Synthesis and Catalytic Evaluation of Novel Mimics of Thiamine Pyrophosphate

KEVIN OGOCHUKWU MADUKA

Synthesis and Catalytic Evaluation of Novel Mimics of Thiamine Pyrophosphate

Kevin Maduka

A thesis submitted in partial fulfilment of the requirements for the degree of

Doctor of Philosophy

Department of Chemistry

Durham University

2020

Declaration

The work described in this thesis was carried out at the Department of Chemistry, Durham University, between October 2015 and November 2019, under the supervision of Dr. AnnMarie O'Donoghue. The material contained has not been previously submitted for a degree at this or any other university. All work has been carried out by the author unless otherwise indicated.

Kevin Maduka

Statement of Copyright

Abstract

The triazolium mimic of thiamine was successfully prepared and isolated using a novel synthetic route, as this compound has not been previously reported in the literature to the best of our knowledge. The route employs inexpensive and commercially available starting material with all reactions carried out in water or ethanol. Thiamine was used to sacrificially to access the intricate 4-aminopyrimidinyl side substituent. In addition to the prime triazolium mimic of thiamine, three other analogues were also prepared starting with different esters and a lactone.

For these, the C3 carbon acid pK_a values of the mimics were determined using a kinetic H/D exchange method. The pseudo first order rate constants k_{ex} (s^{-1}) for exchange were estimated using ^{1}H NMR spectroscopy. Second-order rate constants for deuteroxide ion catalysed exchange (k_{DO}, M^{-1} s^{-1}) were obtained from the slope of the plot of k_{ex} against deuteroxide concentration, which are referred to as kinetic acidities.

Experimental evidence was used to establish the absence of general base catalysis by analysis of H/D exchange in a range of formic acid buffer concentrations at the same buffer ratio. This informed the decision to remove the term for contributions to exchange from buffer catalysis and hence values for k_{DO} may be calculated.

The triazolium based mimics **144, 183-185** show a fifteen-fold increase in acidity towards deuteroxide ion compared to the corresponding native thiamine. This is due to the presence of two extra ring nitrogen atoms which favours the stability of the carbene/ylide. The range of mimics do not show a significant variation in acidity (0.1 unit of pK_a) mostly due to the 5-substituent being relatively far removed from the carbenic carbon atom. Aside from the 5-substituent on the triazolium ring, the mimics were structurally identical otherwise.

Interestingly, the simplest di-methyl triazolium salt **212** studied showed a much lower acidity to the triazolium mimics of thiamine, which suggest the N2-methylpyrimidinyl substituent to

be electron-withdrawing, hence the observed lower pK_a for all the direct triazolium mimics. The N-phenyl triazolium salt previously studied in the group showed similar kinetic acidities compared to the novel mimics which suggest similar effects between the N2-phenyl and the N2CH_2-pyrimidinyl substituent. This is an important observation as it shows the triazolium mimics have closely similar acidity to one of the most widely used and versatile triazolium organocatalysts.

The reactions of the triazolium mimics with a range of typical aldehydes used in NHC-transformations were then explored (Scheme 7.2). Analysis of the ^{1}H NMR spectra obtained from the catalytic evaluation of the triazolium mimics show the presence of the hydroxyaryl adduct in the reaction mixture in all cases. Values of k_1, k_{-1} and K for reactions between novel triazolium mimics **144** and **183** were determined by analysis of changes in species concentration on approach to equilibrium. In addition, using global fitting software, values of forward, reverse and equilibrium constants were estimated from fitting reaction data. The 2-hydroxyethyl triazolium mimic **144** consistently gave larger forward rate constants across the board compared to thiamine **7**. In addition, the 2-subtituent effect previously observed and reported by our group was found to hold true for the new mimics prepared in this work especially with ortho substrate **213**.

In silico binding studies of TPP-dependent enzymes using crystal structures from the protein data bank have been reported using docking software. The results demonstrate the potential for the new diphosphate mimic to hydrogen bond using its N1 atom at the active site of TPP dependent enzymes. Triazolium and thiazolium organocatalysts show different chemoselectivities in a range of transformations and triazoliums demonstrate a broader reaction scope. It is hoped that the diverse chemistry of triazolium organocatalysts can be harnessed at TPP-dependent enzyme active sites.

ABBREVIATIONS

ADP	adenosine diphosphate
AHAS	acetohydroxyacid synthase
AHAS	acetohydroxy acid synthase
Ala	alanine
Arg	arginine
Asn	asparagine
Asp	aspartic acid
ATP	adenosine triphosphate
BAL	benzaldehyde lyase
BFD	benzoyl formate decarboxylase
CHD	cyclohexane-1,2-dione hydrolase
COSY	homonuclear correlation spectroscopy
Cys	cysteine
DCE	dichloroethane
DCM	dichloromethane
DEPT	distortionless enhancement by polarization transfer
DMF	dimethylformamide
DXP	1-deoxy-d-xylulose 5-phosphate
EPR	electron paramagnetic resonance spectroscopy
ESI	electrospray ionization technique
ESR	electron spin resonance spectroscopy
FAD	flavin adenine dinucleotide
FT-IR	fourier transform infrared spectroscopy
GA	generic algorithm
GCMS	gas chromatography coupled mass spectrometry
Gln	glutamine
Glu	glutamic acid
Gly	glycine
GOLD	genetic optimization for ligand docking
His	histidine
HMP	hydroxymethylpyrimidine phosphate
HMP-PP	4-amino-2-methyl-5-hydroxymethylpyrimidine pyrophosphate
HSQC	heteronuclear single quantum correlation experiment
Ile	isoleucine
IS	internal standard
LCMS	liquid chromatography - mass spectrometry
Leu	leucine
Lys	lysine
MC	monte carlo
Met	methionine
NAD	nicotinamide adenine dinucleotide
NEt3	triethylamine
NHC	N-heterocyclic carbene
NMR	nuclear magnetic resonance
NMR	nuclear magnetic resonance
PAC	phenylacetylcarbinol
PDC	pyruvate decarboxylase
Phe	phenylalanine
PLP	pyridoxal-5′-phosphate
Pro	proline
RDS	receptor depth scaling
RMSD	root mean square deviation
Ser	serine
ThDP	*thiamine* diphosphate
Thr	threonine
TK	transketolase
TPP	*thiamine* pyrophosphate
TQD	triple quadrupole mass spectrometer
Trp	tryptophan
TrPP	triazolium pyrophosphate
Tyr	tyrosine
UPLC	ultra-performance liquid chromatography
Val	valine
β-HPA	beta-hydroxypyruvate

Page left intentionally blank

Table of Contents

Chapter One

1 Introduction

1.1 Carbenes

Carbenes are a class of non-charged, reactive species which have a bivalent carbon atom with an electron sextet[1]. This configuration, which is not in good agreement with the octet rule, means the two labile electrons in the valence shell of the carbene can adopt two distinct configurations[2]. Using quantum mechanics, Lennard-Jones and co-workers in 1951 modelled methylene carbene in two different ground states but did not distinguish which one was more stable. Firstly, both may fill up the highest molecular orbital giving rise to a "singlet carbene" or, conversely, each resides in separate, degenerate orbitals to give a "triplet carbene".

A singlet carbene is a very active and transient species, which is expected due to it having a lone pair of electrons in a relatively low energy orbital. Evidence from electron paramagnetic studies (EPR) show both electrons lie in the same sp^2 hybridized orbital, as they are not observable by EPR. Also, X-ray crystal structure show it's in the same plane with the carbon and two other atoms, with an orthogonal p-orbital (Figure 1.1). Both electrons have opposing spins and can be seen to confer a localized negative charge to the central carbon atom. This may be considered an ylide or a zwitterion, with a positive charge in the empty p-orbital and a negative charge in the sp^2 orbital. For methylene, the simplest carbene existing in singlet state, the H−C̈−H bond angle is 103°.

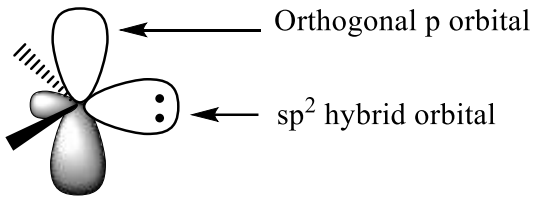

Figure 1.1 Orbital representation of a singlet carbene.

Similarly, triplet carbenes are also sp^2 hybridized but with each electron having same spin, hence do not occupy the same orbital. This is observable by ESR spectroscopy as these electrons are unpaired. Thus, triplet carbenes could be considered to be as 'dual radical'

species: one sp^2 electron in the same plane along with the central carbon atom and two other atoms, while the other electron occupies the orthogonal p-orbital.

However, unlike singlet carbenes, this arrangement is not so rigid, because just one electron in an sp^2 orbital offers less 'push' or steric constraint to other two adjacent sp^2 orbitals, resulting in a larger H−C̈−H bond angle, 136°, for triplet methylene (Figure 1.2). X-ray crystal studies show the bond angle of triplet carbenes varies between 130° – 150°, which strongly suggests a bent configuration.

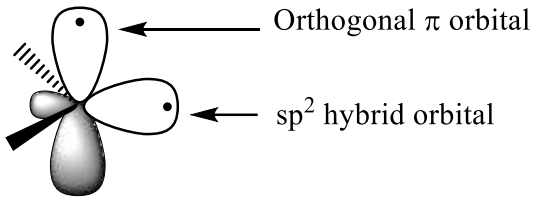

Figure 1.2 Orbital representation of a triplet carbene

1.2 N-Heterocyclic Carbenes (NHCs) - Structures and properties

NHC's are a remarkable class of carbenes which have generated a lot of interest in the last couple of decades. Structurally, they contain a heterocyclic ring with one or more nitrogen atom(s). This opens an array of subclasses within the NHC family each classified based on number of nitrogen atoms and ring size. The nitrogen atom(s) offer a dual stabilisation effect on the carbene carbon atom. Firstly, they are α-electron withdrawing, which inductively reduces the occupation on the sp^2 orbital occupied by the electron lone pair of the carbenium atom. Secondly, they are π-electron donating, which also stabilizes the empty p-orbital of the carbenium atom.

As discussed in the previous section, NHC's are derived from the nitrogen-containing heterocycles, and their naming follows a similar pattern, with the terminal –e, replaced by –ylidene in most cases. Several of these classes have been synthesized, some of which are the thiazol-2-ylidenes **1** , triazol-2-ylidenes **2**, imidazol-2-ylidenes **3** and imidazolin-2-ylidenes **4**

(Figure 1.3). Overall, the dominating feature that influences the stability of these carbenes are the ring heteroatoms.

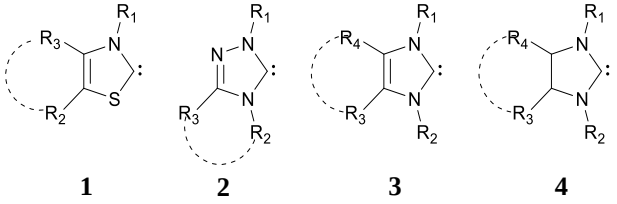

Figure 1.3 General types of N-heterocyclic carbenes (NHCs)

1.3 NHC's as organocatalysts

N-Heterocyclic carbenes have seen use as catalysts in several organic reactions requiring C-C bond formation[3]. The benzoin condensation, involving formal dimerization of benzaldehyde **5** to give 2-hydroxy-1,2-di(phenyl)ethenone **6**, was first reported by Wohler and Liebig in 1832 and catalysed by cyanide ion[4]. Later, Ugai[5] demonstrated it could also be catalysed by a thiamine **7** (Scheme 1.1)**,** and a range of other thiazolium-derived salts.

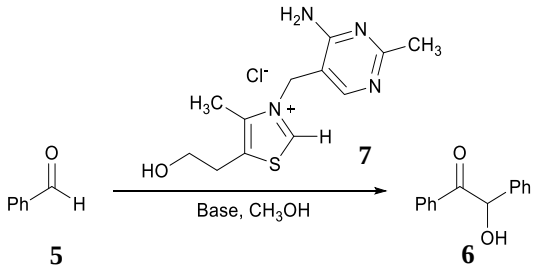

Scheme 1.1 Thiamine catalysed benzoin condensation reaction

This discovery was further expanded upon by Mizuhara and Handler[6] to show that thiamine could also catalyse formation of acetoin **8** and acetate **9** from acetaldehyde **10** and diacetyl **11**, known to occur in living cells, and even went on further to verify previous results that the thiazolium moiety was the active site for catalysis using a thiamine scaffold (Scheme 1.2).

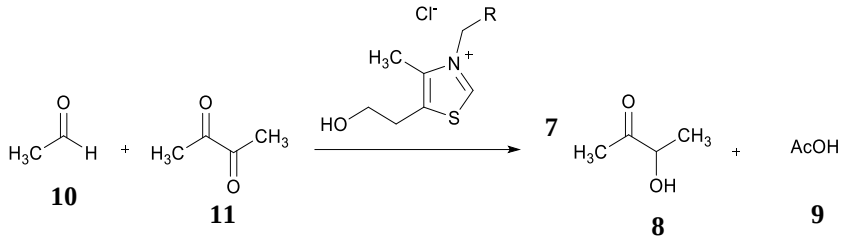

Scheme 1.2 Thiamine catalysed acetoin formation from acetaldehyde and diacetyl

This reaction is said to proceed by a nucleophilic acyl anion (umpolung) intermediate, as postulated by Breslow[7], demonstrated using deuterium oxide to show mobility (or acidity) of the C(2) proton on a number of thiamine salts **12** (Scheme 1.3). Hence under basic conditions, the acidic proton can be lost, leading to a similar mechanism as the classic cyanide catalysed reaction (Scheme 1.4). At this time, the active form of the catalyst was typically drawn in ylidic form, however, it was later recognised that the carbene resonance structure was important.

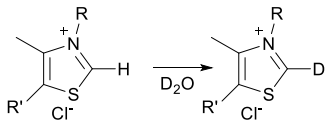

Scheme 1.3 H/D exchange reaction of thiamine salts 12 in D_2O

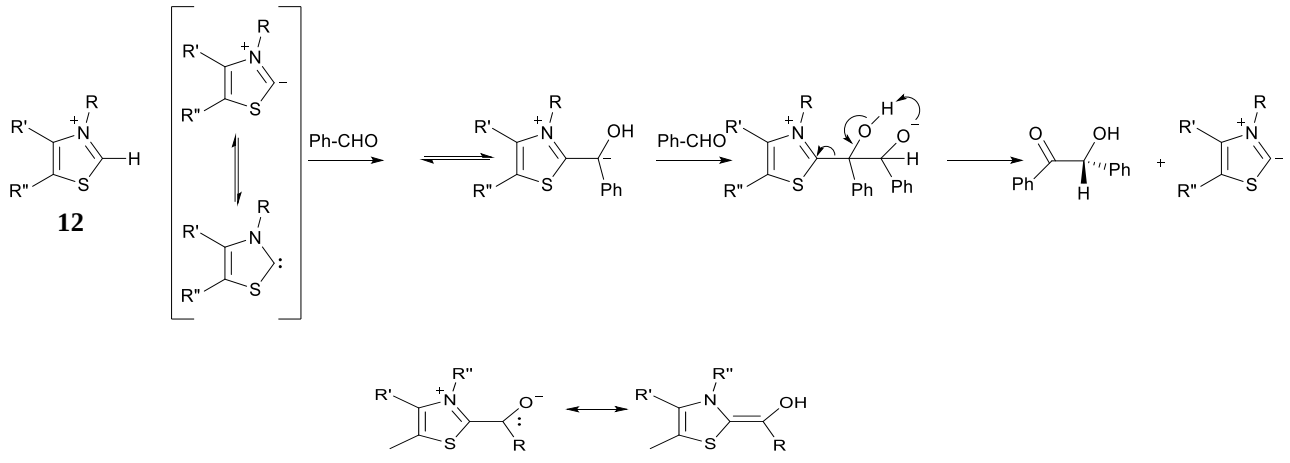

Scheme 1.4 Mechanism for thiamine catalysed benzoin condensation proposed by Breslow [7]

Thereafter, interest in carbene catalysis increased, since NHC's are inexpensive and biodegradable in comparison to transition metals, thereby affording low-cost and eco-friendly alternatives to traditional catalysts.

Along the same lines, Sheehan [8], reported the first homogenous asymmetric benzoin condensation using a chiral thiazolium salt, (*S*)-4-methyl-3-(1-naphthyl)-ethylthiazolium bromide **13** with a 22 % ee of benzoin **6**. This result was subsequently improved upon by the same group, albeit only marginally, using a similar precatalyst **14** (Scheme 1.5).

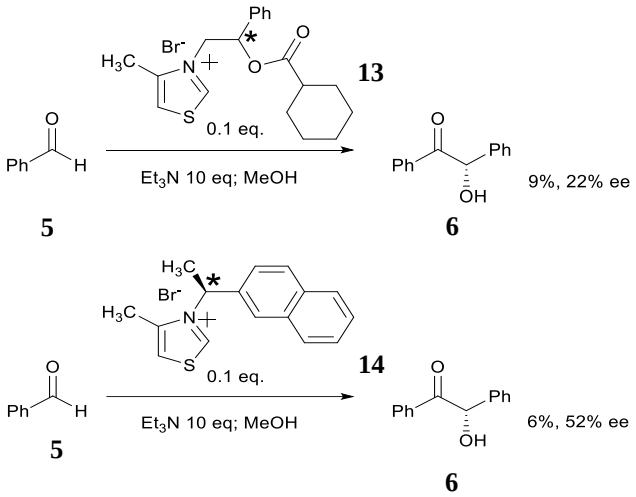

Scheme 1.5 First asymmetric benzoin condensation

After this moderately successful use of chiral thiazolium salts to control stereoselectivity in the benzoin condensation, several groups reported progressively increased yields (Table 1.1), using diverse variations of chiral thiazolium salts **15–18**. This finally culminated in the work of Leeper et al.[9], achieving 80 % ee, using bicyclic triazolium salt **19** as precatalyst.

Table 1.1 Stereoselectivity timeline of the NHC catalysed benzoin condensation reaction

Year	Catalyst	Yield %	ee %
1980 Takagi [10]	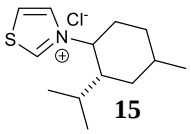 **15**	20	35
1993 Lopez [11]	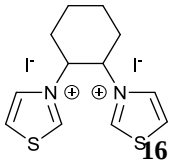 **16**	21	26
1996 Enders [12]	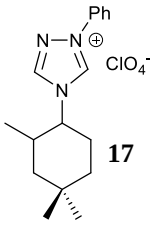 **17**	66	75
1997 Leeper [13]	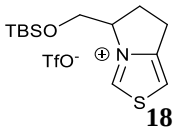 **18**	50	21
1998 Leeper [14]	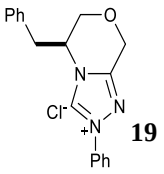 **19**	45	80

Overall, bicyclic triazoliums salts offer better control over enantioselectivity as catalysts in the benzoin condensation, as seen from Table 1.1. Enders et al[15] further modified the bicyclic triazolium ring with a *tert*-butyl group, precatalyst **20**, resulting in much improved enantioselectivity (Scheme 1.6).

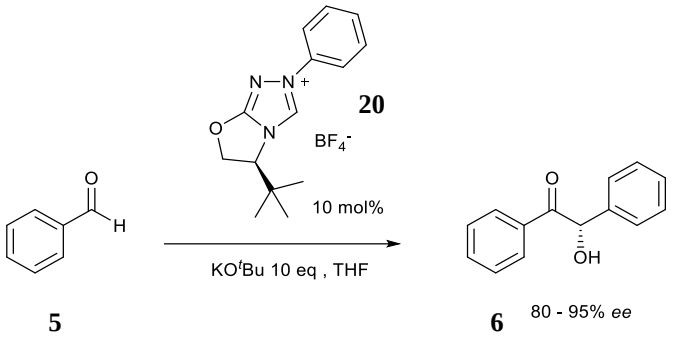

Scheme 1.6 Asymmetric variant of benzoin condensation, catalysed by chiral triazolium ion 20

The *tert*-butyl group on the bicyclic ring of precatalyst **20** creates steric hindrance thus blocking one face of the Breslow intermediate **21** effectively allowing for higher enantioselectivity. (Scheme 1.7) Enantiomers are mirror images (in pairs) while diastereomers are non-mirror images.

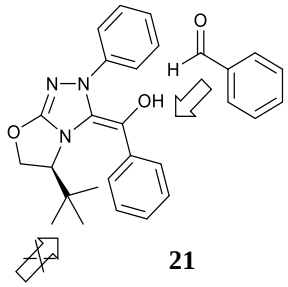

Scheme 1.7 Postulated transition state model 21 to explain the facial selectivity in the asymmetric benzoin condensation in the presence of precatalyst 20

With further introduction of bulky substituents on bicyclic thiazolium salts, Connon et al.[16], using a similar triazolium salt **22** with N-pentafluorophenyl and diphenylhydroxy methyl replacing phenyl and *tert*-butyl groups respectively, showed excellent enantioselectivity (Scheme 1.8). The pentafluorophenyl substituent enhances acidity and the hydroxide group is hydrogen bond donating: these factors combine to give a highly active and efficient catalyst.

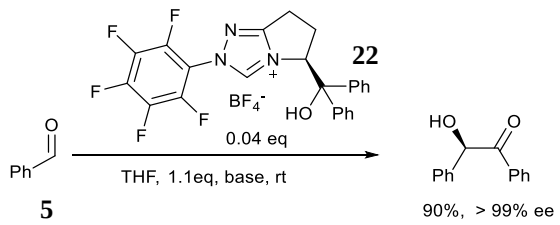

Scheme 1.8 Highly enantioselective benzoin condensation involving a bifunctional protic precatalyst 21

In addition to the benzoin condensation (1,2- addition), NHCs have also been used to catalyse Stetter reactions (1,4-addition) which also proceeds *via* the Breslow intermediate and was first reported by Stetter et al.[17] in 1974. However, unlike the benzoin condensation reaction, the final step to product formation in the Stetter reaction is not usually reversible (Scheme 1.9)

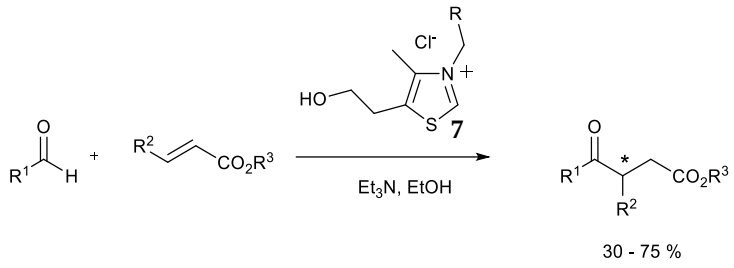

Scheme 1.9 Thiazolium ion catalysed intermolecular Stetter reaction

The Stetter reaction gives product with a stereogenic centre **23**, as expected of a prochiral substrate **24**, leading to a racemic mixture of both isomers. Enders et al.[12] reported the first application of NHC's in an asymmetric Stetter reaction using a triazolium precatalyst **25** (Scheme 1.10).

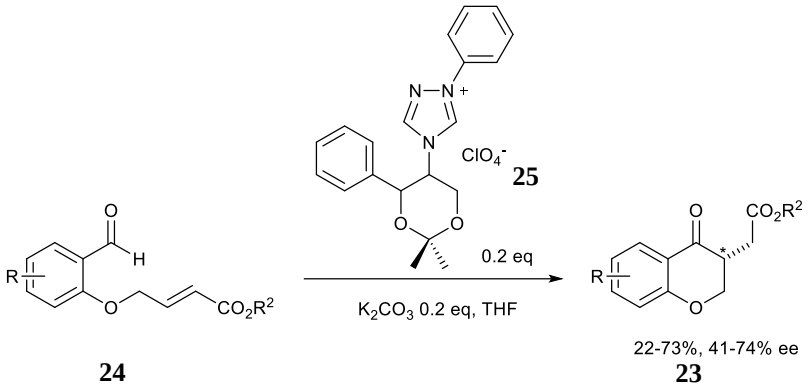

Scheme 1.10 First asymmetric Stetter reaction catalysed by NHC precatalyst 25

Following up on the work of Enders, Rovis et al.[18] reported a highly enantioselective intramolecular Stetter reaction with up to 95% ee for compound **26** (Scheme 1.11). This was achieved using an aminoindanol-derived precatalyst **27** giving optimal yields and enantioselectivities using salicylaldehyde derived starting material **28**.

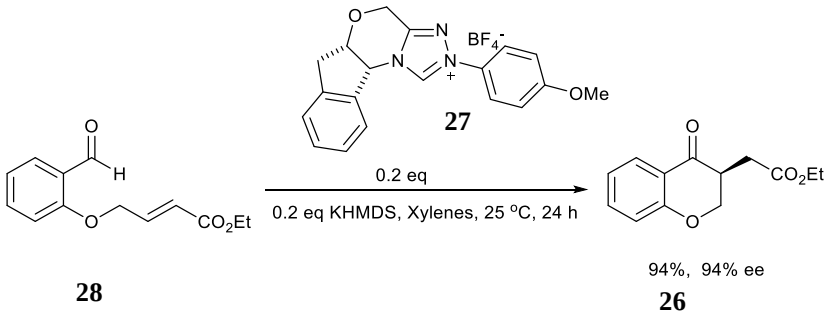

Scheme 1.11 Highly enantioselective Stetter reaction using NHC precatalyst 27

The group extended intramolecular Stetter reactions[19], using phenyl-alanine derived NHC precatalyst **29** in reaction of glyoxamides **30** and alkylidenemalonates **31** (Scheme 1.12). Using catalyst **29** also gave excellent yields reacting glyoxyamides with alkylidene ketoamides **32** (Scheme 1.13)**.**

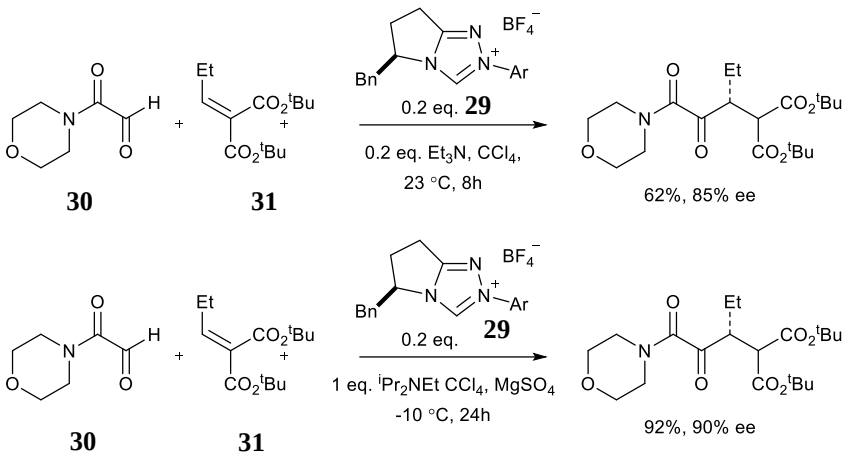

Scheme 1.12 Reactions of glyoxamides 30 with alkylidenmalonates 31

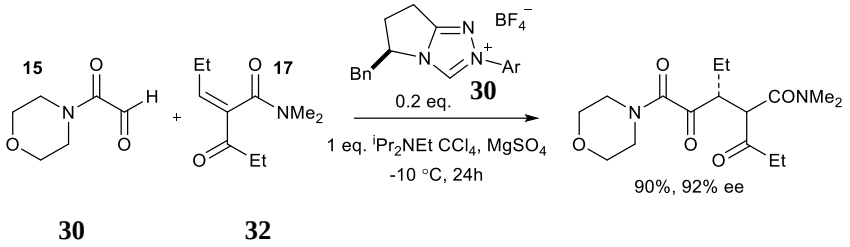

Scheme 1.13 Reaction of glyoxamides 30 with alkylidene ketoamides 32

More recently, NHC organocatalysis has been extended to hydroacylation of enol ethers **33**. The group of She[20] in 2008, reported the intramolecular hydroacylation to benzofuranones **34** in excellent yields using a thiazolium salt precatalyst **35**. This hydroacylation leads to a new chiral centre in the benzofuranone product, however no stereoselectivity was reported (Scheme 1.14).

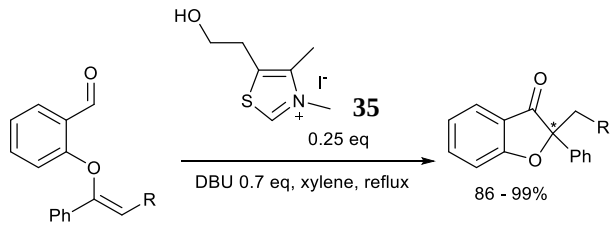

Scheme 1.14 Intramolecular hydroacylation of enol ethers 33

As usual with reactions of this type, proceeding *via* a prochiral intermediate, a chiral centre is introduced, and a racemic product formed. However, using a bicyclic triazolium ring precatalyst **36**, which has been shown previously to give good enantioselectivity, Glorius et al.[21] in 2011, reported a similar reaction, the intramolecular acylation of unactivated alkenes **37** with excellent enantioselectivities **38** This was achieved using NHC generated from L-phenyl alaninol derived triazolium salt (Scheme 1.15).

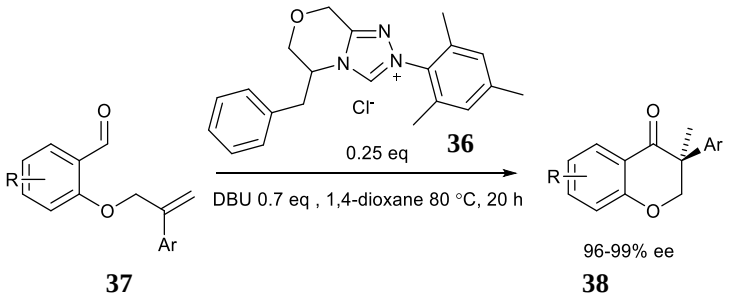

Scheme 1.15 Intramolecular acylation using bicyclic triazolium precatalyst 36

NHCs are indeed a versatile class compounds for effecting organocatalysis, and in addition to mechanisms proceeding *via* an acyloin intermediates (benzoin condensations and Stetter reactions) as discussed in previous literature examples, catalysis has also been reported to advance *via* a zwitterionic homoenolate-type intermediate **39 (**Scheme 1.16 (b)). Synthesis

of γ-butyrolactones **40** *via* an NHC stabilized homoenolate intermediate **39**, is reported by Glorius[22] by reacting several α,β-enal **41** with aldehydes **42** using 1,3-dimesitylimidazolium chloride precatalyst **43** (Scheme 1.16).

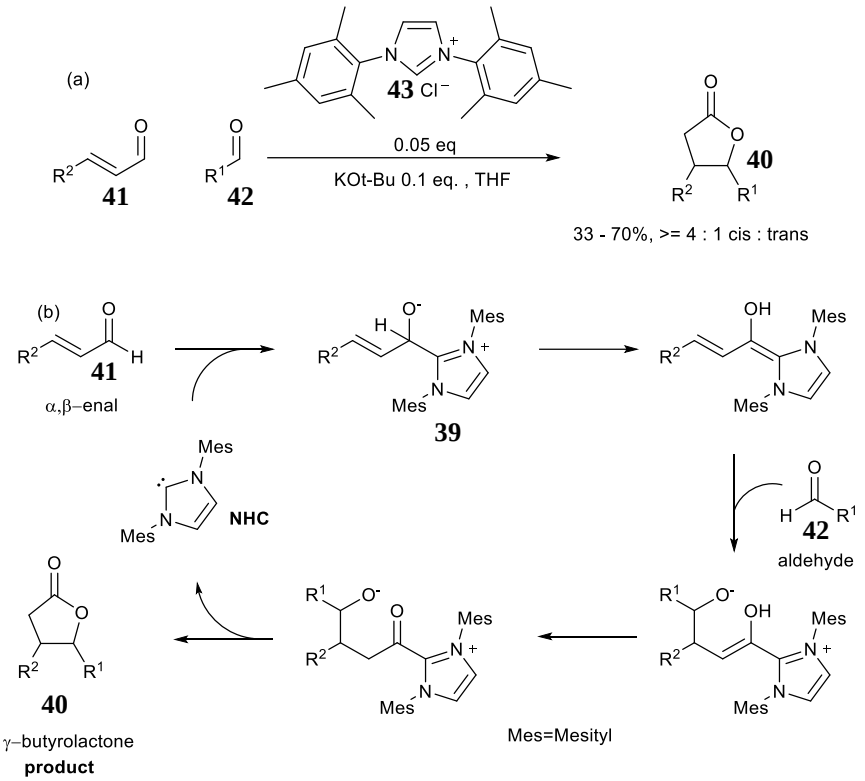

Scheme 1.16 (a) General route and (b) plausible mechanism of NHC-catalysed γ-butyrolactone 40 formation

A similar pathway was proposed by Bode et al. for the formation of substituted γ-butyrolactone **44** via direct annulation of enals **45** and aldehydes **46** [23] using the same 1,3-dimesitylimidazoliumchloride precatalyst **43** (Scheme 1.17).

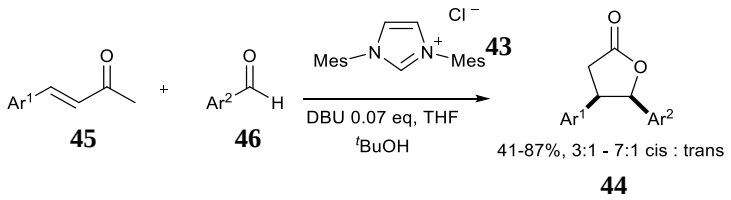

Scheme 1.17 Enal-aldehyde annulations to give substituted lactones 44

Subsequently, using an aminoindanol-derived triazolium precatalyst **47** an array of other transformations was achieved: azadiene **48** Diels-Alder[24] (Scheme 1.18), cyclopentene **49** forming annulations of 4-oxoenoates **50** [25] (Scheme 1.19), bicyclic-β-lactam **51** formation from enals **52** and unsaturated N-sulfonyl ketimines **53** [26] (Scheme 1.20), enantioselective cyclopentane-fused lactone **54** synthesis [27] (Scheme 1.21), and most recently, generation of ester enolate equivalents from α,β-unsaturated aldehydes **55** to give highly enantioselective hetero-Diels-Alder reactions [28] (Scheme 1.22).

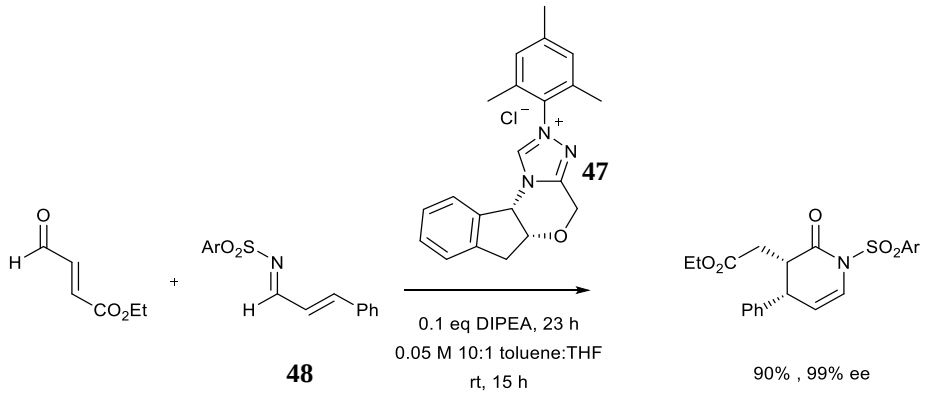

Scheme 1.18 Azadiene-Diels Alder type reaction

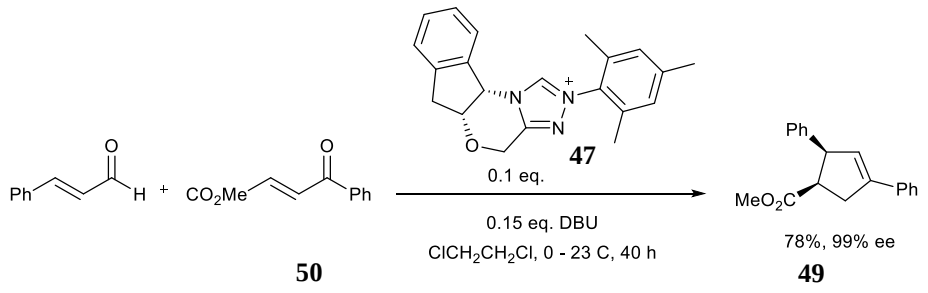

Scheme 1.19 Substituted cyclopentene 49 forming annulations of 4-oxoenoates 50

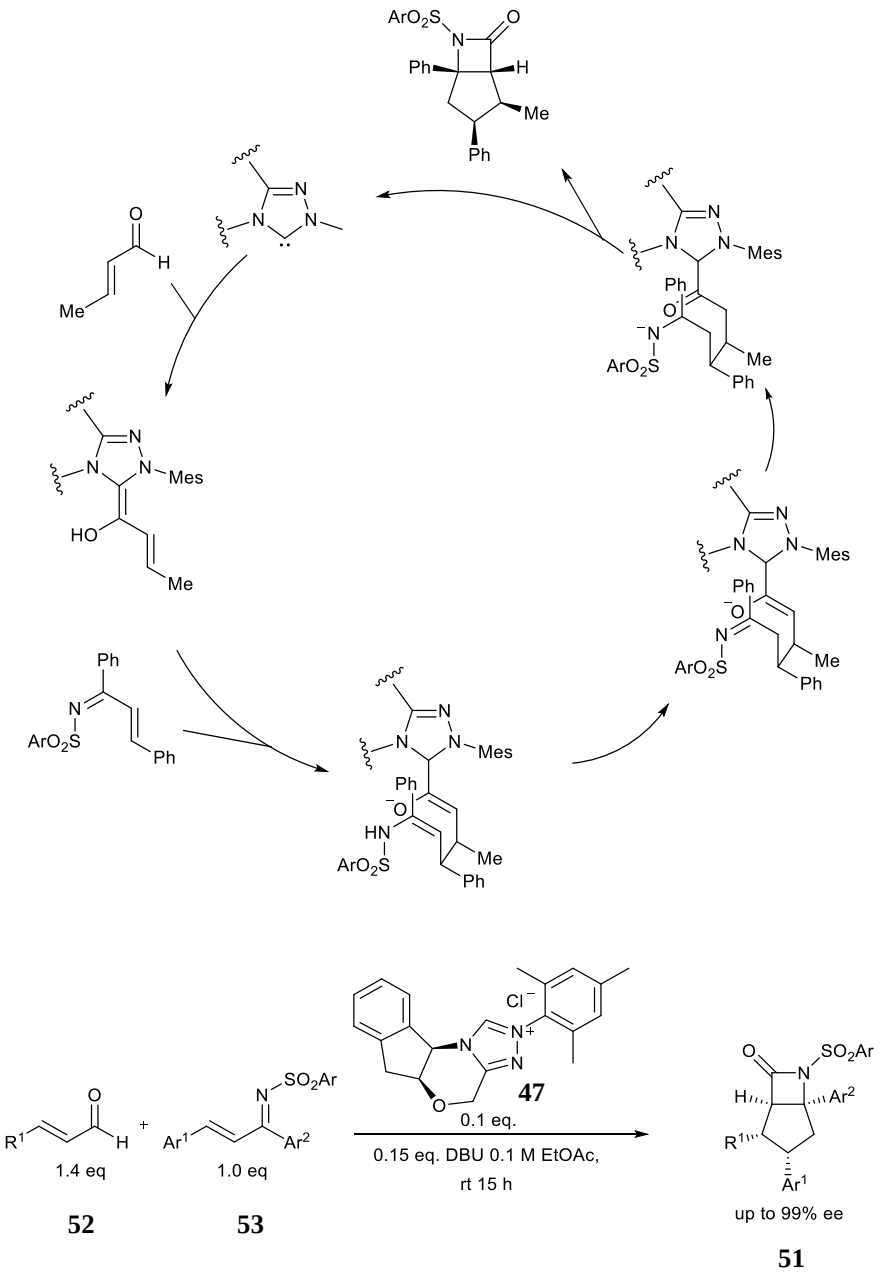

Scheme 1.20 Bicyclic-β-lactam 51 synthesis from enals 52 and unsaturated N-sulfonyl ketimines 53

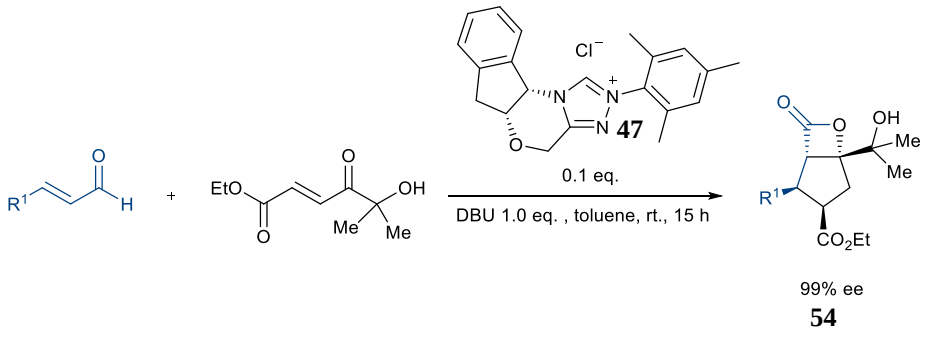

Scheme 1.21 Synthesis of cyclopentane-fused lactone 54

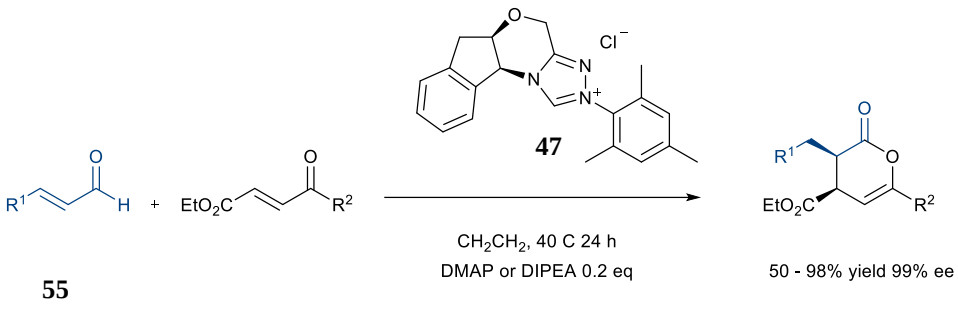

55

Scheme 1.22 Generation of ester-enolate equivalent from α,β-unsaturated aldehydes

The potential of NHCs in catalysis for generating homoenolate stabilized intermediates leading to coupling reactions was further investigated by Chi et al.[29], using benzodienones **56** and enals **57** to effect a highly regio- and stereoselective cascade annulation. This reaction, achieved using the same aminoindanol derived triazolium catalyst **47**, furnishes three successive reactive carbon centres, affording the convenience of quickly making fairly complex phenanthrene type motifs **58** (Scheme 1.23).

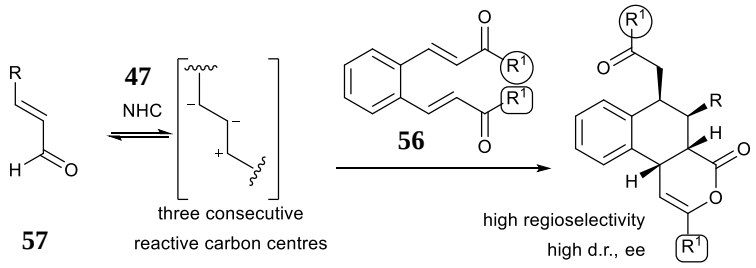

57 **58**

Scheme 1.23 Highly regioselective annulations of unsymmetrical benzodienones 56 with enals 57

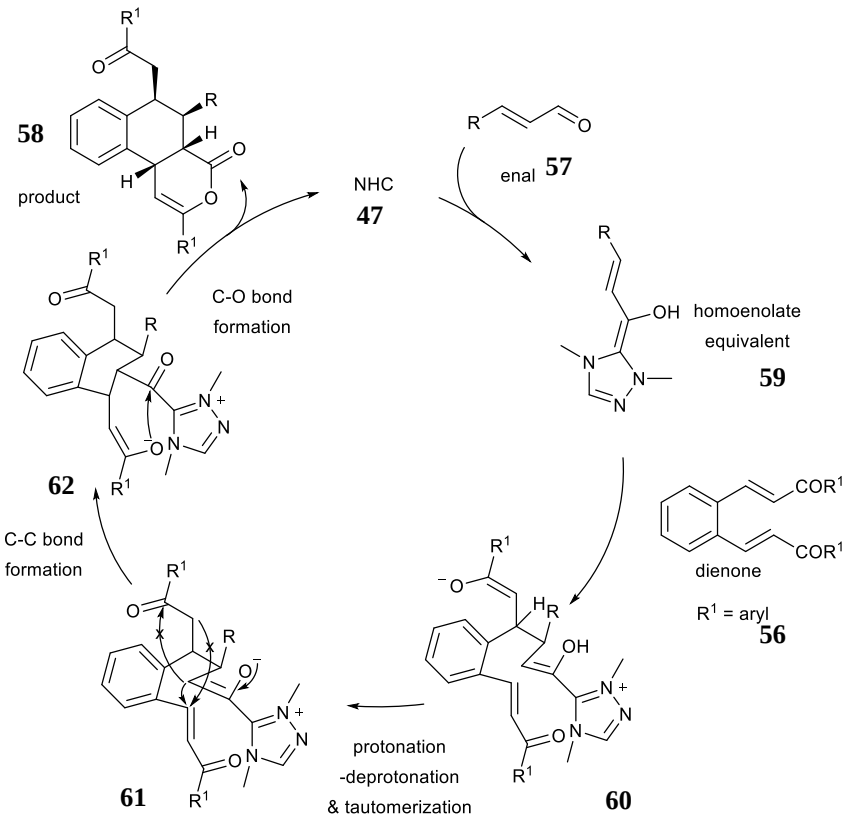

Scheme 1.24 Postulated catalytic cycle for lactone 58 formation

All of the three reactive carbon centres of the enals **57** are involved in new C−C and C−O bond formations to generate the cascade products **58** containing four stereogenic centres. Mechanistically, the reaction proceeds exclusively through Michael-type additions of the *β*- and *α*-carbon atoms of enal **57** to the two enone branches of the dienone **56,** and subsequent intramolecular enol ester formation to yield the products.

Scheme 1.24 shows the postulated reaction pathway beginning with formation of intermediate **59** as a homoenolate equivalent[30]. This is followed by a Michael-type addition to one branch of dienone to give intermediate **60**. Protonation at carbon, deprotonation at oxygen and tautomerization of **60** gives intermediate **61**, which exclusively undergoes intramolecular 1,4-addition of the enal *α*-carbon atom to the other branch of the dienone to afford intermediate **62**.

The final step of the catalytic cycle is the formation of an enol ester to generate the cascade product **58**.

1.4 Synthetic potential of NHCs in chemomimetic biocatalysis

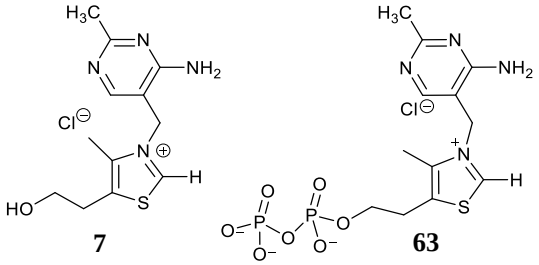

Figure 1.4 The structures of thiamine 7 and thiamine pyrophosphate 63

The recent organocatalytic work largely derives from thiamine pyrophosphate-based precursors. Early interest in this area stemmed from a desire for a mechanistic understanding of the role of thiamine **7** as a cofactor in biology. A number of biological reactions that utilize thiamine pyrophosphate (TPP) **63** are shown as follows (Scheme 1.25).

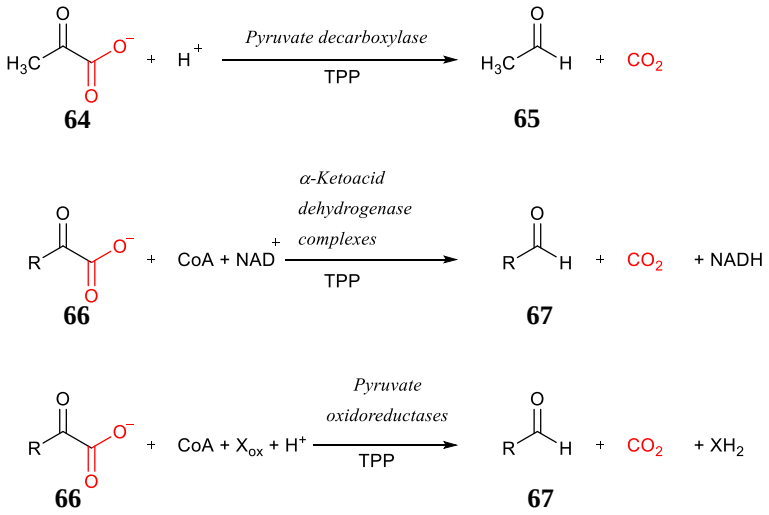

Scheme 1.25 Typical reactions of thiamine pyrophosphate (TPP)-dependent enzymes

As shown in Scheme 1.25 PDC catalyses the conversion of pyruvate **64** into acetaldehyde **65**, α-ketoacid dehydrogenase converts branched chain alpha keto acids **66** into

aldehydes **67**. All of these are implicated to involve an initial deprotonation to give the active thiazolyl carbene followed by onwards reactions by a mechanism very similar to those outlined in previous section. There has been limited research focused on utilizing this enzyme catalysis for synthetic purposes. One of such applications is the use of acetohydroxy acid synthase (AHAS) in the synthesis of (*R*)-phenylacetylcarbinol (PAC) **68**, which is then converted by treatment with inorganic reagents to give the end product ephedrine **69** (Scheme 1.26).

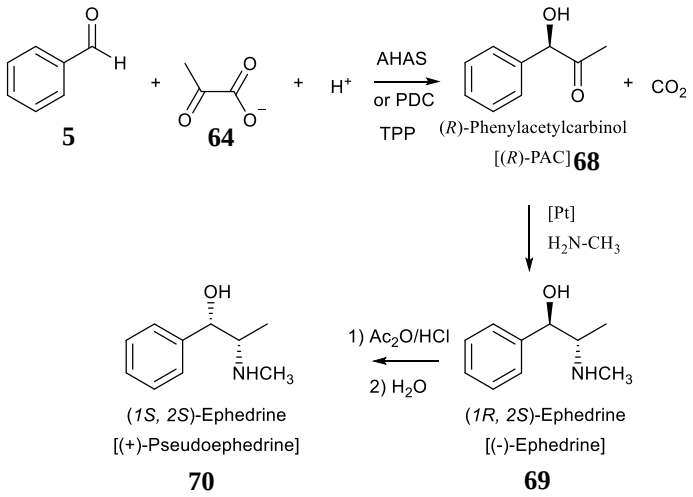

Scheme 1.26 Production of ephedrine 69 and pseudoephedrine 70 from (*R*)-PAC

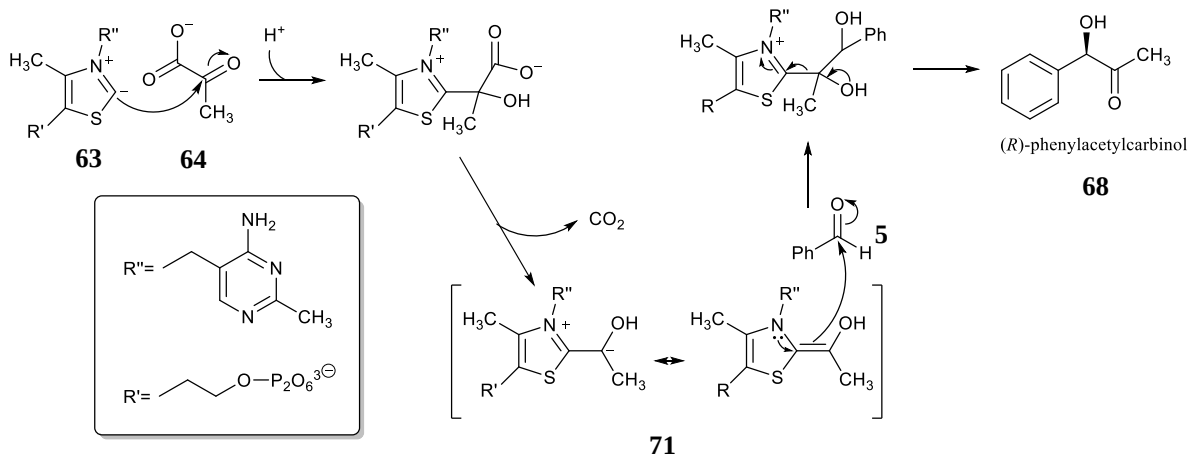

Scheme 1.27 General reaction mechanism for AHAS and PDC mediated (*R*)-PAC 68 synthesis

The first step in the mechanistic sequence is the generation of the carbenic C_2H of the thiazolium in TPP **63** at the AHAS active site, followed by nucleophilic addition to the pyruvate substrate **64** (Scheme 1.27) The N3 of the thiazolium ring then acts as an electron sink, which facilitates the C−C bond cleavage of the substrate leading to loss of carbon dioxide. Further reaction of intermediate **71** with benzaldehyde **5** affords the product (*R*)-PAC **68** in high enantioselectivity.

In general, it was observed that *meta*- and *para*-substituted aromatic aldehydes give better conversion for the formation of α-hydroxy ketones than *ortho*-substituted isomers with AHAS[31].

Synthesis of (*S*)-2-hydroxypropiophenone [(*S*)-2-HPP] **72** (Scheme 1.28) has also been achieved using benzoylformate decarboxylase (BFD), which primarily catalyses the non-oxidative C-C bond breaking of benzoyl formate to benzaldehyde[32]. Chemomimetic use of this enzyme for carboligase activity was first reported by Wilcocks and co-workers[33] and with

subsequently improved enantioselectivities using BFD derived from different bacteria; *P. putida* sourced BFD gave 91 to 92% ee while crude extracts from *A. calcoaceticus* gave conversions to practically enantiomerically pure form with > 98% ee of (*S*)-2-HPP.

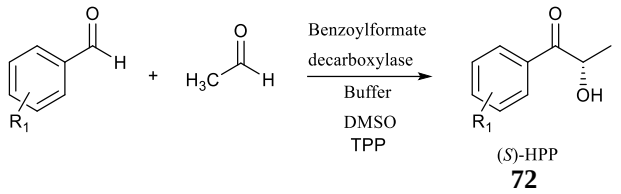

Scheme 1.28 Benzoylformate decarboxylase mediated asymmetric C-C bond formation reaction

Meta-substituted aromatic aldehydes were found to give better enantioselectivities than corresponding *ortho*-substituted analogues,[34] which highlighted the importance of bulk and inductive characteristics of the substituents in amplifying catalytic activity and *ee*.

Pyruvate decarboxylase (PDC) is easily the most studied in the class of TPP-dependent enzymes, owing to its key role in the fermentation of ethanol and in the conversion of glucose to pyruvate. First reported by Neuberg and co-workers in 1921, as the active component in yeast[35], PDC has been widely applied in various biocatalytic syntheses involving carboligation reactions[36 37]. In the synthesis of (*S*)-phenylacetylcarbinol **74**, decarboxylation of pyruvic acid **73**, then further C-C bond formation with benzaldehyde **5** gives the product (**Scheme 1.29**).

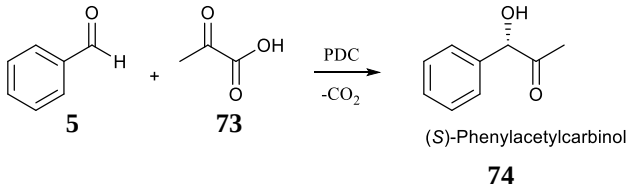

Scheme 1.29 Synthesis of (*S*)-PAC

1.5 Metal Carbenes

Bench stable metal carbenes were first discovered in 1964 by Fisher,[38] based on chromium, molybdenum and tungsten, and still generate interest till date due to their use in alkene (olefin) metathesis. Carbene complexes formed by group 6 metals are broadly grouped by ligand type as either electrophilic or nucleophilic. Electrophilic carbenes or *Fisher carbenes* are commonly found with low oxidation state metals paired with ligands such as CO. Conversely, nucleophilic carbenes or *Schrock carbenes* are normally observed with metals in their highest oxidation state. The ligands are typically described with reference to the spin states of their hypothetical free carbenes. Although Schrock carbenes are treated as triplet species having lone electrons in orbitals usable for metal-directed σ- and π-bonding, in contrast, Fisher carbenes are regarded as singlets with low-lying π* orbitals and a carbon-centred LUMO (Figure 1.5). Subsequently, bonding for a Schrock (alkylidene) type carbene ligand is comparable to a classic double bond. The metal-carbon π-bond represents the HOMO, which, by virtue of the higher electro-positivity of the metal relative to carbon, births nucleophilic character. Theoretical studies for the most part, have shown significant disparity in bonding between Fisher and Schrock carbenes of Group 6 metals,[39] in particular when contrasted to their carbyne analogues.[40]

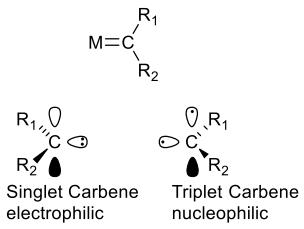

Figure 1.5 Types of metal carbene bond

The first reported alkylidene (nucleophilic) complex **75** was synthesized by Schrock using $[Ta(CH_2{}^tBu]_3Cl_2]$ compound[41] with neopentyl lithium (Scheme 1.30). [42] The mixture generates $[Ta(CH_2{}^tBu)_5]$ a reactive intermediate which readily gives neopentane and alkylidene via α-hydrogen abstraction. [43] By showing that chemically reversible deprotonation may occur at the carbene carbon

atom, Schrock also recorded the first carbyne complex. Currently, this procedure remains commonplace for generating nucleophilic carbenes using a range of transition metals.

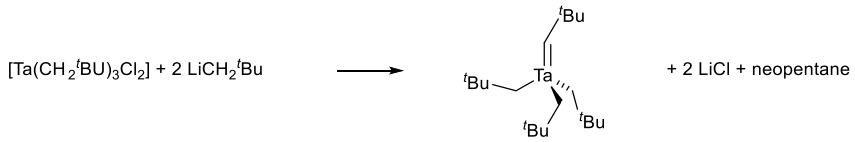

75

Scheme 1.30 Synthesis of the first Schrock metal carbene

The need to make catalysts for olefin metathesis, generated early interest to develop versatile nucleophilic carbene complexes. Several other metals were explored aside from tantalum, culminating with Schrock reporting the first alkylidene compound of tungsten. [44] These Tungsten type Schrock carbenes were obtained by treating phosphines with the trialkylalkylidyne compound, $[W(\equiv C^tBu)(CH_2{}^tBu)_3]$ but were dormant for the metathesis of alkenes. Following this, several other tungsten based alkylidenes were prepared incorporating extra ligands. In particular, tungsten alkylidene **76** having the oxo-ligand which is actively π-donating [45] was prepared using a tantalum complex **77** (Scheme 3). [46] Compound **76** was activated to give the catalytically active specie using aluminium trichloride.

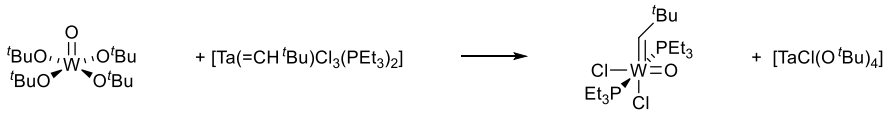

77 **76**

Scheme 1.31 Preparation of tungsten complex 76

Although the oxo ligand proved favourable for catalytic activity in the olefin metathesis, [47] its minuteness promotes coordinative clustering around the metal, hindering reactivity. To prevent this, Schrock replaced the oxo ligand with an imido ligand (NR^{2-}), which eliminated the need to employ aluminium trichloride as activator. [48] However, first generation tungsten complexes showed slow reactivity and narrow functional group tolerance, this lead to their molybdenum analogues being explored for quicker and broader catalytic activity. [49] Early days preparation

of these molybdenum alkylidenes **78** employed triethylamine in catalytic amounts to effect nitrogen to carbon proton transfer within an alkylidyne compound **79** (Scheme 4). Synthesis of compound **78** marked a breakthrough point in the history of carbene chemistry, providing the foundations for three decades of active groundwork into advancing olefin metathesis catalysis.

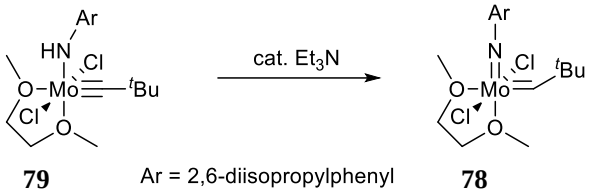

Scheme 1.32 Preparation of molybdenum complex

1.6 Project Aims

The use of enzymes in catalysis offers potential control over the stereochemistry of product obtained. This parallels their role in biosynthesis, where precise control over stereoselectivity is paramount and invariably a key factor in molecular functionality. Exploiting this property of enzymes opens new possibilities to access a wide range of scaffolds with excellent enantioselectivities.

To date TPP has been employed in biocatalysis for a relatively limited range of enzymatic transformations and only native thiazolium co-factors have been explored. By contrast, in organocatalysis there are much broader applications of TPP mimics. More recently, triazolium salts have proven to be more efficient and versatile as promoters for a wider spectrum of organocatalytic transformations[50]. Our aim, therefore, is to harness recent developments in organocatalysis in a biocatalytic context. Central to this proposition is replacing the natural thiazolium of TPP with a triazolium unit.

Figure 1.6 Proposed replacement of TPP thiazolium unit with a triazolium core

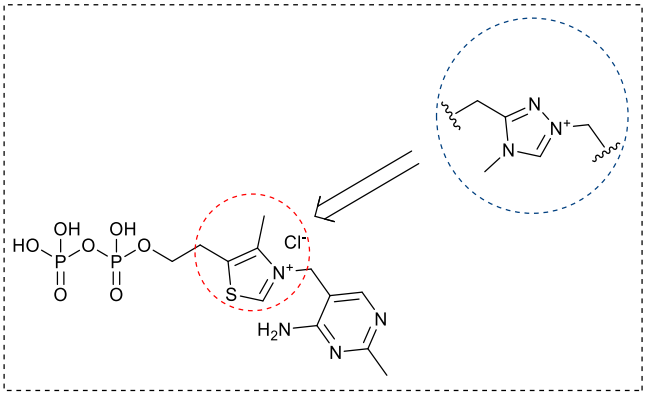

Firstly, we aim to synthesize a small molecule triazolium mimics of thiamine for initial scoping experimentation. This includes the synthesis of a direct like-for-like triazolium mimic of TPP. In addition to this, measurement of the kinetic acidities and pK_a's at the C_3H position of the prepared mimics will be evaluated, given that deprotonation is prerequisite to give the active carbene species. Furthermore, since the benzoin and Stetter reactions are often employed as benchmarks for organic catalysts, evaluation of the new mimics by measuring rate and equilibrium constants for formation of the first key intermediate, the hydroxyaryl adduct, using a range of substituted benzaldehyde derivatives will be attempted.

Prior to employing novel triazolium mimic at the active site of TPP dependent enzymes, in silico screening of the mimics using enzyme docking software is proposed to model active site interactions with protein residues versus the native TPP-cofactor. This would inform on the choice of enzyme(s) to use initially for in vitro assays and ultimately test for biocatalytic activity with a variety of aldehydic substrates and acceptors in the presence and absence of enzymes. Our particular longer-term goal is to harness the different product selectivities and broader reaction scope possible with triazolium organocatalysts versus thiazolium analogues at the active sites of TPP-dependent enzymes.

1.7 References

1. W. Schmid, *Justus Liebigs Annalen der Chemie*, 1855, **93**, 83-88.
2. J. Lennard–Jones and J. Pople, *Discussions of the Faraday Society*, 1951, **10**, 9-18.
3. D. Enders, O. Niemeier and A. Henseler, *Chem. Rev.*, 2007, **107**, 5606-5655.
4. Wöhler and Liebig, *Annalen der Pharmacie*, 1832, **3**, 249-282.
5. R. T. T. Ukai, T. A. Dokawa, *J. Pharm. Soc. Jpn.*, 1943, **63**, 296-300.
6. S. Mizuhara and P. Handler, *J. Am. Chem. Soc.*, 1954, **269**, 1951-1953.
7. R. Breslow, *J. Am. Chem. Soc.*, 1958, **80**, 3719-3726.
8. J. C. Sheehan and D. H. Hunneman, *J. Am. Chem. Soc.*, 1966, **88**, 3666-3667.
9. R. L. Knight, *Tetrahedron Lett.*, 1998, **38**, 3611-3614.
10. W. Tagaki, Y. Tamura and Y. Yano, *Bull. Chem. Soc. Jpn.*, 1980, **53**, 478-480.
11. J. Martí, *Tetrahedron Lett.*, 1993, **34**, 521-524.
12. D. Enders, K. Breuer and J. H. Teles, *Helv. Chim. Acta*, 1996, **79**, 1217-1221.
13. R. L. Knight and F. J. Leeper, *Tetrahedron Lett.*, 1997, **38**, 3611-3614.
14. R. L. Knight and F. J. Leeper, *J. Chem. Soc., Perkin Trans. 1*, 1998, DOI: 10.1039/a803635g, 1891-1894.
15. D. Enders and U. Kallfass, *Angew. Chem. Int. Ed.*, 2002, **41**, 1743-1745.
16. L. Baragwanath, C. A. Rose, K. Zeitler and S. J. Connon, *J. Org. Chem.*, 2009, **74**, 9214-9217.
17. H. Stetter and H. Kuhlmann, *Angew. Chem. Int. Ed. Engl.*, 1974, **13**, 539-539.
18. M. S. Kerr, J. R. D. Alaniz and T. Rovis, *J. Am. Chem. Soc.*, 2002, **124**, 10298-10299.
19. Q. Liu, S. Perreault and T. Rovis, *J. Am. Chem. Soc.*, 2008, **130**, 14066-14067.
20. J. He, S. Tang, J. Liu, Y. Su, X. Pan and X. She, *Tetrahedron*, 2008, **64**, 8797-8800.
21. I. Piel, M. Steinmetz, K. Hirano, R. Frohlich, S. Grimme and F. Glorius, *Angew. Chem. Int. Ed.*, 2011, **50**, 4983-4987.
22. C. Burstein and F. Gloriuns, *Angew. Chem.*, 2004, **116**, 6331-6334.
23. S. S. Sohn, E. L. Rosen and J. W. Bode, *J. Am. Chem. Soc.*, 2004, **126**, 14370-14371.
24. M. He, J. R. Struble and J. W. Bode, *J. Am. Chem. Soc.*, 2006, **128**, 8418-8420.
25. P. C. Chiang, J. Kaeobamrung and J. W. Bode, *J. Am. Chem. Soc.*, 2007, **129**, 3520-3521.
26. M. He and J. W. Bode, *J. Am. Chem. Soc.*, 2008, **130**, 418-419.
27. J. Kaeobamrung and J. W. Bode, *Org. Lett.*, 2009, **11**, 677-680.
28. J. Kaeobamrung, M. C. Kozlowski and J. W. Bode, *Proc. Natl. Acad. Sci. U.S.A.*, 2010, **107**, 20661-20665.
29. X. Fang, K. Jiang, C. Xing, L. Hao and Y. R. Chi, *Angew. Chem. Int. Ed.*, 2011, **50**, 1910-1913.

30. E. M. Phillips, T. E. Reynolds and K. A. Scheidt, *J. Am. Chem. Soc.*, 2008, **130**, 2416-2417.

31. S. Engel, M. Vyazmensky, D. Berkovich, Z. Barak and D. M. Chipman, *Biotechnol. Bioeng.*, 2004, **88**, 825-831.

32. E. Prosen and O. P. Ward, *J. Ind. Microbiol.*, 1994, **13**, 287-291.

33. R. Wilcocks, O. P. Ward, S. Collins, N. J. Dewdney, Y. Hong and E. Prosen, *Appl. Environ. Microbiol.*, 1992, **58**, 1699-1704.

34. P. Domínguez de María, M. Pohl, D. Gocke, H. Gröger, H. Trauthwein, T. Stillger, L. Walter and M. Müller, *Eur. J. Org. Chem.*, 2007, **2007**, 2940-2944.

35. J. A. Barnett, *Yeast*, 2003, **20**, 509-543.

36. O. P. Ward and A. Singh, *Curr. Opin. Biotechnol.*, 2000, **11**, 520-526.

37. B. Rosche, V. Sandford, M. Breuer, B. Hauer and P. L. Rogers, *J. Mol. Catal. B: Enzym.*, 2002, **19-20**, 109-115.

38. E. Fischer and A. Maasböl, *Angew. Chem. Int. Ed. Engl.*, 1964, **3**, 580-581.

39. (a)J. J. Low and W. A. Goddard, *J. Am. Chem. Soc.*, 1984, **106**, 6928-6937; (b)S. F. Vyboishchikov and G. Frenking, *Chem. Eur. J.*, 1998, **4**, 1428-1438.

40. S. F. Vyboishchikov and G. Frenking, *Chem. Eur. J.*, 1998, **4**, 1439-1448.

41. W. Mowat and G. Wilkinson, *J. Chem. Soc., Dalton Trans.*, 1973, DOI: 10.1039/DT9730001120, 1120-1124.

42. R. R. Schrock, *J. Am. Chem. Soc.*, 1974, **96**, 6796-6797.

43. (a)L. Li, M. Hung and Z. Xue, *J. Am. Chem. Soc.*, 1995, **117**, 12746-12750; (b)J. K. Abbott, L. Li and Z.-L. Xue, *J. Am. Chem. Soc.*, 2009, **131**, 8246-8251.

44. D. Clark and R. Schrock, *J. Am. Chem. Soc.*, 1978, **100**, 6774-6776.

45. R. Schrock, S. Rocklage, J. Wengrovius, G. Rupprecht and J. Fellmann, *J. Mol. Catal.*, 1980, **8**, 73-83.

46. J. H. Wengrovius and R. R. Schrock, *Organometallics*, 1982, **1**, 148-155.

47. (a)M. Mocella, R. Rovner and E. Muetterties, *J. Am. Chem. Soc.*, 1976, **98**, 4689-4690; (b)J. Kress, M. Wesolek, J.-P. Le Ny and J. A. Osborn, *J. Chem. Soc., Chem. Commun.*, 1981, 1039-1040.

48. S. F. Pedersen and R. R. Schrock, *J. Am. Chem. Soc.*, 1982, **104**, 7483-7491.

49. J. S. Murdzek and R. R. Schrock, *Organometallics*, 1987, **6**, 1373-1374.

50. D. M. Flanigan, F. Romanov-Michailidis, N. A. White and T. Rovis, *Chem. Rev.*, 2015, **115**, 9307-9387.

Chapter Two

2 Synthesis of Triazolium mimics of TPP

Foreword

This chapter gives a detailed stepwise development of a new route to preparing mimics of thiamine. The first section outlines the synthesis of thiamine pyrophosphate in living cells, and synopsis of current literature reporting on the preparation of structures incorporating the thiazole and triazole motif. Preparation of triazolium based mimics of thiamine using a novel route is discussed in the second section. Lastly, synthesis of various analogues based on the mimic is detailed in the third section.

2.1 Introduction

2.1.1 Biosynthesis of Thiamine (pyrophosphate)

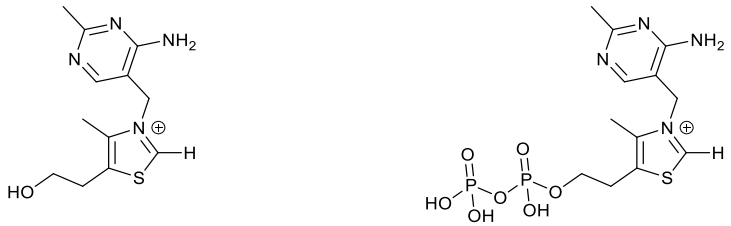

7 **63**

Figure 2.1 Thiamine 7 and Thiamine pyrophosphate 63

All life forms require thiamine **7** to make use of energy stored in food, however, animals cannot directly synthesise it and therefore have to source it from dietary intake[1]. Conversion of thiamine into its bioactive phosphoester, thiamine pyrophosphate (TPP) **63** (also known as cocarboxylase or thiamine diphosphate ThDP) occurs in most living organisms including humans using specific enzymes. Currently it is made in a large-scale industrial process and marketed as a food supplement for both humans and animals alike. Processing of foods to increase shelf life tends to degrade thiamine content, hence, common sources of thiamine include natural delicacies such as fish, red meat, and bran. Thiamine is the first water-soluble

vitamin discovered and the term "vitamin" was coined from the assumption that thiamine was a **vit**al **amine**. Indeed, its names also lend to this scheme, as a sulfur (**thia**) containing **amine**. It was soon found that not all vitamins contain amino groups, but the label (vitamins), however, has stood the test of time.

Thiamine deficiency in humans is generally characterized by symptoms which may be attributed to a lack of vitality, such as irritability, dyspnea, loss of consciousness and atrophy of muscle tissue. Nursing mothers are particularly susceptible to privation during lactation, especially in developing countries where processed foods may not be adequately fortified with synthetic thiamine. In most first-world countries, thiamine deficiency is usually due to alcohol addiction, because ethanol affects absorption in the liver. Aside from being used as a food supplement, it is also administered as a drug to cure certain maladies such as the Leigh syndrome, wet and dry beriberi, and avian encephalomyelitis[2].

In *Archae*, a prehistoric single-celled organism that lacks a true nucleus, thiamine is made by coupling the thiazolium and aminopyrimidine units, which are made separately. The thiazolium ring is made by coupling glycine **80** with nicotinamide adenine dinucleotide (NAD) **81** using thiazole synthase Thi4 (Scheme 2.1). This gives ADP-bound thiazole carboxylate **82**, which is hydrolysed by nudix hydrolase to form the target thiazole carboxylase-monophosphate[3] **83**.

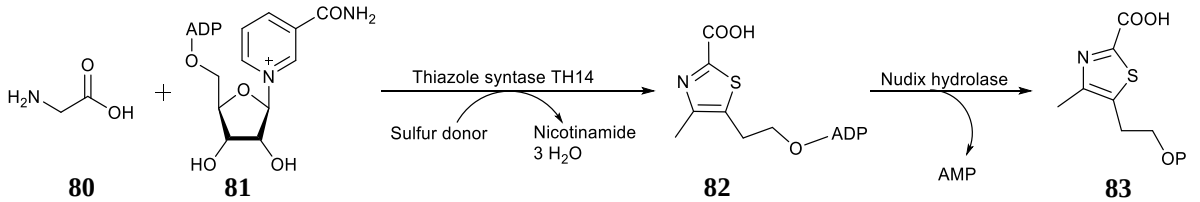

Scheme 2.1 Synthesis of the monophosphate thiazolium moiety in *Archae* from glycine 80

Synthesis of the aminopyrimidine ring is achieved by coupling L-histidine **84** with bioactive vitamin B_6 or pyridoxal-5′-phosphate (PLP) **85** (Scheme 2.2) in the presence of hydroxymethylpyrimidine phosphate synthase to give HMP-phosphate **86**, which is converted

to hydroxymethylpyrimidine pyrophosphate (HMP-Pp) **87** by phosphomethylpyrimidine kinase. The final step is reversible based on the energy needs of the cell, with the forward step using adenosine triphosphate (ATP) and generating adenosine diphosphate (ADP).

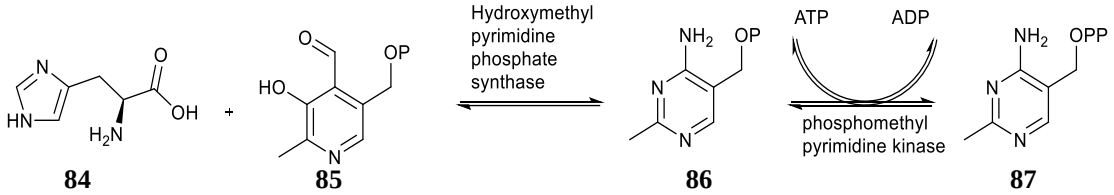

Scheme 2.2 Synthesis of the diphosphate pyrimidine moiety in *Archae* from histidine 84

Both pre-formed thiazolium-monophosphate **83** and hydroxymethylpyrimidine pyrophosphate **87** rings are first combined to give thiamine monophosphate **88** by thiamine phosphate synthase. Dephosphorylation using thiamine phosphate phosphatase to give thiamine **7**, and finally pyrophosphorylation using thiamine pyrophosphokinase gives the bioactive diphosphate form **63** (Scheme 2.3) because it lacks thiamine-phosphate kinase for direct pyrophosphorylation[4].

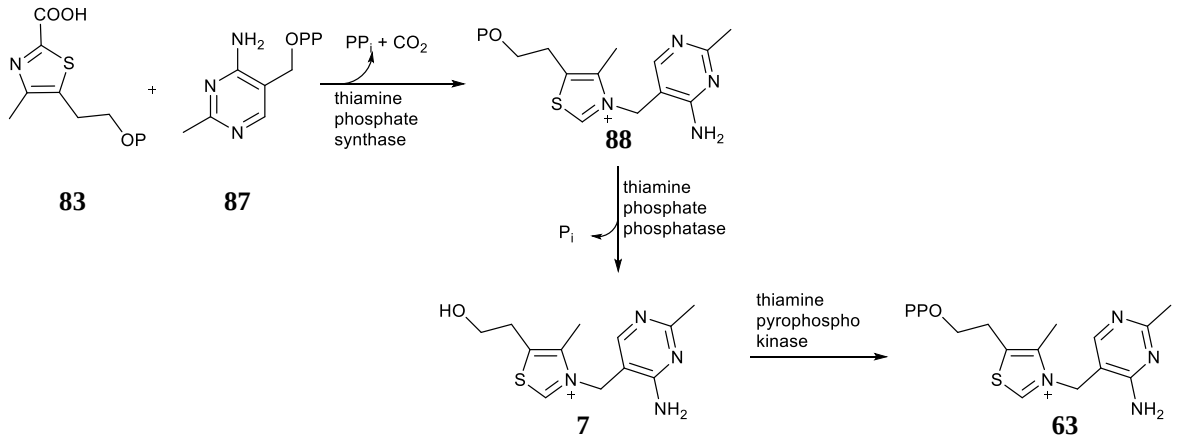

Scheme 2.3 Coupling of the thiazole and pyrimidine components of ThDP 63 in *Arcae* bacteria

The biosynthesis of thiamine pyrophosphate in E. coli follows a slightly modified pathway (Scheme 2.4) from *Archae* because it possesses the enzyme thiamine-phosphate kinase for direct phosphorylation of the monophosphate to give the diphosphate ester[5]. Tyrosine **89,** 1-

Deoxy-D-xylulose 5-phosphate (DXP) **90** and cysteine **91** are converted by thiazole synthase to give thiazole-monophosphate **92**. In addition, 5-aminoimidazole ribotide **93** is modified by hydroxymethylpyrimidine-phosphate synthase to give mono-phosphorylated aminopyrimidine (HMP-P) **94**, and subsequently by phosphomethylpyrimidine kinase to give di-phosphorylated aminopyrimidine (HMP-Pp) **95**. Both heterocycles are combined by thiamine phosphate synthase to make thiamine monophosphate **88**, and finally by thiamine monophosphate kinase to give the native cofactor TPP **63.**

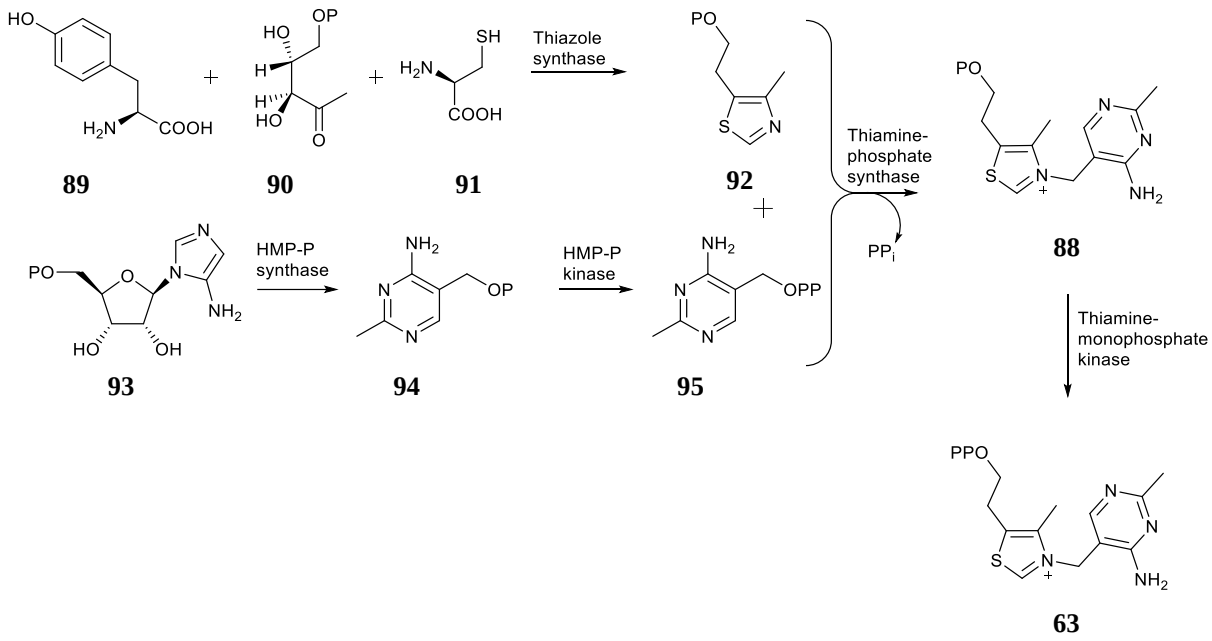

Scheme 2.4 Biosynthesis of thiamine pyrophosphate 63 in *Escherichia coli*

Plants are capable of producing thiamine[6] **7**, wherein the two rings are independently made using specific enzymatic pathways and coupled to give monophosphate ester **88**. Further enzyme catalysed reactions give the active diphosphate form depending on the immediate requirements of the cell[7]. Thiamine is usually the preferred form to treat deficiencies, even though it is not bioactive without pyrophosphorylation. Five other pyrophosphate analogues are known to date with TPP being the most important for enzymatic reactions (Figure 2.2).

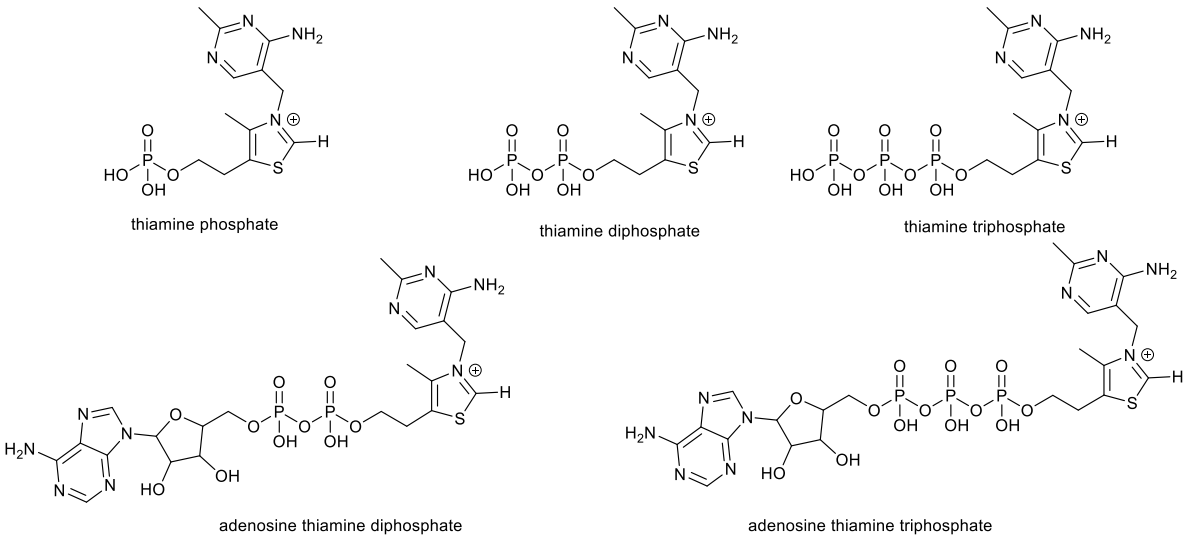

Figure 2.2 Phosphate esters of thiamine

2.1.2 Synthesis of thiazoles

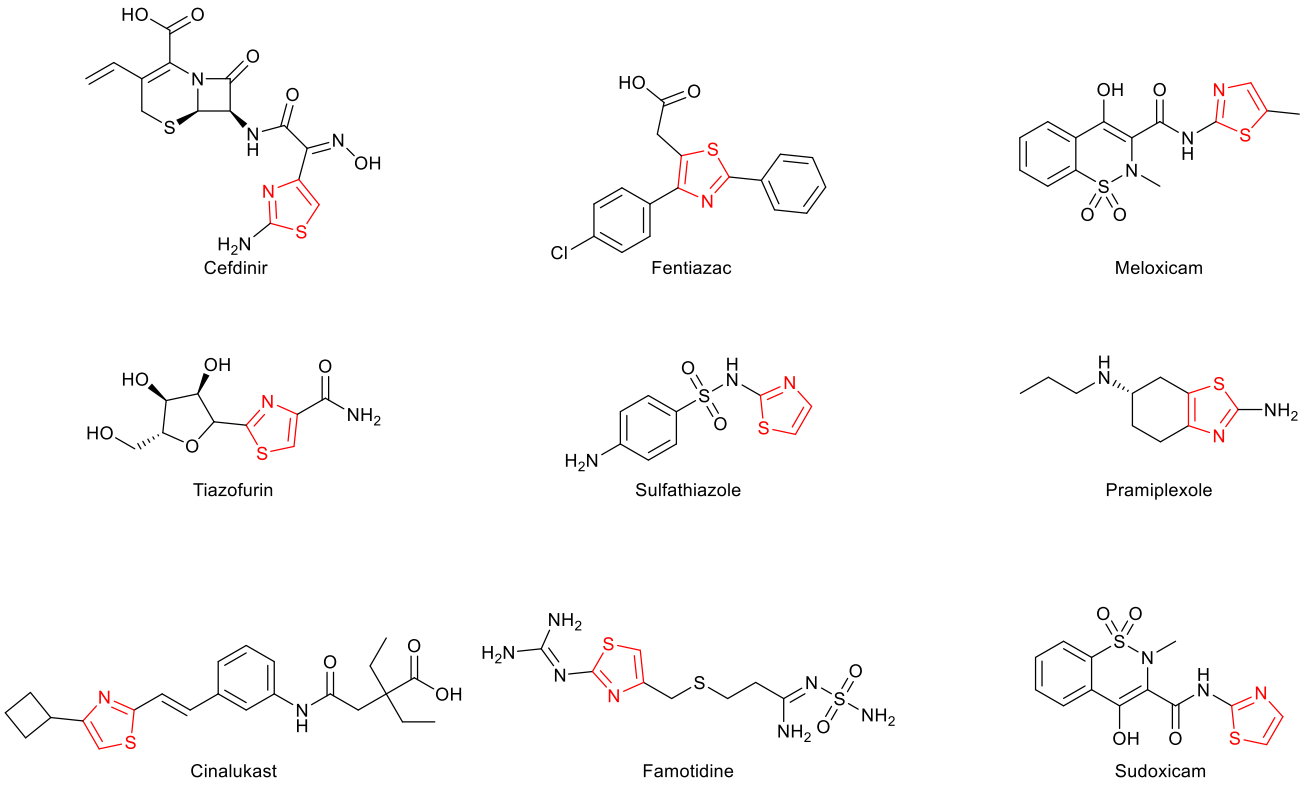

Figure 2.3 Commercially available bioactive compounds incorporating the thiazolium subunit

Thiazoles have been well known to chemists for well over a hundred years *e.g.* as the catalytically active unit in vitamin B_1 (thiamine)[8]. A range of pharmaceutical compounds

incorporate the thiazolium subunit (Figure 2.3**)**, which makes developing facile routes to its synthesis commercially attractive. One of the earliest methods for its preparation is the Hantzsch cyclization[9] (eponymous of Arthur Rudolf Hantzch, a German chemist), which involves reacting a thioamide **96** with halo ketone **97** usually in ethanol (Scheme 2.5).

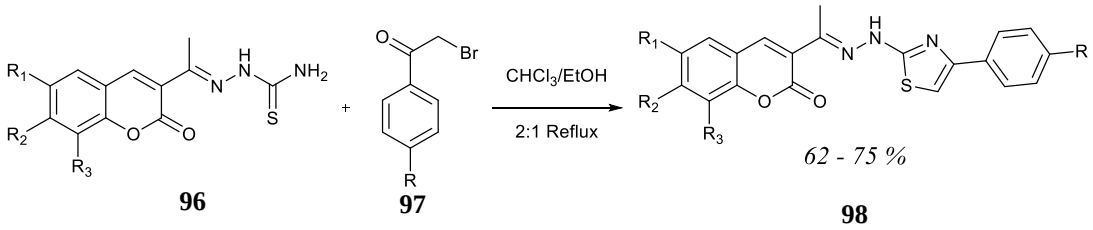

Scheme 2.5 Hantzsch cyclization in ethanol to give thiazole 98

The thiazole-coumarin type structures **98** shown have been investigated by Li[10] and present possible inhibitory properties towards a range of bacterial strains when tested *in silico* using docking software. Although the reaction conditions are not mild and require the use of noxious precursors, the yields are favourable.

A different approach to assemble thiazoles employs potassium thiocyanate reacting with variously substituted oximes **99** and anhydrides **100** in the presence of copper iodide[11]. As illustrated in **Scheme 2.6**, a catalytic amount of copper (I) iodide promotes the severance of the N—O and S—C bonds. It is proposed that a transition metal catalysed [3+1+1] cyclization via **101** effectively affords assorted analogues **102** with substitution at the 2-, 4- and 5-positions in satisfactory yields. Although a few copper salts were used initially, including CuBr, CuCl and $Cu(OAc)_2$, it was found that CuI gave the best yields. Palladium and silver halides were also screened, but these reactions did not progress to detectable/isolable products.

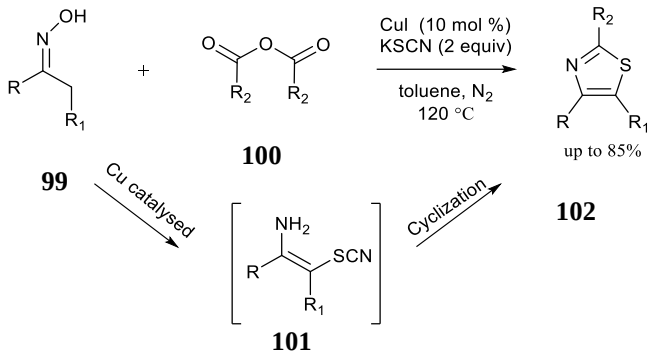

Scheme 2.6 Cyclization via metal catalysis to give thiazoles

For cases where 2,4-disubstituted thiazoles **103** are required, the Hantzsch cyclisation would compel the use of unstable α-haloaldehydes, which in turn, are contrived by direct halogenation of the corresponding aldehyde. This drawback is easily overcome by the use of terminal alkynes **104**, sulfonyl azides **105** and thiono esters **107** catalysed by a copper and rhodium coupled system[12].

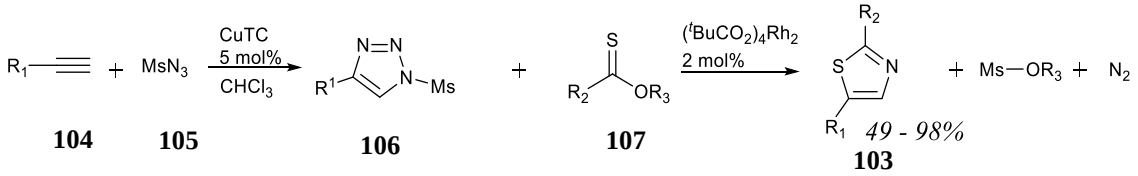

Scheme 2.7 Syntheses of 2,5-disubstituted thiazole 103 via metal catalysed coupling

The alkyne **104** first adds on to the sulfonyl azide **105**, aided by copper(I) thiophene-2-carboxylate (CuTC) to form a 1,2,3-triazole **106**. The next and final step sees the newly formed 1-sulfonyl-1,2,3-triazole **106** react with the thiono ester **107,** catalysed by a rhodium(II) trimethylacetate dimer, to give the target substituted thiazole **103** (Scheme 2.7**)**. In addition, the substituted triazole intermediate **106** can be used as a starting material in the synthesis of metallocarbenes[13].

Recently, the group of Jiao[14] has developed a direct route to thiazoles by reacting elemental sulfur in the presence of oxygen with substituted amines **108** and aldehydes **109** (Scheme 2.8). Straight chain amines have been successfully coupled using this route with relative ease.

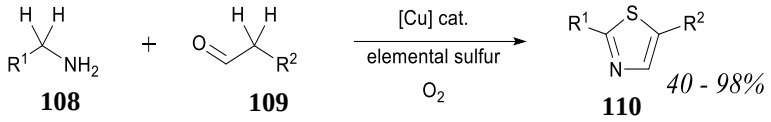

Scheme 2.8 Copper catalysed coupling of aldehyde and amines with sulfur to give thiazoles 110

The authors posit that the carbon-hydrogen sp^3 hybridized bonds of both starting reagents would interact with elemental sulfur to give the target thiazole **110**. However, copper is likely to get poisoned by sulphur, hence the need for oxygen in the reaction, which is mild enough not to react with either amine or aldehyde on the reaction timescale.

2.1.3 Synthesis of Triazoles

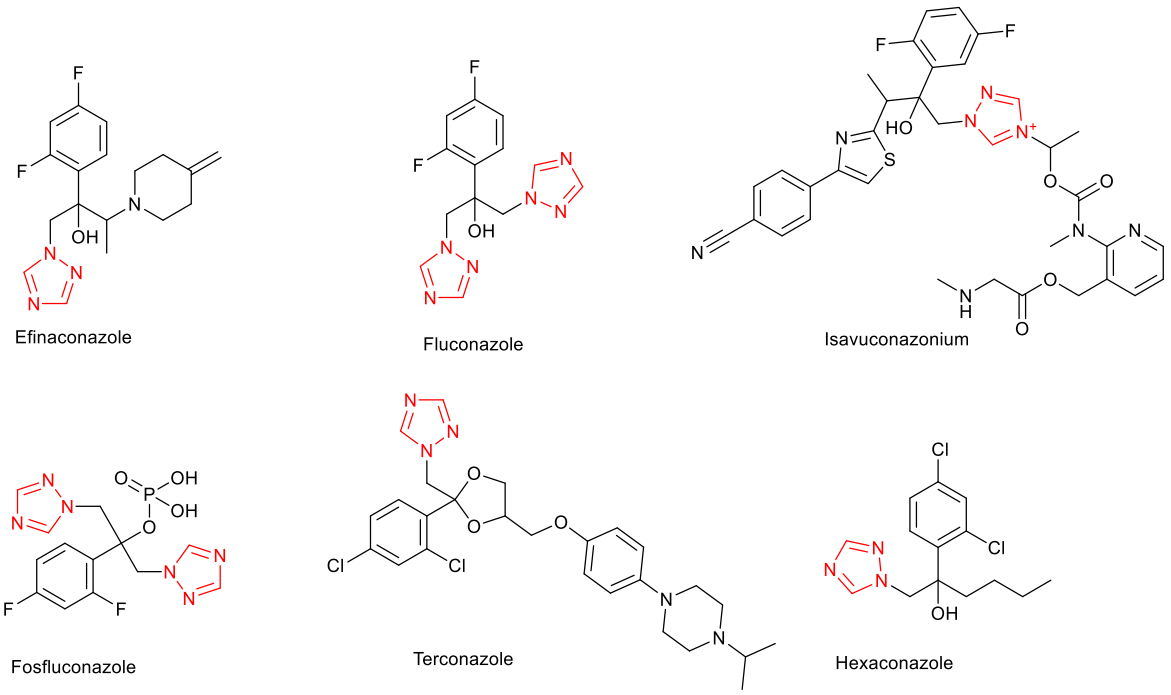

Figure 2.4 Antifungal drugs incorporating a 1,2,4-triazole unit

The synthesis of triazoles is very well-established in organic chemistry owing to their diverse range of applications as biologically active compounds. A broad range of commercially available antifungal drugs incorporate triazoles in their structure (Figure 2.4). Furthermore, triazole derivatives have been adapted for use as anticancer, antitumor, antimigraine and chelating agents. Given that our target mimic would incorporate a triazolium core, it is therefore useful to explore reported procedures for accessing substituted triazoles.

1,2,4-triazoles may be prepared by reacting monosubstituted hydrazines **111** and formamide **112** [15]. This reaction proceeds in the presence of microwave irradiation without the need for a catalyst. Although the reactions conditions are quite rigorous, with the use of high temperatures and extreme pressure, this is countered by the short reaction times, typically less than half an hour required for completion. In addition, the process is amenable to the use of various aryl and alkyl substituents on the N-1 position. Functionalization of the 1-position on the triazole

ring **113** was achieved by using variously substituted hydrazines, with moderate to good results. 4-Methoxyphenylhydrazine gave the best overall yield of 76%, while cyclohexyl hydrazine gave the lowest isolated yield (54%) (Scheme 2.9).

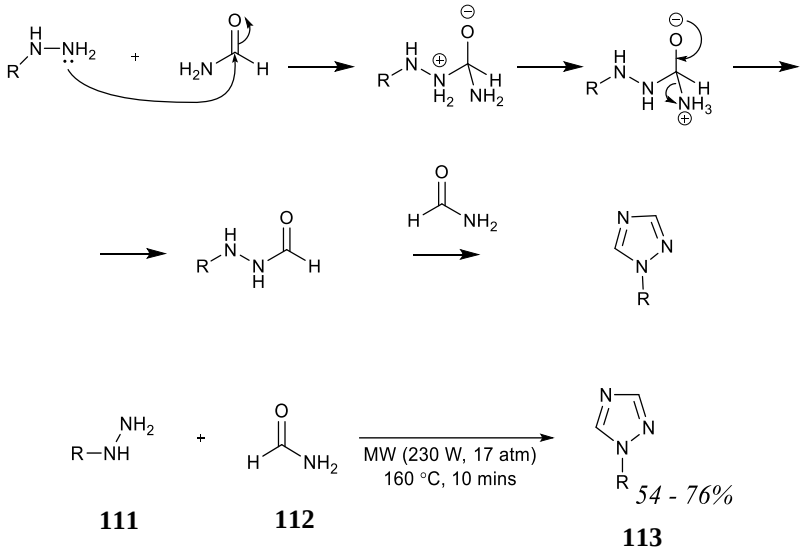

111 **112** **113**

Scheme 2.9 Synthesis of monosubstituted triazoles 113 using microwave irradiation

A much milder technique has been developed for the synthesis of 1,2,4-triazoles using electrodes continuously supplied with a direct current[16]. Mono and disubstituted triazoles were obtained in moderate to good yields by reacting ammonium acetate, arylhydrazines **114**, paraformaldehyde and alcohols **115** as water-soluble solvents (Scheme 2.10). Methanol, dimethylformamide, and acetonitrile were used as solvents with methanol giving the highest yields overall. The use of different solvents such as pentanol and isopropanol gave the corresponding substituted triazole product **116**, which supports the in-situ conversion of the alcohol to aldehyde via a radical type mechanism. When acetonitrile, dimethylformamide or dimethyl sulfoxide were used, the triazole product was only barely detectable without any isolable yields.

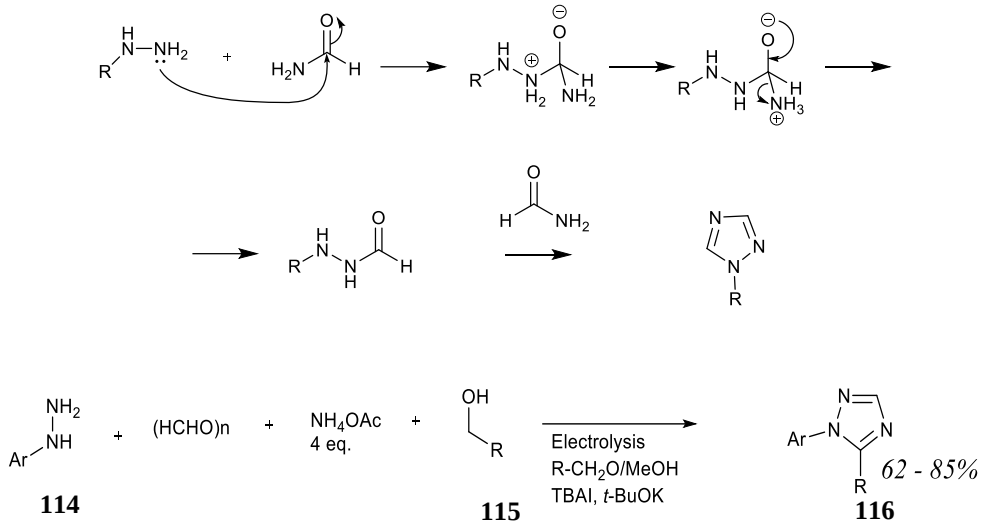

Scheme 2.10 Electro synthetic reaction of aryl hydrazines to furnish disubstituted triazoles 116

The reaction conditions are milder in comparison to the microwave type transformations, and reaction times are longer, with typical completion times of a few hours. Use of various salts as electrolytes gave an interesting mix of results. For instance, starting with NaI, the target phenyltriazole saw a 62% yield. Using potassium, ammonium or n-tetra butyl ammonium iodide gave better results with the t-butyl ammonium salt having the largest yield of 82%.

The group of Cruz have successfully made triazoles using a single mix process, with twenty-one analogues[17]. In the procedure, several substituted anilines **117**, which were readily available commercially, were first condensed with triethylorthoformate to form the imidate **118** and then reacted with tosylamidoxime **119** to give the target triazole **120 (**Scheme 2.11**)**. Although the yields reported were moderate to low (7 – 65%), it is advantageous to note that the reaction does not require the use of transition metal catalysis and has a broad substrate scope.

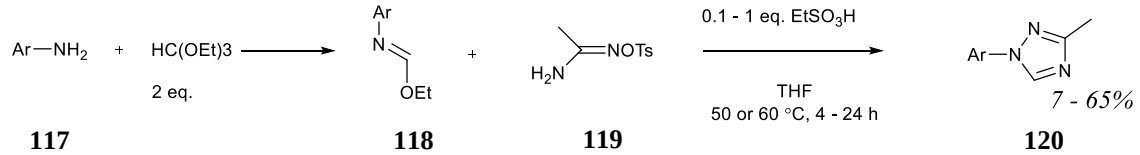

Scheme 2.11 One-pot synthesis of triazoles using substituted anilines

Recently, iodine has been successfully employed as a catalyst in the synthesis of trisubstituted 1,2,4-triazoles[18]. This approach uses hydrazones **121** and primary amines **122** in the presence of atmospheric oxygen to give the target triazole **123**. This one-pot synthesis gives excellent regioselective control. Variations in the concentration of iodine used alluded to a 0.2 equivalent giving optimal yields, however, the removal of iodine completely resulted in minimal yields.

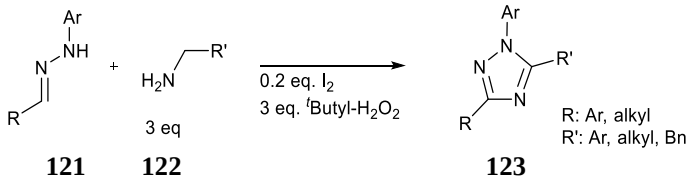

121 **122** **123**

Scheme 2.12 Iodine promoted synthesis of trisubstituted triazoles 123

Xi et al[19] have demonstrated the use of isocyanides in accessing disubstituted triazoles. In this procedure, aryl diazonium salts **124** are cyclized with substituted isocyanides **125** in the presence of silver (I) ions (Scheme 2.13) to give 1,3-disubstituted triazoles **126**. This route is amenable to a diverse range of substrates and provides good functional group tolerance. Excellent yields were obtained (up to 85%) using dichloroethane (DCE) as a solvent, however, the use of DMF did not favour conversion into products.

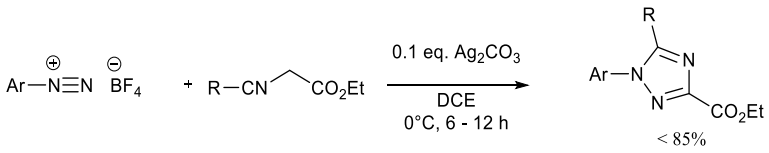

124 **125** **126**

Scheme 2.13 Silver catalysed reaction of isocyanides with diazonium salts to give triazoles

A catalyst-free approach, using cyanamide coupling with aldehydes has been developed by the group of He[20]. Herein, aromatic aldehyde **127** is first treated with cyanamide **128** to give the cyanoimidate **129**, which is then treated with phenylhydrazine **130** refluxing in methanol to give the target triazole **131**. N-Bromosuccinimide **132** was employed to act an oxidizing agent, with cyanamide **128** providing one of the triazole ring nitrogens. This route is agreeable to an

expansive range of alkyl and aryl substituents on the aromatic aldehyde, with the highest yield (92%) recorded using benzaldehyde as a model substrate.

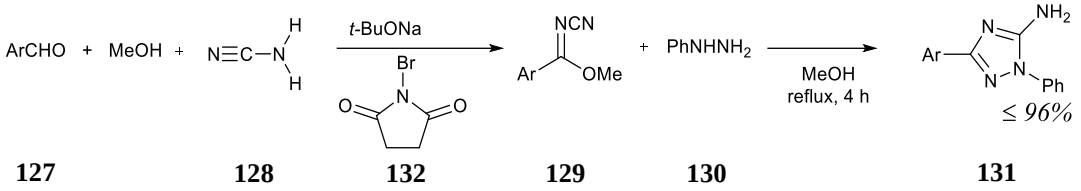

Scheme 2.14 Synthesis of substituted triazoles using cyanamide as a nitrogen source

As none of the previously reported routes gave a direct method for making our target mimic, we designed a novel route for the total synthesis of our direct triazolium analogues of thiamine. This is further discussed in the next section.

2.2 Synthesis of triazolium mimic analogue of thiamine 7

One of the overall aims of this project is to synthesise a triazolium analogue **133** of thiamine pyrophosphate **63** as shown in **Scheme 2.15**. Surprisingly to date, there has been no report of this molecule in the literature, to the best of our knowledge, despite the widespread use of triazolium salts as organocatalysts and the biomimetic links to TPP **63**.

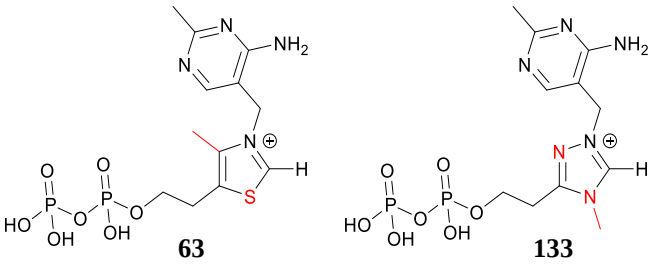

Scheme 2.15 Coenzyme Thiamine Pyrophosphate (TPP) 63 and proposed triazole mimic 133

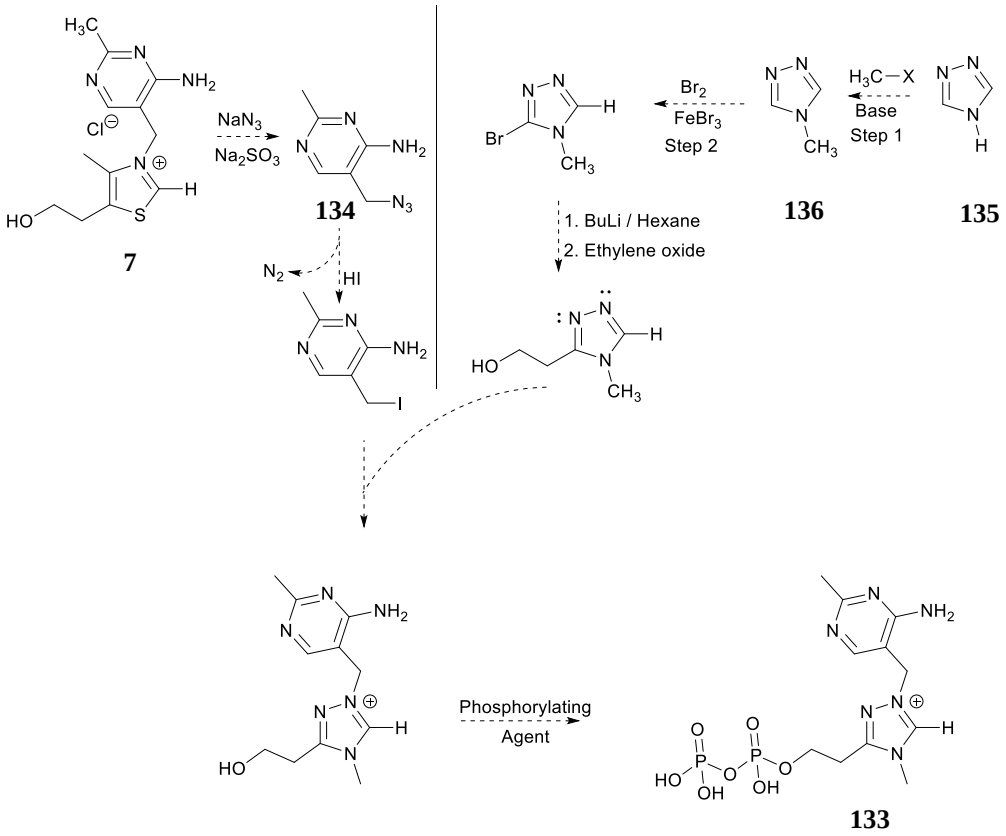

Scheme 2.16 Proposed synthesis of triazole TPP analogue 133

In order to prepare the triazole, the route shown in (Scheme 2.16) was initially proposed. Starting with commercially available thiamine hydrochloride salt **7** and reacting with sodium azide in the presence of sodium sulphite would give 5-azidomethyl-2-methylpyrimidine-4-ylamine **134**, with the intention of further reaction with sodium iodide. The first step, however, did not proceed to isolable product and further attempts to derivatise azido-pyrimidine **134** using hydroiodic acid were unsuccessful.

In addition, attempted methylation of 1,2,4-triazole **135** gave mixtures of mono **136** and di-methylated products which proved difficult to separate. Further attempts at proceeding with the route shown in Scheme 2.16 were therefore abandoned and an alternative synthetic procedure was considered.

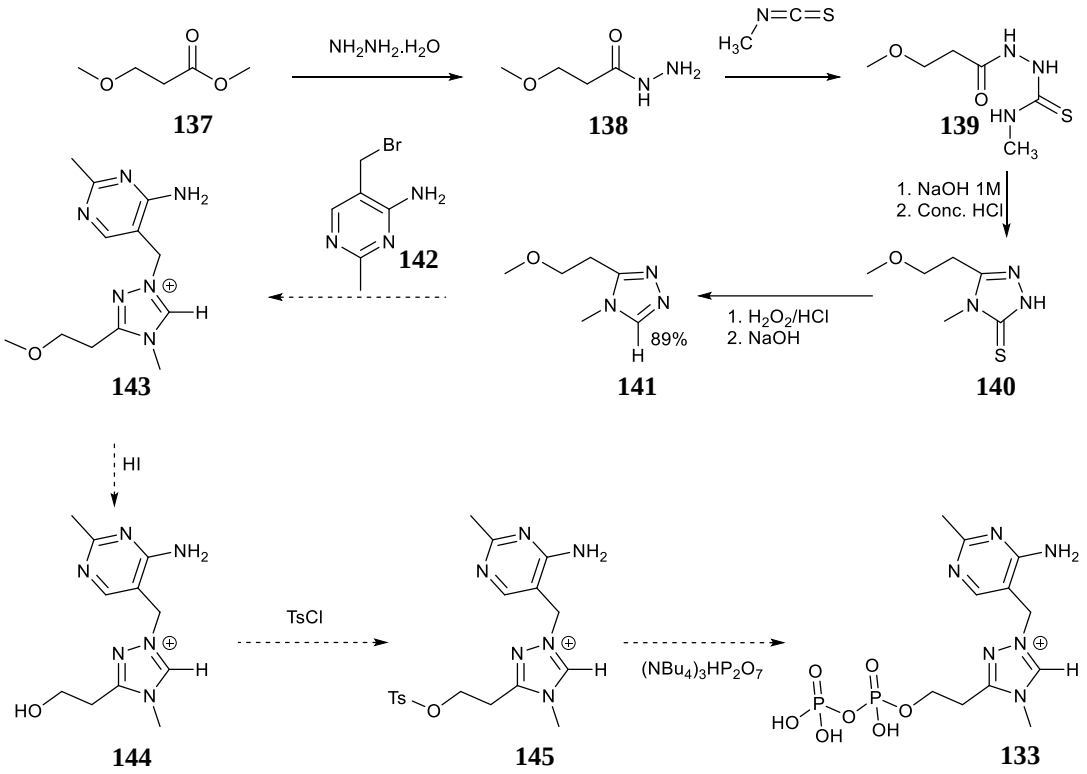

Scheme 2.17 Alternative synthetic procedure towards triazole TPP mimic 133

The route above (Scheme 2.17) shows a different approach to preparing proposed triazole analogue of TPP **133**. In this route, methyl 3-methoxypropanoate **137** is first converted to the hydrazide **138** by reacting with commercially available hydrazine monohydrate. The hydrazide is then treated with methyl isothiocyanate to give the carbothioamide **139**. Onward cyclization in dilute sodium hydroxide, gives the thione intermediate **140**, which can be desulfurized using hydrogen peroxide to give the neutral triazolium compound **141**.

Alkylation at N1 of triazolium **141** with freshly prepared 5-(bromomethyl)-2-methylpyrimidin-4-amine **142** would then give the triazolyl salt **143** and the methoxy side chain can be potentially hydrolysed using HI to give the target mimic **144**. Tosylation of the alcohol **144**, and pyrophosphorylation of the tosylate **145**, in pyridine and acetonitrile respectively, would give the target TPP cofactor mimic **133**.

Our attempts to carry through Scheme 2.17 progressed only as far as the neutral triazolium compound **141** (89% yield). Several trials at preferential alkylation of the neutral triazolium compound **141** using a pyridinium benzyl bromide **146** as a trial alkylating agent under a variety of conditions gave a mixture of isomers of the target triazolyl salt **147** in solution, however, isolation of the desired salt was not fruitful (Scheme 2.18). In addition, N-alkylation was attempted at the thione **140** stage, however, this also was unsuccessful.

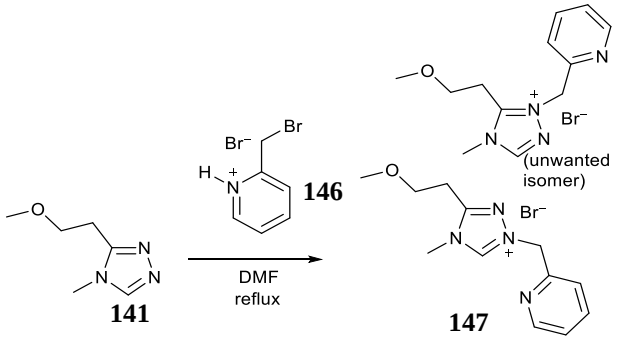

Scheme 2.18 Attempted selective N2 alkylation of triazolium 141

A new route (Scheme 2.19) was then considered, where all the required substituents would already be attached "pre-cyclization", hence, circumventing the need for alkylation following the ring-forming step.

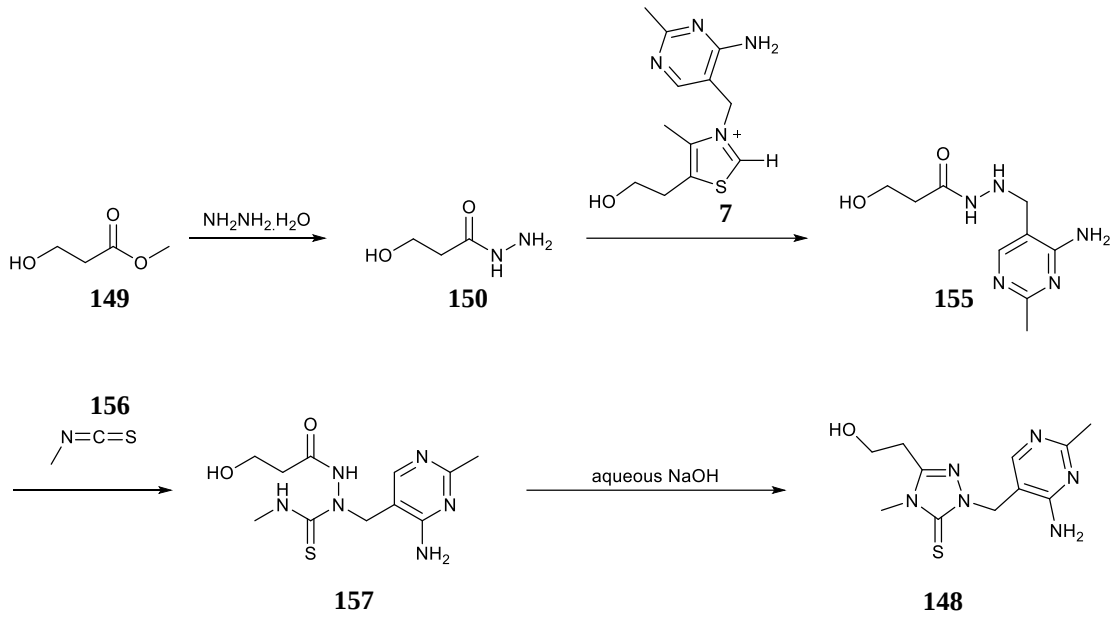

149 **150** **7** **155** **156** **157** **148**

Scheme 2.19 Alternate route to thione mimic synthesis

Using the above route shown in Scheme 2.19, the formation of the thione **148** was achieved with the 4-aminopyrimidinyl substituent attached to the desired bridging nitrogen atom, with relative ease, however, the overall yield was initially lower than desired (15% by NMR spectroscopy). We employed a different starting ester **149** in order to bypass the need to convert methylated analogue **143** to the preferred pendant alcohol **144**. The first step to give the hydrazide **150** was quick (less than one hour) and purification achieved by concentration under reduced pressure to remove excess hydrazine. In practice, residual hydrazine monohydrate was present in the product hydrazide **150** and carried through to the next step outcompetes the hydrazide to give the hydrazinomethyl derivative **151** (Scheme 2.20). This newly formed hydrazinomethyl derivative **151** easily decomposes into the more stable amino methyl product **152**. Hence the hydrazides from the first step was washed with DCM to remove residual hydrazine monohydrate.

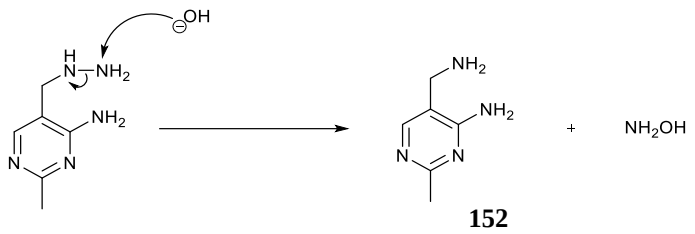

152

Scheme 2.20 decomposition reaction of hydrazine 151 to give 152 under basic conditions

Furthermore, it was necessary to also consider that over alkylation was possible to give di- or tri-alkylated products **153** and **154**, as the mono-alkylated initial product **155** is more nucleophilic than the acyl hydrazide **150**.

Subsequent treatment with thiamine **7**, using three equivalents of substituted hydrazide **150** in the presence of bisulphite gave the 4-aminopyrimidine adduct compound **155** which was used without further purification (Scheme 2.19 above). A threefold excess of the hydrazide **150** was used to ensure a better yield of the mono alkylated product **155** in preference over the other possible (di and tri) alkylation side products (Scheme 2.21).

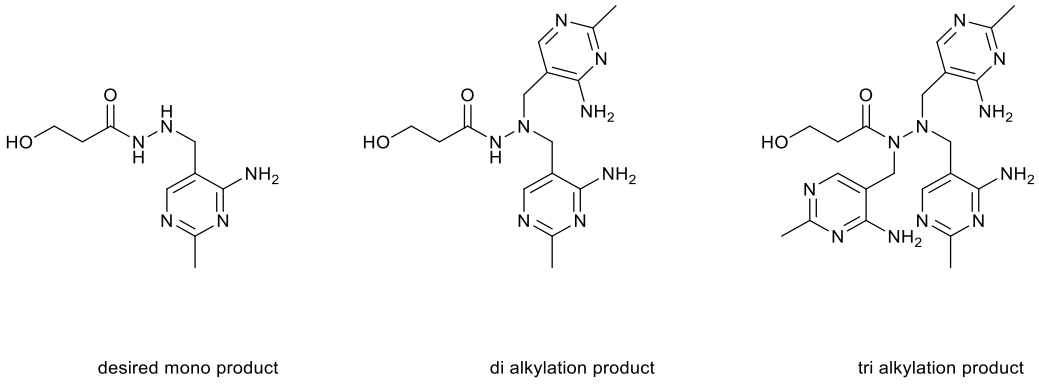

Scheme 2.21 Desired monoalkylation product and possible side products from reaction with thiamine 7

The reaction was monitored by NMR spectroscopy and shows clean conversion of thiamine **7** to the desired product **155**. This was evidenced by the complete disappearance of the bridging

methylene −C*H*$_2$−signal of thiamine at 5.44 ppm(A) and observation of a corresponding new singlet at 3.82 ppm(B), due to aryl linker methylene of the monoalkylated product **155** (Figure 2.5). The reaction mixture was maintained at p*H* ~4.0 at the start, hence the acidic C$_2$*H* (C) of thiamine can be observed at 9.51 ppm in D_2O. The pyrimidinyl hydrogen of thiamine (D) appears as a singlet at 7.90 ppm and the peaks due to the two methylene C*H*$_2$'s of the hydroxyethyl side substituent (E & F) as triplets at 3.77 and 3.08 ppm. The pyrimidinyl methyl and thiazolium methyl of thiamine (G & H) appear as singlets at 2.50 and 2.43 ppm respectively. The two CH_2's of the acyl hydrazide starting material **150 (I & J)** appear as triplets at 3.73 and 2.34 ppm respectively. After all the thiamine (limiting reactant) present in the reaction mixture has been used up, the peak previously due to the C$_2$*H* of thiamine now appears at 8.86 ppm (K) due to neutral thiazole side product **158**.

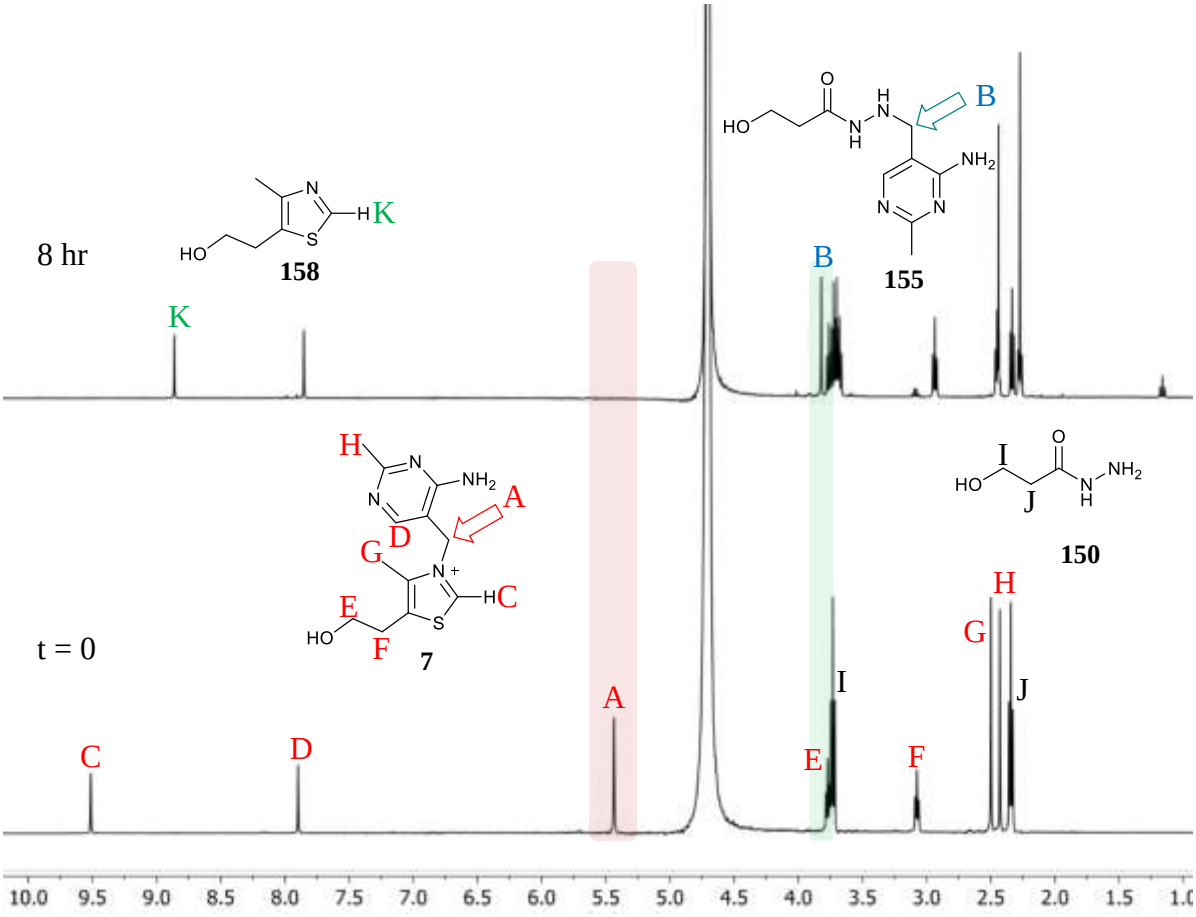

Figure 2.5 Overlay of the NMRs of reaction mixture of hydrazide 150 and thiamine 7 in degassed water

This crude N'-alkylated hydrazide was reacted with methyl isothiocyanate **156** to give the carbothioamide **157** intermediate and cyclised by refluxing in 0.05M sodium hydroxide to give the thione product. The thione **148** is insoluble in water and a white precipitate forms upon cooling, which can be easily filtered off and washed with deionized water (57%). Attempts to grow single crystals of the 2-hydroxy ethyl thione derivative **148** were not successful.

Desulfurization of the thione **148** to give the target triazolyl salt **144** was attempted by suspending the thione in dichloromethane at 0 °C in an ice-bath and adding one equivalent of hydrochloric acid, followed by dropwise addition of two equivalents of 30 % (w/w) hydrogen peroxide in water over 15 mins (Scheme 2.22). The reaction mixture was left to stir overnight

at room temperature. Upon completion, analysis of the reaction mixture showed complete conversion of the thione to the target triazolyl salt.

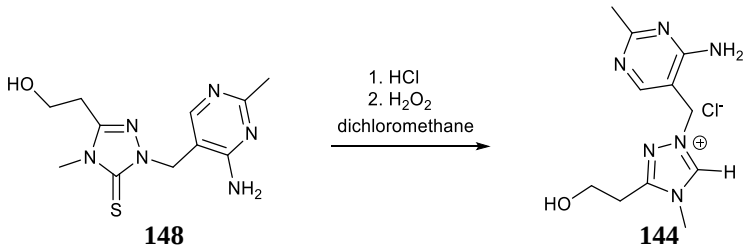

148 **144**

Scheme 2.22 Desulfurization of the thione intermediate 148

The complete conversion of thione **148** was evidenced by the disappearance of the trace at 0.3 minutes with m/z 281 for the thione and the appearance of the peak at 0.19 minutes with m/z 249 which could be attributed to the triazolium component of target salt **144**. NMR analysis shows a shift of the singlet due to the methylene bridge of the thione at 5.1 ppm in D_2O to 5.5 ppm for the triazolyl salt. This is expected as the introduction of a formal positive charge on the "bridging" nitrogen atom would pull electron density away from the methylene linker. In addition, a new peak is observed, corresponding to the triazolyl **144** C_5−H at 9.9 ppm. The acidic proton exchanges instantaneously with deuterium when dissolved in D_2O, hence, a spectrum was acquired in dilute DCl to observe the C_3-H peak. The chemical shift of this proton varies with acidity, tending to decrease in very acidic media. This observation suggests additional protonation states exist at higher DCl concentrations (Scheme 2.23).

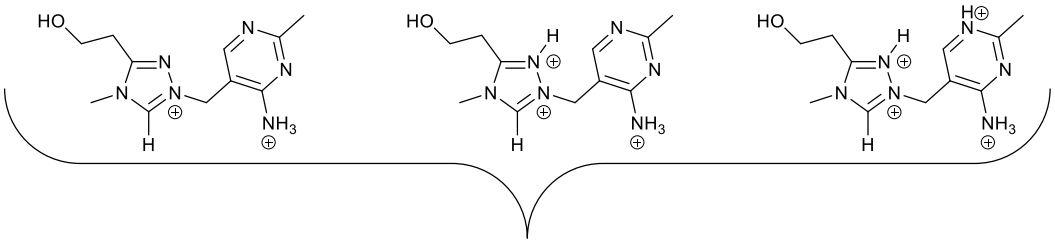

144

Scheme 2.23 Additional protonation states of the triazolyl mimic 144 at low p*H*'s

Attempts to purify the salt **144** via silica column chromatography were unsuccessful, even though a varied mix of solvent systems was employed. High-performance liquid chromatography was not successful either. The chromatogram shows only a single peak which suggests a relatively pure sample, but upon concentration of the eluent fraction, the NMR spectrum shows degradation of the compound. A change of counter ion from chloride to tetrafluoroborate did not give the desired pure product. Attempts at precipitation by increasing the p*H* of the solution led to ring-opening of the salt to give undesired side products.

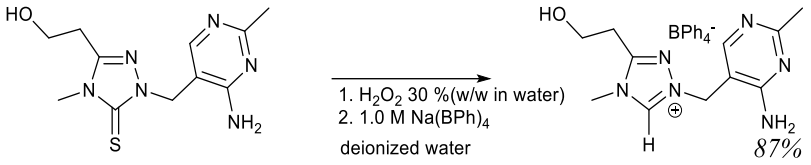

148 **159**

Scheme 2.24 Lipophilic tetraphenylborate counterion as a precipitating agent

Finally, after a few trials, isolation was efficacious using the lipophilic tetraphenyl borate counterion. This was achieved by suspending the thione **148** in deionized water in an ice bath and treating dropwise with hydrogen peroxide. Upon complete desulfurization, monitored by LCMS and TLC, freshly prepared sodium tetraphenylborate was added to precipitate the crude target salt **159**, which was filtered off and washed with deionized water. Attempts at recrystallization using methanol/water mixtures were unsuccessful. Ethanol showed good promise for purification and growing single crystals of the salt, solvating easily at ambient

laboratory temperatures but precipitating rather quickly below 10 °C. Several attempts to recrystallize from ethanol, however, gave "quasi" crystals, which were unsuitable for X-ray analysis. Acetonitrile was found to easily dissolve the salt under ambient laboratory conditions, but it remained soluble even at sub-zero temperatures.

After numerous attempts, with various solvent mixtures, it was found that making up a saturated solution of the salt **159** in methanol and dichloroethane at 40 °C, with very slow cooling in a 10 mL slim glass vial or NMR tube to a supersaturated solution, which when left for about a week, resulted in crystals suitable for X-ray crystallographic analysis.

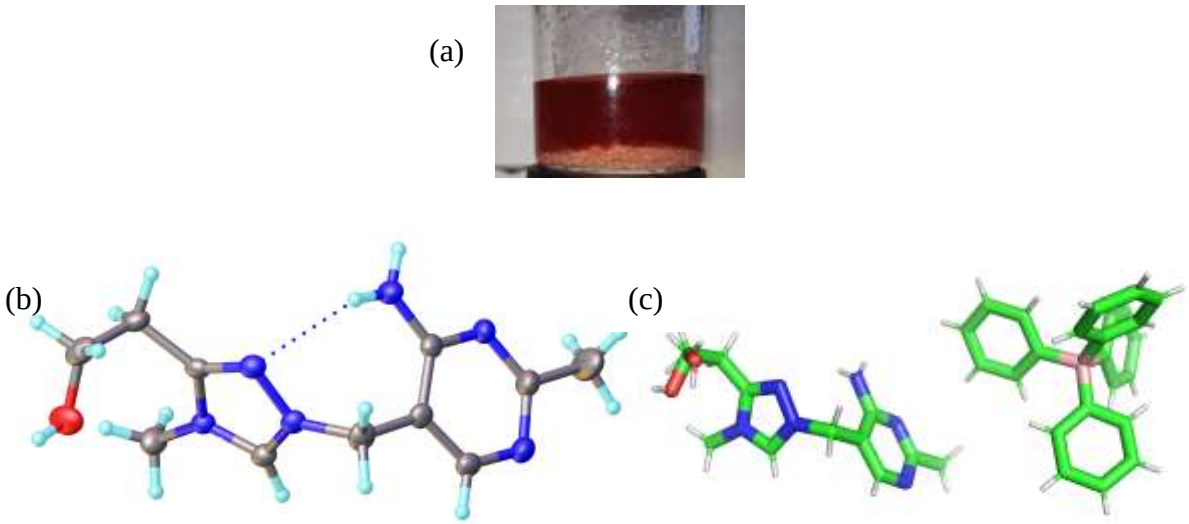

Figure 2.6 Crystal structure of target triazolyl mimic 159 (a) solid crystals in a glass vial (b) cation only (c) packing diagram including the tetraphenylborate counterion

Upon full recrystallisation of the triazolyl salt **159** using the successful conditions, the next and final step was to add the pyrophosphate side chain to give the target cofactor mimic. Attempts to achieve this initially involved using tosyl chloride in pyridine to first convert the pendant alcohol to a better leaving group and then stirring in the presence of a source of pyrophosphate anion (Scheme 2.25). This procedure is not as straight forward in practice given that the pyrophosphate anion is notoriously unstable in water and easily decomposes to give the monophosphate anion.

In addition, the triazolyl salt **144** is only usefully soluble in water and methanol, which are protic solvents, whereas the reaction requires ideally a polar aprotic solvent such as acetonitrile. Choice of counterion affects the solubility of the salt in the desired solvent. For instance, using the lipophilic tetraphenylborate ion, the triazolyl salt **159** becomes readily soluble in organic solvents, however, since our overall aim is to target binding activity at TPP dependent enzyme active sites, in aqueous solution much less bulky counterions, such as chloride or tetrafluoroborate are much preferred.

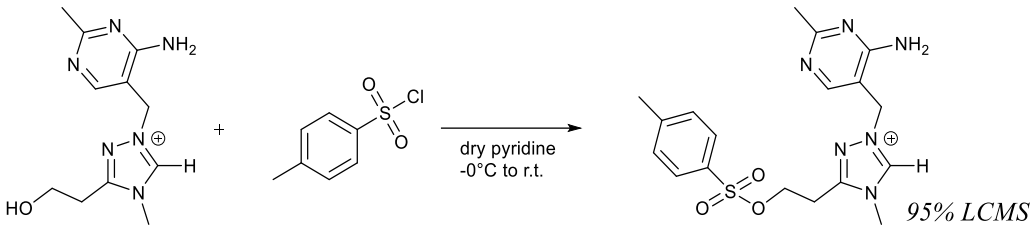

144 **160** **161**

Scheme 2.25 Tosylation of triazolyl salt 144

Using the standard textbook procedure for tosylation in pyridine with a four-fold excess of tosylchloride **160**, analysis by LCMS of the reaction mixture show almost complete conversion into the desired product. However, isolation of the tosylate **161** was not successful because it remains in the aqueous layer during workup.

2.3 Synthesis of analogues of the triazolium mimic

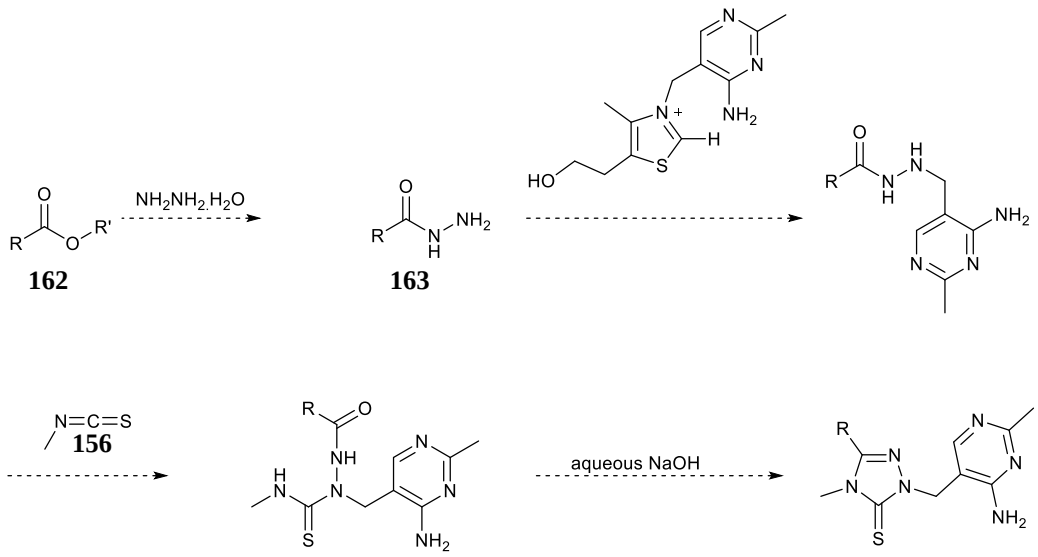

Scheme 2.26 General synthesis of analogues based on the triazolium mimic

In addition to making the triazolium analogue of thiamine, we attempted to prepare several other analogues of thiamine differing only in substitution at the 5-position of the triazolium ring by using various esters **162** as starting material for preparing the hydrazide **163** (Scheme 2.26). Further details are presented below. Initially, the synthesis of analogues of thione **148** will be discussed followed by the final oxidation step.

2.3.1 Synthesis of analogues of thione 148

2.3.1.1 Synthesis of 5-methyl thione analogue

Ethyl acetate **164** was selected as a model ester for initial scoping experimentation and fine-tuning the new synthetic route because it was relatively inexpensive, readily available and easy to use. Treatment of ethyl acetate with hydrazine monohydrate gave the acethydrazide **165** in excellent yield (98%), and upon cooling, formed a white crystalline solid. In the next step, acethydrazide **165** was reacted with thiamine **7**, to give N' alkylated acethydrazide intermediate **166**, and upon further reaction with methyl isothiocyanate **156** gave the carbothioamide **167**, which was filtered off and used in the next step without further purification (Scheme 2.27).

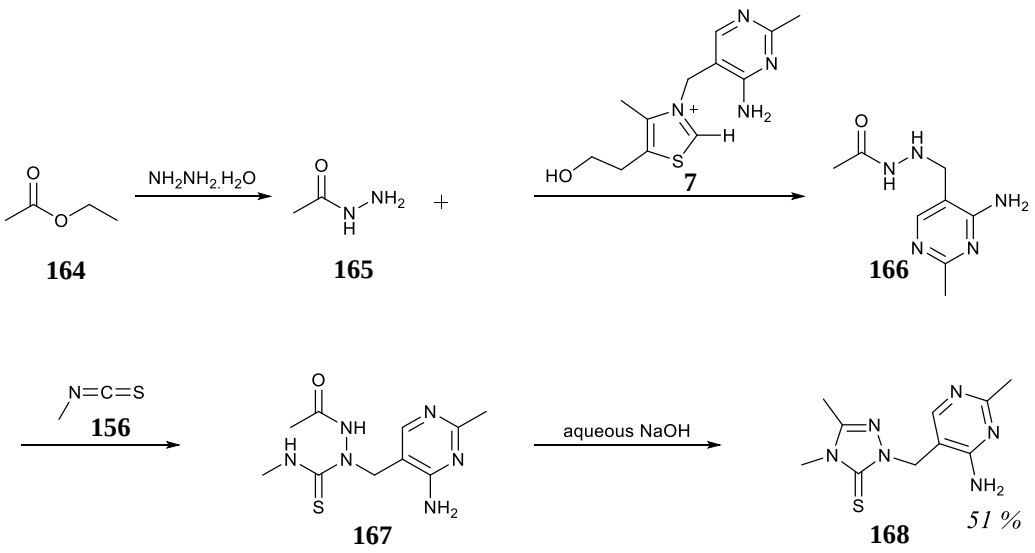

Scheme 2.27 Synthesis of methyl thione triazolium analogue 168

Cyclization of the carbothioamide **167** by heating under reflux in basic conditions gave the desired thione **168**, which was precipitated out of the basic solution upon cooling as translucent fine white needles. It is quite useful to note that at room temperature thione **168** is insoluble in water at p*H* 6 and above. Recrystallization was achieved by dissolving in dilute aqueous HCl and leaving the solution to slowly evaporate in a partially covered conical flask at the back of a fume hood over several weeks, upon which fine transparent needles where observed and collected for single X-ray crystallographic analysis (Figure 2.7).

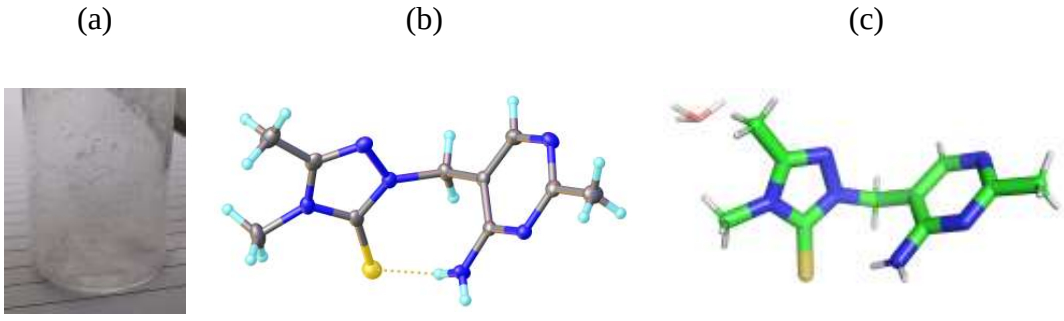

Figure 2.7 Crystal structure of methyl thione intermediate 168 (a) solid crystals (b) cation (c) packing diagram including the hydrate water molecule, with hydrogen disordered over two positions

The structure conclusively shows that the desired N2 alkylation of the triazole was achieved, to give the target methyl aminopyrimidine substituent on the bridging nitrogen (Figure 2.7). Also, the methyl group carried through from methylisothiocyanate **156** is attached at the N4 nitrogen of the triazolium ring in **168** as required. In addition, the 4-amino substituent of the pyrimidine ring remained intact for the duration of the experiment, suggesting that it is less nucleophilic than the primary amine functional group of the carbothioamide **167**.

2.3.1.2 Synthesis of 5(3-hydroxypropyl) thione analogue 169

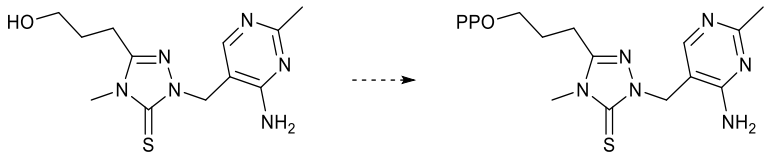

169 **170**

Scheme 2.28 Proposed pyrophosphate ester analogue 170

In addition to making the methyl analogue **168**, we decided to make 3-hydroxypropyl analogue **169** owing to the presence of the pendant alcohol which offers promise for further derivatization to give a pyrophosphate ester mimic **170** (Scheme 2.28).

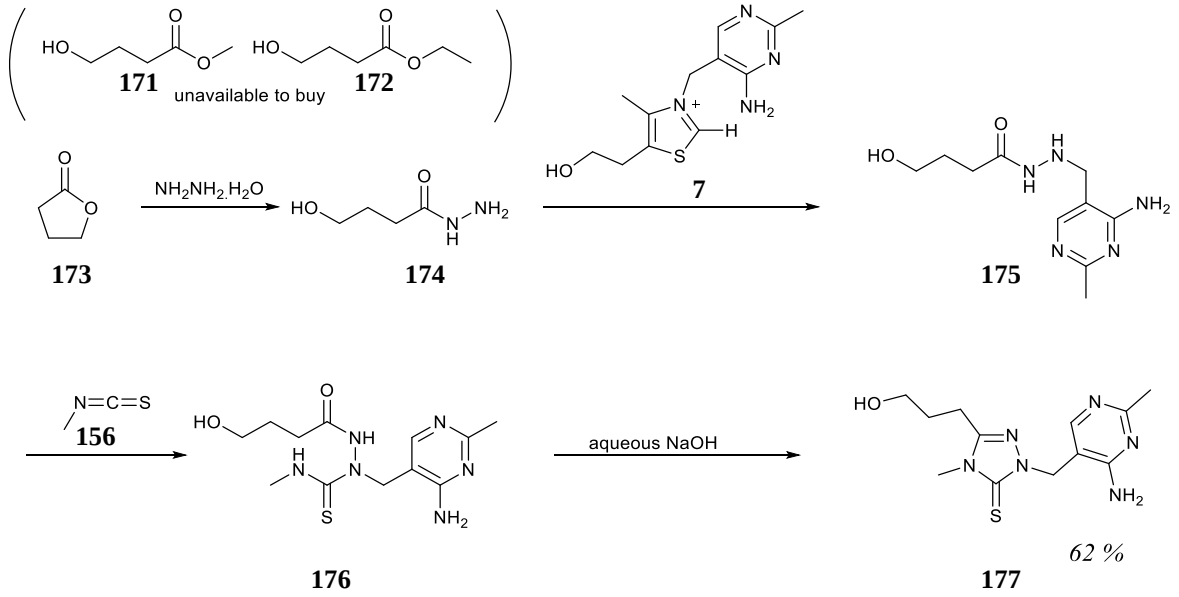

Scheme 2.29 Synthesis of 3-hydroxypropyl thione analogue 177

The desired esters for this first step, methyl **171** or ethyl-4-hydroxybutanoate **172** were not commercially available hence we resorted to instead using relatively inexpensive γ-butyrolactone **173** (Scheme 2.29). The lactone **173** was reacted with 2 equivalents of hydrazine monohydrate to give the desired 4-hydroxyhydrazide **174** in high yield (97%). The product, which conveniently precipitates upon standing, was collected by filtration and washed with cold hexane, considering that (unlike acethydrazide **165**) it was found to dissolve in DCM. Reacting the hydrazide **174** with thiamine **7** afforded the N' alkylation product **175**, which was used directly in the next step without further purification. Treatment of the alkylation product **175** with methylisothiocyanate **156** gave the carbodiimide **176**, which was removed by filtration and refluxed in aqueous sodium hydroxide to give the target thione **177** in moderate isolated yield (62%). Slow cooling of the reaction mixture at 50 °C gave rise to needle-like crystals of the thione **177**, which were filtered off, washed with water and dried for X-ray analysis.

Figure 2.8 Crystal structure of 3-hydroxypropyl thione analogue 177 (a) sample (b) crystal structure (c) packing diagram

We were delighted with the results of the X-ray crystallographic analysis (Figure 2.8), because it shows that the hydroxy appendage could survive treatment with methylisothiocyanate in refluxing ethanol from the third step and refluxing in sodium hydroxide in the final step (Scheme 2.29, page 71). The bridging methylene does not suffer from lability associated with the thiamine **7** under basic conditions as it is still attached to a formally neutral nitrogen atom, at the thione stage, hence it is a fairly bench stable compound across a broad range of p*H*. Hydrogen bonding between the exocyclic nitrogen and the sulfur atom suggest proximity of

the 4-aminopyrimidino substituent to the C_3 position of the triazol-3-thione when the molecule lies in a 'V-conformation'. This pose is of interest in the target salt, as it offers the promise of intramolecular deprotonation to give the catalytically active carbene form.

2.3.1.3 Synthesis of 2-hydroxypropyl thione analogue

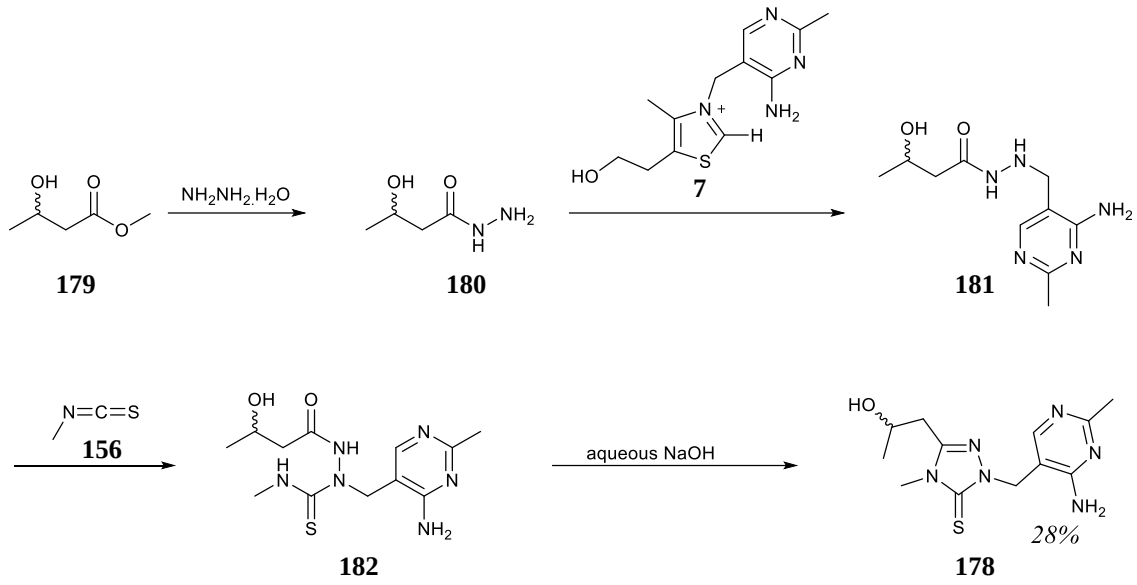

Scheme 2.30 Synthesis of 2-hydroxypropyl thione analogue 178

Further, in order to test alternative mimics for TPP **63** dependent enzyme screening, we elected to make the 2-hydroxypropyl analogue **178** as, in terms of the exocyclic hydroxy positioning, it is the closest in structure to our target triazolium catalyst mimic **159**. Starting with methyl 3-hydroxybutyrate **179**, which was commercially available as a racemic mixture, and reacting it with hydrazine monohydrate, the reaction mixture gave a solid precipitate within an hour of stirring, without external intervention (Scheme 2.30). The resulting solid, after removal of excess hydrazine monohydrate by filtration, was washed with cold hexane and dried to give the target hydrazide **180**. Reacting the hydrazide **180** with thiamine **7** gave the N2 alkylation intermediate **181**, which was dried and used in the next step without further purification. Treatment of compound **181** with methyl isothiocyanate **156** gave the carbothioamide **182** in solution, however, unlike the other carbothioamides previously prepared, the solution had to be cooled to 5 °C in order to observe a precipitate. Refluxing carbothioamide derivative **182**

in aqueous sodium hydroxide completed the cyclization step. Upon cooling the reaction mixture, a white amorphous precipitate was observed and filtered to give the corresponding thione **178** in overall low yield (28%).

Attempts at recrystallization from a hot water solution gave 'quasi-crystals' which were not suitable for further analysis. However, after washing **178** with deionized water, and upon making up a saturated solution in 1M HCl and leaving to slowly evaporate in a partly covered sample vial over several weeks, large cuboid-shaped crystals were observed suitable for X-ray crystallographic analysis.

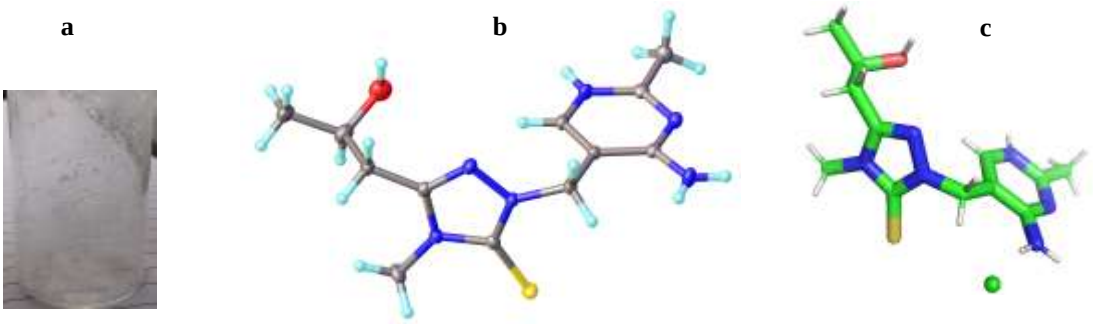

Figure 2.9 Crystal structure of 2-hydroxypropyl thione analogue 178 (a) solid crystal (b) crystal structure (c) packing diagram showing chloride counterion

X-ray analysis of thione **178** shows the exocyclic amino nitrogen to be further away from the triazolium C3. This may simply be the result of preferential solid-state lattice packing. Also, the thione **178** appears to be stable in both acidic and basic conditions, even under reflux. The oxygen bound to carbon appears to be chiral, but only one enantiomer is shown in the crystal structure (Figure 2.9). The solid-state crystal packing show both enantiomers as mirror images of each other with the respective chloride counterion (green ball) sandwiched between each pair. The oxygen atom shown in red alternatively point upward and downwards in each crystal lattice column. The chloride atom in the centre appears to have a strong coordinating influence on the shape of the crystal lattice at the thione structure seems centred around it.

Figure 2.10 X-ray solid state crystal lattice diagram of isopropyl thione analogue 178 showing enantiomers

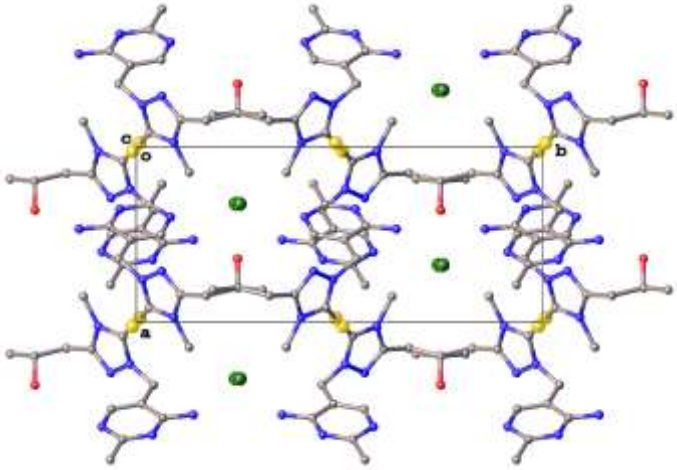

2.3.2 Synthesis of analogues of triazolium mimic 159

The following section details preparation of analogues of triazolium mimic **159** with methyl, isopropyl and hydroxypropanoyl linkers.

2.3.2.1 Synthesis of methyl triazolium tetraphenyl borate analogue 183

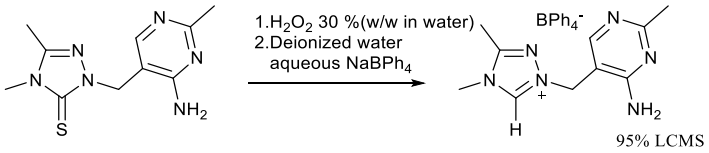

168 **183**

Scheme 2.31 Desulfurization of methyl thione 168 to give target triazolium analogue 183

Desulfurization of thione **168** to give triazolium salt **183** was carried out by treating with hydrogen peroxide in deionized water. The reaction was monitored by LCMS, evidenced by the complete disappearance of the peak at retention time 0.25 minutes due to starting thione **168** and appearance of a single peak at 0.19 minutes with m/z 219 attributed to the target salt **183**. Initially hydrochloric acid was added to access the chloride salt but attempts at recrystallization from the solution preferentially gave common table salt crystals. Upon completion, freshly prepared sodium tetraphenyl borate in deionized water was added which

instantaneously gave a white precipitate. The precipitate was filtered and washed with deionized water and dried to give the methyl triazolium analogue **183**.

Attempts to recrystallize from DCM were unsuccessful because **183** dissolves to give a clear solution but upon evaporation, leaves an orange oily residue. Methanol and ethanol both gave semi-shiny white solids upon slow evaporation of their saturated solutions. A 1:1 mixture of water: ethanol resulted in a white amorphous powder, which suggests that the presence of water favours faster precipitation of the salt from solution. Finally, making up a concentrated solution of the salt in 50:50 methanol: dichloroethane at 50°C in a glass vial and very slow cooling to room temperature gave big shiny crystals of the salt. The solution was noticed to go orange due to some conversion of the tetraphenylborate ion to the triphenyl boron compound, but the crystals remained colourless.

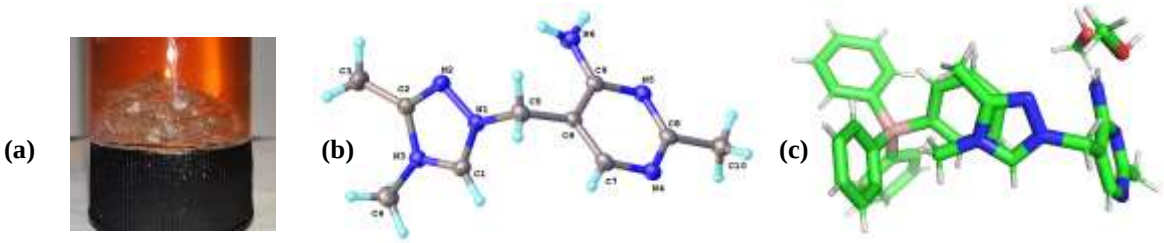

Figure 2.11 Crystal structure of the methyl triazolium tetraphenylborate analogue 183 (a) solid crystals (b) cation (c) packing data showing tetraphenylborate counterion and solvent methanol

The results show the clean conversion of the thione to the triazolium salt with retention of the 1,2,4-triazole ring. The NCN bond angle increases on going from the thione **168** (103.52°) to the triazolium salt **183** (107.7°) by 4.2° on forming the cation. ^{1}H NMR spectra in DCl confirms the presence of the acidic C3-H atom by observable exchange with deuterium.

2.3.2.2 Synthesis of 2-hydroxypropyl triazolium tetraphenyl borate analogue 184

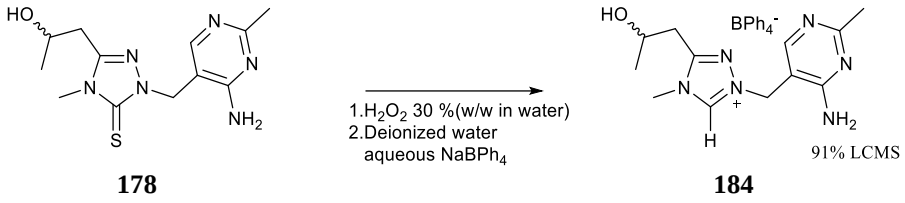

Scheme 2.32 Synthesis of 2-hydroxypropyl triazolium tetraphenyl borate analogue 184

Desulfurization of thione **178** to give triazolium salt **184** was carried out by treating with hydrogen peroxide in deionized water. The reaction was monitored using LCMS, evidenced by the complete disappearance of the peak at retention time 0.23 minutes due to starting thione **96** and appearance of a single peak at 0.19 minutes with m/z 263 attributed to the target salt **184**. Upon completion, freshly prepared sodium tetraphenyl borate in deionized water was added which instantaneously gave a white precipitate upon contact with the reaction mixture. The precipitate was filtered off and washed with deionized water and dried to give the methyl triazolium analogue **184**. Recrystallization was achieved by making up a supersaturated solution of the salt in dichloroethane and methanol at 40 °C in a glass vial and leaving to cool slowly, in a darkened fume hood, to prevent decomposition of the anion into triphenylborane.

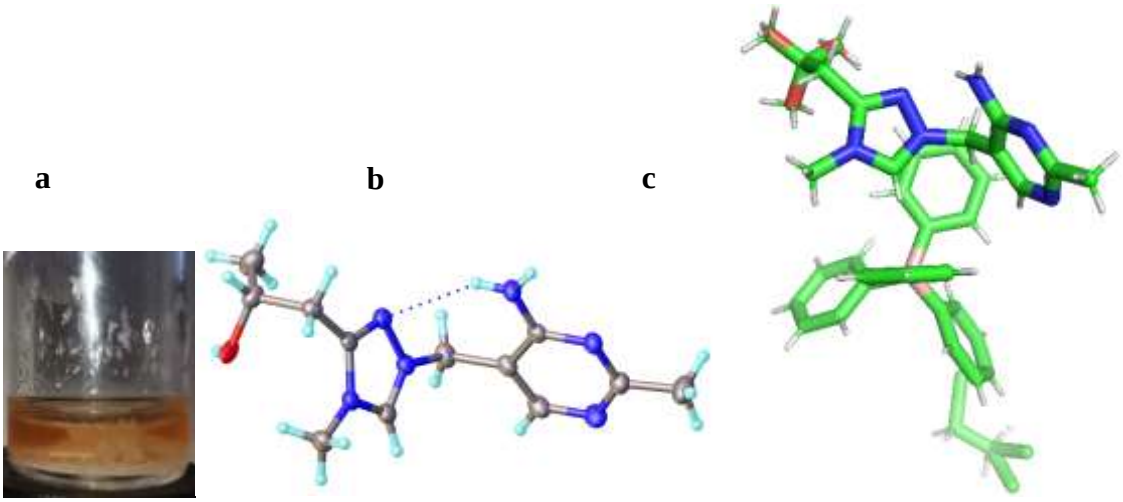

Figure 2.12 Crystal Structure of 2-hydroxypropyl triazolium tetraphenyl borate salt 184 (a) solid crystal sample (b) cation only (c) packing data showing tetraphenylborate counterion

In the crystal packing diagram, (Figure 2.12) the tetraphenyl borate counterion lies in proximity directly underneath the triazolium ring of the cation, suggesting a strong coordination between the ion pair. The exocyclic nitrogen sits within hydrogen bonding distance of the N1 triazolium atom, which shows that the extra nitrogen introduced to the mimic on going from the thiazole to the triazole may increase its propensity for binding at TPP dependent enzyme active sites. Again, the N2 of the triazole serves as the bridging atom as desired, with the NCN bond angle increasing on going from the thione to the triazolium cation.

2.3.3 Synthesis of 4-hydroxybutyl triazolium tetraphenyl borate analogue 185

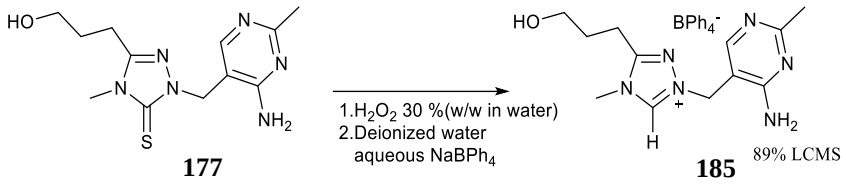

Scheme 2.33 Synthesis of 2-hydroxypropyl triazolium tetraphenyl borate analogue 185

Desulfurization of thione **177** to give triazolium salt **185** was carried out by treating with hydrogen peroxide in deionized water. The reaction was monitored by LCMS, evidenced by the complete disappearance of the peak at retention time 0.25 minutes due to starting thione **177** and appearance of a single peak at 0.19 minutes with m/z 219 attributed to the target salt **185**. Upon completion, freshly prepared sodium tetraphenyl borate in deionized water was added, which instantaneously gave a white precipitate. The precipitate was removed by filtration, washed with deionized water and dried to give the methyl triazolium analogue as a white powder **185**. Attempts at crystallization are still ongoing and all other characterization data confirm purity.

2.4 Conclusions

As outlined in the aims of this chapter, the triazolium mimic of thiamine was successfully prepared and isolated using a novel synthetic route, as this compound has not been previously reported in the literature to the best of our knowledge. The route employs inexpensive and

commercially available starting material with all reactions carried out in water or ethanol. Thiamine was used to sacrificially to introduce the intricate 4-aminopyrimidinyl side substituent.

In addition to the prime triazolium mimic of thiamine, three other analogues were also prepared starting with different esters and a lactone (Figure 2.13). These salts will be used in the next chapters for kinetic studies. X-Ray crystal structures were obtained for structural elucidation by employing the use of sodium tetraphenyl borate salt.

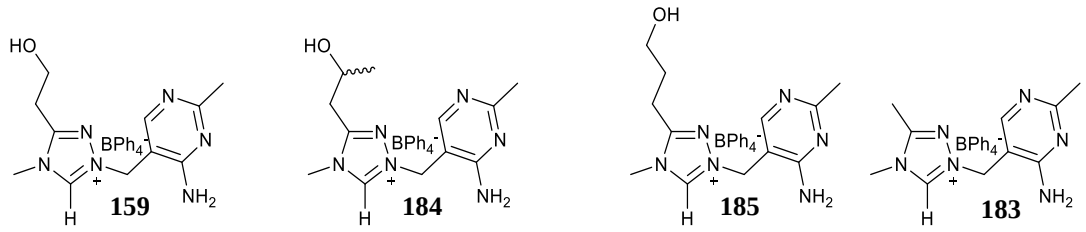

Figure 2.13 Novel triazolium mimics of thiamine prepared from newly developed facile synthetic route

Furthermore, during the synthesis of the triazolium mimics, stable thione intermediates were also isolated in the penultimate step (Figure 2.14). These were recrystallized and fully characterized as they have not been previously reported in the literature to the best of our knowledge. The thiones are bench stable under ambient laboratory conditions, samples prepared remained pure and dry in an open sample vial for three years and counting.

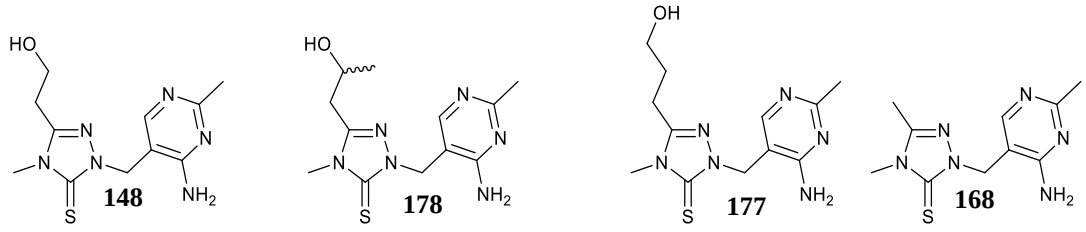

Figure 2.14 Thione intermediates isolated and fully characterized

The use of methylisothiocyanate **156** to provide the 4-methyl substituent was successful and gives and easy route to derivatization of the triazolium ring on the four position. Bench stable

hydrazides (Figure 2.15) were also isolated in the first step of the synthesis. All hydrazides isolated present as crystalline solids and were fully characterised.

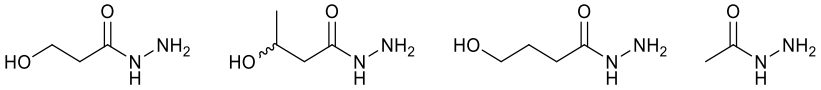

150 **169** **174** **165**

Figure 2.15 Hydrazide crystals successfully isolated from the first step of the synthetic route

2.5 References

1. R. R. Williams and J. K. Cline, *J. Am. Chem. Soc.*, 1936, **58**, 1504-1505.
2. P. Attaluri, A. Castillo, H. Edriss and K. Nugent, *Am J Med Sci*, 2018, **356**, 382-390.
3. A. Chatterjee, N. D. Abeydeera, S. Bale, P. J. Pai, P. C. Dorrestein, D. H. Russell, S. E. Ealick and T. P. Begley, *Nature*, 2011, **478**, 542-546.
4. J. A. Maupin-Furlow, *B Group Vitamins-Current Uses and Perspectives*, 2018, 9-31.
5. R. Leonardi and P. L. Roach, *J. Biol. Chem.*, 2004, **279**, 17054-17062.
6. M. E. Webb, A. Marquet, R. R. Mendel, F. Rebeille and A. G. Smith, *Nat. Prod. Rep.*, 2007, **24**, 988-1008.
7. S. E. Bocobza and A. Aharoni, *Trends Plant Sci.*, 2008, **13**, 526-533.
8. J. Rehbein, S.-M. Ruser and J. Phan, *Chem. Sci.*, 2015, **6**, 6013-6018.
9. S. K. Yusufzai, H. Osman, M. S. Khan, B. M. A. Razik, S. Mohamad, O. Sulaiman, J. A. Gansau, N. Johansah, M. O. Ezzat, T. Parumasivam, M. M. Rosli and I. A. Razak, *Med. Chem. Res.*, 2018, **27**, 1647-1665.
10. L. Wang, Z.-G. Ma, X.-J. Wei, Q.-Y. Meng, D.-T. Yang, S.-F. Du, Z.-F. Chen, L.-Z. Wu and Q. Liu, *Green Chem.*, 2014, **16**, 3752-3756.
11. X. Tang, J. Yang, Z. Zhu, M. Zheng, W. Wu and H. Jiang, *J. Org. Chem.*, 2016, **81**, 11461-11466.
12. T. Miura, Y. Funakoshi, Y. Fujimoto, J. Nakahashi and M. Murakami, *Org. Lett.*, 2015, **17**, 2454-2457.
13. H. M. L. Davies and J. S. Alford, *Chem. Soc. Rev.*, 2014, **43**, 5151.
14. X. Wang, X. Qiu, J. Wei, J. Liu, S. Song, W. Wang and N. Jiao, *Org. Lett.*, 2018, **20**, 2632-2636.
15. G. Shelke, V. Rao, M. Jha, T. Cameron and A. Kumar, *Synlett*, 2015, **26**, 404-407.
16. N. Yang and G. Yuan, *J. Org. Chem.*, 2018, **83**, 11963-11969.
17. A. Tam, I. S. Armstrong and T. E. La Cruz, *Org. Lett.*, 2013, **15**, 3586-3589.
18. Z. Chen, H. Li, W. Dong, M. Miao and H. Ren, *Org. Lett.*, 2016, **18**, 1334-1337.
19. J. Q. Liu, X. Shen, Y. Wang, X. S. Wang and X. Bi, *Org. Lett.*, 2018, **20**, 6930-6933.
20. P. Yin, W.-B. Ma, Y. Chen, W.-C. Huang, Y. Deng and L. He, *Org. Lett.*, 2009, **11**, 5482-5485.

Chapter Three

3 Deuterium Exchange Experiments

Foreword

Given that the loss of proton is essential to understanding catalytic activity of these compounds, it is useful to accurately quantify the acidity constant of thiamine in comparison to the novel triazolium mimics made in the previous chapter. This chapter presents work in estimating the kinetic acidities of triazolium salts derived from thiamine. Section 3.1 gives an overview of the reported methodology to determine pK_a values of azolium salts. Adaptation of the H/D exchange method to obtain experimental values of the C3-H acidity of the triazolium mimics discussed in Chapter 2 is given in Section 3.2. Discussions of the observed trends and comparison between this work and reported literature values are detailed in Section 3.3. Finally, Section 3.4 gives a summary of the results obtained.

3.1 Introduction

This section will overview the relevant pK_a literature for a range of conjugate acids of N-heterocyclic carbenes, in particular triazolium salts. Firstly, detailed reported literature procedures to determine carbon acid pK_a values for triazolium salts will be discussed. In addition, the results of previous publications from our research group proposing various mechanisms for deuterium exchange will be explained.

3.1.1 Procedures to determine carbon acidity

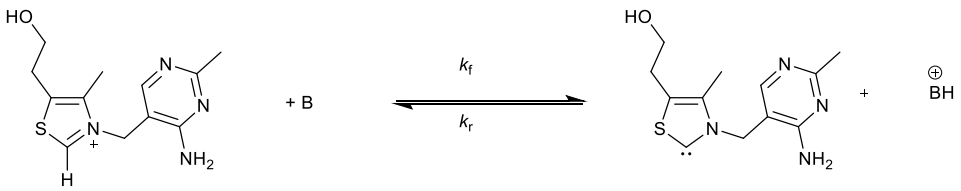

7 **7'**

Scheme 3.1 Thiamine 7 dissociation to give its active carbene form 7'

Thiamine **7** has been long known to catalyse the benzoin condensation following deprotonation in the presence of a base to give its active carbene form 7**'** (Scheme 3.1) in a reaction similar to the action of cyanide on benzaldehyde. Several techniques exist to rank the pK_a values of

carbenes as K_a values are less portable for direct comparison between conjugate acids[1] (**Equation 3.1**). The pK_a of thiamine has been estimated by several research groups giving values ranging from 12 -19[2]. The estimate reported by Washabaugh[2] of ~ 18 employed a robust and reliable kinetic approach.

$$pK_a = -\log K_a \qquad \textbf{Equation 3.1}$$

This technique employs the link between the rate constant for deprotonation of the conjugate acid to give the active carbene and the reverse reprotonation to give the acid form (Equation 3.2). The forward step is much slower than the reverse protonation as established for thiamine (Scheme 3.1). Measurement of the forward deprotonation step is achieved by isotopic replacement/exchange. Using plots of observed rate constants for H/D exchange versus p*D* for several thiazolium salts, Washabaugh found that deuteroxide ion also contributes to the overall forward rate. The reverse rate is relatively fast, e.g., for diphenylcarbene, at the diffusion limit in water-based solutions[1b]. Thiazolium salts including thiamine **7** used in these experiments remained otherwise unchanged during the exchange process with no parallel reactions.

Using the pD-rate profiles for deuterium exchange, the forward rate constant for carbene formation could be estimated. In addition, Washabaugh repeated the process with the labelled C_2-Deuterium and C_2-Tritium and found kinetic isotope effects on deprotonation of between 2.9 – 14.7 for H/D and H/T. Also, these data showed a marked discrepancy from the (Swain-Schaad) relation expected for a process involving rate-limiting proton transfer. This deviation from the Swain-Schaad equation confirms the presence of significant internal return where the reverse re-protonation is competitive with diffusional reorganization of solvent and provides evidence that reprotonation is at the diffusional limit. These authors using rate constants for H/D exchange for k_f and a value of $k_d \sim 10^{10}$ s^{-1} for k_r, pK_a values of 17-19 were

determined for the thiazolium salts studied. (Equation 3.3). K_a^{BH} refers to the acid dissociation constant of the conjugate acid of the base employed, B.

$$\frac{K_a^{Thiamine}}{K_a^{BH}} = \frac{k_f}{k_r} \qquad \textbf{Equation 3.2}$$

$$log\left(K_a^{Thiamine}\right) = log\left(K_a^{BH} \times \frac{k_f}{k_r}\right)$$

$$\mathrm{p}K_a^{Thiamine} = log K_a^{BH} + \log\frac{k_r}{k_f} \qquad \textbf{Equation 3.3}$$

The result was followed up by Amyes *et al.*[3] using imidazolium ions as substrates and at constant ionic strength maintained by potassium chloride (Table 3.1). Experimental rates for deprotonation for the imidazolium substates studied were markedly lower than for corresponding thiazolium ions previously reported by Washabaugh in literature[2]. The pK_as reported for the imidazolium salts **186–191** were in the range 21.2 – 23.8 units. The presence of bulky dialkyl substituents on the imidazolium ring tends to favour a relatively lower pK_a value since electron donating alkyl substituents stabilise the cationic conjugate acid relative to the formally neutral carbene.

Table 3.1 pK_as of imidazolium salts reported by Amyes[3]

Salt	k_{DO} (M^{-1} s^{-1})	k_{HO} (M^{-1} s^{-1})	pK_a
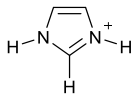 **186**	3.7×10^1	1.5×10^1	23.8
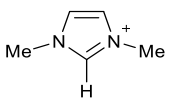 **189**	2.5×10^2	1.0×10^2	23.0

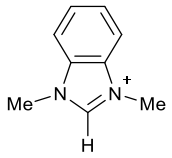 **190**	5.74×10^3	2.39×10^3	21.6
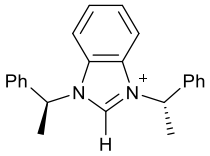 **191**	1.48×10^4	6.17×10^3	21.2

Amyes also discussed variations in carbon acidity between substituted thiazolium, imidazolium and oxazolium salts (Table 3.2)[3]. Oxazolium salt **194** had the lowest pK_a (16.9) of all the salts studied due to the greater electronegativity of oxygen relative to sulfur and nitrogen which destabilises the cationic conjugate acid relative to the neutral carbene. The imidazolium salts **186** and **189** were reported to have a higher pK_a values by around 3.7 units than corresponding thiazolium substrates **192** and **193**. However, although the thiazolium salts have a lower pK_a than the imidazolium salts, the imidazolylidene carbenes are more stable relative to the neutral azole than the corresponding thiazolylidene carbenes. This was shown to be the case by Amyes[3] and was attributed to the better π-donating capacity of nitrogen to carbon than sulfur[4].

Table 3.2 Rate constants for C-2 proton exchange for azolium substrates discussed by Amyes[3]

Salt	k_{DO} (M^{-1} s^{-1})	k_{HO} (M^{-1} s^{-1})	pK_a
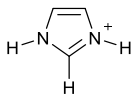 **186**	3.7×10^1	1.5×10^1	23.8
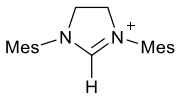 **187**	1.19×10^{-3}	4.96×10^3	21.3

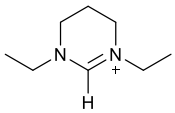 **188**	3.5×10^{-3}	1.45×10^{2}	27.8
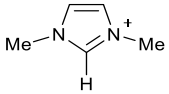 **189**	2.5×10^{2}	1.0×10^{2}	23.0
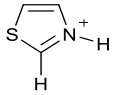 **192**	3.1×10^{5}	1.3×10^{5}	19.9
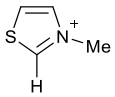 **193**	8.2×10^{5}	3.4×10^{5}	19.5
 **194**	7.2×10^{7}	3.0×10^{7}	16.9

Several imidazolium, dihydroimidazolium and tetrahydropyrimidinium salts have been investigated by Higgins[5] to further probe their observed kinetic acidities (Table 3.2). In this report the imidazolium salts were shown to have lower pK_as very similar to the corresponding substituted dihydroimidazolium salts. The tetrahydropyrimidinium salts had much higher pK_a values of ~28, which is about 8 units greater than the imidazolium salts studied.

Massey et al., using the same technique, presented an elegant assessment of pK_a values for a range of carbene heterocycles based on the triazolium structure[6]. Exchange experiments were monitored for twenty triazolium salts in deuterated solutions at a range of pD values with ionic strength kept constant at I = 1.0 (KCl) and at 25 °C. At higher pD's, the acidity was maintained using acetic acid buffer solutions, hence the effect of buffer catalysis on the experimental rate constant for H/D exchange was investigated. This was done using two model substrate azolium salts **195** and **196** (Figure 3.1). Buffer catalysis was not observed for these exchange

experiments using the model salts. Previous reports in the literature also did not observe buffer catalysis in effect for several carbene precatalysts studied[3]. This means the process follows a specific base catalysed rate law.

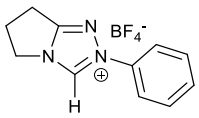

195

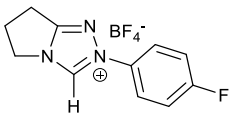

196

Figure 3.1 Model substates used to probe the effect of buffer catalysis on observed pseudo-first-order rate constant for H/D exchange k_{ex}

Most of the triazolium salts studied by the Massey *et al.* show a positive correlation between the rate constant k_{ex} and p*D*. The fit of log k_{ex} vs p*D* with Equation 3.4 for most of the substrates studied is a straight line of slope unity (K_w represents the ionic product of deuterium oxide[7] at 25 °C, $10^{-14.87}$, γ_{DO} represents the activity coefficient for deuteroxide). This first-order dependence on DO^- for nearly all the salts studied supports hydrogen-deuterium exchange through mechanism A (Scheme 3.2).

$$\log k_{ex} = \log\left(\frac{k_{DO}K_w}{\gamma_{DO}}\right) + pD \qquad \textbf{Equation 3.4}$$

$$k_{ex} = k_{\mathrm{DO}}[DO^-] \qquad \textbf{Equation 3.5}$$

The abstraction of a proton from generic triazolium mimic **197** by deuteroxide ion to form intermediate **198●HOD** initiates pathway A (Scheme 3.2). Reorganization of intermediate **198●HOD** to **198●DOL** (L = H or D) for facile replacement of deuterium and subsequent deuteration gives deuterated precatalyst **197d**. Given that the solvent concentration (~ 55 M) is far greater than substrate concentration (~ 2 mM), the deuteration step is essentially

irreversible, therefore, the observed pseudo-first-order rate constant depicts the slowest step, formation of **198●HOD** from substrate **197** and deuteroxide.

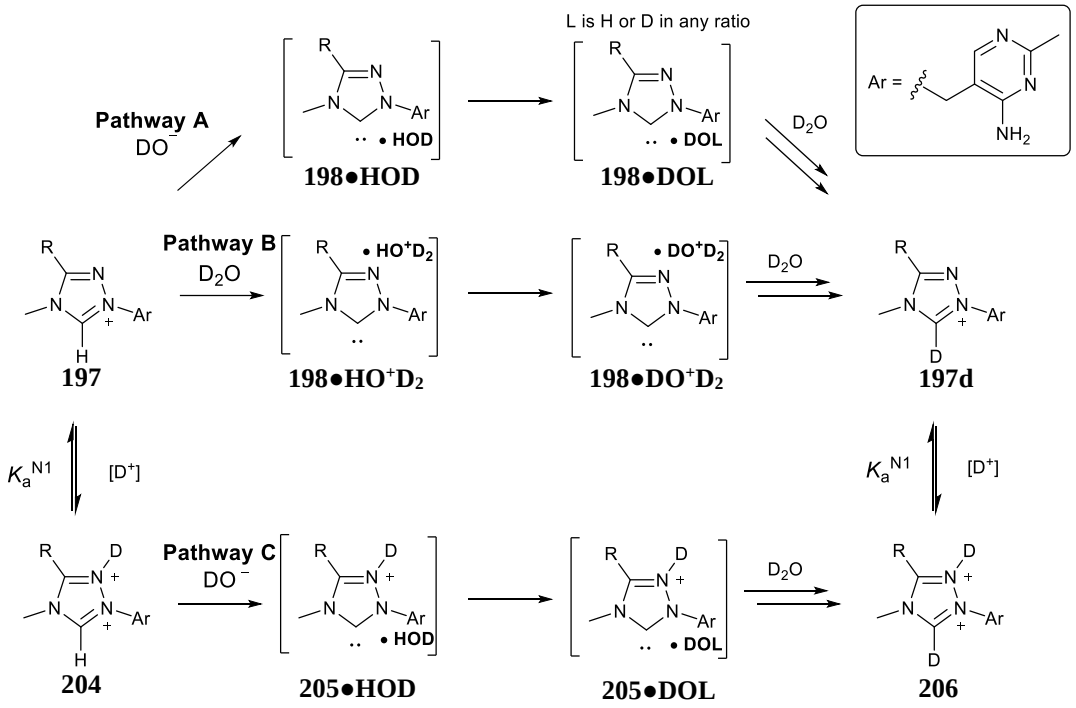

Scheme 3.2 Proposed pathways for the exchange of proton for deuterium of representative mimic 197

Analysis of the log k_{ex} **−** p*D* profiles shows that for some of the salts studied **200 – 202** (Figure 3.2) at p*D*s less than one, the correlation between log k_{ex} and p*D* deviates from unity, suggesting the onset of H/D exchange through alternative pathways. In particular, the pentafluorophenyl triazolium salt **203** displays a more distinct deviation from the trend compared with all other salts. The onset of deviation from a slope of unity starts at p*D* 2 and at the lowest p*D* values, a significant downward break is observed. Since the ionic strength of all solutions prepared was maintained at I = 1.0 using potassium chloride where necessary, attributing this observation to a medium effect was ruled out. To further probe this, exchange was initiated in 1.24 and 2.0 M DCl, and corroborates the downward break previously observed.

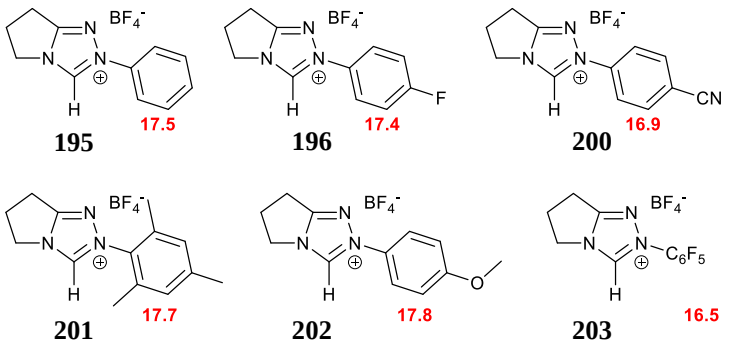

Figure 3.2 Select triazolium salts reported by O'Donoghue and co-workers, p*K*as shown in red

The deviation of the plots from unity slope at lower p*D*s was explained by the presence of other mechanisms for exchange in addition to pathway A. Proton abstraction from triazolium ion **197** by solvent deuterium oxide could give intermediate **198.HOD**$_2^+$. Given that log k_{ex} is not p*D*-independent and continues to decrease with p*D*, an additional pathway involving protonation at N1 must also be inferred. As one mechanistic option, deuteration **197** at N1 to give dicationic species **204** reduces the amount of substrate available for the two previous pathways described (A and B) and may explain the continued partial dependence of log k_{ex} on p*D* at lower p*D*s[8]. Subsequent proton abstraction at C3 of **204** by deuteroxide ion would give a monocationic intermediate **205●HOD**, followed by rearrangement and deuterium transfer to give dicationic exchange product **206**.

$$\log_{10}k_{ex} = \log_{10}\left[\frac{K_a^{N1}\left(\left(\left(\frac{k_{DO}K_w}{\gamma_{DO}}\right)\right)10^{pD}\right)}{\left(K_a^{N1} + 10^{-pD}\right)}\right]$$

Equation 3.6

The authors posit that the presence of pathway A is well modelled by Equation 3.6, although it does not apply to the remaining two pathways (B and C). Data sets for the pentafluoro phenyl salt **203** is incompatible at lower p*D*s with Equation 3.6, therefore, a modified version to account for both pathways B and C with protonation at N1 is needed.

Chiral triazolium salts (Figure 3.3) were also accessed for exchange at C3-H to determine kinetic acidities. Due to their insolubility in water, acetonitrile (33% v/v) was used as a cosolvent to dissolve the substrates. To gauge the effect of acetonitrile on rates of exchange, triazolium salts **195** (N-phenyl) and **203** (N-pentafluoro phenyl) were studied in D_2O/perdeuterated acetonitrile (2:1 D_2O/CD_3CN) as well as D_2O only. At p*D*s above 0.06, exchange was complete before the acquisition of the first spectrum for compound **203**. However, for all the other salts, spectra could be acquired for p*D*s up to 3.6. The onset of altered dependence on p*D* occurred at higher p*D* than for deuterium oxide only solutions for **208**. In general, a positive correlation of log k_{ex} with p*D* was observed for all the chiral salts studied (**200**–**203**) at p*D* > 2.

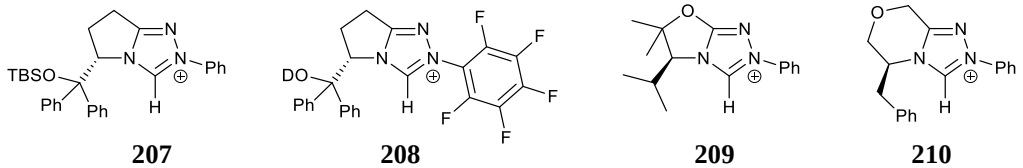

Figure 3.3 Chiral triazolium salts studied by the O'Donoghue group

Electron-withdrawing N-aryl substituents tend to favour an increase in pK_a, for example the N-pentafluorophenyl salt **203** (pK_a = 16.5) is 1.0 unit lower than for corresponding N-phenyl salt **195** (pK_a = 17.5) (Figure 3.2). This is expected as better stabilization of the formally neutral carbene relative to the cationic triazolium ion is achieved by electron-withdrawing substituents. Also, the electron donating N-paramethoxyphenyl salt **202** (pK_a = 17.8) is 0.3 units higher than for corresponding N-phenyl salt **195** (pK_a = 17.5) which reflects destabilization of the neutral carbene relative to its conjugate acid. A similar trend is seen in the other three N-aryl substituted triazolium salts with the N-parafluoro **196** and **200** cyano showing a lower pK_a than for the N-phenyl salt. It is also noteworthy to mention with relevance to the present project that the predicted C3-H pK_a for dicationic triazolium ion **204** is lower than for monocationic **197** i.e. the effect of N1 protonation is to decrease pK_a at C3-H. So far as stated earlier there has

not been a direct like for like comparison of triazolium based thiamine derivative. The following section attempts to provide experimental pK_a values for these direct thiamine mimics.

3.2 Results

The following section details experimental procedures for obtaining pseudo-first-order rate constants of exchange from NMR data, second-order deuteroxide-catalysed rate constants and pK_a determination of several azolium salts.

3.2.1 Deuterium Exchange Kinetic Analysis of Triazolium Salts

Triazolium salt analogues incorporating the 2−(4-amino-2-methyl-pyrimidinyl) ring (Figure 3.4) were monitored for kinetic hydrogen/deuterium replacement in D_2O at 25 °C, at constant ionic strength I = 1.0 (KCl) and at a spread of pD values. Replacement of the C_3-H hydrogen for deuterium was monitored to completion by proton NMR spectroscopy evidenced by the disappearance of the corresponding singlet peak at ~ 9.9 – 9.5 ppm. These data informed the quantification of pseudo-first and second-order rate constants for H/D exchange, and ultimately, assessment of C_3-H acidity values. Novel triazolium salts **144** and **183 – 185** were prepared as described in Chapter 2. Residual sodium tetrafluoroborate is present in all these samples. However, we believe this will have minimal effect on the kinetic H/D exchange data as saturating ionic strength conditions are used (I = 1.0 (KCl)). The tetrafluoroborate salt was accessed by using sodium tetrafluoroborate in place of sodium tetraphenyl borate in the final oxidation step of the thione leading to formation of the triazolium salt. Furthermore, the tetrafluoroborate anion is non-nucleophilic and counterion effects in aqueous solution on H/D exchange have previously been shown to be similar or within experimental error (k_{ex} ± 10%)[6] . Apart from a small amount residual of $NaBF_4$ these salts were pure by NMR spectroscopy

(^{1}H, ^{13}C, COSY, ^{13}C DEPT) and high-resolution mass spectrometry. N-phenyl triazolium salt **195** was prepared according to a known literature procedure. The H/D exchange of this salt has been studied previously by the group, thus it is included as a reference for comparison. Thiazolium salts **7** (Cl^- and NO_3^-) and dimethyltriazolium salt **212** were purchased from Sigma Aldrich. H/D exchange for dimethyl triazolium salt **212** has not been previously reported. Jencks reported an aqueous pK_a value of 18 for salt **7-Cl**.[2]

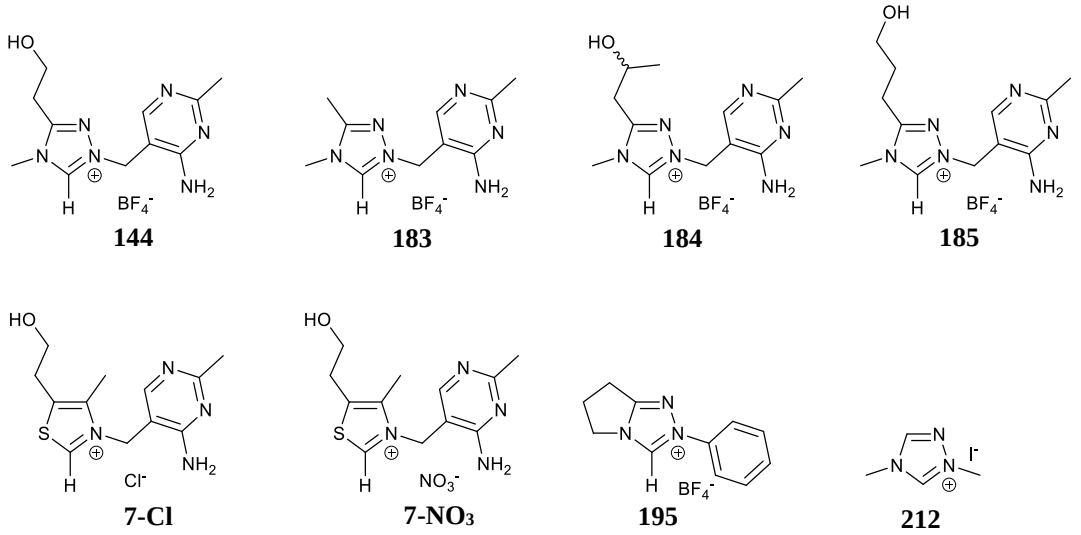

Figure 3.4 Triazolium analogues of thiamine 7 studied and selected triazolium precatalysts

3.2.2 Determination of pseudo-first-order rate constants for deuterium exchange (k_{ex})

Reaction to monitor replacement of hydrogen for deuterium was normally commenced by preparing a solution of DCl, formic or acetic acid buffer in D_2O for p*D* values between 0 – 4.5 at 25 °C and ionic strength I = 1.0 (KCl) with CH_3OD as internal standard (0.5 mM). Stock solutions of the substrate in D_2O could not be prepared owing to the rapid C3−H/D exchange under these conditions, above p*D* 4-5. For the procedure, 1.5 mL of buffer at 25 °C was added to ~1 mg of the sample, and 0.75 mL of the solution put directly in an NMR tube to be analysed immediately, while the p*D* of the remaining solution in the mixing vial was taken. The

substrates are very soluble and dissolve instantaneously. After the exchange was complete, the solution in the NMR tube was transferred to a vial and a p*D* value taken. This was found to remain the same within error (±0.03) compared to the value at the start of the experiment.

In all cases, the rate of replacement of hydrogen for deuterium was monitored by the disappearance of the singlet peak due to the substrate C3−*H* (A_{C3H}) compared to the internal standard monodeuterated methanol C*H*$_3$OD (A_{CH3OD}) at 3.3. ppm. Equation 3.7 was used to compute the proportion of unexchanged salt remaining *f*(s), and by extension, pseudo-first-order rate constants for replacement using a semilogarithmic graph of *f*(s) versus time (Equation 3.8).

$$f(\mathrm{s}) = \frac{\left(\frac{A_{C3-H}}{A_{CH3OD}}\right)\mathrm{t}}{\left(\frac{A_{C3-H}}{A_{CH3OD}}\right)\mathrm{t} = 0} \qquad \textbf{Equation 3.7}$$

$$f(\mathrm{s}) = \mathrm{e}^{-k\mathrm{t}}$$

$$\ln f(\mathrm{s}) = -k_{\mathrm{ex}}\mathrm{t} \qquad \textbf{Equation 3.8}$$

3.2.2.1 2-[(4-amino-2-methylpyrimidin-5-yl)methyl]-4-methyl-4*H*-1,2,4-triazol-3-ium-5-yl]ethanoyl tetrafluoroborate

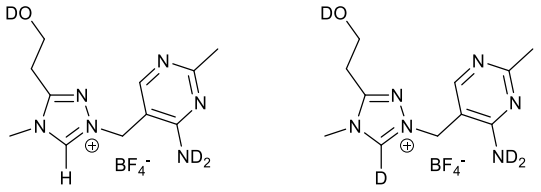

144 **144d**

Scheme 3.3 Hydroxyethanoyl triazolium mimic 144 and deuterated analogue 144d

Triazolium tetrafluoroborate salt **144** was converted to **144d** (Scheme 3.3) at a range of p*D* values, monitored by ^{1}H NMR spectroscopy (400 MHz) to enable determination of pseudo-first-order rate constants.

Figure 3.5 presents an overlay of spectra acquired for the reaction at p*D* 3.44 at three intervals during the experiment. The disappearance of the singlet peak due to the triazolium C3-H (A) at 9.71 ppm is evidence for replacement of hydrogen for deuterium. The progress of replacement of hydrogen for deuterium was quantified with respect to the singlet signal associated with the three equivalent non-acidic hydrogens of the internal standard, mono-deuterated methanol (IS)(CH_3OD) at 3.31 ppm.

The signal due to the pyrimidinyl proton (B) of the triazolium salt **144** appear as a singlet at 8.14 ppm. The large singlet at 8.1 ppm is owing to the formyl proton of the formic acid buffer. The bridging methylene protons (C) attached to the cationic nitrogen atom, joining the two aromatic rings, give a singlet peak at 5.54 ppm. The terminal methylene of the propyl alcohol side chain $-CH_2CH_2OD$ (D) appears as a triplet at 3.84 ppm. The signal corresponding to the triazolium ring N−methyl (E) appears as a singlet at 3.72 ppm. The pendant alcohol methylene, proximal to the triazolium ring $-CH_2CH_2OD$ (F) corresponds to the triplet at 3.15 ppm. A signal corresponding to the pyrimidinyl methyl (G) appear as a singlet at 2.64 ppm. Apart from the C_3H (A) all other peaks (B-G) remained the same and integrated equivalently for the

duration of the experiment. All the peaks were integrated relative to the internal standard, monodeuterated methanol, and remained constant, which confirms that only exchange of the C_3H for deuterium is occurring under these reaction conditions and timescale.

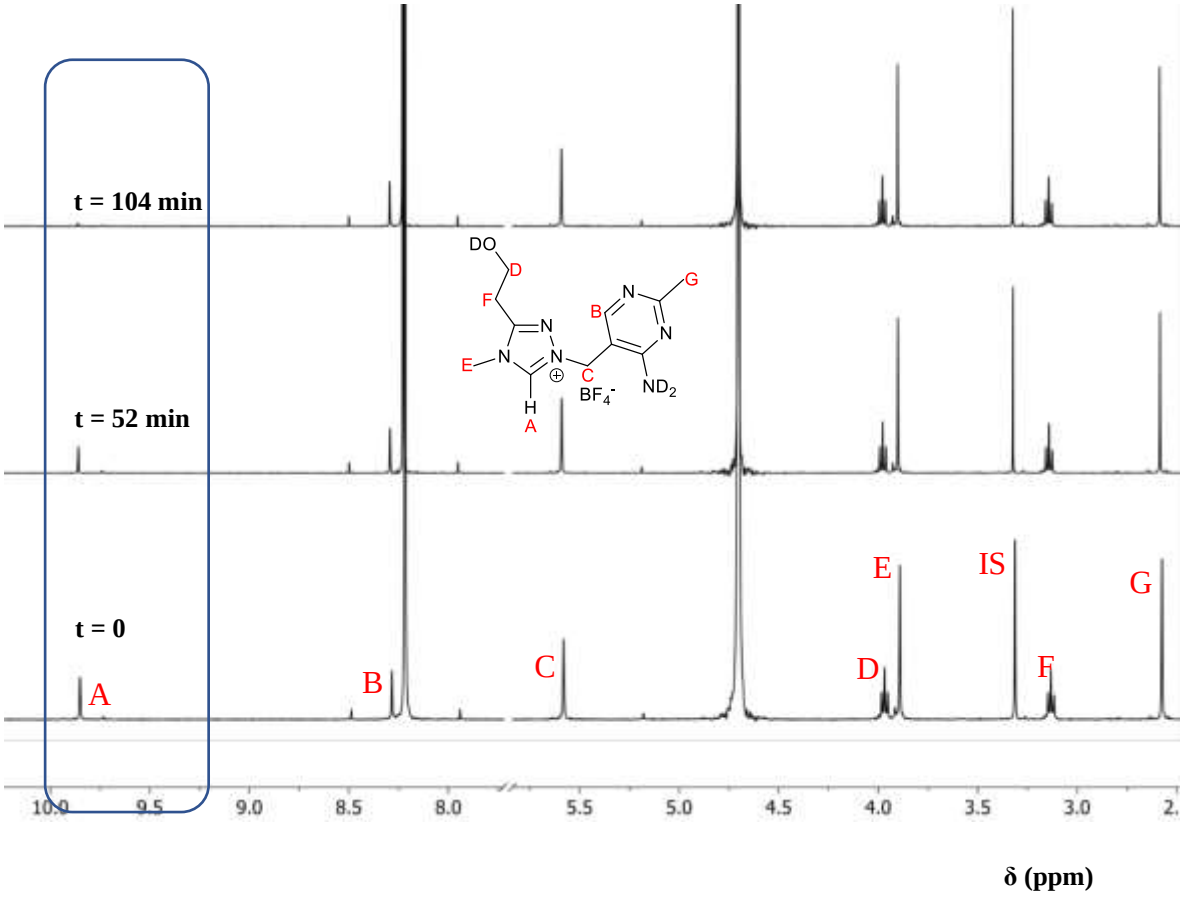

Figure 3.5 **Representative ^{1}H NMR spectra at 400 MHz of triazolium salt 144 (p*D* 3.44) in formic acid buffer obtained during exchange of the C3-H (s, 9.6 ppm) for deuterium in D_2O at 25 °C and *I* = 1.0 (KCl) [Internal standard, monodeuterated methanol CH_3OD (s, 3.31 ppm)]**

Pseudo-first-order rate constants for substitution of proton for deuterium at the C_3-H position were derived from the gradient of the semi-logarithmic plots of the fractions of exchange of substrate *f*(s) against time at each p*D* (3.44). Previous work done in the group established the activity coefficient γ_{DO} = 0.73 for the laboratory electrode under our conditions at *I* = 1.0 (KCl)[9]. Equation 3.9 was applied to calculate the concentration of deuteroxide ion in solution

using the established literature value for the ionic product of deuterium oxide, K_w at 25 °C (pK_w = 14.87 [7]).

$$[DO^-] = \frac{10^{(pD - pK_w)}}{\gamma_{DO}} \qquad \textbf{Equation 3.9}$$

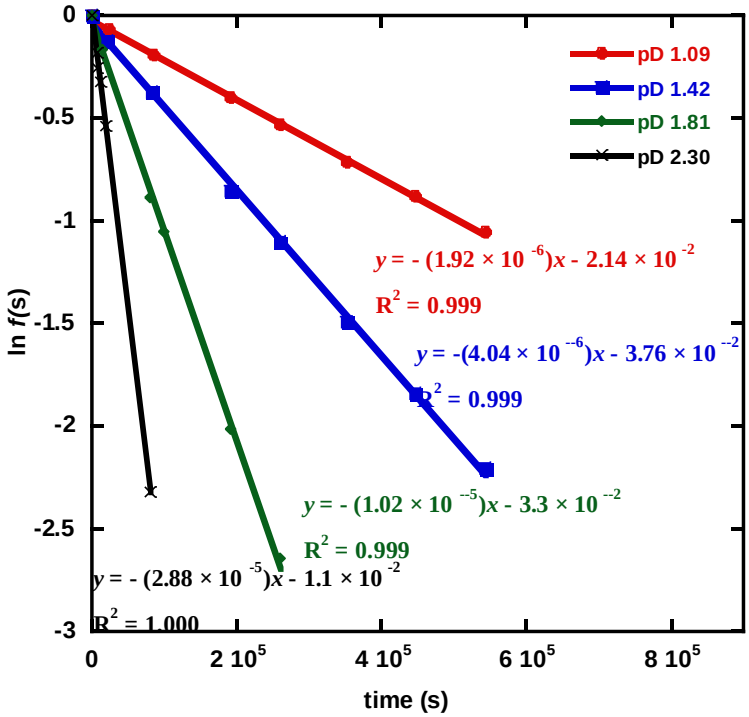

Figure 3.6 **Semilogarithmic plots of the fraction of unexchanged substrate against time for the deuterium exchange reaction of hydroxyethanoyl triazolium salt 144 in DCl solutions in D_2O at 25 ºC and I = 1.0 (KCl)**

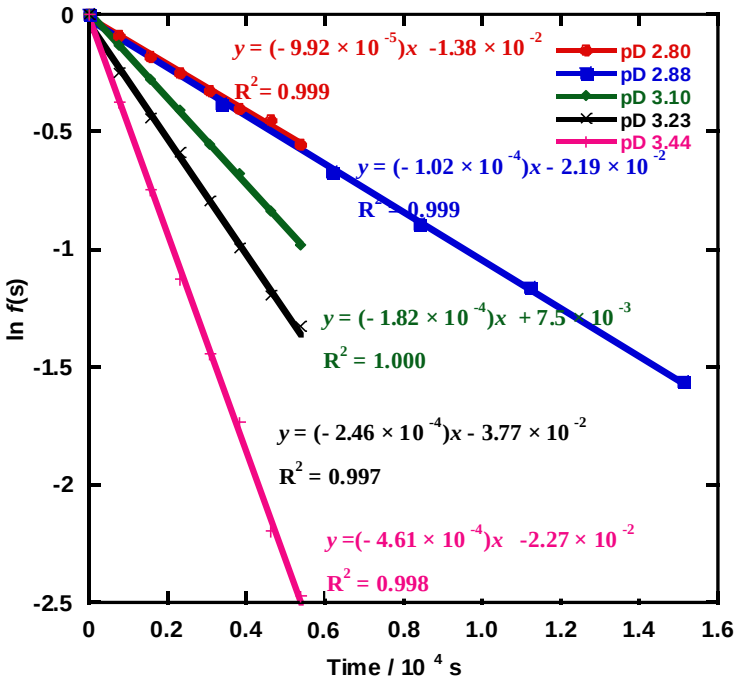

Figure 3.7 **Semilogarithmic plots of the fraction of unexchanged substrate against time for the deuterium exchange reaction hydroxyethanoyl triazolium salt 144 in DCl solutions (pD 2.80) and formic acid (pD 2.88 – 3.44) buffers (0.1 M) in D_2O at 25 °C and I = 1.0 (KCl)**

Table 3.3 shows the observed first-order rate constants for C3−H/D exchange versus p*D* for hydroxyethanoyl triazolium mimic **144** obtained from the gradient of the plot of ln *f*(s) versus time (Appendix A Table A.1).

Table 3.3 **Summary of p*D* and pseudo first-order rate constants for H/D exchange for substrate 144**

p*D*	k_{ex}, s^{-1} [a]	DCl/Buffer
1.09	1.92×10^{-6}	DCl
1.42	4.04×10^{-6}	"
1.81	1.02×10^{-5}	"
2.30	2.88×10^{-5}	"
2.80	9.85×10^{-5}	Formic Acid 0.1 M

2.88	1.02×10^{-4}	“
3.04	1.64×10^{-4}	“
3.10	1.80×10^{-4}	“
3.23	2.40×10^{-4}	“
3.44	4.55×10^{-4}	“

(a) Error margins 6%

3.2.2.2 1-((4-amino-2-methylpyrimidin-5-yl)methyl)-3,4-dimethyl-4H-1,2,4-triazol-1-ium tetrafluoroborate

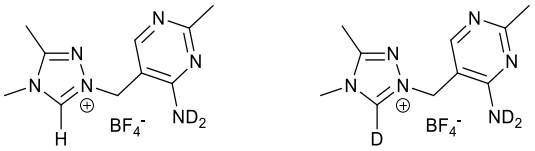

183 **183d**

Scheme 3.4 Methyl triazolium mimic 183 and deuterated analogue 183d

Triazolium tetrafluoroborate salt **183** was converted to analogue **183d** (Scheme 3.4) by replacement of hydrogen for deuterium at a range of p*D* values, monitored by ^{1}H NMR spectroscopy (400 MHz) to enable determination of pseudo-first-order rate constants.

Figure 3.8 presents an overlay of spectra acquired for the reaction at p*D* 2.76 at three intervals during the experiment. The disappearance of the singlet peak due to the triazolium C3-H (A) at 9.83 ppm is evidence for replacement of hydrogen for deuterium. The progress of replacement of hydrogen for deuterium was quantified with respect to the singlet signal associated with three equivalent non-acidic hydrogens of the internal standard, mono-deuterated methanol (IS)(CH_3OD) at 3.34 ppm.

The signal due to the pyrimidinyl proton (B) of the triazolium salt **183** appears as a singlet at 8.30 ppm. The large singlet at 8.1 ppm is owing to the formyl proton of the formic acid buffer. The bridging methylene protons (C) attached to the cationic nitrogen atom, joining the two aromatic rings, give a singlet peak at 5.59 ppm. The signal corresponding to the triazolium ring N−methyl (D) appears as a singlet at 3.88 ppm. A signal corresponding to the C_5 methyl of the triazolium ring C−CH_3 (E) appears as a quintet at 2.61 ppm. A signal corresponding to the pyrimidinyl methyl (F) appears as a singlet at 2.55 ppm. Apart from the C_3H (A) all other peaks (B-F) remained the same and integrated equivalently for the duration of the experiment. All the peaks were integrated relative to the internal standard, monodeuterated methanol and

remained constant, which confirms that only exchange of the C_3H for deuterium is occurring under these reaction conditions and timescale.

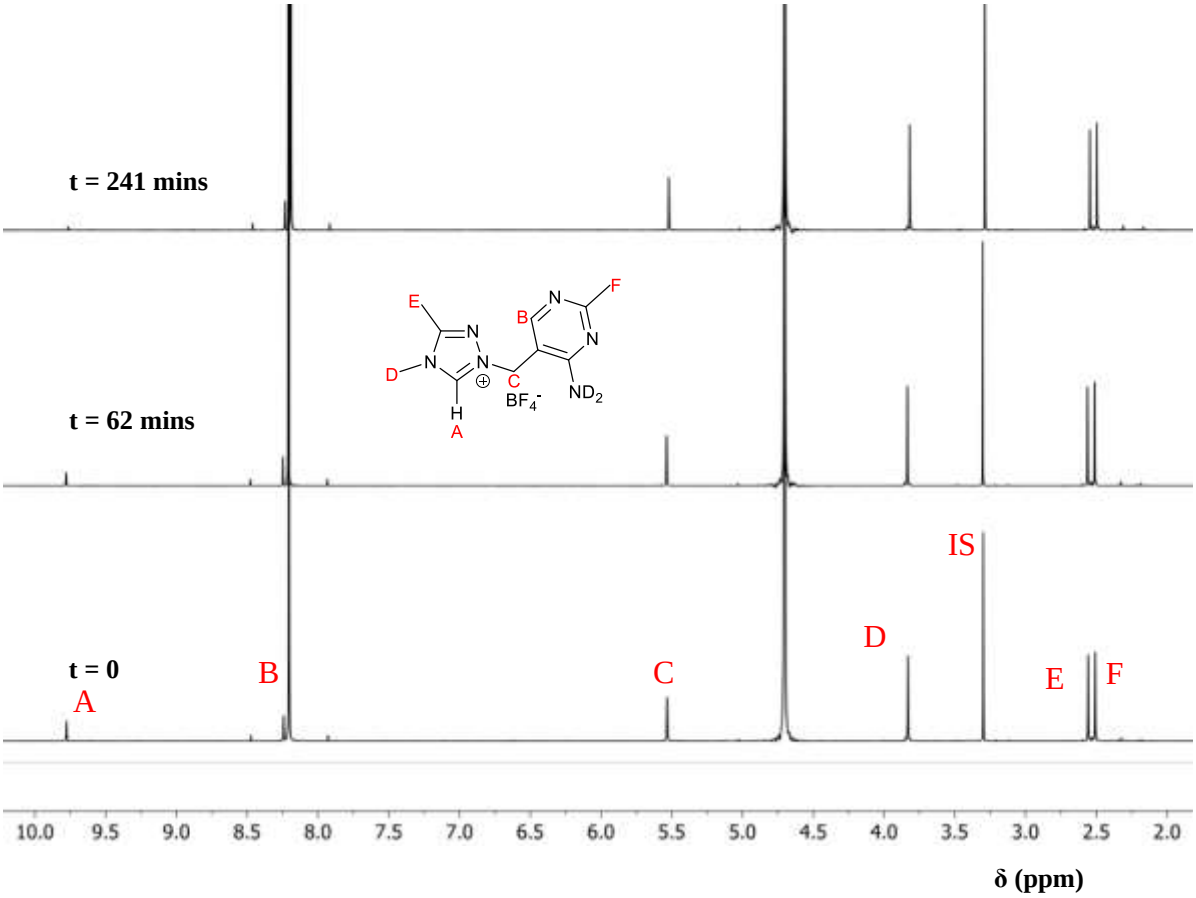

Figure 3.8 **Representative ^{1}H NMR spectra at 400 MHz of methyl triazolium salt 183 (p*D* 2.76) acquired during exchange of the C3-H (s, 9.9 ppm) for deuterium in D_2O at 25 °C and *I* = 1.0 (KCl) [Internal standard, monodeuterated methanol CH_3OD (s, 3.3 ppm)]**

Figure 3.9 **Semilogarithmic plots of the fraction of unexchanged substrate 183 against time for the deuterium exchange reaction methyl triazolium salt 183 in solutions of DCl and formic acid buffer in D_2O at 25 ºC and *I* = 1.0 (KCl)**

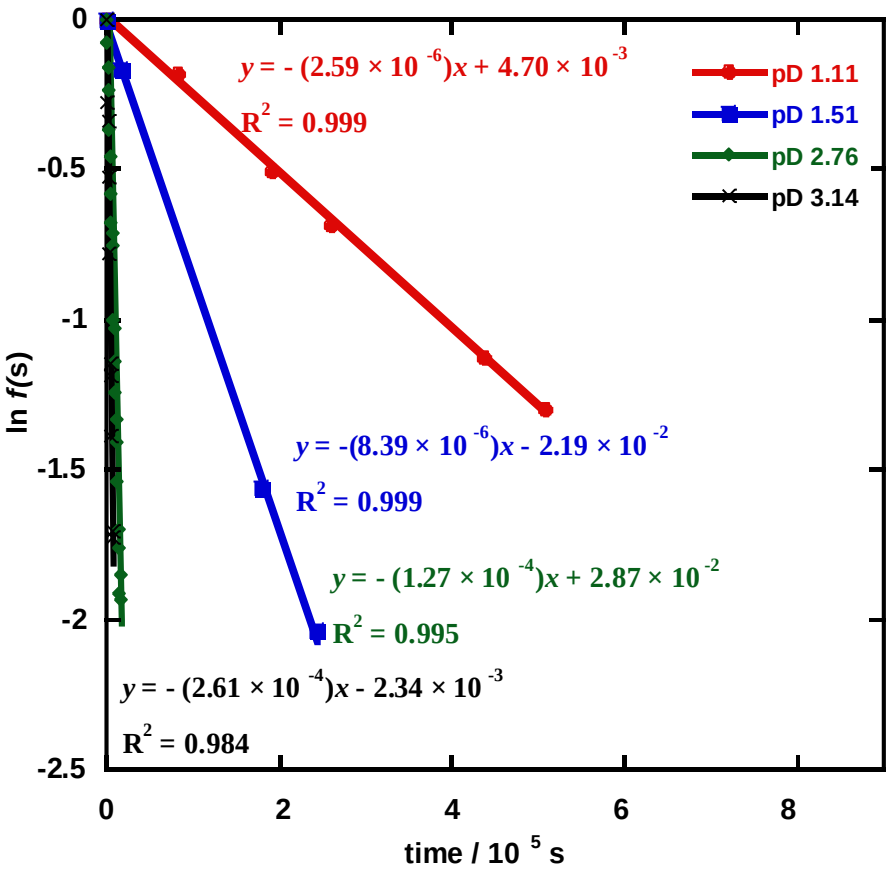

Table 3.4 shows the observed first-order rate constants for C_3−H/D exchange versus p*D* for 5-methyl triazolium mimic **183** obtained from the gradient of the plot of ln *f*(s) versus time (For reaction data see Appendix A Table A.2).

Table 3.4 **Data summary of p*D* and pseudo first order rate constants for H/D exchange for salt 183**

p*D*	k_{ex}, s^{-1}	*DCl/Buffer*
0.94	1.13×10^{-6}	DCl
1.11	2.59×10^{-6}	"
1.51	8.40×10^{-6}	"
2.76	1.30×10^{-4}	Formic acid 0.1M
3.14	2.61×10^{-3}	"

3.2.2.3 1-((4-amino-2-methylpyrimidin-5-yl)methyl)-3-(2-hydroxypropyl)-4-methyl-4H-1,2,4-triazol-1-ium tetrafluoroborate

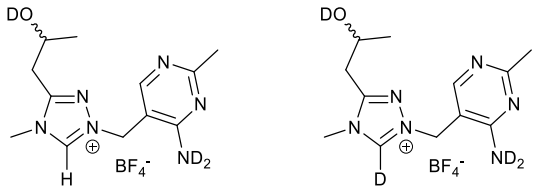

184 **184d**

Scheme 3.5 Isopropyl triazolium mimic 184 and deuterated analogue 184d

Triazolium tetrafluoroborate salt **184** was converted to compound **184d** (Scheme 3.5) by replacement of hydrogen for deuterium at a range of p*D* values, monitored by ^{1}H NMR spectroscopy (400 MHz) to enable determination of pseudo-first-order rate constants.

Figure 3.10 presents an overlay of spectra acquired for the reaction at p*D* 2.78 at three intervals during the experiment. The disappearance of the singlet peak due to the triazolium C3-H (A) at 9.83 ppm is evidence for replacement of hydrogen for deuterium. The progress of replacement of hydrogen for deuterium was quantified with respect to the singlet signal due to three equivalent non-acidic hydrogens from the internal standard, mono-deuterated methanol (IS)(C*H*$_3$OD) at 3.31 ppm.

The signal due to the pyrimidinyl proton (B) of the triazolium salt **184** appears as a singlet at 8.31 ppm. The large singlet at 8.2 ppm is owing to the formyl proton of the formic acid buffer. The bridging methylene protons (C) attached to the cationic nitrogen atom, joining the two aromatic rings, give a singlet peak at 5.57 ppm. A signal corresponding to the central methinyl C(OD)−*H* of the pendant isopropyl alcohol (D) appears as a sextet at 4.09 ppm. The signal corresponding to the triazolium ring N−methyl (E) appears as a singlet at 3.87 ppm. The pendant alcohol methylene, proximal to the triazolium ring (F) corresponds to the multiplet at

3.23 – 2.91 ppm. A signal corresponding to the pyrimidinyl methyl (G) appear as a singlet at 2.55 ppm. The terminal methyl of the isopropyl alcohol side chain −C*H*$_3$ (H) appears as a doublet at 1.24 ppm. Apart from the C_3H (A) all other peaks (B-H) remained the same and integrated equivalently for the duration of the experiment. All the peaks were integrated relative to the internal standard, monodeuterated methanol and remained constant, which confirms that only exchange of the C_3H for deuterium is occurring under these reaction conditions and timescale.

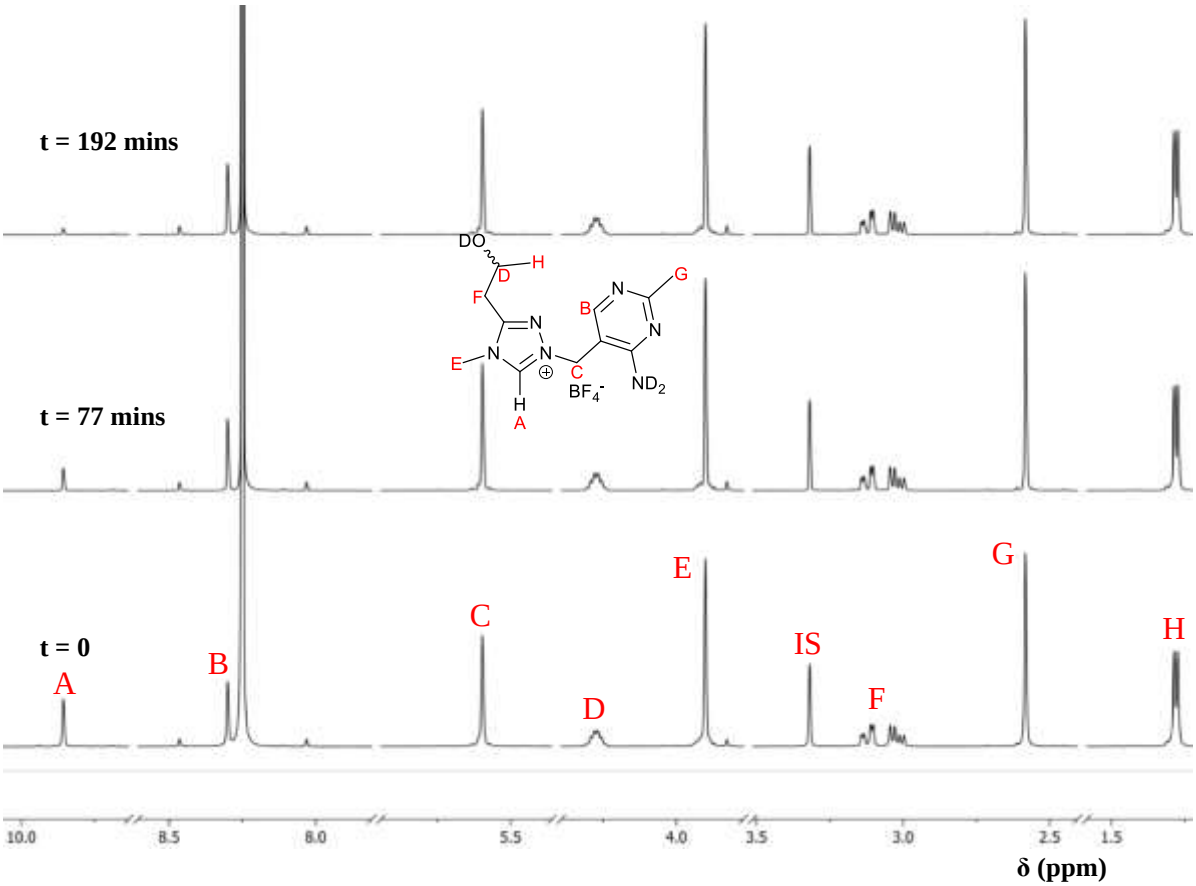

Figure 3.10 Representative ^{1}H NMR spectra at 400 MHz of isopropyl triazolium salt 184 (pD 2.78) acquired during exchange of the C3-H (s, 9.9 ppm) for deuterium formate buffer at 25 °C and *I* = 1.0 (KCl) [Internal standard, monodeuterated methanol CH_3OD (s, 3.3 ppm)]

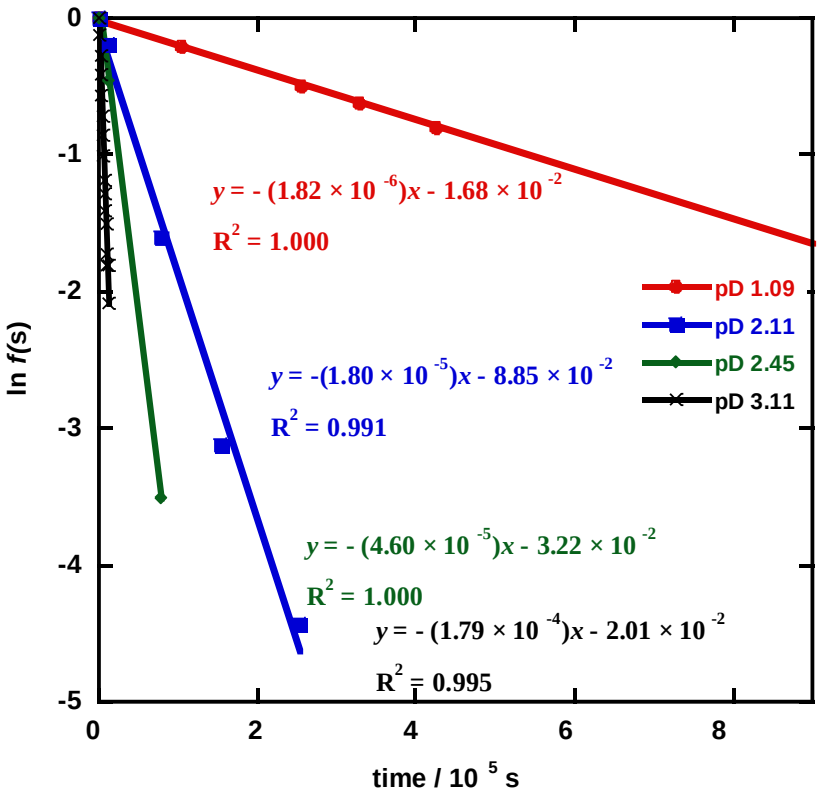

Figure 3.11 Semilogarithmic plots of the fraction of unexchanged substrate against time for the deuterium exchange reaction isopropyl triazolium salt 184 in solutions of DCl in D_2O at 25 °C and I = 1.0 (KCl)

Table 3.5 shows the observed first-order rate constants for C3-H /D exchange versus p*D* for 5-isopropyl triazolium mimic **184** obtained from the gradient of the plot of ln *f*(s) versus time (For reaction data see Appendix A Table A.3).

Table 3.5 Summary of p*D* and pseudo first-order rate constants for H/D exchange of salt 184

p*D*	k_{ex}, s^{-1}	DCl/Buffer
1.09	1.83×10^6	DCl
1.82	9.57×10^6	"
2.11	1.80×10^5	"
2.45	4.60×10^5	Formic Acid 0.1M
3.11	1.84×10^4	"

3.2.2.4 1-((4-amino-2-methylpyrimidin-5-yl)methyl)-3-(3-hydroxypropyl)-4-methyl-4*H*-1,2,4-triazol-1-ium tetrafluoroborate

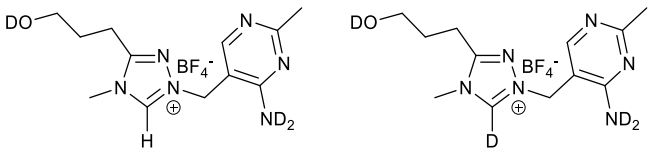

185 **185d**

Scheme 3.6 Propyl triazolium mimic 185 and deuterated analogue 185d

Triazolium tetrafluoroborate salt **185** was converted to analogue **185d** (Scheme 3.6) by replacement of hydrogen for deuterium at a range of p*D* values, monitored by ^{1}H NMR spectroscopy (400 MHz) to enable determination of pseudo-first-order rate constants.

Figure 3.12 presents an overlay of spectra acquired for the reaction at p*D* 2.14 at three intervals during the experiment. The disappearance of the singlet peak due to the triazolium C3-H (A) at 9.81 ppm is evidence for replacement of hydrogen for deuterium. The progress of replacement of hydrogen for deuterium was quantified with respect to the singlet signal due to three equivalent non-acidic hydrogens on the internal standard, mono-deuterated methanol (IS)(CH_3OD) at 3.31 ppm. The signal due to the pyrimidinyl proton (B) of the triazolium salt **185** appears as a singlet at 8.27 ppm. The large singlet at 8.1 ppm is owing to the formyl proton of the formic acid buffer. The bridging methylene protons (C) attached to the cationic nitrogen atom, joining the two aromatic rings, give a singlet peak at 5.56 ppm. The signal corresponding to the triazolium ring N−methyl (D) appears as a singlet at 3.86 ppm. The terminal methylene of the propyl alcohol side chain $-CH_2OD$ (E) appears as a triplet at 3.66 ppm. The pendant alcohol methylene, proximal to the triazolium ring (F) corresponds to the triplet at 2.94 ppm. A signal corresponding to the pyrimidinyl methyl (G) appears as a singlet at 2.58 ppm. A signal

corresponding to the central methylene of the 3-hydroxypropanoyl side chain −CH_2− (H) appears as a distinct quintet at 1.99 ppm. Apart from the C_3H (A), all other peaks (B-H) remained the same and integrated equivalently for the duration of the experiment. All the peaks were integrated relative to the internal standard, monodeuterated methanol, and remained constant. This observation confirms that only exchange of the C_3H for deuterium is occurring under these reaction conditions and timescale.

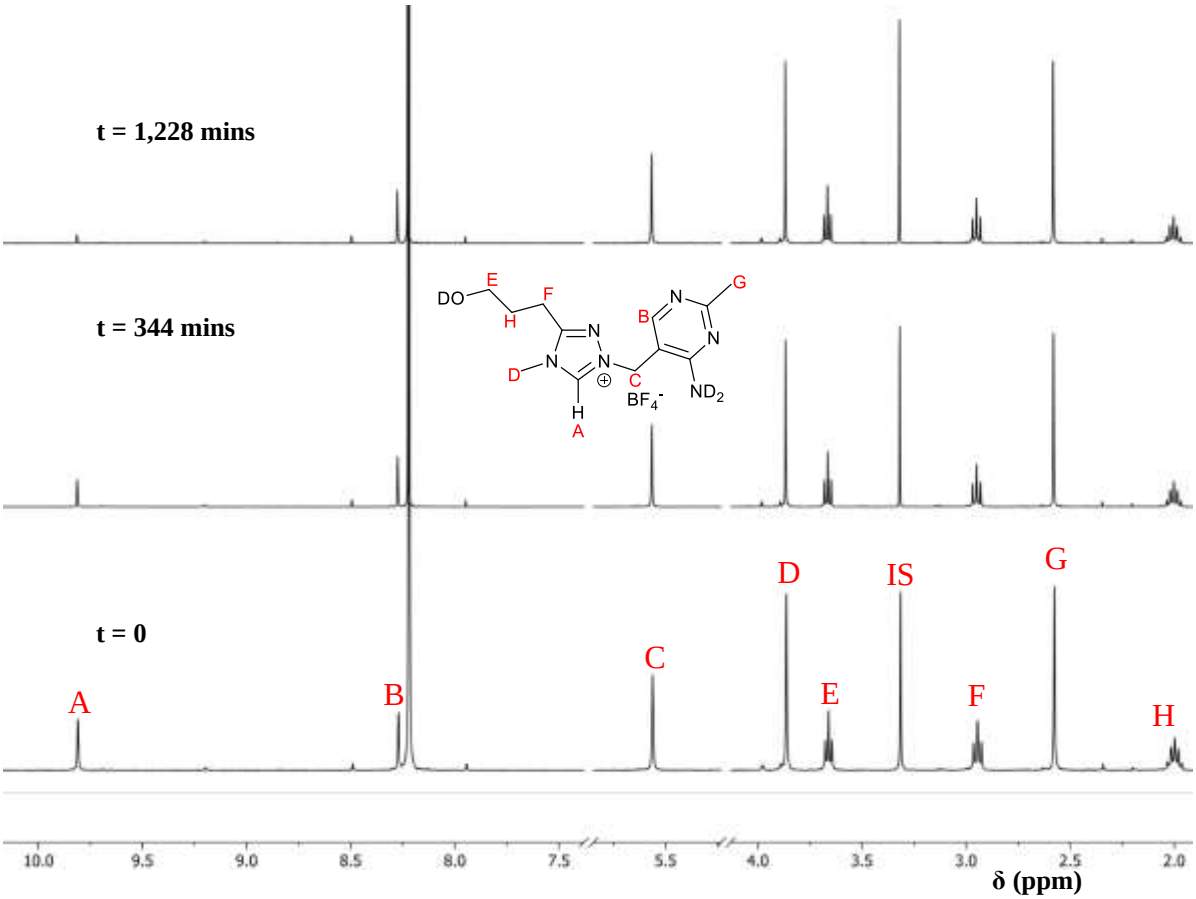

Figure 3.12 Representative ^{1}H NMR spectra at 400 MHz of 3-hydroxypropyl triazolium salt 185 (p*D* 2.14 formate buffer) acquired during exchange of the C3-H (s, 9.9 ppm) for deuterium in formate buffer at 25 °C and *I* = 1.0 (KCl) [Internal standard, monodeuterated methanol CH_3OD (s, 3.3 ppm)]

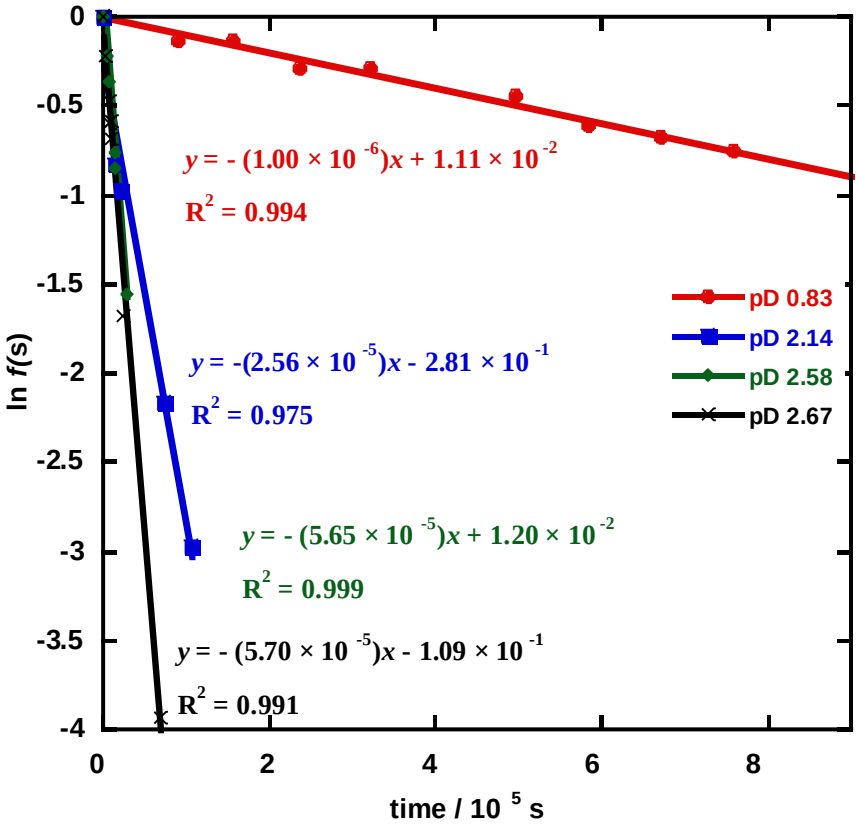

Figure 3.13 Semilogarithmic plots of the fraction of unexchanged substrate against time for the deuterium exchange reaction hydroxypropanoyl triazolium salt 185 in buffered solutions of DCl and formate buffer in D_2O at 25 ºC and I = 1.0 (KCl)

Table 3.6 shows the observed first-order rate constants for C3-H /D exchange versus p*D* for 5-hydroxypropanoyl triazolium mimic **185** obtained from the gradient of the plot of ln *f*(s) versus time (For reaction data see Appendix A Table A.4).

Table 3.6 Summary of p*D* and pseudo first order rate constants for H/D exchange for salt 185

p*D*	k_{ex}, s^{-1}	DCl/Buffer
0.83	1.00×10^{-6}	DCl
2.24	2.57×10^{-5}	"
2.48	4.46×10^{-5}	Formic Acid 0.1M
2.58	5.56×10^{-5}	"
2.67	6.92×10^{-5}	"

3.2.2.5 Thiamine chloride

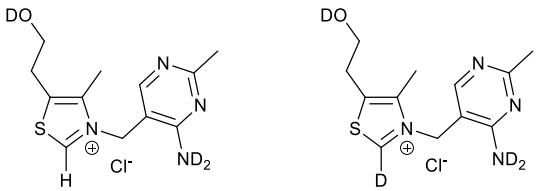

7-Cl **7d-Cl**

Scheme 3.7 Thiamine chloride 7-Cl and deuterated compound 7d-Cl

Thiamine chloride **7-Cl** was converted to analogue **7d-Cl** by replacement of hydrogen for deuterium at a range of p*D* values, monitored by ^{1}H NMR spectroscopy (400 MHz) to enable determination of pseudo-first-order rate constants. Figure 3.14 presents an overlay of spectra acquired for the reaction at p*D* 2.14 at three intervals during the experiment. The disappearance of the singlet peak due to the triazolium C_3H (A) at 9.65 ppm is evidence for replacement of hydrogen for deuterium. The progress of replacement of hydrogen for deuterium was quantified with respect to the singlet signal due to three equivalent non-acidic hydrogens due to the internal standard, mono-deuterated methanol (IS)(CH_3OD) at 3.31 ppm.

The large singlet at 8.2 ppm is owing to the formyl proton of the formic acid buffer. The signal due to the pyrimidinyl proton (B) of the triazolium salt **7** appear as a singlet at 8.03 ppm. The bridging methylene protons (C) attached to the cationic nitrogen atom, joining the two aromatic rings, give a singlet peak at 5.55 ppm. The pendant alcohol terminal methylene, distal to the thiazolium ring $-CH_2OD$ (D) corresponds to the triplet at 3.86 ppm. The methylene of the ethyl alcohol side chain, proximal to the thiazolium ring (E) appears as a triplet at 3.17 ppm. A signal corresponding to the C_4 methyl of the thiazolium ring $C-CH_3$ (F) appear as a singlet at 2.61 ppm. A signal corresponding to the pyrimidinyl methyl (G) appear as a singlet at 2.53 ppm. Apart from the C_3H (A) all other peaks (B - G) remained the same and integrated equivalently

for the duration of the experiment. All the peaks were integrated relative to the internal standard, monodeuterated methanol, and remained constant, which confirms that only exchange of the C_3H for deuterium is occurring under these reaction conditions and timescale.

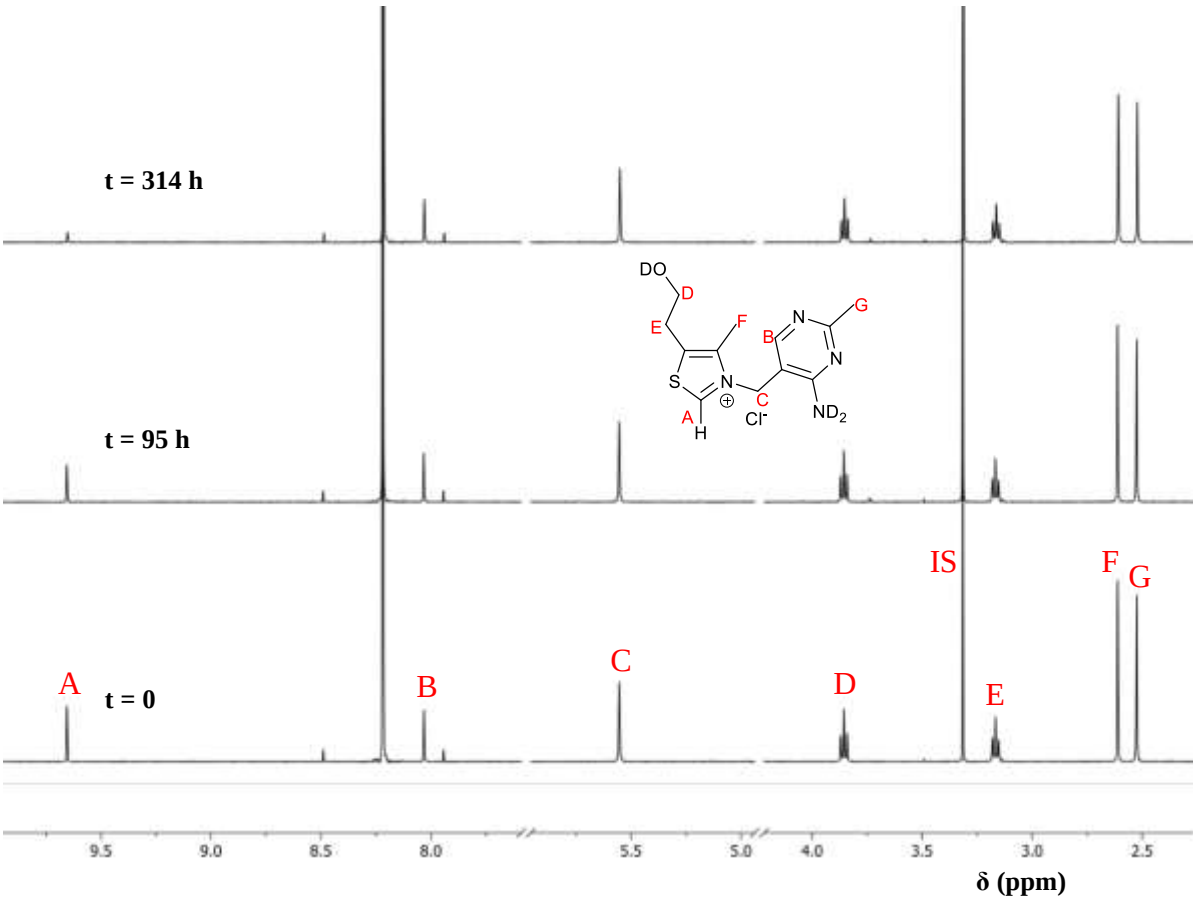

Figure 3.14 Representative ^{1}H NMR spectra at 400 MHz of thiamine chloride 7-Cl (p*D* 2.20 formate buffer) acquired during exchange of the C2−H (s, 9.7 ppm) for deuterium in D_2O at 25 °C and *I* = 1.0 (KCl) [Internal standard, monodeuterated methanol CH_3OD (s, 3.3 ppm)]

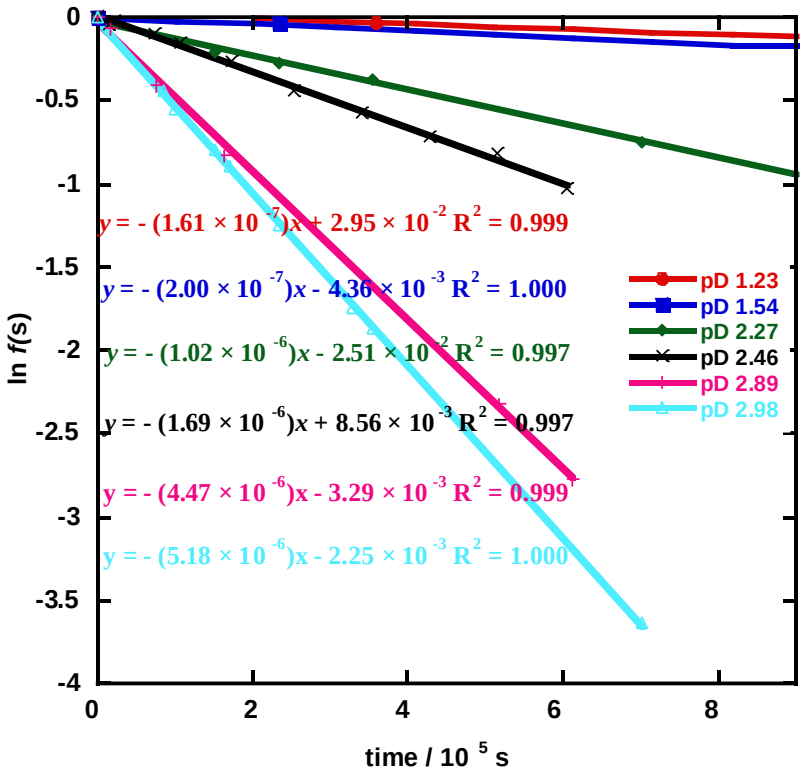

Figure 3.15 Semilogarithmic plots of the fraction of unexchanged substrate against time for the deuterium exchange reaction thiamine chloride salt 7-Cl in solutions of DCl and formate buffer in D_2O at 25 ºC and *I* = 1.0 (KCl)

Table 3.7 shows the observed first-order rate constants for C2-H /D exchange versus p*D* for thiamine chloride **7**-Cl obtained from the gradient of the plot of ln *f*(s) versus time (For reaction data see Appendix A Table A.5).

Table 3.7 Summary of p*D* and pseudo first order rate constants for H/D exchange for salt 7-Cl

p*D*	k_{ex}, s^{-1}	*DCl/Buffer*
1.23	1.02×10^{-7}	DCl
1.54	2.01×10^{-7}	“
2.27	1.02×10^{-6}	“
2.39	1.68×10^{-6}	Formic acid 0.1M
2.86	4.47×10^{-6}	“
2.98	5.18×10^{-6}	“

3.04	5.59×10^{-6}	“

3.2.2.6 Thiamine mononitrate

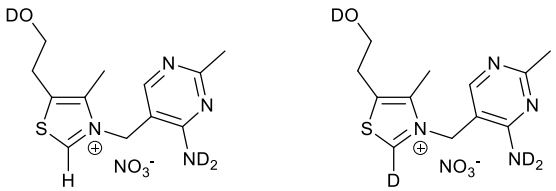

7-NO3 **7d-NO3**

Scheme 3.8 Thiamine mononitrate 7- NO_3 and deuterated compound 7d-NO_3

To study the effect of the counterion on H/D exchange, thiamine mononitrate **7-NO_3** was converted to compound **7d-NO_3** (Scheme 3.8) by replacement of hydrogen for deuterium at a range of p*D* values, monitored by ^{1}H NMR spectroscopy (400 MHz) to enable determination of pseudo-first-order rate constants.

Figure 3.16 presents an overlay of spectra acquired for the reaction at p*D* 1.80 at three intervals during the experiment. The disappearance of the singlet peak due to the triazolium C2-H (A) at 9.65 ppm is evidence for replacement of hydrogen for deuterium. The progress of replacement of hydrogen for deuterium was quantified with respect to the singlet signal due to three equivalent non-acidic hydrogens due to the internal standard, mono-deuterated methanol (IS)(CH_3OD) at 3.31 ppm.

The large singlet at 8.2 ppm is owing to the formyl proton of the formic acid buffer. The signal due to the pyrimidinyl proton (B) of the triazolium salt **7-NO_3** appear as a singlet at 8.05 ppm. The bridging methylene protons (C) attached to the cationic nitrogen atom, joining the two aromatic rings, give a singlet peak at 5.56 ppm. The pendant alcohol terminal methylene, distal to the thiazolium ring $-CH_2OD$ (D) corresponds to the triplet at 3.86 ppm. The methylene of the ethyl alcohol side chain, proximal to the thiazolium ring (E) appears as a triplet at 3.17 ppm. A signal corresponding to the C_4 methyl of the thiazolium ring $C-CH_3$ (F) appears as a

singlet at 2.62 ppm. A signal corresponding to the pyrimidinyl methyl (G) appears as a singlet at 2.53 ppm. Apart from the C_3H (A) all other peaks (B - G) remained the same and integrated equivalently for the duration of the experiment. All the peaks were integrated relative to the internal standard, monodeuterated methanol and remained constant, which confirms that only exchange of the C_3H for deuterium is occurring under these reaction conditions and timescale.

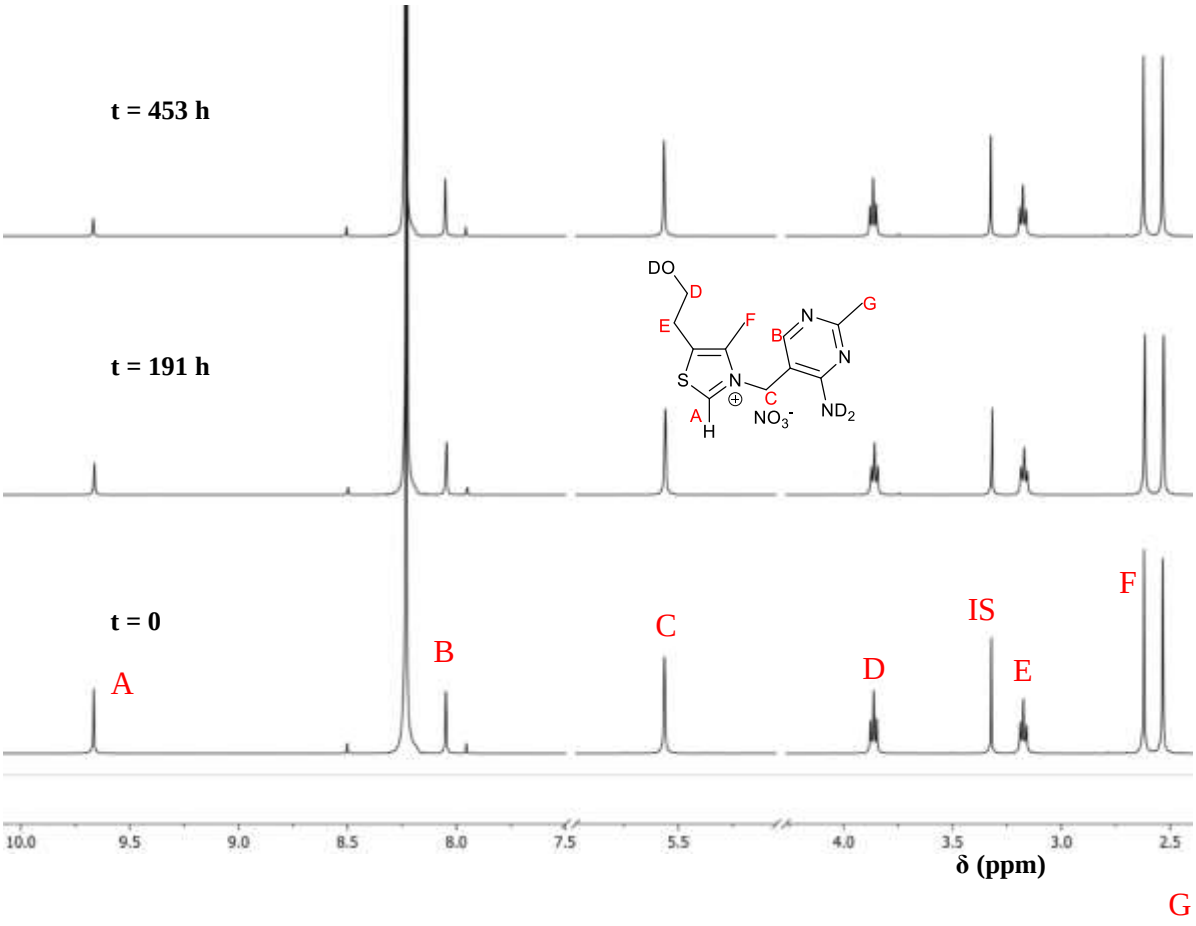

Figure 3.16 Representative ^{1}H NMR spectra at 400 MHz of thiamine mononitrate 7-NO_3 (p*D* 1.80) acquired during exchange of the C2−H (s, 9.67 ppm) for deuterium in DCl or formate buffer in D_2O at 25 °C and *I* = 1.0 (KCl) [Internal standard, monodeuterated methanol CH_3OD (s, 3.3 ppm)]

Figure 3.17 **Semilogarithmic plots of the fraction of unexchanged substrate against time for the deuterium exchange reaction thiamine mononitrate salt 7-NO_3 in solutions of DCl in D_2O at 25 °C and *I* = 1.0 (KCl)**

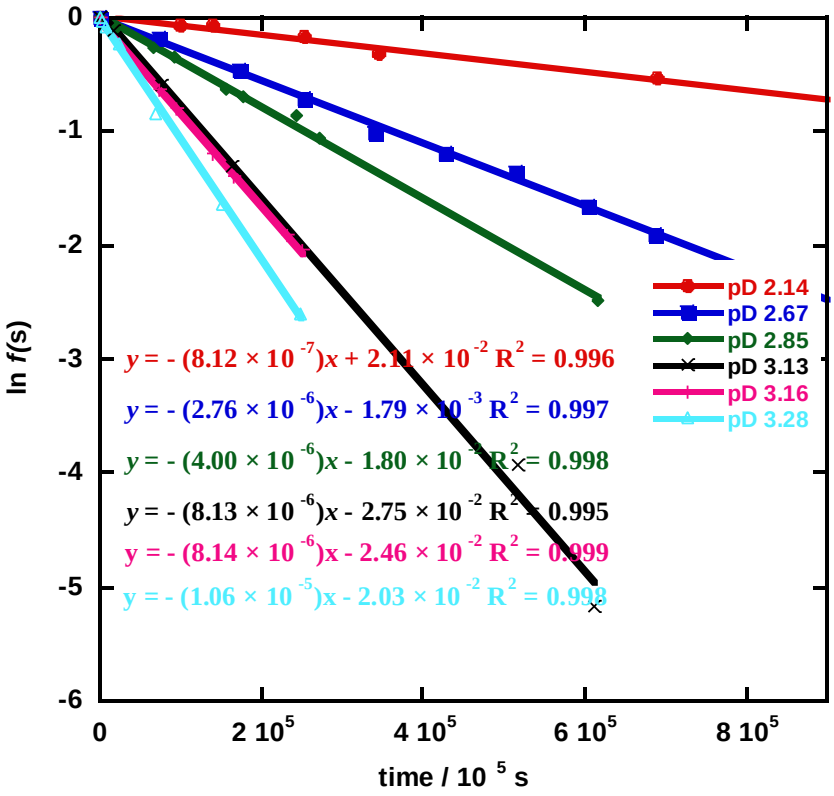

Table 3.8 shows the observed first-order rate constants for C2-H /D exchange versus p*D* for thiamine chloride **7**-NO_3 obtained from the gradient of the plot of ln *f*(s) versus time (For reaction data see Appendix A Table A.6)

Table 3.8 **Summary of p*D* and pseudo first order rate constants for H/D exchange of salt 7-NO_3**

p*D*	k_{ex}, s^{-1}	*DCl/Buffer*
2.14	8.12×10^{-7}	DCl
2.67	2.76×10^{-6}	Formic Acid 0.1M
2.85	4.00×10^{-6}	“
3.13	8.13×10^{-6}	“
3.16	8.14×10^{-6}	“
3.28	1.06×10^{-5}	“

3.2.2.7 2-phenyl-6,7-dihydro-5*H*-pyrrolo[2,1-c][1,2,4]triazol-2-ium

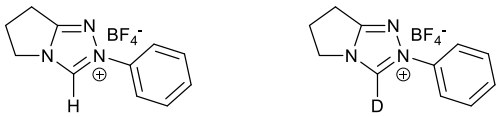

195 **195d**

Scheme 3.9 N-Phenyl triazolium salt 195 and deuterated analogue 195d

Triazolium salt **195** was converted to analogue **195d** (Scheme 3.9) by replacement of hydrogen for deuterium at a range of p*D* values, monitored by ^{1}H NMR spectroscopy (400 MHz) to enable determination of pseudo-first-order rate constants.

Figure 3.18 presents an overlay of spectra acquired for the reaction at p*D* 2.40 at three intervals during the experiment. The disappearance of the singlet peak due to the triazolium C3-H (A) at 10.27 ppm is evidence for replacement of hydrogen for deuterium. The progress of replacement of hydrogen for deuterium was quantified with respect to the singlet signal due to three equivalent non-acidic hydrogens due to the internal standard, mono-deuterated methanol (IS)(CH_3OD) at 3.31 ppm.

The large singlet at 8.2 ppm is owing to the formyl proton of the formic acid buffer. Signals corresponding to the *ortho*-CH, *meta*-CH and *para*-CH groups on the phenyl ring (B & C) appear as two sets of multiplets at 7.61 and 7.73 ppm. The peaks corresponding to the three methylenes on the fused ring appear as two sets of triplets at 4.51 and 3.26 ppm and a quintet at 2.87 ppm (D, E & F). Apart from the C_3H (A) all other peaks (B - F) remained the same and integrated equivalently for the duration of the experiment. All the peaks were integrated relative to the internal standard, monodeuterated methanol and remained constant, which confirms that only exchange of the C_3H for deuterium is occurring under these reaction conditions and timescale.

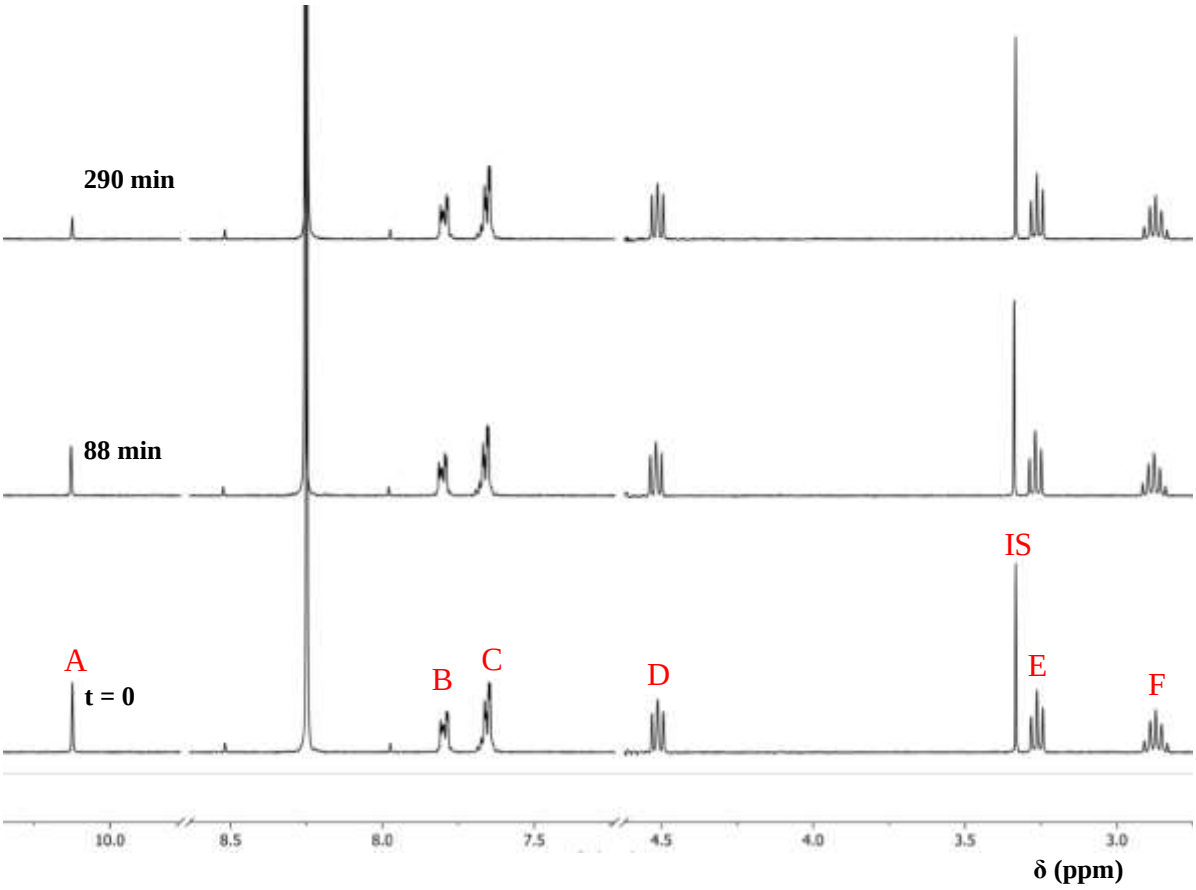

Figure 3.18 **Representative ^{1}H NMR spectra at 400 MHz of triazolium salt 195 (p*D* 2.40 formate buffer) obtained during exchange of the C3-H (s, 10.2 ppm) for deuterium in D_2O at 25 °C and *I* = 1.0 (KCl) [Internal standard, monodeuterated methanol CH_3OD (s, 3.3 ppm)]**

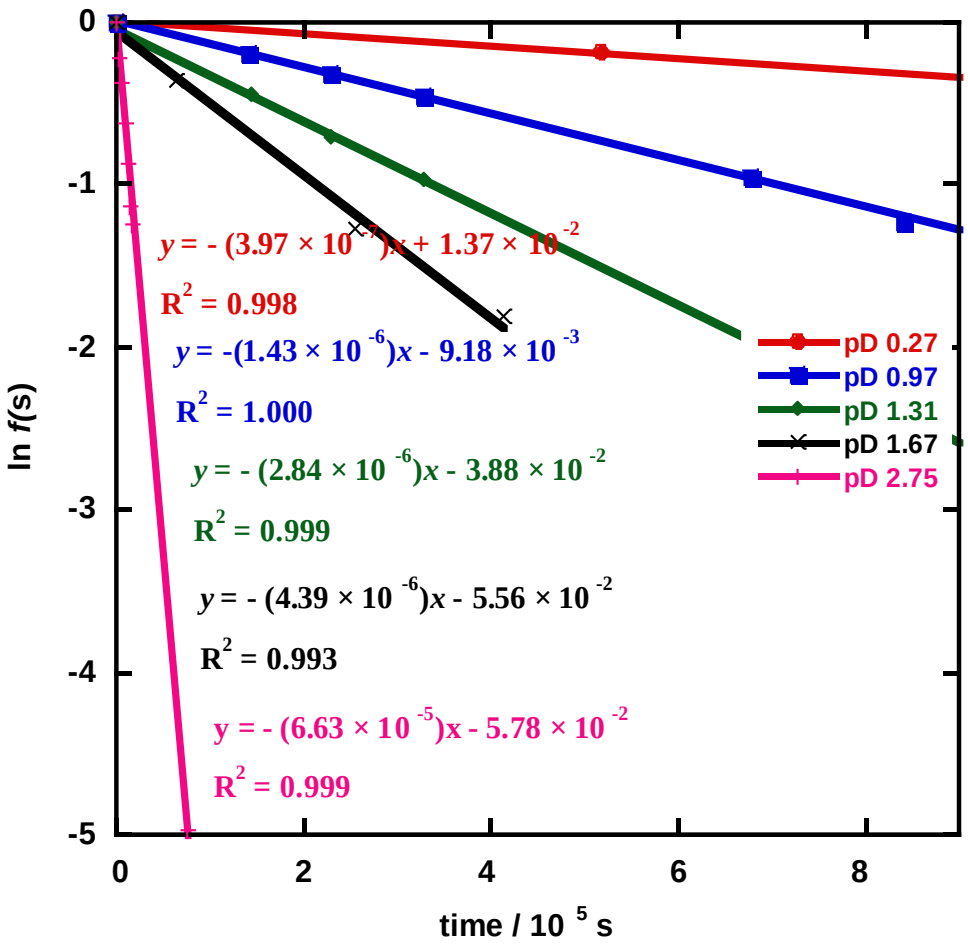

Figure 3.19 **Semilogarithmic plots of the fraction of unexchanged substrate against time for the deuterium exchange reaction of N-phenyl triazolium salt 195 in solutions of DCl in D_2O at 25 ºC and *I* = 1.0 (KCl)**

Table 3.9 shows the observed first-order rate constants for C3-H /D exchange versus p*D* for N-phenyl triazolium salt **195** at obtained from the gradient of the plot of ln *f*(s) versus time (For reaction data see Appendix A Table A.7).

Table 3.9 **Data summary of p*D* and pseudo first-order rate constants for H/D exchange salt 195**

p*D*	k_{ex}, s^{-1}	DCl/Buffer
0.27	3.97×10^{-7}	DCl
0.97	1.44×10^{6}	"

1.21	3.23×10^{-6}	“
1.34	2.84×10^{-6}	“
1.57	4.39×10^{-6}	“
2.27	2.28×10^{-5}	“
2.65	5.55×10^{-5}	Formic Acid 0.1M
2.75	6.63×10^{-5}	“
3.75	6.88×10^{-4}	“

3.2.2.8 1,4-dimethyl-4H-1,2,4-triazol-1-ium iodide

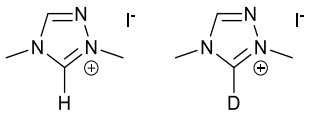

212 **212d**

Scheme 3.10 Triazolium salt 212 and deuterated analogue 212d

Triazolium salt **212** was converted to analogue **212d** by replacement of hydrogen for deuterium at a range of p*D* values, monitored by ^{1}H NMR spectroscopy (400 MHz), to enable determination of pseudo-first-order rate constants.

Figure 3.20 presents an overlay of spectra acquired for the reaction at p*D* 1.80 at three intervals during the experiment. The disappearance of the singlet peak due to the triazolium C3-H (A) at 9.68 ppm is evidence for replacement of hydrogen for deuterium. The progress of replacement of hydrogen for deuterium was quantified with respect to the singlet signal due to three equivalent non-acidic hydrogens due to the internal standard, mono-deuterated methanol (IS)(CH_3OD) at 3.32 ppm.

The signal due to the C_5H (B) of triazolium salt **212** appears as a singlet at 8.76 ppm. The large singlet at 8.2 ppm is owing to the formyl proton of the formic acid buffer. The peaks corresponding to the cationic N^+−methyl (C) appear as a singlet at 4.11 ppm. The signal corresponding to the triazolium ring N−methyl (D) appears as a singlet at 3.95 ppm. Apart from the C_3H (A) and C_5H, all other peaks (B & D) remained the same and integrated equivalently for the duration of the experiment. All the peaks were integrated relative to the internal standard, monodeuterated methanol and remained constant, which confirms that only

exchange of the C_3H and C_5H for deuterium is occurring under these reaction conditions and timescale.

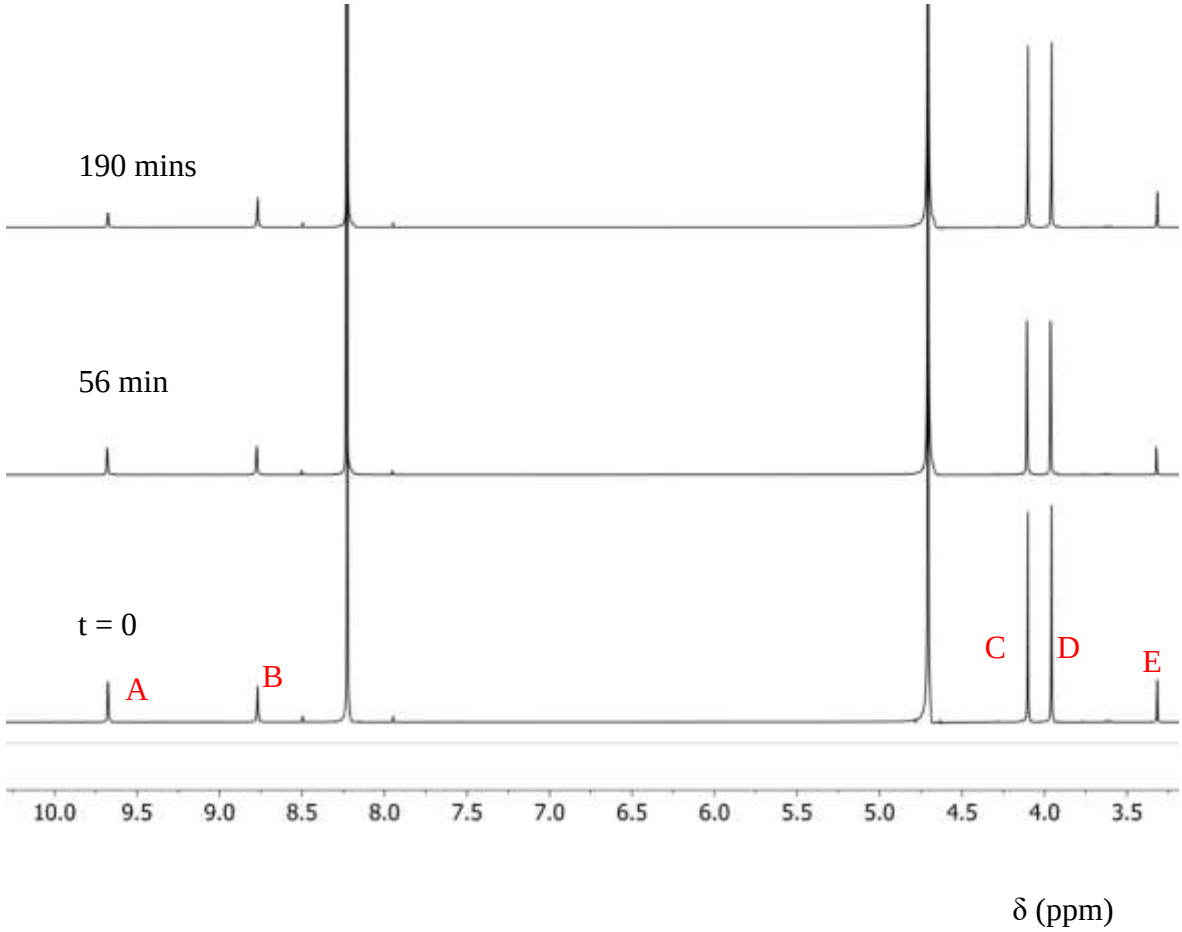

Figure 3.20 Representative ^{1}H NMR spectra at 400 MHz of dimethyl triazolium salt 212 (p*D* 1.80 formate buffer) acquired during exchange of the C3-H (s, 9.68 ppm) for deuterium in D_2O at 25 °C and *I* = 1.0 (KCl) [Internal standard, monodeuterated methanol CH_3OD (s, 3.3 ppm)]

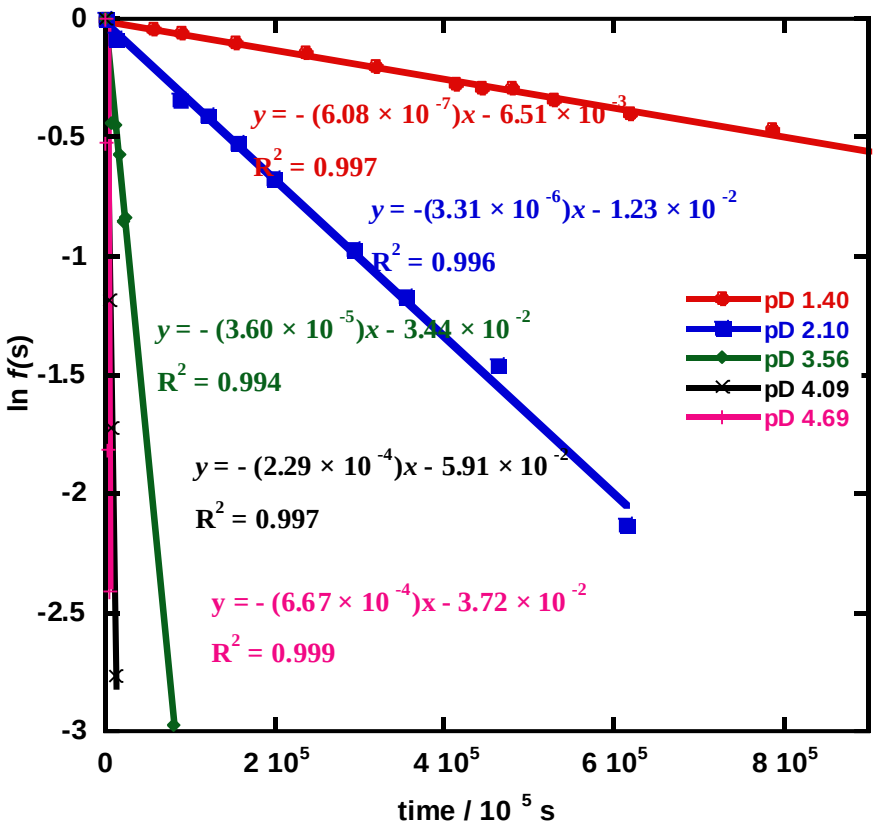

Figure 3.21 **Semilogarithmic plots of the fraction of unexchanged substrate against time for the deuterium exchange reaction of dimethyl triazolium salt 212 in buffered solutions of DCl, formate or acetate buffer in D_2O at 25 °C and *I* = 1.0 (KCl)**

Table 3.10 shows the observed first-order rate constants for C3-H /D exchange versus p*D* for dimethyl triazolium salt **212** at obtained from the gradient of the plot of ln *f*(s) versus time (Appendix A Table A.8).

Table 3.10 **Data summary of p*D* and pseudo first order rate constants for H/D exchange**

p*D*	k_{ex}, s^{-1}	*DCl/Buffer*
1.40	6.08×10^{-7}	DCl
2.10	3.31×10^{-6}	"
3.56	3.60×10^{-5}	Acetic Acid 0.1M
4.09	2.29×10^{-4}	"
4.69	6.67×10^{-4}	"

3.2.3 Second-order rate constant for deuteroxide ion catalysed exchange

Pseudo-first-order rate constant for replacement of hydrogen for deuterium (k_{ex}), comprise buffer base (k_B[B]), deuterium oxide (k_{D2O}) and deuteroxide ion (k_{DO}[DO^-]) contributions (Equation 3.10).

$$k_{ex} = k_{DO}[DO^-] + k_{D2O} + k_B[B] \qquad \textbf{Equation 3.10}$$

Earlier works published in the group determined contributions from solvent and buffer base to be insignificant under these reaction conditions and timescale for the H/D exchange of N-aryl triazolium salts. For one representative salt, we sought to verify that for our new mimics, with the N-alkyl appendage, the observation of no buffer catalysis still holds. Experiments at a fixed buffer ratio and varying concentrations of buffer were employed to assess this using triazolium mimic **144** as a model substrate. Increases in k_{ex} with increasing buffer concentration would imply that general-base catalysis exists for our salt.

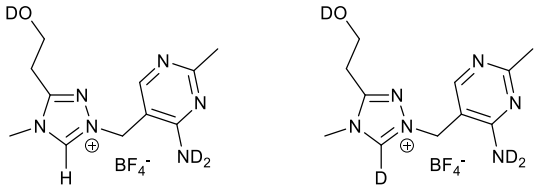

Scheme 3.11 Substrate 144 used for probing the effect of buffer catalysis

First-order rate constants for deuteroxide ion-catalysed exchange of the C3-H of triazolium salt **144** to form deuterated product **144d** were determined by ^{1}H NMR spectroscopy (400 MHz). Experiments were performed in formic acid buffers at a fixed buffer ratio. ^{1}H NMR spectral chemical shifts have been previously presented for **144**.

Reaction data for experimentally observed first-order rate constants for exchange (k_{ex}) at four buffer concentrations ([buffer] = 0.10 – 0.25 M) are presented in Table A.9 (Appendix A). k_{ex}

(s^{-1}) values were determined from slopes of semi-logarithmic plots of *f*(s) against time at each buffer concentration (Figure 3.22).

Figure 3.22 **Semilogarithmic plots of the fraction of unexchanged substrate against time for the H/D-exchange reaction of triazolium ion (144) in formic acid buffer solutions (50% f_B) at buffer base concentrations 100 mM (●), 150 mM (□), 200 mM (◇) and 250 mM (×) in D_2O at 25 °C and *I* = 1.0 (KCl)**

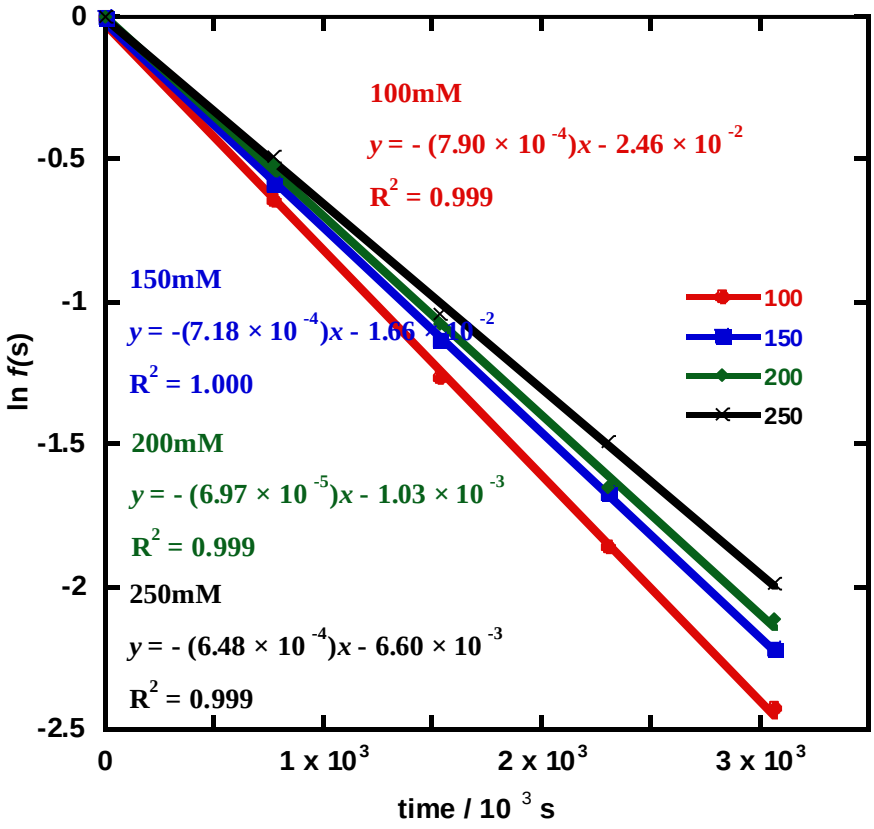

Values of k_{ex} (s^{-1}) as a function of the concentration of the buffer base are shown in Table 3.11. The ratio of rate constants, k_{rel}, obtained using Equation 3.11, is a measure of the relative difference in the experimentally observed rate constant for exchange, k_{ex} (s^{-1}), and contribution to rate from deuteroxide ion-catalysed exchange, $k_{DO}[DO^-]$ (s^{-1}),

where k_{DO} ($\mathbf{M^{-1}\ s^{-1}}$) is determined from rate measurements in un-buffered solution. This equation allows us to account for small changes in p*D* that occur upon dilution at constant ionic strength and buffer ratio.

$$k_{rel} = \frac{k_{ex}}{k_{DO}[DO^-]} = \frac{(k_{DO}[DO^-] + k_B[B])}{k_{DO}[DO^-]} = 1 + \frac{k_B[B]}{k_{DO}[DO^-]} \qquad \textbf{Equation 3.11}$$

Table 3.11 Pseudo-first-order rate constants for exchange, k_{ex} (s^{-1}), of the C3-H of triazolium ion (144) for deuterium in 50% f_B formic acid buffered solutions of D_2O at 25 ºC and I = 1.0 (KCl)

Buffer Concentration [B] (mM)[a]	p*D*	$[B]/[DO^-]$[b]	k_{ex}, s^{-1} [c]	k_{rel}
100	3.63	1.27×10^9	7.90×10^{-4}	1.17
150	3.62	1.95×10^9	7.18×10^{-4}	1.09
200	3.61	2.66×10^9	6.97×10^{-4}	1.08
250	3.61	3.23×10^9	6.48×10^{-4}	1.00

(a) Concentration of free base ($HCOO^-$) formate form of buffer. (b) Ratio of concentrations of $HCOO^-$ to deuteroxide ion. (c) Experimentally observed pseudo-first-order rate constant for exchange of C(3)-H of triazolium **144** (d) Ratio of first-order rate constant for exchange of C3-H (k_{ex}) to first-order rate term for deuteroxide ion-catalysed exchange only ($k_{DO}[DO^-]$), as described in Equation 2.8, where $k_{DO} = 8.58 \times 10^7\ \mathbf{M^{-1}\ s^{-1}}$

Figure 3.23 Plot of the ratio of rate constants k_{rel} against ([B]/[DO$^-$])

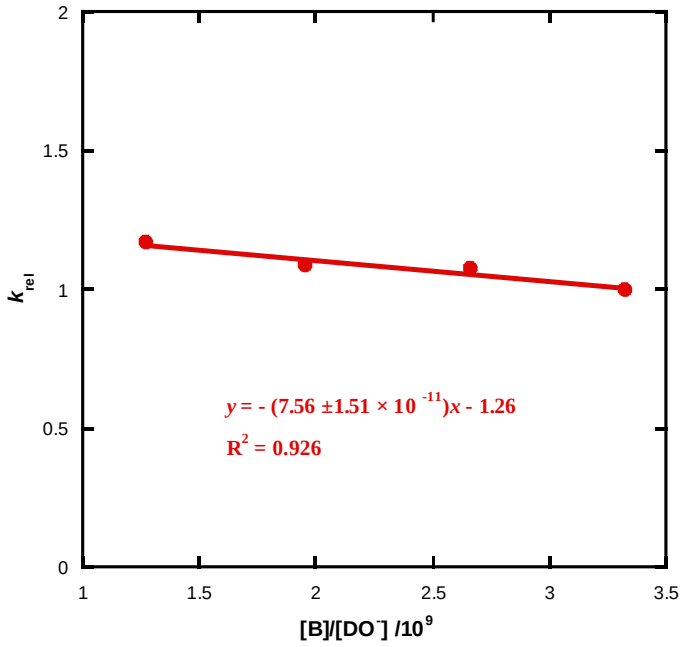

The plot (Figure 3.23) of varying buffer concentration against observed pseudo first-order rate constants does not show significant change on increasing buffer concentration. In fact the observed rate constants k_{ex} decrease as buffer concentration increases, however this is partly owing to lower observed p*D* values at higher buffer concentration. The ratio of k_B to k_{DO} is found to be 7.56 (±1.51) × 10^{-11} from the slope of the plot. This value is very small and negligible compared to k_{DO} and thus the exchange may be considered as specific-base catalysed for the mimics studied in this work. Therefore, changes in buffer concentrations do not significantly affect the rate of exchange under our experimental conditions. As buffer catalysis is absent Equation 3.10 simplifies to Equation 3.12. Thus, we can obtain k_{DO} as the slope of the plot of k_{ex} against deuteroxide concentration.

$$k_{ex} = k_{DO}[DO^-] \qquad \textbf{Equation 3.12}$$

Plots of k_{ex} against deuteroxide concentration for all the salts studied in this chapter are shown in Figures 3.24 −3.31 . p*D* rate profiles are included in the appendix section B.

Figure 3.24 Plot of rate constant k_{ex} against deuteroxide concentration [DO^-] for mimic 144

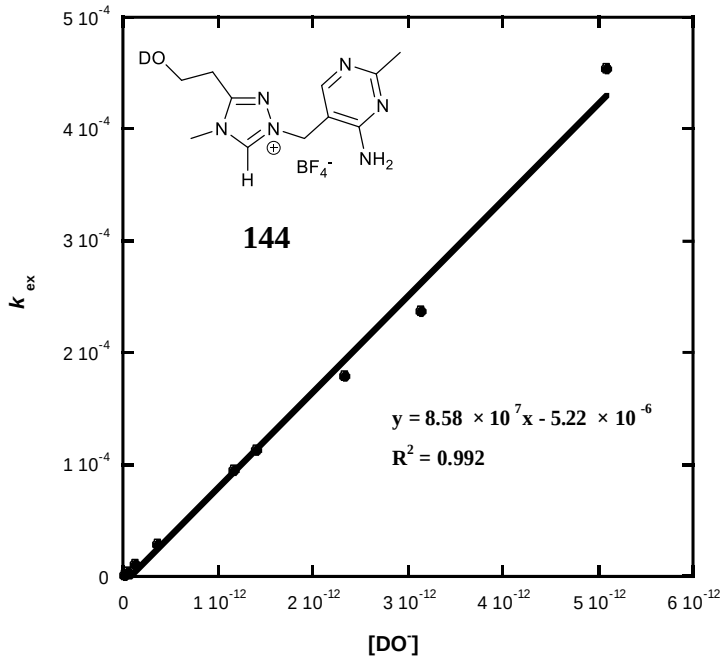

Figure 3.25 Plot of rate constant k_{ex} against deuteroxide concentration [DO^-] for mimic 184

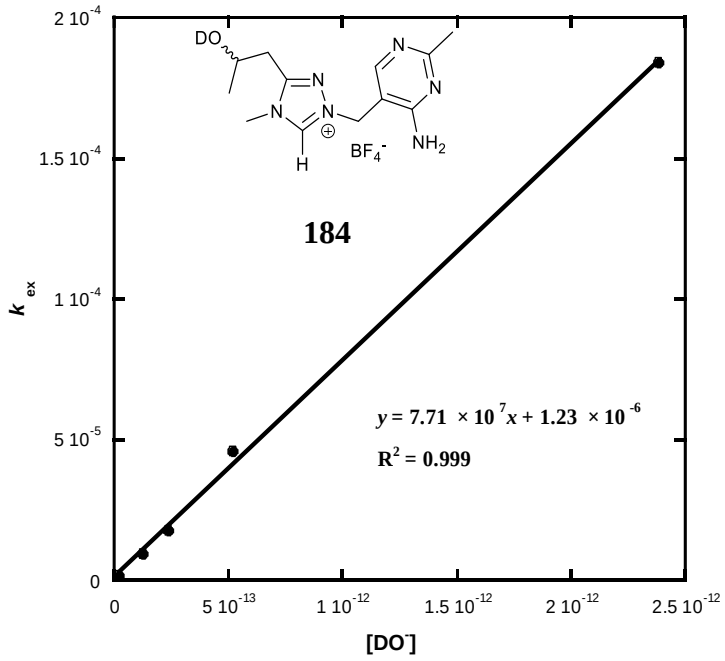

Figure 3.26 Plot of rate constant k_{ex} against deuteroxide concentration [DO^-] for mimic 183

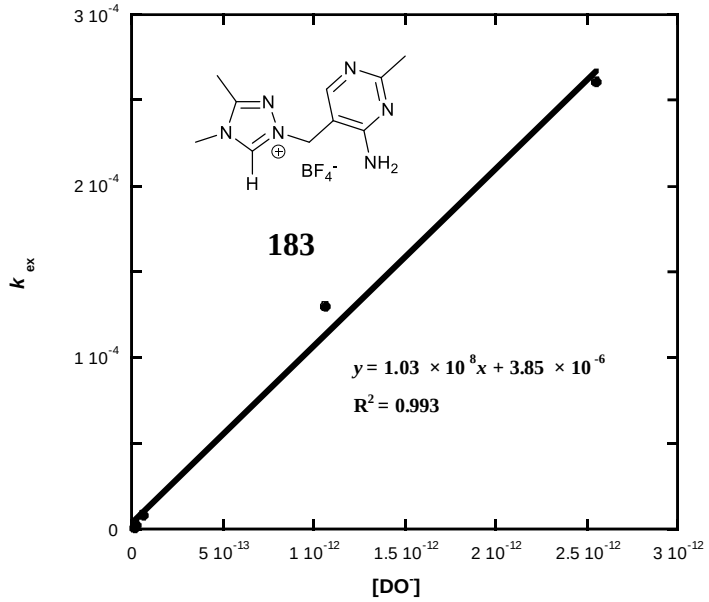

Figure 3.27 Plot of rate constant k_{ex} against deuteroxide concentration [DO^-] for mimic 185

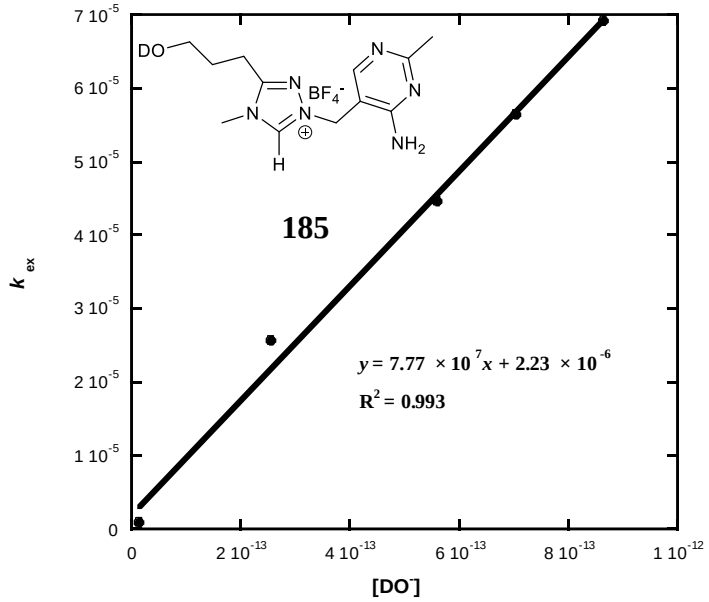

Figure 3.28 Plot of rate constant k_{ex} against deuteroxide concentration [DO^-] for thiamine chloride 7-Cl

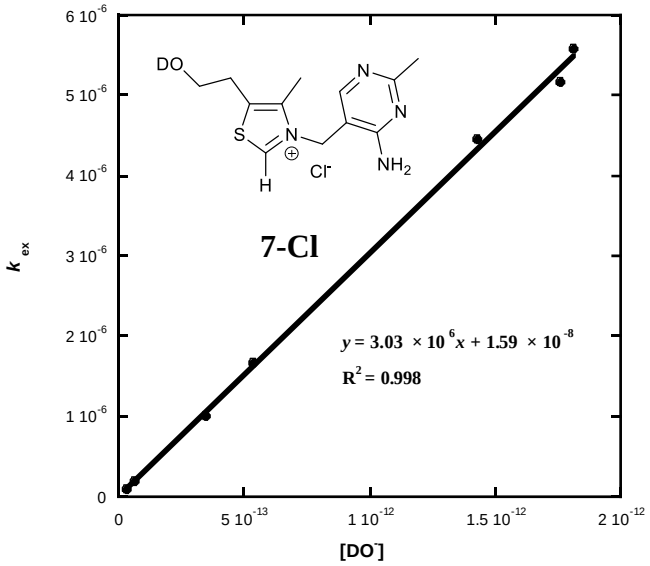

Figure 3.29 Plot of rate constant k_{ex} against deuteroxide concentration [DO^-] for thiamine mononitrate 7-NO_3

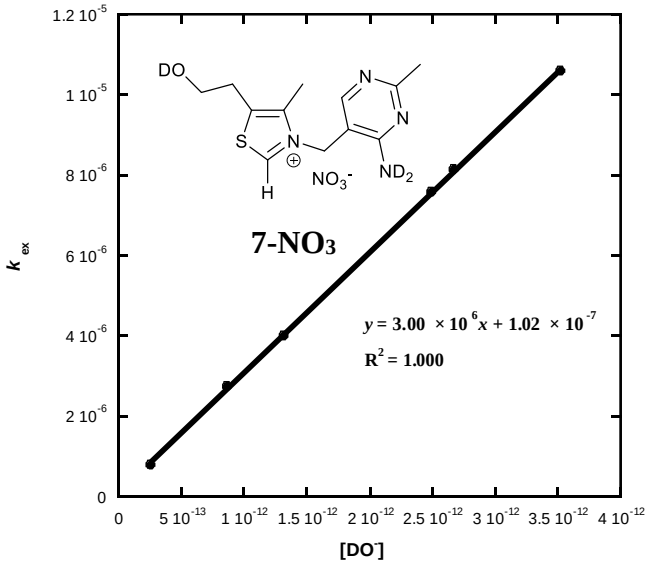

Figure 3.30 Plot of rate constant k_{ex} against deuteroxide concentration [DO^-] for triazolium salt 195

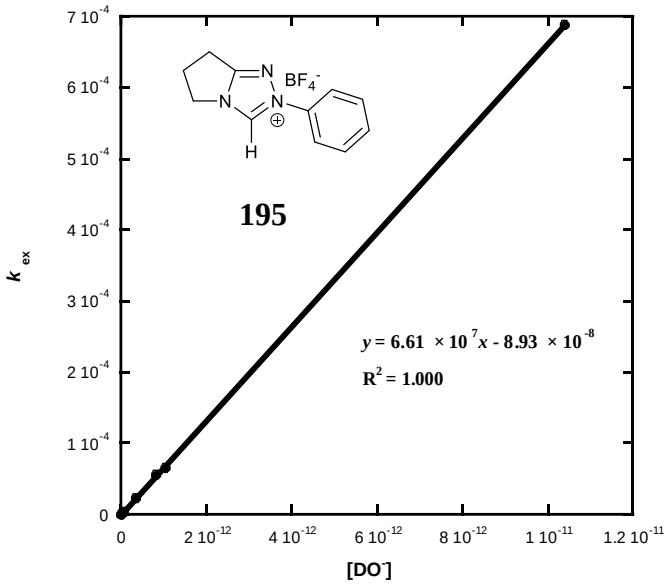

Figure 3.31 Plot of rate constant k_{ex} against deuteroxide concentration [DO^-] for triazolium salt 212

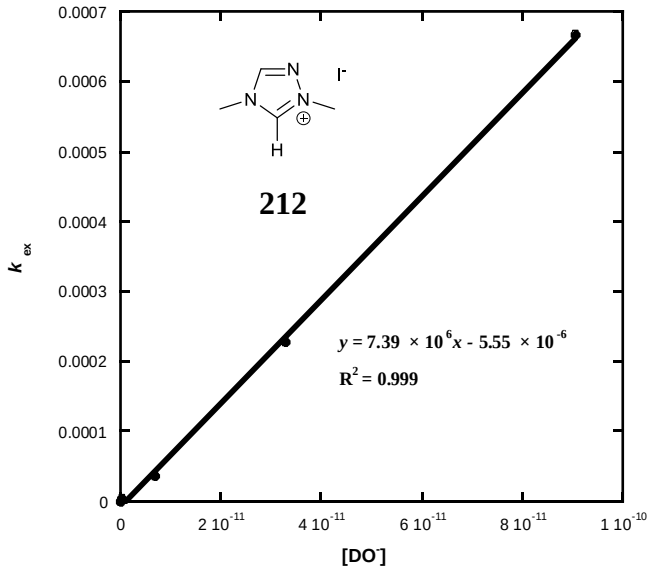

Second-order rate constants obtained from the plot of k_{ex} and deuteroxide concentration for all the salts studied are shown in the Table 3.12.

Table 3.12 Rate constants for exchange of the C3−H of triazolium mimics for deuterium in D_2O at 25 °C and I =1.0 (KCl)

	Substrate	k_{DO}[a] ($M^{-1}\,s^{-1}$)
144	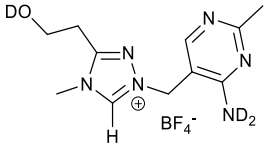	k_{DO} = 8.58 (± 0.30) × 10^7 $M^{-1}\,s^{-1}$ intercept = −5.22 (± 6.68) × 10^{-6} s^{-1}
184	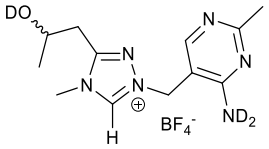	k_{DO} = 7.71 (± 0.15) × 10^7 $M^{-1}\,s^{-1}$ intercept = 1.23 (± 1.66) × 10^{-6} s^{-1}
183	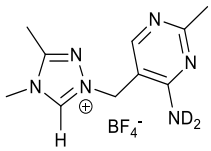	k_{DO} = 1.03 (± 0.05) × 10^8 $M^{-1}\,s^{-1}$ intercept = 3.85 (± 6.06) × 10^{-6} s^{-1}
185	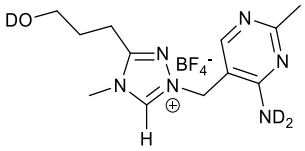	k_{DO} = 7.77 (± 0.37) × 10^7 $M^{-1}\,s^{-1}$ intercept = 2.23 (± 2.10) × 10^{-6} s^{-1}
7-Cl	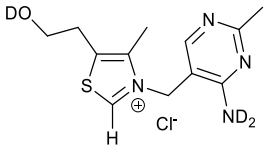	k_{DO} = 3.03 (± 0.05) × 10^6 $M^{-1}\,s^{-1}$ intercept = 1.59 (± 5.97) × 10^{-6} s^{-1}
7-NO_3	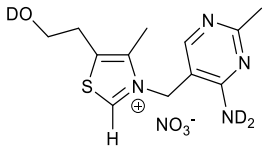	k_{DO} = 3.00 (± 0.02) × 10^6 $M^{-1}\,s^{-1}$ intercept = 1.02 (± 0.48) × 10^{-6} s^{-1}

195	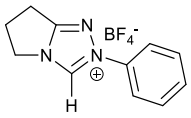	$\boldsymbol{k_{DO}} = 6.61\ (\pm\ 0.01) \times 10^{7}\ \mathbf{M^{-1}\ s^{-1}}$ intercept = 8.93 (± 38.4) × 10^{-6} s^{-1}
212	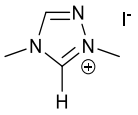	$\boldsymbol{k_{DO}} = 7.39\ (\pm\ 0.12) \times 10^{6}\ \mathbf{M^{-1}\ s^{-1}}$ intercept = 5.55 (± 4.99) × 10^{-6} s^{-1}

3.2.4 Estimation of k_{HOH}, k_{HO} and pK_a

Carbon acid pK_a values may be determined by using the second-order rate constants from experimental H/D exchange for the triazolium mimics studied in this thesis. The rate constants are related to the acid dissociation constant K_a and the ionic product of water by a modified Henderson-Hasselbalch equation (Equation 3.13) derived from combining equations from the self-ionization of water and reaction with the azolium salts studies in solution (Scheme 3.12).

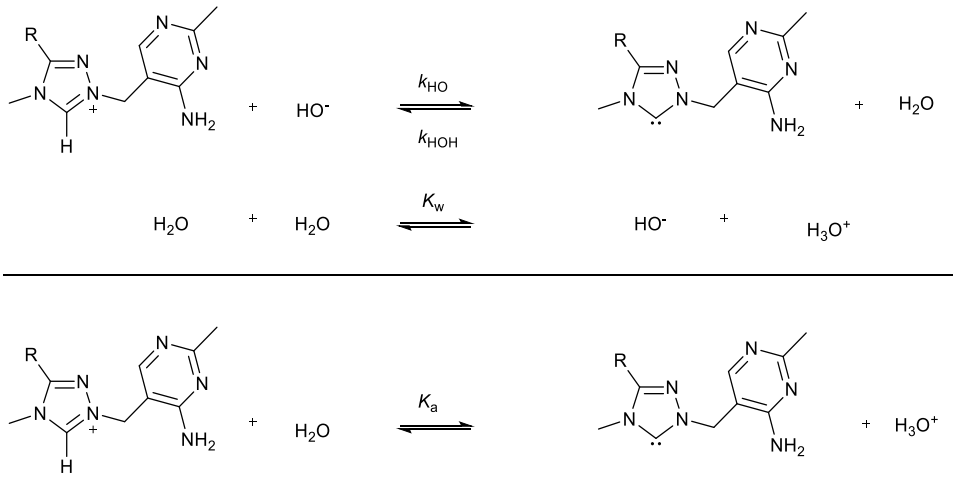

Scheme 3.12 Self ionization of water and reaction with generic triazolium mimic

$$\mathrm{p}K_{\mathrm{a}} = \mathrm{p}K_{\mathrm{w}} + \log_{10}\left(\frac{k_{\mathrm{HOH}}}{k_{\mathrm{HO}}}\right) \qquad \textbf{Equation 3.13}$$

Due to the lower solution basicity of hydroxide relative to deuteroxide, the value of k_{HO} may be obtained from k_{DO} by applying the secondary isotope effect relationship k_{DO}/k_{HO} =2.4[2]. As discussed in section 3.1 solvent reorganization was shown to be the rate-limiting step for the hydrogen to deuterium exchange experiments. Owing to solvent reorganization being rate-limiting for the forward step, it is therefore implied to be rate-determining for the reverse step to give the precatalyst (principle of microscopic reversibility). Consequently, the rate constant for protonation of the carbene may be taken to be that of solvent reorganization[10] (Equation 3.14).

$$k_{\mathrm{HOH}} = k_{\mathrm{reorg}} \approx 10^{11}\mathrm{s}^{-1} \qquad \textbf{Equation 3.14}$$

Kinetic specific catalysis (acid or base) refers to a reaction rate showing only a kinetic dependence on the concentration of the specific acid or base (H^+ or OH^- in water). Kinetic general catalysis (acid or base) additionally involves kinetic contributions to the rate from buffer species (BH^+ or B). Enzymes and functional groups may stabilize a transition state by donation or accepting a proton. For this work, the formate and acetate buffer base species could potentially contribute to the rate. However, the observation of no significant increase in observed pseudo-first-order rate constant for exchange at fixed p*D* implies the absence of general base catalysis. The rate constants and pK_a values determined for all the salts determined in this chapter are shown in Table 3.13.

Table 3.13 Summary of rate constants and pK_a values for azolium salts determined in this report

Substrate	k_{DO}[a] ($M^{-1}\,s^{-1}$)	k_{HO}[b] ($M^{-1}\,s^{-1}$)	pK_a[c]
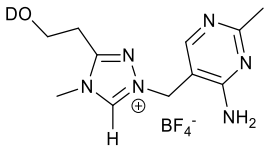 **144**	8.58×10^7	3.58×10^7	17.4
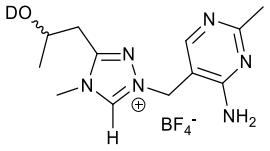 **184**	7.71×10^7	3.21×10^7	17.5
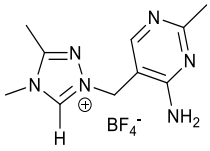 **183**	1.03×10^8	4.29×10^7	17.4
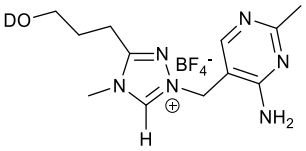 **185**	7.77×10^7	3.24×10^7	17.5
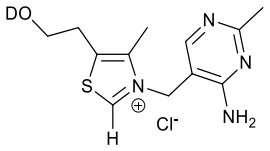 **7-Cl**	3.03×10^6	1.26×10^6	18.9
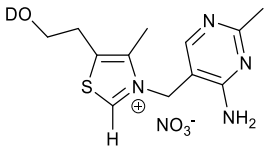 **7-NO_3**	3.00×10^6	1.25×10^6	18.9
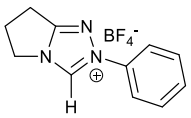 **195**	6.62×10^7 6.82×10^{7d}	2.76×10^7 2.83×10^{7d}	17.6 (17.5[d])

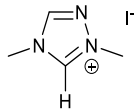 **212**	7.39×10^6	3.80×10^6	18.5

(a) Second order rate constants for deprotonation of the substrate ion at triazolium C(2) or C(3) by deuteroxide ion in D_2O. (b) Second-order rate constants for deprotonation of substrate at C(2) or C(3) by hydroxide ion in H_2O, calculated from the experimental value for k_{DO}, using an estimated secondary solvent isotope effect of $k_{DO}/k_{HO} = 2.4$ (c) Carbon acid pK_a for ionization of the substrate ion at C(2) in H_2O, calculated using Equation 3.13 (d) Results from previous group publication[6]

3.3 Discussion

This part compares data from the previous section with reported literature values and explains the various trends observed in the results. Analysis of the effect of substituents, counterion, ring heteroatom and speciation are discussed.

3.3.1 Effect of substituents on proton chemical shifts

Table 3.14 summarizes the chemical shifts for all N-heterocyclic azolium the salts used. The acidic (exchangeable) C3−H proton appears between 9.65 and 10.27 ppm, within a 0.7 ppm range. The highest value seen is due to the N-phenyl salt **195**, and the lowest due to both thiamine salts **7**. The triazolium analogues of thiamine all come up at 9.83 ppm except for the direct mimic **144** which appears at 9.71 ppm. The C3-H of N-phenyl salt **195** at 10.29 ppm is substantially higher than all others (9.65 – 9.83ppm) likely attributable to the absence of a donating N2-bridging alkyl group. This slight variation may be attributed to the p*D* of the buffered solution. The proton due to the Aryl−CH appears between 8.05 and 8.31 ppm for the salts bearing the 4-aminopyrimidinyl substituent. The highest chemical shift is due to the 5-methyl triazolium mimic **184** at 8.31 ppm.

Table 3.14 Proton NMR chemical shifts for azolium salts studied in D_2O

	Substrate	C3−H	Aryl−CH	N2−CH_2	N3−CH_3	Aryl−CH_3
144	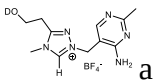 a	9.71	8.14	5.54	3.72	2.64
184	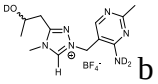 b	9.83	8.30	5.59	3.88	2.55
183	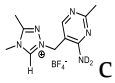 c	9.83	8.31	5.57	3.87	2.55

185	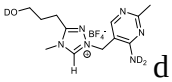 d	9.81	8.27	5.56	3.86	2.58
7-Cl	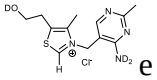 e	9.65	8.03	5.55	n/a	2.53
7-NO$_3$	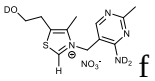 f	9.65	8.05	5.56	n/a	2.53
195	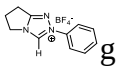 g	10.27	n/a	n/a	n/a	n/a
212	 h	9.68	n/a	n/a	n/a	n/a

NMR conditions for each salt as follows (a)p*D* 3.44 (b)p*D* 2.76 (c)p*D* 2.78 (d)p*D* 2.14 (e)p*D* 2.20 (f)p*D* 1.80 (g)p*D* 2.40 (h)p*D* 1.80

Overall the bridging methylene peak appears at approximately the same shift for all the salts studied at approximately 5.5 ppm, which suggests the protons to be in similar electronic environments i.e. attached to both a cationic nitrogen and a substituted pyrimidine. The shift due to the triazolium N-methyl appears at about 3.8 ppm for the four mimics synthesized. This value is highest for the 5-isopropyl derivative **183** and appears at 3.88 ppm. The pyrimidinyl methyl appears at ~ 2.5 ppm for the mimics and native thiamine. This is to be expected as it is far removed from any variations in the structure of the analogues for a marked difference in the chemical shift observed.

3.3.2 Alkyl versus aryl substituent effects on C3-H kinetic acidities towards deuteroxide ion, k_{DO} ($M^{-1}s^{-1}$) and C3−H pK_a values

Using values of kinetic acidities k_{DO} ($M^{-1}s^{-1}$), estimated from Section 3.2, pK_a values could be calculated for triazolium mimics **144**, **184**, **183**, **185**, **195, 212** and thiamine **7** (Cl^- and NO_3^-). The highest k_{DO} ($M^{-1}s^{-1}$) value was 1.03×10^8 **M^{-1} s^{-1}** for C5-isopropyl mimic **183** and the

lowest value reported among the salts incorporating a triazolium ring was for di-methyl salt **212** at 7.39×10^6 $\mathbf{M^{-1}\,s^{-1}}$ as presented in Table 3.12. This represents a fourteen-fold increase in kinetic acidity on going from a simple methyl substituent (**212**) to a 2-methyl-4-aminopyrimidinyl substituent (**183**). The increase in kinetic acidity towards deuteroxide for **183** may be explained by the presence of the pendant pyrimidine ring with electron withdrawing nitrogens, which better stabilizes the neutral carbene form relative to its positively charged conjugate acid. This increase in kinetic acidity (k_{DO}), and resulting decrease in pK_a, on going from salt **183** to salt **212** can also potentially be attributed to the presence of the electron withdrawing oxygen atom on the C5 substituent. As all novel thiamine mimics **144**, **183 – 185** have higher k_{DO} values and lower pK_as than for **212**, this confirms the net electron-withdrawing effect of the N_2CH_2-pyrimidinyl and C5-alkoxy groups.

Within the series of N2-methyl-4aminopyrimidinyl substituted triazolium salts, the pK_a only varies between 17.4 and 17.5 and kinetic acidity k_{DO} by varies 1.3 fold. The simple 5-methyl substituted salt **183** (pK_a = 17.4) is the lowest in the range and the 5-isopropyl substituted salt **184** (pK_a = 17.5) has the highest value. This small change may potentially be attributed to the length of the alkyl chain, with the isopropyl substituent being more electron-donating than the simple methyl substituent, which favours stabilization of the positively charged conjugate acid relative to the neutral carbene resulting in a slightly lower kinetic acidity k_{DO} and hence higher pK_a. This change is small across the series (0.1 pK_a unit), and close to experimental error (± 10 % in k_{DO}), reflecting the great similarity among the mimics and the fact that the N5 substituent is well removed from the C3−H.

3.3.3 Thiazole versus triazole comparison on C(3)-H carbon acid pK_a values

Until now, a direct like for like comparison has not been made for thiamine and any direct triazolium derivative to the best of our knowledge where only the central heterocycle has been

changed. The triazole mimic **144** ($\boldsymbol{k_{DO}} = 8.58 \times 10^7\ \mathbf{M^{-1}\,s^{-1}}$) is fifteen-fold more reactive toward deuteroxide than thiamine **7** ($\boldsymbol{k_{DO}} = 3.0 \times 10^6\ \mathbf{M^{-1}\,s^{-1}}$) with like-for-like substitution, thus the effect of replacing the sulfur with two nitrogen atoms is an increase in acidity at C3-H (Table 3.12). The results show good agreement with the observed chemical shifts of the C3−H of triazolium salt **144** (δ 9.71 ppm) and C2−H of thiamine **7** (δ 9.65 ppm), suggesting that the triazolium ring system is more electron-withdrawing overall than the corresponding thiazolium ring, due to the greater π-donating ability of nitrogen toward carbon[4, 11]. This increase in electron-withdrawing character on going from thiazolium to triazolium results in the increase in acidity observed between the mimics **144**, **184**, **183**, **185**, **195** and natural thiamine **7**. This work estimates the pK_a of thiamine to be 18.9 and its corresponding triazolium derivative to be 17.4 at I = 1.0 (KCl) at 25 °C. Previous studies by Jencks determined the acidity of thiamine as pK_a = 18 at I = 2.0 (KCl) and 30 °C[3].

3.3.4 Comparison of triazolium mimics with N-phenyl salt

Surprisingly, the N-phenyl salt **195** shows similar kinetic acidity ($\boldsymbol{k_{DO}} = 6.62 \times 10^7\ \mathbf{M^{-1}\,s^{-1}}$) compared to triazolium mimics studied **144**, **183 – 185** ($\boldsymbol{k_{DO}} = [7.71{-}10.3] \times 10^7\ \mathbf{M^{-1}\,s^{-1}}$). This is about a 1.1 fold increase for the C5-isopropyl triazolium mimic **184** and 1.5 fold increase compared to the dimethyl triazolium mimic **183**. Considering that the N-phenyl salt **195** has a direct aryl substituent attached to the N2 atom of the triazolium ring, while the novel triazolium mimics have an alkyl CH_2 appendage, one might expect salt **195** to have a higher k_{DO} value. However, the CH_2-pyrimidyl substituent has three nitrogen atoms, and also the potential for N-protonation, which would increase C3-H acidity.

3.3.5 Effect of counterion on the second-order rate constants

For the range of mimics studied, **144**, **184**, **183**, **185**, **195** the counter ion used was tetrafluoroborate (BF_4^-). For native thiamine **7**, the chloride **7-Cl** ($3.03 \times 10^6\ \mathbf{M^{-1}\,s^{-1}}$) and the nitrate **7-NO$_3$** ($3.00 \times 10^6\ \mathbf{M^{-1}\,s^{-1}}$) show negligible difference in kinetic acidities towards

deuteroxide ion, with the chloride salt being only marginally more acidic than the nitrate salt. A 1.01-fold increase in k_{DO} is observed upon on going from the nitrate to the chloride counterion which is well within experimental error. Given that the exchange reactions were conducted at saturating ionic strength (I=1.0 (KCl)), using millimolar concentrations of the azolium salts, it is reasonable that the change in counterion has minimal effect. Previous studies by our group show the effect of counterion to be minimal as the fully aqueous conditions favours hydrogen bonding with deuterium oxide minimizing the effect of the counterion. Overall the data suggest that the change in counterion can only lead to a maximum of 1.1 times effect so the main difference is due to the central heterocycle.

3.3.6 Effect of speciation on the pK_a values of the triazolium salts

The triazolium mimics studied **144**, **184**, **183**, **185**, **195** and thiamine which bears the 2-aminopyrimidinyl substituent may potentially exist in aqueous solution in various protonated states (**Scheme 3.13**). Given that the observed acidity of our triazolium salts is relatively high compared to the di-alkyl triazolium salt **212** studied, it is important to consider the speciation of the triazolium mimics under the conditions of our exchange. The pK_a of the pyrimidinium cation is reported in the literature to be 1.5 - 2 units[12], however, this value will be substantially decreased owing to the adjacent cationic azolium ion. Similarly, the exocyclic amino pK_a will be decreased owing to the adjacent triazolium cation. For example, the pK_a of $N^+H_3N^+H_3$ is −1 in water whereas that for $N^+H_3NH_2$ is ~8[13], showing a large pK_a decrease with an adjacent positive charge.

Given that the exchanges were monitored at pDs 0 − 4 above these pK_as, the extent of diprotonation is likely small (e.g. A in Scheme 3.13) Since the plot of log k_{ex} vs pD deuteroxide concentration does not show any marked deviation from unity, the triazolium mimics are likely

to exist in solution in only one monocationic speciation state for the range of p*D* used to obtain the plots.

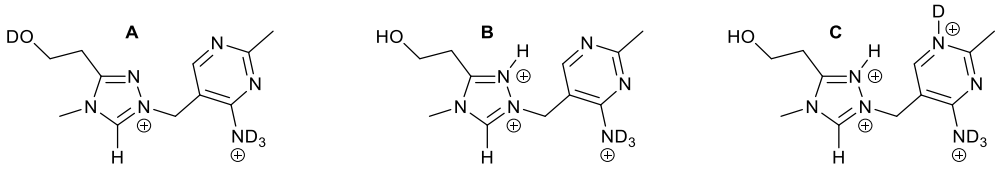

144

Scheme 3.13 Possible protonation states of triazolium mimic 144 in solution

3.4 Conclusion

For these studies, the carbon acid pK_a values for several novel triazolium-based mimics of thiamine were determined using a kinetic H/D exchange method. The pseudo-first-order rate constants k_{ex} (s^{-1}) for exchange were estimated using ^{1}H NMR spectroscopy. Second-order rate constants for deuteroxide ion catalysed exchange (k_{DO}, $M^{-1}\,s^{-1}$) were obtained from the slope of the plot of k_{ex} against deuteroxide concentration, which are referred to as kinetic acidities.

Experimental evidence was used to establish the absence of general-base catalysis by analysis of H/D exchange in a range of formic acid buffer concentrations at the same buffer ratio. This informed the decision to remove the term for contributions to exchange from buffer catalysis and hence values for k_{DO} may be calculated.

The triazolium based mimics **144, 183-185** show a fifteen-fold increase in acidity towards deuteroxide ion than for corresponding native thiamine **7**. This is due to the presence of two extra ring nitrogen atoms which favours the stability of the carbene/ylide. The range of mimics do not show a significant variation in acidity (0.1 unit of pK_a) mostly due to the 5-substituent being relatively far removed from the carbenic carbon atom. Aside from the 5-substituent on the triazolium ring, the mimics were structurally identical otherwise.

Interestingly, the di-alkyl triazolium salt studied showed a much lower acidity to the triazolium mimics of thiamine, which suggest the N2-methylpyrimidinyl substituent to be electron-withdrawing, hence the observed lower pK_a for all the direct triazolium mimics. The N-phenyl triazolium salt previously studied in the group showed similar kinetic acidities compared to the novel mimics which suggest similar effects between the N2-phenyl and the N2CH_2-pyrimidinyl substituent. This is an important observation as it shows the triazolium mimics have closely similar acidity to one of the most widely used and versatile triazolium organocatalysts.

3.5 References

1. (a)F. G. Bordwell, *Acc. Chem. Res.*, 1988, **21**, 456-463; (b)F. G. Bordwell, W. S. Matthews and N. R. Vanier, *J. Am. Chem. Soc.*, 1975, **97**, 442-443; (c)A. Streitwieser, J. C. Ciula, J. A. Krom and G. Thiele, *J. Org. Chem.*, 1991, **56**, 1074-1076; (d)A. Streitwieser, D. Z. Wang, M. Stratakis, A. Facchetti, R. Gareyev, A. Abbotto, J. A. Krom and K. V. Kilway, *Can. J. Chem.*, 1998, **76**, 765-769.
2. M. W. Washabaugh and W. P. Jencks, *Biochemistry*, 1988, **27**, 5044-5053.
3. T. L. Amyes, S. T. Diver, J. P. Richard, F. M. Rivas and K. Toth, *J. Am. Chem. Soc.*, 2004, **126**, 4366-4374.
4. J. Kapp, C. Schade, A. M. El-Nahasa and P. von Ragué Schleyer, *Angew. Chem. Int. Ed. Engl.*, 1996, **35**, 2236-2238.
5. E. M. Higgins, J. A. Sherwood, A. G. Lindsay, J. Armstrong, R. S. Massey, R. W. Alder and A. C. O'Donoghue, *Chem. Commun.*, 2011, **47**, 1559-1561.
6. R. S. Massey, C. J. Collett, A. G. Lindsay, A. D. Smith and A. C. O'Donoghue, *J. Am. Chem. Soc.*, 2012, **134**, 20421-20432.
7. A. K. Covington, R. A. Robinson and R. G. Bates, *J. Phys. Chem.*, 1966, **70**, 3820-3824.
8. J. Bouffard, B. K. Keitz, R. Tonner, G. Guisado-Barrios, G. Frenking, R. H. Grubbs and G. Bertrand, *Organometallics*, 2011, **30**, 2617-2627.
9. R. S. Massey and A. C. O'Donoghue, Ph.D., Durham University, 2013.
10. A. C. O'Donoghue and R. S. Massey, in *Contemporary Carbene Chemistry*, John Wiley & Sons, Inc, Hoboken, NJ, 2013, DOI: 10.1002/9781118730379.ch3, pp. 75-106.
11. F. Bernardi, A. Bottoni and A. Venturini, *J. Am. Chem. Soc.*, 1986, **108**, 5395-5400.
12. T. M. Krygowski, H. Szatyłowicz and J. E. Zachara, *J. Org. Chem.*, 2005, **70**, 8859-8865.
13. S. F. Nelsen, D. T. Rumack, L. W. Sieck and M. Meot-Ner, *J. Am. Chem. Soc.*, 1988, **110**, 6303-6308.

Chapter Four

4 Catalytic Evaluation of Triazolium Mimics

Foreword

Central to this project is the proposed replacement of the thiazole of thiamine pyrophosphate with a 1,2,4-triazolium ring. This chapter focuses on initial scoping experimentation to compare the relative catalytic efficiencies of thiamine and the triazolium mimics prepared in the present work, in coupling a range of aldehydic substrates, under identical conditions with a focus on the first step for reaction of NHC and aldehyde. As already discussed in the introductory chapter, the catalytic cycle begins with initial deprotonation of the C_2H of the thiazolium active site in thiamine to give the active carbenic form. This chapter focuses on the comparison of reaction rates and concentration profiles of both thiamine and the triazolium analogues prepared.

4.1 Introduction

4.1.1 Comparative Kinetic Studies of the Benzoin Condensation

Wohler and Liebig were the first to report the use of cyanide to catalyse the conversion of benzaldehyde **5** to benzoin **6**[1]. Much later on, Ugai[2] reported the self-condensation of **5** to give **6** in the presence of thiamine **7** and a weak base. The catalytic action of **7** was attributed to its thiazole ring by Mizuhara[3]. Breslow[4] put forward the now widely accepted model by observing deuterium exchange between the thiazolium cation and its carbenic/ylide form (Scheme 4.1). This mechanism was derived from work previously published by Lapworth[5] on the cyanide catalysed formation of benzoin **6**.

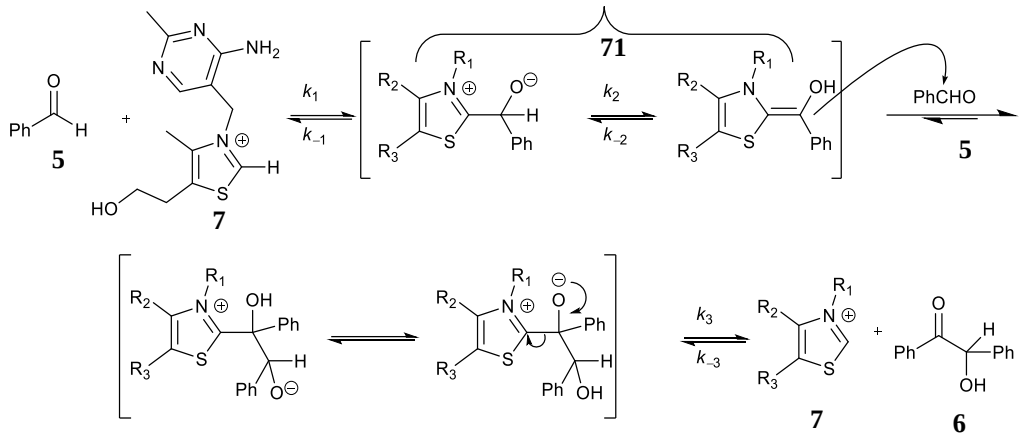

Scheme 4.1 Mechanism proposed by Breslow for thiamine 7 catalysed benzoin 6 formation[4]

Much later, Leeper et al.[6] reported a detailed kinetic investigation of the benzoin condensation in methanol promoted by a N-benzyl thiazolium catalyst **215**. Concentrations of the species present in the reaction mixture were monitored using ^{1}H NMR spectroscopy at 27 °C. Experiments were performed using known concentrations of substrate under pre-steady-state conditions to facilitate easy determination of stepwise rate constants in the mechanistic pathway (Scheme 4.2). During the course of the reaction, the hydroxyaryl adduct **216** was identified as a relatively stable intermediate. The authors posited that any other intermediate formed was transient on the NMR timescale, including the putative Breslow intermediate **217**.

The authors inferred that the interconversion between the precatalyst **215** and its active carbenic form was fast on the NMR timescale for the experiment conducted, and studies of isotopic exchange by the O'Donoghue group supports this[7].

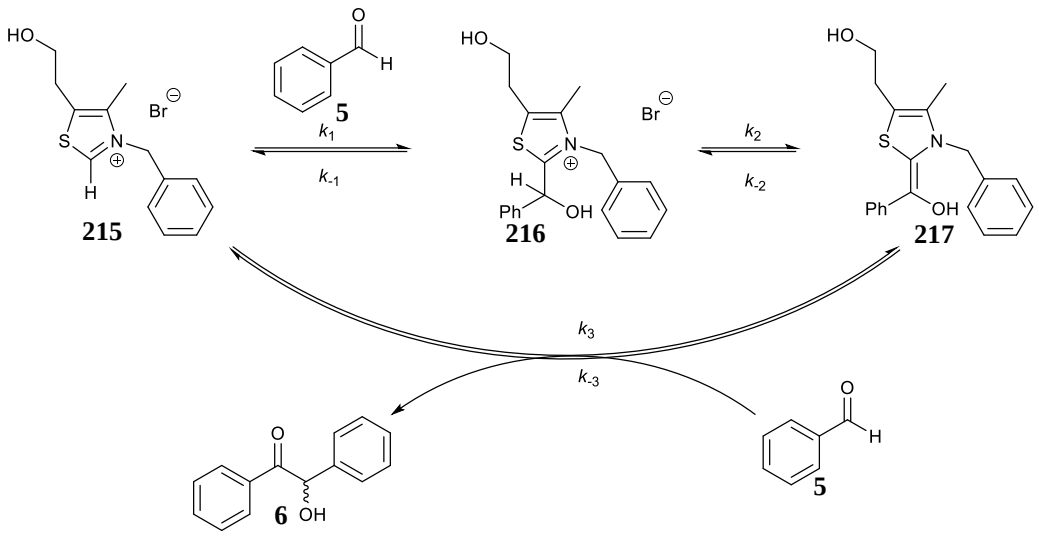

Scheme 4.2 Kinetic studies by Leeper of the benzoin condensation by N-benzyl thiazolium salt 215

Representative peaks due to the substrate (benzaldehyde) **5,** adduct **216**, and product **6** (benzoin) in comparison to the unbound thiazolium ion **215**, were integrated to give the concentration of each species for the duration of the experiment. Rate constants (k_1, k_2 and k_3) were determined for each step, from fitting concentration plots to rate equations. All three steps were found to contribute significantly to the overall rate.

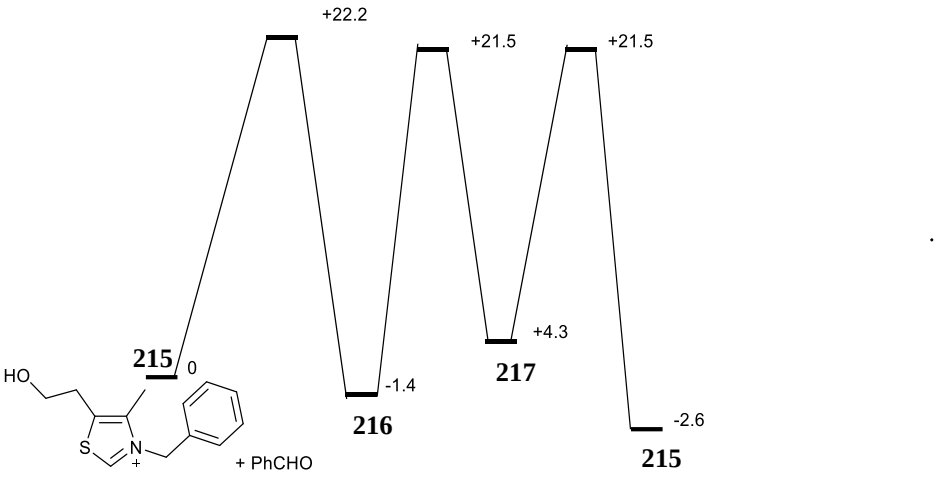

Figure 4.1 Free energy profile for the benzoin condensation reaction of benzaldehyde (1M) catalysed by benzyl thiamine 215 at 27 °C determined from experimental rate constants

A free energy profile was obtained from free energies of activation determined using the rate constants. Estimates of the pK_a of a O-methylated analogue of **216, 218** 15.5 (Figure 4.2) were used to give the activation energy of the Breslow intermediate because this could not be obtained using the concentration plot.

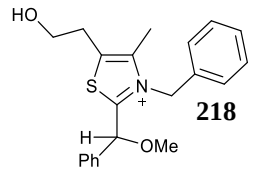

218

Figure 4.2 Methylated analogue of the adduct 218

The kinetic deuterium isotope effect, i.e., change in rate of reaction upon substituting proton for deuterium, was found to be $k_H/k_D \cong 3.4$ for benzaldehyde-d supporting Breslow intermediate **217** formation being at least partially rate limiting. A considerable inverse solvent isotope effect $k_D/k_H \cong 5.9$ for deuterio methanol was obtained, which was attributed to slowing down reverse protonation of **217** to favour more product formation.

4.1.2 Isolation of hydroxyaryl adduct: the proposed first intermediate for NHC-catalysis of aldehydic transformations

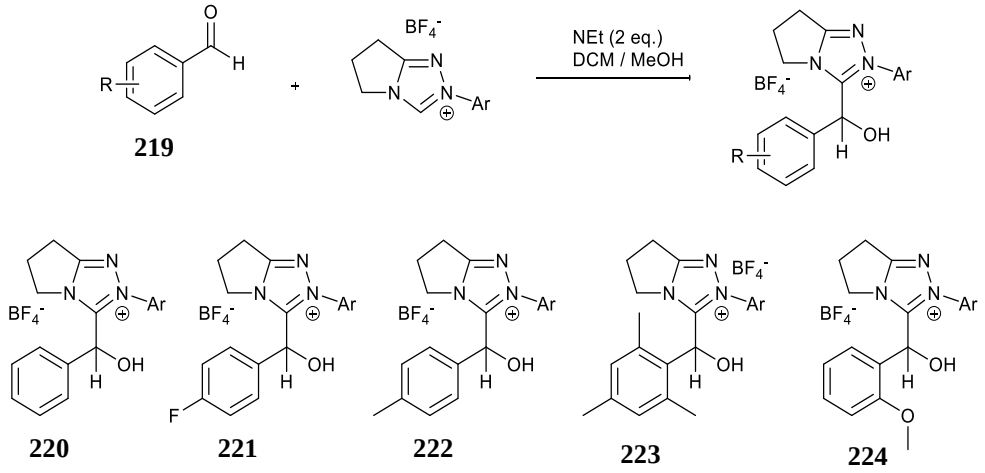

Scheme 4.3 formation of hydroxy aryl adduct

Previous work in our group by Massey prepared several 3-(hydroxybenzyl)triazolium derivatives from aryl aldehydes and triazolium salts by addition of triethylamine. However, these were found to revert to the aldehyde and triazolium ion under basic conditions relatively rapidly. Furthermore, attempts at purification using conventional normal phase silica gel column chromatography was ineffective, but reverse phase chromatography gave pure compounds in low yields. Adducts with a 2-methoxy substituent on the phenyl ring were more stable than the others and could be separated using silica gel normal phase column chromatography.

Figure 4.3 Proton and Carbon NMR chemical shifts for the adduct and ketone tautomer

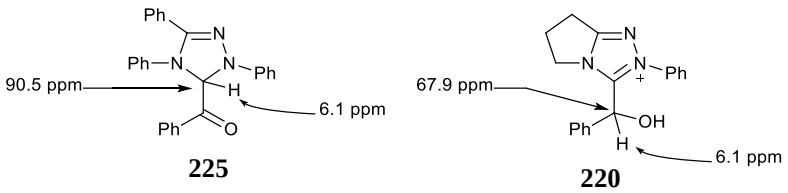

The ketone tautomer **225** of the Breslow intermediate derived from a triphenyl triazolium precatalyst was reported in the literature by Berkessel[8] with the proton chemical shift for the C(3)-H similar to that of the C(α)-H for the isolated phenyl adduct **220** (Figure 4.3).

Corroboratory evidence for proof of structure was however obtained using ^{1}H, ^{13}C HSQC NMR spectroscopy, showing the C(α) chemical shift to be 67.9 ppm, about 20 ppm units lower than for the ketone tautomer **225** reported (90.5 ppm).

In addition, Massey successfully obtained crystal structures of three adducts, phenyl **220**, parafluoro **221** and parамethyl **222** derivatives, which gives unambiguous proof of structure. These were isolated from solutions of DCl (~ 0.1 M) in deuterated water with the chloride counterion (Figure 4.4).

Figure 4.4 **X-ray crystal structures obtained by Massey for adducts N-aryl 220, 221 and 222. (Reproduced with permission from Chemical Science. Copyright © The Royal Society of Chemistry 2013)[9]**

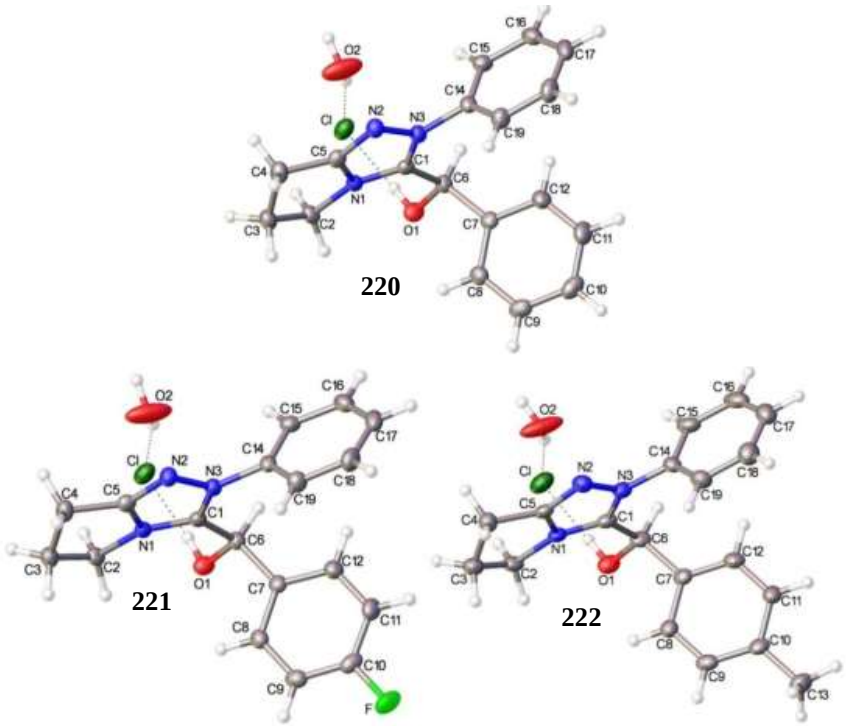

4.1.3 Effect of aryl aldehyde substituent on hydroxyaryl adduct formation

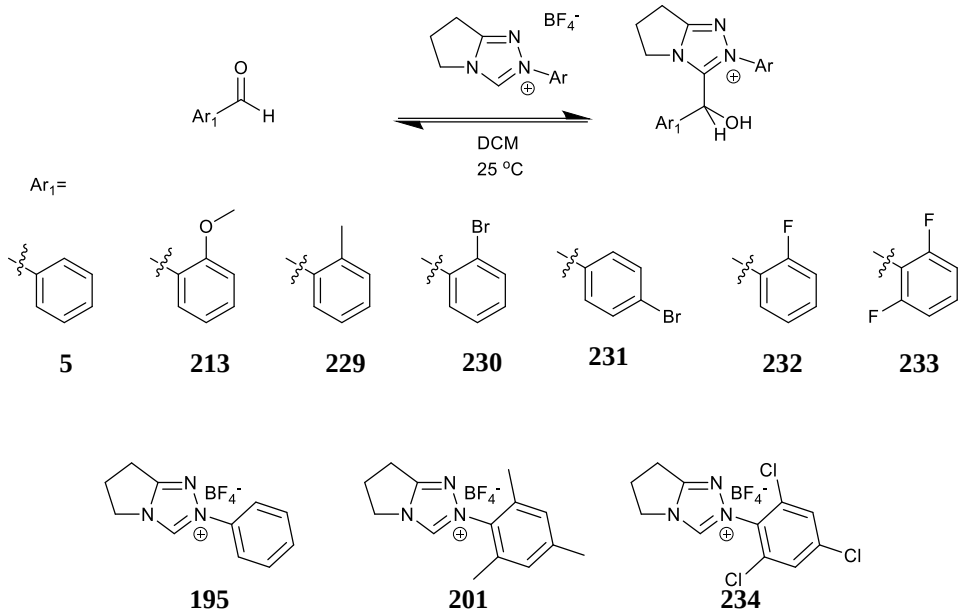

5 **213** **229** **230** **231** **232** **233**

195 **201** **234**

Table 4.1 **Equilibrium constants *K* for 3-(hydroxybenzyl)azolium adduct formation [10]**

NHC	Ar_1	K^{exp} [M^{-1}]
195	**5**	3
195	**213**	56
201	**5**	31
201	**213**	143
234	**5**	39
234	**213**	301
201	**229**	16
201	**230**	332
201	**231**	15
201	**232**	150
201	**233**	785

Table 4.1 shows the values of equilibrium constants *K* for a range of aryl aldehydes reacting with three triazolium precatalysts[10]. These values were determined experimentally by ^{1}H NMR spectroscopy under pre-steady state stoichiometric conditions with < 10 % benzoin product formation. The results from Table 4.1 above show the largest *K* value for the reaction between N-mesityl catalyst **201** and aldehyde 2,6-difluorobenzaldehyde **233** giving K^{exp} = 785 M^{-1}. The smallest *K* value for the series was between N-phenyl catalyst **195** and benzaldehyde **5** with K^{exp} = 3 M^{-1}. This demonstrates that substitution on the aromatic rings can significantly affect the equilibrium constant.

Comparing the reaction of the three catalysts **195**, **201** and **234** with 2-methoxybenzaldehyde **213**, suggests that the 2,4,6-trichlorophenyl **234** precatalyst gives the largest *K* value of K^{exp} = 301 M^{-1} which is about six-fold the value for the unsubstituted N-phenyl catalyst **195** K^{exp} = 56 M^{-1}**.** This effect is also observed with the 3-halo-substituted substrates, for example, the reaction between 4-bromobenzaldehyde **231** and the N-mesityl catalyst gave K^{exp} = 15 M^{-1} however using 2-bromobenzaldehyde **230** gave K^{exp} = 332 M^{-1}, a substantial 22-fold increase. Also, adding a halogen to the 6-position further increased the experimentally observed *K* value. For example, N-mesityl catalyst **201** and aldehyde 2,6-difluorobenzaldehyde **233** giving K^{exp} = 785 M^{-1}.

In order to further probe these observed effects, rate constants for formation of 3-(hydroxybenzyl)azolium adducts were obtained. Kinetic measurements had not been previously reported at the time for triazolium promoted benzoin or Stetter reactions. Pre-steady state conditions were used to monitor the reaction of aldehyde **28**, which is a commonly used test substrate for the intramolecular Stetter reaction. The Stetter reaction is closely related to

the benzoin condensation with identical proposed reaction steps up to the Breslow intermediate. The main difference lies with the onward second molecule of aldehyde for the benzoin reaction whereas the Stetter reaction involves a Michael-type acceptor.

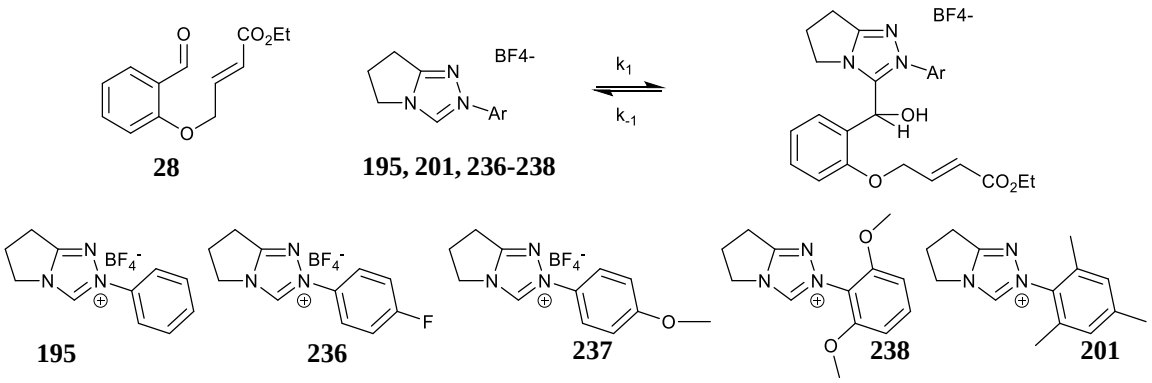

Scheme 4.4 Measurement of rate and equilibrium constants for 3-(hydroxybenzyl)azolium adduct formation from aldehyde 28

Table 4.2 shows values of equilibrium constants using variously substituted N-aryl triazolium catalysts.

Table 4.2 Measurement of rate and equilibrium constants for 3-(hydroxybenzyl)azolium adduct formation

N-aryl substituent	k_1 $M^{-1}s^{-1}$	k_{-1} s^{-1}	K^{exp} M^{-1}	K^{fit} M^{-1}
195	1.52×10^{-2}	4.76×10^{-5}	319	394
236	4.89×10^{-2}	9.45×10^{-5}	383	433
237	1.28×10^{-2}	3.09×10^{-5}	414	555
238	1.07×10^{-2}	$\leq 1.01 \times 10^{-7}$	$>1 \times 10^{5}$	7034
201	3.85×10^{-2}	1.25×10^{-5}	3082	3414

Pseudo-second-order rate constants (k_1, $M^{-1}s^{-1}$) and equilibrium constants (K^{exp}, M^{-1}) were obtained from kinetic analysis of the reaction mixture prior to notable product formation (< 5 %). Reaction of the NHC with aldehyde is preceded by initial deprotonation of the precatalyst

by triethylamine base. The base is recycled by protonation of the initial hydroxyanion adduct giving rise to a pseudo-second-order process.

From the table, the parafluorophenyl substituted catalyst **236** gave the largest value of $k_1 = 4.89 \times 10^{-2}\ M^{-1}s^{-1}$ while the lowest value was obtained using the 2,6-dimethoxyphenyl catalyst **238,** $k_1 = 1.07 \times 10^{-2}\ M^{-1}s^{-1}$, a difference of ~5-fold. The N-phenyl catalyst **195** gave a value of $k_1 = 1.52 \times 10^{-2}\ M^{-1}s^{-1}$ which is less than half the value for the mesityl catalyst **199** $k_1 = 3.85 \times 10^{-2}\ M^{-1}s^{-1}$.

4.2 Concentration profiles by ^{1}H NMR spectroscopy for triazolium mimics

As outlined in the introduction, previous studies have shown triazolium precatalysts to be in rapid equilibrium with a range of different types of aldehydes for both typical benzoin and Stetter processes. In order to evaluate the novel triazolium mimics prepared in the present work, we have done analogous experiments with our triazolium mimics and a range of aldehydes (Figure 4.5).

Using ^{1}H NMR spectroscopy, the reactions of aldehydes **213, 240-244** and catalysts **7, 144, 183** and **212** were monitored using carefully measured concentrations in triethylamine-buffered (2:1 NEt_3:HCl) methanol-d_4. The use of 0.04M of catalyst enables easy detection of any stable intermediate(s) formed during the course of the reaction such as the hydroxyaryl adduct. Concentration profiles were obtained for thiamine and several other triazolium mimics under these reaction conditions.

Figure 4.5 NHC-precatalysts and aldehydes studied in this work

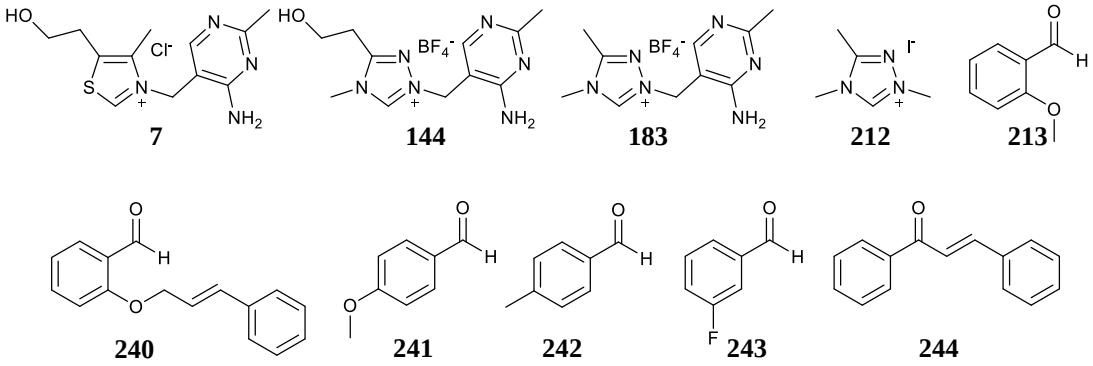

4.2.1 Reaction of 2-methoxybenzaldehyde 213 in the presence of 2-hydroxyethyl triazolium precatalyst 144

2-Hydroxyethyltriazolium precatalyst **144** (0.04 M), triethylamine (0.107 M), triethylamine hydrochloride salt (0.053 M) in deuterated methanol (CD_3OD) were pre-mixed in a rigorously dried NMR tube. 2-Methoxybenzaldehyde **213** (0.06 M) was added and mixed thoroughly to commence the reaction. The reaction was transferred to an NMR instrument with the probe

maintained at 25 °C. NMR spectra were recorded continuously for the duration of the experiment with each acquisition taking approximately 4 min. An overlay of spectra acquired at two time points during the experiment is presented below (Figure 4.6).

Figure 4.6 **Overlay of ^{1}H NMR spectra at 500 MHz for the reaction of 2-hydroxyethyltriazolium (0.04 M) precatalyst 144 and 2-methoxybenzaldehyde (0.06 M) 213 in methanol-d$_4$ at 25 °C and 0.16 M triethylamine buffer.**

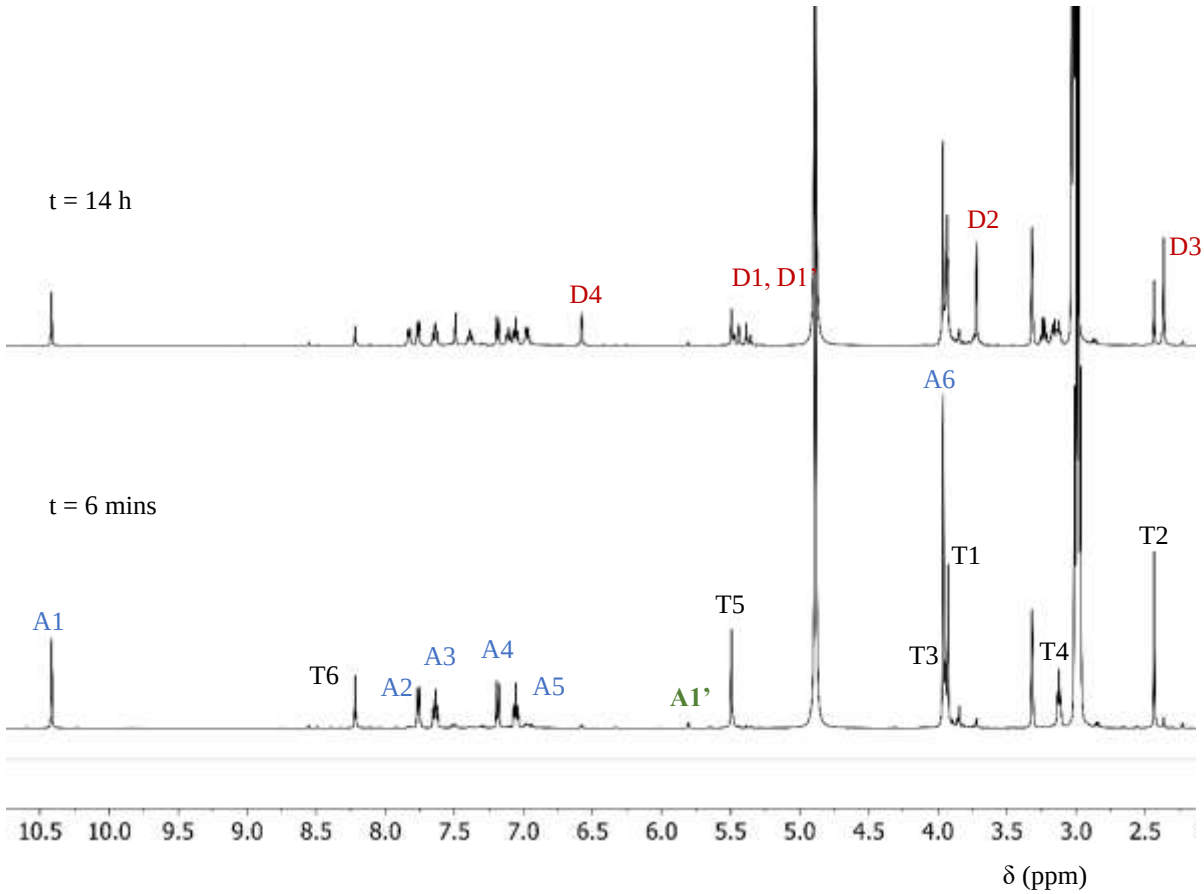

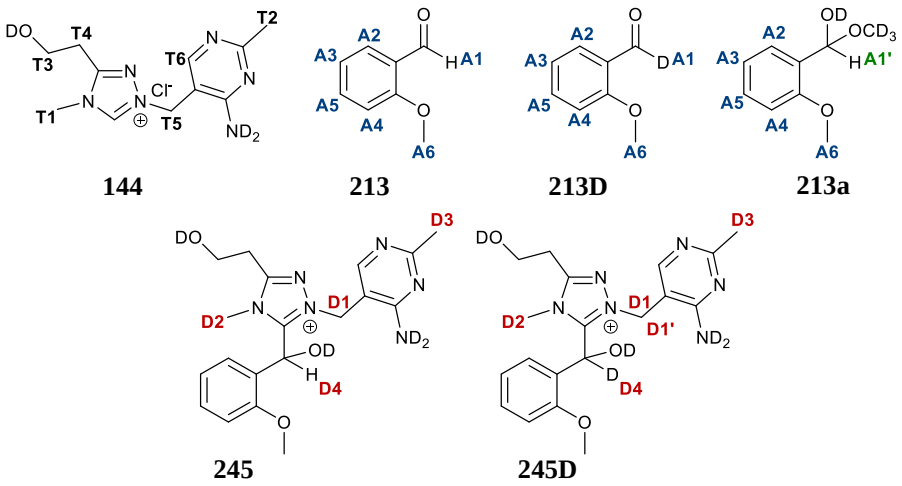

Scheme 4.5 Chemical shift assignments of the proton NMR peaks for the reaction species present in solution

At the start of the reaction, analysis shows exclusively C(3)−D deuterated 2-hydroxyethyltriazolium precatalyst **144**, the C(2)−H (9.7 ppm) having been completely exchanged owing to the basic conditions used. The diagnostic benzoin product peak (6.11 ppm) CO(*H*OH) was not seen for the duration of the experiment. The disappearance of precatalyst **144** and aldehyde **213** is closely matched by the appearance of adduct **245,** there is a small amount of deuteration of both aldehyde and adduct to give **213D** and **245D** respectively. Distinct peaks for each species present in solution were used to estimate its concentration by integration. The singlet peak appearing at 3.93 ppm (T1) corresponds to the triazolium methyl of unbound **144**. The singlet appearing at 2.43 ppm (T2) represents the pyrimidinyl methyl of free **144**. The peaks for the hydroxyethyl side chain of **144** appear as triplets at 3.94 ppm (T3-*sandwiched between A6 and T1*) and 3.12 ppm (T4). The bridging methylene of **144** presents as a singlet at 5.49 ppm (T5) and the pyrimidinyl C−*H* as a singlet at 8.21 ppm (T6).

The singlet peak appearing at 10.41 ppm (A1) represents the aldehydic hydrogen of 2-methoxybenzaldeyde **213**. The doublet at 7.76 ppm (A2) corresponds to the ortho proton C-*H* on the aldehyde phenyl ring. The triplet at 7.64 ppm (A3) represents one of the meta proton C-*H* on the aldehyde ring. The doublet at 7.18 ppm (A4) represents one of the meta C-*H* of the

aldehyde and the triplet at 7.06 ppm (A5) represents the para proton C-*H* on the aldehyde. The singlet at 3.96 ppm (A6) corresponds to the methoxy hydrogens of **213**.

Over time the presence of triazolium precatalyst-aldehyde adduct **245** can be detected by the appearance of duplicate peaks alongside those of triazolium precatalyst at slightly lower chemical shifts. The bridging methylene of the adduct **245** presents as two doublets due to the two diastereotopic protons at 5.35 – 5.47 ppm (D1 and D1'). The singlet at 2.37 ppm (D2) represents the adduct triazolium N-methyl. The singlet at 2.37 ppm (D3) corresponds to the adduct pyrimidinyl methyl and was used to quantify the total concentration of adduct as the reaction progresses. The exchangeable hydrogen of the hydroxyaryl adduct appears as a singlet at 6.58 ppm (D4) and was used to estimate the concentration of protonated adduct present in solution.

The concentration of 2-hydroxyethyltriazolium precatalyst was quantified using the singlet signal due to the methyl on its pyrimidinyl ring at 2.43 ppm (T2) with the total amount of triazolium represented by A_{T2} + A_{D3} so that, with the known concentration of triazolium precatalyst of 0.04 M, the catalyst concentration is given by Equation 4.1. The triplet signal due to the 2-hydroxyethyl sidechain on the precatalyst (T3) overlapped with the N-methyl (T1) of the free precatalyst **144** and o-methoxy peak (A6) of the free aldehyde **213**, hence could not be used for integration. The bridging methylene of unbound precatalyst (T5) integrated 2:3 with the lone pyrimidinyl methyl (T2) during the reaction.

$$[catalyst] = \frac{A_{T2}}{A_{T2} + A_{D3}} \times 0.04 \qquad \textbf{Equation 4.1}$$

2-Methoxybenzaldehyde **213** used in this study forms a hemiacetal adduct **213a** in methanolic solution, like other benzylic aldehydes (**Scheme 4.6**). The singlet at 5.81ppm (A1') represents the hemiacetal proton of the methanolic adduct **213a**. The previous report by Leeper did not

consider this speciation[6]. For **213**, f_{ald} (fraction of aldehyde remaining in solution) was found to be 0.939 from previous group work[11].

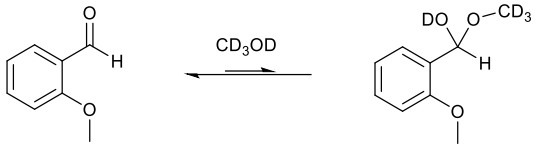

213 **213a**

Scheme 4.6 2-methoxybenzaldehyde 213 and its methanolic hemiacetal 213a

For an authentic assessment of concentration profiles over time, the value of the aldehyde present needs to be adjusted to account for the hemiacetal formation. C(O)H 2-methoxybenzaldehyde was resolved using the singlet signal at 10.41 ppm (A1). The concentration of deuterated aldehyde C(O)D was obtained by subtracting the protonated from the total concentration. The term in red $(A_{T2} + A_{D3})$ represents the starting concentration of catalyst and is used as internal standard throughout.

$$[\text{aldehyde tot}] = \frac{1}{f_{ald}} \times \frac{A_{A2}}{\left(\frac{(A_{T2} + A_{D3})}{3}\right)} \times 0.04 \qquad \textbf{Equation 4.2}$$

$$[\text{aldehyde H}] = \frac{1}{f_{ald}} \times \frac{A_{A1}}{\left(\frac{(A_{T2} + A_{D3})}{3}\right)} \times 0.04 \qquad \textbf{Equation 4.3}$$

$$[\text{aldehyde D}] = [\text{aldehyde tot}] - [\text{aldehyde H}] \qquad \textbf{Equation 4.4}$$

$$[\text{adduct tot}] = \frac{A_{D3}}{A_{T2} + A_{D3}} \times 0.04 \qquad \textbf{Equation 4.5}$$

$$[\text{adduct H}] = \frac{A_{D4}}{\left(\frac{(A_{T2} + A_{D3})}{3}\right)} \times 0.04 \qquad \textbf{Equation 4.6}$$

$$[\text{adduct D}] = [\text{adduct tot}] - [\text{adduct H}] \qquad \textbf{Equation 4.7}$$

4.2.2 Kinetic reaction of aldehyde 240 in the presence of 2-hydroxyethyl triazolium precatalyst 144

2-Hydroxyethyltriazolium precatalyst **144** (0.04 M), triethylamine (0.107 M), triethylamine hydrochloride salt (0.053 M) in deuterated methanol (CD_3OD) were incubated in a rigorously dried NMR tube. Aldehyde **240** (0.05 M) was added and mixed thoroughly to commence the reaction. The reaction was transferred to an NMR instrument with the probe maintained at 25 °C. NMR spectra were recorded continuously for the duration of the experiment with each acquisition approximately 4 min. An overlay of spectra acquired at two points during the experiment is presented below (Figure 4.7).

Figure 4.7 **Overlay of ^{1}H NMR spectra at 500 MHz for the reaction of 2-hydroxyethyltriazolium precatalyst 144 and aldehyde 240 in methanol-d_4 at 25 °C and 0.16 M triethylamine buffer.**

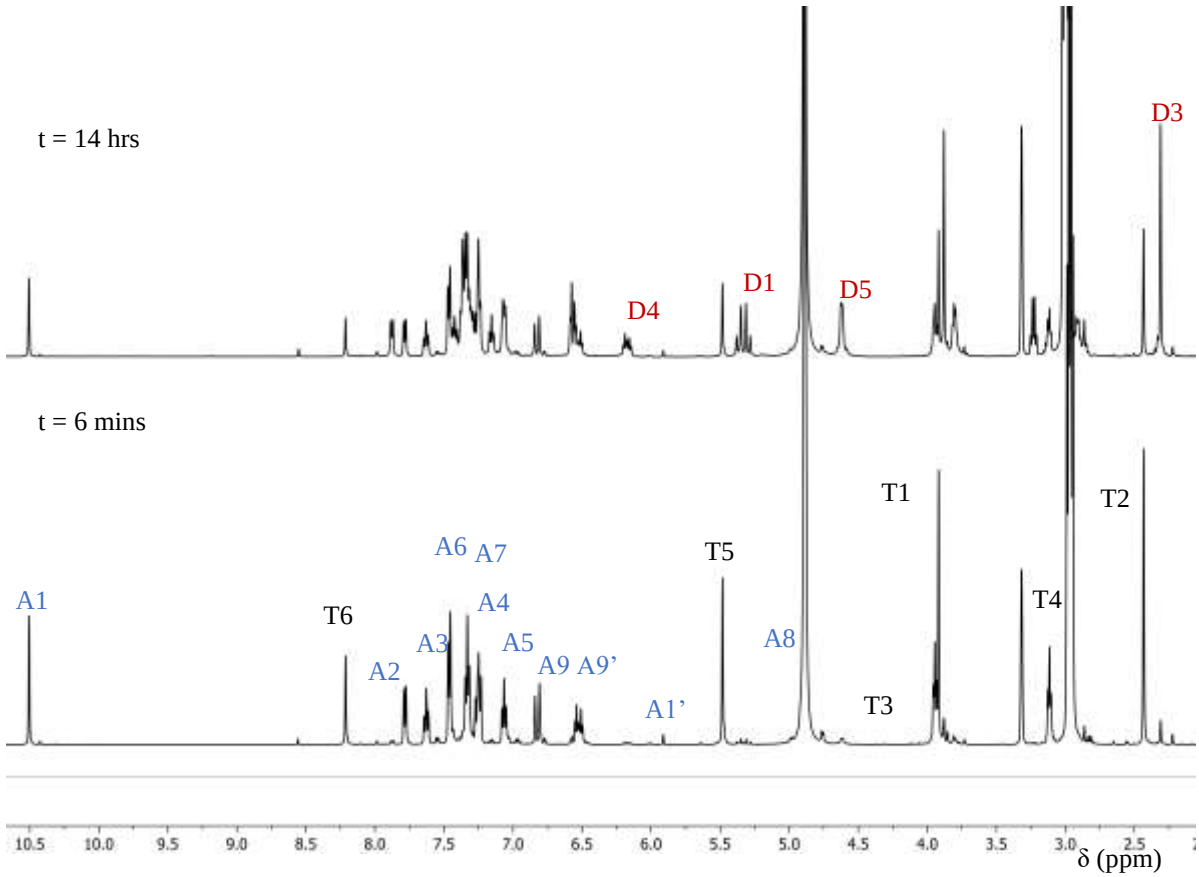

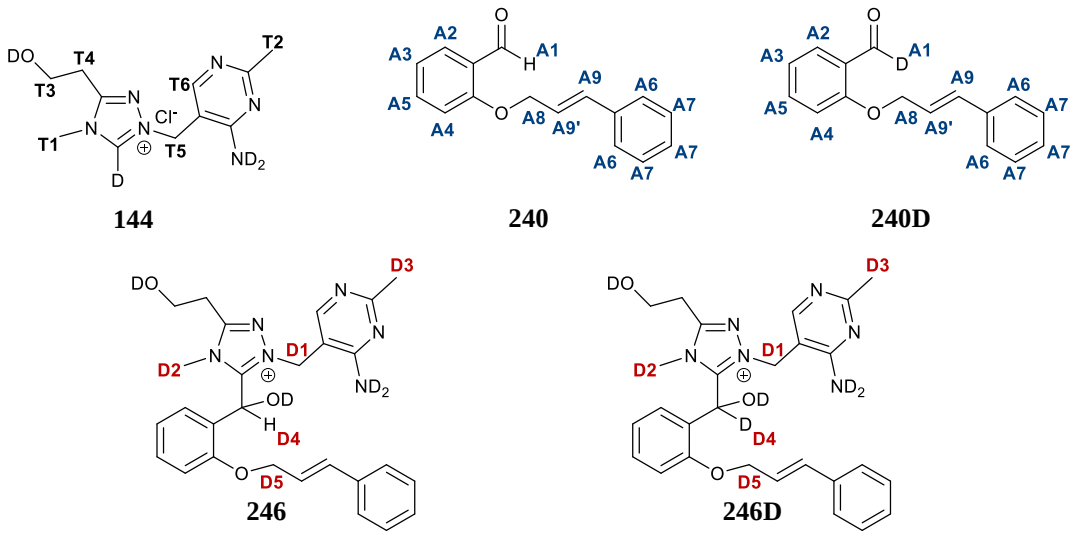

Scheme 4.7 Chemical shift assignments of the proton NMR peaks for the reaction species present in solution

At the start of the reaction, analysis shows exclusively C(3)−D deuterated 2-hydroxyethyltriazolium precatalyst **144**, the C(2)−H (9.7 ppm) having been completely exchanged owing to the basic conditions used. Distinct peaks for each species present in solution were used to estimate its concentration by integration. The singlet peak appearing at 3.92 ppm (T1) corresponds to the triazolium methyl of unbound **144**. The singlet appearing at 2.43 ppm (T2) represents the pyrimidinyl methyl of free 2-hydroxyethyltriazolium precatalyst. The peaks for the hydroxyethyl side chain of **144** appears as triplets at 3.94 ppm (T3) and 3.11 ppm(T4). The bridging methylene of **144** presents as a singlet at 5.48 ppm (T5) and the pyrimidinyl C−H as a singlet at 8.21 ppm (T6). The concentration of **144** was quantified using the singlet signal due to the methyl on its pyrimidinyl ring at 2.43 ppm (T2) (Equation 4.8). The bridging methylene of unbound precatalyst (T5) integrated 2:3 with the lone pyrimidinyl methyl (T2) during the reaction.

The singlet peak appearing at 10.50 ppm (A1) represents the aldehydic hydrogen of aldehydic substrate **240**. The doublet at 7.78 ppm (A2) corresponds to the ortho proton C-*H* on the aldehyde phenyl ring. The triplet at 7.63 ppm (A3) represents the meta proton C-*H* on the

aldehyde ring. The doublet at 7.18 ppm (A4) represents the other meta proton C-*H* of the aldehyde **240** and the triplet at 7.11 (A5) represents the para proton on position 5 of the aldehyde ring. The ortho protons of the pendant phenyl ring (A6) on the aldehyde **240** appears as a doublet at 7.45 ppm and the meta and para protons (A7) as a multiplet at 7.42−7.28 ppm. The peak due to the methylene, O-C*H*$_2$CH=CHPh (A8) is overlapped by the water peak at 4.8 ppm. The peak due to the proton proximal to the phenyl ring on the alkene O-CH$_2$CH=C*H*Ph appears as a doublet (A9) at 6.54 ppm while the distal proton O-CH$_2$C*H*=CHPh (A9') appears as a doublet at 6.79 ppm.

Over time the presence of triazolium precatalyst-aldehyde adduct **246** can be detected by the appearance of new peaks alongside those of triazolium precatalyst at slightly lower chemical shifts. The bridging methylene of the adduct presents as a doublet of doublets due to the two diastereotopic protons at 5.26 – 5.41 ppm (D1). The singlet at 2.37 ppm (D3) corresponds to the adduct pyrimidinyl methyl and used to quantify the total concentration of adduct as the reaction progresses. The exchangeable hydrogen of the hydroxyaryl adduct appears as a multiplet at 6.12−6.29 ppm (D4) and used to estimate the concentration of protonated adduct **246** present in solution. The singlet at 4.61 ppm D5 represents the adduct methylene, O-C*H*$_2$CH=CHPh. The peaks due to D1 and D3 on the adduct **246** integrate 2:3 for the duration of the experiment.

$$[catalyst] = \frac{A_{T2}}{A_{T2} + A_{D3}} \times 0.04 \qquad \textbf{Equation 4.8}$$

$$[\text{aldehyde tot}] = \frac{1}{f_{\text{ald}}} \times \frac{A_{A2}}{\left(\frac{(\text{A}_{\text{T2}} + \text{A}_{\text{D3}})}{3}\right)} \times 0.04 \qquad \textbf{Equation 4.9}$$

$$[\text{aldehyde H}] = \frac{1}{f_{\text{ald}}} \times \frac{A_{A1}}{\left(\frac{(\text{A}_{\text{T2}} + \text{A}_{\text{D3}})}{3}\right)} \times 0.04 \qquad \textbf{Equation 4.10}$$

$$[\text{aldehyde D}] = [\text{aldehyde tot}] - [\text{aldehyde H}] \quad \textbf{Equation 4.11}$$

$$[\text{adduct tot}] = \frac{A_{D3}}{\mathrm{A_{T2}} + \mathrm{A_{D3}}} \times 0.04 \quad \textbf{Equation 4.12}$$

$$[\text{adduct H}] = \frac{A_{D4}}{\left(\frac{(\mathrm{A_{T2}} + \mathrm{A_{D3}})}{3}\right)} \times 0.04 \quad \textbf{Equation 4.13}$$

$$[\text{adduct D}] = [\text{adduct tot}] - [\text{adduct H}] \quad \textbf{Equation 4.14}$$

4.2.3 Kinetic reaction of 4-methoxybenzaldehyde 241 in the presence of 2-hydroxyethyl triazolium precatalyst 144

2-Hydroxyethyltriazolium precatalyst **144** (0.04 M), triethylamine (0.107 M) and triethylamine hydrochloride salt (0.053 M) in deuterated methanol (CD_3OD) were incubated in a rigorously dried NMR tube. 4-Methoxybenzaldehyde **241** (0.058 M) was added and mixed thoroughly to commence the reaction. The reaction was transferred to an NMR instrument with the probe maintained at 25 °C. NMR spectra were recorded continuously for the duration of the experiment with each acquisition approximately 4 min. An overlay of spectra acquired at three time points during the experiment is presented below (Figure 4.8).

Figure 4.8 **Overlay of ^{1}H NMR spectra at 500 MHz for the reaction of 2-hydroxyethyltriazolium precatalyst 144 and 4-methoxybenzaldehyde (para anisaldehyde) 241 in methanol-d_4 at 25 °C and 0.16 M triethylamine buffer**

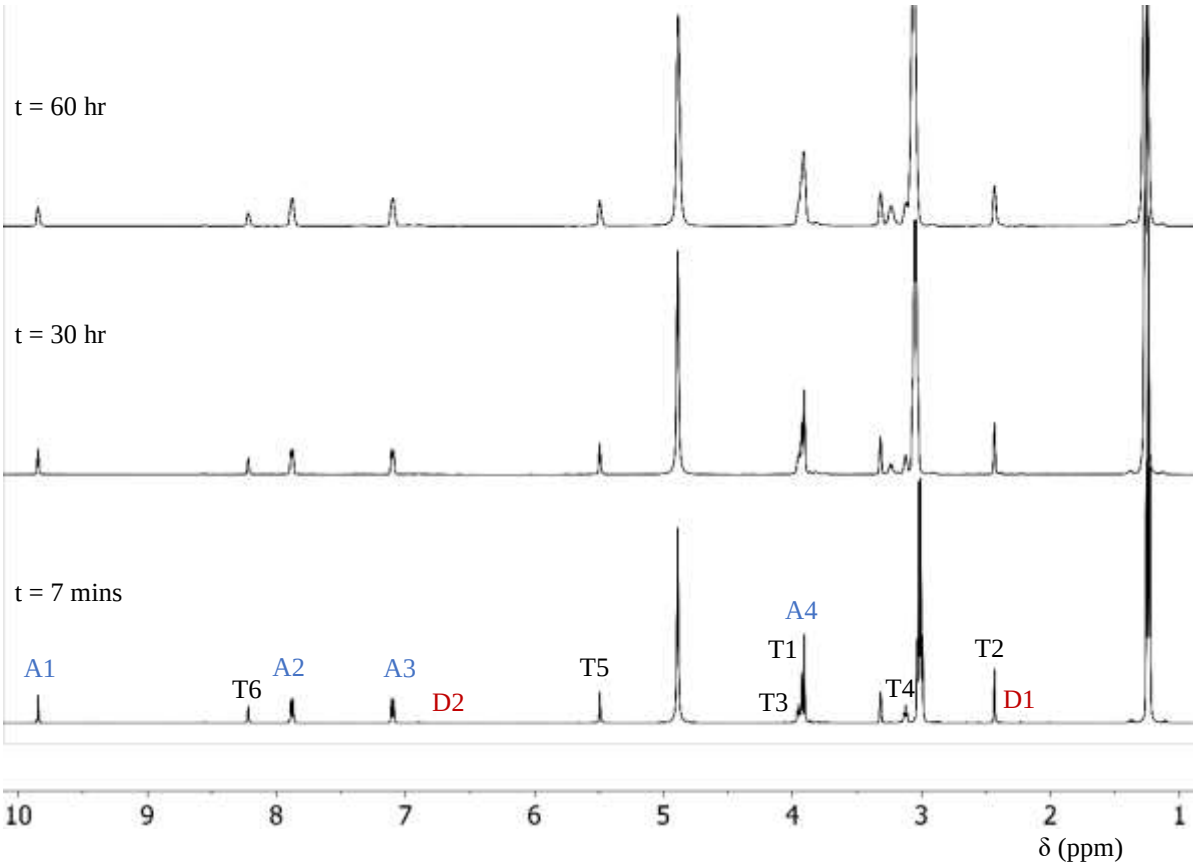

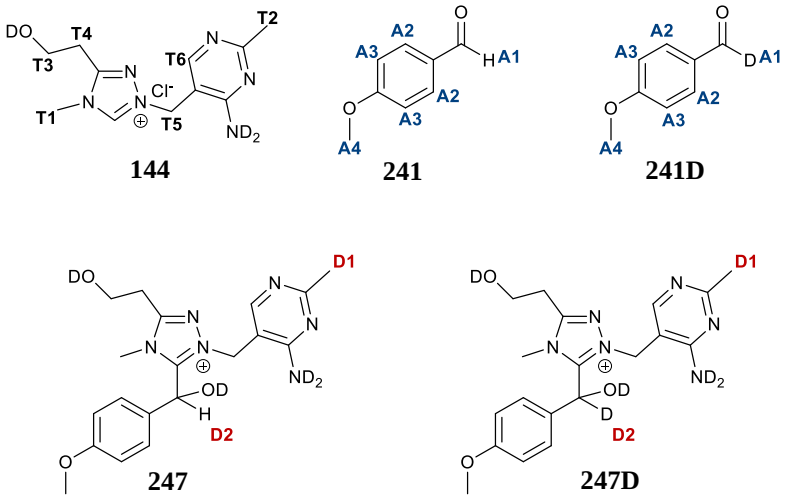

Scheme 4.8 Chemical shift assignments of the proton NMR peaks for the reaction species present in solution

At the start of the reaction, analysis shows exclusively C(2)−D deuterated 2-hydroxyethyltriazolium precatalyst **144**, the C(2)−H (9.7 ppm) having been completely exchanged owing to the basic conditions used. Distinct peaks for each species present in solution were used to estimate its concentration by integration. The singlet peak appearing at 3.93 ppm (T1- *sandwiched between A4 and T3*) corresponds to the triazolium N-methyl of unbound **144**. The singlet appearing at 2.43 ppm (T2) represents the pyrimidinyl methyl of free **144**. The peaks for the hydroxyethyl side chain of **144** appear as triplets at 3.96 ppm (T3) and 3.12 ppm (T4). The bridging methylene of the **144** presents as a singlet at 5.49 ppm (T5) and the pyrimidinyl C−H as a singlet at 8.22 ppm (T6).

The singlet peak appearing at 9.84 ppm (A1) represents the aldehydic hydrogen of 4-methoxybenzaldeyde **241**. The doublet at 7.87 ppm (A2) corresponds to the pair of equivalent ortho protons C-*H* on the aldehyde phenyl ring. The doublet at 7.11 ppm (A3) represents the pair of equivalent meta protons C-*H* on the aldehyde ring. The singlet at 3.91 ppm (A4) represents the para methoxy-OCH_3 **144**.

Initially the presence of triazolium precatalyst-aldehyde adduct **247** can be detected by the appearance of duplicate peaks alongside those of triazolium precatalyst **144** at slightly lower chemical shifts. The hardly visible singlet at 2.23 ppm (D1) corresponds to the adduct pyrimidinyl methyl and used to quantify the total concentration of adduct **247** as the reaction progresses. The exchangeable hydrogen of the hydroxyaryl adduct **247** appears as a tiny singlet at 6.58 ppm (D2) and was used to estimate the concentration of protonated adduct present in solution.

The concentration of 2-hydroxyethyltriazolium precatalyst was quantified using the singlet signal due to the methyl on its pyrimidinyl ring at 2.43 ppm (T2) (Equation 4.15).

$$[catalyst] = \frac{A_{T2}}{(A_{T2} + A_{D1})} \times 0.04$$ **Equation 4.15**

$$[\text{aldehyde tot}] = \frac{1}{f_{\text{ald}}} \times \frac{\left({}^{A_{A2}}/_{2}\right)}{\left(\frac{(\text{A}_{\text{T2}} + \text{A}_{\text{D1}})}{3}\right)} \times 0.04$$ **Equation 4.16**

$$[\text{aldehyde H}] = \frac{1}{f_{\text{ald}}} \times \frac{A_{A1}}{\left(\frac{(\text{A}_{\text{T2}} + \text{A}_{\text{D1}})}{3}\right)} \times 0.04$$ **Equation 4.17**

$$[\text{aldehyde D}] = [\text{aldehyde tot}] - [\text{aldehyde H}]$$ **Equation 4.18**

$$[\text{adduct tot}] = \frac{A_{D1}}{\text{A}_{\text{T2}} + \text{A}_{\text{D1}}} \times 0.04$$ **Equation 4.19**

$$[\text{adduct H}] = \frac{A_{D2}}{\left(\frac{(\text{A}_{\text{T2}} + \text{A}_{\text{D1}})}{3}\right)} \times 0.04$$ **Equation 4.20**

$$[\text{adduct D}] = [\text{adduct tot}] - [\text{adduct H}]$$ **Equation 4.21**

4.2.4 Kinetic reaction of 4-methoxybenzaldehyde 241 and chalcone 244 in the presence of 2-hydroxyethyl triazolium precatalyst 144

2-Hydroxyethyltriazolium precatalyst **144** (0.04 M), triethylamine (0.107 M) and triethylamine hydrochloride salt (0.053 M) in deuterated methanol (CD_3OD) were incubated in a rigorously dried NMR tube. 4-Methoxybenzaldehyde **241** (0.11 M) and chalcone **244** (0.15 M) were added and mixed thoroughly to commence the reaction. The reaction was transferred to an NMR instrument with the probe maintained at 25 °C. NMR spectra were recorded continuously for the duration of the experiment with each acquisition approximately 4 min. An overlay of spectra acquired at three two points during the experiment is presented below (Figure 4.9).

Figure 4.9 **Overlay of ^{1}H NMR spectra at 500 MHz for the reaction of 2-hydroxyethyltriazolium precatalyst 144 4-methoxybenzaldehyde 241 and chalcone 244 in methanol-d_4 at 25 °C and 0.16 M triethylamine buffer**

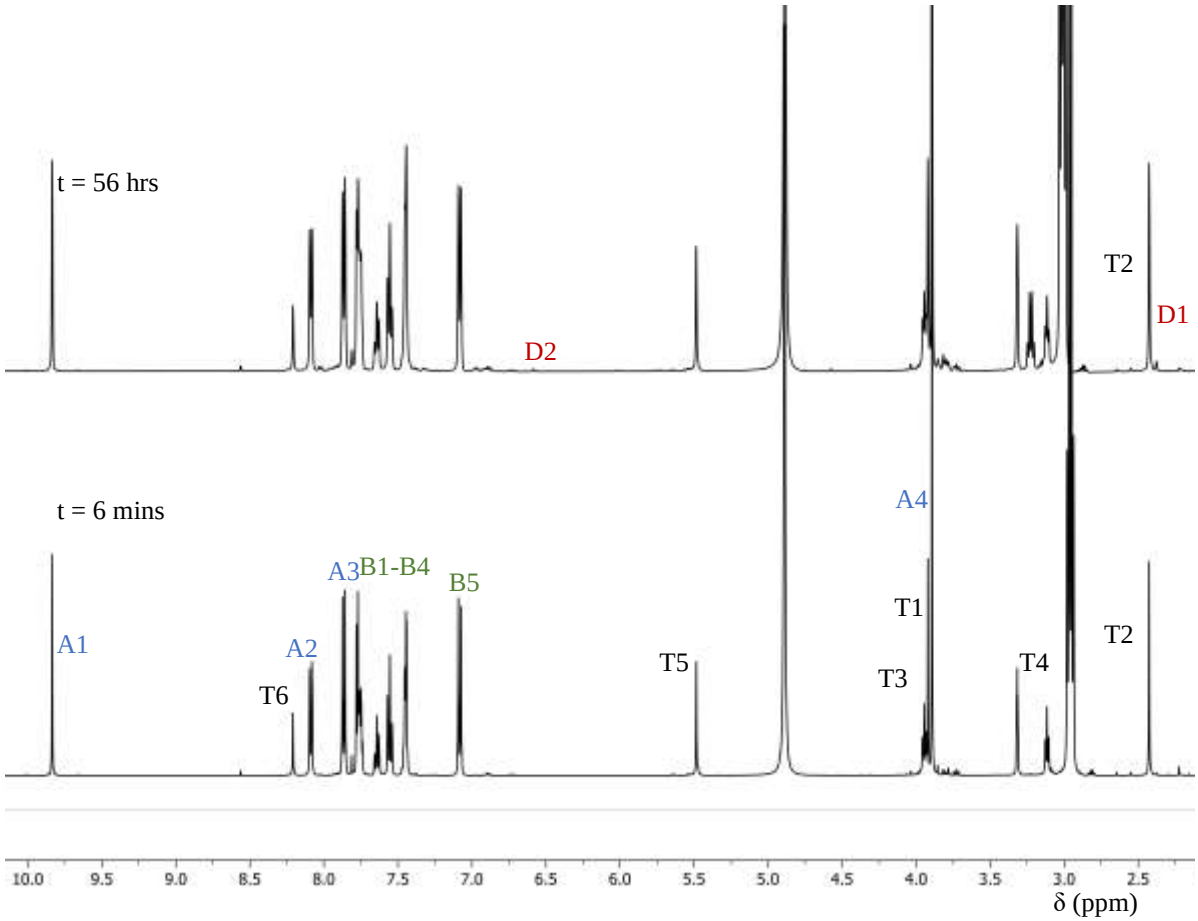

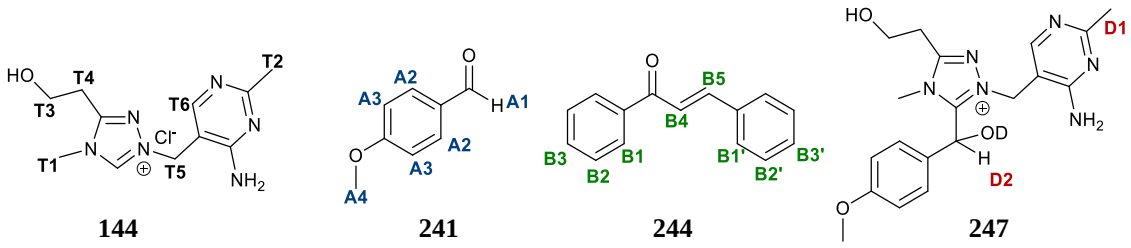

144 **241** **244** **247**

Scheme 4.9 Chemical shift assignments of the proton NMR peaks for the reaction species present in solution

At the start of the reaction, analysis shows exclusively C(2)−D deuterated 2-hydroxyethyltriazolium precatalyst **144**, the C(2)−H (9.7 ppm) having been completely exchanged owing to the basic conditions used. Distinct peaks for each species present in solution were used to estimate its concentration by integration. The singlet peak appearing at 3.92 ppm (T1) corresponds to the triazolium N-methyl of unbound 2-hydroxyethyltriazolium precatalyst. The singlet appearing at 2.43 ppm (T2) represents the pyrimidinyl methyl of free 2-hydroxyethyltriazolium precatalyst. The peaks for the hydroxyethyl side chain of **144** appear as triplets at 3.95 ppm (T3) and 3.12 ppm (T4). The bridging methylene of **144** presents as a singlet at 5.48 ppm (T5) and the pyrimidinyl C−H as a singlet at 8.21 ppm (T6).

The singlet peak appearing at 9.84 ppm (A1) represents the aldehydic hydrogen of 4-methoxybenzaldeyde **241**. The doublet at 7.87 ppm (A2) corresponds to the pair of equivalent ortho protons C-*H* on the aldehyde phenyl ring and the doublet at 7.11 ppm (A3) represents the pair of equivalent meta protons C-*H* on the aldehyde ring. The singlet at 3.91 ppm (A4) represents the para methoxy CH_3 of aldehyde. Peaks due to the phenyl rings B1 – B3 (and B1' – B3') of chalcone **244** appear as multiplets between 7.52 and 7.79 ppm. The peak corresponding to the ethylene bridge proton, proximal to the carbonyl, B4 appear as a doublet at 7.39 ppm, while the proton distal to the carbonyl, B5 appears as a doublet at 7.09 ppm.

At the start of the reaction, the presence of triazolium precatalyst-aldehyde adduct **247** can be detected by the appearance of duplicate peaks alongside those of triazolium precatalyst **144** at slightly lower chemical shifts. The tiny singlet at 2.22 ppm (D1) corresponds to the adduct **247** pyrimidinyl methyl and used to quantify the total concentration of adduct as the reaction progresses. The exchangeable hydrogen of the hydroxyaryl adduct appears as a tiny singlet at 6.58 ppm (D2) and used to estimate the concentration of protonated adduct present in solution. The concentration of **144** was quantified using the singlet signal due to the methyl on its pyrimidinyl ring at 2.43 ppm (T2) (Equation 4.22).

$$[catalyst] = \frac{A_{T2}}{A_{T2} + A_{D1}} \times 0.04$$ **Equation 4.22**

$$[\text{aldehyde tot}] = \frac{1}{f_{\text{ald}}} \times \frac{\left({}^{A_{A2}}/_{2}\right)}{\left(\frac{(\text{A}_{\text{T2}} + \text{A}_{\text{D1}})}{3}\right)} \times 0.04$$ **Equation 4.23**

$$[\text{aldehyde H}] = \frac{1}{f_{\text{ald}}} \times \frac{A_{A1}}{\left(\frac{(\text{A}_{\text{T2}} + \text{A}_{\text{D1}})}{3}\right)} \times 0.04$$ **Equation 4.24**

$$[\text{aldehyde D}] = [\text{aldehyde tot}] - [\text{aldehyde H}]$$ **Equation 4.25**

$$[\text{adduct tot}] = \frac{A_{D1}}{\text{A}_{\text{T2}} + \text{A}_{\text{D1}}} \times 0.04$$ **Equation 4.26**

$$[\text{adduct H}] = \frac{A_{D2}}{\left(\frac{(\text{A}_{\text{T2}} + \text{A}_{\text{D1}})}{3}\right)} \times 0.04$$ **Equation 4.27**

$$[\text{adduct D}] = [\text{adduct tot}] - [\text{adduct H}]$$ **Equation 4.28**

$$[Chalcone] = \frac{A_{B5}}{\left(\frac{(\text{A}_{\text{T2}} + \text{A}_{\text{D1}})}{3}\right)} \times 0.04$$

4.2.5 Kinetic reaction of 4-methylbenzaldehyde 242 in the presence of 2-hydroxyethyl triazolium mimic 144

2-Hydroxyethyltriazolium precatalyst **144** (0.04 M), triethylamine (0.107 M) and triethylamine hydrochloride salt (0.053 M) in deuterated methanol (CD_3OD) were incubated in a rigorously dried NMR tube. 4-Methylbenzaldehyde **242** (0.12 M) was added and mixed thoroughly to commence the reaction. The reaction was transferred to an NMR instrument with the probe maintained at 25 °C. NMR spectra were recorded continuously for the duration of the experiment with each acquisition taking approximately 4 min. An overlay of spectra acquired at two time points during the experiment is presented below (Figure 4.10).

Figure 4.10 Overlay of ^{1}H NMR spectra at 500 MHz for the reaction of 2-hydroxyethyltriazolium precatalyst 144 and 4-methylbenzaldehyde (para tolualdehyde) 242 in methanol-d$_4$ at 25 °C and 0.16 M triethylamine buffer

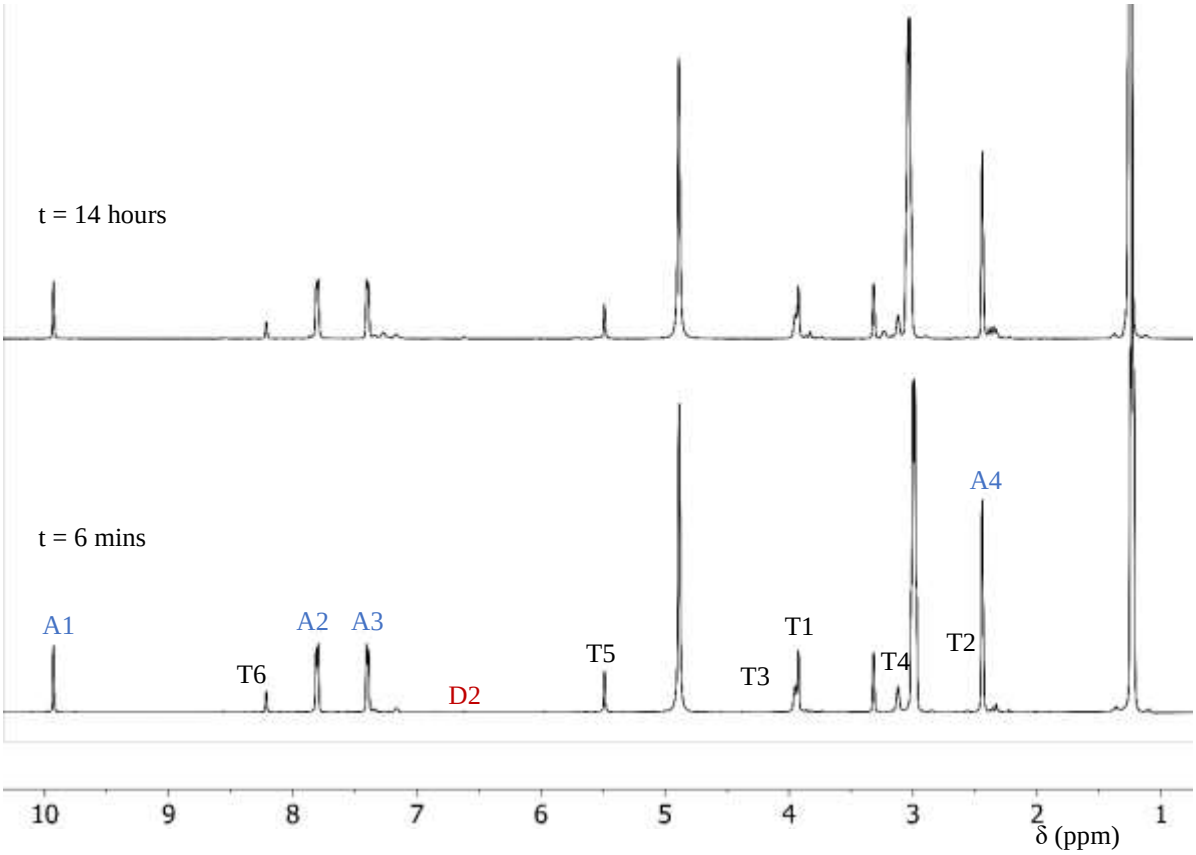

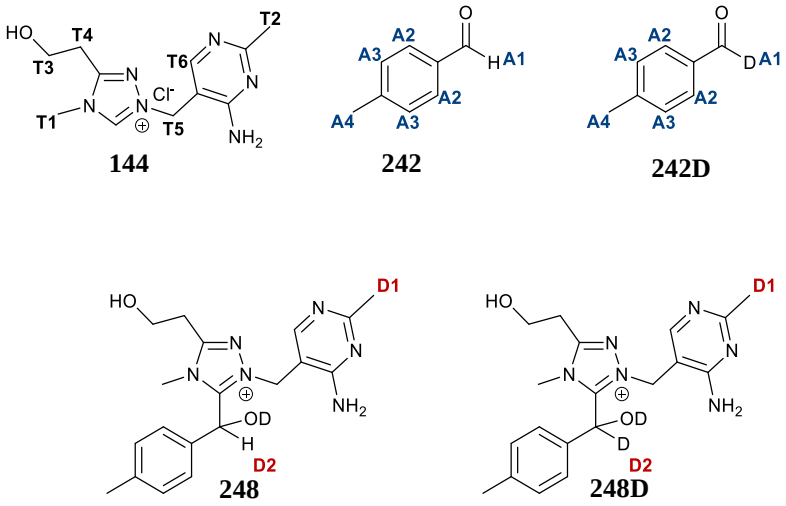

Scheme 4.10 Chemical shift assignments of the proton NMR peaks for the reaction species present in solution

At the start of the reaction, analysis shows exclusively C(2)−D deuterated 2-hydroxyethyltriazolium precatalyst **144**, the C(2)−H (9.7 ppm) having been completely exchanged owing to the basic conditions used. The benzoin product peak (6.11 ppm) was not seen for the duration of the experiment. Distinct peaks for each species present in solution were used to estimate its concentration by integration. The singlet peak appearing at 3.93 ppm (T1) corresponds to the triazolium N-methyl of unbound **144**. The singlet appearing at 2.43 ppm (T2) represents the pyrimidinyl methyl of free **144**. The peaks for the hydroxyethyl side chain of 2-hydroxyethyltriazolium precatalyst appear as triplets at 3.96 ppm (T3) and 3.12 ppm (T4). The bridging methylene of **144** presents as a singlet at 5.49 ppm (T5) and the pyrimidinyl C−H as a singlet at 8.21 ppm (T6).

The singlet peak appearing at 9.93 ppm (A1) represents the aldehydic hydrogen of 4-methylbenzaldehyde **242**. The doublet at 7.79 ppm (A2) corresponds to the pair of equivalent ortho protons C-*H* on the aldehyde phenyl ring. The doublet at 7.40 ppm (A3) represents the pair of equivalent meta protons C-*H* on the aldehyde ring. The singlet at 2.44 ppm (A4) represents the para methyl CH_3 of aldehyde.

Initially the presence of triazolium precatalyst-aldehyde adduct **248** can be detected by the appearance of duplicate peaks alongside those of triazolium precatalyst at slightly lower chemical shifts. The tiny singlet at 2.22 ppm (D1) corresponds to the adduct pyrimidinyl methyl and was used to quantify the total concentration of adduct **248** as the reaction progresses. The exchangeable hydrogen of the hydroxyaryl adduct appears as a tiny singlet at 6.61 ppm (D2) and was used to estimate the concentration of protonated adduct present in solution.

The concentration of 2-hydroxyethyltriazolium precatalyst was quantified using the singlet signal due to the pyrimidinyl ring C-H at 8.21 ppm (T6) (Equation 4.29).

$$[catalyst] = \frac{A_{T6}}{\left(\frac{(3A_{T6} + A_{D1})}{3}\right)} \times 0.04 \qquad \textbf{Equation 4.29}$$

$$[\text{aldehyde tot}] = \frac{1}{f_{\text{ald}}} \times \frac{\left({}^{A_{A2}}/_{2}\right)}{\left(\frac{(3\text{A}_{\text{T6}} + \text{A}_{\text{D1}})}{3}\right)} \times 0.04 \qquad \textbf{Equation 4.30}$$

$$[\text{aldehyde H}] = \frac{1}{f_{\text{ald}}} \times \frac{A_{A1}}{\left(\frac{(3\text{A}_{\text{T6}} + \text{A}_{\text{D1}})}{3}\right)} \times 0.04 \qquad \textbf{Equation 4.31}$$

$$[\text{aldehyde D}] = [\text{aldehyde tot}] - [\text{aldehyde H}] \qquad \textbf{Equation 4.32}$$

$$[\text{adduct tot}] = \frac{A_{D1}}{3\text{A}_{\text{T6}} + \text{A}_{\text{D1}}} \times 0.04 \qquad \textbf{Equation 4.33}$$

$$[\text{adduct H}] = \frac{A_{D2}}{\left(\frac{(3\text{A}_{\text{T6}} + \text{A}_{\text{D1}})}{3}\right)} \times 0.04 \qquad \textbf{Equation 4.34}$$

$$[\text{adduct D}] = [\text{adduct tot}] - [\text{adduct H}] \qquad \textbf{Equation 4.35}$$

4.2.6 Kinetic reaction of 3-fluorobenzaldehyde 243 in the presence of 2-hydroxyethyl triazolium mimic 144

2-Hydroxyethyltriazolium precatalyst **144** (0.04 M), triethylamine (0.107 M), triethylamine hydrochloride salt (0.053 M) in deuterated methanol (CD_3OD) were incubated in a rigorously dried NMR tube. 3-Fluorobenzaldehyde **243** (0.05 M) was added and mixed thoroughly to commence the reaction. The reaction was transferred to an NMR instrument with the probe maintained at 25 °C. NMR spectra were recorded continuously for the duration of the experiment with each acquisition taking approximately 4 min. An overlay of spectra acquired at two time points during the experiment is presented below (Figure 4.11).

Figure 4.11 Overlay of ^{1}H NMR spectra at 500 MHz for the reaction of 2-hydroxyethyltriazolium precatalyst 144 and 3-fluorobenzaldehyde 243 in methanol-d_4 at 25 °C and 0.16 M triethylamine buffer

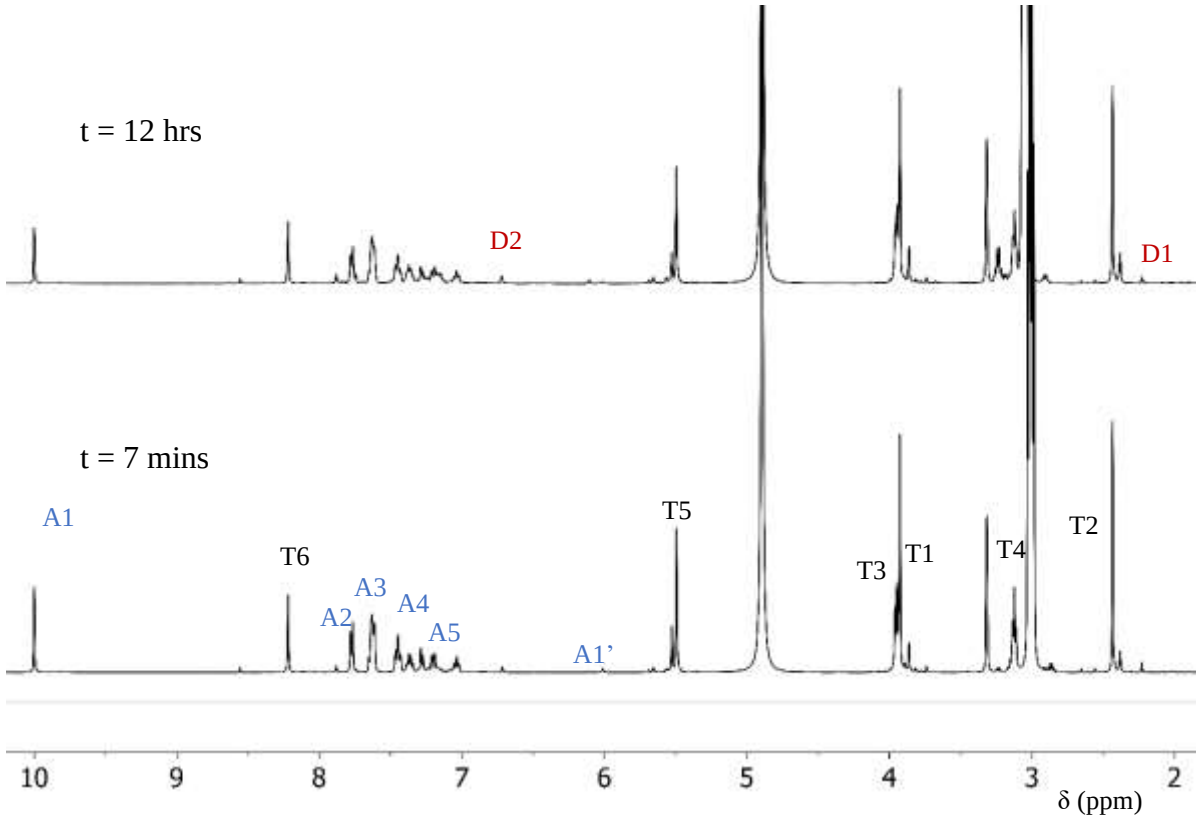

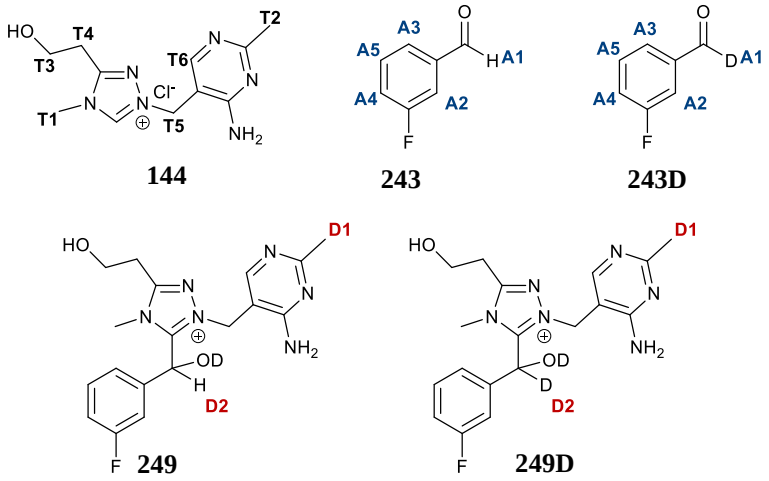

Scheme 4.11 Chemical shift assignments of the proton NMR peaks for the reaction species present in solution

At the start of the reaction, analysis shows exclusively C(2)−D deuterated 2-hydroxyethyltriazolium precatalyst **144**, the C(2)−H (9.7 ppm) having been completely exchanged owing to the basic conditions used. Distinct peaks for each species present in solution were used to estimate its concentration by integration. The singlet peak appearing at 3.93 ppm (T1) corresponds to the triazolium N-methyl of unbound **144**. The singlet appearing at 2.43 ppm (T2) represents the pyrimidinyl methyl of free **144**. The peaks for the hydroxyethyl side chain appear as triplets at 3.95 ppm (T3) and 3.12 ppm (T4) and the bridging methylene -C*H*$_2$ presents as a singlet at 5.49 ppm (T5) and the pyrimidinyl C−H as a singlet at 8.22 ppm (T6).

The singlet peak appearing at 10.00 ppm (A1) represents the aldehydic hydrogen of 3-fluorobenzaldeyde **243**. The doublet at 7.78 ppm (A2) corresponds to the ortho proton C-*H* on the aldehyde ring. The doublet at 7.40 ppm (A3) represents the other ortho proton C-*H* on the aldehyde ring. The multiplet at 7.42-7.46 ppm (A4) represents the para C*H* of aldehyde **243**. The multiplet at 7.29-7.32 ppm (A5) represents the meta C*H* of aldehyde **243**. The signals due to the protons A4 and A5 are split into multiplets due to the meta fluorine atom [12]. Impurity peaks are also present in the slightly aged sample of **243** used likely owing to oxidation to the

3-fluorobenzoic acid. For **243**, f_{ald} (fraction of aldehyde remaining in solution) was found to be 0.943 from the integrated spectra.

The presence of triazolium precatalyst-aldehyde adduct **249** can be detected by the appearance of new peaks alongside those of triazolium precatalyst at slightly lower chemical shifts. The tiny singlet at 2.23 ppm (D1) corresponds to the adduct pyrimidinyl methyl and used to quantify the total concentration of adduct as the reaction progresses. The exchangeable hydrogen of the hydroxyaryl adduct **249** appears as a tiny singlet at 6.71 ppm (D2) and used to estimate the concentration of protonated adduct present in solution.

The concentration of **144** was quantified using the singlet signal due to the methyl of the pyrimidinyl ring C-H_3 at 2.43 ppm (T2). (Equation 4.36).

$$[catalyst] = \frac{A_{T2}}{A_{T2} + A_{D1}} \times 0.04 \quad \textbf{Equation 4.36}$$

$$[\text{aldehyde tot}] = \frac{1}{f_{\text{ald}}} \times \frac{A_{A2}}{\left(\frac{(\text{A}_{\text{T2}} + \text{A}_{\text{D1}})}{3}\right)} \times 0.04 \quad \textbf{Equation 4.37}$$

$$[\text{aldehyde H}] = \frac{1}{f_{\text{ald}}} \times \frac{A_{A1}}{\left(\frac{(\text{A}_{\text{T2}} + \text{A}_{\text{D1}})}{3}\right)} \times 0.04 \quad \textbf{Equation 4.38}$$

$$[\text{aldehyde D}] = [\text{aldehyde tot}] - [\text{aldehyde H}] \quad \textbf{Equation 4.39}$$

$$[\text{adduct tot}] = \frac{A_{D1}}{\text{A}_{\text{T2}} + \text{A}_{\text{D1}}} \times 0.04 \quad \textbf{Equation 4.40}$$

$$[\text{adduct H}] = \frac{A_{D2}}{\left(\frac{(\text{A}_{\text{T2}} + \text{A}_{\text{D1}})}{3}\right)} \times 0.04 \quad \textbf{Equation 4.41}$$

$$[\text{adduct D}] = [\text{adduct tot}] - [\text{adduct H}] \quad \textbf{Equation 4.42}$$

4.2.7 Kinetic reaction of 2-methyoxybenzaldehyde 213 in the presence of methyl triazolium mimic 183

Methyl triazolium mimic **183** (0.08 M), triethylamine (0.107 M), triethylamine hydrochloride salt (0.053 M) in deuterated methanol (CD_3OD) were incubated in a rigorously dried NMR tube. 2-Methoxybenzaldehyde **213** (0.083 M) was added and mixed thoroughly to commence the reaction. The reaction was transferred to an NMR instrument with the probe maintained at 25 °C. NMR spectra were recorded continuously for the duration of the experiment with each acquisition taking approximately 4 min. An overlay of spectra acquired at two time points during the experiment is presented below (Figure 4.12).

Figure 4.12 Overlay of ^{1}H NMR spectra at 500 MHz for the reaction of methyl triazolium precatalyst 183 and 2-methoxybenzaldehyde 213 in methanol-d_4 at 25 °C and 0.16 M triethylamine buffer

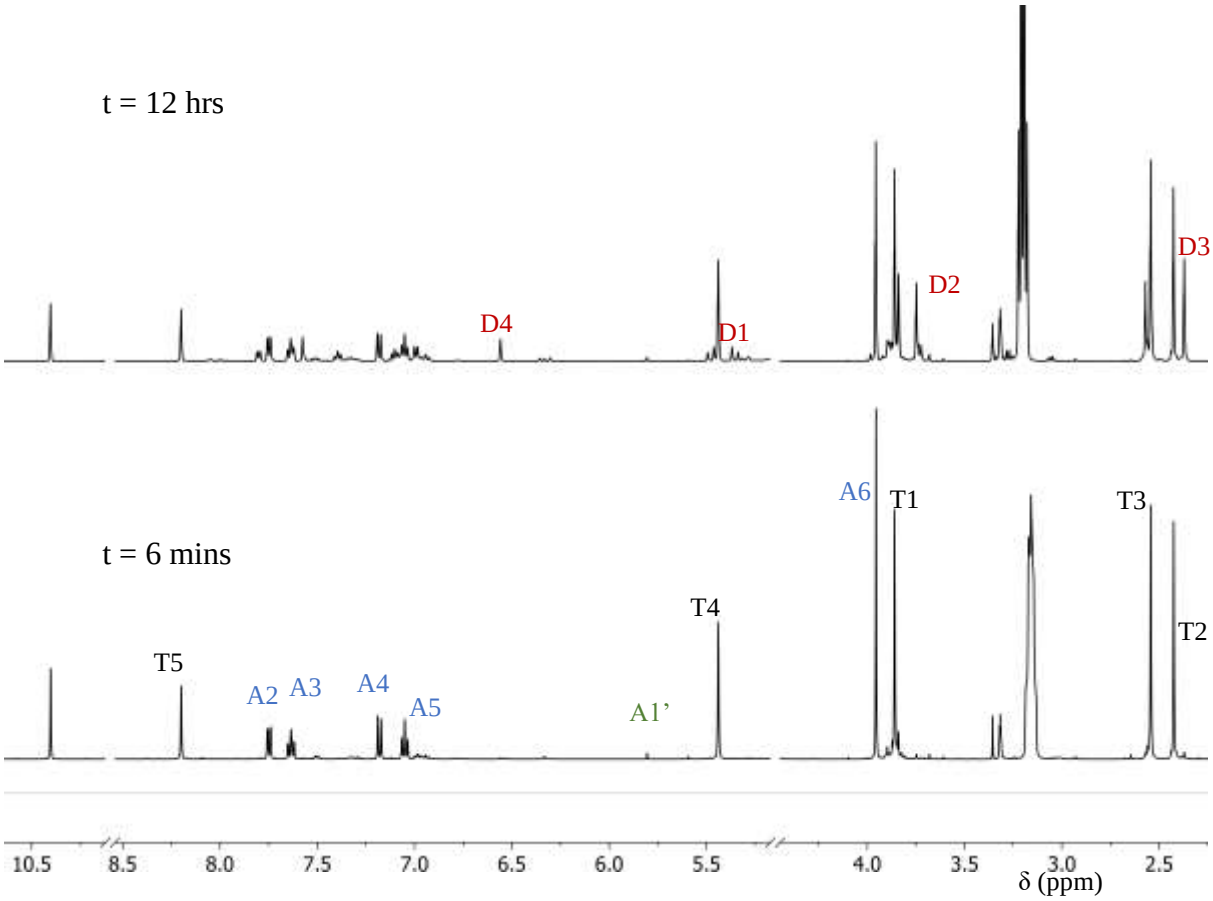

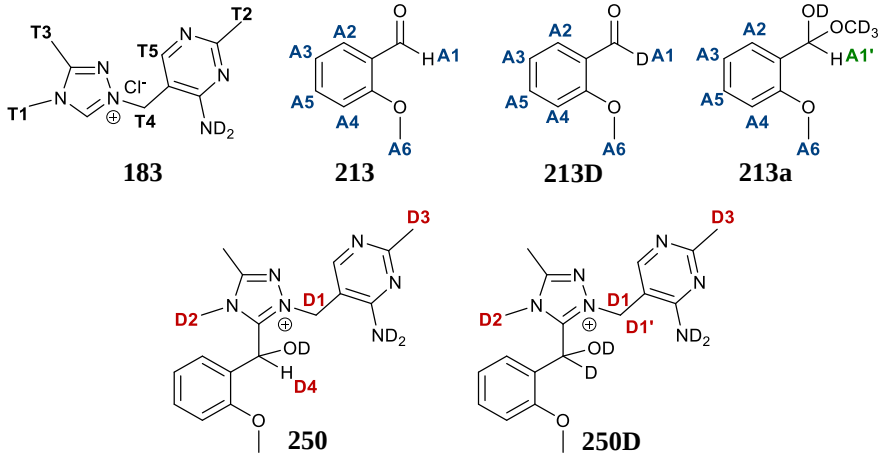

Scheme 4.12 Chemical shift assignments of the proton NMR peaks for the reaction species present in solution

At the start of the reaction, analysis shows exclusively C(2)−D deuterated methyltriazolium precatalyst **183**, the C(2)−H (9.7 ppm) having been completely exchanged owing to the basic conditions used. Distinct peaks for each species present in solution were used to estimate its concentration by integration. The singlet peak appearing at 3.86 ppm (T1) corresponds to the triazolium N-methyl of unbound **183**. The singlet appearing at 2.43 ppm (T2) represents the pyrimidinyl methyl of free **183**. The peaks for the triazolium C5-methlyl appear as a singlet at 2.54 ppm (T3) and the bridging methylene -CH_2 presents as a singlet at 5.44 ppm (T4) and the pyrimidinyl C−H as a singlet at 8.20 ppm (T5).

The singlet peak appearing at 10.40 ppm (A1) represents the aldehydic hydrogen of 2-methoxybenzaldeyde **213**. The doublet at 7.75 ppm (A2) corresponds to the ortho proton C-*H* on the aldehyde phenyl ring. The triplet at 7.63 ppm (A3) represents one of the meta C-*H* on the aldehyde ring. The doublet at 7.19 ppm (A4) represents the other meta C-*H* of the aldehyde and the triplet at 7.05 ppm (A5) represents the para C-*H* on the aldehyde. The singlet at 3.95 ppm (A6) corresponds to the methoxy hydrogens of **213**.

The presence of triazolium precatalyst-aldehyde adduct **250** can be detected by the appearance of new peaks alongside those of triazolium precatalyst at slightly lower chemical shifts. The multiplet at 5.24-5.40 ppm (D1) corresponds to the bridging methylene on **250.** The methyl of the pyrimidinyl ring on **250** appears as a singlet at 2.37 ppm (D3) and was used to quantify the total concentration of **250** as the reaction progresses. The exchangeable hydrogen of the hydroxyaryl adduct **250** appears as a tiny singlet at 6.56 ppm (D4) and used to estimate the concentration of protonated adduct present in solution. The concentration of **183** was quantified using the singlet signal due to the methyl of the pyrimidinyl ring C-H_3 at 2.43 ppm (T2) (Equation 4.43).

$$[catalyst] = \frac{A_{T2}}{A_{T2} + A_{D3}} \times 0.08 \qquad \textbf{Equation 4.43}$$

$$[\text{aldehyde tot}] = \frac{1}{f_{\text{ald}}} \times \frac{A_{A2}}{\left(\frac{(\text{A}_{\text{T2}} + \text{A}_{\text{D3}})}{3}\right)} \times 0.08 \qquad \textbf{Equation 4.44}$$

$$[\text{aldehyde H}] = \frac{1}{f_{\text{ald}}} \times \frac{A_{A1}}{\left(\frac{(\text{A}_{\text{T2}} + \text{A}_{\text{D3}})}{3}\right)} \times 0.08 \qquad \textbf{Equation 4.45}$$

$$[\text{aldehyde D}] = [\text{aldehyde tot}] - [\text{aldehyde H}] \qquad \textbf{Equation 4.46}$$

$$[\text{adduct tot}] = \frac{A_{D3}}{\text{A}_{\text{T2}} + \text{A}_{\text{D3}}} \times 0.08 \qquad \textbf{Equation 4.47}$$

$$[\text{adduct H}] = \frac{A_{D4}}{\left(\frac{(\text{A}_{\text{T2}} + \text{A}_{\text{D3}})}{3}\right)} \times 0.08 \qquad \textbf{Equation 4.48}$$

$$[\text{adduct D}] = [\text{adduct tot}] - [\text{adduct H}] \qquad \textbf{Equation 4.49}$$

4.2.8 Kinetic reaction of 2-methoxybenzaldehyde 213 in the presence of precatalyst 212

Methyl triazolium mimic **212** (0.08 M), triethylamine (0.107 M), triethylamine hydrochloride salt (0.053 M) in deuterated methanol (CD_3OD) were incubated in a rigorously dried NMR tube. 2-Methoxybenzaldehyde **213** (0.18 M) was added and mixed thoroughly to commence the reaction. The reaction was transferred to an NMR instrument with the probe maintained at 25 °C. NMR spectra were recorded continuously for the duration of the experiment with each acquisition taking approximately 4 min. An overlay of spectra acquired at two time points during the experiment is presented below (Figure 4.13).

Figure 4.13 Overlay of ^{1}H NMR spectra at 500 MHz for the reaction of methyl triazolium precatalyst 212 and 2-methoxybenzaldehyde 213 in methanol-d_4 at 25 °C and 0.16 M triethylamine buffer

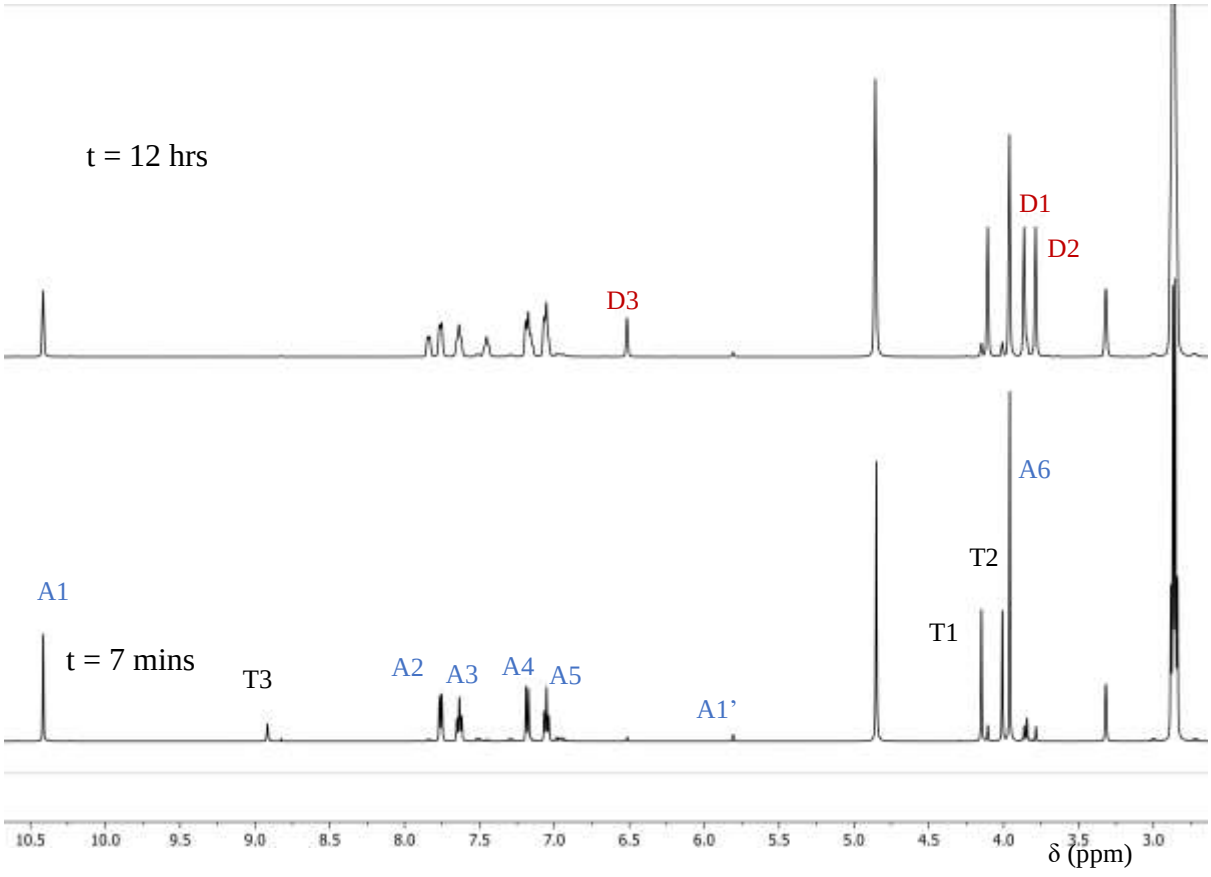

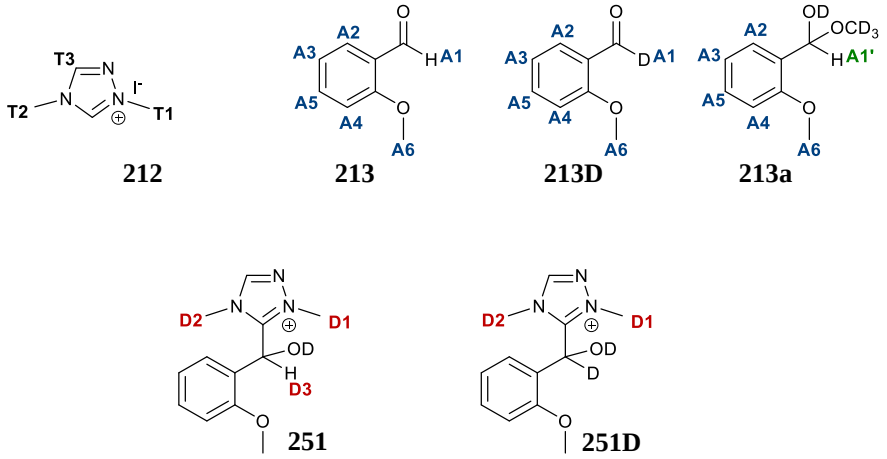

Scheme 4.13 Chemical shift assignments of the proton NMR peaks for the reaction species present in solution

At the start of the reaction, analysis shows exclusively C(2)−D deuterated precatalyst **212**, the C(2)−H (9.7 ppm) having been completely exchanged owing to the basic conditions used. Distinct peaks for each species present in solution were used to estimate its concentration by integration. The singlet peak appearing at 4.14 ppm (T1) corresponds to the triazolium N2-methyl of unbound **212**. The singlet appearing at 4.01 ppm (T2) represents N4- methyl of free **212**. The peak for the triazolium C5-*H* is partially exchanged for deuterium and appears as a singlet at 8.91 ppm (T3) which is completely exchanged during the course of the reaction.

The singlet peak appearing at 10.41 ppm (A1) represents the aldehydic hydrogen of 2-methoxybenzaldeyde **213**. The doublet at 7.75 ppm (A2) corresponds to the ortho proton C-*H* on the aldehyde phenyl ring. The triplet at 7.64 ppm (A3) represents one of the meta C-*H* on the aldehyde ring. The doublet at 7.17 ppm (A4) represents one of the meta C-*H* of the aldehyde and the triplet at 7.05 ppm (A5) represents the para C-*H* on the aldehyde. The singlet at 3.96 ppm (A6) corresponds to the methoxy hydrogens of **213**.

The presence of triazolium precatalyst-aldehyde adduct **251** can be detected by the appearance of new peaks alongside those of triazolium precatalyst at slightly lower chemical shifts. The singlet at 3.86 ppm (D1) corresponds to the N2-methyl on **251.** The N4-methyl appears as a singlet at 3.78 ppm (D2) and was used to quantify the total concentration of **251** as the reaction

progresses. The exchangeable hydrogen of the hydroxyaryl adduct **251** appears as a singlet at 6.51 ppm (D3) and used to estimate the concentration of protonated adduct present in solution. The concentration of **212** was quantified using the singlet signal due to the N2-methyl N^{+}-CH_3 at 2.43 ppm (T1).

$$[catalyst] = \frac{A_{T1}}{A_{T1} + A_{D2}} \times 0.08 \qquad \textbf{Equation 4.50}$$

$$[\text{aldehyde tot}] = \frac{1}{f_{\text{ald}}} \times \frac{A_{A2}}{\left(\frac{(\text{A}_{\text{T1}} + \text{A}_{\text{D2}})}{3}\right)} \times 0.08 \qquad \textbf{Equation 4.51}$$

$$[\text{aldehyde H}] = \frac{1}{f_{\text{ald}}} \times \frac{A_{A1}}{\left(\frac{(\text{A}_{\text{T1}} + \text{A}_{\text{D2}})}{3}\right)} \times 0.08 \qquad \textbf{Equation 4.52}$$

$$[\text{aldehyde D}] = [\text{aldehyde tot}] - [\text{aldehyde H}] \qquad \textbf{Equation 4.53}$$

$$[\text{adduct tot}] = \frac{A_{D2}}{\text{A}_{\text{T1}} + \text{A}_{\text{D2}}} \times 0.08 \qquad \textbf{Equation 4.54}$$

$$[\text{adduct H}] = \frac{A_{D3}}{\left(\frac{(\text{A}_{\text{T1}} + \text{A}_{\text{D2}})}{3}\right)} \times 0.08 \qquad \textbf{Equation 4.55}$$

$$[\text{adduct D}] = [\text{adduct tot}] - [\text{adduct H}] \qquad \textbf{Equation 4.56}$$

4.2.9 Kinetic reaction of 2-methoxybenzaldehyde 213 in the presence of thiamine 7

Thiamine hydrochloride **7** (0.04 M), triethylamine (0.107 M), triethylamine hydrochloride salt (0.053 M) in deuterated methanol (CD_3OD) were incubated in a rigorously dried NMR tube. 2-Methoxybenzaldehyde **213** (0.04 M) was added and mixed thoroughly to commence the reaction. The reaction was transferred to an NMR instrument with the probe maintained at 25 °C. NMR spectra were recorded continuously for the duration of the experiment with each acquisition taking approximately 4 min. An overlay of spectra acquired at three time points during the experiment is presented below (**Figure 4.14**).

Figure 4.14 Overlay of ^{1}H NMR spectra at 500 MHz for the reaction of thiamine 7 and 2-methoxybenzaldehyde 213 in methanol-d_4 at 25 °C and 0.16 M triethylamine buffer.

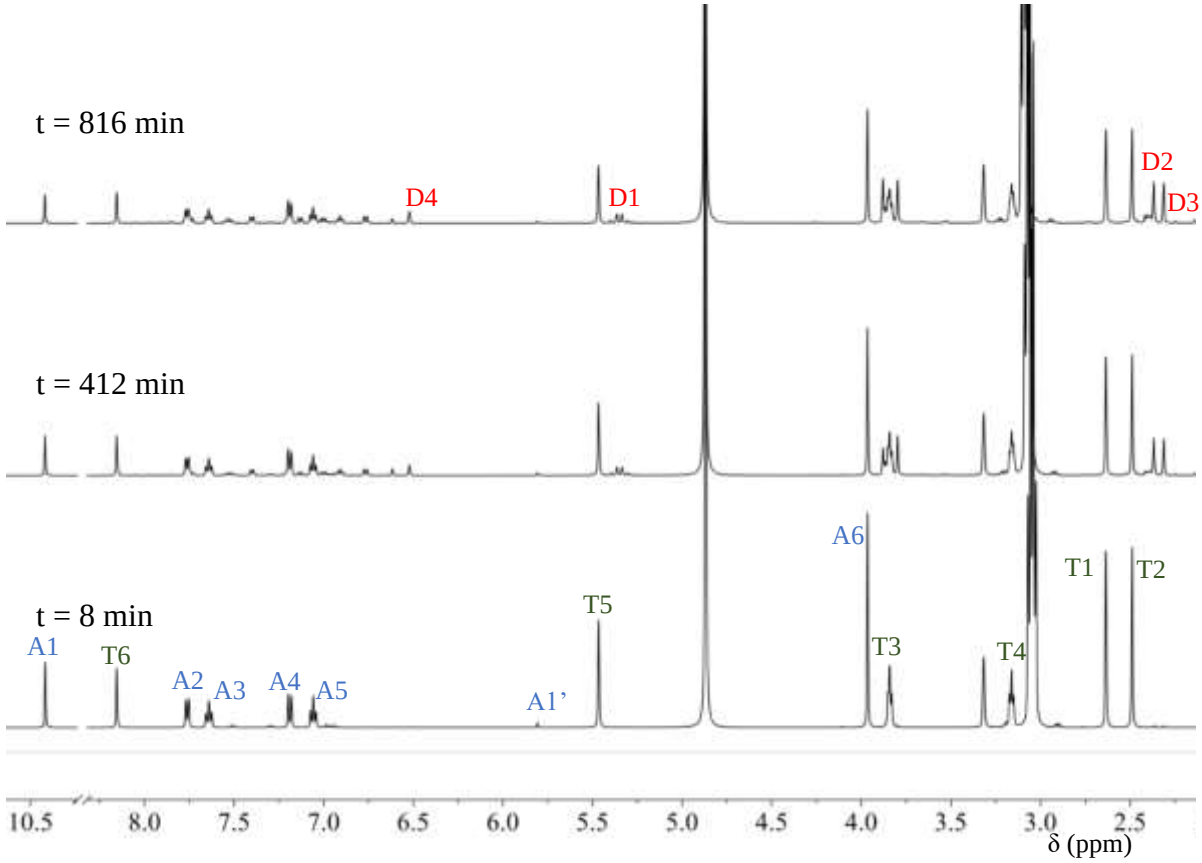

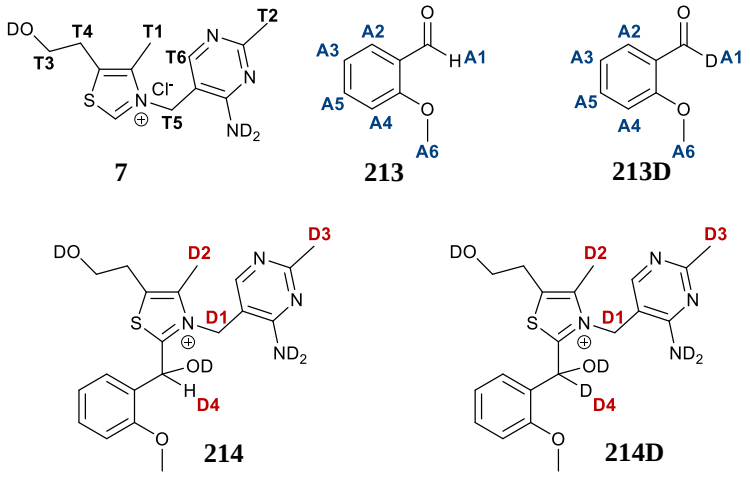

Scheme 4.14 Assignments of the proton NMR for the reaction species present in solution

At the start of the reaction, analysis shows exclusively C(2)−D deuterated thiamine **7**, the C(2)−H (9.6 ppm) having been completely exchanged owing to the basic conditions used. The benzoin product peak C*H*OH (6.11 ppm) was not seen for the duration of the experiment. Distinct peaks for each species present in solution were used to estimate concentration by integration. The singlet peak appearing at 2.64 ppm (T1) corresponds to the thiazolium methyl of unbound thiamine. The singlet appearing at 2.49 ppm (T2) represents the pyrimidinyl methyl of free thiamine. The peaks for the hydroxyethyl side chain of thiamine appear as triplets at 3.84 ppm (T3) and 3.16 ppm (T4). The bridging methylene of thiamine presents as a singlet at 5.47 ppm (T5) and the pyrimidinyl C−H as a singlet at 8.16 ppm (T6).

The singlet peak appearing at 10.42 ppm (A1) represents the aldehydic hydrogen of 2-methoxybenzaldeyde **213**. The doublet at 7.75 ppm (A2), triplet at 7.64 ppm (A3), doublet at 7.18 ppm (A4) and the triplet at 7.06 ppm (A5) correspond to aryl C-Hs on the aldehyde **213**. The singlet at 3.97 ppm (A6) corresponds to the methoxy hydrogens of **213**.

Overtime the presence of thiamine-aldehyde adduct **214** can be detected by the appearance of duplicate peaks alongside those of thiamine at slightly lower chemical shifts. Although the

adduct has not been isolated, its peaks can be inferred by comparison with other mimics (adduct) prepared. The bridging methylene of the adduct presents as a multiplet due to the two diastereotopic protons at 5.25 – 5.42 ppm (D1). The singlet at 2.37 ppm (D2) represents the adduct thiazolium methyl. The singlet at 2.31 ppm (D3) corresponds to the adduct pyrimidinyl methyl and may be used to quantify the total concentration of adduct as the reaction progresses. The exchangeable hydrogen of the hydroxyaryl adduct appears as a broad singlet at 6.52 ppm (D4) and used to estimate the concentration of protonated adduct present in solution.

The concentration of thiamine precatalyst was quantified using the singlet signal due to the lone methyl on its thiazolium ring (2.61 ppm) ((T1) (Equation 4.57). The catalyst is present only as free catalyst or adduct, no other peaks were observed by NMR. The triplet signal due to the 2-hydroxyethyl sidechain on thiamine (T3) overlapped with two other singlet signals due to the adduct, hence could not be used for integration. The bridging methylene of unbound thiamine (T5) integrated 2:3 with the lone thiazolium methyl (T1) during the reaction.

$$[catalyst] = \frac{A_{T1}}{A_{T1} + A_{D3}} \times 0.04 \qquad \textbf{Equation 4.57}$$

$$[\text{aldehyde tot}] = \frac{1}{f_{\text{ald}}} \times \frac{A_{A6}}{\text{A}_{\text{T1}} + \text{A}_{\text{D3}}} \times 0.04 \qquad \textbf{Equation 4.58}$$

$$[\text{aldehyde H}] = \frac{1}{f_{\text{ald}}} \times \frac{A_{A1}}{\left(\frac{(\text{A}_{\text{T1}} + \text{A}_{\text{D3}})}{3}\right)} \times 0.04 \qquad \textbf{Equation 4.59}$$

$$[\text{aldehyde D}] = [\text{aldehyde tot}] - [\text{aldehyde H}] \qquad \textbf{Equation 4.60}$$

$$[\text{adduct tot}] = \frac{A_{D3}}{(\text{A}_{\text{T1}} + \text{A}_{\text{D3}})} \times 0.04 \qquad \textbf{Equation 4.61}$$

$$[\text{adduct H}] = \frac{A_{D4}}{\left(\frac{(\text{A}_{\text{T1}} + \text{A}_{\text{D3}})}{3}\right)} \times 0.04$$ **Equation 4.62**

$$[\text{adduct D}] = [\text{adduct tot}] - [\text{adduct H}]$$ **Equation 4.63**

4.2.10 Concentration Profiles

For the reactions between a range of aldehydes and azolium precatalyst studied in the previous section, the concentration profiles are shown below (**Figure 4.15 - Figure 4.23**). In each case, the concentration of catalyst was used was 0.04M due to the limit for solubility of thiamine in methanol-d_4 at 25 °C. Various concentration of aldehyde were used and in cases where conversion into the adduct was relatively slow, a large excess of aldehyde was used in attempt to favour onward formation of the adduct.

Figure 4.15 Concentration profile for the self-condensation of 2-methoxybenzaldehyde 213 (0.06M), catalysed by triazolium mimic (144) (0.04 M), in 0.107M NEt_3 and 0.107 M NEt_3·DCl in methanol-d_4

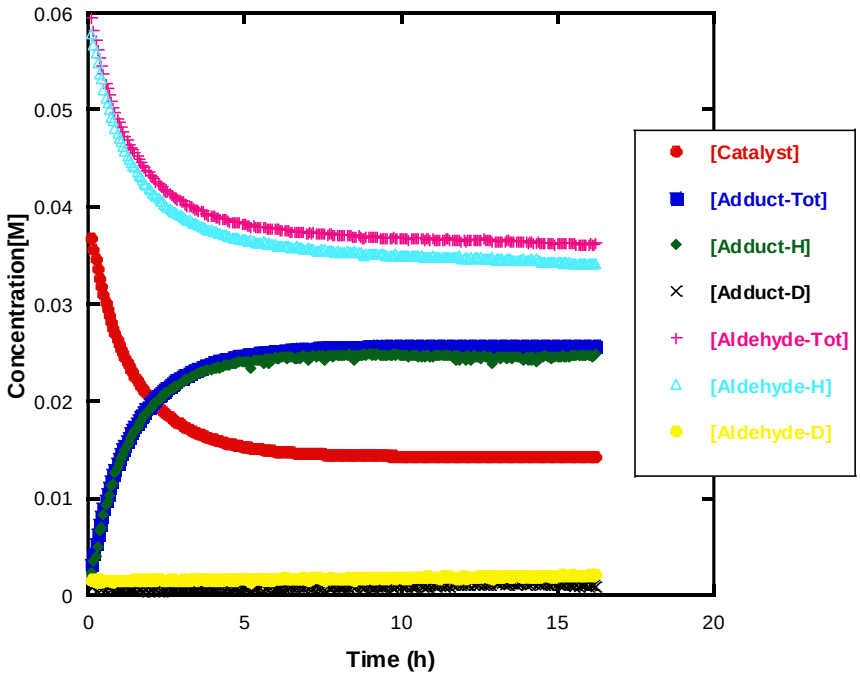

Figure 4.16 **Concentration profile for the self-condensation of aldehyde 240 (0.05M), catalysed by triazolium mimic (144) (0.04 M), in 0.107 M NEt3 and 0.107 M NEt_3·DCl in methanol-d_4**

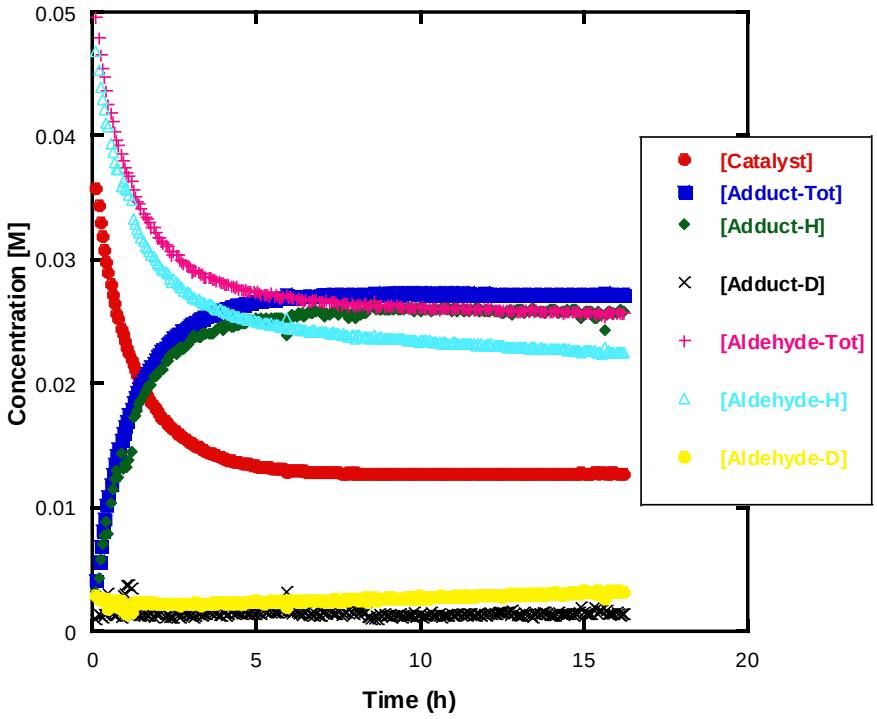

Figure 4.17 **Concentration profile for the self-condensation of 4-methoxybenzaldehyde (0.06M), catalysed by triazolium mimic (144) (0.04 M), in 0.107M NEt_3 and 0.107 M NEt_3·DCl in methanol-d_4**

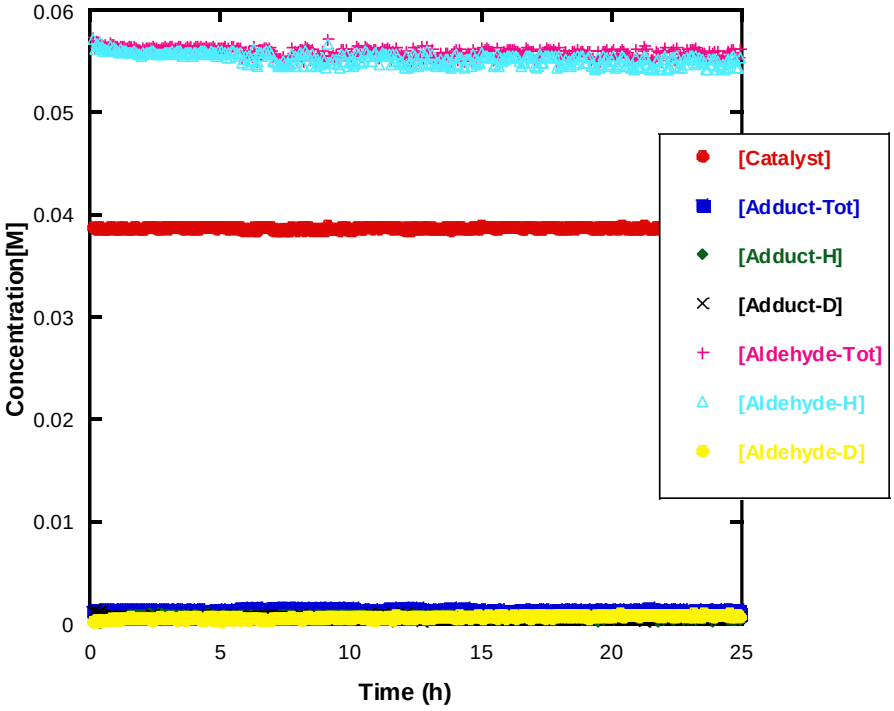

Figure 4.18 **Concentration profile for the self-condensation of 4-methoxybenzaldehyde 241 (0.15 M) and chalcone 244 (0.13 M), catalysed by triazolium mimic (144) (0.04 M), in 0.107M NEt_3 and 0.107 M NEt_3·DCl in methanol-d_4**

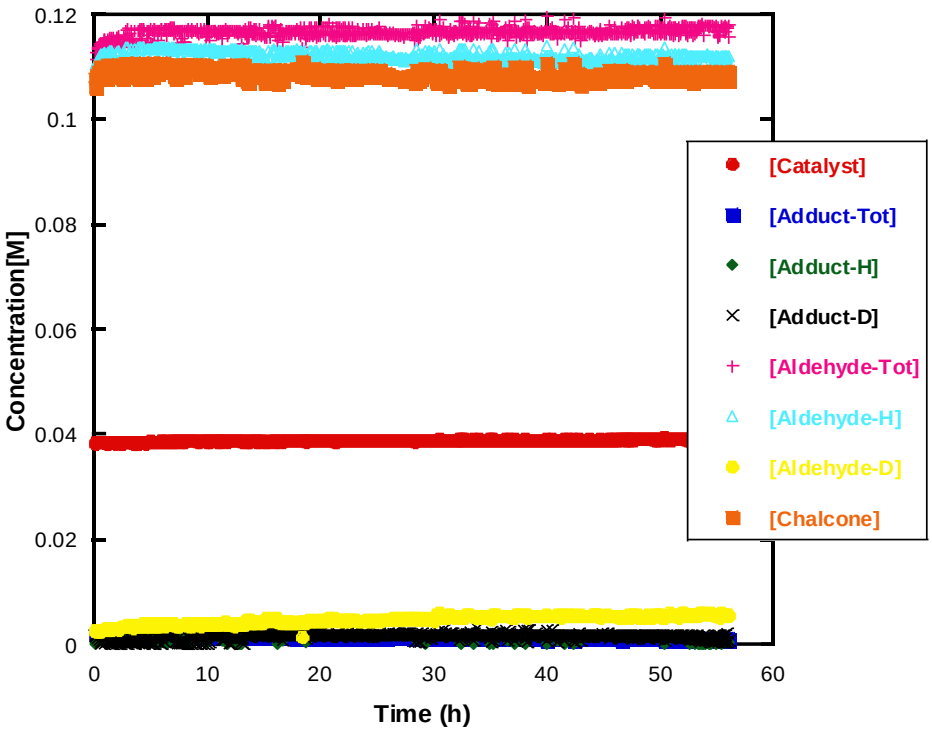

Figure 4.19 **Concentration profile for the self-condensation of 4-methylbenzaldehyde 242 (0.13 M), catalysed by triazolium mimic (144) (0.04 M), in 0.107M NEt_3 and 0.107 M NEt_3·DCl in methanol-d_4**

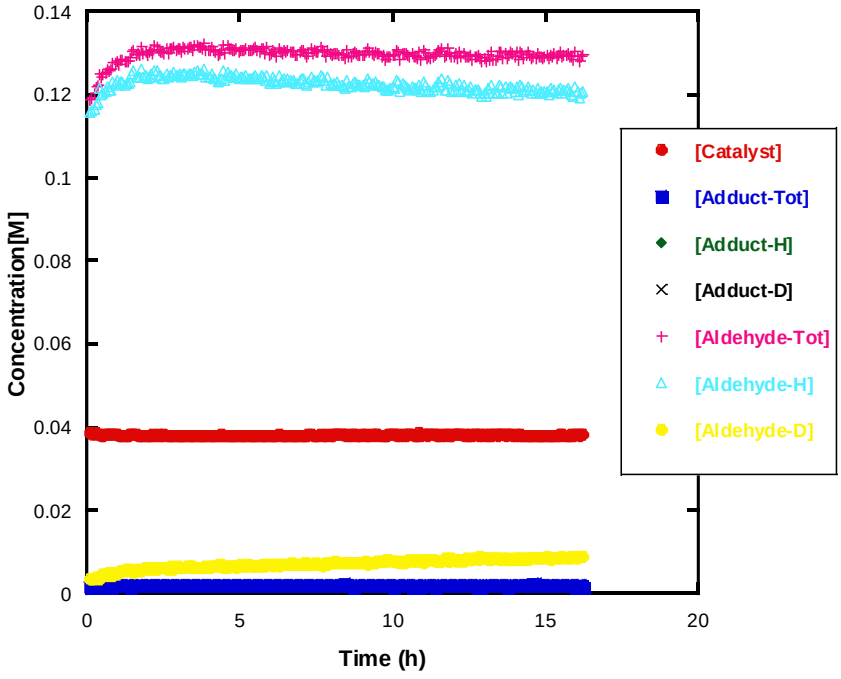

Figure 4.20 **Concentration profile for the self-condensation of 3-fluorobenzaldehyde 243 (0.05 M), catalysed by triazolium mimic (144) (0.04 M), in 0.107 M NEt_3 and 0.107 M NEt_3·DCl in methanol-d_4**

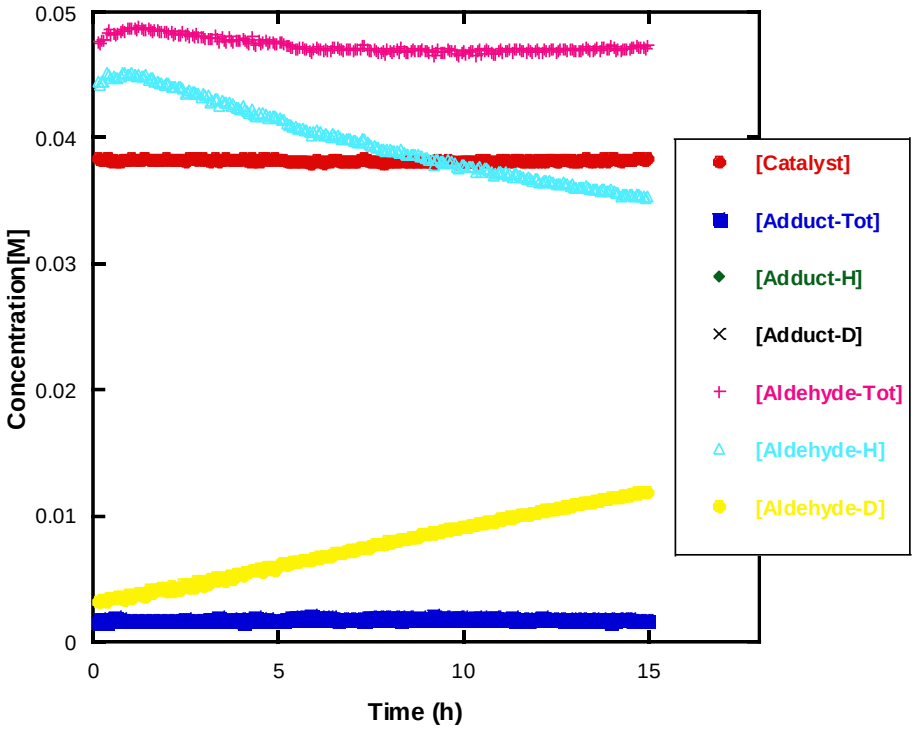

Figure 4.21 **Concentration profile for the self-condensation of 2-methoxybenzaldehyde 213 (0.083 M), catalysed by triazolium mimic (183) (0.08 M), in 0.107 M NEt_3 and 0.107 M NEt_3·DCl in methanol-d_4**

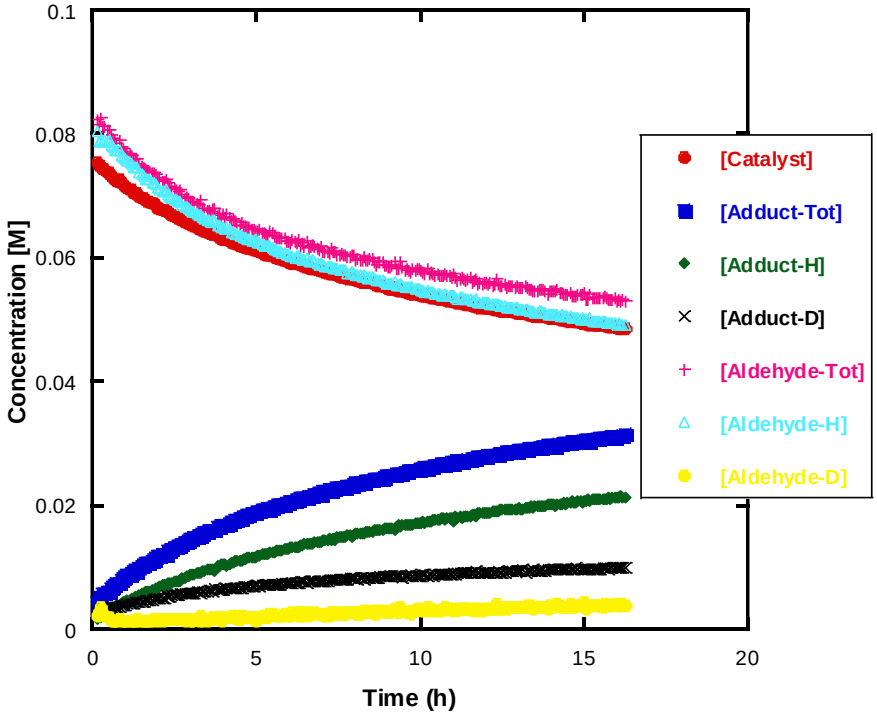

Figure 4.22 **Concentration profile for the self-condensation of 2-methoxybenzaldehyde (213) (0.18M), catalysed by precatalyst (212) (0.08 M), in 0.107M NEt_3 and 0.107 M NEt3·DCl in methanol-d_4**

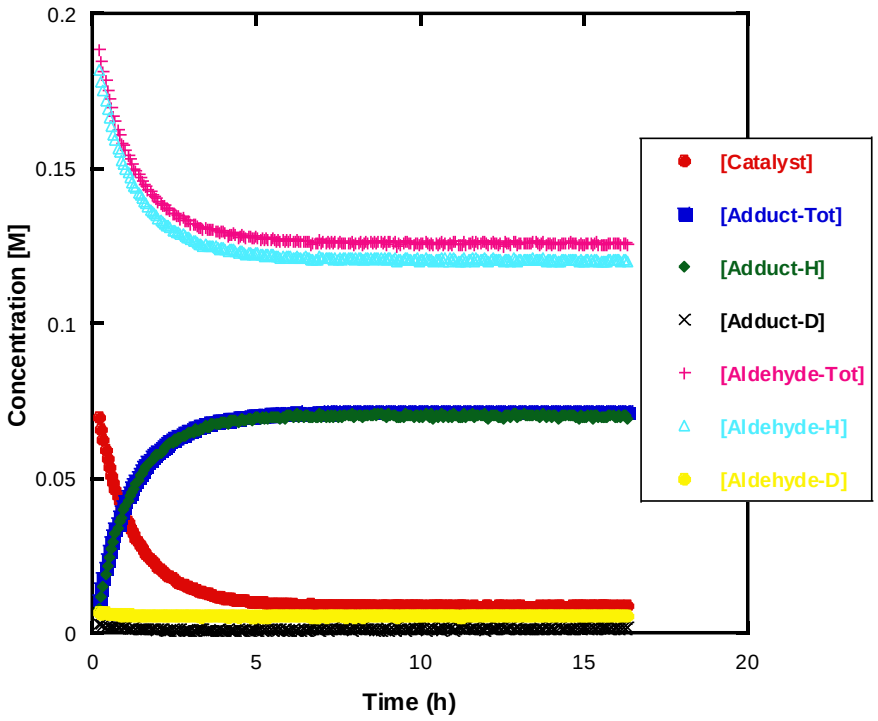

Figure 4.23 **Concentration profile for the self-condensation of 2-methoxybenzaldehyde (213) (0.05M), catalysed by thiamine (7) (0.04 M), in 0.107M NEt_3 and 0.107 M NEt3·DCl in methanol-d_4**

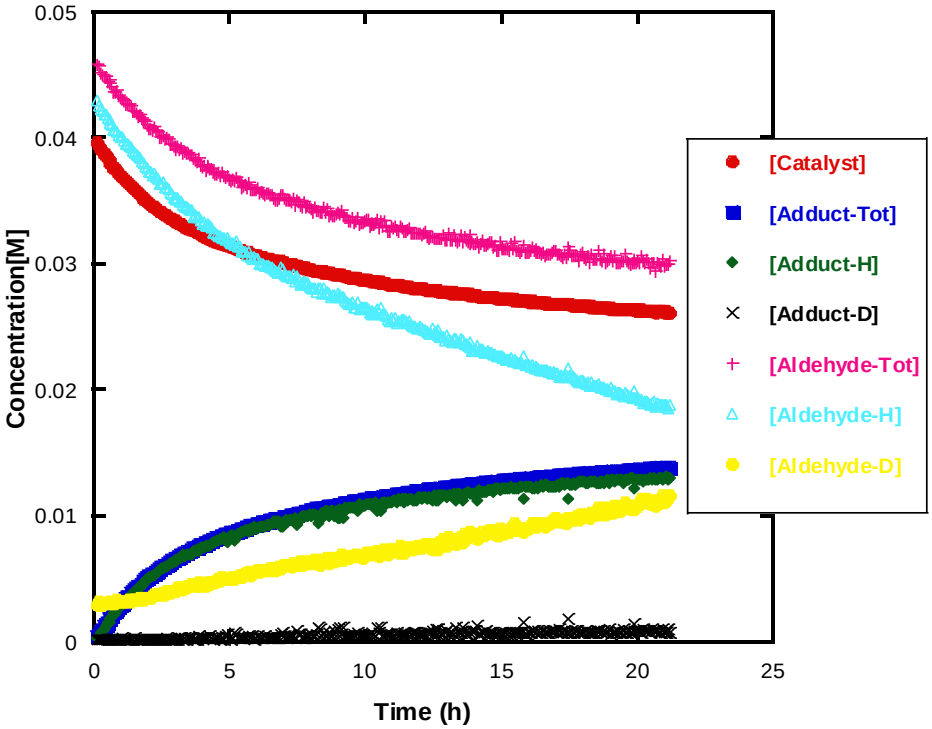

4.2.11 Determination of Rate Constants for Formation of Hydroxyaryl Adduct

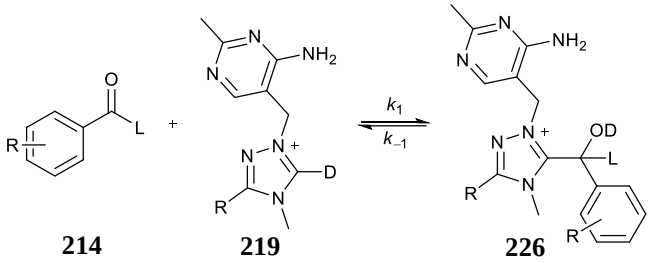

214 **219** **226**

Scheme 4.15 Formation of hydroxyaryl adduct from reaction between triazolium mimic 219 and generic aldehyde 214

Scheme 4.15 above represents the reaction between substituted aldehyde **214** and generic triazolium salt **219** to give the corresponding hydroxyaryl adduct **226**. Previous work by Zhu[11], developed a reliable method to estimate the values of k_1 and k_{-1} units for the adduct association and dissociation rate constants, respectively. Herein, the pre-equilibrium state leading onwards to the hydroxyaryl adduct may be regarded as a pseudo-second-order reaction (Equation 4.64).

$$\frac{d[\text{cat}]}{dt} = -k_1[\text{cat}][\text{ald}] + k_{-1}[\text{add}] \qquad \textbf{Equation 4.64}$$

Firstly, after plotting the concentration profiles, the equilibrium constant for hydroxyaryl adduct formation K (M^{-1}), can be estimated by using the concentration values at equilibrium for catalyst, aldehyde and adduct (Equation 4.65).

$$K = \frac{[\text{add (tot)}]_e}{[\text{cat}]_e \times [\text{ald (tot)}]_e} \qquad \textbf{Equation 4.65}$$

One advantage of the new method developed by Zhu is that varying starting concentrations of catalyst and substrate may be used to arrive at the desired rate constants. The prevailing concentration for substrate and adduct may be obtained using Equation 4.67 and Equation 4.68, respectively. Using the newfound value for *K*, the reverse rate constant for formation of the

hydroxy aryl adduct k_{-1} may be eliminated from the differential expression using Equation 4.69.

$$\frac{d[\text{cat}]}{dt} = -k_1[\text{cat}][\text{ald}] + k_{-1}[\text{add}] \qquad \textbf{Equation 4.66}$$

$$[\text{ald}] = [\text{ald}]_0 - ([\text{cat}]_0 - [\text{cat}]) \qquad \textbf{Equation 4.67}$$

$$[\text{add}] = [\text{cat}]_0 - [\text{cat}] \qquad \textbf{Equation 4.68}$$

$$k_{-1} = \frac{k_1}{K} \qquad \textbf{Equation 4.69}$$

For simplicity, the terms for aldehyde concentration, [ald] was replaced by "*y*", and similarly, catalyst concentration changed to "*x*" to give a simplified differential rate expression (Equation 4.70). The value of k_1 may be found from the gradient of the plot of *x* as a function of time *t* (Equation 4.71).

$$\frac{dx}{dt} = -k_1 x(y_0 - x_0 + x) + \frac{k_1}{K}(x_0 - x) \qquad \textbf{Equation 4.70}$$

$$k_1 \text{t} = \frac{1}{\sqrt{(y_0 - x_0 + \frac{1}{K})^2 + \frac{4x_0}{K}}} \left| \ln\left(\frac{x - x_1}{x - x_2}\right) \right|_{x_0}^{x}, \text{where} \qquad \textbf{Equation 4.71}$$

$$x_1 = \frac{-\left(y_0 - x_0 + \frac{1}{K}\right) + \sqrt{(y_0 - x_0 + \frac{1}{K})^2 + \frac{4x_0}{K}}}{2} \text{ and}$$

$$x_2 = \frac{-\left(y_0 - x_0 + \frac{1}{K}\right) - \sqrt{(y_0 - x_0 + \frac{1}{K})^2 + \frac{4x_0}{K}}}{2}$$

Correspondingly, hydroxyaryl adduct concentration may be used to estimate the value of k_1. This is achieved by modifying the differential expression (Equation 4.64) to reflect adduct formation, [add] = *z*, (Equation 4.72).

$$-\frac{dz}{dt} = -k_1(x_0 - z)(y_0 - z) + \frac{k_1}{K}z \qquad \textbf{Equation 4.72}$$

$$k_1 \mathrm{t} = \frac{1}{\sqrt{(x_0 + y_0 + \frac{1}{K})^2 - 4x_0y_0}} \left| \ln\left(\frac{z - z_1}{z - z_2}\right) \right|_0^z \quad where \qquad \textbf{Equation 4.73}$$

$$z_1 = \frac{\left(x_0 + y_0 + \frac{1}{K}\right) + \sqrt{(x_0 + y_0 + \frac{1}{K})^2 - 4x_0y_0}}{2}, \textit{ and}$$

$$z_2 = \frac{\left(x_0 + y_0 + \frac{1}{K}\right) - \sqrt{(x_0 + y_0 + \frac{1}{K})^2 - 4x_0y_0}}{2} \quad .$$

In addition, the rate of dissociation of adduct to give catalyst and substrate k_{-1} may also be obtained by analogous derivation. The differential expression (Equation 4.72) may be modified to give Equation 4.74, and onwards integration, gives the desired rate function Equation 4.75.

$$-\frac{dz}{dt} = -Kk_{-1}(x_0 - z)(y_0 - z) + k_{-1}z \qquad \textbf{Equation 4.74}$$

$$k_{-1} \mathrm{t} = \frac{1}{K\sqrt{(x_0 + y_0 + \frac{1}{K})^2 - 4x_0y_0}} \left| \ln\left(\frac{z - z_1}{z - z_2}\right) \right|_0^z \qquad \textbf{Equation 4.75}$$

$$z_1 = \frac{\left(x_0 + y_0 + \frac{1}{K}\right) + \sqrt{(x_0 + y_0 + \frac{1}{K})^2 - 4x_0y_0}}{2}, \text{ and}$$

$$z_2 = \frac{\left(x_0+y_0+\frac{1}{K}\right)-\sqrt{(x_0+y_0+\frac{1}{K})^2-4x_0y_0}}{2}$$

The values for k_1, k_{-1} and K may also be obtained by fitting the concentrations of adduct, aldehyde and catalyst from initiation of the reaction to equilibrium before any significant onward reaction to give the benzoin product using global fitting software (Berkeley Madonna, Version 10.1.2). There was insufficient adduct formation to enable reliable determination of k_1, k_{-1} and K for aldehydic substrates **241 - 243**.

Table 4.3 Rate constants and equilibrium constants for hydroxyaryl adduct formation determined by manual fitting [a, b, c]

Catalyst	Aldehyde	k_1, $M^{-1}s^{-1}$ [a]	k_{-1}, s^{-1} [b]	K, M^{-1} [c]
	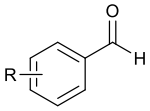			
Thiamine **7**	R = 2-OMe **213**	5.02×10^{-4}	2.88×10^{-5}	17.4
Ethylene Mimic **139**	R = 2-OMe **213**	2.31×10^{-3}	4.66×10^{-5}	49.5
	R = 2-$OCH_2(CH)_2$Ph **240**	3.53×10^{-3}	4.29×10^{-5}	82.3
	R = 4-MeO **241**	-	-	-
	R = 4-Me **242**	-	-	-
	R = 3-F **243**	-	-	-
Methyl Mimic **178**	R = 2-OMe **213**	2.11×10^{-4}	1.76×10^{-5}	12.0
Precatalyst **205**	R = 2-OMe **213**	1.39×10^{-3}	2.05×10^{-5}	67.7

(a)Obtained from the gradient of the plot of x as a function of time t Equation 4.57 (b) Calculated from values of k_1 (M^{-1} s^{-1}) and K (M^{-1}) (c) Calculated using equilibrium concentrations Equation 4.51

4.3 Global fitting to obtain k_1, k_{-1} and K

Global fitting software (Berkeley Madonna, Version 10.1.2) was used to fit the concentration profiles shown in Section 4.3 using the simplified mechanism shown below. The mechanism is shown in Scheme 4.16 below. Values of K fit were obtained from the values of k_1 and k_{-1} obtained from the fitting software using Equation 4.69.

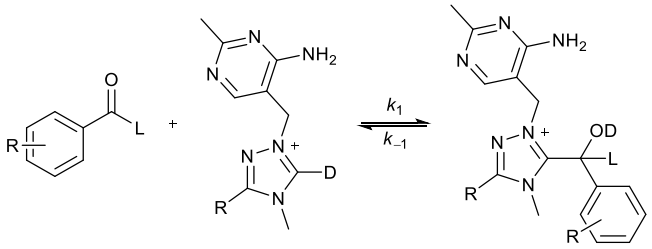

Scheme 4.16 First step to give the hydroxy aryl adduct

Figure 4.24 Concentration profile for the self-condensation of 2-methoxybenzaldehyde (0.06 M), catalysed by triazolium mimic (144) (0.04 M), in 0.107 M NEt_3 and 0.107 M NEt_3·DCl in methanol-d_4 fitted using Berkeley Madonna global fitting software

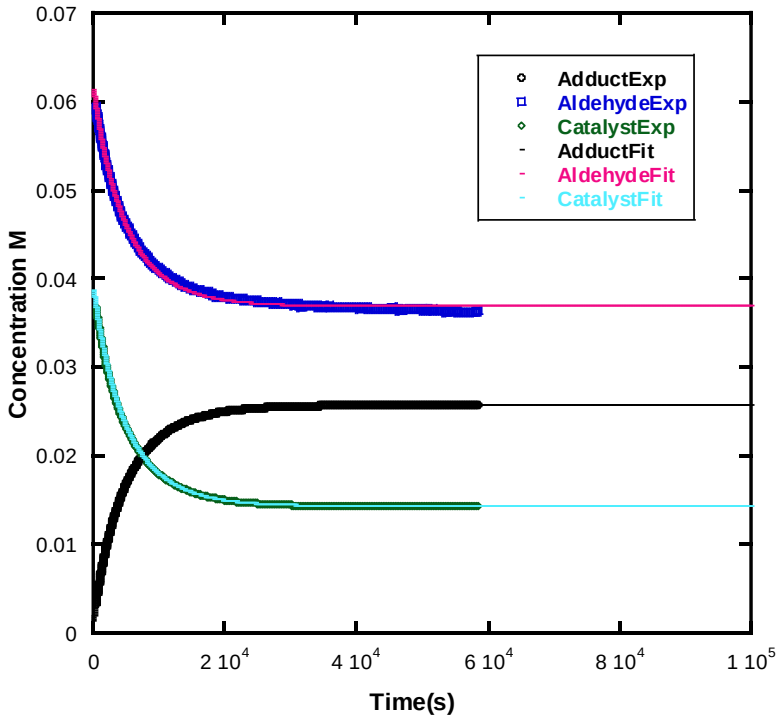

Figure 4.25 **Concentration profile for the self-condensation of aldehyde 240 (0.05 M), catalysed by triazolium mimic (144) (0.04 M), in 0.107 M NEt_3 and 0.107 M NEt_3·DCl in methanol-d_4 fitted using Berkeley Madonna global fitting software**

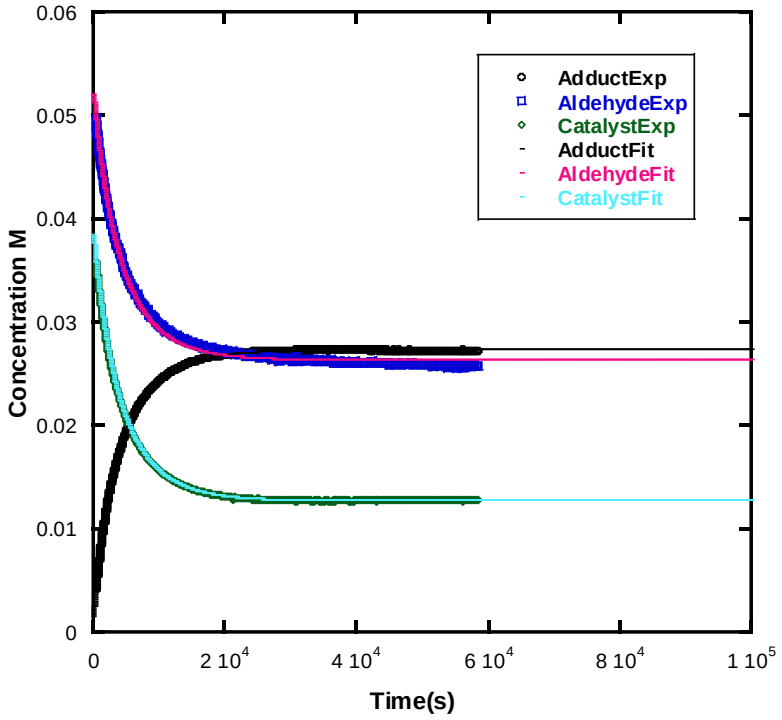

Figure 4.26 **Concentration profile for the self-condensation of 2-methoxybenzaldehyde (0.08 M), catalysed by methyl triazolium mimic (183) (0.08 M), in 0.107 M NEt_3 and 0.107 M NEt_3·DCl in methanol-d_4 fitted using Berkeley Madonna global fitting software**

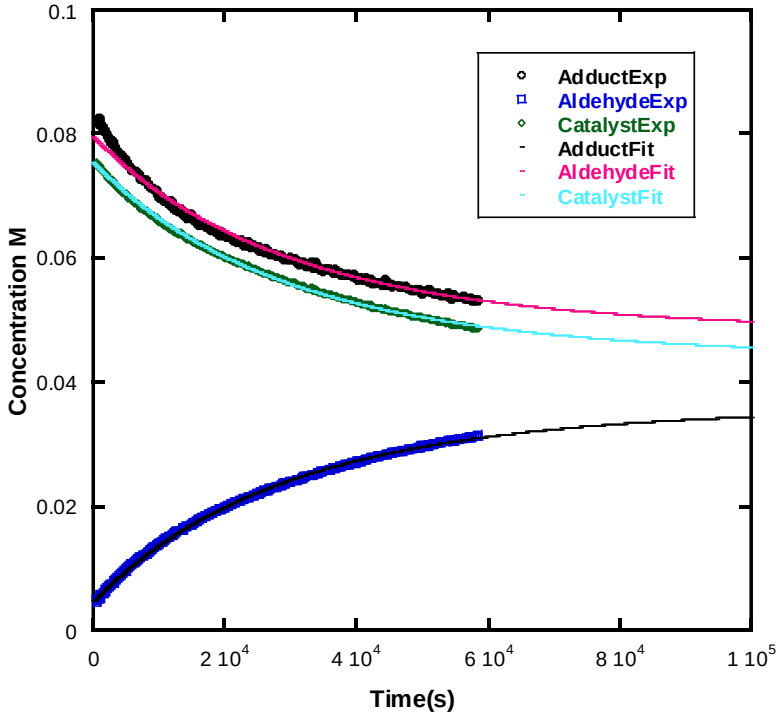

Figure 4.27 **Concentration profile for the self-condensation of 2-methoxybenzaldehyde (0.18 M), catalysed by triazolium precatalyst (212) (0.08 M), in 0.107 M NEt_3 and 0.107 M NEt_3·DCl in methanol-d_4 fitted using Berkeley Madonna global fitting software**

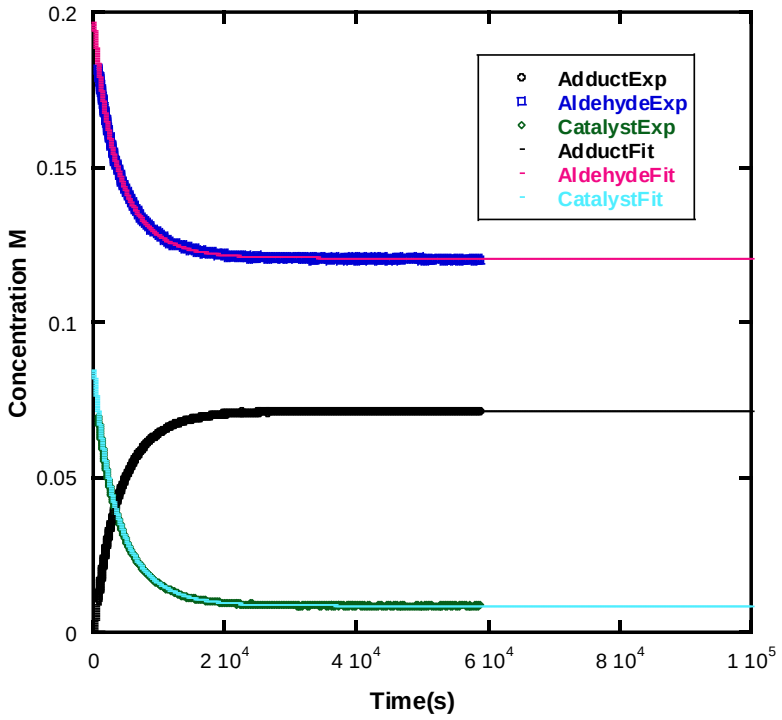

Figure 4.28 **Concentration profile for the self-condensation of 2-methoxybenzaldehyde (213) (0.05M), catalysed by thiamine (7) (0.04 M), in 0.107 M NEt_3 and 0.107 M NEt_3·DCl in methanol-d_4 fitted using Berkeley Madonna global fitting software**

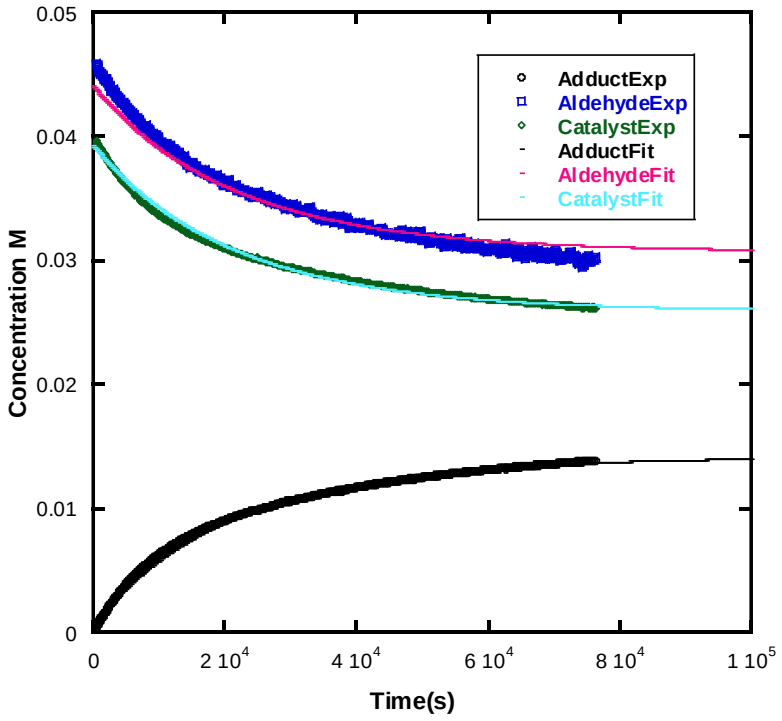

The Table 4.4 shows the values of forward and reverse rate constant obtained from fitting with global fitting software Berkeley Madonna. These results are in good agreement with those obtained from 'manual fitting' in excel.

Table 4.4 Rate constants obtained from global fitting

Catalyst	Aldehyde	k_1, $M^{-1}s^{-1}$ [a]	k_{-1}, s^{-1} [a]	K, M^{-1} [a]
	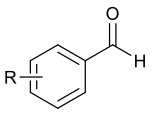			
Thiamine **7**	R = 2-OMe **213**	3.83×10^{-4}	2.15×10^{-5}	17.8
Ethylene Mimic **144**	R = 2-OMe **213**	2.31×10^{-3}	4.66×10^{-5}	49.5
	R = 2-$OCH_2(CH)_2Ph$ **240**	3.56×10^{-3}	4.34×10^{-5}	82.0
Methyl Mimic **183**	R = 2-OMe **213**	1.92×10^{-4}	1.15×10^{-5}	16.7
Precatalyst **212**	R = 2-OMe **213**	1.39×10^{-3}	2.01×10^{-5}	69.2

(a)Obtained by global fitting according to Equation 4.50 using concentrations of catalyst, aldehyde and adduct

4.4 Discussion

This section compares data from the previous section for k_1, k_{-1} and K with reported literature values and analyses the various trends observed in the results. Analysis of the effect of substituents, counterion, and ring heteroatom are discussed.

4.4.1 Thiamine versus triazolium mimic effect on equilibrium constant *K*

The equilibrium constant is three times larger for the triazolium **144** catalysed reaction than for thiamine **7** (K = 49.5 vs 17.4 M^{-1}) using aldehyde **213**, which shows that more of the adduct product is present in the equilibrium reaction mixture for the triazolium **144** catalysed reaction. The C_3H pK_a of **144** is about one pK_a unit lower than **7** at the C2 position. The adduct formation from triazolium/thiazolium has two steps: firstly, carbene formation by deprotonation of precatalyst and secondly, addition of carbene to aldehyde. A lower pre-catalyst pK_a will increase the concentration of carbene at equilibrium. However, assuming nucleophilicity parallels basicity, this would be expected to decrease rate of addition of NHC to aldehyde. This trend is seen with the rest of the triazolium salts studied, except for the methyl triazolium mimic **183** (K = 12.0 M^{-1}) which is less by 5.4 units than for thiamine **7** (Table 4.3). Comparing this result with previously reported data (Table 4.1), the K value for thiamine **7** (K = 17.4 M^{-1}) is smaller than for the N-phenyl substituted triazolium precatalyst **195** (K = 56 M^{-1}) using the same substrate 2-methoxy benzaldehyde **213** by 3 fold. Both the N-mesityl **201** (K = 143 M^{-1}) and N-2,4,6-trichlorophenyl (K = 301 M^{-1}) triazolium precatalysts K values are 8 and 17 fold larger for the same substrate **213** in comparison to thiamine. This consistently demonstrates that triazolium precatalysts favour higher equilibrium constant values in comparison to thiamine **7.**

The value of K for thiamine **7** and **213** (17.4 M^{-1}) is 6-fold higher than for triazolium salt N-phenyl **195** and benzaldehyde **5** (K = 3 M^{-1}). Also, the K value for N-mesityl catalyst **201** and substrates 2-methylbenzaldehyde **229** (K = 16 M^{-1}) and para bromobenzaldehyde **231** (K = 15

M^{-1}) are marginally lower than for thiamine **7** and **213** (17.4 M^{-1}). This demonstrates that choice of substrate, in this case, benzaldehyde **5**, can counterbalance catalytic efficiency given the reported ortho-substituent effect of aldehyde **213** on this equilibrium.

The triazolium mimic **144** equilibrium value with substrate **213** (49.5 M^{-1}) is similar to the value reported using N-phenyl catalyst **195** and 2-methoxybenzaldeyde **213** (K = 56 M^{-1}). This suggests the effect of the different N-substituent on both catalysts to be closely matched, although the N-phenyl catalyst is slightly (1.1-fold) higher. Comparing these K values with the value reported for the reaction between N-mesityl catalyst **201** and substrate 2-methoxybenzaldehyde **213** (K = 143 M^{-1}) gives a substantial 3-fold increase. This observation can be in part attributed to the steric effect of the mesityl ring, as its orthogonal orientation to the triazolium ring in the precatalyst is more amenable to approach of the aldehyde[13]. Furthermore, the value for K using N-2,4,6-trichlorophenyl catalyst **234** and substrate **213** (K = 301 M^{-1}) shows a 6-fold increase. This demonstrates that the equilibrium position is shifted to favour adduct formation upon additional heteroatom substitution at the ortho-positions, which again demonstrates the 2-substituent effect in these systems[10].

In addition, the triazolium mimic **144** shows a 2-fold increase in K values from substrate **213** (49.5 M^{-1}) to aldehyde **240** (82.3 M^{-1}). Using N-phenyl catalyst **195** with a related intramolecular Stetter substrate **28** (K = 319 M^{-1}) gives a 4-fold increase in equilibrium constant compared to mimic **144** and **240 (**

). The difference is even larger for N-mesityl catalyst **201** and intramolecular substrate **28** (K = 3082 M^{-1}) representing a massive 38-fold increase. Again, the mesityl ring shows a strong disposition to favour adduct formation. These data demonstrate that triazolium ion **144** in general leads to larger equilibrium constant values K in comparison to the thiazolium ion and shows similar aldehydic substituent effect trends to previously studied N-aryl triazolium catalysts.

4.4.2 Thiamine versus triazolium mimic effect on forward rate constant k_1

For the reaction between thiamine **7** and 2-methoxybenzaldehyde **213**, a value of $k_1 = 3.83 \times 10^{-4}\ M^{-1}s^{-1}$ was obtained, which is considerably lower than for the reaction of triazolium mimic **144** with the same substrate **213** $k_1 = 2.31 \times 10^{-3}\ M^{-1}s^{-1}$. This represents a direct like for like comparison and establishes the triazolium **144** as the faster catalyst. This result is pleasing because it shows that preparing the mimic for use as a cofactor in enzymatic reaction shows good promise. Similar results are seen for previously reported triazolium salts from our group[10]. N-phenyl salt **195** and 2-methoxy benzaldehyde **213** gave a value of $k_1 = 3.44 \times 10^{-2}\ M^{-1}s^{-1}$ which represents a substantial 90-fold increase in forward rate constant k_1 in comparison to thiamine **7** and 2-methoxybenzaldehyde **213**. Surprisingly, the reaction between N-phenyl salt **195** and 4-methoxy benzaldehyde **241** gave a value of $k_1 = 2.86 \times 10^{-3}\ M^{-1}s^{-1}$ which is still much higher than reaction between thiamine **7** and 2-methoxybenzaldehyde **213**.

Previously reported forward rate constant values for the N-aryl substituted catalysts and substrate **28** were consistently higher than for thiamine or any of the triazolium mimics prepared and may be attributed to the higher stability of the corresponding adduct in relation to the aldehyde. For example, N-parafluoro phenyl precatalyst **236** and substrate **28** gave a value of $k_1 = 4.89 \times 10^{-2}\ M^{-1}s^{-1}$ (Table 4.2 page 154) which is 125 times larger than for thiamine **7** and 2-methoxybenzaldehyde **213** ($k_1 = 3.83 \times 10^{-4}\ M^{-1}s^{-1}$).

4.4.3 Alkyl versus aryl substituent effects on forward rate constants

Comparing the values of rate constants for the triazolium salts studied shows that the 2-hydroxyethyl triazolium mimic **144** gave a k_1 value of $2.31 \times 10^{-3}\ M^{-1}s^{-1}$ which is about twice for precatalyst **212** which gave the smallest k_1 value of $1.39 \times 10^{-3}\ M^{-1}s^{-1}$ with the same

substrate 2-methoxybenzaldehyde **213**. This demonstrates that the pendant 2-hydroxyethyl and 2-methylpyrimidine side chains can promote the first step to give the adduct. In addition, the pK_a of **144** is lower by one unit than for **212** which favours more of the active carbene form present in solution. N-Phenyl salt (pK_a 17.5) **195** and 2-methoxy benzaldehyde **213** gave a value of $k_1 = 3.44 \times 10^{-2}\,M^{-1}s^{-1}$ which represents a substantial 15 fold increase in forward rate constant k_1 in comparison to mimic **144** and 2-methoxybenzaldehyde **213** ($k_1 = 2.31 \times 10^{-3}$ $M^{-1}s^{-1}$).

A similar trend is observed with all the other N-aryl substituted precatalysts previously reported in the group[10]. For example, the N-parafluoro phenyl precatalyst **236** and intramolecular Stetter substrate **28** gave a value of $k_1 = 4.89 \times 10^{-2}\,M^{-1}s^{-1}$ (

) which is 14-fold bigger than for 2-hydroxyethyl triazolium mimic **144** and aldehyde **240** (k_1 = $3.53 \times 10^{-3}\,M^{-1}s^{-1}$) (Table 4.3). In addition, N-paramethoxy phenyl precatalyst **237** and intramolecular Stetter substrate **28** gave a value of $k_1 = 1.28 \times 10^{-2}\,M^{-1}s^{-1}$ (

) which is 4 fold larger than for 2-hydroxyethyl triazolium mimic **144** and aldehyde **240** (k_1 = $3.53 \times 10^{-3}\,M^{-1}s^{-1}$) (Table 4.3). The N-2,6-dimethoxyphenyl precatalyst **238** gave a lower value for intramolecular Stetter substrate **28** ($k_1 = 1.28 \times 10^{-2}\,M^{-1}s^{-1}$) representing a 3-fold increase in comparison to mimic **144** and aldehyde **240** . The reaction between triazolium mimic **144** and 4-methylbenzaldehyde **242** needs further investigation as concentration of reactants does not normally increase during the course of reaction **Figure 4.19**.

4.4.4 Alkyl versus aryl substituent effects on reverse rate constants

The values of reverse rate constants k_{-1} for the triazolium salts studied shows that the 2-hydroxyethyl triazolium mimic **144** gave a k_{-1} value of $4.66 \times 10^{-5}\,s^{-1}$ which is about 2.6 fold greater than that for methyl mimic **183** which gave the lowest k_{-1} value of $1.76 \times 10^{-5}\,s^{-1}$ with

substrate 2-methoxybenzaldehyde **213** (Table 4.3). Reaction between N-phenyl salt **195** and Stetter substrate **28** gave a value of k_{-1} = 4.76 × 10^{-5} s^{-1}, which is almost the same in comparison to mimic **144** and 2-methoxybenzaldehyde **213** (k_{-1} = 4.66 × 10^{-5} s^{-1}). This demonstrates that the rate of reverse reaction from the adduct to give back the aldehyde and catalyst is favoured to the same extent by both catalyst mimic **144** and N-phenyl precatalyst **195.**

A similar trend is observed with all the other N-aryl substituted precatalysts previously reported in the group[10]. For example, the N-parafluoro phenyl precatalyst **236** and intramolecular Stetter substrate **28** gave a value of k_{-1} = 9.45 × 10^{-5} s^{-1} (

) which is only 2-fold faster than for 2-hydroxyethyl triazolium mimic **144** and aldehyde **240** (k_{-1} = 4.29 × 10^{-5} s^{-1}) (Table 4.3). In addition, N-paramethoxy phenyl precatalyst **237** and intermolecular Stetter substrate **28** gave a value of k_{-1} = 3.09 × 10^{-5} s^{-1} (

) which is marginally smaller than for 2-hydroxyethyl triazolium mimic **144** and aldehyde **240** (k_{-1} = 4.29 × 10^{-5} s^{-1}) (Table 4.3). This demonstrates that mimic **144** is faster than precatalyst **237** for the reverser reaction to give catalyst and aldehyde in this case. The N-2,6-dimethoxyphenyl precatalyst **238** gave the lowest reverse rate constant k_{-1} value for series of N-aryl triazolium precatalysts reported with intramolecular Stetter substrate **28** (k_{-1} = ≤ 1.01 × 10^{-7} s^{-1}) representing a two orders of magnitude decrease in comparison to mimic **144** and aldehyde **240** . It can be inferred that the adduct is more stabilized relative to the precatalyst **238** due to the two heteroatom substitution at positions 2 and 6.

4.4.5 Comparison of rate constants obtained from 'manual fitting' and global fitting

The values obtained from fitting reaction data in Berkeley Madonna global fitting computational software closely matched those obtained from manual fitting in most cases. These results are summarized in Table 4.5 below.

Table 4.5 Comparison of rate constants obtained from 'manual fitting' and global fitting

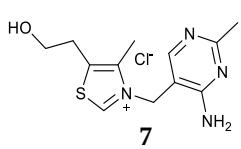

7

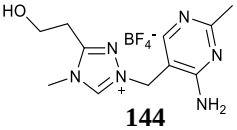

144

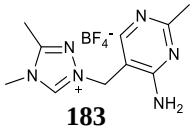

183

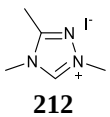

212

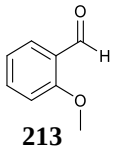

213

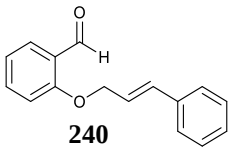

240

Catalyst	Aldehyde	k_1, $M^{-1}s^{-1}$ [a]	k_1, $M^{-1}s^{-1}$ [b]	k_{-1}, s^{-1} [c]	k_{-1}, s^{-1} [b]	K, M^{-1} [d]	K, M^{-1} [a]
7	**213**	5.02×10^{-4}	3.83×10^{-4}	2.88×10^{-5}	2.15×10^{-5}	17.8	17.4
144	**213**	2.31×10^{-3}	2.31×10^{-3}	4.66×10^{-5}	4.66×10^{-5}	49.5	49.5
144	**240**	3.53×10^{-3}	3.56×10^{-3}	4.29×10^{-5}	4.34×10^{-5}	82.0	82.3
183	**213**	2.11×10^{-4}	1.92×10^{-4}	1.15×10^{-5}	1.15×10^{-5}	16.7	12.0
212	**213**	1.39×10^{-3}	1.39×10^{-3}	2.01×10^{-5}	2.01×10^{-5}	69.2	67.7

(a) Obtained from the gradient of the plot of x as a function of time t Equation 4.57 (b) Obtained by global fitting according to Equation 4.50 using concentrations of catalyst, aldehyde and adduct (c) Calculated from values of k_1 (M^{-1} s^{-1}) and K (M^{-1}) (d) Calculated using equilibrium concentrations Equation 4.51

The largest variance in k_1 was observed for reaction between thiamine **7** and 2-methoxybenzaldehyde **213**; a value of $k_1 = 5.02 \times 10^{-4}\,M^{-1}s^{-1}$ was obtained from manual fitting and $k_1 = 3.83 \times 10^{-4}\,M^{-1}s^{-1}$ from using fitting software for the forward rate constant (a difference of ~ 30 %). The reverse rate constants obtained show a similar trend of $k_{-1} = 2.88 \times 10^{-5}\,s^{-1}$ and $k_{-1} = 2.15 \times 10^{-5}\,s^{-1}$ for manual and global fitting respectively. The equilibrium

constant for this reaction was similar for both manual fitting and software fitting 17.8 and 17.4 M^{-1}, respectively.

The triazolium mimic **144** shows closely matched values for k_1, k_{-1} and K to 2 decimal places for both manual and global fitting for its reaction with aldehyde **213** and only marginal variation with substrate **240** (Table 4.5)**.** Triazolium catalyst **183** does show a slight variation in values for k_1 and K using manual fitting $k_1 = 2.11 \times 10^{-4}\ M^{-1}s^{-1}$ and $K = 16.7$ compared to $k_1 = 1.92 \times 10^{-4}\ M^{-1}s^{-1}$ and $K = 12.0$ obtained from software fitting. In addition triazolium catalyst **212** does show good agreement in values for k_1, k_{-1} and K using manual fitting $k_1 = 1.39 \times 10^{-3}\ M^{-1}s^{-1}$, $k_{-1} = 2.01 \times 10^{-5}\ s^{-1}$ and $K = 69.2$ compared to $k_1 = 1.39 \times 10^{-3}\ M^{-1}s^{-1}$, $k_{-1} = 2.01 \times 10^{-5}\ s^{-1}$ and $K = 67.7$ from software fitting. These results are pleasing and show the values obtained from the two methods are comparable.

4.5 Conclusion

Triazolium mimics prepared in chapter 2 have been screened for catalytic efficacy. The 2-hydroxyethyl triazolium mimic **144** consistently gave larger forward rate constants across the board compared to thiamine **7**. Values of k_1, k_{-1} and K were determined using manual fitting of experimental data. In addition, using global Berkeley Madonna fitting software, values of forward, reverse and equilibrium constants were estimated from computational fitting. Several other substrates, **241 - 243** were screened for reaction with the range of precatalyst used in this study. Triazolium salts were demonstrated to be more efficient in the reactions for the formation of the hydroxy aryl adduct. The 2-substituent effect previously observed and reported by our group[10] was found to hold true for the new mimics prepared in this work especially with ortho substrate **213**.

4.6 References

1. Wöhler and Liebig, *Annalen der Pharmacie*, 1832, **3**, 249-282.
2. R. T. T. Ukai, T. A. Dokawa, *J. Pharm. Soc. Jpn.*, 1943, **63**, 296-300.
3. S. Mizuhara and P. Handler, *J. Am. Chem. Soc.*, 1954, **269**, 1951-1953.
4. R. Breslow, *J. Am. Chem. Soc.*, 1958, **80**, 3719-3726.
5. A. Lapworth, *J. Chem. Soc. Trans.*, 1903, **83**, 995-1005.
6. M. J. White and F. J. Leeper, *J. Org. Chem.*, 2001, **66**, 5124-5131.
7. E. M. Higgins, J. A. Sherwood, A. G. Lindsay, J. Armstrong, R. S. Massey, R. W. Alder and A. C. O'Donoghue, *Chem. Commun.*, 2011, **47**, 1559-1561.
8. A. Berkessel, S. Elfert, V. R. Yatham, J. M. Neudorfl, N. E. Schlorer and J. H. Teles, *Angew Chem Int Ed Engl*, 2012, **51**, 12370-12374.
9. R. S. Massey and A. C. O'Donoghue, Ph.D., Durham University, 2013.
10. C. J. Collett, R. S. Massey, J. E. Taylor, O. R. Maguire, A. C. O'Donoghue and A. D. Smith, *Angew. Chem. Int. Ed.*, 2015, **54**, 6887-6892.
11. J. Zhu and A. C. O'Donoghue, Ph.D., Durham University, 2019.
12. R. Wasylishen and T. Schaefer, *Can. J. Chem.*, 2011, **49**, 3216-3228.
13. (a)B. Maji, M. Breugst and H. Mayr, *Angew. Chem. Int. Ed.*, 2011, **50**, 6915-6919; (b)F. Ragone, A. Poater and L. Cavallo, *J. Am. Chem. Soc.*, 2010, **132**, 4249-4258.

Chapter Five

5 Docking Studies of Triazolium Mimics of Thiamine

Foreword

In Chapter 5, the results of computational docking of the new thiamine co-factor mimics at the active site of six thiamine pyrophosphate-dependent enzymes will be presented and discussed. As O-pyrophosphorylation of thiamine must occur to give an active cofactor, the o-pyrophosphate of the mimic was assessed.

5.1 Introduction

Docking software is useful to explore how well a cofactor or another potential substrate or inhibitor, interacts with residues at an enzyme active site. In principle, this is achieved by first "reading" the ligand structure and creating several possible conformations, based on σ-bonds present in the molecule. This gives insights into the energy dynamics and the attraction and repulsion principles can be tested to give the most stable conformation. Secondly, all the rotamers generated in the first step, are then assessed to see how well each bind at the active site of the protein.

There are quite a few algorithms in use to determine if a ligand would give strong interactions with the target protein, but in general, most do not quantify binding affinities. Instead, results are sums displayed as a scoring function to be graded by comparison with the natural cofactor. This method is important because docking programs are calibrated by extracting a native ligand from the active site of protein X-ray crystal structure, and the software attempts to reposition it at the same cavity. The result is juxtaposed with experimental values to score the program. A root mean square distance (R.M.S.D.) difference of 2.0 Å or less is considered a good fit[1] in comparison to the native ligand. This is useful for defining structure-activity relationships and ab-initio screening to determine whether a proposed structure is likely to be biologically active.

5.1.1 Test algorithm

Various binding modes may exist between a ligand and protein molecules, and although modern-day computers have become a lot faster and affordable, having to generate all hypothetical pose would be tedious and excessively time-consuming. It is therefore imperative to design a filter (algorithm) to comb through conformers which show good promise out of the exhaustive array of poses.

A good number of algorithms exist with this aim in mind and are grouped based on the order of degrees of freedom permitted for ligand. In the most basic model, both ligand and protein are considered inflexible which results in six degrees of freedom in total – three translational and three rotational. One common example of a software that employs this approach is DOCK. Herein the filter is fashioned to identify ligands which rigidly fit in the hollow pockets at the business end of the protein. Analysis is accomplished using continuous spheres, similar to an electron density map, with each one generated using the atomic radii of the ligand atoms. If the internal length is a match for a ligand – protein pair, the result is said to be positive. PhDOCK, Ph4DOCK and SANDDOCK are also based on this matching algorithm.

Another widely used method is incremental construction, where the ligand is parsed into sections which allow for flexible docking through rotatable bonds. One of the sections is used as a pivot point attached to the protein molecule and is usually a rigid part of the ligand such as a ring system. Each section of the ligand is then progressively added, and the most favourable poses used in the next stepwise addition until all the complete ligand molecule is docked. This method makes the algorithm relatively faster than the matching method previously discussed. Incremental construction (IC) is popular with DOCK 4.0, MacDock, FLOG, SKELGEN and SLIDE. This method is however only suitable for small ligands with only a few segments and may not be practical using more elaborate ligands.

Worthy of note among protein–ligand docking algorithms reported in the literature is the Monte Carlo (MC) simulation. In this the ligand is prepared by incremental bond rotation across several non-rigid bonds. Each generated pose is then appraised at the binding site of the protein using molecular mechanics generated energy calculations and passed on or accepted for the next cycle. Previously discussed algorithms usually favour a lower energy for each pose, however, for the Monte Carlo technique, the base energy level is a function of another parameter T (simulated annealing) and can result in favourable higher energy barriers. This method (Monte Carlo) is used in several programs such as GlamDock, PRODOCK, RiboDock and AutoDock.

Genetic Algorithm (GA) employ the use of a global minima to filter off preferred docking poses. This approach is derived from the Darwinian theory of evolution wherein the fittest are selected for use. A large set of ligands is generated and assigned a ranked fitness using a scoring function. This process is repeated with only the top-scoring ligands reused in the next step over several 'generations' of results. Mutations are introduced using a random change in the fragment of a ligand. GA is employed in popular docking programmes such as AutoDock, Darwin, Divaldi, Gold.

5.1.2 Scoring Function

The algorithms discussed above allow each software to list generated conformers in order of best fit at the binding site of the protein. This is arrived at by gauging the binding energy using several parameters to give a realistic value in the least amount of time. The scoring functions currently employed in the literature can be based on empirical data, force field or knowledge[2]. Force field equations may be refined by including terms accounting for van der Waals interactions, bond lengths, angles and strains [3]. Ab initio mechanical calculations and experimental data are often employed to derive force field functions.

$$E = \sum_i \sum_j \left(\frac{A_{ij}}{r_{ij}^{12}} - \frac{B_{ij}}{r_{ij}^{6}} + \frac{q_i q_j}{\varepsilon(r_{ij}) r_{ij}} \right)$$ **Equation 5.1**

In the equation above, i represents the protein and j represents the ligand, the van der Waals parameter is represented by B, the distance between the protein atom and ligand atom by r_{ij}, and the atomic charges by ε. Solvent effects are implicated by the dielectric constant ε, however desolvation effects are not accounted for especially when treating charged ligands. This could lead to discrepancies in results which may favour highly charged ligands. A more holistic approach would account for solvent interaction with ligands at the binding site.

To solve this problem, Shoichet et al. included parameters to account for solvent effects using an indirect model, which employed the Poisson-Boltzmann derived electrostatic potential map of the protein[4]. Lennard-Jones potentials were used to account for the van der Waals interactions between atoms and the protein-ligand interaction was determined using computer generated electrostatic interactions with DelPhi[5]. Results obtained from this revised function corrected for solvent interaction were found to be in good agreement with experimental binding free energies. DockScore[6] , GoldScore[7] and HADDOCK Score[8] employ this method.

5.2 Enzymatic docking using GOLD Suite

For this study, GOLD software offered as part of the Cambridge crystallographic suite is used for actual docking experiments. In addition to GOLD, Hermes®, which is also bundled as part of the software suite, is applied to prepare both ligand and enzyme pre-docking. This may involve deleting any native ligand already bound at the active site, before testing the target cofactor mimic.

Genetic algorithm or GA is employed in GOLD to run docking experiments. This is a subset of evolutionary formula, closely based on the Darwinian concept of natural selection. The set

of rules defining protein-ligand interactions in GA may be fine-tuned to give rise to several different scoring functions, each more suited to specific binding needs. Four notable scoring functions in GOLD are Goldscore, ChemScore, Astex Statistical Potential, ChemPLP and ChemScore RDS.

ChemPLP (Piecewise Linear Potential) has been placed first out of twenty scoring functions accessed in terms of scoring, ranking and docking power[9]. In line with this, all the docking experiments performed herein were done using ChemPLP. *Scoring power* refers to an algorithm's ability to generate different conformations of the ligand, *ranking* refers to the linear ordering of the generated poses in order of best fit, and *docking* refers to the ability of the program to identity the native pose of the natural ligand from a set of conformers. In order to generate, rank and predict the best pose, ChemPLP closely models the piecewise linear potential function (PLP) with additional hydrogen bonding and cation affinity parameters **Equation 5.2**. In addition to these, all atoms are classed as belonging to a donor, acceptor, or both, nonpolar, metal, H or charged hydrogen, CH-donor or charged acceptor[10].

$$fitness_{PLP} = -(w_{PLP}.f_{PLP} + W_{lig-clash}.f_{lig-clash} + w_{lig-tors}.f_{lig-tors} + f_{chem-cov} + w_{prot}.f_{chem-prot} + w_{cons}.f_{cons} \qquad Equation\ 5.2$$

PLP fitness scores for each pose generated by GOLD are interpreted as "lower is better", hence a negative number is indicative of a better docked pose. Push-pull interactions between enzyme and small molecule atoms are also accounted for by PLP. Default predetermined parameters are assigned to all atoms types based on these attraction and repulsion potential. The ligand clash potential is added to prevent conflict between docked poses and is arrived using **Equations 5.3** and **5.4** below.

$$f_{dist(r,w,rr_{clash})} = \begin{cases} 0 \\ w.\dfrac{(r_{clash}^2 - r^2)}{r^2} \end{cases} \quad if\ r > r_{clash}\ , otherwise \ldots\ldots\ldots Equation\ 5.3$$

$$f_{clash} = w_{clash} \cdot \sum_{c \in C_{clash}} f_{dist}\left(\overrightarrow{\|c_{pa}c_{pa}\|}, c_{w,}\, c_{r_{clash}}\right) \quad \ldots\ldots\ldots Equation\ 5.4$$

An exhaustive description of all the terms in the equation is given in the literature cited[10].

The following sections detail experiments done using X-ray crystal structures of thiamine pyrophosphate-dependent enzymes downloaded from the protein data bank https://www.rcsb.org/ and using GOLD docking suite.

Crystal structures used for all experiments were downloaded in the .pdb format for compatibility with GOLD. The first step was to load the enzyme structure to identify the ligands present and the docking pocket(s). Once the target TPP is identified, it is deleted, and a cavity file is created describing its co-ordinates as the target docking area. Some enzyme structures present with multiple active sites (dimers, tetramers, etc.) and other ligands perched around, but for the purpose of this experiment, only one active site is treated for docking.

For all the enzymes downloaded, the conformation of TPP **63** at the docking pocket was found to be very similar irrespective of substrate specificity or parent organism. GOLD docking software treats the metal magnesium/calcium cation as part of the cofactor structure hence it deletes it, along with the cofactor when creating the cavity file from the active site. Using an alternative crystal structure visualizer, PyMOL®, the metal cation was not treated as part of the cofactor (e.g., **Figure 5.1**), however, we proceeded to use GOLD for screening studies as PyMOL does not have the capability for docking.

Figure 5.1 TPP at the active site of the Inferred ancestral pyruvate decarboxylase 5NPU

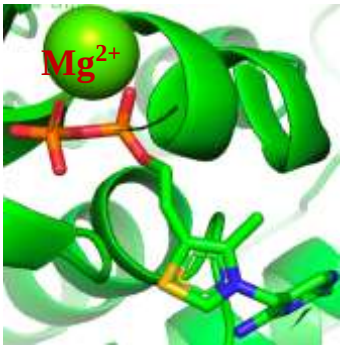

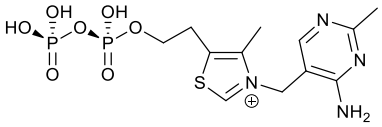

TPP 63

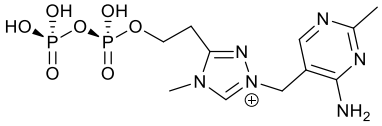

TrPP 133

After preparing the crystal structure for docking, a mimic file triazolyl thiamine pyrophosphate (TrPP.mol) was created using TPP **63** extracted from the active site, by replacing the S1 and C4 of the thiazolium ring with nitrogen. The methyl on the C4 of thiamine was placed on the N4 of the triazolyl ring. The metal cation remained attached to the pyrophosphate chain on TrPP **133** used for this study. Also, the native cofactor TPP **63** extracted was loaded back as a comparison with TrPP for each sample run. The following section describes the six TPP enzyme's family screened for in silico docking with TrPP **133**.

5.2.1 Acetohydroxyacid synthase

Acetohydroxy acid synthase or AHAS (also known as acetolactate synthase) is a thiamine pyrophosphate-dependent enzyme commonly found in plant cells and promotes the initiation sequence for the formation of three amino acids – valine **257**, leucine **258** and isoleucine **259** [11]. Specifically, a glycine residue is responsible for the interaction with thiamine pyrophosphate cofactor essential for catalysis. AHAS fosters the decarboxylation of pyruvate **252** to give the enamine complex (acyl anion equivalent) **253**, upon which further condensation with either 2-ketobutyrate **232** or pyruvate gives aceto hydroxybuyrate **255** or acetolacate **256**, respectively. Action by other enzymes gives the target branched chain amino acids[12].

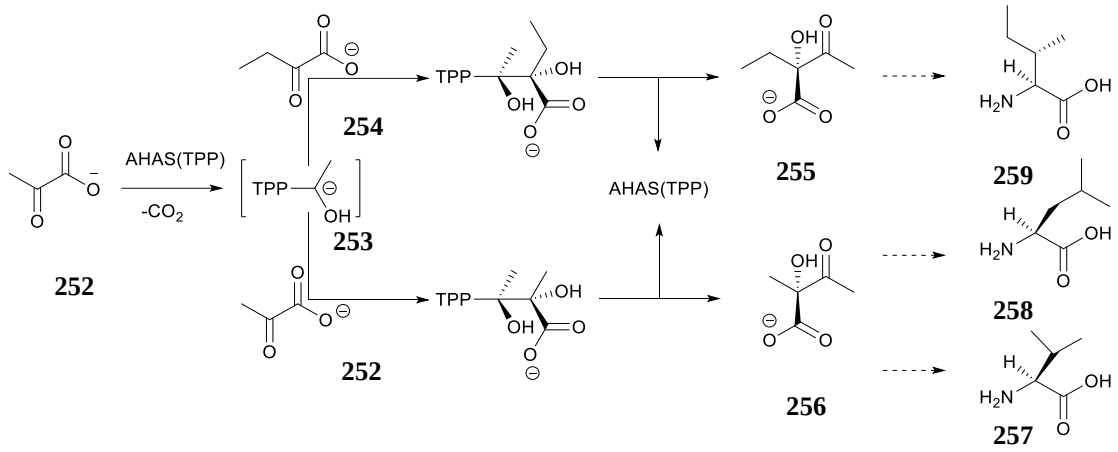

Scheme 5.1 Reaction pathways promoted by TPP bound AHAS

The active site of AHAS with thiamine pyrophosphate TPP is shown in Figure 5.2. Crystallization of the enzyme protein was done with imazaquin **260** complexed within its scaffold. The crystal structure exists as a tetramer of four equivalent subunits, each having a TPP cofactor at its active site. FAD (flavin adenine dinucleotide) is present within each subunit, and may be explained as a vestigial remnant since it is also present in pyruvate oxidase[13] and adopts a similar orientation and position in both enzymes[14]. The imidazolinone-derived herbicide does not binds to the active site neither does it displace the natural cofactor, but works by stalling/barricading substrate progression to the C(2) –H of thiamine pyrophosphate by sitting within 5 Å of the thiazolium ring[14]. Hence, the crystal structure is therefore suitable as a candidate for protein-ligand docking studies because the active site is structurally intact for biocatalysis. TPP at the binding pocket interacts with several protein residues, which locks it in a "V-conformation" using the pyrophosphate side chain bound to the magnesium cation and the aminopyrimidine ring hydrogen bonded to nearby protein residues.

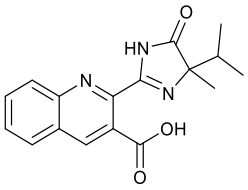

260

Scheme 5.2 Structure of imazaquin inhibitor

(a)

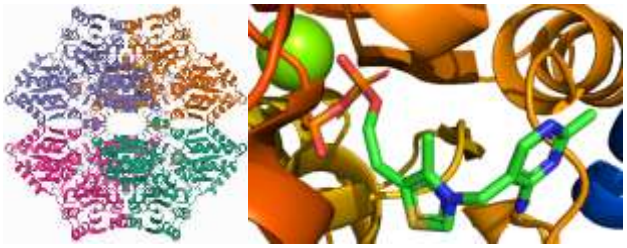

(b)

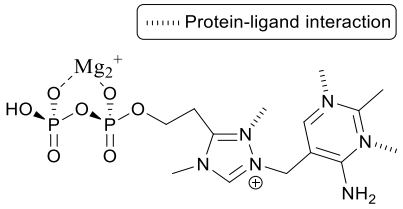

Figure 5.2: (a) Natural cofactor TPP at *arabidopsis thaliana* AHAS 1Z8N active site (b) Structure of Triazolyl Pyrophosphate mimic (TrPP)

Table 5.1 below shows a representative summary of the results from screening mimic TrPP **133**, with crystal structure 1Z8N AHAS sourced from *Arabidopsis thaliana* using the method described in the previous section with GOLD. Results for the remaining five enzymes are included in the Appendix.

Table 5.1: Results of docking TrPP 133 at active site of *Arabidopsis thaliana* AHAS 1Z8N

No:	Docked Pose	RMSD[a]	B[b]	H-B[c]	L-C[d]	L-T[e]	N-P[f]	R[g]	PLP Fitness	Rank
1	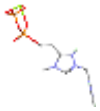	26.6	135.3	-1.5	0.1	1.1	-26.5	24.9	-134.3	2
2	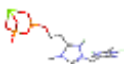	25.8	119.1	-2.4	0.0	1.2	-37.3	40.7	-122.7	6
3	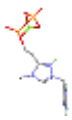	27.2	123.9	-3.1	0.0	0.5	-26.7	37.6	-130.2	4

4	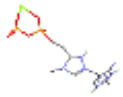	24.9	113.0	-1.0	0.0	0.5	-30.1	49.6	-136.0	**1st**
5	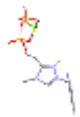	27.3	113.1	3.5	0.0	0.5	-32.6	34.2	-121.5	8
6	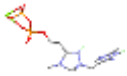	25.2	104.8	-1.8	0.0	0.5	-28.8	44.7	-122.6	7
7	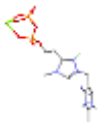	26.7	123.8	0.1	1.3	0.3	-27.9	25.1	-124.5	5
8	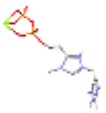	25.8	118.2	-1.4	0.0	1.6	-18.8	28.5	-131.2	3
9		27.1	115.7	0.8	0.0	0.8	-30.5	28.8	-118.2	9
10		27.2	115.8	1.7	1.7	0.6	-34.8	29.2	-115.8	10
Native TPP 63 redocked										
1		8.1	9.0	-1	0	1.4	-9.0	14.8	64.07	1
2	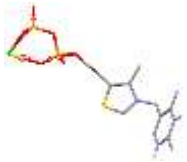	8.1	-0.7	-1	0	1.2	-11.6	8.5	77.95	2

3	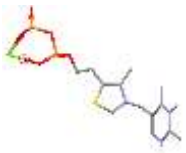	8.1	-3	-1	0	0.8	-9.1	9.0	78.58	3

[a] RMSD: root mean square deviation of mimic ligand atoms pose from the natural cofactor original pose; [b] B: buried term (polar-non polar); [c] H-B; hydrogen bonding term; [d] L-C; ligand clash term; [e] L-T; ligand torsion term; [f] N-P: non polar term; [g] R: ligand repulsion term.

5.2.2 Benzaldehyde lyase (BAL)

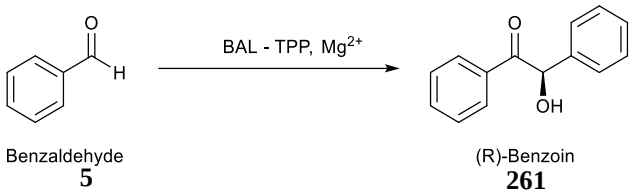

Scheme 5.3 Synthesis of (R)-Benzoin from benzaldehyde catalysed by BAL

Benzaldehyde lyase (BAL) is a TPP-dependent enzyme that catalyses the stereoselective formation of (*R*)-benzoin **261** from two molecules of benzaldehyde **5**. Analysis of its X-ray crystal structure extracted from *pseudomonas fluorescens* at 2.4 Å show that the cofactor (TPP) is anchored at the pyrophosphate and aminopyrimidine ends in two separate subunits of the enzyme resulting in a relatively loose thiazolium ring in the middle[15]. The enzyme also catalyses the reverse cleavage of R-benzoin in *pseudomonas fluorescens* which provides the only source of carbon and energy for the plant using TPP as cofactor. The enzyme is highly substrate stereospecific, only accepts the *R*-enantiomer for benzoin, which makes it a great candidate for use in synthetic carboligations.

Figure 5.3 X-ray crystal structure of Benzaldehyde lyase BAL tetramer 2AG0 with inset showing TPP between two subunits red and green.

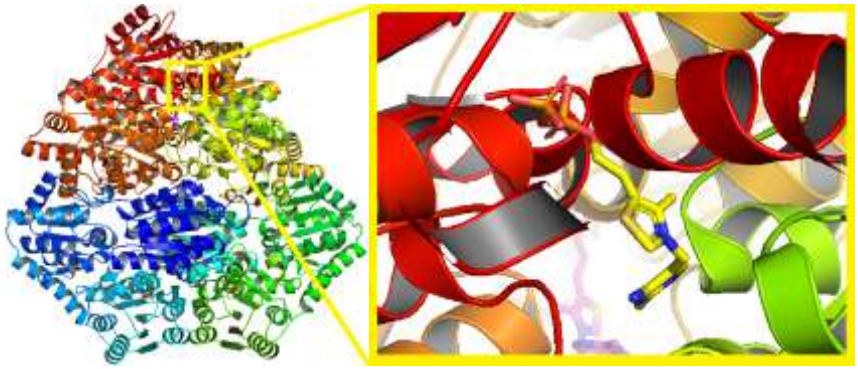

Using the procedure described in the previous section, six crystal structures of BAL were screened with TrPP and the results for 2AG0 are shown in Table 5.2. Results for the remaining five enzymes are included in the appendix.

Table 5.2 Results of docking TrPP at active site of 2AG0 BAL

No:	Docked Pose	RMSD[a]	B[b]	H-B[c]	L-C[d]	L-T[e]	N-P[f]	R[g]	PLP Fitness	Rank
1	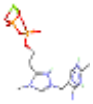	7.6	-6.7	-0.8	0.0	0.6	-47.1	1.0	51.4	1st
2		7.2	-7.7	-1.0	0.0	1.0	-51.0	4.2	52.5	3
3		7.3	-7.9	-1.0	0.0	0.7	-49.8	5.0	51.6	2
Native TPP 63 redocked										
1		1.4	-0.9	-1.0	0.0	1.2	-9.3	9.9	83.5	

2	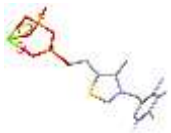	1.4	-4.5	-1.2	0.0	1.2	-9.4	13.6	80.6	
3		1.5	-1.5	-1.0	0.1	1.8	-5.7	10.7	76.7	

[a] RMSD: root mean square deviation of mimic ligand atoms pose from the natural cofactor original pose; [b] B: buried term (polar-non polar); [c] H-B; hydrogen bonding term; [d] L-C; ligand clash term; [e] L-T; ligand torsion term; [f] N-P: non polar term; [g] R: ligand repulsion term.

5.2.3 Benzoylformate decarboxylase

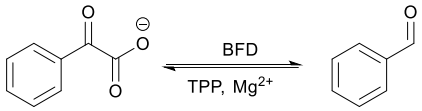

262 **5**

Scheme 5.4 Decarboxylation of benzoylformate by TPP bound BFD

The non-oxidative decarboxylation of benzoylformate to benzaldehyde and carbon dioxide is catalysed by benzoylformate decarboxylase BFD using cofactor TPP[16]. BFD also catalyses the enantioselective carboligation as a side reaction in bacteria which is still currently being investigated by biochemists[17]. BFD found in *Pseudomonas putida* promotes the breakdown of aromatic molecules in the mandelate catabolism[18], an auxiliary metabolic pathway for converting (*R*)-mandelate into a source of carbon and energy for growth. BFD is part of the decarboxylase group of TPP-dependent enzymes, which make up the largest group[19].

The crystal structure of BFD expressed from its cloned gene has been determined by Hasson[20]. Several TPP dependent enzymes show comparable active site structure: one glutamate is almost always present, as well as *one dual* histidine residue[15,16,17]. However, specificity and

substrate selectivity are determined by other residues parked within and around the active site[18,19].

Figure 5.4 X-ray crystal structure of benzoylformate decarboxylase tetramer 1BFD tetramer with inset showing TPP in the active site of the green subunit

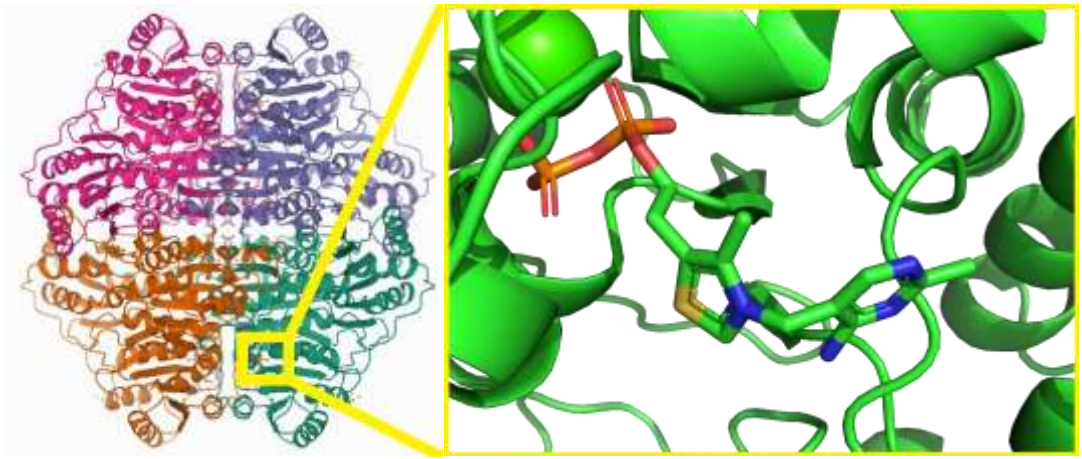

Using the procedure described in the previous section, six crystal structures of BFD were screened with TrPP and the results for 1BFD are shown in Table 5.3. Results for the remaining twelve enzymes are included in the Appendix.

Table 5.3 Results of docking TrPP at active site of 1BFD BFD

No:	Docked Pose	RMSD[a]	B[b]	H-B[c]	L-C[d]	L-T[e]	N-P[f]	R[g]	PLP Fitness	Rank
1	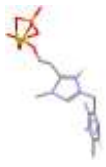	9.5	-4.8	-1.2	0.4	0.4	-23.8	3.1	42.0	1

2	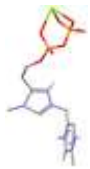	9.0	-6.3	-1.8	0.0	0.9	-40.2	2.8	43.7	5
3	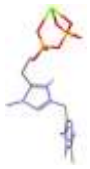	8.9	-9.5	-1.7	0.0	0.8	-39.7	2.5	45.9	8
4	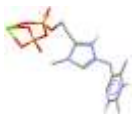	9.4	-2.3	-1.1	0.0	0.8	-43.6	2.9	42.8	3
5	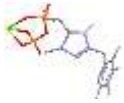	9.3	-2.9	-0.5	0.0	0.4	-42.7	2.7	44.1	6
6	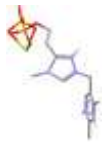	9.1	-3.6	-2.0	1.3	0.6	-9.7	4.0	42.9	4
7	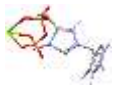	9.1	-6.4	-1.9	0.0	0.8	-41.1	2.0	47.2	10
8	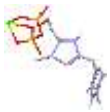	9.4	-7.4	-2.2	0.0	0.7	-40.1	2.6	45.8	7
9	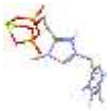	9.2	-8.0	-1.9	0.0	0.7	-40.3	2.1	46.5	9
10	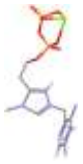	9.0	-3.2	-0.5	0.0	0.7	-47.3	4.3	42.4	2
Native TPP 63 redocked										

1		1.1	-2.1	-1.0	0.0	1.2	-9.6	16.8	64.3	
2	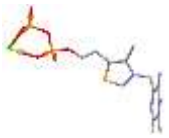	1.7	-2.8	-0.9	0.0	0.5	-6.1	20.5	64.3	
3	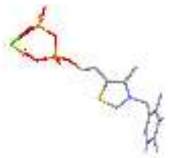	1.7	-2.1	-1.0	0.0	0.6	-9.0	18.7	64.2	

[a] RMSD: root mean square deviation of mimic ligand atoms pose from the natural cofactor original pose; [b] B: buried term (polar-non polar); [c] H-B; hydrogen bonding term; [d] L-C; ligand clash term; [e] L-T; ligand torsion term; [f] N-P: non polar term; [g] R: ligand repulsion term.

5.2.4 Cyclohexane-1,2-dione hydrolase and Pyruvate dehydrogenase

Cyclohexane-1,2-dione hydrolase CDH is a TPP-dependent enzyme that promotes the conversion of cyclohexane-1,2-dione **263** to give 6-oxohexanoic acid **264** via a ring opening reaction (Scheme 5.5 (a)).

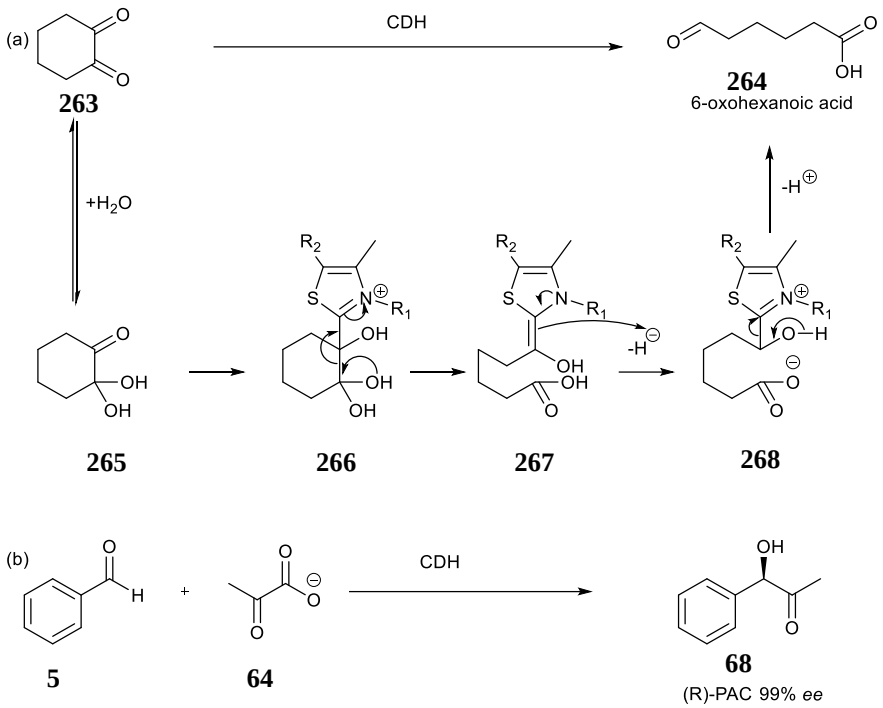

Scheme 5.5 Reactions natively catalysed by CDH

The carbon to carbon bond cleavage of dione **263** is proposed to be triggered by attack of TPP ylide on one of the carbonyl carbon of its monohydrate **265** [21]. The tetrahedral intermediate formed **266** in turn decomposes to give the carboxylic acid **267.** Addition of a proton to the enamine of **267** gives **268** and successive elimination of TPP furnishes the final product **264**. In addition, CDH also catalyses the asymmetric condensation between pyruvate **64** and benzaldehyde **5** to give (R)-PAC (phenyl acetyl carbinol) [22]. Several benzaldehydes are also converted into their analogous PAC derivatives[23]. A crystal structure of natal CDH has been reported in the literature by Steinbach depicting a tetramer with each identical sub-unit housing a FAD and one TPP cofactor molecule [24].

Using the procedure described in the previous section, two crystal structures of CHD were screened with TrPP and the results for 4D5E are shown in Table 5.7. Results for the second enzyme are included in the appendix along with results from twelve TPP-dependent pyruvate dehydrogenase enzymes.

Figure 5.5 **X-ray crystal structure of Cyclohexane-1,2-dione hydrolase tetramer 4D5E tetramer with inset showing TPP in the active site of one subunit**

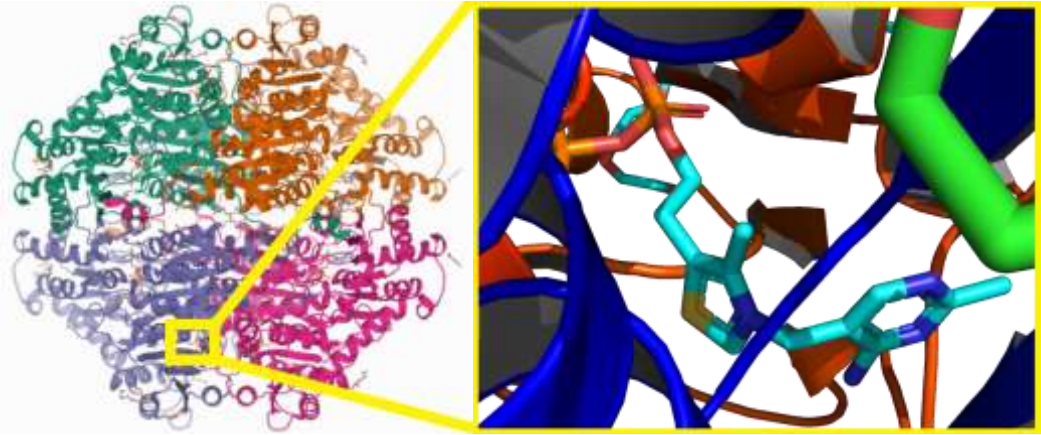

Table 5.4: Results of docking TrPP at active site of 4D5E CDH

No:	Docked Pose	RMSD[a]	B[b]	H-B[c]	L-C[d]	L-T[e]	N-P[f]	R[g]	PLP Fitness	Rank
1		3.9	-6.8	-0.8	0.0	1.1	-29.9	28.6	25.1	3
2	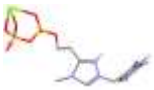	4.1	-4.9	-3.0	0.0	1.1	-28.9	31.9	22.5	2
3		3.9	-6.7	-1.0	0.0	1.4	-27.7	27.8	21.6	1
Native TPP 63 redocked										
1	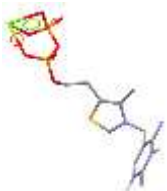	1.4	-4.6	-1.0	0.0	1.0	-32.5	20.9	81.3	

2	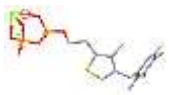	0.7	-0.8	-1.0	0.0	1.1	-26.7	20.2	71.8	
3		1.5	2.1	-1.5	2.6	1.3	-19.7	18.4	75.7	
4	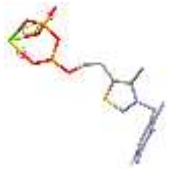	1.5	-3.4	-1.0	0.0	0.9	-16.1	18.6	87.8	
5		1.5	-2.6	-1.0	0.0	1.4	-17.8	21.5	85.7	

[a] RMSD: root mean square deviation of mimic ligand atoms pose from the natural cofactor original pose; [b] B: buried term (polar-non polar); [c] H-B; hydrogen bonding term; [d] L-C; ligand clash term; [e] L-T; ligand torsion term; [f] N-P: non polar term; [g] R: ligand repulsion term.

5.2.5 Pyruvate Decarboxylase

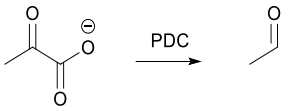

252 **269**

Scheme 5.6 Decarboxylation of pyruvate by PDC

Pyruvate decarboxylase PDC is a very well-researched TPP-dependent enzyme which has been used for centuries in the fermentation of carbohydrate to give alcohol. It also catalyses the conversion of pyruvate **252** into acetaldehyde **269 (**Scheme 5.6**)** which is typical of its presence in yeast and many bacteria. The acetaldehyde is then usually reduced to alcohol by an alcohol dehydrogenase (ADH). Engineered strains of both enzymes sourced from *Z. mobilis* have been used to increase ethanol production from glycerol yield by more than 300 percent[25].

Figure 5.6 X-ray crystal structure of PDC tetramer 1OVM tetramer with inset showing TPP in the active site of one subunit

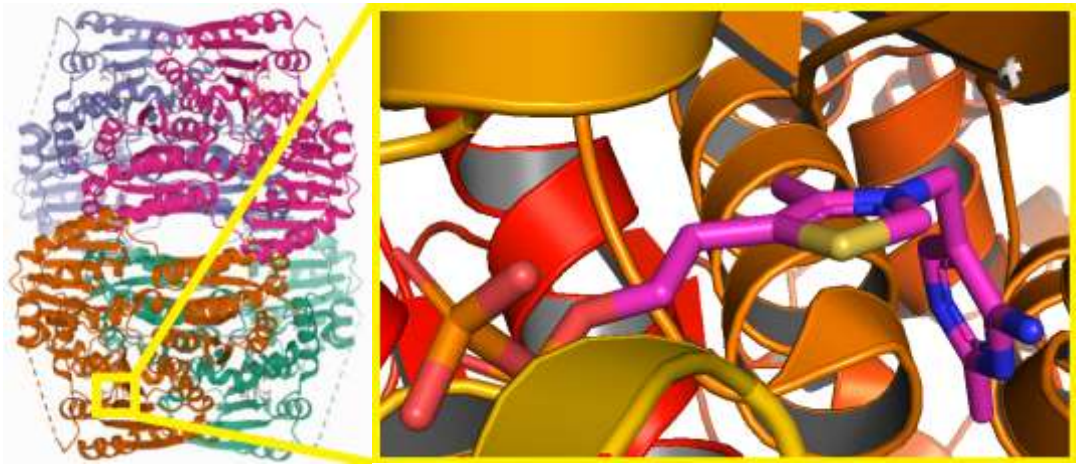

Crystal structures of PDC (Figure 5.6) shows it normally exists as a dimer of dimers, with four identical subunits, each with one active site. For every active site in the PDC tetramer, two glutamates Glu-477 and -51 are invariably present, and contribute to keeping the TPP bound in a rigid V-conformation[28]. PDC enzymes sourced from a range of living organisms show closely similar structures, with molecular weights between 240 and 260 kDa[26].

Figure 5.7 Cofactor-binding site of 1OVM PDC showing residues interaction with TPP within 3.2 Angstroms

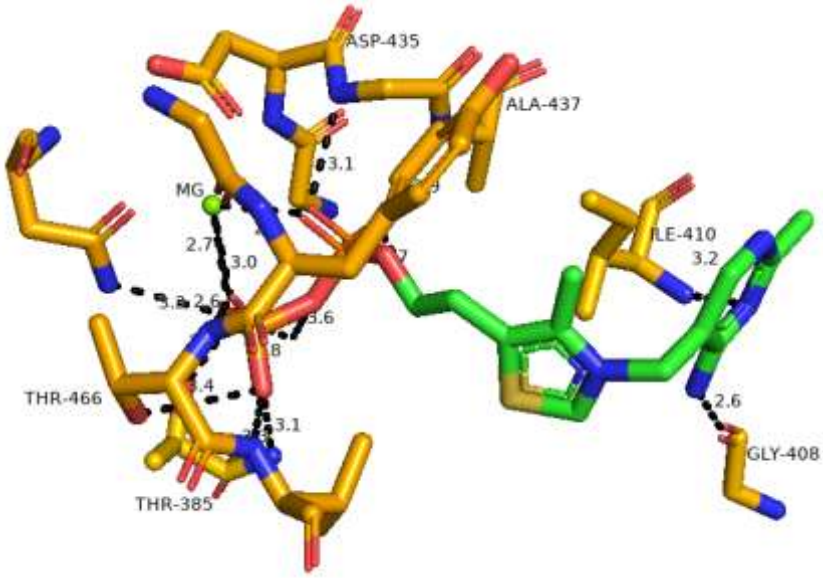

At the active site of 10VM PDC, the TPP cofactor (shown in red and green) is bound by at least six protein residues (shown in marigold) within 3.2 Angstroms (Figure 5.7). Four of these residues' ASP-435, ALA-437, THR-466 and THR-385 surround the pyrophosphate side chain which coordinates with the magnesium cation. The two other protein residues GLY-408 and ILE-410 are within 2.6 and 3.2 angstroms respectively of the aminopyrimidine side chain of TPP. The thiazolium ring is in the centre and free to bind to substrate for catalytic action.

Using the procedure described in the previous section, thirteen crystal structures of PDC were screened with TrPP **133** and the results for 1OVM are shown in Table 5.5. Results for the remaining twelve crystal structure are included in the appendix.

Table 5.5: Results of docking TrPP at active site of 1OVM PDC

No:	Docked Pose	RMSD[a]	B[b]	H-B[c]	L-C[d]	L-T[e]	N-P[f]	R[g]	PLP Fitness	Rank
1		4.0	-5.6	-1.0	0.0	0.5	-41.8	18.2	37.0	4
2	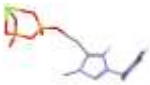	4.3	-9.4	-2.2	0.0	1.2	-41.8	25.6	38.7	5
3	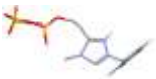	4.0	-5.0	-1.4	0.0	1.4	-30.1	16.0	36.3	3
4		4.2	-1.5	-2.0	0.0	0.6	-17.1	13.9	36.1	2
5	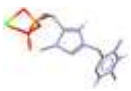	8.7	13.8	-3.0	0.0	0.6	-43.6	6.4	39.2	7
6		8.8	4.5	-3.0	0.0	0.9	-36.5	9.2	41.8	9
7		4.0	-5.3	-1.0	0.0	1.0	-43.2	17.2	41.8	8
8	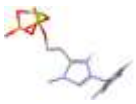	3.9	3.0	-1.0	0.0	0.6	-4.8	19.3	32.3	1st
9	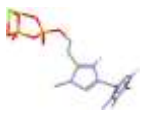	4.0	-9.3	-1.0	0.0	1.2	-45.9	19.1	42.4	10
10	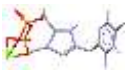	8.7	4.3	-3.0	0.0	1.1	-35.7	9.1	39.0	6
Native TPP 63 redocked										

1	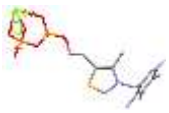	0.4	-6.5	-1.0	0.0	1.4	-24.2	16.2	98.1	
2	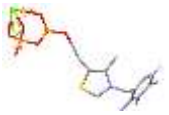	0.5	-5.2	-1.3	0.0	1.3	-25.3	14.0	99.6	
3	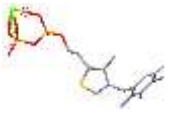	0.4	-5.4	-1.0	0.0	0.7	-24.8	15.3	99.5	

[a] RMSD: root mean square deviation of mimic ligand atoms pose from the natural cofactor original pose; [b] B: buried term (polar-non polar); [c] H-B; hydrogen bonding term; [d] L-C; ligand clash term; [e] L-T; ligand torsion term; [f] N-P: non polar term; [g] R: ligand repulsion term.

5.2.6 Transketolase

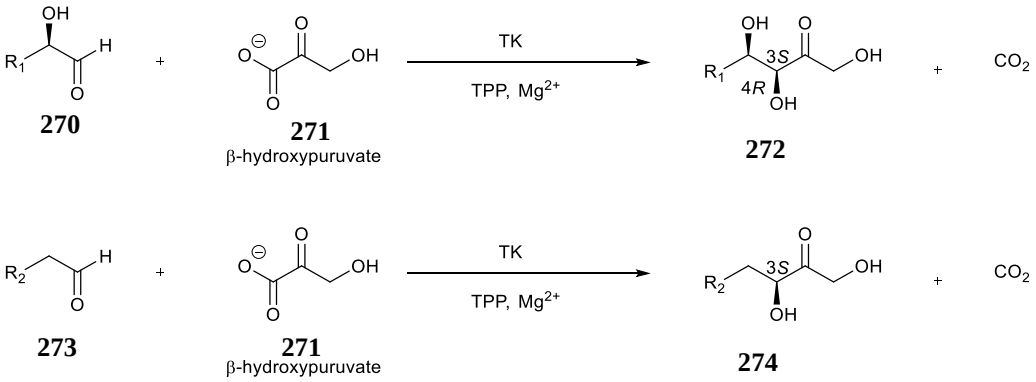

Scheme 5.7 Stereoselective synthesis of α-hydroxyketones using TK

Transketolase (TK) is a TPP dependent enzyme present in all living organisms. It catalyses two reactions in the pentose phosphate pathway and one in the Calvin cycle of photosynthesis. The substrates must be in the right stereo configuration in order to enter the rather striated channel leading into the active site, this in turn controls the specificity of the enzyme[38]. TK shows great promise in organocatalysis for making a spectrum of α,α'-dihydroxy ketones, which are building blocks for ketosugars and 2-amino-1,3-diols. Classic organic synthesis of these

compounds require multiple steps leading to less than optimal yields, for example synthesis of aromatic 1,3-dihydroxyketones using a five-step scheme[27].

Also reported in the literature is a single step enzyme catalysed synthesis of racemic 1,3-dihydroxyketones. TK provides a stereoselective single step reaction to access useful 1,3-dihydroxyketones using a wide range of aldehyde acceptors as substrate. Remarkably, using a broad scope of aliphatic aldehyde acceptors, and beta hydroxypyruvate (β-HPA) **271** as a ketol donor, stereoselective coupling have been successful with TK sourced from spinach, yeast, and *E. coli* (Scheme 5.7), generation of carbon dioxide as a by-product makes the reaction practically irreversible[28]. Wild type TK enzymes accept (2*R*-) α-hydroxylated aldehydes **270** to give (3S, 4R) products **272**. Use of non-α-hydroxylated aldehydes **273** results in the (3S) stereochemistry **274**.

Figure 5.8 X-ray crystal structure of 1ITZ TK tetramer with inset showing TPP in the active site of one subunit

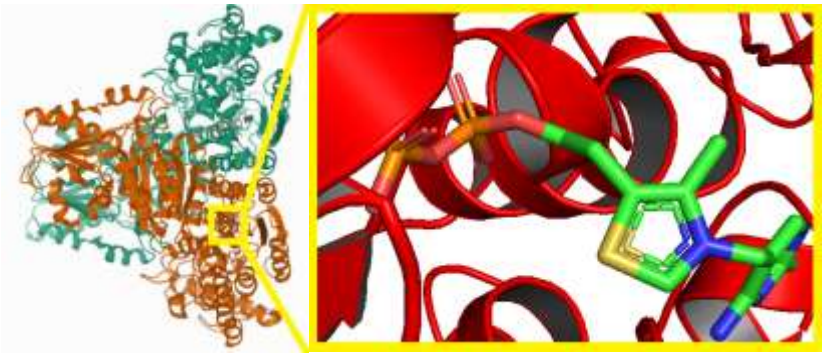

A crystal structure of TK in complex with TPP (Figure 5.8) sourced from maize (*zea mays)* gene plastid has been obtained and solved using molecular replacement [29]. Expression of the gene was done using recombinant fusion proteins thioredoxin of E. coli and cleaved with thrombin, to give plastid TK. The enzyme exists as a homodimer with C2 symmetry and each

subunit parsed into three domains. The active sites are sandwiched between the subunits in the interface region.

Figure 5.9 Cofactor-binding site of 1ITZ TK showing residues interaction with TPP within 3.5 Angstroms

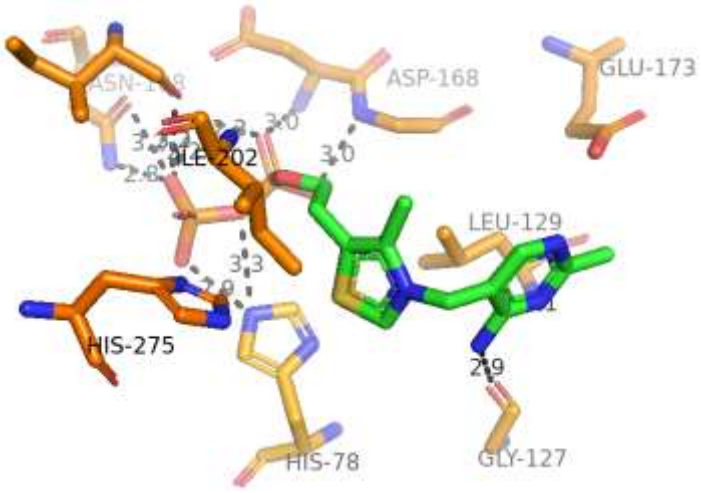

At the active site of 1ITZ TK, the TPP cofactor (shown in red and green) is bound by at least six protein residues (shown in marigold) within 3.5 Å (Figure 5.9). Four of these residues' ASN-118, ASP-168, ILE-202 and HIS-275 surround the pyrophosphate side chain which coordinates with the magnesium cation. The two other protein residues GLY-127 and LEU-129 are within 2.9 and 3.1 Å respectively of the aminopyrimidine side chain of TPP. The thiazolium ring is in the centre and free to bind to substrate for catalytic action.

Using the procedure described in the previous section, thirteen crystal structures of PDC were screened with TrPP **133** and the results for 1ITZ are shown in Table 5.6. Results for the remaining enzymes are included in the Appendix.

Table 5.6: Results of docking TrPP at active site of 1ITZ TK

No:	Docked Pose	RMSD[a]	B[b]	H-B[c]	L-C[d]	L-T[e]	N-P[f]	R[g]	PLP Fitness	Rank
1	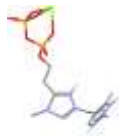	13.3	-4.1	0.0	0.0	0.9	-26.8	1.0	27.5	4
2		13.4	-6.0	-0.7	0.0	0.7	-22.1	3.8	23.9	2
3	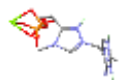	12.6	-2.9	-1.3	0.0	0.8	-26.2	0.9	26.9	3
4		15.4	-5.5	0.0	0.0	1.2	-17.5	0.4	20.2	1
5		13.4	-2.2	-1.0	0.0	0.9	-29.6	0.7	30.0	7
6		13.3	-5.0	0.0	0.0	0.7	-29.2	1.1	31.8	10
7		13.1	-2.8	0.0	0.0	0.1	-28.9	0.9	31.6	9
8		12.7	-4.1	0.0	0.0	0.7	-26.8	1.6	27.8	5
9		14.7	-6.3	-1.1	0.0	0.8	-24.9	1.6	29.0	6

10	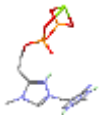	15.0	-8.1	-1.9	0.0	1.1	-25.3	1.1	31.4	8
Native TPP 63 redocked										
1	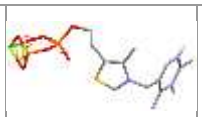	1.0	-3.9	-3.1	0.0	1.9	-38.6	5.4	89.2	
2	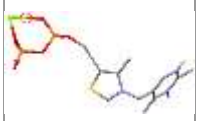	0.7	-3.8	-2.2	0.0	1.3	-21.4	17.5	87.7	
3	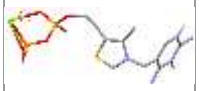	0.8	-8.6	-2.7	0.0	1.3	-34.6	18.4	87.7	

[a] RMSD: root mean square deviation of mimic ligand atoms pose from the natural cofactor original pose; [b] B: buried term (polar-non polar); [c] H-B; hydrogen bonding term; [d] L-C; ligand clash term; [e] L-T; ligand torsion term; [f] N-P: non polar term; [g] R: ligand repulsion term.

5.3 Discussion

For this work, six families of TPP-dependent enzymes were screened in silico with TrPP **133** and each class will be discussed separately below. The overall aim is to select four protein strains for expression and testing with the new mimic TrPP.

Table 5.7 shows the summary of results from docking structure of TrPP **133** with six crystal structures of AHAS (acetohydroxyacid synthase) sourced from *Arabidosis thaliana*, *Saccharomyces cerevisiae* and *Candida albicans.* For each of the crystal structure studies, ten best docking poses were selected from several hundreds of poses generated using GA (genetic algorithm). Only the best ranked ligand pose for each crystal structure is shown in the table, i.e. the pose with the most negative PLP fitness score.

Table 5.7 Summary of results from screening AHAS TPP dependent enzymes with TrPP

Enzyme	Source	RMSD	PLP Score	Rank
	***TPP* 63**	**8.1**	**64.1**	
3E9Y	‘’	**9.1**	**-367.8**	**1st**
5IMS	*Saccharomyces cerevisiae*	2.9	3.8	3rd
6BD3	‘’	11.8	34.2	5th
6BD9	‘’	13.1	26.7	4th
6DEK	*Candida albicans*	9.3	48.9	6th

Results from the Table 5.7 above show that docking with structure 1Z8N from *Arabidopsis thaliana* gave the second-best fitness score of −136 and crystals from 3E9Y from the same plant gave the best fitness of −367.8. The least fit ligand pose of the series was from docking using yeast (*Candida albicans*) sourced 6DEK crystal structure with a scoring fitness of 48.9.

RMSD values obtained are interpreted the same as the PLP fitness scores with low numbers representing a better fit. The results show a different trend from the PLP scores as the best RSMD value was given by yeast sourced (*Saccharomyces cerevisiae*) 5IMS at RMSD=2.9. This value is only about twice the value obtained by redocking TPP back into the active site RMSD=1.4. Results for the two best PLP candidates 3E9Y and 1Z8N are RMSD=9.1 and RMSD=22.4 respectively. Given that the RMSD values empirically calculates the average distance between the docked ligand TrPP **133** pose at the protein active site superimposed with the native cofactor TPP pose, it is therefore a better estimate or guide for fitness than the overall PLP fitness score. Results from crystal structures 6BD3 and 6BD9 gave RMSD values midway within the series of RMSD = 11.8 and RMSD = 13.9.

Figure 5.10 Best docking pose generated for TrPP 133 at 3E9Y active site by GOLD PLP score = −367.8 RMSD=9.1

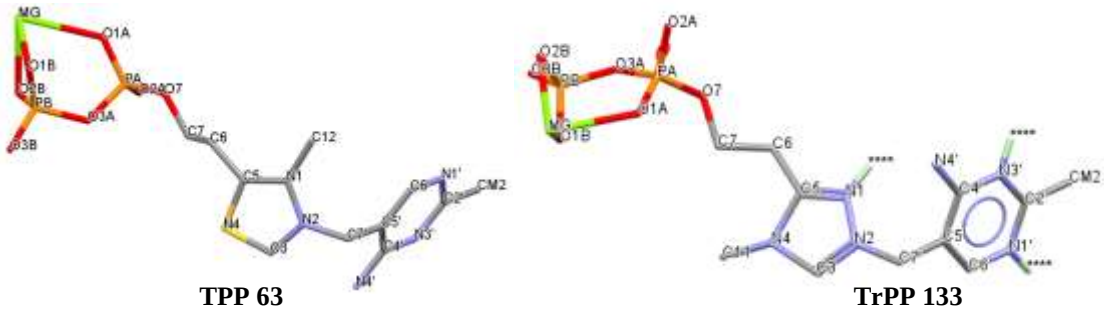

TPP 63 **TrPP 133**

The stick structure above (Figure 5.10) show the conformation of TrPP **133** at the active site of 3E9Y. The bond angle at the bridging methylene (N2−C7'−C5' 108.67 °) is a mere 0.57 ° bigger compared to native cofactor TPP (108.10 °). This represents a close similarity to the conformation of TPP at the active site of 3E9Y. However, the exocyclic 4-amino substituent on the pyrimidinyl ring is pointing 'upwards and away from the carbenic C3 of the triazole ring in the generated pose. By contrast, in the native factor at the active site of 3E9Y, the 4-amino substituent points downwards and towards the carbenic C2 of the thiazolium ring. Several papers have implicated this conformation as preferred for an intramolecular deprotonation step preceding attack of substrate at the active site[30]. In addition, there exists the potential for

hydrogen bonding at the N1 atom of the triazolium ring of TrPP **133** at the active site which is absent in the native cofactor TPP.

Table 5.8 shows the summary of results from docking structure of TrPP 133 with six crystal structures of Benzaldeyde lyase BAL sourced from *Pseudomonas fluorescens* and *putida*. For each of the crystal structures studies, ten best docking poses were selected from several hundreds of poses generated using GA (genetic algorithm). Only the best-ranked ligand pose for each crystal structure is shown in the Table 5.8 below, i.e. the pose with the least PLP fitness score.

Table 5.8 Summary of results from screening Benzaldeyde lyase BAL TPP dependent enzymes with TrPP 133

Enzyme	Source	RMSD	PLP Score	Rank
	***TPP* 63**	**1.4**	**83.5**	
2AG1	‘’	8.7	49.1	4th
2UZ1	‘’	8.8	41.9	3rd
3D7K	*unspecified*	8.2	38.1	2nd
3IAE	***Pseudomonas putida***	**13.1**	**36.4**	**1st**
3IAF	‘’	8.6	53.9	6th

From Table 5.8 above, docking **133** TrPP with structure 3IAE gave the best fitting result of 36.4 and structure 3IAF gave the least fitting result of 53.9. This represents a difference of 15 PLP score units showing a narrower variation within the series of protein strains. The least fit ligand pose of the series was from docking using gram-negative bacterium (*Pseudomonas putida*) sourced 3IAF crystal structure with a scoring fitness of 53.9.

RMSD values show a contrasting progression from the PLP scores - the best RSMD value was given by enzyme 3D7K at RMSD = 8.2. This value is about five units smaller than for the best PLP score enzyme 3IAE RMSD = 13.1. The rest of the series have RMSD values hovering around 8 units. This shows that the poses are quite similar in terms of mean distances compared to the native cofactor TPP.

Figure 5.11 Best docking pose generated for TrPP 133 at 3IAF active site by GOLD PLP score = 36.4 RMSD=13.1

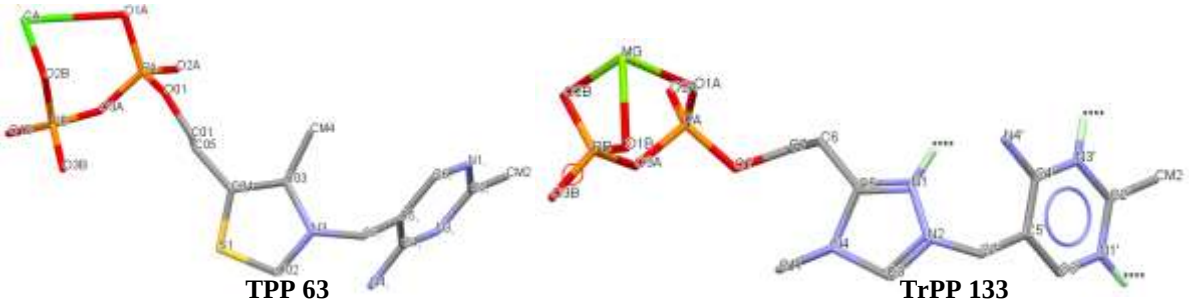

TPP 63 **TrPP 133**

The stick structure above (Figure 5.11) show the conformation of TrPP **133** at the active site of 3IAF. The bond angle at the bridging methylene (N2−C7'−C5' 108.67 °) is 3.16 ° lower compared to native cofactor TPP (111.83 °) (Table 5.9 below). This represents a close similarity to the conformation of TPP at the active site of 3IAF. In addition, the exocyclic 4-amino substituent on the pyrimidinyl ring is pointing 'upwards and away from the carbenic C3 of the triazole ring in the generated pose. Again, in the native factor at the active site of 3IAF, the 4-amino substituent points downwards and towards the carbenic C2 of the thiazolium ring. This may be due to the potential for hydrogen bonding at the N1 position of the triazolium ring of **133**, which is not present in the thiazolium of native TPP **63**.

Table 5.9 Bond angles at the bridging methylene of TrPP best docking pose at 3IAF

TPP 63				TrPP 133			
Atom1	**Atom2**	**Atom3**	**Angle**	**Atom1**	**Atom2**	**Atom3**	**Angle**
C03	N3	C02	108.2	**C5'**	**C7'**	**N2**	**108.67**
C03	N3	C7,	123.73	C5'	C7'	H7'1	109.92
C02	N3	C7,	128.06	C5'	C7'	H7'2	109.96
N3	**C7,**	**C5,**	**111.83**	N2	C7'	H7'1	109.98
C7,	C5,	C6,	120.16	N2	C7'	H7'2	109.94
C7,	C5,	C4,	119.95	H7'1	C7'	H7'2	108.38

Table 5.10 below shows the summary of results from docking structure of TrPP 133 with twelve crystal structures of BFD (benzoylformate decarboxylase) sourced from *Pseudomonas putida*, *Saccharomyces pastorianus* and *Polynucleobacter necessarius.* For each of the crystal structures studies, ten best docking poses were selected from several hundreds of poses generated using GA (genetic algorithm). Only the best ranked ligand pose for each crystal structure is shown in the table, i.e. the pose with the most negative PLP fitness score.

Table 5.10 Summary of results from screening Benzoylformate decarboxylase BFD TPP dependent enzymes with TrPP 133

Enzyme	Source	RMSD	PLP Score	Rank
	***TPP* 63**	1.1	64.3	
1PI3	‘’	8.9	36.4	5th
1QPB	*Saccharomyces pastorianus*	8.4	33.5	4th
2V3W	*Pseudomonas putida*	**8.4**	**2.1**	**1st**
3FSJ	‘’	5.6	38.4	6th

4GG1	‘’	11.7	40.6	9th
4GM0	‘’	9.7	31.5	3rd
4GM1	‘’	8.9	39.9	8th
4K9Q	*Polynucleobacter necessarius*	11.7	38.9	7th
4MPR	*Pseudomonas putida*	9.0	41.1	10th
5DEI	‘’	3.9	78.9	12th
6A50	‘’	6.8	13.6	2nd

From Table 5.10 above, docking **133** TrPP with structure 2V3W (*Pseudomonas putida*) gave the best fitting result of 2.1 and structure 5DEI from *Pseudomonas putida* gave the least fitting result of 78.9. This represents a difference of ~77 PLP score units showing a wide variation within the series of protein strains screened. Enzyme 1QPB sourced from *Saccharomyces pastorianus* gave a PLP score of 33.5 ranking fifth among the series while 4K9Q *Polynucleobacter necessaries* ranked seventh with a PLP score of 38.9.

Results from the RMSD column (Table 5.10 above) show that the best score 5DEI RMSD = 3.9, is in stark contrast to its PLP score ranking (12th). This demonstrates the variance between the RMSD parameter and the overall ranking by PLP score. Both 4GG1(*Pseudomonas putida*) and 4K9Q (*Polynucleobacter necessarius*) gave the least favourable RMSD of 11.7.

Figure 5.12 Best docking pose generated for TrPP 133 at 2V3W active site by GOLD PLP score = 2.1 RMSD = 8.4

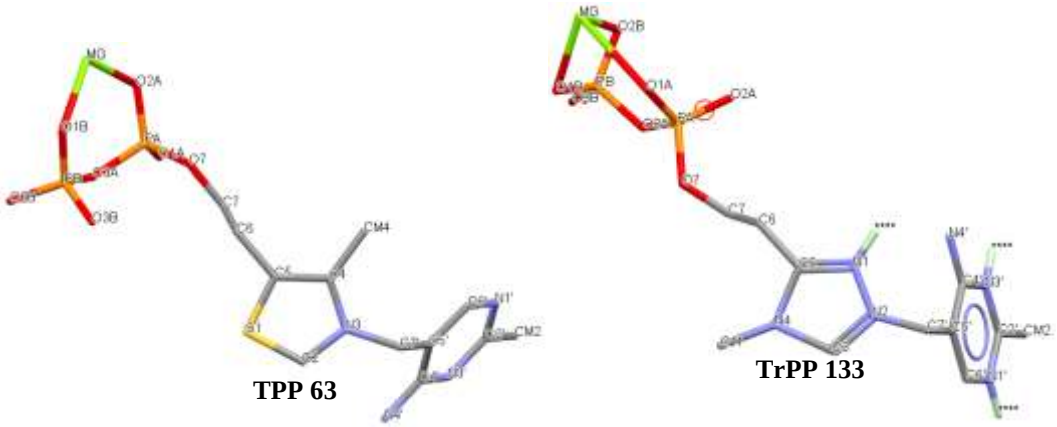

Table 5.11 Bond angles at the bridging methylene of TrPP best docking pose at 2V3W

TPP 63				TrPP 133			
Atom1	**Atom2**	**Atom3**	**Angle**	**Atom1**	**Atom2**	**Atom3**	**Angle**
C4'	C5'	C7'	121.35	**C5'**	**C7'**	**N2**	**108.67**
C6'	C5'	C7'	118.74	C5'	C7'	H7'1	109.93
N1'	C6'	C5'	119.82	C5'	C7'	H7'2	109.96
C5'	**C7'**	**N3**	**117.64**	N2	C7'	H7'1	109.97
C7'	N3	C2	124.05	N2	C7'	H7'2	109.93
C7'	N3	C4	125.97	H7'1	C7'	H7'2	108.37

The stick structure above (Figure 5.12) show the conformation of TrPP **133** at the active site of 2V3W. The bond angle at the bridging methylene (C5'–C7'– N2 108.67 °) is ~ 9 ° lower compared to native cofactor TPP (117.64 °) (Table 5.11). The pyrophosphate side chain in both mimic and cofactor adopt closely similar conformations, as the magnesium cation sits atop. The exocyclic 4-amino substituent on the pyrimidinyl ring is pointing 'upwards and away from the carbenic C3 of the triazole ring in the generated pose. However, in the native factor at the active site of 2V3W, the 4-amino substituent points downwards and towards the carbenic C2 of the thiazolium ring. For this enzyme structure 2V3W, three other poses generated all have

their exocyclic amino group pointing downwards towards the C3 of the triazolium ring (Figure 5.13).

Figure 5.13 Poses generated for 2V3W with the exocyclic NH_2 'pointing downwards' with respect to the triazolium ring

Table 5.12 below shows the summary of results from docking structure of TrPP **133** with thirteen crystal structures of PDC (Pyruvate decarboxylase) sourced from *Enterobacter cloacae, Azospirillum brasilense, Kluyveromyces lactis, Zymomonas mobilis, Gluconacetobacter diazotrophicus and Pseudomonas putida.* For each of the crystal structures studies, ten best docking poses were selected from several hundreds of poses generated using GA (genetic algorithm). Only the best ranked ligand pose for each crystal structure is shown in the table, i.e. the pose with the most negative PLP fitness score.

Table 5.12 Summary of results from screening Pyruvate decarboxylase PDC TPP dependent enzymes with TrPP 133

Enzyme	Source	RMSD	PLP Score	Rank
	***TPP* 63**	**0.4**	**98.1**	
2NXW	*Azospirillum brasilense*	3.9	28.3	5th
2VJY	*Kluyveromyces lactis*	9.0	22.7	3rd
2V4K	unspecified	7.7	29.0	7th
2WVA	*Zymomonas mobilis*	3.8	22.6	2nd
2WVG	''	9.4	30.1	8th
4COK	*Gluconacetobacter diazotrophicus*	8.9	24.4	4th
4MZX	*Pseudomonas putida*	8.7	39.5	12th
4ZP1	***Zymomonas mobilis***	**36.1**	**-293.5**	**1st**

5NPU	Artificial gene sequencing	5.0	71.9	13th
5TMA	*Zymomonas mobilis*	9.1	37.9	11th
6EFG	*Kluyveromyces lactis*	14.6	28.3	5th
6EFH	‘’	8.9	36.0	10th

From Table 5.12 above, docking **133** TrPP with structure 4ZP1 (*Zymomonas mobilis*) gave the best fitting result of -293.5 and structure 5NPU gave the least fitting result of 71.9. This represents a difference of ~365 PLP score units showing a wide variation within this range of PDC enzymes. Enzyme 2VJY sourced from *Kluyveromyces lactis* (yeast) gave a PLP score of 22.7 ranking third among the series while 2NXW *Azospirillum brasilense* (bacteria) ranked fifth with a PLP score of 28.3.

Results from the RMSD column (Table 5.12 above) show that the best score 2WVA RMSD = 3.8, is similar to its PLP score ranking (2nd). This is closely followed by 1OVM (*Enterobacter cloacae*) and 2NXW (*Azospirillum brasilense*) both registering an RMSD value of 3.9. Surprisingly, 4ZP1 (*Zymomonas mobilis*) gave the least favourable RMSD of 36.1 given that it ranked best in terms of overall PLP score.

Figure 5.14 Best docking pose generated for TrPP 133 at 4ZP1 active site GOLD PLP score = -293.1 RMSD = 36.1

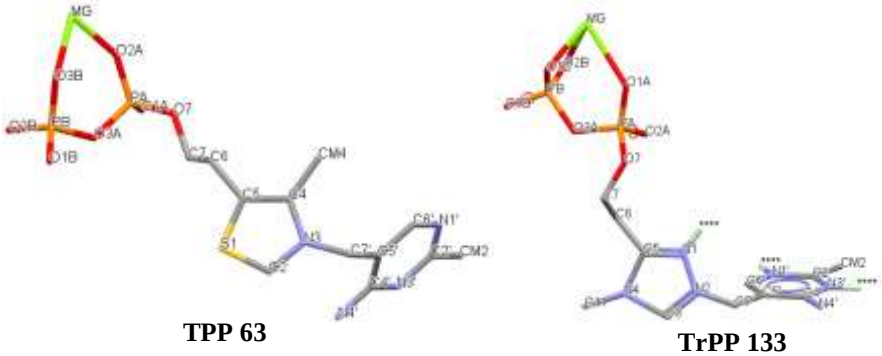

TPP 63 **TrPP 133**

Table 5.13 shows the bond angles at the bridging methylene $C7H_2$ in TPP and TrPP at the active site of 4ZP1.

Table 5.13 Bond angles at the bridging methylene of TrPP best docking pose at 4ZP1

TPP 63				**TrPP 133**			
Atom1	**Atom2**	**Atom3**	**Angle**	**Atom1**	**Atom2**	**Atom3**	**Angle**
C4'	C5'	C7'	121.42	**C5'**	**C7'**	**N2**	**108.67**
C6'	C5'	C7'	119.08	C5'	C7'	H7'1	109.92
N1'	C6'	C5'	120.43	C5'	C7'	H7'2	109.96
C5'	**C7'**	**N3**	**114.82**	N2	C7'	H7'1	109.97
C7'	N3	C2	124.46	N2	C7'	H7'2	109.94
C7'	N3	C4	124.92	H7'1	C7'	H7'2	108.37

The stick structure above (Figure 5.14) show the conformation of TrPP **133** at the active site of 4ZP1. The bond angle at the bridging methylene (C5'−C7'− N2 108.67 °) is ~ 6 ° lower compared to native cofactor TPP (114.82°) (Table 5.13). The pyrophosphate side chain in both mimic and cofactor adopt closely similar conformation, as the magnesium cation sits atop. The aminopyrimidinyl ring lies in a plane perpendicular to the triazolium ring while exocyclic 4-amino substituent on the pyrimidinyl ring is points away from the triazole ring in the generated pose. However, in the native factor at the active site of 4ZP1, the 4-amino substituent points downwards and towards the carbenic C2 of the thiazolium ring suggesting the possibility of intramolecular deprotonation.

A summary of results from TrPP docking five pyruvate dehydrogenase enzymes using GOLD is shown in Table 5.14.

Table 5.14 Summary of results from screening Pyruvate dehydrogenase TPP dependent enzymes with TrPP 133

Enzyme	Source	RMSD	PLP Score	Rank
	***TPP* 63**	1.4	81.3	
1NI4	*Homo sapiens*	3.1	71.3	5th
2OZL	‘’	3.9	19.8	3rd
3EXE	**‘’**	**2.8**	**-4.8**	**1st**
3EXF	‘’	8.8	51.7	4th

From Table 5.14 above, docking **133** TrPP with structure 3EXE (*Homo sapiens*) gave the best fit result of -4.8 and structure 1NI4 gave the least fit result of 71.3. This represents a difference of ~76 PLP score units. Enzyme 1L8A sourced from *Escherichia coli* (bacteria) gave a PLP score of 19.4 ranking second among the series while human 3EXF *(Homo sapiens)* ranked fourth with a PLP score of 51.7.

Results from the RMSD column (Table 5.14 above) show that the best score 3EXE RMSD = 2.8, is matched to its PLP score ranking (1st). This is closely followed by 1NI4 (*Homo sapiens*) registering an RMSD value of 3.1 (2nd) surprisingly ranked fifth by overall PLP score. Remarkably bacteria sourced 1L8A (*Escherichia coli*) gave the least favourable RMSD of 9.2 (5th) given that it ranked second best in terms of overall PLP score.

Figure 5.15 Best docking pose generated for TrPP 133 at 3EXE active site GOLD PLP score = -4.8 RMSD = 2.8

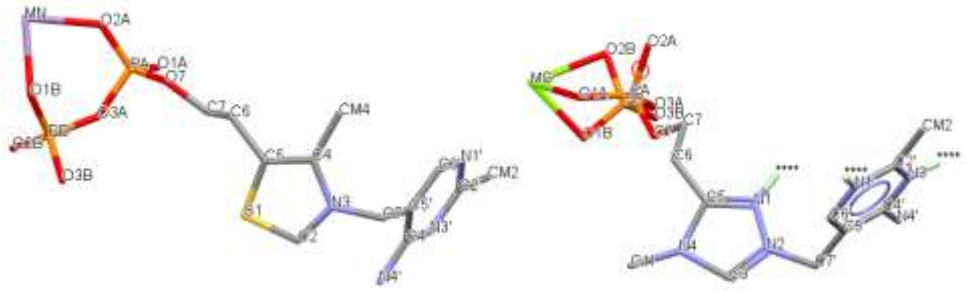

TPP 63 **TrPP 133**

Table 5.15 shows the bond angles at the bridging methylene $C7H_2$ in TPP and TrPP at the active site of 3EXE.

Table 5.15 Bond angles at the bridging methylene of TrPP best docking pose at 3EXE

TPP 63				**TrPP 133**			
Atom1	**Atom2**	**Atom3**	**Angle**	**Atom1**	**Atom2**	**Atom3**	**Angle**
C4'	C5'	C7'	124.06	**C5'**	**C7'**	**N2**	**108.67**
C6'	C5'	C7'	117.49	C5'	C7'	H7'1	109.93
N1'	C6'	C5'	117.75	C5'	C7'	H7'2	109.96
C5'	**C7'**	**N3**	**104.82**	N2	C7'	H7'1	109.97
C7'	N3	C2	124.57	N2	C7'	H7'2	109.94
C7'	N3	C4	123.3	H7'1	C7'	H7'2	108.38

As shown in Figure 5.15 , the stick structure of cofactor TPP is bound to a magnesium cation (purple) at its pyrophosphate side chain in contrast to the mimic TrPP which has a magnesium cation (green). In the native factor TPP the manganese cation sits above the pyrophosphate side chain while the magnesium cation in the mimic TrPP sits to the left of the pyrophosphate side chain. Bond angle at the bridging methylene (C5'−C7'− N2 108.67 °) is only ~ 2 ° larger compared to native cofactor TPP (104.82°) indicating a closely matched V-conformation

(Table 5.15). The aminopyrimidinyl ring lies above the triazolium ring in the generated pose and does not come within hydrogen bonding distance of the triazolium C3.

A summary of results from TrPP docking twelve transketolase (TK) enzymes using GOLD is shown in Table 5.16.

Table 5.16 Summary of results from screening Transketolase TK TPP dependent enzymes with TrPP 133

Enzyme	Source	RMSD	PLP Score	Rank
	***TPP* 63**	**1.0**	**89.2**	
1ITZ	*Zea mays*	15.4	20.2	3
1QGD	*Escherichia coli*	8.3	23.2	6
1R9J	*Leishmania mexicana*	8.7	21.2	4
3M34	*Campylobacter jejuni*	9.3	36.0	10
3M49	‘’	3.9	22.7	5
3MOS	*Homo sapiens*	9.5	33.4	8
3OOY	‘’	10.9	12.0	2
3RIM	*Mycobacterium tuberculosis*	12.3	25.0	7
4C7X	*Lactobacillus salivarius*	5.8	34.4	9
5ND5	***Chlamydomonas reinhardtii***	**8.9**	**10.9**	**1st**
5XS6	*Scheffersomyces stipitis*	9.0	37.8	11

From Table 5.16 above, docking **133** TrPP with alga sourced 5ND5 (*Chlamydomonas reinhardtii*) gave the best fit result of 10.9 and structure 1GPU from yeast gave the least fit result of 40.2 ranking twelfth. This represents a difference of ~29 PLP score units. Enzyme 3OOY (*Homo sapiens*) gave a PLP score of 12 ranking second among the series while 1R9J *(Leishmania mexicana)* ranked fourth with a PLP score of 21.2. 3RIM sourced from bacteria (*Mycobacterium tuberculosis*) registered a PLP score of 25.0 ranking fifth.

Results from the RMSD column (Table 5.16 above) show that the best score 3M49 RMSD = 3.9, shows a divergence from its PLP score ranking (5th). The second best RMSD value is given by 4C7X (*Lactobacillus salivarius*) registering an RMSD value of 5.8 (2nd) surprisingly ranked ninth by overall PLP score. Remarkably bacteria sourced 1ITZ (*Zea mays*) gave the least favourable RMSD of 15.4 (12th) given that it ranked third best in terms of overall PLP score

Figure 5.16 Best docking pose generated for TrPP 133 at 5ND5 active site GOLD PLP score = 10.9 RMSD = 8.9

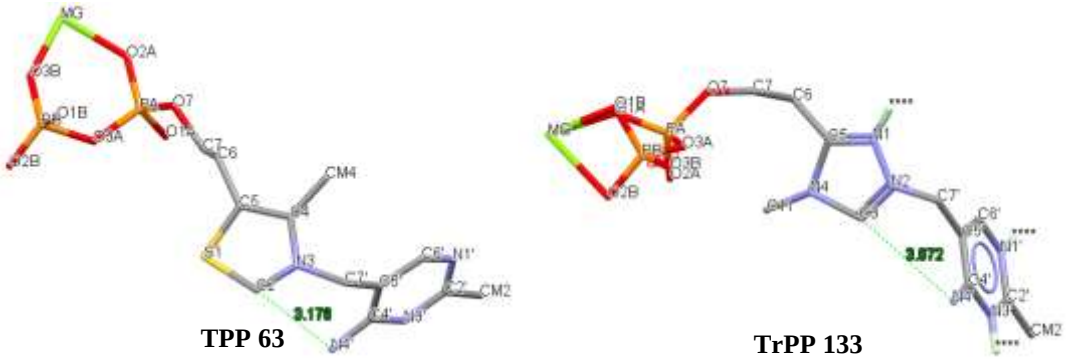

Table 5.17 Bond angles at the bridging methylene of TrPP best docking pose at 5ND5

TPP 63				TrPP 133			
Atom1	**Atom2**	**Atom3**	**Angle**	**Atom1**	**Atom2**	**Atom3**	**Angle**
C6'	C5'	C7'	122.36	**C5'**	**C7'**	**N2**	**108.67**
N1'	C6'	C5'	124.9	C5'	C7'	H7'1	109.93
C5'	**C7'**	**N3**	**111.7**	C5'	C7'	H7'2	109.96
C7'	N3	C2	129.8	N2	C7'	H7'1	109.97
C7'	N3	C4	119.63	N2	C7'	H7'2	109.94
C2	N3	C4	110.25	H7'1	C7'	H7'2	108.37

The stick structure above (Figure 5.16) show the conformation of TrPP **133** at the active site of 5ND5. The bond angle at the bridging methylene (C5'–C7'– N2 108.67 °) is ~ 3° lower

compared to native cofactor TPP (111.7 °) (Table 5.17). The magnesium cation on the TrPP sits to the left of the pyrophosphate side chain, however, in TPP docked at 5ND5 active site, it sits atop the diphosphate linker. The aminopyrimidinyl ring lies in a similar in the generated pose compared to the TPP, with similar distance between the exocyclic nitrogen (N7) and the C3-carbon – 3.2 and 3.8 Å respectively. In addition, the exocyclic amino group point downwards and towards the carbenic centre in both cases.

Figure 5.17 Overall comparison of the range of PLP fitness scores of enzyme families screened

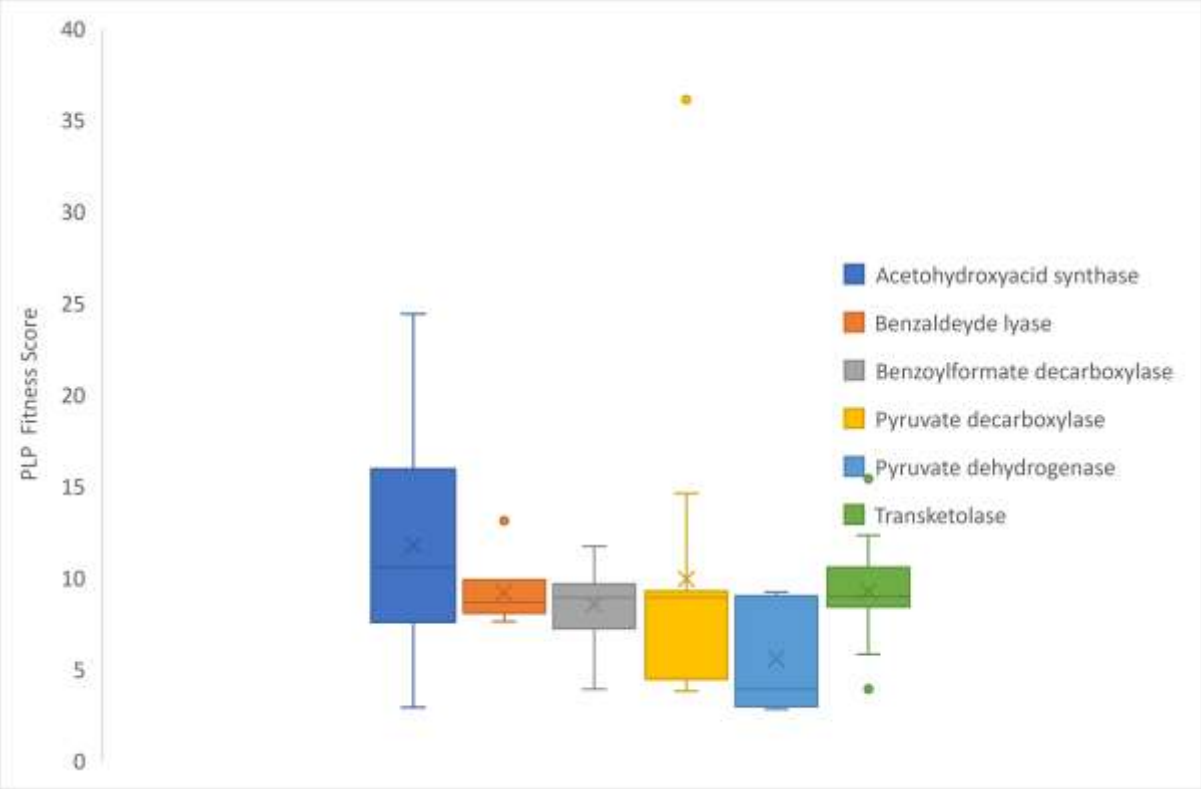

Figure 5.18 Overall comparison of the range of RMSD scores of enzyme families screened

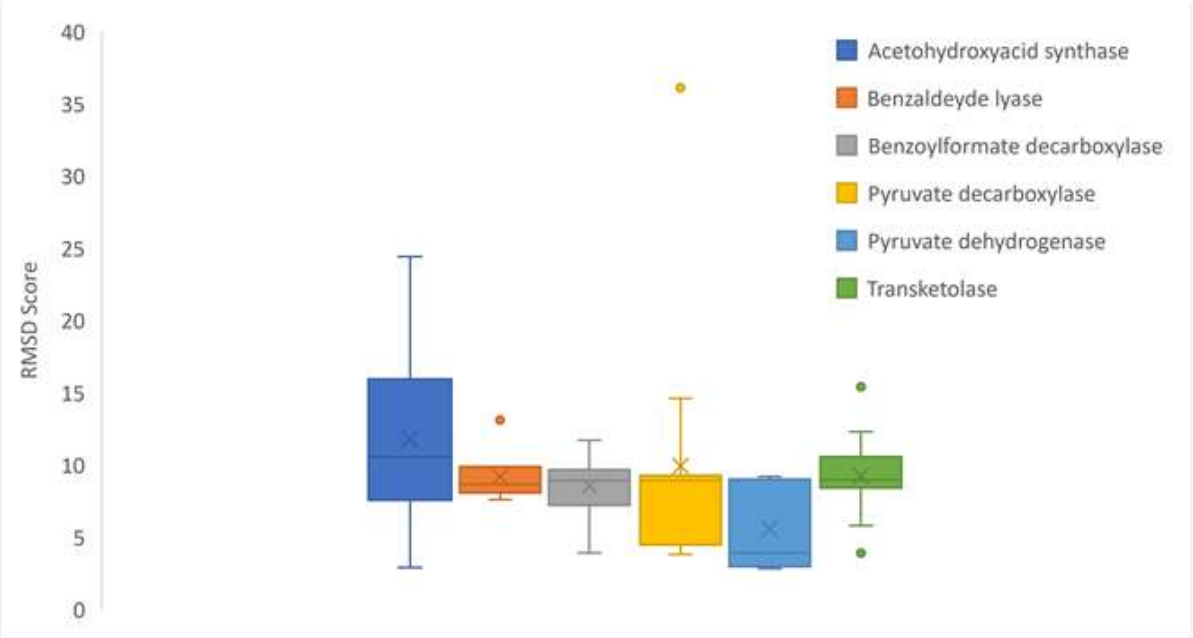

Figure 5.17 shows the plot of overall comparison of PLP scores obtained from the families of TPP-dependent enzymes studied. The median value is marked with an x across the bar in the plot. From the plot, enzymes sourced from AHAS class gave the lowest PLP values i.e. better fit. The other families of enzymes registered fitting score above zero. Enzymes from the BFD class gave the least variance in scoring values. This may suggest that the residues present are better conserved in this family leading to closely similar active sites within the BFD family.

Figure 5.18 shows the plot of overall RMSD values for all the enzyme classes screened in this work. Enzymes from the AHAS class showed a wider divergence in relation to the rest of the families. In general, the triazolium ring of the mimic docks in the same conformation of the thiazole of TPP, which makes the C3-H of the triazolium ring accessible to target substrates. RMSD values for BAL class gave the least deviation, with values ranging between 7 and 13. This is larger than for the redocked cofactor which gave RMSD values less than 2. Overall, both plots show that there may be a good chance for binding at the active site since there exists

protein residues withing hydrogen bonding distance of the docked mimic TrPP and the variance in RMSD compared to native redocked TPP is the result of repositioning the methyl from C5 of thiamine in TPP to the N4 of the mimic triazolium in TrPP.

5.4 Summary

In total 54 of TPP-dependent enzymes from six families were screened for binding poses with triazolium TrPP 128. Using GOLD docking software and PLP scoring function, the proteins were ranked by order of best fit, i.e. lowest energy. In addition, RMSD values were compared to match similarity between docked poses generated and the natural conformation of TPP at the active site. Furthermore, bond angles at the bridging methylene of TrPP at active sites were compared against values obtained for the native cofactor. In cases where the conformation show promise for intramolecular deprotonation, distances between the exocyclic amino group and the carbenic centre were measures come within 3.8 Å.

The overall data from all the enzymes studied were compared in two plots of PLP score and RMSD value. The plots show good promise for in vivo docking as the active site is spacious enough to fit the artificial cofactor TrPP.

5.5 References

1. M. L. Verdonk, J. C. Cole, M. J. Hartshorn, C. W. Murray and R. D. Taylor, *Proteins.*, 2003, **52**, 609-623.
2. D. B. Kitchen, H. Decornez, J. R. Furr and J. Bajorath, *Nat. Rev. Drug Discov.*, 2004, **3**, 935-949.
3. N. Huang, C. Kalyanaraman, J. J. Irwin and M. P. Jacobson, *J. Chem. Inf. Model.*, 2006, **46**, 243-253.
4. B. K. Shoichet, A. R. Leach and I. D. Kuntz, *Proteins.*, 1999, **34**, 4-16.
5. A. Nicholls and B. Honig, *J. Comput. Chem.*, 1991, **12**, 435-445.
6. E. C. Meng, B. K. Shoichet and I. D. Kuntz, *J. Comput. Chem.*, 1992, **13**, 505-524.
7. D. K. Jones-Hertzog and W. L. Jorgensen, *J. Med. Chem.*, 1997, **40**, 1539-1549.
8. M. van Dijk, A. D. J. van Dijk, V. Hsu, R. Boelens and A. M. J. J. Bonvin, *Nucleic Acids Res.*, 2006, **34**, 3317-3325.
9. T. Cheng, X. Li, Y. Li, Z. Liu and R. Wang, *J. Chem. Inf. Model.*, 2009, **49**, 1079-1093.
10. O. Korb, T. Stützle and T. E. Exner, *J. Chem. Inf. Model.*, 2009, **49**, 84-96.
11. D. Chipman, Z. e. Barak and J. V. Schloss, *Biochim. Biophys. Acta. Prot. Struct. Mol. Enzym.*, 1998, **1385**, 401-419.
12. K. Tittmann, M. Vyazmensky, G. Hübner, Z. e. Barak and D. M. Chipman, *Proc. Natl. Acad. Sci. U.S.A.*, 2005, **102**, 553-558.
13. Y. Y. Chang and J. E. Cronan, *J. Bacteriol.*, 1988, **170**, 3937-3945.
14. J. A. McCourt, S. S. Pang, J. King-Scott, L. W. Guddat and R. G. Duggleby, *Proc. Natl. Acad. Sci. U.S.A.*, 2006, **103**, 569.
15. Z. Maugeri and P. Domínguez de María, *J. Mol. Catal. B: Enzym.*, 2014, **107**, 120-123.
16. G. D. Hegeman, *Methods Enzymol.*, 1970, DOI: 10.1016/0076-6879(71)17262-X.
17. R. Wilcocks, O. P. Ward, S. Collins, N. J. Dewdney, Y. Hong and E. Prosen, *Appl. Environ. Microbiol.*, 1992, **58**, 1699-1704.
18. I. C. Gunsalus, C. F. Gunsalus and R. Y. Stanier, *J. Bacteriol.*, 1953, **66**, 538-542.
19. F. H. Andrews and M. J. McLeish, *Bioorg. Chem.*, 2012, **43**, 26-36.
20. M. S. Hasson, A. Muscate, M. J. McLeish, L. S. Polovnikova, J. A. Gerlt, G. L. Kenyon, G. A. Petsko and D. Ringe, *Biochemistry*, 1998, DOI: 10.1021/bi973047e.
21. R. Bakule and F. A. Long, *J. Am. Chem. Soc.*, 1963, **85**, 2309-2312.
22. S. Loschonsky, T. Wacker, S. Waltzer, P. P. Giovannini, M. J. McLeish, S. L. A. Andrade and M. Müller, *Angew. Chem. Int. Ed.*, 2014, DOI: 10.1002/anie.201408287.
23. S. Loschonsky, S. Waltzer, S. Fraas, T. Wacker, S. L. A. Andrade, P. M. H. Kroneck and M. Müller, *ChemBioChem*, 2014, **15**, 389-392.

24. A. Steinbach, S. Fraas, J. Harder, E. Warkentin, P. M. H. Kroneck and U. Ermler, *The FEBS Journal*, 2012, **279**, 1209-1219.

25. W.-K. Hong, C.-H. Kim, S.-Y. Heo, L. H. Luo, B.-R. Oh and J.-W. Seo, *Biotechnol. Lett*, 2010, **32**, 1077-1082.

26. S. Koenig, D. Svergun, M. H. J. Koch, G. Huebner and A. Schellenberger, *Biochemistry*, 1992, **31**, 8726-8731.

27. M. Fetizon, P. Goulaouic and I. Hanna, *Tetrahedron Lett.*, 1985, **26**, 4925-4928.

28. A. G. Datta and E. Racker, *J. Biol. Chem.*, 1961, **236**, 617-623.

29. S. Gerhardt, S. Echt, M. Busch, J. Freigang, G. Auerbach, G. Bader, W. F. Martin, A. Bacher, R. Huber and M. Fischer, *Plant Physiol*, 2003, **132**, 1941-1949.

30. R. Kluger and K. Tittmann, *Chem. Rev.*, 2008, **108**, 1797-1833.

Chapter Six

6 Experimental

6.1 Materials

Chemicals used were bought from Sigma Aldrich, Alfa Aesar, Apollo scientific and Tokyo Chemicals. Deuterated solvents were bought from Cambridge Isotope Laboratories.

6.2 Instrumentation

NMR Spectroscopy: Proton and carbon NMR (Nuclear magnetic resonance) spectra were recorded as shown in Table 6.1 below:

Table 6.1 NMR spectrometer frequencies

Spectrometer	*Operating Frequencies and Nuclei*
Bruker Avance III-HD-400 (A4)	399.95 MHz for ^{1}H, 100.57 MHz for ^{13}C
Bruker Avance III-HD-400 (B4)	400.07 MHz for ^{1}H, 100.60 MHz for ^{13}C
Bruker Neo- 400 (N4)	400.20 MHz for ^{1}H, 100.63 MHz for ^{13}C
Varian DD2- 500 (C5)	499.53 MHz for ^{1}H, 125.61 MHz for ^{13}C
Varian VNMRS-600 (P6)	599.42 MHz for ^{1}H, 150.72 MHz for ^{13}C
Varian VNMRS-700 (D7)	699.73 MHz for ^{1}H, 175.95 MHz for ^{13}C

Spectral analyses were recorded in the order: chemical shift (ppm), integration, multiplicity (s = singlet, d = doublet, t= triplet, q = quartet, qu = quintet, s = sextet, m = multiplet), coupling constants (Hz) and assignment. Monodeuterated methanol (CH_3OD) was used as internal standard in water.

Table 6.2 NMR solvents and reference signals

solvent	**δ_H, ppm**
acetonitrile-d_3	1.99
deuterium oxide-d_2	4.81
dimethyl sufoxide-d_6	2.49
methanol-d_4	3.31

Infra-Red Spectroscopy: Infrared spectra were recorded using neat liquid or solid samples on a Perkin Elmer FT-IR Frontier spectrometer.

UV-Visible Spectroscopy: Ultraviolet to visible spectra were recorded using samples dissolved in ethanol in a 1.00 cm pathlength quartz cuvette on Varian Cary 50 and Varian Cary 100 Bio Spectrophotometers maintained at 25°C.

HPLC: Chromatograms were run on a Puriflash 420 Interchim chromatography machine.

LC-MS(ESI): Liquid Chromatography-Mass Spectrometry coupled analysis using an electrospray ionization technique was accomplished using a TQD (Triple Quadrupole) mass spectrometer and an Acquity UPLC (Ultra-Performance Liquid Chromatography) (Waters Ltd, UK). Positive and negative ions are produced alternatively between 100 – 2000 amu. An inbuilt photodiode array detector gives an absorption plot between 210 to 400 nm.

GCMS: Gas Chromatography Coupled-Mass Spectrometry analysis was carried out on a Shimadzu QP2010-Ultra at 70ev for a mass range inclusive between 35 to 650 amu.

Elemental Analysis: Solid samples were analysed using an Exeter CE-440 Elemental Analyser

Melting points: were measured using a Gallenkamp melting point apparatus.

6.3 Synthesis of Hydrazides

6.3.1 Acethydrazide

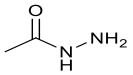

165

Ethyl acetate **164** (1.0 ml, 10 mmol) and hydrazine monohydrate 64−65 % (2.0 ml, 26 mmol) were stirred at room temperature for 4h after which the mixture was concentrated under reduced pressure at 50 °C to give a clear viscous liquid. The crude residue was cooled to −10 °C and triturated with ice-cold dichloromethane (10 mL) to give the title compound as a white crystalline solid (0.65 g, 85 %) with spectroscopic data in accordance with literature values[1]. **mp**: 58 °C; **IR** ν_{max}/cm^{-1}; 1525 (bend NH_2), 1620 (C=O), 3210 (stretch NH) **^{1}H NMR** (400 MHz, D_2O): δ_H 1.8 (3H, s, CH_3); **^{13}C NMR** (101 MHz, D_2O): δ_C 19.6 (CH_3), 172.6 (C=O).

6.3.2 3-Methoxypropanehydrazide

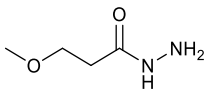

138

Methyl 3-methoxy propionate **137** (1.0 ml, 8.5 mmol) and, hydrazine monohydrate 64−65 % in water (2.0 ml, 26 mmol) were stirred at room temperature for 4h. The mixture was

concentrated under reduced pressure to give the title compound as an oily liquid (0.65 g, 85 %) **IR** ν_{max}/cm^{-1}; 1526 (bend NH_2), 1627 (C=O), 3287 (stretch NH); **^{1}H NMR** (400 MHz, D_2O): δ_H 2.33 (2H, t, *J*=6.0, (C=O)CH_2), 3.19 (3H, s, O−CH_3), 3.55 (2H, t, *J*=6.0, O−CH_2); **^{13}C NMR** (101 MHz, D_2O): δ_C 33.9 (CH_2), 57.9 (O-CH_2), 67.9 (O−CH_3), 172.9 (C=O); ***m/z*** (ES+): 119 [M+H] HRMS: **HRMS** (ES+): $[M+H]^+$ $C_4H_{11}N_2O_2^+$requires 119.0821 found 119.0818 (-2.5 ppm).

6.3.3 3-Ethoxypropanehydrazide

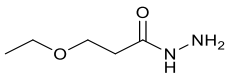

211

Ethyl 3-ethoxy propionate (1.0 ml, 6.8 mmol) and hydrazine monohydrate 64−65 % in water (2.0 ml, 26 mmol) were stirred at room temperature for 4h. The mixture was then concentrated under reduced pressure to give the title compound as an oily liquid (0.81 g, 90%) **IR** ν_{max}/cm^{-1}; 3275, 2975, 1618, 1535, 1444, 1099; **^{1}H NMR** (400 MHz, D_2O): δ_H 1.06 (3H, t, *J*=7.1, CH_3), 2.37 (2H, t, *J*=6.1, CH_2), 3.46 (2H, q, *J*=7.1, CH_2), 3.64 (2H, t, *J*=6.1, CH_2) ; **^{13}C NMR** (101 MHz, D_2O): δ_C 14.0 (CH_3), 34.0 (CH_2), 65.7 (CH_2), 66.5 (CH_2), 172.9 (C=O) ; ***m/z*** (ES+): 132 ; **HRMS:** calc. for $C_5H_{13}N_2O_2$ 133.0977 found: 133.0968 (-6.8 ppm).

6.3.4 3-Hydroxybutanehydrazide

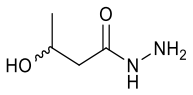

180

Ethyl 3-hydroxybutyrate (1.0 ml, 7.5 mmol), hydrazine monohydrate 64−65 % in water (2.0 ml, 26 mmol) and ethanol (3.0 ml) were stirred at room temperature for 4h. The mixture was cooled to −30 °C. Clear crystals formed, which were filtered and washed with ice-cold dichloromethane (10 ml), and dried to give the title compound as a transparent crystalline solid (0.6 g, 68%) **m.p.** 78 °C; **IR** ν_{max}/cm^{-1}: 3292, 3163, 1620, 1537, 1341; **^{1}H NMR** (400 MHz, D_2O): δ_H 1.09 (3H, d, *J*=6.2, CH_3), 2.23 (2H, d, *J*=6.5, CH_2), 3.95 – 4.12 (1H, m, CH); **^{13}C NMR** (101 MHz, D_2O): δ_C 21.8 (CH_3), 42.8 (CH_2), 64.8 (CH), 172.7 (C=O) ; ***m/z*** (ES+): 119($[M+H]^+$, 100%); **HRMS** (ES+): $[M+H]^+$ $C_4H_{11}N_2O_2^+$requires 119.0821 found 119.0817 (-3.4 ppm).

6.3.5 3-Hydroxypropanehydrazide

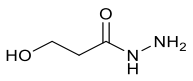

150

3-Hydroxypropionate (1.0 ml, 8.5 mmol) and hydrazine monohydrate 64−65 % in water (2.0 ml, 26 mmol) were stirred at room temperature for 4h. The mixture was concentrated under reduced pressure at 50 ℃ to give a clear residue, which was cooled to −10 ℃ and washed with

cold diethyl ether to give the title compound as a white crystalline solid (0.75 g, 74 %) **mp**: 80 – 82 °C; **IR** ν_{max}/cm^{-1}: 3300 and 3190 (NH) 1620 (OH) 1530 (CO); **^{1}H NMR** (400 MHz, D_2O): δ_H 2.29 (2H, t, *J*=6.1 , CH_2), 3.70 (2H, t, *J*=6.1, CH_2); **^{13}C NMR** (101 MHz, D_2O): δ_C 36.5, 57.6, 173.2 (C=O); ***m/z*** (ES+): 105 ($[M+H]^+$, 100%); **HRMS** [M+H]+ $C_3H_9N_2O_2$ requires 105.0664 found 105.0663 (-1.0 ppm).

6.3.6 4-Hydroxybutanehydrazide

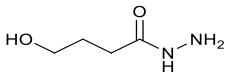

174

γ-Butyrolactone **173** (1.0 ml, 14 mmol) and hydrazine monohydrate (2.0 ml, 26 mmol) were stirred at room temperature for 4h. The mixture was then concentrated under reduced pressure at 50 ℃ to give a clear residue, which was cooled to −10 ℃ washed with ice-cold diethyl ether (10 ml) and dried to give the title compound as a white crystalline solid (0.84 g, 50 %) **m.p.** 78 °C; **IR** ν_{max}/cm^{-1}**:** 3301, 3193, 3117, 2958, 2933, 1633, 1530, 1469, 1450, 1369, 1300, 1258, 1043, 1008; **^{1}H NMR** (400 MHz, D_2O): δ_H 1.68 – 1.57 (2H, m, CH_2), 2.08 (2H, t, *J*=7.6, CH_2), 3.40 (2H, t, J=6.5, CH_2); **^{13}C NMR** (101 MHz, D_2O): δ_C 27.5 (CH_2), 30.2 (CH_2), 60.6 (CH_2), 175.0 (C=O) ; ***m/z*** (ES+): 133 [M+H]; **HRMS** [M+H]+ $C_4H_{11}N_2O_2$ requires 119.0821 found 119.0851 (-5.0 ppm)

6.4 Synthesis of Thione Intermediates

6.4.1 General procedure A

To the corresponding hydrazide (8 mmol) stirring in 30 ml of water at room temperature was added thiamine mononitrate (1.0 g, 3.0 mmol) and the solution adjusted to p*H* 4 using 1.0M hydrochloric acid to aid solubility and maintain the stability of the substrate. After degassing the stirring mixture for 15 minutes, sodium bisulphite (0.04 g, 0.3 mmol) was added under argon and the reaction mixture maintained at 80 ℃ for 8 h. Upon completion, the mixture was concentrated under reduced pressure, the residue dried and used in the next step without further purification. To the dry residue was added absolute ethanol (30 ml) and methyl isothiocyanate (1.0 g, 14 mmol) under an inert atmosphere, and the mixture was refluxed for 4 h. The solid in the resulting white suspension was removed by filtration, dried, dissolved in 0.1M NaOH (30 ml) and refluxed for 24 h. Upon cooling a white precipitate formed, which was removed by filtration, washed with deionized water, and dried under vacuum to yield the target thione intermediate.

6.4.2 1-((4-amino-2-methylpyrimidin-5-yl)methyl)-3,4-dimethyl-1*H*-1,2,4-triazole-5(4*H*)-thione

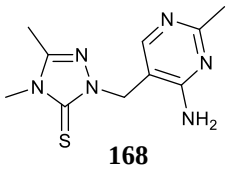

168

Using general procedure **A**, acethydrazide **165** (0.60 g, 8.1 mmol) was reacted to yield the title compound as a white, crystalline solid (0.66 g, 29 %). λ_{max}**(**EtOH**)/nm** 235 (ε/dm^3 mol^{-1} cm^{-1}

12, 400); **^{1}H NMR** (400 MHz, D_2O): δ_H 2.05 (3H, s, aryl-CH_3), 2.24 (3H, s, CH_3), 3.19 (3H, s, N–CH_3), 4.96 (2H, s), 7.80 (1H, s, aryl ortho-H); **^{13}C NMR** (101 MHz, D_2O): δ_C 10.3, 20.7, 31.2, 45.2, 109.3, 143.0, 151.6, 162.1, 163.1, 165.0 (C=S); ***m/z*** (ES+): 251 [M+H] ;**HRMS** (ES+): $[M+H]^+$ $C_{10}H_{15}N_6S$ requires 219.1351, found 219.1345.

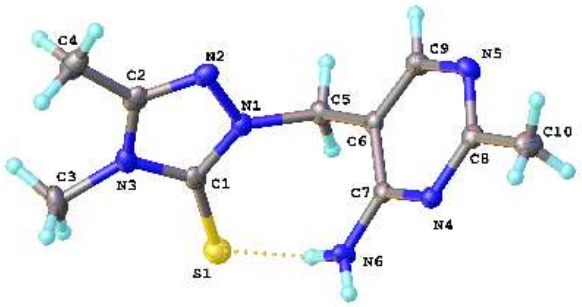

Synthesis of 2-[2-[(4-amino-2-methylpyrimidin-5-yl)methyl]-4-methyl-1,2,4-triazol-3-thione-5-yl]2-methoxyethanol

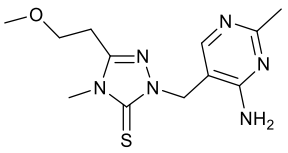

227

Using general procedure **A**, 3-methoxypropanehydrazide **138** (1.0 g, 7.6 mmol) was reacted to yield the title compound as a white solid (0.39 g, 17 %). **λ_{max}(EtOH)/nm** 257 (ε/dm^3 mol^{-1} cm^{-1} 13, 900); **^{1}H NMR** (400 MHz, D_2O): δ_H 2.43 (3H, s, CH_3), 2.92 (2H, t, *J*=6.1, CH_2), 3.21 (3H, s, N–CH_3), 3.42 (3H, s, O–CH_3), 3.67 (2H, t, *J*=6.1, CH_2), 5.17 (2H, s, CH_2), 8.00 (1H, s, *aryl*-C-H); **^{13}C NMR** (101 MHz, D_2O): δ_C 20.7 (*aryl*-CH_3), 25.2 (CH_2), 31.5 (CH_3), 45.5 (CH_2), 58.0 (CH_3), 67.8 (CH_2) , 109.3 (*aryl*-C), 143.3 (*aryl*-C), 151.9 , 162.3 , 163.4 , 165.5 (C=S); ***m/z*** (ES+): 295 $[M+H^+]$.

Synthesis of 2-[2-[(4-amino-2-methylpyrimidin-5-yl)methyl]-4-methyl-1,2,4-triazol-3-thione-5-yl]-2-ethoxyethanol

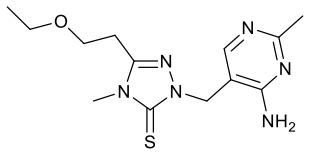

228

Using general procedure **A**, 3-ethoxypropanehydrazide (0.70 g, 7.6 mmol) was reacted to yield the title compound as a white solid (0.601 g, 39 %). **λ_{max}(**EtOH**)/nm** 234 (ε/dm^3 mol^{-1} cm^{-1} 14, 090); **^{1}H NMR** (400 MHz, D_2O): δ_H 0.89 (3 H, t, *J*=7.1, CH_3), 2.38 (3 H, s, CH_2), 2.85 (2 H, t, *J*=6.2, CH_2), 3.35 (2 H, q, *J*=7.1, CH_2), 3.36 (3 H, s, N−CH_3), 3.65 (2 H, t, *J*=6.2, CH_2), 5.12 (2 H, s, CH_2), 7.98 (1 H, s, aryl ortho−CH); **^{13}C NMR** (101 MHz, D_2O): δ_C 20.7 (*aryl*-CH_3), 25.5 (CH_2), 27.2 (CH_2), 31.3 (CH_3), 45.9 (CH_2), 58.4 (CH_3), 67.6 (CH_2) , 109.7 (*aryl*-C), 143.1 (*aryl*-C), 151.3 , 162.5 , 163.1 , 165.3 (C=S) ; ***m/z*** (ES+): 309 [M+H$^+$] **HRMS** (ES+): [M+H]$^+$ $C_{13}H_{20}N_6OS$ requires 309.1501, found 309.1498

6.4.3 2-[2-[(4-amino-2-methylpyrimidin-5-yl)methyl]-4-methyl-1,2,4-triazol-3-thione-5-yl]2-hydroxypropanol

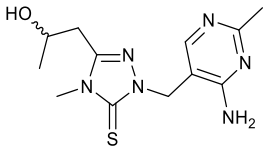

178

Using general procedure **A**, 3-hydroxybutanehydrazide **180** (1.3 g, 7.6 mmol) was reacted to yield the title compound as a white solid (0.561 g, 24 %). **λ_{max}(**EtOH**)/nm** 238 (ε/dm^3 mol^{-1} cm^{-1} 13, 870); **^{1}H NMR** (400 MHz, D_2O): δ_H 1.13 (3H, d, *J*=6.3, alkyl−CH_3), 2.44 (3H, s, aryl−CH_3), 2.59 – 3.02 (2H, m, aryl−CH_2), 3.43 (3H, s, N−CH_3), 3.89 – 4.30 (1H, m, aryl−CH), 5.19 (2H, s, CH_2), 8.03 (1H, s, aryl ortho−CH); **^{13}C NMR** (101 MHz, D_2O): δ_C 20.7, 21.7, 31.7, 33.7, 45.5, 65.0, 109.3, 143.2, 151.9, 162.3, 163.3, 165.4 (C=S); ***m/z*** (ES+): $[M+H]^+$ 295 **HRMS** (ES+): $[M+H]^+$ $C_{12}H_{18}N_6OS$ requires 295.1341, found 295.1339 (−0.7 ppm).

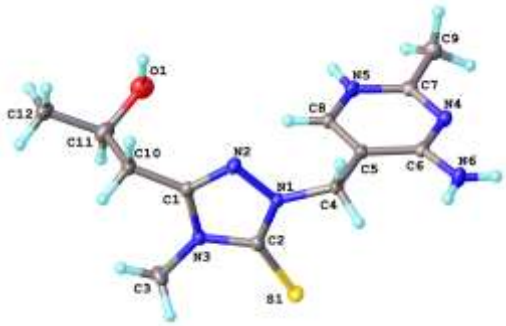

6.4.4 2-[2-[(4-amino-2-methylpyrimidin-5-yl)methyl]-4-methyl-1,2,4-triazol-3-thione-5-yl]propanol

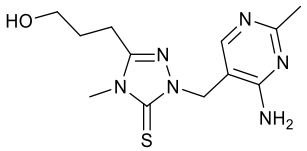

177

Using general procedure **A**, 4-hydroxybutyric acid hydrazide **174** (1.2 g, 7.6 mmol) was reacted to yield the title compound as a white crystalline solid (0.44 g, 19 %); **λ_{max}(**EtOH**)/nm** 230, 253 (ε/dm^3 mol^{-1} cm^{-1} 14, 700); **^{1}H NMR** (400 MHz, D_2O): δ_H 1.81 (2H, q, *J*=6.7, alkyl−CH_2), 2.44 (3H, s, aryl−CH_3), 2.70 (2H, t, *J*=7.6, alkyl−CH_2), 3.41 (3H, s, N−CH_3), 3.53 (2H, t, *J*=6.3, O−CH_2), 5.18 (2H, s, N−CH_2), 8.01 (1H, s, aryl−H); **^{13}C NMR** (101 MHz, D_2O): δ_C 20.8 (CH_3), 21.4, 27.5, 31.3, 45.4, 60.3, 109.4, 143.2, 154.1, 162.3, 163.3, 165.4 (C=S); ***m/z*** (ES+): 295 [M+H] **HRMS:** calc. for $C_{12}H_{19}N_6OS$ 295.1347 found: 295.1341 (2.0 ppm)

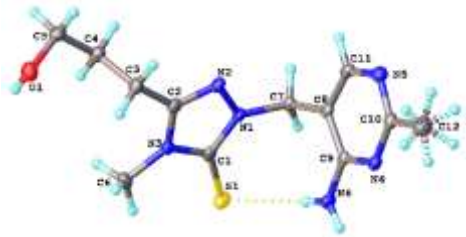

6.4.5 2-[2-[(4-amino-2-methylpyrimidin-5-yl)methyl]-4-methyl-1,2,4-triazol-3-thione-5-yl]ethanol

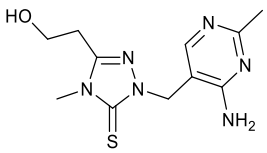

148

Following general procedure **A**, 3-hydroxypropionic acid hydrazide **150** (1.0 g, 7.6 mmol) was reacted to yield the title compound as a white solid (0.901 g, 57 %);**^{1}H NMR** (400 MHz, D_2O): δ_H 2.42 (3H, s, CH_3), 2.87 (2H, t, *J*=7.6, CH_2), 3.43 (3H, s, CH_3), 3.79 (2H, t, *J*=7.6, CH_2), 5.18 (2H, s, CH_2), 8.00 (1H, s, aryl−CH); **^{13}C NMR** (101 MHz, D_2O): δ_C 20.8 (CH_3), 21.4, 27.5, 31.3, 45.4, 60.3, 109.4, 143.2, 154.1, 162.3, 163.3, 165.4; ***m/z*** (ES+): 281 [M+H] ; **HRMS** calc. for $C_{11}H_{17}N_6OS$ 281.1180 found: 281.1185 (−1.8 ppm).

6.5 Synthesis of Triazolyl Tetrafluoroborate Salts

6.5.1 General Procedure B

To the corresponding thione (3 mmol) was added freshly prepared 1.0M tetrafluoroboric acid in water (0.5 ml) and the solution was left to stir for 10 minutes at room temperature. Upon cooling in an ice bath, hydrogen peroxide 40% w/w in water (2 ml, 17.4 mmol) was then added dropwise with continuous stirring at 0 °C and left stirring at room temperature for 3h. The clear solution was then carefully neutralized to ~p*H* 7 using sodium bicarbonate and immediately lyophilized to give the target triazolyl salt as a white hygroscopic solid.

6.5.2 2-[2-[(4-amino-2-methylpyrimidin-5-yl)methyl]-4-methyl-1,2,4-triazol-3-ium-5-yl]propanoyl tetrafluoroborate

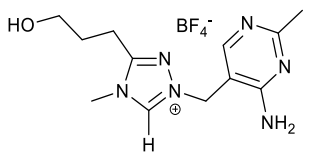

185

Following general procedure **B**, 4-hydroxybutyric thione **169** (0.7 g, 2.4 mmol) was reacted to give the title compound as a white solid (0.814, 97%). **^{1}H NMR** (400 MHz, DCl, p*D* 2.0): δ_H 1.87 – 1.99 (2H, m, alkyl–CH_2), 2.49 (3H, s, aryl−CH_3), 2.87 (2H, t, *J*=7.5, alkl–CH_2), 3.59 (2H, t, *J*=6.3, alkyl–CH_2), 3.78 (3H, s, N−CH_3), 5.46 (2H, s, bridging CH_2), 8.16 (1H, s, aryl C−H), 9.68 (1H, s, C3−H); **^{13}C NMR** (101 MHz, D_2O): δ_C 20.2, 21.0, 27.3, 32.7, 48.1, 60.1, 107.1, 143.6, 145.6, 157.5, 163.3, 163.4; **^{19}F NMR** (376 MHz, D_2O) δ_F −150.7(s, BF_4). ***m/z*** (ES+): 263$[M]^+$; **HRMS** (ES+): $[M-BF_4]^+$ $C_{12}H_{19}N_6O$ requires 263.1620, found 263.1620 (0.0 ppm).

6.5.3 2-[2-[(4-amino-2-methylpyrimidin-5-yl)methyl]-4-methyl-1,2,4-triazol-3-ium-5-yl]ethanoyl tetrafluoroborate

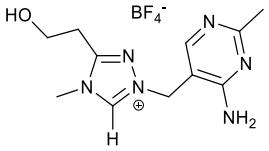

144

Following general procedure **B**, 3-hydroxypropanoic acid thione **148** (0.8 g, 2.9 mmol) was reacted to give the title compound as a white solid (0.527 g ,73%); **^{1}H NMR** (400 MHz, DCl, p*D* 2.0): δ_H 2.32 (3H, s, aryl−CH_3), 2.77 (2H, t, *J*=8.0, CH_2), 3.51 (2H, t, *J*=8.0, CH_2), 3.89 (3H, s, N−CH_3), 5.58 (2H, s, CH_2), 8.11 (1H, s, aryl C−H), 9.72 (1H, s, C3−H); **^{13}C NMR** (101 MHz, D_2O): δ_C 22.1, 27.0, 32.3, 48.5, 58.3, 106.0, 143.4, 151.8, 155.9, 163.0, 165.6; ***m/z*** (ES+): 249$[M]^+$; **HRMS** (ES+): $[M-BF_4]^+$ $C_{11}H_{17}N_6O$ requires 249.1469, found 249.1464 (−5.5 ppm).

6.5.4 2-[(4-amino-2-methylpyrimidin-5-yl)methyl]-4,5-dimethyl-1,2,4-triazol-3-ium-5-yl tetrafluoroborate

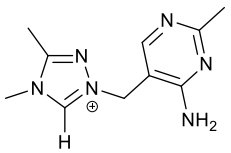

183

Following general procedure **B**, methyl thione **168** (0.72 g, 2.9 mmol) was reacted to give the title compound as a white solid (0.88 g, 91%); **^{1}H NMR** (400 MHz, DCl, p*D* 2.0): δ_H 2.44 (3H, s, aryl C−H_3), 2.44 (3H, s, triazolium C−H_3), 3.74 (3 H, s, NC−H_3), 5.45 (2 H, s, bridging C−H_2), 8.16 (1 H, s, aryl C−H), 9.69 (1 H, s, C3−H).; **^{13}C NMR** (101 MHz, D_2O): δ_C 9.3, 20.9, 33.0, 48.0, 107.3, 143.4, 145.2, 155.5, 163.1, 163.5; ***m/z*** (ES+): 219$[M-BF_4]^+$; **HRMS** (ES+): $[M-BF_4]^+$ $C_{10}H_{15}N_6$ requires 291.1358, found 219.1351 (−3.2 ppm)

6.5.5 2-[2-[(4-amino-2-methylpyrimidin-5-yl)methyl]-4-methyl-1,2,4-triazol-3-ium-5-yl]-2-hydroxyoxypropanoyl tetrafluoroborate

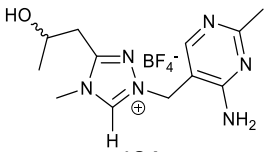

184

Following general procedure **B**, 3-hydroxybutyric thione **178** (0.8 g, 2.9 mmol) was reacted to give the title compound as a white solid (0.86 g, 85%); **^{1}H NMR** (400 MHz, DCl, p*D* 2.0): δ_H 1.25 (3 H, d, *J*=8.0 alkyl C−H_3), 2.55 (3 H, s, aryl C−H_3), 2.94−3.16 (2 H, m, C−H_2), 3.87 (3 H, s), 4.19 – 4.31 (1 H, m), 5.57 (2 H, s), 8.27 (1 H, s), 9.83 (1 H, s, C3−H); **^{13}C NMR** (101 MHz, D_2O): δ_C 21.8, 22.6, 32.5, 32.6, 33.2, 48.7, 65.1, 106.5, 151.6, 155.3, 162.6, 166.0; ***m/z*** (ES+): 263$[M+H]^+$; **HRMS** (ES+): $[M-BF_4]^+$ $C_{12}H_{19}N_6O$ requires 263.1620, found 263.1630 (3.8 ppm).

6.6 Synthesis of Triazolyl Tetraphenylborate Salts

6.6.1 General Procedure C

To the corresponding thione (3 mmol) was added freshly prepared deionized water (5 ml) and the suspension left to stir for 10 minutes at room temperature. Upon cooling in an ice bath, hydrogen peroxide 40% w/w in water (2 ml, 17.4 mmol) was added dropwise to the suspension with continuous stirring at 0 ℃ and the resulting suspension left stirring at room temperature for 3h. The clear solution was then carefully treated with freshly prepared 1.0 M sodium tetraphenylborate (5 ml) to give a white precipitate, which was filtered, washed with deionized water (10 mL), dried and recrystallized to give the target compound as shiny white crystals.

6.6.2 1-((4-amino-2-methylpyrimidin-5-yl)methyl)-3-(2-hydroxyethyl)-4-methyl-4*H*-1,2,4-triazol-1-ium tetraphenylborate

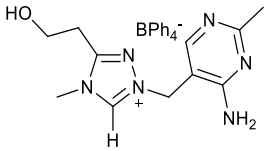

159

Following general procedure **C**, thione **148** (1.1 g, 3.8 mmol) was reacted to give the title compound as a white solid (1.9 g, 93%); **mp**: 127 °C; **IR** ν_{max}/cm^{-1}: 3434, 3056, 1598, 1668, 1478, 1426; **λ_{max}(EtOH)/nm:** 227 ($\varepsilon/dm^3\ mol^{-1}\ cm^{-1}$ 25, 800); **^{1}H NMR** (400 MHz, CD_3CN): δ_H 2.42 (3H, s, aryl−CH_3), 3.02 (2H, t, *J*=6.0, alkyl−CH_2), 3.74 (3H, s, N−CH_3), 3.82−3.92 (2H, m, alkyl−CH_2), 5.28 (2H, s, bridging CH_2), 6.87 (4H, t, *J*=12.0, [BPh_4^-, para aryl−CH]), 7.02 (8H, t, *J* = 8.0, [BPh_4^-, meta aryl−CH]), 7.28−7.33 (8H, m, [BPh_4^-, ortho aryl−CH]), 8.14 (1H, s, pyrimidinyl C−H), 8.96 (1H, s, C3−H); **^{13}C NMR** (101 MHz, D_2O): δ_C 25.0, 27.4, 33.3, 49.9, 58.5, 105.1, 121.8, 125.6, 135.7, 142.3, 155.9, 158.2, 161.9, 164.1, 164.5, 169.1; ***m/z*** (ES+): 263$[M+H]^+$; **HRMS** (ES+): $[M-BPh_4]^+$ $C_{12}H_{19}N_6O$ requires 249.1469, found 249.1464 (−5.5 ppm).

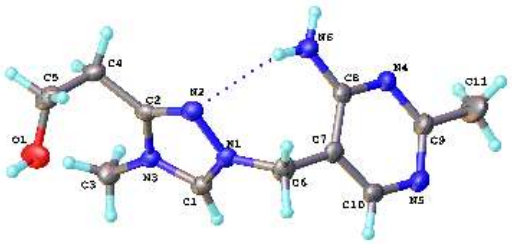

6.6.3 1-((4-amino-2-methylpyrimidin-5-yl)methyl)-3-(2-hydroxypropyl)-4-methyl-4H-1,2,4-triazol-1-ium tetraphenylborate

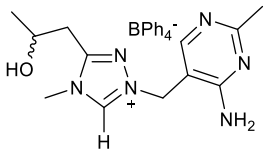

178

Following general procedure **C**, thione **178** (0.5 g, 1.8 mmol) was reacted to give the title compound as a white solid (1.04 g, 94 %), **mp**: 137; **IR** ν_{max}/cm^{-1}: 3054, 2010, 1979, 1654, 1579, 1478, 1426; **λ_{max}(**EtOH**)/nm** 260 (ε/dm^3 mol^{-1} cm^{-1} 23, 600); **^{1}H NMR** (400 MHz, CD_3CN): δ_H 1.26 (2H, d, *J*=6.0, alkyl−CH_3), 2.49 (3H, s, aryl−CH_3), 2.80−3.04 (2H, m, alkyl−CH_2), 3.74 (3H, s, N−CH_3), 4.08−4.18 (1H, m, alkyl CH), 5.19 (2H, s, bridging CH2), 6.87 (4H, t, *J* = 6.0, [BPh_4^-, para aryl−CH]), 7.03 (8H, t, *J* = 6.0, [BPh_4^-, meta aryl−CH]), 7.25−7.37 (8H, m, [BPh_4^-, ortho aryl−CH]), 7.91 (1H, s, pyrimidinyl C−H), 8.79 (1H, s, C3−H); **^{13}C NMR** (101 MHz, CD_3CN): δ_C 22.4, 32.8, 33.6, 48.7, 65.4, 106.4, 117.4, 121.8, 125.7, 135.7, 142.8, 155.7, 163.1, 163.6, 164.1, 164.6; ***m/z*** (ES+): 263$[M+H]^+$; **HRMS** (ES+): $[M-BPh_4]^+$ $C_{12}H_{19}N_6O$ requires 263.1620, found 263.1630 (3.8 ppm)

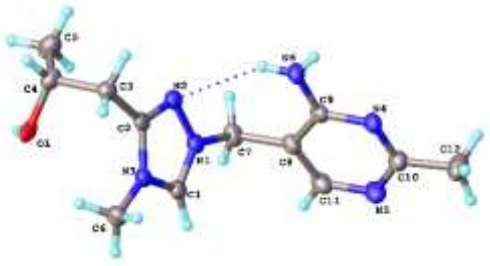

6.6.4 1-((4-amino-2-methylpyrimidin-5-yl)methyl)-3,4-dimethyl-4H-1,2,4-triazol-1-ium tetraphenylborate

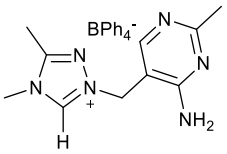

183

Following general procedure **C**, thione **168** (0.5 g, 2.0 mmol) was reacted to give the title compound as a shiny crystalline solid (0.8 g , 74 %); **mp**: 131°C; **IR** ν_{max}/cm^{-1}: 3052, 1619, 1560, 1585, 1477, 1426, 1233, 1031; **λ_{max}(EtOH)/nm** 228 ($\varepsilon/dm^3\ mol^{-1}\ cm^{-1}$ 24, 100); **^{1}H NMR** (600 MHz, CD_3CN): δ_H 2.37 (3H, s, aryl−CH_3), 2.45 (3H, s, triazolium CH_3), 3.50 (3H, s, N−CH_3), 4.95 (2H, s, bridging CH_2), 6.88 (4H, t, *J* = 6 *Hz*, [BPh_4^-, para aryl−CH]), 7.16 (8H, t, *J*=6.0 [BPh_4^-, meta aryl−CH]), 7.34−7.40 (8H, m, [BPh_4^-, ortho aryl−CH]), 7.55 (1H, s, pyrimidinyl C−H), 8.22 (1H, s, C3−H); **^{13}C NMR** (101 MHz, D_2O): δ_C 9.5, 21.9, 33.1, 48.1, 106.8, 115.2, 117.4, 121.9, 125.8, 129.6, 135.7, 142.7, 146.1, 154.8; ***m/z*** (ES+): 219$[M+H]^+$; **HRMS** (ES+): $[M-BPh_4]^+$ $C_{10}H_{15}N_6$ requires 291.1358, found 219.1351 (−3.2 ppm).

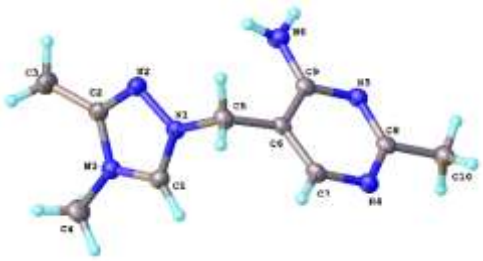

6.6.5 2-[2-[(4-amino-2-methylpyrimidin-5-yl)methyl]-4-methyl-1,2,4-triazol-3-ium-5-yl]propanoyl tetraphenylborate

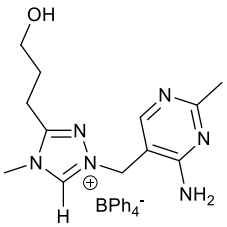

185

Following general procedure **C**, thione **177** (1.2 g, 4.0 mmol) was reacted to give the title compound as a shiny crystalline solid (2.1 g , 92 %), **mp**: 115°C; **IR** ν_{max}/cm^{-1}: 3209, 3054, 2165, 2037, 1654, 1581, 1531, 1478, 1426, 1266, 1150; **λ_{max}(**EtOH**)/nm** 205 ($\varepsilon/dm^3\ mol^{-1}\ cm^{-1}$ 19, 300); **^{1}H NMR** (400 MHz, CD_3CN): δ_H 1.91 (2H, qu, *J*=8.0, alkyl−CH_2), 2.51 (3H, s, aryl−CH_3), 2.87 (2H, t, *J*=4.0, alkyl−CH_2), 3.60 (2H, t, *J*=4.0, alkyl−CH_2), 3.70 (3H, s, N−CH_3), 5.19 (2H, s, bridging CH2), 6.86 (4H, t, *J* = 6.0, [BPh_4^-, para aryl−CH]), 7.02 (8H, t, *J* = 6.0, [BPh_4^-, meta aryl−CH]), 7.27−7.36 (8H, m, [BPh_4^-, ortho aryl−CH]), 7.88 (1H, s, pyrimidinyl C−H), 8.82 (1H, s, C3−H); **^{13}C NMR** (101 MHz, CD_3CN): δ_C 9.5, 20.5, 22.0, 28.3, 38.0, 48.4, 59.7, 106.8, 115.1, 117.4, 121.8, 125.8, 125.7, 129.6, 135.7, 135.7, 135.7, 135.7, 142.7, 146.1, 154.8, 163.2, 163.2, 163.4, 163.8, 164.1, 164.4; ***m/z*** (ES+): 263$[M+H]^+$; **HRMS** (ES+): $[M-BPh_4]^+$ $C_{12}H_{19}N_6O$ requires 263.1620, found 263.1620 (0.0 ppm).

6.7 Summary of Attempted Syntheses

6.7.1 1,2,4-triazole and trimethyloxonium tetrafluoroborate

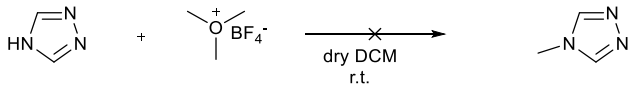

135 **136**

1,2,4-triazole **135** (0.05g, 0.7 mmol) was added to a solution of trimethyloxonium tetrafluoroborate (0.21 g, 1.4 mmol) in dry DCM at room temperature, under an inert atmosphere, and stirred for 72h. The reaction was monitored by LCMS, however separation

from other isomers to give the target monomethylated triazole **136** proved unsuccessful using silica chromatography 98:2 (DCM:MeOH).

6.7.2 1,2,4-triazole and 2-(bromomethyl)pyridine hydrobromide

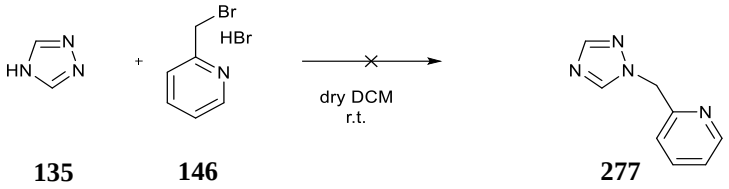

135 **146** **277**

1,2,4-triazole **135** (0.05g, 0.7 mmol) was added to a solution of 2-bromomethyl-pyridine hydrobromide **146** (0.36 g, 1.4 mmol) in dry DCM at room temperature, under an inert atmosphere, and stirred for 72h. The triazole remained as white suspension and did not appear to dissolve in DCM. The reaction was monitored by LCMS and did not show conversion into the desired product **277**.

6.7.3 1,2,4-triazole and 2-(bromomethyl)pyridine hydrobromide in DMF

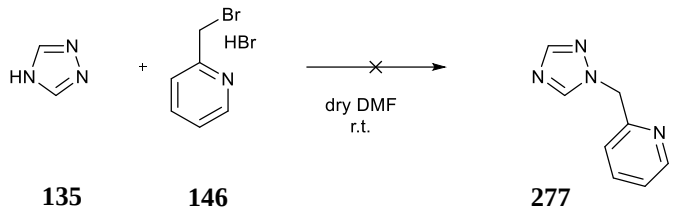

135 **146** **277**

1,2,4-triazole **135** (0.05g, 0.7 mmol) was added to a solution of 2(bromomethyl)pyridine hydrobromide **146** (0.36 g, 1.4 mmol) in dry DMF at room temperature, under an inert atmosphere, and stirred for 72h. The reaction was monitored by LCMS and did not show conversion into the desired product **277**. It was observed, however, that the p*H* of the solution was ~2 as the alkylating agent was commercially sold as the acid salt.

6.7.4 1,2,4-triazole and 2-(bromomethyl)pyridine hydrobromide in *tert*-butoxide

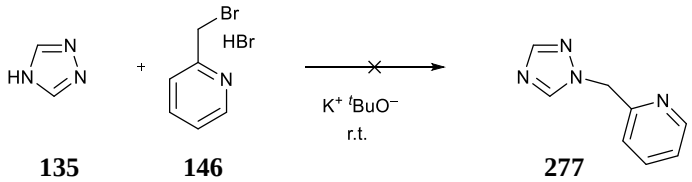

135 **146** **277**

1,2,4-triazole **135** (0.077g, 1.0 mmol) was added to a solution of potassium tert-butoxide (0.12g, 0.9 mmol) in tert-butanol (5 mL) and stirred open to air for 1h at room temperature. 2(bromomethyl)pyridine hydrobromide **146** (0.26 g, 1.0 mmol) was added to a solution of potassium tertiary butoxide (0.13 g, 1.1 mmol) in *tert*-butanol (5 mL) and stirred open to the air, for 1h at room temperature. Both mixtures were added together and mixed thoroughly, and left to stir at room temperature for 72 h. The resulting mixture was concentrated under reduced pressure to yield a yellow liquid and a white gelatinous precipitate. The residue was purified by column chromatography to give a crude pale-yellow oil. Analysis showed the presence of the target compound **277** but purification using silica chromatography 98:2 (DCM:MeOH) from other isomers present was unsuccessful.

6.7.5 1,2,4-triazole and 2-(bromomethyl)pyridine hydrobromide with sodium carbonate

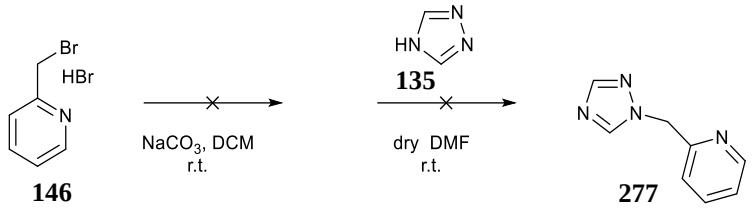

2-Bromomethyl-pyridine hydrobromide **146** (0.53 g, 2.1 mmol) was added to sodium carbonate (0.26 g, 2.4 mmol) in a vial containing DCM (20 mL) and mixed thoroughly. The resulting solution was left standing for 15 minutes and triturated with water (20ml). The organic phase was washed with water (× 20 mL) to ensure complete neutralization of the acid salt. The organic layer was then collected and concentrated under reduced pressure, and added to a solution of 1,2,4-triazole **135** (0.08 g, 1.0 mmol) in dry DMF. The reaction mixture was then left to stir for 72 h. Upon completion, analysis by LCMS suggest the desired alkylation product **277** present in the mixture, but purification by silica chromatography 98:2 (DCM:MeOH) was unsuccessful.

6.7.6 1,2,4-triazole, trimethyloxonium tetrafluoroborate and potassium carbonate

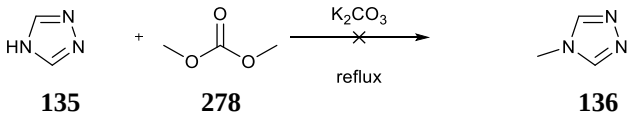

Dimethyl carbonate **278** (5 mL, 59 mmol) was added to a mixture of 1,2,4-triazole **135** (0.58 g, 8.3 mmol) and K_2CO_3 (0.58 g, 4.2 mmol). The resulting suspension was heated under reflux overnight. The reaction mixture was concentrated under reduced pressure to give a white residue however, isolation of the target compound **136** by silica chromatography 98:2 (DCM:MeOH) was unsuccessful.

6.7.7 6,7-dihydro-5*H*-pyrrolo[2,1-c][1,2,4]triazol-2-ium tetrafluoroborate

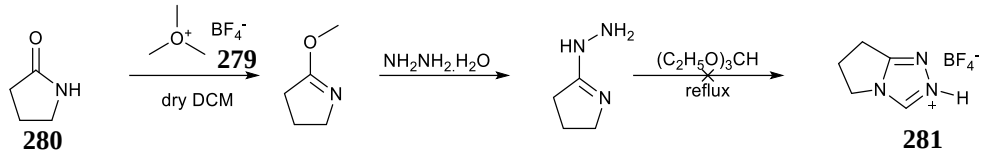

Trimethyloxonium tetrafluoroborate **279** (0.45 g, 3 mmol) was added to a solution of 2-pyrrolidinone **280** (0.24 g, 2.8 mmol) in dry DCM (16 mL) and stirred under argon for 24 h. Hydrazine monohydrate (0.3 mL) was added to the mixture and left to stir for under argon at room temperature for 48h. Upon completion, the mixture was concentrated under reduced pressure to give a residue, which was dissolved in methanol (2.5 mL) and triethyl orthoformate (5 mL, 29.7 mmol), and refluxed for 24 h. Upon completion, the solvent was removed under reduced pressure and the residue washed with ethyl acetate. Analysis of the resulting solid does not suggest the presence of the title compound **281**, hence further purification was not attempted.

6.7.8 6,7-dihydro-5*H*-pyrrolo[2,1-c][1,2,4]triazol-2-ium chloride

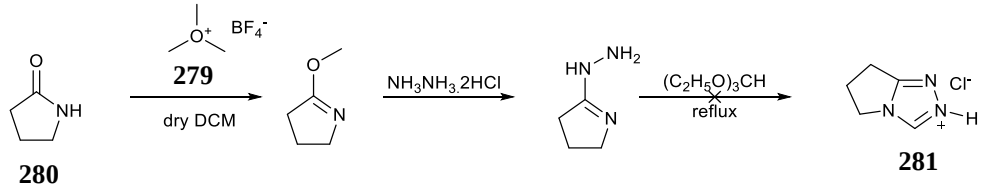

Trimethyloxonium tetrafluoroborate **279** (0.45 g, 3 mmol) was added to a solution of 2-pyrrolidinone **280** (0.24 g, 2.8 mmol) in dry DCM (16 mL) and stirred under argon for 24 h. Hydrazine dihydrochloride (0.31 g, 3.0 mmol) was added to the mixture and left to stir for under argon at room temperature for 48h. Upon completion, the mixture was concentrated under reduced pressure to give a residue which was dissolved in methanol (2.5 mL) and triethyl orthoformate (2.5 mL, 15 mmol) and refluxed for 24 h. Upon completion, the solvent was removed under reduced pressure and the residue washed with ethyl acetate. Analysis of the resulting crude solid does not suggest the presence of the desired product **281**, hence further purification was not attempted.

6.7.9 3,4-dimethyl-4*H*-1,2,4-triazole

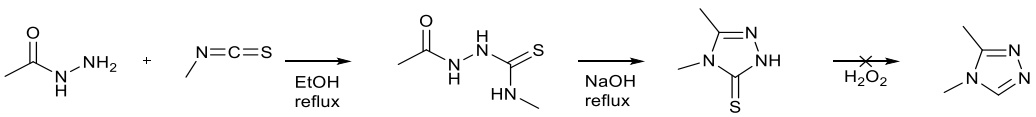

165 **156** **282** **283** **284**

Acethydrazide **165** (74 mg, 1.0 mmol) was added to a solution of methyl isothiocyanate **156** (72 mg, 1.0 mmol) in 5 mL of ethanol. Upon completion, the mixture was concentrated under reduced pressure, then 1.0 M sodium hydroxide (5 mL) added to the residue **282** and refluxed for 10h. Upon cooling the solution was concentrated under reduced pressure to give a white solid **283**. This was dissolved in DCM (5 mL), at 0 °C in an ice bath, and 40% w/w hydrogen peroxide (1 mL) added dropwise over 15 minutes and left to stir for 2 h. After completion of the reaction, monitored by LCMS, the reaction mixture was concentrated under reduced pressure to give an oily residue. Analysis by NMR and LCMS showed the presence of **284**. Further purification by chromatography (98:2 DCM:MeOH) to give the title compound **284** was unsuccessful.

6.7.10 3-(2-methoxyethyl)-4-methyl-4H-1,2,4-triazole

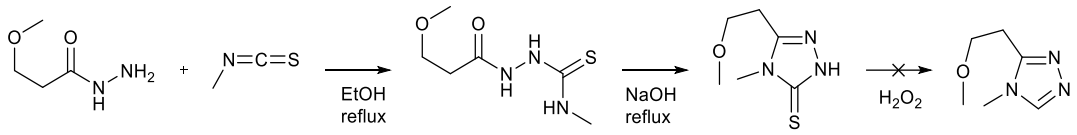

138 **156** **285** **286** **287**

3-Methoxypropanehydrazide **138** (118 mg, 1.0 mmol) was added to a solution of methyl isothiocyanate **156** (72 mg, 1.0 mmol) in 5 mL of ethanol. The mixture was refluxed for 5h. Upon completion, the mixture was concentrated under reduced pressure and 1.0 M sodium hydroxide (5 mL) added to the residue **285** and refluxed for 10h. Upon cooling the solution was concentrated under reduced pressure to give a white solid **286**. This was dissolved in DCM (5 mL), at 0°C in an ice bath, and 40% w/w hydrogen peroxide (1 mL) added dropwise over 15 minutes and left to stir for 2 h. After completion of the reaction, monitored by LCMS, the reaction mixture was concentrated under reduced pressure to give an oily residue. Further purification by chromatography (98:2 DCM:MeOH) to give the title compound **287** was unsuccessful.

6.7.11 1-benzyl-3-(2-methoxyethyl)-4-methyl-4*H*-1,2,4-triazol-1-ium chloride

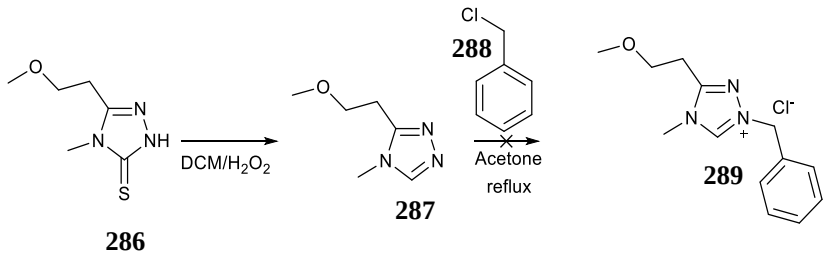

286 **287** **288** **289**

5-(2-methoxyethyl)-4-methyl-2,4-dihydro-3H-1,2,4-triazole-3-thione **286** (0.17g , 1.0 mmol) was dissolved in DCM (5 mL), at 0 °C in an ice bath, and 40% w/w hydrogen peroxide (1 mL) added dropwise over 15 minutes and left to stir for 2 h. After completion of the reaction, monitored by LCMS, the reaction mixture was concentrated under reduced pressure to give an oily residue **287**. The residue was dissolved in acetone and benzyl chloride **288** (1.7 mL, 1.5 mmol) was added dropwise with continuous stirring over 10 minutes and the mixture refluxed for 15h. The reaction was monitored by LCMS and did not suggest the presence of the title compound **289** in the mixture, hence further purification was not attempted.

6.7.12 1-hexyl-3-(2-methoxyethyl)-4-methyl-4H-1,2,4-triazol-1-ium bromide

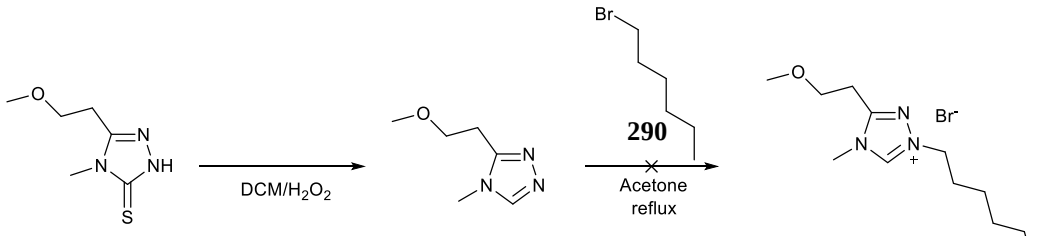

286 **287** **291**

5-(2-methoxyethyl)-4-methyl-2,4-dihydro-3H-1,2,4-triazole-3-thione **286** (0.17g , 1.0 mmol) was dissolved in DCM (5 mL), at 0 °C in an ice bath, and 40% w/w hydrogen peroxide (1 mL) added dropwise over 15 minutes and left to stir for 2 h. After completion of the reaction, monitored by LCMS, the reaction mixture was concentrated under reduced pressure to give an oily residue **287**. The residue was dissolved in acetone and bromohexane **290** (1.4 mL, 1.5 mmol) was added dropwise with continuous stirring over 10 minutes and the mixture refluxed for 15h. The reaction was monitored by LCMS and did not suggest the presence of the title compound **291** in the mixture, hence further purification was not attempted.

6.7.13 1-hexyl-3,4-dimethyl-4H-1,2,4-triazol-1-ium bromide

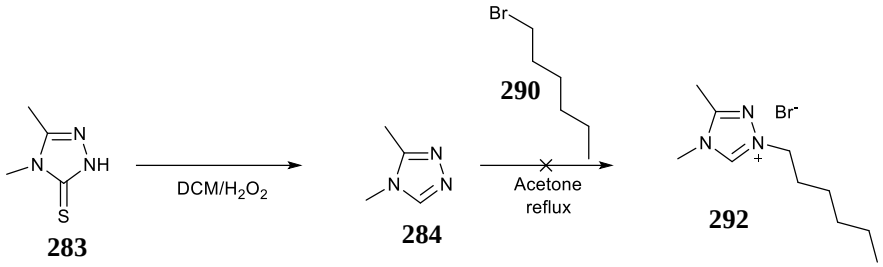

283 **284** **292**

4,5-dimethyl-2,4-dihydro-3H-1,2,4-triazole-3-thione **283** (0.13g , 1.0 mmol) was dissolved in DCM (5 mL), at 0 °C in an ice bath, and 40% w/w hydrogen peroxide (1 mL) added dropwise over 15 minutes and left to stir for 2 h. After completion of the reaction, monitored by LCMS, the reaction mixture was concentrated under reduced pressure to give an oily residue **284**. The residue was dissolved in acetone and bromohexane **290** (1.4 mL, 1.5 mmol) was added dropwise with continuous stirring over 10 minutes and the mixture refluxed for 15h. The reaction was monitored by LCMS and did not suggest the presence of the title compound **292** in the mixture, hence further purification was not attempted.

6.7.14 3-(2-methoxyethyl)-4-methyl-1-(pyridin-2-ylmethyl)-4H-1,2,4-triazol-1-ium bromide

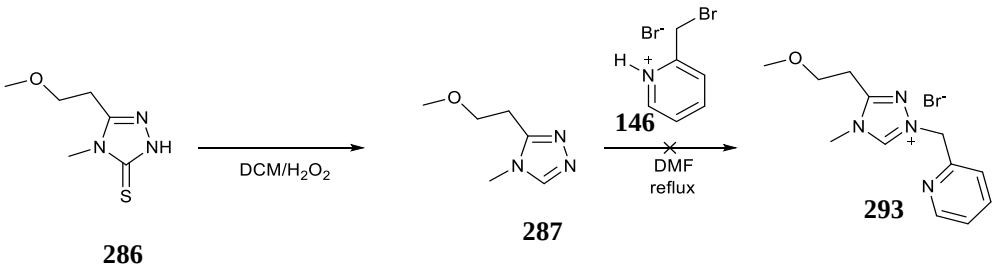

286 **287** **146** **293**

5-(2-methoxyethyl)-4-methyl-2,4-dihydro-3H-1,2,4-triazole-3-thione **286** (0.17g , 1.0 mmol) was dissolved in DCM (5 mL), at 0 °C in an ice bath, and 40% w/w hydrogen peroxide (1 mL) added dropwise over 15 minutes and left to stir for 2 h. After completion of the reaction, monitored by LCMS, the solution was concentrated under reduced pressure to give an oily residue **287**. The residue was dissolved in DMF and 2-(bromomethyl)pyridine hydrobromide **146** (0.25 g, 1.0 mmol) was added portion wise with continuous stirring over 10 minutes and the mixture refluxed for 15h. The reaction was monitored by LCMS and did not suggest the presence of the title compound **293** in the mixture, hence further purification was not attempted.

6.7.15 1,2,4-trimethyl-4H-1,2,4-triazole-1,2-diium ditetrafluoroborate

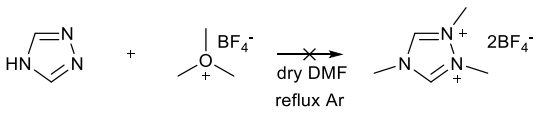

135 **279** **294**

1,2,4-triazole **135** (0.28 g, 4.0 mmol) and trimethyloxonium tetrafluoroborate **279** (0.59 g, 4.0 mmol) in dry DMF (20 mL) were stirred and refluxed under argon overnight. Upon completion, analysis by LCMS did not provide evidence for the presence of the trialkylation product in solution **294**. Purification of the reaction mixture was therefore not attempted.

6.7.16 N'-benzyl-3-hydroxypropanehydrazide

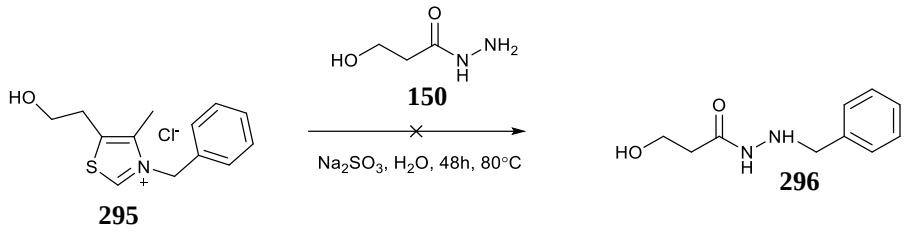

3-benzyl-5-(2-hydroxyethyl)-4-methylthiazol-3-ium chloride **295** (1.0 g, 3.7 mmol), hydrazide **150** (1.0 g, 8.5 mmol) and sodium sulphite (0.04 g, 0.03 mmol) were dissolved in degassed water (30 mL) under argon and stirred at 80 °C for 48h. NMR and LCMS analysis of the reaction mixture shows no perceptible change in concentration of the starting material and no evidence of desired product **296**. The reaction was therefore not pursued any further.

6.7.17 2-(4-methylthiazol-5-yl)ethan-1-ol

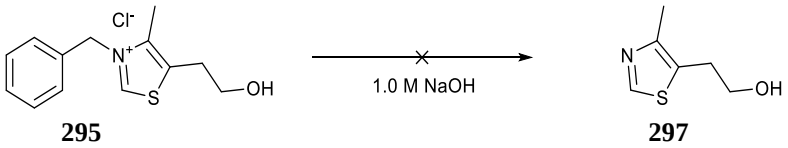

3-benzyl-5-(2-hydroxyethyl)-4-methylthiazol-3-ium chloride **295** (1.0 g, 3.7 mmol) was dissolved in degassed aqueous 1.0 M NaOH (30 mL) and sodium sulphite (0.04 g, 0.03 mmol) stirred for 48h. NMR and LCMS analysis of the reaction mixture shows no perceptible change in concentration of the starting material **295** and no trace of product **297** formation.

6.7.18 Benzyl hydrazine

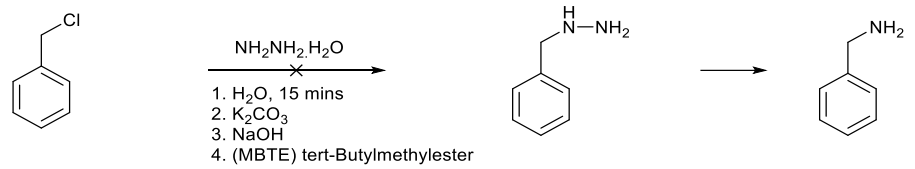

288 **298** **299**

Hydrazine monohydrate 40% w/w (2.0 mL, 26 mmol) was added to a solution Benzyl chloride **288** (1.13 g, 9.0 mmol) of in water (1.0 mL) at room temperature and stirred for 15 mins. Potassium carbonate (2.4 g, 17 mmol) was added and stirred at 40 °C for 24 h. Upon completion, 2.0 g of sodium hydroxide in 8.0 mL of water and 20 mL MBTE (tert-butyl methyl ester) was added with vigorous stirring. The organic layer was separated and concentrated under reduced pressure, and the residue dissolved in hexane (5 mL) and left overnight in the fridge after which crystals were observed. NMR and LCMS analysis of the product suggests it to be phenylmethanamine **299**, from the decomposition of the desired title compound **298** under the reaction conditions.

6.7.19 5-(hydrazineylmethyl)-2-methylpyrimidine

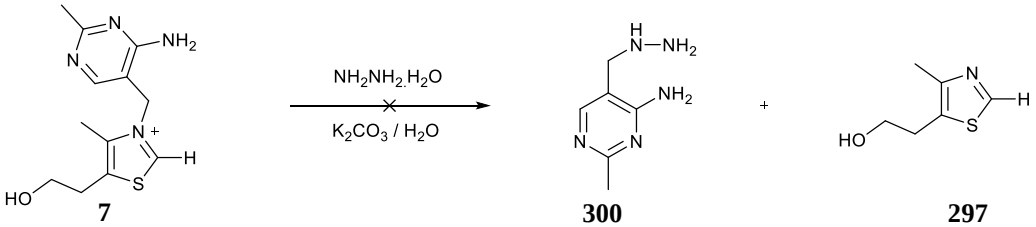

7 **300** **297**

Thiamine **7** (1.0 g, 3.0 mmol) was dissolved in water (30 mL), Hydrazine monohydrate (1.0 mL, 20 mmol) and potassium carbonate (0.7 g, 5.0 mmol) were added and the mixture stirred at room temperature of 24h. Analysis of the reaction mixture showed the disappearance of the starting material, presence of the side product **297** but no trace of the desired title compound **300**.

6.7.20 2-benzyl-6,7-dihydro-5H-pyrrolo[2,1-c][1,2,4]triazol-2-ium chloride

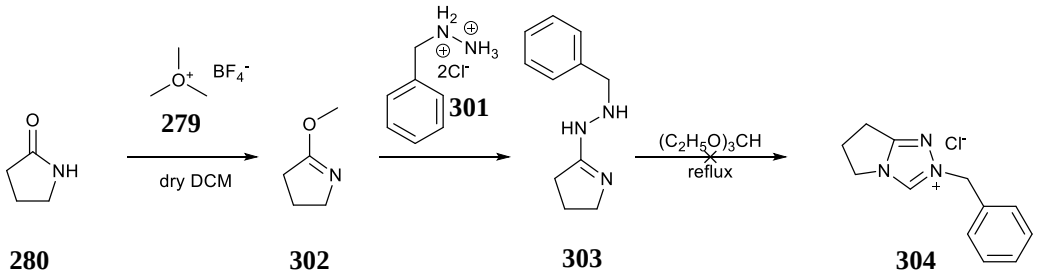

Trimethyloxonium tetrafluoroborate **279** (0.45 g, 3.0 mmol) was added to a solution of 2-pyrrolidinone **280** (0.24 g, 2.8 mmol) in dry DCM (15 mL) and stirred under argon for 24 h. Benzylhydrazine dihydrochloride **301** (0.27 g, 2.2 mmol) was added to the mixture **302** and left to stir under argon at room temperature for 48h. Upon completion, the mixture was concentrated under reduced pressure to give a residue **303**, then dissolved in methanol (2.5 mL) and triethyl orthoformate (2.5 mL, 15 mmol) and refluxed for 24 h. Upon completion, the solvent was removed under reduced pressure and the residue washed with ethyl acetate. Analysis suggests the presence of the title compound **304** in the mixture, however, purification was unsuccessful by chromatography (98:2 DCM:MeOH).

6.7.21 ethyl 3-hydroxypropanoate

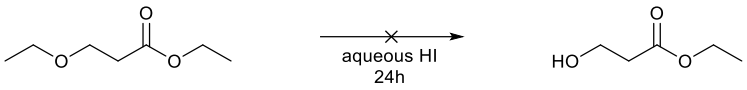

305 **306**

Hydroiodic acid (3.0 mL, 12 mmol) was added dropwise to a solution of ethyl-3-ethoxypropionate **305** (2.0 mL, 12 mmol) at 0 °C, with vigorous stirring. After 24 hours, the reaction mixture was extracted into DCM (3 × 3 mL) and combined organic layers concentrated under reduced pressure to give a dark residue. Analysis of the residue and aqueous phase did not suggest the presence of mostly unreacted starting material and not the title compound **306**, therefore further purification was not attempted.

6.7.22 N'-((4-amino-2-methylpyrimidin-5-yl)methyl)-3-ethoxypropanehydrazide

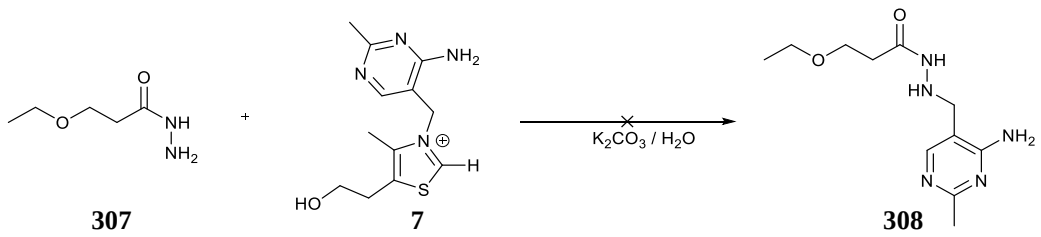

307 **7** **308**

Thiamine hydrochloride **7** (1.0 g, 3.0 mmol) was added to a solution of 3-ethoxypropanehydrazide **307** (0.4 mg, 3 mmol) and potassium carbonate (0.8 g, 6.0 mmol) in distilled water (10 mL) and stirred at room temperature for 48 h. Upon completion, analysis of the reaction mixture did not suggest the formation of the title compound **308**, hence, further purification was not attempted.

6.7.23 5-(iodomethyl)-2-methylpyrimidin-4-amine

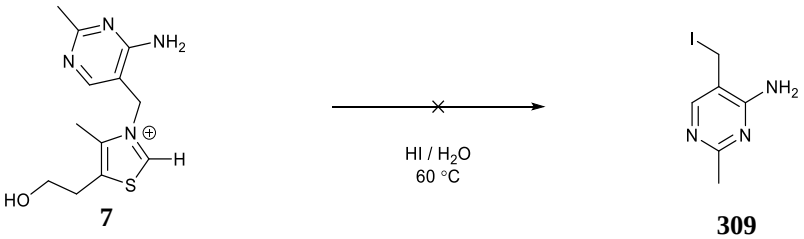

7 **309**

Thiamine hydrochloride **7** (0.34 g, 1.0 mmol) was dissolved in water (5.0 mL) and hydroiodic acid 48% w.w. (1.0 mL) added dropwise. The reaction mixture was stirred at 60 °C for 24h. Analysis of the reaction mixture did not suggest the presence of the title compound **309** nor a decrease in the concentration of the starting material.

6.7.24 N'-benzyl-3-ethoxypropanehydrazide

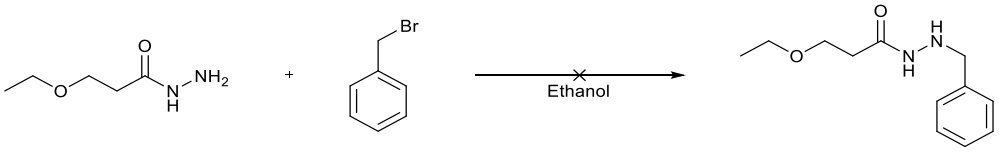

307 **310** **311**

3-Ethoxypropanehydrazide **307** (0.27 g, 2.0 mmol) and benzyl bromide **310** (1.0 mL, 6.0 mmol) were stirred in ethanol (5.0 mL) at 60 °C for 24h. Analysis by NMR and LCMS of the reaction mixture suggested the presence of the target compound **311**, but subsequent purification by chromatography (98:2 DCM:MeOH) was unsuccessful.

6.7.25 N'-((4-amino-2-methylpyrimidin-5-yl)methyl)acetohydrazide

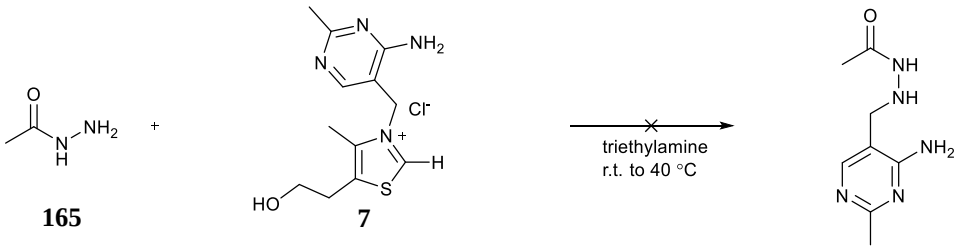

165 **7** **166**

Acetohydrazide **165** (0.07 g, 1.0 mmol) and thiamine chloride **7** (0.33 g, 1.0 mmol) were dissolved in triethylamine (5 mL) and stirred at room temperature to 40 °C for 48 hours. Analysis of the reaction mixture did not suggest the formation of the title compound **166**, hence purification was not attempted.

6.7.26 benzylhydrazine

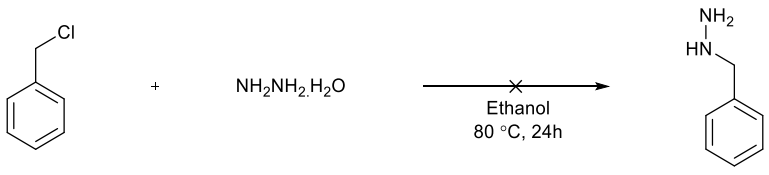

288 **298**

Hydrazine monohydrate (8.0 mL, 160 mmol) was added to ethanol (10 mL) and stirred at 80 °C. Benzyl chloride **288** (2.3 mL, 20 mmol) was added dropwise and left stirring for 24h. Isolation and purification of the crude product **298** by chromatography (98:2 DCM:MeOH) were not successful.

6.7.27 N'-benzyl-3-methoxypropanehydrazide

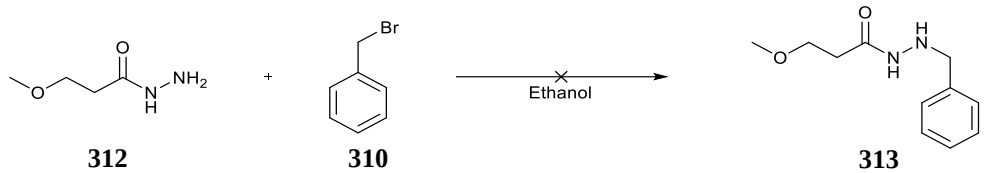

312 **310** **313**

3-Methoxypropanehydrazide **312** (0.24 g, 2.0 mmol) and benzyl bromide **310** (1.0 mL, 6.0 mmol) were stirred in ethanol (5.0 mL) at 60 °C for 24h. Analysis of the reaction mixture suggested the presence of the target compound **313**, but subsequent purification by chromatography (98:2 DCM:MeOH) was unsuccessful.

6.7.28 2-benzyl-5-(2-methoxyethyl)-4-methyl-2,4-dihydro-3H-1,2,4-triazole-3-thione

286 **288** **314**

Thione **286** (0.87 g, 5.0 mmol) was dissolved in DCM (10 mL) and benzyl chloride **288** (0.68 g, 5.0 mmol) added dropwise with continuous stirring at room temperature for 1h. Analysis of the reaction mixture suggested the presence of the target product **314**, however, isolation by chromatography (98:2 DCM:MeOH) was unsuccessful.

6.7.29 2-benzyl-4,5-dimethyl-2,4-dihydro-3*H*-1,2,4-triazole-3-thione

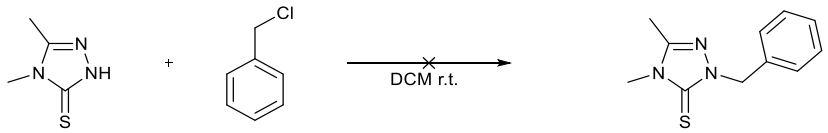

283 **288** **315**

Thione **283** (0.66 g, 5.0 mmol) was dissolved in DCM (10 mL) and benzyl chloride **288** (0.68 g, 5.0 mmol) added dropwise with continuous stirring at room temperature for 1h. Analysis of the reaction mixture suggested the presence of the target product **315**, however, isolation by chromatography (98:2 DCM:MeOH) was unsuccessful.

6.7.30 2-benzyl-5-(2-ethoxyethyl)-4-methyl-2,4-dihydro-3H-1,2,4-triazole-3-thione

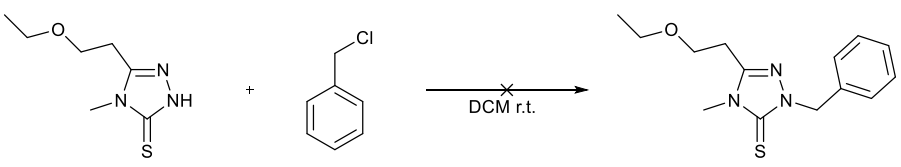

316 **288** **317**

Thione **316** (0.94 g, 5.0 mmol) was dissolved in DCM (10 mL) and benzyl chloride **288** (0.68 g, 5.0 mmol) added dropwise with continuous stirring at room temperature for 1h. Analysis of the reaction mixture suggested the presence of the target product **317**, however, isolation by chromatography (98:2 DCM:MeOH) was unsuccessful.

6.7.31 2-((4-amino-2-methylpyrimidin-5-yl)methyl)-5-(2-ethoxyethyl)-4-methyl-2,4-dihydro-3*H*-1,2,4-triazole-3-thione

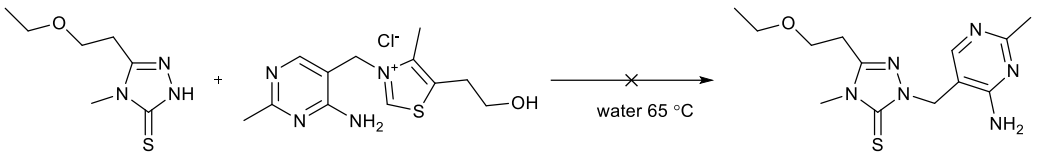

316 **7** **276**

Thione **316** (0.94 g, 5.0 mmol) and thiamine chloride **7** (1.6 g, 5.0 mmol) were dissolved in water (10 mL) and left to stir at 65 °C for 24h. Analysis of the reaction mixture did not suggest conversion to the product **276**.

6.7.32 5-(2-hydroxyethyl)-4-methyl-2,4-dihydro-3H-1,2,4-triazole-3-thione

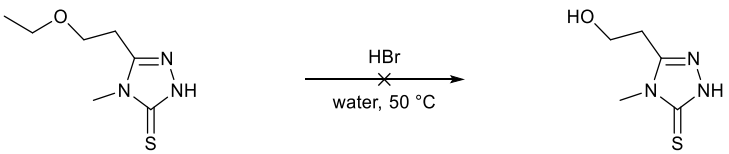

316 **318**

Thione **316** (0.94 g, 5.0 mmol) was dissolved in water (10 mL) and hydrobromic acid (48 w/w % 1.0 ml) added dropwise at room temperature. The reaction mixture was stirred at 50 °C for 24 h. Analysis of the reaction mixture did not suggest the formation of the product **318**.

6.7.33 1-benzyl-2-(3-ethoxypropanoyl)-N-methylhydrazine-1-carbothioamide

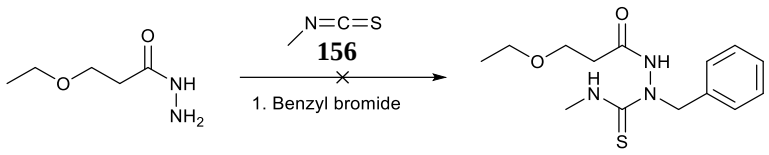

307 **319**

3-Ethoxypropanehydrazide **307** (0.26 g, 2.0 mmol) and benzyl bromide (1.0 mL, 6.0 mmol) were stirred in ethanol (5.0 mL) at 60 °C for 24h. Methylisothiocyanate (0.15 g, 2.0 mmol) was added to the mixture and stirred at room temperature for 24 h. Analysis of the reaction mixture did not suggest the formation of the product **319**.

6.7.34 3-hydroxypropanehydrazide

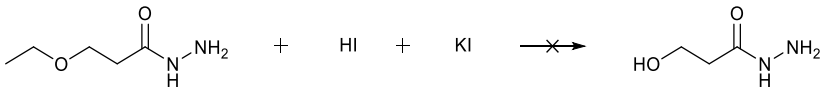

307 **150**

3-Ethoxypropanehydrazide **307** (1.3 g, 10 mmol) was dissolved in a solution of potassium iodide (1.7 g, 10 mmol) and hydroiodic acid (1.0 mL) in water (10.0 mL) and stirred at room

temperature for 24 h. Analysis of the reaction mixture by NMR and LCMS suggested some conversion into product **150**, however, isolation by chromatography (98:2 DCM:MeOH) was unsuccessful.

6.7.35 methyl 3-((trimethylsilyl)oxy)propanoate

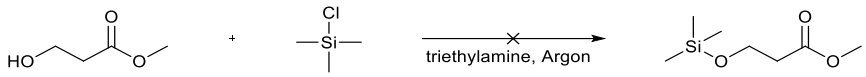

149 **320** **321**

Methyl 3-hydroxypropanoate **149** (0.5 g, 4.2 mmol) was stirred in triethylamine (10 mL) and trimethylsilyl chloride **320** (0.7 g, 6.0 mmol) added portion-wise under argon. The mixture was left to stir for 24h. Analysis of the reaction mixture does not suggest the formation of the target compound **321**.

6.7.36 2-(1-((4-amino-2-methylpyrimidin-5-yl)methyl)-4-methyl-5-thioxo-4,5-dihydro-1H-1,2,4-triazol-3-yl)ethyl 4-methylbenzenesulfonate

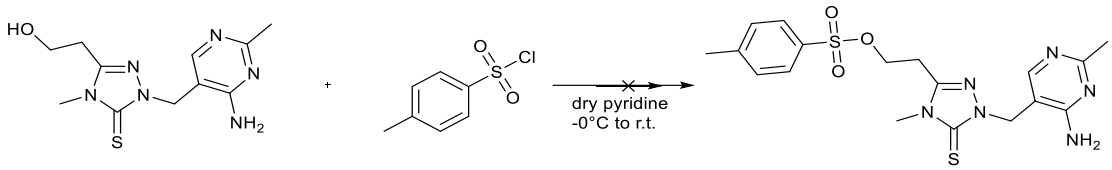

148 **160** **322**

Thione **148** (0.84 g, 3.0 mmol) was dissolved in pyridine (10 mL) at 0 °C and left stirring for 15 minutes. 4-Methylbenzenesulfonyl chloride **160** (2.3 g, 12.0 mmol) was added in portions over 30 mins, under argon, and the mixture left to stir at room temperature for 2h. Analysis of

the reaction mixture suggests the near-complete conversion of starting material to some product, however, isolation of the desired product **322** was by chromatography (98:2 DCM:MeOH) unsuccessful.

6.7.37 1-((4-amino-2-methylpyrimidin-5-yl)methyl)-3-(2-hydroxyethyl)-4-methyl-4H-1,2,4-triazol-1-ium

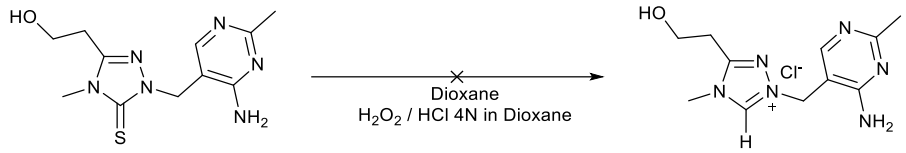

148 **144**

Thione **148** (0.84 g, 3.0 mmol) was dissolved in dioxane (10 mL) and 4N HCl in dioxane (0.1 mL) and stirred at room temperature. Hydrogen peroxide 40 w/w % (1.0 mL, 10 mmol) was added dropwise over 5 mins and stirred at room temperature for 2h. Analysis of the reaction mixture suggested complete conversion into the desired product **144**, however, attempted purification by silica chromatography (98:2 DCM:MeOH) was unsuccessful.

6.7.38 1-((4-amino-2-methylpyrimidin-5-yl)methyl)-3-(3-hydroxypropyl)-4-methyl-4H-1,2,4-triazol-1-ium

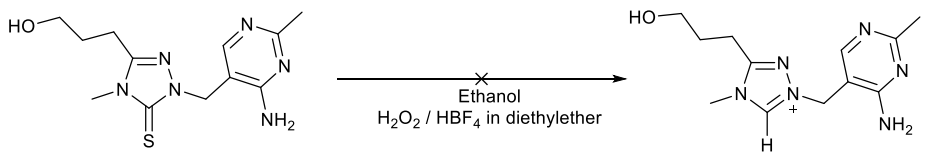

148 **144**

Thione **148** (0.88 g, 3.0 mmol) was dissolved in ethanol (10 mL) and 2M HCl in diethyl ether (0.1 mL) and stirred at room temperature. Hydrogen peroxide 40 w/w % (1.0 mL, 10 mmol) solution in water (1.0 mL, 10 mmol) was added dropwise over 5 mins and stirred at room temperature for 2h. Analysis of the reaction mixture suggested complete conversion into the desired product **144**, however, attempted purification by silica gel chromatography (98:2 DCM:MeOH) was unsuccessful.

6.7.39 1-((4-amino-2-methylpyrimidin-5-yl)methyl)-4-methyl-3-(2-(tosyloxy)ethyl)-4H-1,2,4-triazol-1-ium chloride

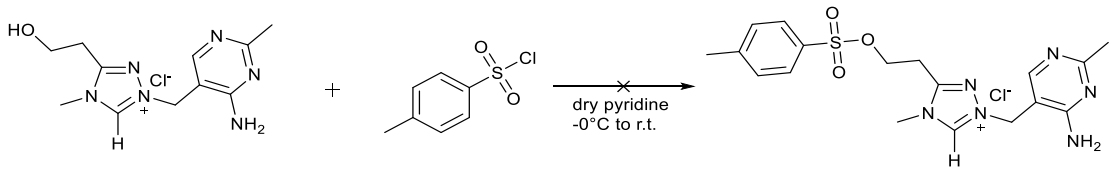

144 **160** **145**

Triazolium salt **144** (0.86 g, 3.0 mmol) was dissolved in pyridine (10 mL) at 0 °C and left stirring for 15 mins. 4-Methylbenzenesulfonyl chloride **160** (2.3 g, 12.0 mmol) was added in portions over 30 mins, under argon, and the mixture left to stir at room temperature for 2h. Analysis of the reaction mixture suggested the near-complete conversion of starting material, however, isolation of the desired product **145**, by silica gel chromatography (98:2 DCM:MeOH) was unsuccessful.

6.7.40 1-((4-amino-2-methylpyrimidin-5-yl)methyl)-5-(hydroxy(2-methoxyphenyl)methyl)-3-(2-hydroxyethyl)-4-methyl-4H-1,2,4-triazol-1-ium

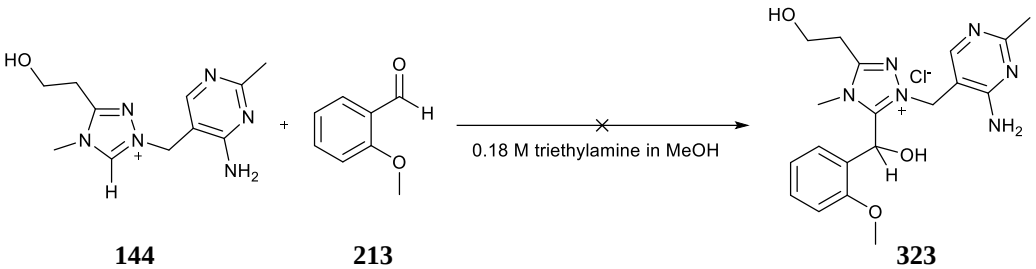

144 **213** **323**

Triazolium salt **144** (0.86 g, 3.0 mmol) was dissolved in triethylamine (2.0 mL) and methanol (10 mL) at room temperature and left stirring for 15 mins. 2-Methoxybenzaldehyde **213** (1.6 g, 12.0 mmol) was added and the mixture left to stir at room temperature for 18h. Analysis of the reaction mixture suggests the near-complete conversion of starting material, however, isolation of the desired product **323**, by silica gel chromatography (98:2 DCM:MeOH) was unsuccessful.

6.7.41 1-((4-amino-2-methylpyrimidin-5-yl)methyl)-3-(2-((hydroxy(phosphonooxy)phosphoryl)oxy)ethyl)-4-methyl-4*H*-1,2,4-triazol-1-ium chloride

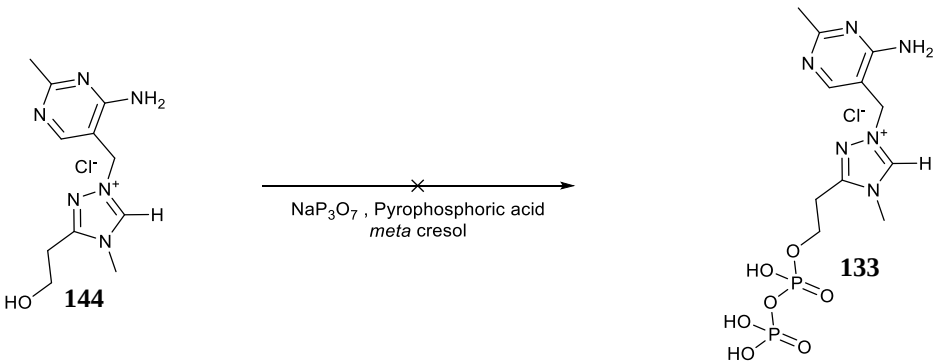

To a stirring solution of triazolium salt **144** (0.05 g, 0.1 mmol) in *m*-cresol (2.0 mL) was added sodium pyrophosphate (0.1g , 0.3 mmol) and polyphosphoric acid (0.1 g) and left stirring at 120 °C for 4h. Analysis of the reaction mixture suggests the formation of the target pyrophosphate **133**, however, subsequent purification by silica gel chromatography (98:2 DCM:MeOH) was unsuccessful.

6.8 Kinetic Section

6.8.1 Preparation of Solutions

DCl solution was prepared by serial dilution from commercially sourced stock solutions and subsequent titration against standard solutions of NaOH. Stock solutions of potassium acetate and potassium formate were prepared by carefully weighing out rigorously dry potassium acetate and dissolving in D_2O. Further mixing with varying amounts of already prepared DCl, and maintaining ionic strength with KCl, to give various buffer solutions at different free base ratios.

6.8.2 p*H*, p*D* instrumentation

All solution used in the exchange studies were maintained at 25 °C measured with a Radiometer Analytical RadioLab® p*H* 210 standard p*H* meter fitted with a radiometer electrode filled with saturated KCl solution. Calibration of the setup is at intervals of 1.6 – 4.0, 4.0 – 7.0 (phosphate), and 7.0 – 10.0 (borate) and 10.0 – 12.45 (saturated calcium chloride). The reading of the pH meter was determined by adding 0.4 to the instrument reading.

Previous work in our group by past PhD student[2] found the activity of coefficient for hydroxide ion (γ_{HO}) for the model of electrode in use to be 0.72 using Equation 6.1 below.

$$10^{(pH-pK_w)} = \gamma_{OH}[OH^-]$$ **Equation 6.1**

6.8.3 Parameters for NMR Spectroscopic Kinetic Experiments

Exchange reactions of all mimics synthesised and studied ^{1}H NMR spectra were normally measured on a 400 MHz spectrometer with parameters set for 4 s acquisition time, 20 s relaxation delay, 8298.8 sweep width and pulse angle of 90 °. Exchange experiments with half-lives shorter than half an hour were thermostated directly in the NMR instrument at 25 °C using a 20 s relaxation delay, 4 s acquisition time, and 32 transients giving a total time of about 13 minutes. Before integration, the spectral overlay were collectively baseline and phase-corrected, using a sixth-order Bernstein polynomial fit and a zero filling to 64K spectrum size using the Mestrenova software.

For H/D exchange experiments, sample peaks were weighted with the peak due to the internal standard (monodeuterated methanol CH_3OD), arbitrarily set to 1000 integral units for ease of comparison.

Fitting of kinetic data was done using Berkerley Madonna fitting software version 10.1.2 and plots were obtained using Kaleidagraph software version 4.5.0.

6.9 References

1. A. J. Fugard, B. K. Thompson, A. M. Z. Slawin, J. E. Taylor and A. D. Smith, *Org. Lett.*, 2015, **17**, 5824-5827.
2. R. S. Massey and A. C. O'Donoghue, Ph.D., Durham University, 2013.

Chapter Seven

7 Conclusion and Future Work

The triazolium mimic of thiamine **144** was successfully prepared and isolated using a novel synthetic route, as this compound has not been previously reported in the literature to the best of our knowledge. Thiamine was used to sacrificially access the intricate 4-aminopyrimidinyl substituent. In addition to the direct triazolium mimic of thiamine, three other analogues were also prepared **183-185**. X-Ray crystal structures were obtained for structural elucidation by employing the use of sodium tetraphenyl borate salt. Following all the syntheses of the novel triazolium mimics, and attempts at pyrophosphorylation at the pendant alcohol linker to access **133**, further work is required to prepare their diphosphate analogues for comparison with TPP **63**. This may be attempted by direct pyrophosphorylation with organic reagents or by using enzyme phosphorylase e.g. thiamin pyrophosphokinase (TK).

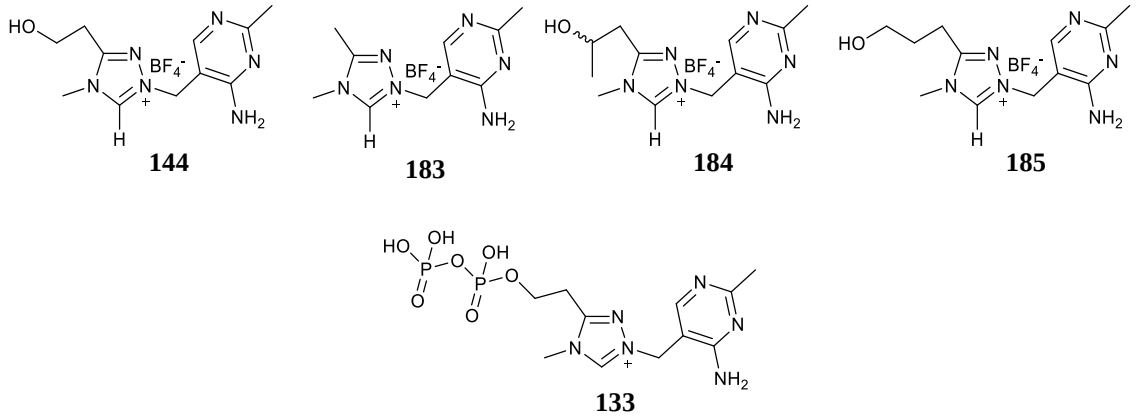

Scheme 7.1 Novel triazolium mimics 144, 183-185 of thiamine and target pyrophosphate mimic 133

Furthermore, during the synthesis of the triazolium mimics, stable thione intermediates were also isolated in the penultimate step (Figure 7.1). These were recrystallized and fully characterized as they have not been previously reported in the literature to the best of our knowledge. The thiones are bench stable under ambient laboratory conditions and samples prepared remained pure and dry in an open sample vial for three years and counting. Pyrophosphorylation may also be attempted using thione **148** as it is relatively stable under basic conditions.

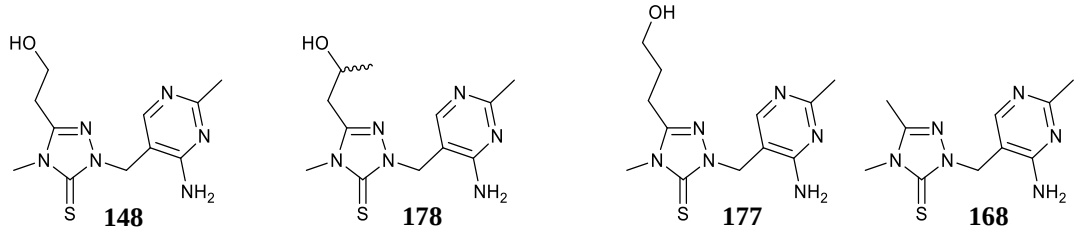

Figure 7.1 Thione intermediates isolated and fully characterized

Carbon acid pK_a values for the novel triazolium based mimics **144, 183-185** have been determined using a kinetic H/D exchange method. The pseudo first order rate constants k_{ex} (s^{-1}) for exchange were estimated using ^{1}H NMR spectroscopy. Second-order rate constants for deuteroxide ion catalysed exchange (k_{DO}, M^{-1} s^{-1}) were obtained from the slope of the plot of k_{ex} against deuteroxide concentration, which are referred to as kinetic acidities or protofugalities. Experimental evidence was used to establish the absence of general base catalysis by analysis of H/D exchange in a range of formic acid buffer concentrations at the same buffer ratio. This informed the decision to remove the term for contributions to exchange from buffer catalysis and hence values for k_{DO} may be calculated.

The triazolium based mimics **144, 183-185** show a fifteen-fold increase in acidity towards deuteroxide ion compared to native thiamine **7**. This is due to the presence of two extra ring nitrogen atoms which favours the stability of the carbene/ylide. Interestingly, the simple di-methyl triazolium salt **212** studied showed a much lower acidity to the triazolium mimics of thiamine, which suggest the N2-methylpyrimidinyl substituent to be electron-withdrawing, hence the observed lower pK_a for all the direct triazolium mimics. The N-phenyl triazolium salt previously studied in the group showed similar kinetic acidities compared to the novel mimics which suggest similar effects between the N2-phenyl and the N2CH_2-pyrimidinyl

substituent. This is an important observation as it shows the triazolium mimics have closely similar acidity to one of the most widely used and versatile triazolium organocatalysts.

The p*D* rate profiles indicate that more data point in the range below zero may be acquired to give more complete representation of the behaviour of the mimics under acidic conditions where alternative H/D exchange pathways may be observed. Hence further work is required to probe the behaviour of these salts under strongly acidic conditions although this is not necessary for organocatalysis or enzymatic catalysis, which operate under neutral or mildly basic conditions.

The reactions of the triazolium mimics with a range of typical aldehydes used in NHC-transformations were then explored (Scheme 7.2). Analysis of the ^{1}H NMR spectra obtained from the catalytic evaluation of the triazolium mimics show the presence of the hydroxyaryl adduct in the reaction mixture in all cases. Isolation and purification for unambiguous characterization is therefore required in future work. Recrystallization to establish the stereochemistry at the tetrahedral carbon of the adduct is desirable and may be attempted under acidic conditions. Scheme 7.3 shows the target hydroxy aryl adducts **245 - 250** identified during analysis to give rate and equilibrium constants for formation.

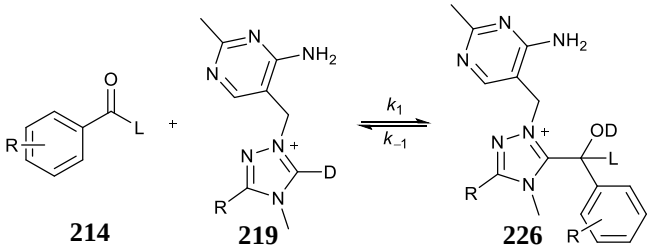

Scheme 7.2 Formation of hydroxyaryl adduct from reaction between triazolium mimic 219 and generic substituted aldehyde 214

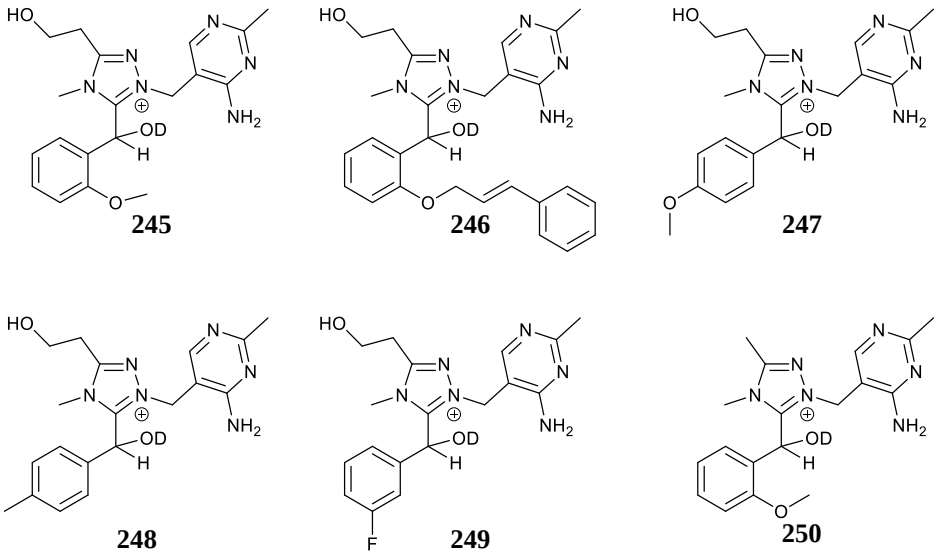

Scheme 7.3 Target hydroxyaryl adducts 245 - 250

Upon successful synthesis of the hydroxyaryl adducts, **245 - 250**, rate constants for dissociation of the adduct to give the aldehyde and catalyst may be accessed and compared with those initially obtained from approaching the equilibrium in the forward direction (Scheme 7.4). This would serve to establish the accuracy of the values obtained by both methods.

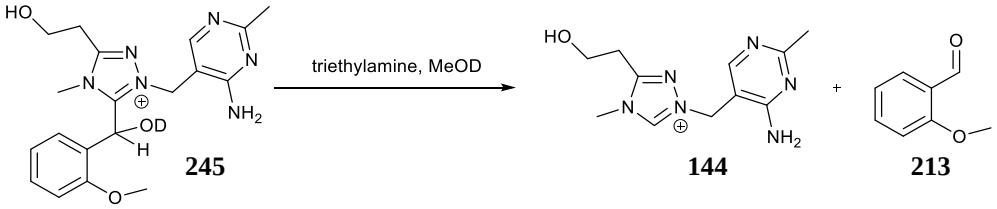

Scheme 7.4 Dissociation kinetics of hydroxyaryl adduct 245

Values of k_1, k_{-1} and K for reactions between novel triazolium mimics **144** and **183** were determined by analysis of changes in species concentration on approach to equilibrium. In addition, using global fitting software, values of forward, reverse and equilibrium constants were estimated from fitting reaction data. The 2-hydroxyethyl triazolium mimic **144** consistently gave larger forward rate constants across the board compared to

thiamine **7**. In addition, the 2-subtituent effect previously observed and reported by our group was found to hold true for the new mimics prepared in this work especially with ortho substrate **213**.

More work is required to screen a broader range of substrate aldehydes with the new precatalysts to probe for further biomimetic transformation.

In silico binding studies of TPP dependent enzymes using crystal structures from the protein data bank have been reported using docking software. The results demonstrate the potential for the new diphosphate mimic to hydrogen bond using its N1 atom at the active site of TPP dependent enzymes. To confirm this, it may be beneficial to probe actual binding using cultured enzymes expressed from plasmid genes and the isolation of crystal structures of the mimic bound within the protein scaffold in comparison with TPP (Figure 7.2) would be desirable although challenging.

Figure 7.2 Crystal structure of TPP at active site of human pyruvate dehydrogenase 3EXE showing manganese cation in purple

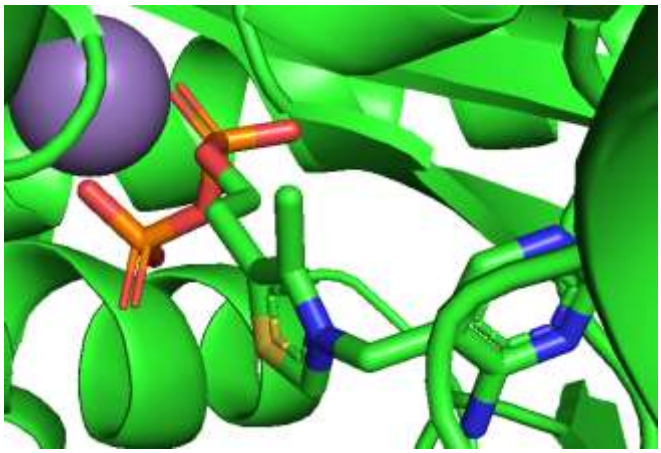

Once binding of the triazolium mimic at the active site has been achieved, catalytic activity may be probed using range of aldehydic substrates to obtain enzyme reaction rates using the Michaelis-Menten equation. Triazolium and thiazolium organocatalysts show different chemoselectivities in a range of transformations and triazoliums demonstrate a broader reaction

scope. It is hoped that the diverse chemistry of triazolium organocatalysts can be harnessed at TPP-dependent enzyme active sites.

Acknowledgements

Above all, I would sincerely like to thank my supervisor, AnnMarie O'Donoghue, for her expert knowledge and guidance over the past three years and eight months. She has been a helpful and kind supervisor. Thanks also to the academic and technical staff who helped to obtain all the NMR and X-ray crystallography data. In addition, I would like to thank all past and present members of the O'Donoghue group and CG115 for their kindness throughout the years. Finally, I would like to thank my mum and dad for their love and support.

8 Appendix

APPENDIX A

A1 Determination of pseudo first-order rate constants for exchange (k_{ex})

Table A.1 Reaction data and first-order rate constants for exchange of the C(3)-H of triazolium salt 144 for deuterium in D_2O solution at 25 °C and I = 1.0 (KCl)

[DCl], M	[DO^-][a], M	time, s	f(s)[b]	ln f(s)	k_{ex}, s^{-1}
		0	1.000	0	
		2.27×10^{04}	0.909	−0.095	
0.08	2.27×10^{-14}	8.40×10^{04}	0.820	−0.199	1.92×10^{-6}
	pD 1.09	1.91×10^{05}	0.645	−0.439	
		3.53×10^{05}	0.479	−0.735	
		4.46×10^{05}	0.403	−0.908	
		5.44×10^{05}	0.333	−1.101	
		0	1.000	0	
		2.07×10^{4}	0.887	−0.120	
0.038	4.86×10^{-14}	8.37×10^{4}	0.688	−0.374	4.04×10^{-6}
	pD 1.42	1.91×10^{5}	0.427	−0.850	
		2.60×10^{5}	0.332	−1.102	
		3.53×10^{5}	0.226	−1.488	
		4.46×10^{5}	0.159	−1.837	
		5.44×10^{5}	0.110	−2.205	
		0	1.000	0.000	
0.016	1.19×10^{-13}	1.45×10^{4}	0.846	−0.167	1.02×10^{-5}
	pD 1.81	8.02×10^{4}	0.412	−0.886	
		9.83×10^{4}	0.349	−1.052	
		1.91×10^{5}	0.133	−2.016	
		2.61×10^{5}	0.071	−2.645	
		0	1.000	0	
0.005	3.69×10^{-13}	6.06×10^{3}	0.834	−0.182	2.88×10^{-5}
	pD 2.30	8.22×10^{3}	0.775	−0.255	

		1.08×10^{4}	0.724	−0.324	
		1.81×10^{4}	0.582	−0.540	
		8.02×10^{4}	0.098	−2.321	
		0	1.000	0	
		7.68×10^{2}	0.915	−0.088	
0.0016	1.17×10^{-12}	1.54×10^{3}	0.836	−0.180	9.85×10^{-5}
	p*D* 2.80	2.30×10^{3}	0.781	−0.248	
		3.07×10^{3}	0.722	−0.326	
		3.84×10^{3}	0.668	−0.403	
		4.61×10^{3}	0.637	−0.450	
		5.38×10^{3}	0.577	−0.549	
		6.14×10^{3}	0.542	−0.612	
		6.91×10^{3}	0.511	−0.672	
		7.68×10^{3}	0.473	−0.748	
		8.45×10^{3}	0.440	−0.821	
		9.22×10^{3}	0.401	−0.915	
		9.98×10^{3}	0.380	−0.967	
		1.08×10^{4}	0.356	−1.032	
		1.15×10^{4}	0.320	−1.138	
		1.23×10^{4}	0.300	−1.205	
		1.31×10^{4}	0.278	−1.280	
		1.38×10^{4}	0.263	−1.336	
		0	1.000	0	
0.001	1.40×10^{-12}	3.36×10^{3}	0.683	−0.381	1.02×10^{-4}
	p*D* 2.88	6.18×10^{3}	0.514	−0.666	
		8.40×10^{3}	0.411	−0.890	
		1.12×10^{4}	0.314	−1.159	
		1.51×10^{4}	0.211	−1.557	
		0	1.000	0	
0.0008	2.02×10^{-12}	7.68×10^{2}	0.888	−0.118	
	p*D* 3.04	1.54×10^{3}	0.765	−0.267	1.64×10^{-4}
		2.30×10^{3}	0.689	−0.373	
		3.07×10^{3}	0.593	−0.522	
		3.84×10^{3}	0.537	−0.622	
		4.61×10^{3}	0.475	−0.745	
		5.38×10^{3}	0.415	−0.879	

		6.14×10^3	0.361	−1.020	
		0	1.000	0	
		7.68×10^2	0.879	−0.128	
0.0008	2.27×10^{-14}	1.54×10^3	0.760	−0.274	1.80×10^{-4}
	p*D* 3.10	2.30×10^3	0.666	−0.407	
		3.07×10^3	0.575	−0.553	
		3.84×10^3	0.508	−0.677	
		4.61×10^3	0.434	−0.835	
		5.38×10^3	0.376	−0.978	
		6.14×10^3	0.336	−1.092	
		6.91×10^3	0.290	−1.238	
		7.68×10^3	0.253	−1.375	
		0	1.000	0	
		7.68×10^2	0.778	−0.251	
0.0006	3.14×10^{-12}	1.54×10^3	0.644	−0.440	2.40×10^{-4}
	p*D* 3.23	2.30×10^3	0.555	−0.589	
		3.07×10^3	0.453	−0.791	
		3.84×10^3	0.370	−0.995	
		4.61×10^3	0.303	−1.193	
		5.38×10^3	0.266	−1.324	
		6.14×10^3	0.219	−1.518	
		6.91×10^3	0.185	−1.687	
		7.68×10^3	0.151	−1.889	
		0	1.000	0	
		7.68×10^2	0.698	−0.375	
0.0004	5.09×10^{-12}	1.54×10^3	0.485	−0.742	4.55×10^{-4}
	p*D* 3.44	2.30×10^3	0.333	−1.123	
		3.07×10^3	0.243	−1.444	
		3.84×10^3	0.177	−1.736	
		4.61×10^3	0.113	−2.197	
		5.38×10^3	0.086	−2.473	
		6.14×10^3	0.063	−2.790	
		6.91×10^3	0.042	−3.181	

(a) Deuteroxide ion concentration calculated using Equation 3.9 (b) Proportion of unexchanged salt calculated using Equation 3.7 (c) Gradient of the plot of ln *f*(s) versus time gave pseudo-first order rate constant for exchange, k_{ex} (s^{-1})

Table A.2 Reaction data and first-order rate constants for exchange of the C(3)-H of triazolium salt 183 for deuterium in D_2O solution at 25 °C and I = 1.0 (KCl)

[DCl], M	$[DO^-]^a$, M	time, s	$f(s)^b$	ln $f(s)$	k_{ex}, s^{-1} ^{c}
		0	1.000	0	
0.11	1.61×10^{-14}	1.72×10^5	0.715	−0.336	1.13×10^{-6}
	pD = 0.94	4.20×10^5	0.547	−0.603	
		1.20×10^6	0.242	−1.418	
		1.46×10^6	0.177	−1.731	
		0	1.000	0	
0.078	2.83×10^{-14}	8.15×10^4	0.834	−0.181	2.59×10^{-6}
	pD = 1.11	1.91×10^5	0.605	−0.502	
		2.59×10^5	0.505	−0.684	
		4.38×10^5	0.324	−1.127	
		5.07×10^5	0.273	−1.299	
0.031	2.55×10^{-12}	0	1.000	0	8.40×10^{-6}
	pD = 1.51	1.56×10^4	0.848	−0.165	
		1.79×10^5	0.210	−1.563	
		2.44×10^5	0.130	−2.039	
		0	1.000	0	
		7.68×10^2	0.930	−0.072	
		1.54×10^3	0.853	−0.159	
		2.30×10^3	0.794	−0.231	
0.0017	1.06×10^{-12}	3.07×10^3	0.694	−0.366	1.30×10^{-4}
	pD = 2.76	3.84×10^3	0.637	−0.452	

		4.61×10^3	0.560	−0.580	
		5.38×10^3	0.510	−0.673	
		6.14×10^3	0.491	−0.712	
		6.91×10^3	0.471	−0.754	
		7.68×10^3	0.368	−0.998	
		8.45×10^3	0.357	−1.031	
		9.22×10^3	0.320	−1.139	
		9.98×10^3	0.289	−1.240	
		1.08×10^4	0.265	−1.330	
		1.15×10^4	0.244	−1.411	
		1.23×10^4	0.214	−1.541	
		1.31×10^4	0.182	−1.701	
		1.38×10^4	0.172	−1.760	
		1.46×10^4	0.148	−1.909	
		1.54×10^4	0.158	−1.848	
		1.61×10^4	0.144	−1.936	
		0	1.000	0	
		7.68×10^2	0.759	−0.276	
0.0007	2.55×10^{-12}	1.54×10^3	0.714	−0.337	2.61×10^{-3}
	pD = 3.14	2.30×10^3	0.593	−0.523	
		3.07×10^3	0.460	−0.777	
		3.84×10^3	0.318	−1.146	
		4.61×10^3	0.306	−1.184	
		5.38×10^3	0.250	−1.388	
		6.14×10^3	0.182	−1.703	
		6.91×10^3	0.178	−1.726	

(a) Deuteroxide ion concentration calculated using Equation 3.9 (b) Proportion of unexchanged salt calculated using Equation 3.7 (c) Gradient of the plot of ln f(s) versus time gave pseudo-first order rate constant for exchange, k_{ex} (s^{-1})

Table A.3 Reaction data and first-order rate constants for exchange of the C(3)-H of triazolium salt 184 for deuterium in D_2O solution at 25 °C and I = 1.0 (KCl)

[DCl], M	[DO^-][a], M	time, s	f(s)[b]	ln f(s)	k_{ex}, s^{-1}
		0	1.000	0	
0.08	2.27×10^{-14}	1.05×10^5	0.815	−0.203	1.83×10^6
	pD 1.09	2.56×10^5	0.612	−0.489	
		3.28×10^5	0.535	−0.624	
		4.25×10^5	0.447	−0.803	
		1.13×10^6	0.126	−2.064	
		0	1.000	0	
0.015	1.22×10^{-13}	1.00×10^5	0.827	−1.438	9.57×10^6
	pD 1.82	2.51×10^5	0.201	−3.034	
		3.24×10^5	0.044	−3.588	
		4.21×10^5	0.011	−3.954	
		0	1.000	0	
0.008	2.38×10^{-13}	1.13×10^4	0.827	−0.188	1.80×10^5
	pD 2.11	7.70×10^5	0.201	−1.601	
		1.54×10^5	0.044	−3.118	
		2.52×10^5	0.011	−4.437	
		0	1.000	0	
0.0035	5.21×10^{-13}	1.13×10^4	0.638	−0.448	4.60×10^5
	pD 2.45	7.69×10^4	0.029	−3.509	
		1.54×10^5	0.011	−4.423	
		2.52×10^5	0.008	−4.776	
		4.46×10^5	0.015	−4.173	
		0	1.000	0	

0.0008	2.38×10^{-12}	7.67×10^{2}	0.880	−0.127	1.84×10^{4}
	p*D* 3.11	1.54×10^{3}	0.755	−0.280	
		2.34×10^{3}	0.663	−0.409	
		3.07×10^{3}	0.566	−0.567	
		3.84×10^{3}	0.487	−0.717	
		4.61×10^{3}	0.426	−0.851	
		5.38×10^{3}	0.363	−1.012	
		6.14×10^{3}	0.304	−1.189	
		6.91×10^{3}	0.278	−1.279	
		7.68×10^{3}	0.243	−1.410	
		8.45×10^{3}	0.220	−1.510	
		9.22×10^{3}	0.177	−1.728	
		9.98×10^{3}	0.163	−1.812	
		1.08×10^{5}	0.164	−1.805	
		1.15×10^{5}	0.124	−2.081	

(a) Deuteroxide ion concentration calculated using Equation 3.9 (b) Proportion of unexchanged salt calculated using Equation 3.7 (c) Gradient of the plot of ln *f*(s) versus time gave pseudo-first order rate constant for exchange, k_{ex} (s^{-1})

Table A.4 Reaction data and first-order rate constants for exchange of the C(3)-H of triazolium salt 185 for deuterium in D_2O solution at 25 °C and *I* = 1.0 (KCl)

[DCl], M	**$[DO^-]^a$, M**	**time, s**	***f*(s)[b]**	**ln *f*(s)**	**k_{ex}, s^{-1}**
		0	1.000	0	
0.15	1.25×10^{-14}	9.01×10^{4}	0.875	−0.134	1.00×10^{-6}
	p*D* 0.83	1.57×10^{5}	0.879	−0.129	

		2.36×10^{5}	0.752	−0.285	
		3.21×10^{5}	0.753	−0.284	
		4.95×10^{5}	0.644	−0.440	
		5.83×10^{5}	0.545	−0.608	
		6.70×10^{5}	0.511	−0.671	
		7.59×10^{5}	0.471	−0.752	
		1.11×10^{6}	0.326	−1.122	
		1.28×10^{6}	0.273	−1.298	
		0	1.000	0	
0.007	2.55×10^{-13}	1.47×10^{4}	0.435	−0.832	2.57×10^{-5}
	p*D* 2.24	2.07×10^{4}	0.378	−0.973	
		7.37×10^{4}	0.115	−2.166	
		1.07×10^{5}	0.051	−2.969	
		0	1.000	0	
0.0033	5.58×10^{-13}	3.24×10^{3}	0.877	−0.131	4.46×10^{-5}
	p*D* 2.48	5.24×10^{3}	0.781	−0.247	
		8.91×10^{3}	0.702	−0.354	
		1.16×10^{4}	0.622	−0.475	
		1.44×10^{4}	0.427	−0.851	
		7.47×10^{4}	0.036	−3.327	
		5.17×10^{5}	0.026	−3.662	
		0	1.000	0	
0.0026	7.03×10^{-13}	4.41×10^{3}	0.804	−0.218	5.56×10^{-5}
	p*D* 2.58	6.94×10^{3}	0.692	−0.368	
		1.33×10^{4}	0.465	−0.766	
		1.53×10^{4}	0.426	−0.852	

		2.79×10^4	0.210	−1.559	
		0	1.000	0	
0.0021	8.64×10^{-13}	2.98×10^3	0.799	−0.224	6.92×10^{-5}
	p*D* 2.67	6.30×10^3	0.622	−0.474	
		7.62×10^3	0.551	−0.596	
		8.84×10^3	0.560	−0.580	
		9.93×10^3	0.506	−0.682	
		2.40×10^4	0.187	−1.679	
		6.83×10^4	0.020	−3.930	

(a) Deuteroxide ion concentration calculated using Equation 3.9 (b) Proportion of unexchanged salt calculated using Equation 3.7 (c) Gradient of the plot of ln *f*(s) versus time gave pseudo-first order rate constant for exchange, k_{ex} (s^{-1})

Table A.5 Reaction data and first-order rate constants for exchange of the C(2)-H of thiamine mononitrate 7-Cl for deuterium in D_2O solution at 25 °C and *I* = 1.0 (KCl)

[DCl], M	**[DO^-]^a, M**	**time, s**	***f*(s)^b**	**ln *f*(s)**	**k_{ex}, s^{-1}**
0.06	3.14×10^{-14}	0	1.000	0	1.02×10^{-7}
	p*D* 1.23	3.60×10^5	0.972	−0.029	
		1.04×10^6	0.901	−0.105	
		1.01×10^7	0.201	−1.603	

0.03	6.41×10^{-14}	0	1.000	0	2.01×10^{-7}
	p*D* 1.54	2.33×10^{5}	0.964	−0.036	
		1.04×10^{6}	0.814	−0.206	
		1.01×10^{7}	0.133	−2.019	
		0	1.000	0	
0.005	3.44×10^{-13}	1.50×10^{5}	0.815	−0.204	1.02×10^{-6}
	p*D* 2.27	2.33×10^{5}	0.757	−0.279	
		3.55×10^{5}	0.691	−0.370	
		7.01×10^{5}	0.472	−0.751	
		1.04×10^{6}	0.339	−1.081	
		0	1.000	0	
		1.47×10^{4}	0.960	−0.041	
0.0035	4.54×10^{-13}	2.07×10^{4}	0.975	−0.026	1.68×10^{-6}
	p*D* 2.39	7.37×10^{4}	0.911	−0.093	
		1.07×10^{5}	0.853	−0.159	
		1.72×10^{5}	0.768	−0.264	
		2.53×10^{5}	0.645	−0.438	
		3.41×10^{5}	0.567	−0.568	
		4.27×10^{5}	0.486	−0.722	
		5.14×10^{5}	0.440	−0.822	
		6.04×10^{5}	0.356	−1.032	
		0	1.000	0	
0.0014	1.34×10^{-12}	1.74×10^{4}	0.932	−0.070	4.47×10^{-6}
	pD 2.86	7.47×10^{4}	0.669	−0.403	
		1.63×10^{5}	0.439	−0.824	
		5.17×10^{5}	0.099	−2.314	

		6.11×10^5	0.063	−2.772	
		0	1.000	0	
0.001	1.76×10^{-12}	8.44×10^4	0.641	−0.445	5.18×10^{-6}
	pD 2.98	9.92×10^4	0.576	−0.551	
		1.50×10^5	0.450	−0.799	
		1.70×10^5	0.410	−0.892	
		2.33×10^5	0.286	−1.252	
		3.28×10^5	0.174	−1.746	
		3.55×10^5	0.155	−1.865	
		7.01×10^5	0.026	−3.633	
		0	1.000	0	
		2.98×10^3	0.972	−0.028	
0.0009	2.03×10^{-12}	6.32×10^3	0.953	−0.048	5.59×10^{-6}
	p*D* 3.04	2.40×10^4	0.910	−0.094	
		6.83×10^4	0.605	−0.503	
		1.51×10^5	0.421	−0.864	
		2.47×10^5	0.245	−1.407	
		3.28×10^5	0.141	−1.956	
		4.15×10^5	0.088	−2.435	
		5.02×10^5	0.051	−2.977	
		5.89×10^5	0.041	−3.204	
		6.79×10^5	0.024	−3.720	
		7.62×10^5	0.013	−4.322	

(a) Deuteroxide ion concentration calculated using Equation 3.9 (b) Proportion of unexchanged salt calculated using Equation 3.7 (c) Gradient of the plot of ln *f*(s) versus time gave pseudo-first-order rate constant for exchange, k_{ex} (s^{-1})

Table A.6 Reaction data and first-order rate constants for exchange of the C(2)-H of thiamine mononitrate 7-NO_3 for deuterium in D_2O solution at 25 °C and I = 1.0 (KCl)

[DCl], M	[DO^-][a], M	time, s	f(s)[b]	ln f(s)	k_{ex}, s^{-1}
		0	1.000	0	
0.007	2.55×10^{-13}	9.89×10^{4}	0.938	−0.064	8.12×10^{-7}
	p*D* 2.14	1.39×10^{5}	0.934	−0.068	
		2.53×10^{5}	0.854	−0.158	
		3.45×10^{5}	0.733	−0.311	
		6.89×10^{5}	0.588	−0.530	
		1.02×10^{6}	0.472	−0.750	
		1.39×10^{6}	0.322	−1.133	
		1.63×10^{6}	0.269	−1.315	
		0	1.000	0	
0.002	8.64×10^{-13}	7.37×10^{4}	0.830	−0.186	2.76×10^{-6}
	p*D* 2.67	1.72×10^{5}	0.631	−0.461	
		2.53×10^{5}	0.492	−0.710	
		3.41×10^{5}	0.366	−1.005	
		4.27×10^{5}	0.302	−1.198	
		5.14×10^{5}	0.257	−1.358	
		6.04×10^{5}	0.190	−1.661	
		6.87×10^{5}	0.148	−1.912	
		8.70×10^{5}	0.093	−2.380	
		1.04×10^{6}	0.050	−2.998	
		1.13×10^{6}	0.049	−3.026	
		0	1.000	0	

0.0014	1.31×10^{-12}	2.13×10^{4}	0.921	−0.082	4.00×10^{-6}
	p*D* 2.85	6.58×10^{4}	0.771	−0.260	
		9.26×10^{4}	0.706	−0.349	
		1.57×10^{5}	0.535	−0.625	
		1.77×10^{5}	0.498	−0.698	
		2.44×10^{5}	0.421	−0.866	
		2.72×10^{5}	0.345	−1.063	
		6.16×10^{5}	0.084	−2.478	
0.0007	2.49×10^{-12}	0	1.000	0	7.59×10^{-6}
	p*D* 3.13	1.74×10^{4}	0.889	−0.118	
		7.47×10^{4}	0.556	−0.587	
		1.63×10^{5}	0.272	−1.302	
		5.17×10^{5}	0.020	−3.921	
		6.12×10^{5}	0.006	−5.166	
0.0007	2.67×10^{-12}	0	1.000	0	8.16×10^{-6}
	p*D* 3.16	7.33×10^{4}	0.536	−0.624	
		9.46×10^{4}	0.452	−0.794	
		1.39×10^{5}	0.303	−1.195	
		1.66×10^{5}	0.248	−1.395	
		2.31×10^{5}	0.149	−1.905	
		2.51×10^{5}	0.131	−2.035	
		0	1.000	0	
0.0005	3.52×10^{-12}	2.98×10^{3}	0.970	−0.031	1.06×10^{-5}
	p*D* 3.28	6.32×10^{3}	0.917	−0.087	
		2.40×10^{4}	0.794	−0.231	
		6.83×10^{4}	0.430	−0.844	

1.51×10^5	0.194	−1.637	
2.47×10^5	0.074	−2.600	

(a) Deuteroxide ion concentration calculated using Equation 3.9 (b) Proportion of unexchanged salt calculated using Equation 3.7 (c) Gradient of the plot of ln *f*(s) versus time gave pseudo-first order rate constant for exchange, k_{ex} (s^{-1})

Table A.7 Reaction data and first-order rate constants for exchange of the C(2)-H of 195 for deuterium in D_2O solution at 25 °C and *I* = 1.0 (KCl)

[DCl], M	[DO^-], M	time, s	*f*(s)	ln *f*(s)	k_{ex}, s^{-1}
	1.72×10^{-14}	0.0	1.000	0	
0.11	p*D* 0.97	3.23×10^3	0.828	-0.189	1.44×10^6
		5.30×10^3	0.728	-0.318	
		8.89×10^3	0.635	-0.454	
		1.16×10^3	0.385	-0.955	
		1.44×10^4	0.294	-1.223	
		1.74×10^4	0.238	-1.435	
		7.46×10^4	0.210	-1.560	
0.54	pD 0.27	0	1.000	0	3.97×10^{-7}
		5.17×10^4	0.840	-0.175	
		1.12×10^6	0.653	-0.426	
		1.74×10^6	0.504	-0.686	
		0	1.000	0.000	

0.002	p*D* 2.75	3.23×10^{3}	0.798	-0.225	6.62×10^{-5}
		5.30×10^{3}	0.686	-0.377	
		8.89×10^{3}	0.536	-0.623	
		1.16×10^{4}	0.423	-0.862	
		1.44×10^{4}	0.321	-1.135	
		1.74×10^{4}	0.289	-1.242	
		7.46×10^{4}	0.007	-4.971	
0.05	p*D* 1.34	0	1.000	0	2.85×10^{-6}
		1.43×10^{5}	0.640	-0.447	
		2.30×10^{5}	0.497	-0.700	
		3.28×10^{5}	0.379	-0.970	
		6.79×10^{5}	0.132	-2.028	
		8.41×10^{5}	0.084	-2.476	
		1.01×10^{6}	0.057	-2.862	
		1.10×10^{6}	0.044	-3.128	
		0	1.000	0	
0.03	p*D* 1.57	6.36×10^{4}	0.697	-0.361	4.39×10^{-6}
		2.55×10^{5}	0.283	-1.264	
		4.13×10^{5}	0.163	-1.812	
		0	1.000	0	
		7.52×10^{4}	0.770	−0.261	

	3.00×10^{-14}	1.03×10^{5}	0.716	−0.335	3.23×10^{-6}
0.06	(p*D* 1.21)	1.57×10^{5}	0.580	−0.544	
		2.51×10^{5}	0.445	−0.809	
		2.53×10^{5}	0.434	−0.835	
		2.64×10^{5}	0.425	−0.855	
		2.78×10^{5}	0.411	−0.889	
		3.12×10^{5}	0.353	−1.040	
		3.21×10^{5}	0.353	−1.040	
		4.52×10^{5}	0.227	−1.483	
		5.10×10^{5}	0.193	−1.648	
		0	1.000	0	
		9.20×10^{3}	0.834	−0.181	
	3.44×10^{-13}	1.43×10^{4}	0.796	−0.228	2.28×10^{-5}
0.005	(p*D* 2.27)	4.87×10^{4}	0.318	−1.144	
		5.63×10^{4}	0.274	−1.295	
		7.71×10^{4}	0.191	−1.655	
		8.44×10^{4}	0.146	−1.921	
		0	1.000	0	
		1.77×10^{3}	0.886	−0.121	
	8.23×10^{-13}	3.95×10^{3}	0.789	−0.237	5.55×10^{-5}
0.002	(p*D* 2.65)	6.70×10^{3}	0.683	−0.381	
		9.31×10^{3}	0.587	−0.534	

		1.27×10^4	0.490	−0.714	
		0	1.000	0	
		4.43×10^2	0.549	−0.599	
	1.04×10^{-11}	1.26×10^3	0.330	−1.108	6.88×10^{-4}
0.0002	(p*D* 3.75)	2.07×10^3	0.192	−1.650	
		2.88×10^3	0.107	−2.234	
		3.69×10^3	0.067	−2.704	
		4.51×10^3	0.040	−3.214	

(a) Deuteroxide ion concentration calculated using Equation 3.9 (b) Proportion of unexchanged salt calculated using Equation 3.7 (c) Gradient of the plot of ln *f*(s) versus time gave pseudo-first order rate constant for exchange, k_{ex} (s^{-1})

Table A.8 Reaction data and first-order rate constants for exchange of the C(2)-H of 212 for deuterium in D_2O solution at 25 °C and *I* = 1.0 (KCl)

[DCl], M	[DO^-][a], M	time, s	*f*(s)[b]	ln *f*(s)	k_{ex}, s^{-1}
		0	1.000	0	
		5.68×10^4	0.962	−0.039	
		9.06×10^4	0.940	−0.061	
		1.54×10^5	0.904	−0.101	
		2.36×10^5	0.871	−0.138	
		3.19×10^5	0.818	−0.201	
	4.64×10^{-14}	4.14×10^5	0.765	−0.268	6.07×10^{-7}
	(p*D* 1.40)	4.45×10^5	0.752	−0.285	

	4.79×10^{5}	0.745	−0.294	
	5.28×10^{5}	0.709	−0.344	
	6.19×10^{5}	0.673	−0.396	
	7.87×10^{5}	0.630	−0.462	
	9.36×10^{5}	0.559	−0.582	
	1.13×10^{5}	0.504	−0.685	
	0	1.000	0	
	1.28×10^{4}	0.920	−0.083	
	8.69×10^{4}	0.713	−0.338	
	1.20×10^{5}	0.669	−0.402	
	1.55×10^{5}	0.594	−0.520	
	1.99×10^{5}	0.512	−0.670	
2.33×10^{-13}	2.94×10^{5}	0.380	−0.968	3.32×10^{-6}
(p*D* 2.10)	3.54×10^{5}	0.310	−0.171	
	4.62×10^{5}	0.233	−1.459	
	6.15×10^{5}	0.119	−2.130	
	0	1.000	0	

	7.64×10^{3}	0.646	−0.437	
6.71×10^{-12}	1.25×10^{4}	0.642	−0.443	3.59×10^{-5}
(p*D* 3.56)	1.64×10^{4}	0.566	−0.569	
	2.45×10^{4}	0.435	−0.833	
	2.06×10^{4}	0.425	−0.855	
	8.13×10^{4}	0.051	−2.967	
	0	1.000	0	
2.3×10^{-11}	4.56×10^{3}	0.306	−1.183	2.36×10^{-4}
(p*D* 4.09)	7.17×10^{3}	0.178	−1.725	
	1.20×10^{4}	0.063	−2.773	
	0	1.000	0	
9.1×10^{-11}	8.96×10^{2}	0.596	−0.517	7.25×10^{-4}
(p*D* 4.69)	2.80×10^{3}	0.163	−1.816	
	3.63×10^{3}	0.090	−2.404	

(a) Deuteroxide ion concentration calculated using Equation 3.9 (b) Proportion of unexchanged salt calculated using Equation 3.7 (c) Gradient of the plot of ln *f*(s) versus time gave pseudo-first order rate constant for exchange, k_{ex} (s^{-1})

Table A.9 Reaction data and pseudo-first-order rate constants for exchange, k_{ex} (s−1), of the C(3)−H of triazolium ion (144) for deuterium in 50% f_B formic acid buffered solutions of D_2O at 25 °C and I = 1.0 (KCl)

[buffer], M	[DO^-][a], M	time, s	f(s)[b]	ln f(s)	k_{ex}, s^{-1}
		0	1.000	0.000	
0.10	8.07×10^{-12}	7.68×10^{2}	0.526	−0.643	7.90×10^{-4}
	(pD 3.64)	1.54×10^{3}	0.283	−1.263	
		2.30×10^{3}	0.156	−1.855	
		3.07×10^{3}	0.088	−2.426	
		0	1.000	0.000	
0.15	7.70×10^{-12}	7.68×10^{2}	0.557	−0.584	7.18×10^{-4}
	(pD 3.62)	1.54×10^{3}	0.323	−1.130	
		2.30×10^{3}	0.189	−1.668	
		3.07×10^{3}	0.109	−2.215	
		0	1.000	0.000	
0.20	7.52×10^{-12}	7.68×10^{2}	0.557	−0.584	6.97×10^{-4}
	(pD 3.61)	1.54×10^{3}	0.323	−1.130	
		2.30×10^{3}	0.189	−1.668	
		3.07×10^{3}	0.109	−2.215	
		0	1.000	0.000	
0.25	8.84×10^{-12}	7.68×10^{2}	0.611	−0.492	6.48×10^{-4}
	(pD 3.68)	1.54×10^{3}	0.353	−1.040	
		2.30×10^{3}	0.225	−1.490	
		3.07×10^{3}	0.137	−1.991	

(a) Concentration of deuteroxide ion calculated using Equation 3.9, where γDO = 0.73; (b) Fraction of unexchanged substrate remaining, *f*(s), calculated using Equation 3.7; (c) Pseudo-first-order rate constant for exchange, *k*ex (s-1), obtained from the slope of the plot of ln *f*(s) against time in Figure 3.22.

p*D* rate profiles for azolium salts studies in the H/D exchange experiments

2hydroxyethyl mimic 139

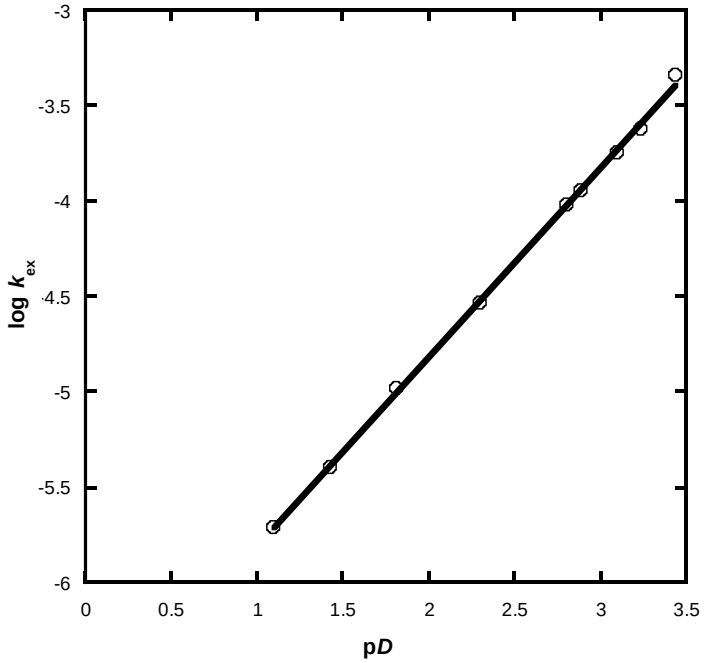

Isopropyl mimic 179

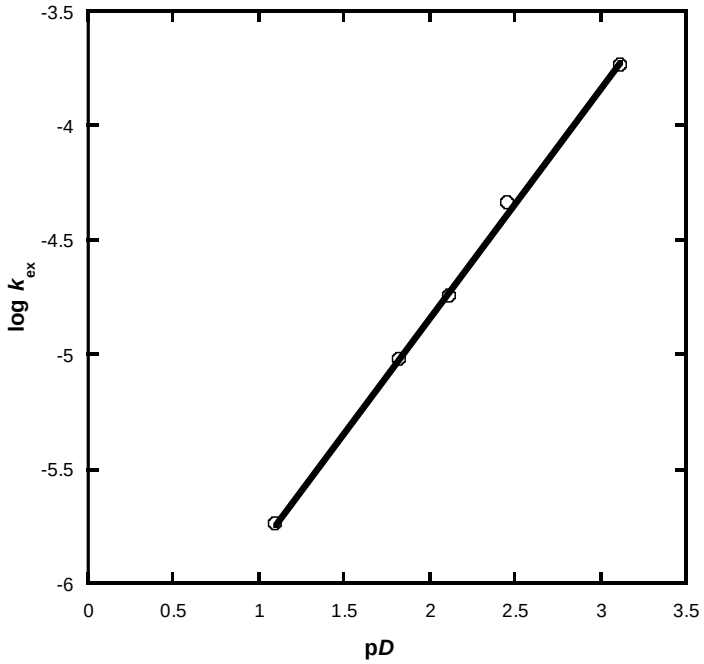

Methyl mimic 178

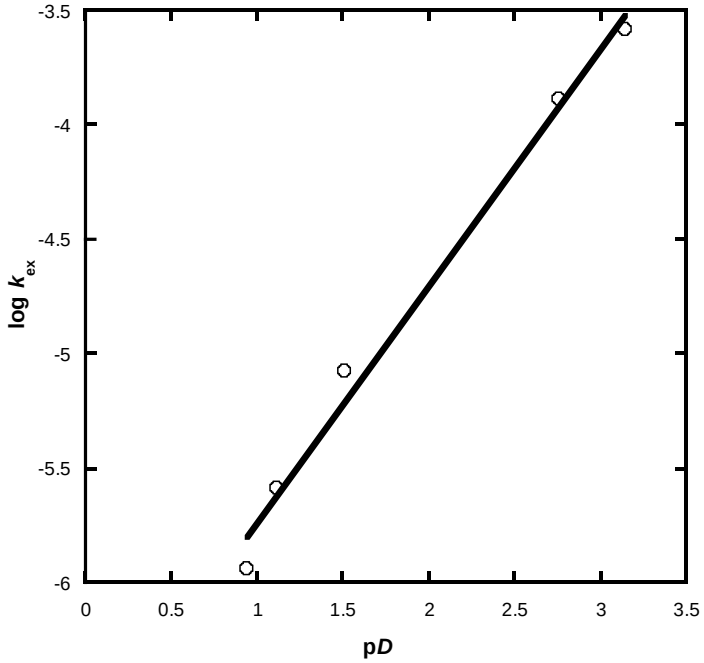

Propyl mimic 180

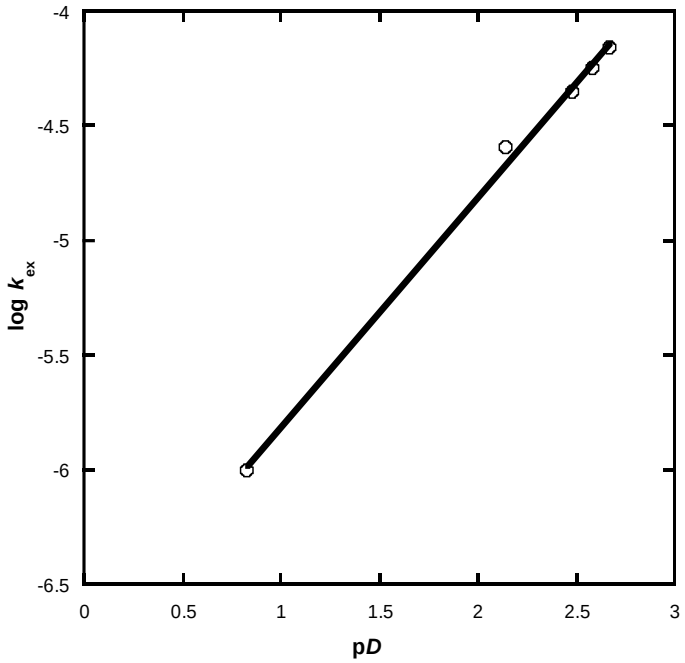

Thiamine HCl 7-Cl

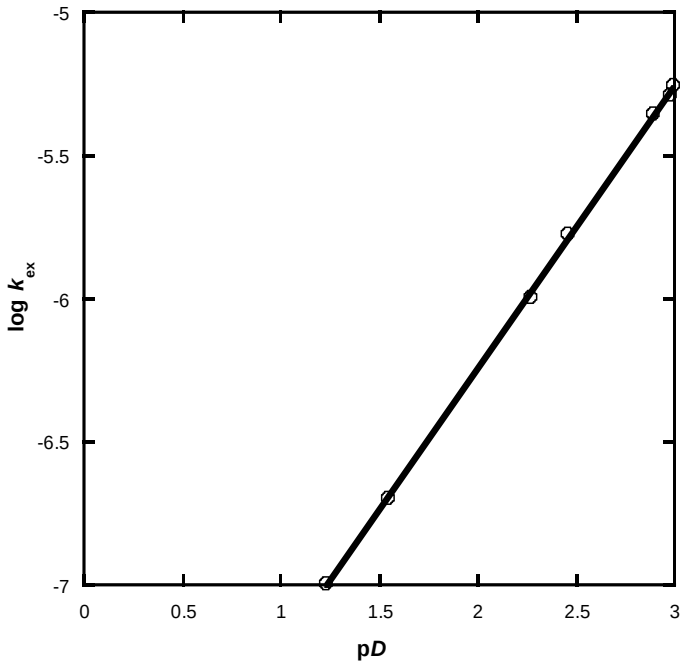

Thiamine mononitrate 7- NO_3

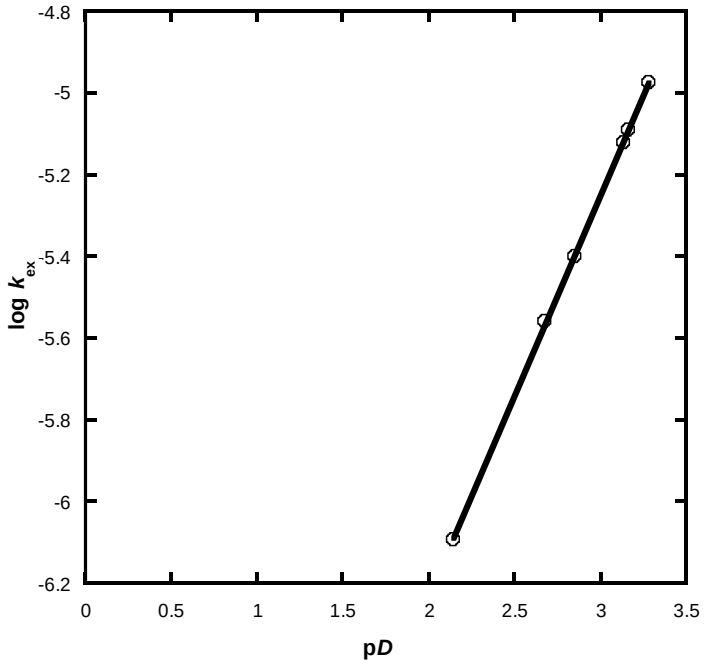

N-phenyl salt 188

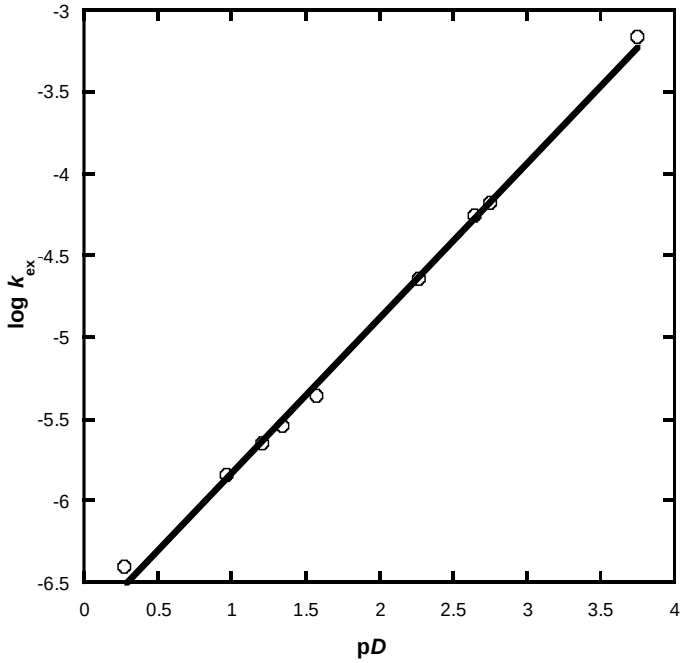

Dimethyl triazolium salt 205

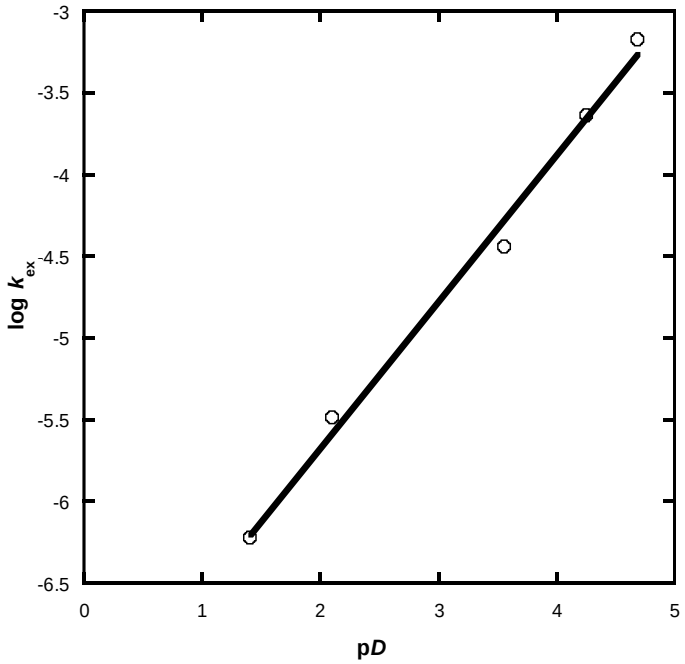

APPENDIX B

Figure B1: Semilogarithmic plots of *x* against time (Equation 4.57) for the reaction of substituted aldehydes with azolium precatalysts **7, 139, 178** and **205**.

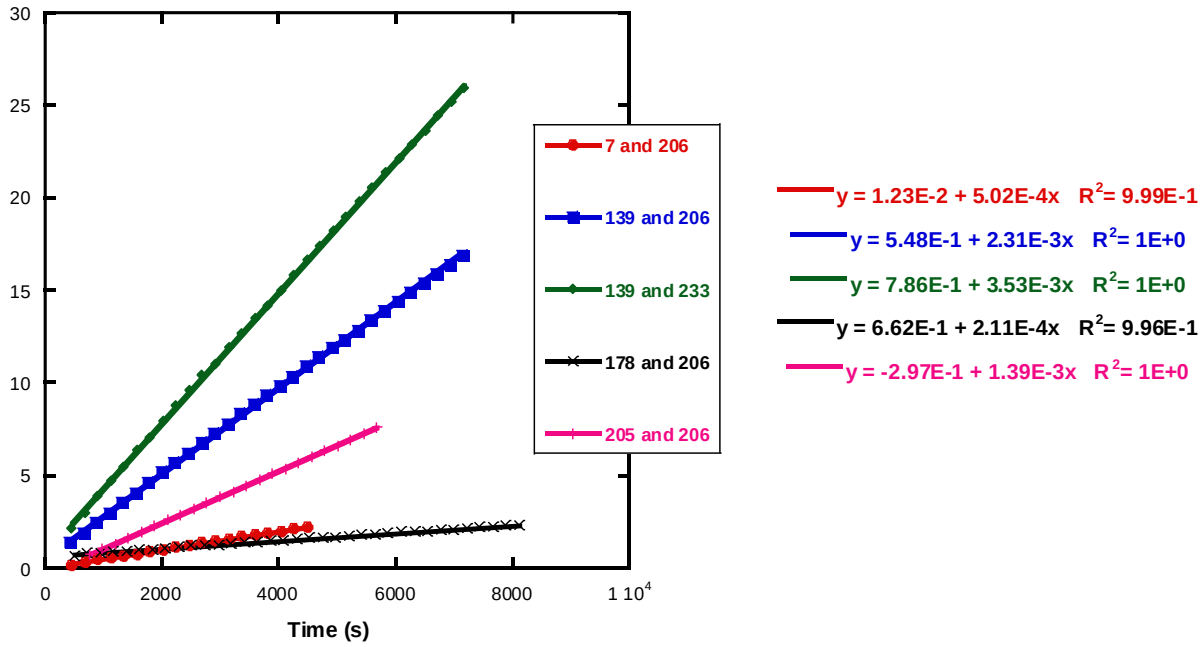

APPENDIX C

C1 X-ray Crystallographic Data

8.1.1.1.1.1.1 *18srv342*

2-((4-amino-2-methylpyrimidin-5-yl)methyl)-5-(3-hydroxypropyl)-4-methyl-2,4-dihydro-3*H*-1,2,4-triazole-3-thione

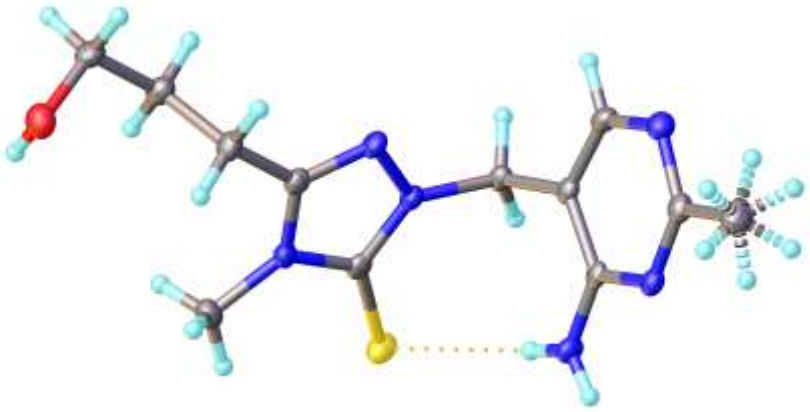

Table 1 Crystal data and structure refinement for 18srv342.	
Identification code	18srv342
Empirical formula	$C_{12}H_{18}N_6OS$
Formula weight	294.38
Temperature/K	120.0
Crystal system	triclinic
Space group	P-1
a/Å	9.0797(6)
b/Å	13.4248(9)
c/Å	13.6498(9)
α/°	117.518(2)

β/°	97.477(3)
γ/°	98.734(3)
Volume/Å^3	1419.89(17)
Z	4
ρ_{calc}g/cm^3	1.377
μ/mm^{-1}	0.234
F(000)	624.0
Crystal size/mm^3	0.36 × 0.08 × 0.07
Radiation	MoKα (λ = 0.71073)
2Θ range for data collection/°	4.662 to 55.996
Index ranges	-11 ≤ h ≤ 11, -17 ≤ k ≤ 17, -18 ≤ l ≤ 18
Reflections collected	27855
Independent reflections	6833 [R_{int} = 0.0700, R_{sigma} = 0.0713]
Data/restraints/parameters	6833/0/386
Goodness-of-fit on F^2	1.019
Final R indexes [I>=2σ (I)]	R_1 = 0.0448, wR_2 = 0.0990
Final R indexes [all data]	R_1 = 0.0756, wR_2 = 0.1094
Largest diff. peak/hole / e Å^{-3}	0.29/-0.29

Table 2 Fractional Atomic Coordinates (×10^4) and Equivalent Isotropic Displacement Parameters (Å^2×10^3) for 18srv342. U_{eq} is defined as 1/3 of of the trace of the orthogonalised U_{IJ} tensor.

Atom	***x***	***y***	***z***	**U(eq)**
S1	8598.7(6)	3953.8(4)	3126.4(4)	23.93(13)
O1	6793.2(16)	4427.9(13)	8602.5(11)	26.3(3)

N1	8763.1(17)	2331.1(13)	3786.6(12)	16.5(3)
N2	8392.2(17)	2036.9(13)	4585.4(12)	18.6(3)
N3	7819.8(17)	3686.7(12)	4882.5(12)	17.1(3)
N4	5925.4(17)	-719.7(13)	678.8(12)	17.8(3)
N5	7303.4(19)	-1578.7(13)	1552.0(13)	22.2(4)
N6	6766(2)	1161.3(15)	1105.0(14)	19.4(3)
C1	8416(2)	3325.8(15)	3936.6(14)	16.9(4)
C2	7828(2)	2884.9(16)	5241.7(14)	18.5(4)
C3	7308(2)	2992.2(17)	6272.0(15)	21.2(4)
C4	8554(2)	3792.6(18)	7348.6(15)	23.8(4)
C5	8063(2)	3925.3(17)	8417.4(16)	24.4(4)
C6	7262(2)	4733.4(16)	5380.8(16)	24.7(4)
C7	9389(2)	1549.8(15)	2873.9(14)	17.6(4)
C8	8242(2)	418.2(15)	2105.6(14)	16.5(4)
C9	6985(2)	298.4(15)	1293.5(14)	15.7(4)
C10	6110(2)	-1596.4(16)	855.5(15)	20.3(4)
C11	8340(2)	-558.6(16)	2164.1(15)	20.8(4)
C12	4874(2)	-2693.7(17)	228.4(17)	28.5(5)
S1A	3768.3(7)	-433.7(4)	3020.5(4)	30.56(14)
O1A	1674.8(16)	3396.3(13)	8356.2(12)	27.8(3)
N1A	3787.2(17)	1828.3(13)	3704.9(12)	17.2(3)
N2A	3357.8(17)	2756.3(13)	4505.8(12)	18.8(3)
N3A	2893.0(18)	1247.5(13)	4774.8(12)	20.2(3)
N4A	973.7(17)	1533.2(13)	684.0(12)	17.6(3)
N5A	2514.5(18)	3445.6(13)	1484.0(13)	21.7(4)
N6A	1677(2)	216.2(14)	1156.0(14)	19.7(3)

C1A	3505(2)	886.2(16)	3834.8(15)	20.0(4)
C2A	2817(2)	2375.6(16)	5143.6(14)	19.1(4)
C3A	2228(2)	3078.1(17)	6149.3(15)	22.1(4)
C4A	3460(2)	3631.9(17)	7250.9(15)	23.9(4)
C5A	2813(2)	4199.7(17)	8296.6(16)	25.8(4)
C6A	2423(3)	519.0(19)	5265.3(18)	31.4(5)
C7A	4427(2)	1923.1(16)	2817.2(15)	18.6(4)
C8A	3312(2)	2144.3(16)	2072.1(14)	16.4(4)
C9A	1994(2)	1284.3(15)	1299.3(14)	15.8(4)
C10A	1265(2)	2601.6(16)	817.8(14)	18.7(4)
C11A	3503(2)	3188.2(16)	2101.6(15)	20.0(4)
C12A	79(2)	2874.5(17)	173.0(16)	24.9(4)

Table 3 Anisotropic Displacement Parameters ($Å^2×10^3$) for 18srv342. The Anisotropic displacement factor exponent takes the form: $-2\pi^2[h^2a^{*2}U_{11}+2hka^*b^*U_{12}+\ldots]$.

Atom	**U_{11}**	**U_{22}**	**U_{33}**	**U_{23}**	**U_{13}**	**U_{12}**
S1	31.3(3)	21.1(2)	19.3(2)	11.8(2)	3.6(2)	1.6(2)
O1	28.5(8)	25.5(8)	25.1(7)	11.6(6)	10.4(6)	6.2(7)
N1	18.8(8)	18.7(8)	12.0(7)	7.4(6)	3.5(6)	5.1(6)
N2	21.1(8)	22.3(8)	13.2(7)	9.3(7)	4.5(6)	5.0(7)
N3	19.0(8)	15.5(8)	13.1(7)	4.7(6)	1.9(6)	3.8(6)
N4	18.8(8)	19.7(8)	12.8(7)	6.6(6)	3.9(6)	4.1(7)
N5	26.8(9)	21.8(8)	19.5(8)	11.1(7)	5.4(7)	6.9(7)
N6	19.1(9)	18.6(9)	15.9(8)	7.0(7)	-1.3(7)	2.1(7)
C1	13.6(9)	17.8(9)	13.6(8)	5.4(7)	-1.2(7)	-0.1(7)
C2	17.7(10)	18.7(9)	15.3(9)	6.9(8)	0.4(7)	2.0(8)

C3	23.9(10)	23.2(10)	16.3(9)	9.0(8)	6.3(8)	5.4(8)
C4	22.1(10)	30.6(11)	19.2(9)	11.7(9)	4.8(8)	9.5(9)
C5	30.9(11)	25.6(10)	19.7(10)	13.5(8)	4.2(8)	8.5(9)
C6	26.7(11)	21.0(10)	23.0(10)	7.1(8)	4.3(8)	9.9(9)
C7	14.9(9)	21.5(9)	14.4(9)	6.6(7)	3.6(7)	6.3(8)
C8	16.3(9)	20.5(9)	11.6(8)	6.3(7)	5.1(7)	5.1(8)
C9	16.8(9)	18.9(9)	10.6(8)	5.7(7)	6.3(7)	4.8(7)
C10	24.6(10)	20.2(9)	15.2(9)	7.4(8)	6.7(8)	5.4(8)
C11	21.3(10)	27.0(10)	14.9(9)	9.9(8)	3.6(7)	9.7(8)
C12	33.6(12)	24.1(11)	25.9(11)	12.5(9)	4.9(9)	2.3(9)
S1A	47.3(4)	25.0(3)	23.1(3)	11.4(2)	11.0(2)	17.9(3)
O1A	30.8(8)	36.0(8)	31.0(8)	24.1(7)	13.0(6)	16.2(7)
N1A	17.2(8)	20.0(8)	13.8(7)	7.8(6)	2.6(6)	4.8(6)
N2A	19.9(8)	21.1(8)	13.3(7)	6.6(6)	2.3(6)	6.5(7)
N3A	24.3(9)	22.1(8)	17.5(8)	11.5(7)	5.2(7)	7.7(7)
N4A	20.4(8)	19.8(8)	13.1(7)	8.4(6)	4.0(6)	4.7(7)
N5A	25.5(9)	20.6(8)	18.9(8)	10.1(7)	5.7(7)	3.7(7)
N6A	19.9(9)	17.7(8)	17.7(8)	7.5(7)	-1.9(7)	2.8(7)
C1A	20.6(10)	24.1(10)	16.2(9)	10.6(8)	2.2(7)	7.1(8)
C2A	17.4(10)	22.4(10)	14.8(9)	8.1(8)	-0.7(7)	4.7(8)
C3A	23.3(10)	25.4(10)	18.5(9)	10.1(8)	6.6(8)	9.0(8)
C4A	23.5(11)	25.2(10)	18.6(9)	8.5(8)	3.5(8)	2.6(8)
C5A	35.1(12)	21.7(10)	20.3(10)	9.5(8)	7.0(9)	8.4(9)
C6A	42.7(13)	32.7(12)	30.0(11)	21.9(10)	14.8(10)	11.8(10)
C7A	14.8(9)	23.8(10)	15.7(9)	9.0(8)	4.0(7)	2.1(8)
C8A	15.7(9)	21.7(9)	11.7(8)	7.8(7)	5.0(7)	4.4(7)

C9A	18.0(9)	19.6(9)	11.2(8)	7.0(7)	8.1(7)	5.7(8)
C10A	22.8(10)	22.1(10)	13.3(9)	9.3(8)	6.7(7)	6.3(8)
C11A	20.2(10)	21.0(10)	14.0(9)	6.2(8)	3.9(7)	0.2(8)
C12A	29.2(11)	25.5(10)	23.0(10)	14.8(9)	3.5(8)	6.9(9)

Table 4 Bond Lengths for 18srv342.

Atom	**Atom**	**Length/Å**		**Atom**	**Atom**	**Length/Å**
S1	C1	1.6818(18)		S1A	C1A	1.6765(19)
O1	C5	1.415(2)		O1A	C5A	1.415(2)
N1	N2	1.383(2)		N1A	N2A	1.378(2)
N1	C1	1.348(2)		N1A	C1A	1.348(2)
N1	C7	1.460(2)		N1A	C7A	1.458(2)
N2	C2	1.310(2)		N2A	C2A	1.306(2)
N3	C1	1.371(2)		N3A	C1A	1.372(2)
N3	C2	1.374(2)		N3A	C2A	1.374(2)
N3	C6	1.455(2)		N3A	C6A	1.463(2)
N4	C9	1.352(2)		N4A	C9A	1.352(2)
N4	C10	1.335(2)		N4A	C10A	1.338(2)
N5	C10	1.335(2)		N5A	C10A	1.337(2)
N5	C11	1.344(2)		N5A	C11A	1.342(2)
N6	C9	1.334(2)		N6A	C9A	1.333(2)
C2	C3	1.493(2)		C2A	C3A	1.486(2)
C3	C4	1.528(3)		C3A	C4A	1.530(3)
C4	C5	1.521(3)		C4A	C5A	1.521(3)
C7	C8	1.502(3)		C7A	C8A	1.500(2)

C8	C9	1.417(2)		C8A	C9A	1.416(2)
C8	C11	1.365(3)		C8A	C11A	1.367(2)
C10	C12	1.498(3)		C10A	C12A	1.497(3)

Table 5 Bond Angles for 18srv342.

Atom	**Atom**	**Atom**	**Angle/°**		**Atom**	**Atom**	**Atom**	**Angle/°**
N2	N1	C7	119.34(14)		N2A	N1A	C7A	120.04(14)
C1	N1	N2	113.08(14)		C1A	N1A	N2A	113.01(14)
C1	N1	C7	127.50(15)		C1A	N1A	C7A	126.93(15)
C2	N2	N1	103.70(14)		C2A	N2A	N1A	104.15(14)
C1	N3	C2	108.06(14)		C1A	N3A	C2A	108.21(15)
C1	N3	C6	124.47(15)		C1A	N3A	C6A	123.93(16)
C2	N3	C6	127.46(15)		C2A	N3A	C6A	127.86(16)
C10	N4	C9	118.18(15)		C10A	N4A	C9A	117.98(15)
C10	N5	C11	115.54(16)		C10A	N5A	C11A	115.47(16)
N1	C1	S1	128.37(14)		N1A	C1A	S1A	128.68(14)
N1	C1	N3	103.77(15)		N1A	C1A	N3A	103.58(15)
N3	C1	S1	127.81(14)		N3A	C1A	S1A	127.70(15)
N2	C2	N3	111.37(15)		N2A	C2A	N3A	111.04(16)
N2	C2	C3	124.53(16)		N2A	C2A	C3A	124.44(17)
N3	C2	C3	124.07(16)		N3A	C2A	C3A	124.51(17)
C2	C3	C4	111.24(15)		C2A	C3A	C4A	111.81(15)
C5	C4	C3	112.72(16)		C5A	C4A	C3A	112.21(16)
O1	C5	C4	112.93(15)		O1A	C5A	C4A	111.98(16)
N1	C7	C8	111.41(14)		N1A	C7A	C8A	112.01(14)

C9	C8	C7	122.53(16)		C9A	C8A	C7A	121.91(16)
C11	C8	C7	121.55(16)		C11A	C8A	C7A	122.08(16)
C11	C8	C9	115.90(16)		C11A	C8A	C9A	116.01(16)
N4	C9	C8	120.13(16)		N4A	C9A	C8A	120.26(16)
N6	C9	N4	116.89(16)		N6A	C9A	N4A	116.93(16)
N6	C9	C8	122.97(17)		N6A	C9A	C8A	122.79(16)
N4	C10	C12	117.67(16)		N4A	C10A	C12A	116.96(16)
N5	C10	N4	125.51(17)		N5A	C10A	N4A	125.63(16)
N5	C10	C12	116.82(17)		N5A	C10A	C12A	117.40(16)
N5	C11	C8	124.53(17)		N5A	C11A	C8A	124.52(17)

Table 6 Hydrogen Bonds for 18srv342.

D	**H**	**A**	**d(D-H)/Å**	**d(H-A)/Å**	**d(D-A)/Å**	**D-H-A/°**
O1	H1	N5A[1]	0.88(3)	2.02(3)	2.889(2)	170(2)
N6	H6A	S1	0.87(2)	2.59(2)	3.4335(18)	163.2(18)
N6	H6B	N4[2]	0.82(2)	2.17(2)	2.988(2)	179(2)
O1A	H1A	N5[3]	0.90(3)	1.91(3)	2.788(2)	165(2)
N6A	H6AA	S1A	0.85(2)	2.65(2)	3.4843(17)	166.8(17)
N6A	H6AB	N4A[4]	0.85(2)	2.13(2)	2.979(2)	176.9(19)

[1]1-X,1-Y,1-Z; [2]1-X,-Y,-Z; [3]1-X,-Y,1-Z; [4]-X,-Y,-Z

Table 7 Selected Torsion Angles for 18srv342.

A	**B**	**C**	**D**	**Angle/°**		**A**	**B**	**C**	**D**	**Angle/°**
C2	C3	C4	C5	179.85(16)		C2A	C3A	C4A	C5A	-171.35(16)
C3	C4	C5	O1	-62.0(2)		C3A	C4A	C5A	O1A	59.9(2)

C4	C3	C2	N2	96.9(2)		C4A	C3A	C2A	N2A	-94.7(2)
C4	C3	C2	N3	-80.9(2)		C4A	C3A	C2A	N3A	83.9(2)
C8	C7	N1	N2	64.93(19)		C8A	C7A	N1A	N2A	-62.1(2)
C8	C7	N1	C1	-111.69(19)		C8A	C7A	N1A	C1A	115.84(19)
C9	C8	C7	N1	75.5(2)		C9A	C8A	C7A	N1A	-70.5(2)
C11	C8	C7	N1	-103.35(19)		C11A	C8A	C7A	N1A	109.14(19)

Table 8 Hydrogen Atom Coordinates (Å×10^4) and Isotropic Displacement Parameters (Å^2×10^3) for 18srv342.

Atom	***x***	***y***	***z***	**U(eq)**
H3A	7034.34	2216.95	6204.33	25
H3B	6380.98	3301.64	6324.65	25
H4A	9479.04	3480.47	7290.59	29
H4B	8829.42	4564.38	7408.78	29
H5A	7797.43	3154.17	8359.86	29
H5B	8933.47	4413.45	9078.89	29
H6C	7195.99	5042.44	4871.88	37
H6D	6267.19	4553.74	5511.78	37
H6E	7955.19	5294.74	6088.18	37
H7A	10314.84	1405.77	3204.79	21
H7B	9693.11	1919.78	2425.85	21
H11	9200.96	-514.12	2672.59	25
H12A	4064.22	-2604.6	-252.96	34
H12B	5304.05	-3332.04	-245.59	34
H12C	4445.85	-2862.21	773.63	34
H12D	5145.19	-3261.3	436.35	34

H12E	3905.36	-2533.86	428.98	34
H12F	4763.57	-3003.69	-590.24	34
H1	7070(30)	5110(20)	8660(20)	54(8)
H6A	7350(20)	1856(19)	1509(18)	23(6)
H6B	6020(30)	1029(18)	611(18)	26(6)
H3AA	1350.04	2578	6196.15	27
H3AB	1856.55	3693.32	6057.86	27
H4AA	3943.06	3030.96	7282.85	29
H4AB	4263.33	4220.94	7252.32	29
H5AA	3653.56	4556.92	8984.59	31
H5AB	2367.95	4822.59	8281.13	31
H6AC	1768.9	-226.7	4665.87	47
H6AD	1852.98	904.36	5838.7	47
H6AE	3331.65	391.35	5620.09	47
H7AA	4723.03	1197.61	2346.55	22
H7AB	5361.81	2562.68	3170.9	22
H11A	4397.06	3771.97	2593.11	24
H12G	-539.23	2155.7	-489.06	37
H12H	582.15	3384.93	-79	37
H12I	-584.02	3261.74	664.81	37
H1A	2160(30)	2890(20)	8430(20)	50(8)
H6AA	2260(20)	-9(17)	1516(17)	21(4)
H6AB	900(20)	-268(18)	642(17)	21(4)

Table 9 Atomic Occupancy for 18srv342.

Atom	***Occupancy***		**Atom**	***Occupancy***		**Atom**	***Occupancy***
H12A	0.5		H12B	0.5		H12C	0.5
H12D	0.5		H12E	0.5		H12F	0.5

****

8.1.1.1.1.1.2 *19srv229*

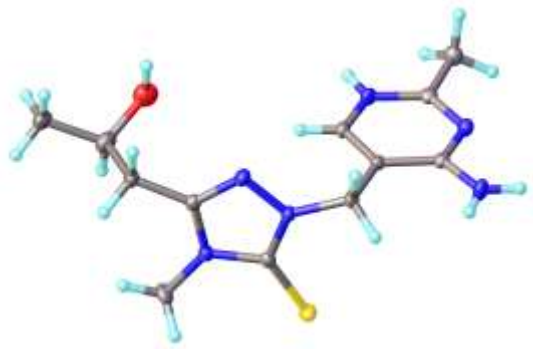

Table 1 Crystal data and structure refinement for 19srv229.	
Identification code	19srv229
Empirical formula	$C_{12}H_{19}ClN_6OS$
Formula weight	330.84
Temperature/K	120.0
Crystal system	monoclinic
Space group	$P2_1/c$
a/Å	7.5503(3)
b/Å	17.5222(7)
c/Å	12.4877(6)
α/°	90
β/°	91.6826(17)
γ/°	90
Volume/Å^3	1651.38(12)

Z	4
ρ_{calc}g/cm^3	1.331
μ/mm^{-1}	0.366
F(000)	696.0
Crystal size/mm^3	0.28 × 0.22 × 0.18
Radiation	MoKα (λ = 0.71073)
2Θ range for data collection/°	4.006 to 58
Index ranges	-10 ≤ h ≤ 10, -23 ≤ k ≤ 23, -17 ≤ l ≤ 17
Reflections collected	25310
Independent reflections	4384 [R_{int} = 0.0284, R_{sigma} = 0.0203]
Data/restraints/parameters	4384/0/213
Goodness-of-fit on F^2	1.103
Final R indexes [I>=2σ (I)]	R_1 = 0.0368, wR_2 = 0.0910
Final R indexes [all data]	R_1 = 0.0433, wR_2 = 0.0937
Largest diff. peak/hole / e Å^{-3}	1.14/-0.32

Table 2 Fractional Atomic Coordinates (×10^4) and Equivalent Isotropic Displacement Parameters (Å^2×10^3) for 19srv229. U_{eq} is defined as 1/3 of of the trace of the orthogonalised U_{IJ} tensor.

Atom	***x***	***y***	***z***	**U(eq)**
Cl1	6746.3(5)	7448.1(2)	3667.4(3)	23.02(10)
S1	10238.2(5)	5087.8(2)	2575.1(3)	18.80(9)
O1	6388.6(18)	2504.2(7)	4671.2(11)	30.0(3)
N1	7582.4(15)	4847.1(7)	3955.1(9)	13.9(2)
N2	7090.6(16)	4372.4(7)	4780.4(10)	16.0(2)
N3	9739.6(15)	4070.7(7)	4203.0(9)	14.2(2)
N4	3548.7(16)	5401.4(7)	952.4(10)	15.6(2)

N5	4006.4(16)	4155.6(7)	1542.8(10)	15.5(2)
N6	4690.5(19)	6406.3(7)	1905.7(11)	19.4(3)
C1	8430.6(18)	3909.1(8)	4914.6(11)	14.6(3)
C2	9184.0(18)	4671.3(8)	3575.1(11)	13.7(3)
C3	11452(2)	3697.5(10)	4091.0(13)	22.2(3)
C4	6397.2(18)	5428.6(8)	3525.0(11)	14.6(3)
C5	5311.4(18)	5140.2(8)	2574.6(11)	13.2(3)
C6	4513.5(18)	5659.0(8)	1815.2(11)	14.3(3)
C7	3286.8(19)	4664.0(8)	851.5(11)	15.3(3)
C8	5016.7(18)	4388.5(8)	2396.9(11)	14.9(3)
C9	2120(2)	4363.9(9)	-30.9(12)	20.2(3)
C10	8496(2)	3278.0(9)	5710.5(12)	18.7(3)
C11	8049(2)	2495.7(9)	5229.0(15)	26.0(3)
C12	8174(3)	1892.5(11)	6111.2(18)	25.3(4)
C12A	9114(13)	2195(6)	4198(8)	32.6(19)

Table 3 Anisotropic Displacement Parameters ($Å^2×10^3$) for 19srv229. The Anisotropic displacement factor exponent takes the form: $-2\pi^2[h^2a^{*2}U_{11}+2hka^*b^*U_{12}+\ldots]$.

Atom	**U_{11}**	**U_{22}**	**U_{33}**	**U_{23}**	**U_{13}**	**U_{12}**
Cl1	26.08(19)	11.55(16)	30.9(2)	-0.88(14)	-8.09(15)	2.38(13)
S1	17.20(17)	22.61(19)	16.78(17)	4.95(14)	3.84(13)	1.36(14)
O1	34.1(7)	23.8(6)	32.0(7)	-5.6(5)	0.1(5)	-3.3(5)
N1	14.2(5)	12.9(5)	14.5(5)	2.2(4)	1.6(4)	1.1(4)
N2	17.5(6)	14.5(6)	16.1(6)	2.9(5)	2.4(4)	0.5(4)
N3	13.3(5)	14.3(5)	14.8(5)	0.9(4)	0.1(4)	1.9(4)
N4	18.2(6)	14.7(6)	13.9(5)	1.3(4)	2.0(4)	1.1(4)
N5	17.5(6)	10.0(6)	18.9(6)	-0.8(5)	0.6(5)	0.1(4)
N6	27.6(7)	12.0(6)	18.5(6)	2.0(5)	-2.7(5)	0.8(5)
C1	16.2(6)	12.8(6)	14.9(6)	-0.5(5)	-0.3(5)	-0.9(5)
C2	13.8(6)	13.5(6)	13.7(6)	-1.9(5)	-1.4(5)	0.2(5)
C3	16.8(7)	26.6(8)	23.1(7)	3.5(6)	1.5(6)	8.8(6)
C4	15.4(6)	11.4(6)	16.9(6)	0.2(5)	0.1(5)	2.1(5)
C5	12.2(6)	12.2(6)	15.2(6)	0.6(5)	3.0(5)	1.5(5)
C6	15.3(6)	13.0(6)	14.7(6)	1.4(5)	4.1(5)	1.5(5)
C7	14.8(6)	17.1(7)	14.1(6)	-0.1(5)	4.1(5)	1.0(5)
C8	14.5(6)	12.8(6)	17.4(6)	2.2(5)	1.2(5)	1.8(5)
C9	21.6(7)	20.7(7)	18.1(7)	-2.4(6)	-1.4(6)	0.0(6)
C10	19.1(7)	16.3(7)	20.5(7)	5.1(6)	-0.9(5)	0.3(5)
C11	29.6(8)	17.3(7)	31.4(9)	2.6(6)	4.9(7)	-1.4(6)
C12	23.5(10)	16.1(9)	36.4(11)	5.8(8)	3.2(8)	-1.1(7)

Table 4 Bond Lengths for 19srv229.

Atom	**Atom**	**Length/Å**		**Atom**	**Atom**	**Length/Å**
S1	C2	1.6685(14)		N5	C7	1.3441(19)
O1	C11	1.417(2)		N5	C8	1.3559(19)
N1	N2	1.3837(16)		N6	C6	1.3207(19)
N1	C2	1.3476(18)		C1	C10	1.487(2)
N1	C4	1.4489(18)		C4	C5	1.5096(19)
N2	C1	1.3041(18)		C5	C6	1.4335(19)

N3	C1	1.3778(18)		C5	C8	1.3530(19)
N3	C2	1.3708(18)		C7	C9	1.486(2)
N3	C3	1.4591(18)		C10	C11	1.530(2)
N4	C6	1.3599(19)		C11	C12	1.528(3)
N4	C7	1.3126(19)				

Table 5 Bond Angles for 19srv229.

Atom	**Atom**	**Atom**	**Angle/˚**		**Atom**	**Atom**	**Atom**	**Angle/˚**
N2	N1	C4	121.50(11)		N1	C4	C5	111.79(11)
C2	N1	N2	112.83(11)		C6	C5	C4	121.05(12)
C2	N1	C4	125.53(12)		C8	C5	C4	122.52(13)
C1	N2	N1	104.23(11)		C8	C5	C6	116.42(13)
C1	N3	C3	128.62(12)		N4	C6	C5	121.24(13)
C2	N3	C1	108.26(11)		N6	C6	N4	116.57(13)
C2	N3	C3	123.12(12)		N6	C6	C5	122.18(14)
C7	N4	C6	118.58(13)		N4	C7	N5	122.27(14)
C7	N5	C8	120.87(13)		N4	C7	C9	120.24(13)
N2	C1	N3	110.96(12)		N5	C7	C9	117.46(13)
N2	C1	C10	124.01(13)		C5	C8	N5	120.54(13)
N3	C1	C10	125.00(13)		C1	C10	C11	113.64(13)
N1	C2	S1	128.04(11)		O1	C11	C10	111.43(13)
N1	C2	N3	103.70(12)		O1	C11	C12	113.37(15)
N3	C2	S1	128.26(11)		C12	C11	C10	109.17(15)

Table 6 Hydrogen Bonds for 19srv229.

D	**H**	**A**	**d(D-H)/Å**	**d(H-A)/Å**	**d(D-A)/Å**	**D-H-A/°**
N6	H6A	Cl1	0.85(2)	2.39(2)	3.2219(15)	167.1(18)
N6	H6B	O1[1]	0.89(2)	1.98(3)	2.8545(18)	168(2)
N5	H5	Cl1[2]	0.81(2)	2.25(2)	3.0552(13)	175(2)
O1	H1	Cl1[3]	1.01(4)	2.20(4)	3.1940(15)	167(3)

[1]1-X,1/2+Y,1/2-Z; [2]1-X,-1/2+Y,1/2-Z; [3]1-X,1-Y,1-Z

Table 7 Selected Torsion Angles for 19srv229.										
A	**B**	**C**	**D**	**Angle/°**		**A**	**B**	**C**	**D**	**Angle/°**
C1	C10	C11	O1	-54.55(18)		C6	C5	C4	N1	-159.00(12)
C1	C10	C11	C12	179.47(14)		C8	C5	C4	N1	21.85(18)
C5	C4	N1	N2	-92.82(15)		C11	C10	C1	N2	99.22(17)
C5	C4	N1	C2	82.64(17)		C11	C10	C1	N3	-78.82(18)

Table 8 Hydrogen Atom Coordinates (Å×10^4) and Isotropic Displacement Parameters (Å^2×10^3) for 19srv229.				
Atom	***x***	***y***	***z***	**U(eq)**
H3A	11442.9	3403.22	3423.54	33
H3B	11674.94	3354.22	4699.64	33
H3C	12387.64	4084.55	4074.61	33
H4A	7099.61	5876.09	3304.88	17
H4B	5592.31	5596.48	4090.68	17
H8	5521.83	4021	2874.51	18
H9A	909.01	4312.24	220.61	30
H9B	2555.37	3863.89	-256.65	30
H9C	2128.05	4717.78	-638.5	30
H10A	7651.59	3391.1	6281.06	22
H10B	9698.77	3257.48	6046.91	22
H11	8974.24	2374.04	4697.97	31
H12A	7357.04	2022.96	6678.66	38
H12B	9387.89	1874.97	6410.11	38
H12C	7856.39	1392.49	5810.8	38
H6A	5300(30)	6612(11)	2413(17)	21(5)
H6B	4220(30)	6709(14)	1399(19)	41(6)
H5	3790(30)	3708(13)	1449(17)	30(6)
H1	5480(50)	2595(18)	5230(30)	84(11)

Table 9 Atomic Occupancy for 19srv229.							
Atom	***Occupancy***		**Atom**	***Occupancy***		**Atom**	***Occupancy***
C12	0.8		C12A	0.2			

Table 10 Solvent masks information for 19srv229.						
Number	**X**	**Y**	**Z**	**Volume**	**Electron count**	**Content**
1	0.050	0.192	0.312	23.4	1.9	?
2	0.050	0.308	0.812	23.4	1.9	?
3	-0.050	0.692	0.188	23.4	1.9	?
4	-0.050	0.808	0.688	23.4	2.0	?

****

8.1.1.1.1.1.3 *18srv385*

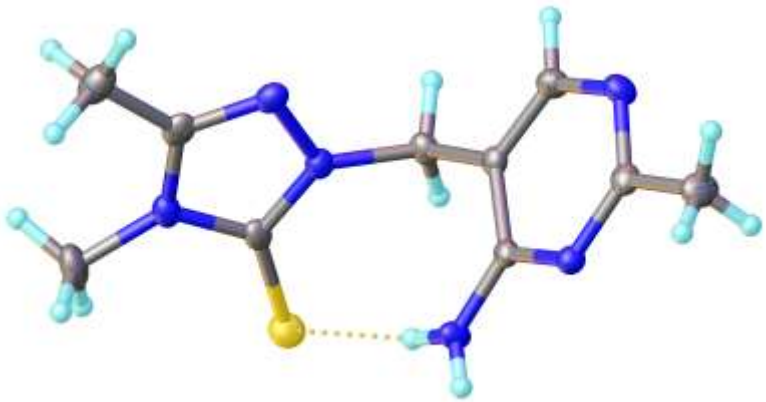

Table 1 Crystal data and structure refinement for 18srv385.	
Identification code	18srv385
Empirical formula	$C_{10}H_{14}N_6S$ x H_2O

Formula weight	268.35
Temperature/K	120.0
Crystal system	triclinic
Space group	P-1
a/Å	4.5666(10)
b/Å	12.070(3)
c/Å	12.682(3)
α/°	69.902(8)
β/°	83.251(8)
γ/°	87.628(8)
Volume/Å^3	651.9(2)
Z	2
ρ_{calc}g/cm^3	1.367
μ/mm^{-1}	0.248
F(000)	284.0
Crystal size/mm^3	0.27 × 0.08 × 0.01
Radiation	MoKα (λ = 0.71073)
2Θ range for data collection/°	5.762 to 58
Index ranges	-6 ≤ h ≤ 6, -16 ≤ k ≤ 16, -17 ≤ l ≤ 17
Reflections collected	13014
Independent reflections	3455 [R_{int} = 0.0601, R_{sigma} = 0.0716]

Data/restraints/parameters	3455/3/231
Goodness-of-fit on F^2	1.030
Final R indexes [I>=2σ (I)]	R_1 = 0.0407, wR_2 = 0.0938
Final R indexes [all data]	R_1 = 0.0804, wR_2 = 0.1045
Largest diff. peak/hole / e $Å^{-3}$	0.32/-0.29

Table 2 Fractional Atomic Coordinates ($\times 10^4$) and Equivalent Isotropic Displacement Parameters ($Å^2 \times 10^3$) for 18srv385. U_{eq} is defined as 1/3 of of the trace of the orthogonalised U_{IJ} tensor.

Atom	***x***	***y***	***z***	**U(eq)**
S1	1731.0(10)	614.9(4)	8072.4(4)	24.92(14)
N1	4311(3)	2643.3(12)	6621.8(12)	17.2(3)
N2	6185(3)	3534.3(12)	6578.2(12)	19.3(3)
N3	5273(3)	2272.9(12)	8317.8(12)	19.6(3)
N4	8971(3)	1440.4(11)	3973.0(11)	16.7(3)
N5	7577(3)	3346.3(12)	2794.8(12)	21.1(3)
N6	6816(3)	584.3(13)	5788.1(13)	19.7(3)
C1	3756(4)	1844.1(14)	7673.0(14)	17.1(4)
C2	6735(4)	3272.6(14)	7623.7(15)	19.8(4)
C3	5368(5)	1719(2)	9528.0(16)	29.1(5)
C4	8666(5)	3959.4(19)	8021(2)	28.8(5)
C5	3016(4)	2666.1(16)	5619.3(14)	18.9(4)
C6	5257(3)	2539.8(14)	4701.4(14)	15.6(3)
C7	6993(3)	1509.4(13)	4830.9(13)	15.3(3)

C8	9127(4)	2346.9(14)	2998.2(14)	18.5(4)
C9	5686(4)	3414.3(15)	3674.6(15)	20.7(4)
C10	11229(5)	2227.5(19)	2044.8(17)	26.4(4)
O1W	2688(3)	4954.4(12)	9412.5(11)	30.9(3)

Table 3 Anisotropic Displacement Parameters ($Å^2×10^3$) for 18srv385. The Anisotropic displacement factor exponent takes the form: $-2\pi^2[h^2a^{*2}U_{11}+2hka^*b^*U_{12}+\ldots]$.

Atom	**U_{11}**	**U_{22}**	**U_{33}**	**U_{23}**	**U_{13}**	**U_{12}**
S1	25.4(3)	24.6(2)	22.1(3)	-5.77(19)	1.96(18)	-2.06(18)
N1	17.7(7)	18.5(7)	16.3(8)	-7.4(6)	-1.2(6)	2.2(5)
N2	16.9(8)	18.0(7)	24.8(8)	-9.8(6)	-2.2(6)	2.7(6)
N3	20.2(8)	23.2(8)	16.9(8)	-9.0(6)	-3.6(6)	6.5(6)
N4	18.5(7)	16.0(7)	15.6(8)	-5.9(6)	-0.2(6)	0.3(5)
N5	24.2(8)	19.6(7)	15.9(8)	-2.1(6)	-1.0(6)	1.8(6)
N6	25.0(8)	16.3(8)	15.2(8)	-4.2(6)	2.3(6)	4.8(6)
C1	16.4(9)	20.3(8)	14.7(9)	-7.3(7)	-0.7(7)	6.3(6)
C2	14.5(9)	22.0(9)	26.4(10)	-13.4(8)	-3.0(7)	7.4(7)
C3	32.3(12)	40.3(12)	15.6(10)	-10.8(9)	-5.0(8)	7.4(10)
C4	23.1(11)	31.4(11)	40.2(13)	-21.7(10)	-9.5(9)	6.9(9)
C5	16.8(9)	22.7(9)	16.9(9)	-6.3(7)	-3.9(7)	4.6(7)
C6	14.4(8)	18.1(8)	16.0(9)	-7.4(7)	-4.2(6)	1.2(6)
C7	16.9(9)	15.9(8)	14.0(9)	-5.5(7)	-3.1(6)	-2.3(6)
C8	18.7(9)	19.7(9)	17.8(9)	-7.3(7)	-0.7(7)	-4.6(6)
C9	22.5(9)	18.6(9)	20.8(10)	-6.2(7)	-4.4(7)	4.1(7)
C10	30.3(12)	24.2(11)	21.3(11)	-6.4(9)	6.4(8)	-0.8(9)
O1W	26.9(8)	41.1(8)	18.8(8)	-3.2(6)	-2.6(6)	2.8(6)

Table 4 Bond Lengths for 18srv385.						
Atom	**Atom**	**Length/Å**		**Atom**	**Atom**	**Length/Å**
S1	C1	1.6733(18)		N4	C8	1.337(2)
N1	N2	1.3841(19)		N5	C8	1.335(2)
N1	C1	1.352(2)		N5	C9	1.352(2)
N1	C5	1.456(2)		N6	C7	1.334(2)
N2	C2	1.306(2)		C2	C4	1.474(3)
N3	C1	1.367(2)		C5	C6	1.502(2)
N3	C2	1.369(2)		C6	C7	1.418(2)
N3	C3	1.454(2)		C6	C9	1.364(2)
N4	C7	1.353(2)		C8	C10	1.496(2)

Table 5 Bond Angles for 18srv385.								
Atom	**Atom**	**Atom**	**Angle/°**		**Atom**	**Atom**	**Atom**	**Angle/°**
N2	N1	C5	120.61(13)		N2	C2	C4	124.90(17)
C1	N1	N2	112.84(14)		N3	C2	C4	123.68(17)
C1	N1	C5	126.43(15)		N1	C5	C6	113.14(14)
C2	N2	N1	103.75(13)		C7	C6	C5	122.76(14)
C1	N3	C2	108.41(14)		C9	C6	C5	121.21(15)
C1	N3	C3	124.83(16)		C9	C6	C7	116.02(15)
C2	N3	C3	126.73(16)		N4	C7	C6	120.29(14)
C8	N4	C7	117.84(14)		N6	C7	N4	117.03(14)
C8	N5	C9	115.10(14)		N6	C7	C6	122.67(15)
N1	C1	S1	127.76(13)		N4	C8	C10	116.92(15)

N1	C1	N3	103.52(14)		N5	C8	N4	126.10(15)
N3	C1	S1	128.71(13)		N5	C8	C10	116.98(15)
N2	C2	N3	111.43(15)		N5	C9	C6	124.58(16)

Table 6 Hydrogen Bonds for 18srv385.

D	**H**	**A**	**d(D-H)/Å**	**d(H-A)/Å**	**d(D-A)/Å**	**D-H-A/°**
N6	H6A	N4[1]	0.829(19)	2.17(2)	3.001(2)	176.0(18)
N6	H6B	S1	0.89(2)	2.62(2)	3.5030(17)	174.4(15)
O1W	H1WA	N5[2]	0.973(5)	1.896(7)	2.858(2)	170(2)
O1W	H1WB	O1W[3]	0.978(5)	1.81(2)	2.750(3)	161(6)
O1W	H1WC	O1W[4]	0.978(5)	1.87(3)	2.737(3)	146(5)

[1]2-X,-Y,1-Z; [2]1-X,1-Y,1-Z; [3]1-X,1-Y,2-Z; [4]-X,1-Y,2-Z

Table 7 Selected Torsion Angles for 18srv385.

A	**B**	**C**	**D**	**Angle/°**		**A**	**B**	**C**	**D**	**Angle/°**
C6	C5	N1	N2	65.53(18)		C7	C6	C5	N1	63.8(2)
C6	C5	N1	C1	-118.57(17)		C9	C6	C5	N1	-117.73(18)

Table 8 Hydrogen Atom Coordinates (Å×10^4) and Isotropic Displacement Parameters (Å^2×10^3) for 18srv385.

Atom	***x***	***y***	***z***	**U(eq)**
H3A	3740(50)	1179(18)	9829(18)	44(6)
H3B	7120(50)	1250(20)	9690(19)	46(6)
H3C	5360(40)	2330(18)	9875(18)	39(6)
H4A	7600(50)	4370(20)	8450(20)	58(7)

H4B	10030(50)	3471(17)	8547(17)	35(6)
H4C	9790(50)	4497(18)	7385(19)	38(6)
H5A	1930(40)	3411(14)	5340(14)	12(4)
H5B	1570(40)	2040(15)	5869(15)	17(4)
H6A	7910(40)	7(17)	5846(15)	25(5)
H6B	5540(40)	536(15)	6388(17)	23(5)
H9	4540(40)	4148(15)	3511(15)	21(5)
H10A	12710(70)	1790(30)	2260(20)	83(10)
H10B	12010(60)	2930(20)	1550(20)	66(8)
H10C	10610(70)	1740(30)	1770(30)	89(11)
H1WA	2800(50)	5486(17)	8633(8)	64(8)
H1WB	4070(120)	5110(60)	9880(50)	100(20)
H1WC	1240(90)	5160(50)	9950(40)	100(20)

Table 9 Atomic Occupancy for 18srv385.

Atom	***Occupancy***		**Atom**	***Occupancy***		**Atom**	***Occupancy***
H1WB	0.5		H1WC	0.5			

****

8.1.1.1.1.1.4 *19srv312*

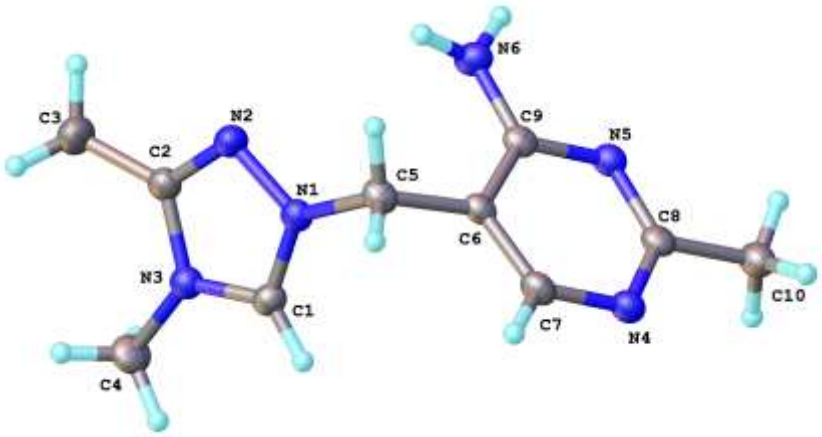

Table 1 Crystal data and structure refinement for 19srv312.	
Identification code	19srv312
Empirical formula	$C_{37}H_{47}BN_6O_3$
Formula weight	634.61
Temperature/K	120.0
Crystal system	orthorhombic
Space group	Pbca
a/Å	15.7186(7)
b/Å	17.8372(8)
c/Å	24.9840(10)
α/°	90
β/°	90
γ/°	90

Volume/Å^3	7004.9(5)
Z	8
ρ_{calc}g/cm^3	1.203
μ/mm^{-1}	0.077
F(000)	2720.0
Crystal size/mm^3	0.46 × 0.31 × 0.08
Radiation	MoKα (λ = 0.71073)
2Θ range for data collection/°	4.164 to 53
Index ranges	-19 ≤ h ≤ 19, -22 ≤ k ≤ 22, -31 ≤ l ≤ 31
Reflections collected	85226
Independent reflections	7260 [R_{int} = 0.1252, R_{sigma} = 0.0762]
Data/restraints/parameters	7260/6/451
Goodness-of-fit on F^2	1.015
Final R indexes [I>=2σ (I)]	R_1 = 0.0504, wR_2 = 0.1122
Final R indexes [all data]	R_1 = 0.0865, wR_2 = 0.1281
Largest diff. peak/hole / e Å^{-3}	0.26/-0.24

Table 2 Fractional Atomic Coordinates (×10^4) and Equivalent Isotropic Displacement Parameters (Å^2×10^3) for 19srv312. U_{eq} is defined as 1/3 of of the trace of the orthogonalised U_{IJ} tensor.

Atom	***x***	***y***	***z***	**U(eq)**
O1S	6317.3(9)	1243.2(8)	4379.6(6)	30.7(4)
C1S	7208.4(14)	1154.9(13)	4466.7(9)	36.8(5)
O2S	6208.5(11)	4543.2(9)	4292.8(6)	40.5(4)
C2S	6178.7(17)	4893.5(14)	3788.6(10)	50.8(7)
O3S	4771.3(12)	3716.6(9)	4489.0(7)	47.4(5)
C3S	4135(2)	4169.1(18)	4666.8(18)	96.1(14)
N1	5667.1(10)	1168.7(8)	5868.1(6)	20.4(3)
N2	6431.1(10)	1502.3(9)	5754.0(6)	25.1(4)
N3	6115.3(10)	1602.9(8)	6611.2(6)	21.2(4)
N4	2827.1(10)	972.0(9)	5389.0(6)	23.9(4)
N5	3436.3(10)	2045.0(9)	4965.5(6)	21.5(4)
N6	4878.9(12)	2166.9(10)	4851.3(7)	25.5(4)
C1	5486.6(12)	1226.6(10)	6381.3(7)	21.9(4)
C2	6689.5(12)	1766.2(11)	6214.7(7)	24.3(4)
C3	7499.6(14)	2174.4(13)	6308.5(9)	37.4(5)
C4	6176.6(14)	1814.7(12)	7176.2(8)	30.5(5)
C5	5202.6(12)	757.7(10)	5444.8(7)	22.6(4)

C6	4344.9(12)	1082.1(10)	5322.1(7)	19.4(4)
C7	3619.5(13)	715.0(11)	5473.9(7)	23.4(4)
C8	2781.2(12)	1637.8(11)	5139.4(7)	21.7(4)
C9	4230.9(12)	1765.3(10)	5041.0(7)	20.1(4)
C10	1908.4(13)	1945.4(12)	5046.6(8)	27.6(5)
C11	5709.8(12)	3488.8(10)	8066.9(7)	20.5(4)
C12	5296.8(13)	2879.8(11)	8305.9(7)	24.5(4)
C13	5732.3(15)	2273.6(11)	8520.9(8)	30.9(5)
C14	6610.2(15)	2255.6(12)	8507.2(8)	35.0(5)
C15	7044.2(14)	2841.5(13)	8270.8(8)	33.2(5)
C16	6602.6(13)	3439.6(11)	8052.5(7)	26.1(4)
C21	5698.9(12)	4955.6(10)	7754.0(7)	20.7(4)
C22	5536.9(12)	5493.9(11)	7356.9(8)	24.8(4)
C23	5911.2(13)	6199.6(11)	7356.5(9)	29.6(5)
C24	6474.3(13)	6395.2(11)	7758.3(9)	31.3(5)
C25	6647.3(13)	5883.9(11)	8157.8(8)	29.1(5)
C26	6262.8(12)	5182.1(11)	8154.5(8)	23.8(4)
C31	5102.5(12)	3822.2(10)	7146.2(7)	19.5(4)

C32	4444.7(12)	3356.5(10)	6974.2(8)	24.6(4)
C33	4438.7(13)	3032.8(11)	6467.9(8)	29.3(5)
C34	5091.2(14)	3165.7(11)	6112.7(8)	29.6(5)
C35	5758.2(14)	3615.6(12)	6272.0(8)	30.4(5)
C36	5761.5(13)	3929.4(11)	6778.6(8)	26.6(5)
C41	4278.6(12)	4350.3(10)	8047.3(7)	19.7(4)
C42	4149.1(12)	4294.7(10)	8601.6(7)	22.4(4)
C43	3415.3(13)	4542.8(11)	8850.8(8)	25.1(4)
C44	2768.9(13)	4873.2(11)	8555.6(8)	25.9(4)
C45	2870.4(13)	4937.4(11)	8005.6(8)	25.6(4)
C46	3604.5(12)	4679.7(10)	7762.5(8)	22.4(4)
B1	5186.5(14)	4153.9(12)	7757.9(8)	19.8(5)

Table 3 Anisotropic Displacement Parameters ($Å^2 \times 10^3$) for 19srv312. The Anisotropic displacement factor exponent takes the form: $-2\pi^2[h^2a^{*2}U_{11}+2hka^*b^*U_{12}+\ldots]$.

Atom	**U_{11}**	**U_{22}**	**U_{33}**	**U_{23}**	**U_{13}**	**U_{12}**
O1S	30.5(9)	35.0(9)	26.8(8)	6.7(7)	2.2(6)	2.8(7)
C1S	29.2(12)	36.9(13)	44.3(13)	1.1(11)	4.4(10)	4.8(10)

O2S	30.6(9)	46.7(10)	44.3(10)	14.3(8)	-3.0(7)	6.5(8)
C2S	49.2(16)	45.7(15)	57.6(16)	21.9(13)	-23.0(13)	-10.2(13)
O3S	41.9(11)	29.8(9)	70.5(12)	6.7(8)	22.4(9)	5.2(8)
C3S	52(2)	54(2)	182(4)	-30(2)	41(2)	7.6(16)
N1	21.4(9)	18.0(8)	21.8(8)	1.8(7)	-1.2(7)	0.0(7)
N2	22.7(9)	27.9(9)	24.5(9)	5.0(7)	-0.3(7)	-3.3(7)
N3	22.7(9)	18.9(8)	21.8(8)	0.5(7)	-0.2(7)	0.4(7)
N4	25.3(9)	23.1(8)	23.2(8)	4.6(7)	-0.7(7)	0.1(7)
N5	24.4(9)	19.4(8)	20.8(8)	0.8(6)	0.4(7)	2.1(7)
N6	26.6(10)	21.5(9)	28.5(9)	4.6(7)	3.5(8)	0.9(8)
C1	21.9(10)	19.3(9)	24.3(10)	1.4(8)	1.3(8)	-1.2(8)
C2	23.5(11)	24.5(10)	24.9(10)	5.4(8)	-1.4(8)	-1.1(8)
C3	29.5(13)	46.7(14)	35.8(12)	7.5(10)	-3.4(10)	-11.3(11)
C4	35.3(12)	33.4(12)	22.9(10)	-7.3(9)	-1.3(9)	-2.8(10)
C5	28.4(11)	18.8(10)	20.6(9)	-1.6(8)	-1.8(8)	1.9(8)
C6	25.3(11)	16.6(9)	16.3(9)	-0.2(7)	-1.9(7)	0.1(8)
C7	29.8(12)	19.4(10)	21.1(10)	3.1(8)	-2.3(8)	1.4(8)
C8	26.3(11)	23.0(10)	15.7(9)	-1.3(8)	0.5(8)	1.6(8)

C9	25.8(11)	17.4(9)	17.1(9)	-2.6(7)	-0.1(8)	-0.1(8)
C10	27.5(11)	30.4(11)	25.0(10)	3.9(9)	0.6(8)	3.9(9)
C11	24.0(10)	19.9(9)	17.6(9)	-4.8(8)	-0.2(8)	1.8(8)
C12	30.4(12)	22.0(10)	21.0(10)	-1.7(8)	-0.5(8)	2.6(9)
C13	47.1(14)	22.6(11)	23.0(10)	0.9(8)	3.8(9)	5.6(10)
C14	47.5(15)	34.0(12)	23.4(11)	-1.2(9)	-2.9(10)	22.8(11)
C15	30.9(12)	42.6(13)	26.1(11)	-5.8(10)	-1.1(9)	15.7(10)
C16	27.3(11)	29.4(11)	21.7(10)	-4.6(8)	1.3(8)	3.5(9)
C21	18.2(10)	21.3(10)	22.6(9)	-4.2(8)	5.2(8)	1.0(8)
C22	20.7(11)	21.1(10)	32.6(11)	-0.2(8)	-1.3(8)	0.2(8)
C23	27.2(12)	20.6(10)	40.8(12)	2.5(9)	5.4(9)	2.5(9)
C24	29.0(12)	19.2(10)	45.6(13)	-7.9(9)	8.3(10)	-6.2(9)
C25	26.3(12)	30.5(11)	30.6(11)	-12.1(9)	4.0(9)	-7.0(9)
C26	22.6(11)	24.4(10)	24.2(10)	-4.5(8)	2.3(8)	-2.2(8)
C31	21.6(10)	16.1(9)	20.9(9)	1.3(7)	-1.0(8)	2.3(8)
C32	24.7(11)	22.9(10)	26.3(10)	-1.9(8)	3.2(8)	-3.5(8)
C33	30.1(12)	27.2(11)	30.5(11)	-7.8(9)	-2.8(9)	-5.4(9)
C34	38.6(13)	28.4(11)	21.9(10)	-6.8(8)	0.4(9)	2.3(10)

C35	32.9(12)	33.5(12)	24.7(10)	-2.7(9)	8.2(9)	-4.0(10)
C36	25.9(11)	28.1(11)	25.8(10)	-4.1(8)	1.5(8)	-4.6(9)
C41	21.3(10)	14.9(9)	22.8(9)	-2.1(7)	-0.7(8)	-3.4(7)
C42	23.2(11)	20.2(9)	23.9(10)	-2.3(8)	-2.5(8)	-0.8(8)
C43	26.7(11)	26.1(10)	22.5(10)	-3.6(8)	2.5(8)	-3.3(9)
C44	19.6(10)	24.7(10)	33.5(11)	-6.8(9)	3.0(9)	-1.4(8)
C45	22.9(11)	21.4(10)	32.4(11)	-1.1(8)	-5.0(9)	1.0(8)
C46	24.5(11)	21.4(10)	21.3(9)	0.0(8)	0.6(8)	-1.1(8)
B1	20.4(11)	18.1(11)	21.0(10)	-1.7(9)	1.5(9)	-2.0(9)

Table 4 Bond Lengths for 19srv312.

Atom	**Atom**	**Length/Å**		**Atom**	**Atom**	**Length/Å**
O1S	C1S	1.426(3)		C13	C14	1.381(3)
O2S	C2S	1.407(3)		C14	C15	1.381(3)
O3S	C3S	1.360(3)		C15	C16	1.385(3)
N1	N2	1.370(2)		C21	C22	1.404(3)
N1	C1	1.317(2)		C21	C26	1.396(3)

N1	C5	1.479(2)		C21	B1	1.641(3)
N2	C2	1.308(2)		C22	C23	1.390(3)
N3	C1	1.326(2)		C23	C24	1.383(3)
N3	C2	1.371(2)		C24	C25	1.379(3)
N3	C4	1.464(2)		C25	C26	1.390(3)
N4	C7	1.344(2)		C31	C32	1.394(3)
N4	C8	1.343(2)		C31	C36	1.398(3)
N5	C8	1.333(2)		C31	B1	1.644(3)
N5	C9	1.358(2)		C32	C33	1.391(3)
N6	C9	1.332(2)		C33	C34	1.377(3)
C2	C3	1.485(3)		C34	C35	1.379(3)
C5	C6	1.499(3)		C35	C36	1.384(3)
C6	C7	1.369(3)		C41	C42	1.403(3)
C6	C9	1.418(3)		C41	C46	1.405(3)
C8	C10	1.496(3)		C41	B1	1.638(3)
C11	C12	1.399(3)		C42	C43	1.383(3)
C11	C16	1.407(3)		C43	C44	1.387(3)

C11	B1	1.637(3)		C44	C45	1.388(3)
C12	C13	1.388(3)		C45	C46	1.383(3)

Table 5 Bond Angles for 19srv312.

Atom	**Atom**	**Atom**	**Angle/°**		**Atom**	**Atom**	**Atom**	**Angle/°**
N2	N1	C5	119.94(14)		C15	C16	C11	122.6(2)
C1	N1	N2	110.93(15)		C22	C21	B1	120.73(16)
C1	N1	C5	128.93(16)		C26	C21	C22	115.06(17)
C2	N2	N1	104.20(15)		C26	C21	B1	124.02(17)
C1	N3	C2	106.58(15)		C23	C22	C21	122.90(19)
C1	N3	C4	126.68(16)		C24	C23	C22	119.94(19)
C2	N3	C4	126.73(16)		C25	C24	C23	118.99(19)
C8	N4	C7	115.12(17)		C24	C25	C26	120.37(19)
C8	N5	C9	117.71(16)		C25	C26	C21	122.74(19)
N1	C1	N3	107.51(16)		C32	C31	C36	115.39(17)
N2	C2	N3	110.78(17)		C32	C31	B1	124.08(16)
N2	C2	C3	125.54(18)		C36	C31	B1	120.14(16)

N3	C2	C3	123.67(17)		C33	C32	C31	122.19(18)
N1	C5	C6	113.51(15)		C34	C33	C32	120.65(19)
C7	C6	C5	120.53(17)		C33	C34	C35	118.72(18)
C7	C6	C9	116.31(17)		C34	C35	C36	120.14(19)
C9	C6	C5	123.16(17)		C35	C36	C31	122.89(19)
N4	C7	C6	124.41(18)		C42	C41	C46	114.83(17)
N4	C8	C10	116.45(17)		C42	C41	B1	123.16(17)
N5	C8	N4	126.27(18)		C46	C41	B1	121.53(16)
N5	C8	C10	117.27(17)		C43	C42	C41	122.85(18)
N5	C9	C6	120.06(17)		C42	C43	C44	120.50(18)
N6	C9	N5	117.14(17)		C43	C44	C45	118.50(18)
N6	C9	C6	122.79(18)		C46	C45	C44	120.22(18)
C12	C11	C16	115.17(17)		C45	C46	C41	123.09(18)
C12	C11	B1	122.06(17)		C11	B1	C21	112.80(16)
C16	C11	B1	122.31(17)		C11	B1	C31	102.59(14)
C13	C12	C11	122.77(19)		C11	B1	C41	112.62(15)
C14	C13	C12	120.1(2)		C21	B1	C31	110.34(15)

C15	C14	C13	119.14(19)		C41	B1	C21	104.11(14)
C14	C15	C16	120.3(2)		C41	B1	C31	114.67(16)

Table 6 Hydrogen Bonds for 19srv312.

D	**H**	**A**	**d(D-H)/Å**	**d(H-A)/Å**	**d(D-A)/Å**	**D-H-A/°**
O2S	H2S	N4[1]	0.89(3)	1.94(3)	2.819(2)	172(3)
O3S	H3S	O2S	0.94(3)	1.80(3)	2.742(2)	177(3)
N6	H6A	O3S	0.93(2)	2.01(2)	2.914(2)	163(2)
N6	H6B	O1S	0.92(3)	2.20(3)	3.036(2)	151(2)

[1]1/2+X,1/2-Y,1-Z

Table 7 Selected Torsion Angles for 19srv312.

A	**B**	**C**	**D**	**Angle/°**		**A**	**B**	**C**	**D**	**Angle/°**
C6	C5	N1	N2	-118.48(18)		C21	B1	C41	C42	-90.4(2)
C6	C5	N1	C1	67.3(2)		C21	B1	C41	C46	81.3(2)
C7	C6	C5	N1	-108.27(19)		C31	B1	C11	C12	-87.53(19)
C9	C6	C5	N1	72.8(2)		C31	B1	C11	C16	84.3(2)

C11	B1	C21	C22	155.66(16)		C31	B1	C21	C22	41.6(2)
C11	B1	C21	C26	-29.7(2)		C31	B1	C21	C26	-143.73(18)
C11	B1	C31	C32	87.4(2)		C31	B1	C41	C42	148.98(17)
C11	B1	C31	C36	-85.1(2)		C31	B1	C41	C46	-39.3(2)
C11	B1	C41	C42	32.2(2)		C41	B1	C11	C12	36.3(2)
C11	B1	C41	C46	-156.16(16)		C41	B1	C11	C16	-151.94(17)
C21	B1	C11	C12	153.77(17)		C41	B1	C21	C22	-81.9(2)
C21	B1	C11	C16	-34.4(2)		C41	B1	C21	C26	92.7(2)
C21	B1	C31	C32	-152.13(18)		C41	B1	C31	C32	-35.0(2)
C21	B1	C31	C36	35.4(2)		C41	B1	C31	C36	152.52(17)

Table 8 Hydrogen Atom Coordinates (Å×10^4) and Isotropic Displacement Parameters (Å^2×10^3) for 19srv312.

Atom	***x***	***y***	***z***	**U(eq)**
H1SA	7452.48	851.43	4177.99	55
H1SB	7303.14	904.01	4810.49	55
H1SC	7481.86	1648.61	4471.31	55
H1S	6246(17)	1420(15)	4071(11)	60(9)

H2SA	6148.76	4510.91	3507.75	76
H2SB	6691.68	5197.74	3738.32	76
H2SC	5674.92	5215.98	3768.58	76
H2S	6740(20)	4423(17)	4382(12)	80(11)
H3SA	4060.67	4588.89	4418.01	144
H3SB	4280.02	4362.72	5022.31	144
H3SC	3604.2	3881.83	4688.19	144
H3S	5269(19)	4002(17)	4434(11)	68(9)
H1	4995.49	1033.78	6555.03	26
H3A	7377.15	2665.13	6467.25	56
H3B	7796.94	2243.53	5967.31	56
H3C	7859.04	1883.95	6552.85	56
H4A	6120.91	2359.88	7209.99	46
H4B	6729.41	1656.74	7318.26	46
H4C	5720.64	1569.34	7378.29	46
H5A	5130.84	229.63	5558.11	27
H5B	5549.43	759.4	5114.09	27
H7	3680.1	246.84	5651.2	28

H10A	1664.78	2110	5388	41
H10B	1546.77	1555.08	4890.18	41
H10C	1941.66	2372.5	4800.78	41
H6A	4789(14)	2619(14)	4678(9)	40(7)
H6B	5409(17)	1953(14)	4815(9)	49(7)
H12	4692.96	2881.34	8321.71	29
H13	5425.88	1870.42	8677.73	37
H14	6911.62	1845.49	8658.43	42
H15	7648.22	2834.26	8257.91	40
H16	6914.76	3832.04	7886.61	31
H22	5154.41	5370.14	7076.05	30
H23	5780.46	6547.4	7080.55	35
H24	6737.96	6874.48	7759.1	38
H25	7031.36	6012.01	8436.79	35
H26	6389.02	4842.42	8436.41	29
H32	3985.27	3257.03	7210.86	30
H33	3979.83	2716.85	6366.08	35
H34	5082.13	2951.6	5764.55	36

H35	6216.49	3710.34	6033.47	36
H36	6232.39	4230.9	6880.92	32
H42	4584.22	4077.21	8815.03	27
H43	3353.67	4486.38	9226.89	30
H44	2267.93	5051.58	8726.03	31
H45	2433.98	5159.03	7795.47	31
H46	3655.55	4727.72	7385.17	27

****

8.1.1.1.1.1.5 *19srv347*

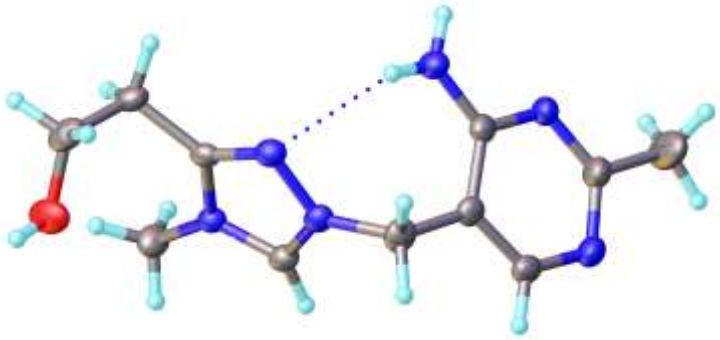

Table 1 Crystal data and structure refinement for 19srv347.	
Identification code	19srv347
Empirical formula	$C_{35}H_{37}BN_6O$
Formula weight	568.51

Temperature/K	120.0
Crystal system	monoclinic
Space group	$P2_1/n$
a/Å	9.0388(3)
b/Å	18.0004(6)
c/Å	20.5112(7)
α/°	90
β/°	93.4831(16)
γ/°	90
Volume/Å^3	3331.05(19)
Z	4
ρ_{calc}g/cm^3	1.134
μ/mm^{-1}	0.070
F(000)	1208.0
Crystal size/mm^3	0.31 × 0.25 × 0.22
Radiation	Mo Kα (λ = 0.71073)
2Θ range for data collection/°	4.526 to 57.998
Index ranges	$-12 \leq h \leq 12$, $-24 \leq k \leq 24$, $-27 \leq l \leq 27$
Reflections collected	51420
Independent reflections	8855 [R_{int} = 0.0405, R_{sigma} = 0.0347]
Data/restraints/parameters	8855/1/396

Goodness-of-fit on F^2	1.039
Final R indexes [I>=2σ (I)]	R_1 = 0.0474, wR_2 = 0.1162
Final R indexes [all data]	R_1 = 0.0724, wR_2 = 0.1278
Largest diff. peak/hole / e $Å^{-3}$	0.29/-0.24

Table 2 Fractional Atomic Coordinates ($\times 10^4$) and Equivalent Isotropic Displacement Parameters ($Å^2 \times 10^3$) for 19srv347. U_{eq} is defined as 1/3 of of the trace of the orthogonalised U_{IJ} tensor.

Atom	***x***	***y***	***z***	**U(eq)**
O1	6766.3(14)	2975.1(6)	8506.0(6)	42.4(3)
O1A	8447(11)	2973(4)	8172(5)	42(2)
N1	5919.4(12)	2954.2(6)	6404.2(5)	23.2(2)
N2	6846.9(12)	3432.8(6)	6752.0(5)	25.0(2)
N3	4840.1(11)	3197.8(6)	7270.9(5)	22.0(2)
N4	4427.6(14)	4107.3(6)	4636.6(5)	30.9(3)
N5	3574.3(14)	2907.9(7)	4318.8(5)	34.7(3)
N6	6199.5(13)	4287.5(6)	5464.2(5)	29.6(3)
C1	4723.0(14)	2818.4(7)	6714.1(6)	23.6(3)
C2	6158.1(14)	3574.7(6)	7282.7(6)	22.0(2)

C3	3724.6(15)	3234.4(8)	7762.8(7)	31.4(3)
C4	6743.4(15)	4045.9(7)	7833.8(6)	28.7(3)
C5	7624.6(16)	3581.5(8)	8335.2(7)	36.2(3)
C6	6302.2(16)	2679.3(8)	5758.9(6)	30.3(3)
C7	5360.4(14)	3035.6(7)	5221.6(6)	24.4(3)
C8	5337.5(14)	3812.9(7)	5110.5(6)	24.3(3)
C9	3607.3(18)	3644.8(8)	4257.9(7)	36.4(3)
C10	4443.5(16)	2621.7(7)	4811.7(6)	28.8(3)
C11	2651(3)	3988.4(11)	3716.4(9)	68.1(7)
C12	7257.6(13)	3749.1(7)	1514.9(7)	24.8(3)
C13	7172.6(14)	3503.8(7)	865.3(7)	29.8(3)
C14	6467.3(15)	2849.2(8)	664.8(8)	36.9(3)
C15	5812.4(16)	2404.9(8)	1117.1(9)	43.0(4)
C16	5884.8(15)	2619.4(8)	1762.5(9)	40.4(4)
C17	6602.0(14)	3278.5(8)	1960.2(8)	31.8(3)
C18	9904.0(13)	4338.0(7)	1568.7(6)	22.4(2)
C19	10577.4(14)	4551.6(7)	999.0(7)	25.9(3)
C20	12043.6(15)	4367.2(7)	884.2(7)	30.2(3)

C21	12883.4(14)	3953.6(7)	1336.9(7)	31.1(3)
C22	12250.6(14)	3723.2(7)	1900.9(7)	29.5(3)
C23	10790.9(14)	3913.5(7)	2010.1(6)	25.2(3)
C24	7524.9(13)	5211.7(7)	1238.1(6)	22.9(3)
C25	6137.0(14)	5220.7(7)	901.1(6)	25.0(3)
C26	5597.9(16)	5838.9(8)	550.2(6)	30.9(3)
C27	6444.3(18)	6473.5(8)	525.4(7)	34.4(3)
C28	7817.4(17)	6491.0(8)	860.6(7)	34.8(3)
C29	8337.8(15)	5873.4(7)	1208.4(7)	29.4(3)
C30	7963.8(14)	4811.7(7)	2445.8(6)	26.2(3)
C31	6565.6(16)	4833.1(7)	2711.5(7)	31.6(3)
C32	6355.4(19)	5139.3(9)	3322.6(8)	41.2(4)
C33	7520(2)	5448.1(9)	3688.7(8)	49.0(4)
C34	8908(2)	5448.1(9)	3441.1(9)	47.7(4)
C35	9116.9(17)	5132.7(8)	2834.5(7)	35.2(3)
B1	8162.4(15)	4521.2(8)	1698.3(7)	22.1(3)

Table 3 Anisotropic Displacement Parameters ($Å^2×10^3$) for 19srv347. The Anisotropic displacement factor exponent takes the form: $-2\pi^2[h^2a^{*2}U_{11}+2hka^*b^*U_{12}+\ldots]$.

Atom	**U_{11}**	**U_{22}**	**U_{33}**	**U_{23}**	**U_{13}**	**U_{12}**
O1	44.9(7)	32.0(6)	47.8(7)	12.0(5)	-19.2(5)	1.4(5)
N1	25.0(5)	18.8(5)	25.4(5)	-0.2(4)	-1.8(4)	3.3(4)
N2	23.8(5)	21.6(5)	29.2(6)	1.0(4)	-1.8(4)	0.0(4)
N3	22.5(5)	19.2(5)	24.0(5)	0.7(4)	-1.0(4)	-1.2(4)
N4	44.6(7)	26.0(6)	21.3(5)	1.7(4)	-4.7(5)	-6.8(5)
N5	49.2(7)	30.2(6)	24.1(6)	-2.9(5)	-2.8(5)	-9.8(5)
N6	35.6(6)	24.5(6)	27.9(6)	0.9(4)	-5.1(5)	-5.8(5)
C1	23.3(6)	19.6(6)	27.3(6)	0.1(5)	-3.4(5)	0.9(5)
C2	22.9(6)	15.7(5)	26.8(6)	3.9(4)	-3.8(5)	0.2(5)
C3	29.2(7)	36.2(7)	29.4(7)	-3.5(6)	7.2(5)	-6.7(6)
C4	32.0(7)	21.2(6)	32.2(7)	-2.0(5)	-3.1(5)	-5.1(5)
C5	34.0(8)	31.3(7)	41.1(8)	-4.9(6)	-15.8(6)	-0.1(6)
C6	35.0(7)	27.0(7)	29.1(7)	-5.2(5)	3.1(6)	9.7(6)
C7	28.0(6)	23.2(6)	22.4(6)	-3.8(5)	5.7(5)	2.2(5)

C8	28.4(6)	25.8(6)	19.3(6)	-1.9(5)	5.6(5)	-3.2(5)
C9	51.8(9)	31.7(7)	24.7(7)	-0.2(5)	-6.3(6)	-9.3(7)
C10	38.9(8)	23.1(6)	25.1(6)	-4.7(5)	7.1(6)	-3.1(5)
C11	103.7(17)	46.2(10)	48.3(10)	8.2(8)	-44.6(11)	-17.8(11)
C12	13.9(5)	20.5(6)	40.0(7)	3.9(5)	2.0(5)	5.0(5)
C13	21.8(6)	24.1(6)	43.4(8)	-1.2(6)	0.7(5)	4.3(5)
C14	26.1(7)	26.6(7)	56.8(10)	-8.0(6)	-6.6(6)	6.1(6)
C15	24.5(7)	22.5(7)	80.3(13)	0.6(7)	-10.0(7)	0.4(6)
C16	19.7(6)	26.7(7)	74.8(12)	18.4(7)	2.2(7)	1.8(5)
C17	18.6(6)	27.4(7)	49.6(8)	10.9(6)	3.8(6)	5.1(5)
C18	17.7(6)	21.1(6)	28.5(6)	-4.1(5)	2.4(5)	-0.9(5)
C19	21.8(6)	23.4(6)	33.1(7)	-1.5(5)	5.3(5)	0.6(5)
C20	24.1(6)	24.4(6)	43.6(8)	-6.8(6)	14.0(6)	-3.1(5)
C21	16.2(6)	25.3(6)	52.5(9)	-12.4(6)	6.1(6)	-0.9(5)
C22	21.2(6)	26.8(7)	39.7(8)	-9.4(6)	-5.5(5)	3.6(5)
C23	22.4(6)	24.9(6)	28.2(6)	-5.2(5)	1.3(5)	1.1(5)
C24	19.9(6)	22.1(6)	27.4(6)	-0.4(5)	8.0(5)	2.2(5)

C25	26.1(6)	22.4(6)	27.1(6)	0.1(5)	5.2(5)	2.2(5)
C26	35.8(7)	31.8(7)	25.1(6)	0.1(5)	1.2(5)	9.6(6)
C27	49.6(9)	27.6(7)	27.2(7)	7.2(5)	11.2(6)	8.8(6)
C28	41.1(8)	23.4(7)	42.2(8)	4.5(6)	20.6(7)	-1.3(6)
C29	22.4(6)	25.9(6)	40.8(8)	1.1(6)	10.0(5)	-0.2(5)
C30	27.3(6)	19.9(6)	32.2(7)	4.9(5)	7.5(5)	6.3(5)
C31	32.2(7)	27.8(7)	36.0(7)	9.6(6)	12.2(6)	11.0(6)
C32	48.5(9)	36.3(8)	41.4(8)	11.0(7)	23.4(7)	19.4(7)
C33	71.6(12)	39.6(9)	37.2(9)	-6.2(7)	14.8(8)	20.1(9)
C34	55.8(11)	38.5(9)	48.5(10)	-18.0(7)	1.6(8)	9.4(8)
C35	35.1(8)	28.6(7)	42.6(8)	-8.2(6)	7.2(6)	4.2(6)
B1	16.4(6)	21.1(6)	29.1(7)	1.7(5)	4.8(5)	1.9(5)

Table 4 Bond Lengths for 19srv347.

Atom	**Atom**	**Length/Å**		**Atom**	**Atom**	**Length/Å**
O1	C5	1.3962(19)		C14	C15	1.385(2)
O1A	C5	1.376(5)		C15	C16	1.377(2)

N1	N2	1.3716(15)		C16	C17	1.400(2)
N1	C1	1.3102(16)		C18	C19	1.4035(18)
N1	C6	1.4738(16)		C18	C23	1.3994(18)
N2	C2	1.3115(17)		C18	B1	1.6457(18)
N3	C1	1.3294(16)		C19	C20	1.3999(18)
N3	C2	1.3698(16)		C20	C21	1.381(2)
N3	C3	1.4706(17)		C21	C22	1.385(2)
N4	C8	1.3435(17)		C22	C23	1.3943(18)
N4	C9	1.3328(18)		C24	C25	1.3952(18)
N5	C9	1.3329(19)		C24	C29	1.4026(18)
N5	C10	1.3447(18)		C24	B1	1.6437(19)
N6	C8	1.3395(16)		C25	C26	1.3968(18)
C2	C4	1.4848(17)		C26	C27	1.377(2)
C4	C5	1.5138(19)		C27	C28	1.382(2)
C6	C7	1.4956(18)		C28	C29	1.388(2)
C7	C8	1.4177(18)		C30	C31	1.4069(18)
C7	C10	1.3653(18)		C30	C35	1.398(2)

C9	C11	1.499(2)		C30	B1	1.6401(19)
C12	C13	1.401(2)		C31	C32	1.393(2)
C12	C17	1.4032(19)		C32	C33	1.373(3)
C12	B1	1.6446(19)		C33	C34	1.382(3)
C13	C14	1.3899(19)		C34	C35	1.391(2)

Table 5 Bond Angles for 19srv347.

Atom	**Atom**	**Atom**	**Angle/°**		**Atom**	**Atom**	**Atom**	**Angle/°**
N2	N1	C6	120.56(11)		C15	C16	C17	120.69(15)
C1	N1	N2	111.18(10)		C16	C17	C12	121.97(15)
C1	N1	C6	128.22(11)		C19	C18	B1	123.17(11)
C2	N2	N1	104.36(10)		C23	C18	C19	115.32(11)
C1	N3	C2	107.06(11)		C23	C18	B1	121.40(11)
C1	N3	C3	126.18(11)		C20	C19	C18	122.55(13)
C2	N3	C3	126.69(11)		C21	C20	C19	120.13(13)
C9	N4	C8	118.01(12)		C20	C21	C22	119.02(12)
C9	N5	C10	115.87(12)		C21	C22	C23	120.24(13)

N1	C1	N3	107.21(11)		C22	C23	C18	122.73(13)
N2	C2	N3	110.19(11)		C25	C24	C29	115.23(12)
N2	C2	C4	125.31(11)		C25	C24	B1	124.51(11)
N3	C2	C4	124.45(11)		C29	C24	B1	120.05(11)
C2	C4	C5	110.50(11)		C24	C25	C26	122.65(13)
O1	C5	C4	108.95(11)		C27	C26	C25	120.17(13)
O1A	C5	C4	123.0(5)		C26	C27	C28	118.97(13)
N1	C6	C7	111.33(10)		C27	C28	C29	120.24(13)
C8	C7	C6	122.94(12)		C28	C29	C24	122.72(13)
C10	C7	C6	121.13(12)		C31	C30	B1	121.52(12)
C10	C7	C8	115.92(12)		C35	C30	C31	115.08(13)
N4	C8	C7	120.53(11)		C35	C30	B1	123.01(12)
N6	C8	N4	116.79(11)		C32	C31	C30	122.30(15)
N6	C8	C7	122.69(12)		C33	C32	C31	120.70(15)
N4	C9	C11	116.71(13)		C32	C33	C34	118.82(15)
N5	C9	N4	125.59(13)		C33	C34	C35	120.28(17)
N5	C9	C11	117.70(13)		C34	C35	C30	122.81(15)

N5	C10	C7	123.99(12)		C12	B1	C18	105.13(10)
C13	C12	C17	115.32(12)		C24	B1	C12	110.82(10)
C13	C12	B1	118.80(11)		C24	B1	C18	111.35(10)
C17	C12	B1	125.81(12)		C30	B1	C12	113.71(10)
C14	C13	C12	123.11(14)		C30	B1	C18	112.02(10)
C15	C14	C13	119.90(15)		C30	B1	C24	103.97(10)
C16	C15	C14	119.00(14)					

Table 6 Hydrogen Bonds for 19srv347.

D	**H**	**A**	**d(D-H)/Å**	**d(H-A)/Å**	**d(D-A)/Å**	**D-H-A/°**
O1	H1	N5[1]	0.84	1.93	2.7649(15)	175.7
N6	H6A	N4[2]	0.88	2.09	2.9493(16)	164.1
N6	H6B	N2	0.88	2.34	3.0819(15)	141.4

[1]1/2+X,1/2-Y,1/2+Z; [2]1-X,1-Y,1-Z

Table 7 Selected Torsion Angles for 19srv347.

A	**B**	**C**	**D**	**Angle/°**		**A**	**B**	**C**	**D**	**Angle/°**

C2	C4	C5	O1	-51.86(16)		C18	B1	C24	C25	136.44(12)
C2	C4	C5	O1A	33.2(6)		C18	B1	C24	C29	-49.10(15)
C5	C4	C2	N2	-89.79(15)		C18	B1	C30	C31	-164.80(11)
C5	C4	C2	N3	87.15(15)		C18	B1	C30	C35	22.82(17)
C7	C6	N1	N2	-106.78(13)		C24	B1	C12	C13	54.47(14)
C7	C6	N1	C1	71.09(16)		C24	B1	C12	C17	-128.82(12)
C8	C7	C6	N1	60.35(17)		C24	B1	C18	C19	-20.60(16)
C10	C7	C6	N1	-118.57(13)		C24	B1	C18	C23	163.41(11)
C12	B1	C18	C19	99.47(13)		C24	B1	C30	C31	74.85(14)
C12	B1	C18	C23	-76.52(14)		C24	B1	C30	C35	-97.53(14)
C12	B1	C24	C25	19.79(17)		C30	B1	C12	C13	171.16(11)
C12	B1	C24	C29	-165.74(11)		C30	B1	C12	C17	-12.14(17)
C12	B1	C30	C31	-45.77(16)		C30	B1	C18	C19	-136.56(12)
C12	B1	C30	C35	141.85(12)		C30	B1	C18	C23	47.45(15)
C18	B1	C12	C13	-65.95(14)		C30	B1	C24	C25	-102.76(13)
C18	B1	C12	C17	110.75(13)		C30	B1	C24	C29	71.71(14)

Table 8 Hydrogen Atom Coordinates (Å×10^4) and Isotropic Displacement Parameters (Å^2×10^3) for 19srv347.

Atom	***x***	***y***	***z***	**U(eq)**
H1	7277.61	2691.91	8755.02	64
H1A	7891.5	2599.62	8130.65	63
H6A	6152.05	4766.74	5380.8	36
H6B	6813.21	4119.98	5779.92	36
H1B	3921.48	2506.86	6568.15	28
H3A	3036.37	3643.56	7656.44	47
H3B	4219.22	3318.86	8194.9	47
H3C	3174.78	2765.29	7764.84	47
H4A	5909.43	4288.93	8041.51	34
H4B	7385.78	4439.34	7666.85	34
H5AA	8550.01	3405.41	8151.7	43
H5AB	7893.54	3884.89	8727.27	43
H5BC	8314.99	3924.85	8577.25	43
H5BD	6915.4	3406	8650.8	43

H6C	6163.61	2134	5740.27	36
H6D	7358.62	2786.43	5696.59	36
H10	4417.93	2099.8	4878.77	35
H11A	3279.57	4213.04	3397.18	102
H11B	2022.53	4372.01	3896.03	102
H11C	2024.61	3604.81	3501.83	102
H13	7618.22	3798.71	546.98	36
H14	6434.51	2706.94	218.16	44
H15	5320.59	1958.66	984.02	52
H16	5443.48	2317.11	2076.94	49
H17	6646.09	3411.02	2409.28	38
H19	10016.55	4832.05	678.97	31
H20	12461.62	4527	494.06	36
H21	13880.42	3828.88	1262.47	37
H22	12813.07	3434.59	2214.49	35
H23	10381.51	3747.95	2400.33	30
H25	5534.26	4788.91	910.59	30

H26	4645.09	5821.66	328.17	37
H27	6089.76	6892.65	281.58	41
H28	8406.95	6927.41	852.92	42
H29	9283.76	5899.71	1435.83	35
H31	5735.9	4631.7	2465.55	38
H32	5396.09	5134.33	3487.84	49
H33	7373.92	5658.17	4104.83	59
H34	9723.46	5664.42	3686.33	57
H35	10084.31	5135.45	2677.57	42

Table 9 Atomic Occupancy for 19srv347.

Atom	***Occupancy***		**Atom**	***Occupancy***		**Atom**	***Occupancy***
O1	0.9		H1	0.9		O1A	0.1
H1A	0.1		H5AA	0.9		H5AB	0.9
H5BC	0.1		H5BD	0.1			

Table 10 Solvent masks information for 19srv347.

Number	X	Y	Z	Volume	Electron count	Content
1	0.500	0.000	1.000	209.4	44.1	2 C2H6O
2	0.000	0.500	0.500	209.4	44.1	2 C2H6O

****

8.1.1.1.1.1.6 *19srv333*

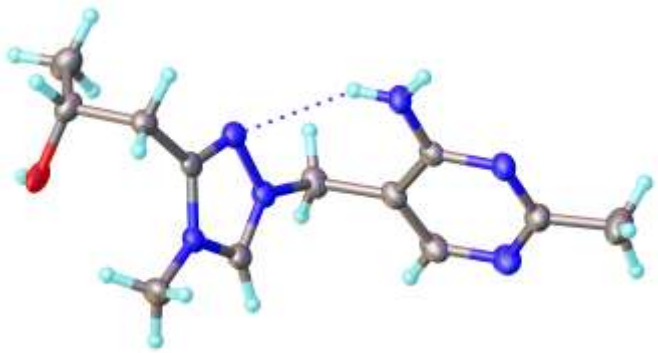

Table 1 Crystal data and structure refinement for 19srv333.	
Identification code	19srv333
Empirical formula	$C_{38}H_{43}BCl_2N_6O$
Formula weight	681.49
Temperature/K	120.0
Crystal system	monoclinic
Space group	$P2_1/n$
a/Å	9.2435(4)

b/Å	18.4354(8)
c/Å	21.1224(9)
α/°	90
β/°	93.4409(16)
γ/°	90
Volume/Å^3	3592.9(3)
Z	4
ρ_{calc}g/cm^3	1.260
μ/mm^{-1}	0.220
F(000)	1440.0
Crystal size/mm^3	0.34 × 0.19 × 0.08
Radiation	Mo Kα (λ = 0.71073)
2Θ range for data collection/°	3.864 to 54
Index ranges	-11 ≤ h ≤ 11, -23 ≤ k ≤ 23, -26 ≤ l ≤ 26
Reflections collected	48290
Independent reflections	7837 [R_{int} = 0.0474, R_{sigma} = 0.0369]
Data/restraints/parameters	7837/1/456
Goodness-of-fit on F^2	1.034
Final R indexes [I>=2σ (I)]	R_1 = 0.0602, wR_2 = 0.1487
Final R indexes [all data]	R_1 = 0.0895, wR_2 = 0.1655
Largest diff. peak/hole / e Å^{-3}	0.92/-0.65

Table 2 Fractional Atomic Coordinates ($\times 10^4$) and Equivalent Isotropic Displacement Parameters ($Å^2 \times 10^3$) for 19srv333. U_{eq} is defined as 1/3 of of the trace of the orthogonalised U_{IJ} tensor.

Atom	***x***	***y***	***z***	**U(eq)**
Cl1	6803.2(10)	8322.5(4)	3811.9(4)	56.9(2)
Cl2	9323.5(15)	8686.8(7)	5073.9(5)	84.2(4)
Cl2A	10321(6)	9128(4)	4894(3)	46.5(16)
C1S	8504(4)	8786.4(19)	3820.0(15)	53.0(8)
C2S	8783(4)	9222(2)	4409.1(16)	67.0(10)
O1	3412(3)	2164.4(12)	1508.7(12)	48.2(7)
O1A	2064(6)	1160(3)	1158(3)	64.0(15)
O1B	1306(4)	1899(3)	1982(2)	38.1(10)
N1	4522(2)	2086.2(10)	3565.0(9)	24.3(4)
N2	3584(2)	1633.3(10)	3227.7(9)	24.4(4)
N3	5449(2)	1918.5(10)	2677.9(9)	23.9(4)
N4	5787(2)	856.7(10)	5299.0(9)	24.9(4)
N5	6732(2)	2000.9(11)	5635.0(10)	32.8(5)
N6	4151(2)	736.5(12)	4451.9(10)	24.7(4)
C1	5632(3)	2253.8(12)	3235.5(11)	26.2(5)
C2	4181(2)	1537.8(12)	2685.2(11)	22.4(5)
C3	3543(2)	1108.4(12)	2144.8(11)	25.3(5)
C4	2551(3)	1571.6(13)	1702.7(12)	30.4(5)
C5	2064(6)	1160(3)	1158(3)	64.0(15)
C5A	1306(4)	1899(3)	1982(2)	38.1(10)

C5B	3412(3)	2164.4(12)	1508.7(12)	48.2(7)
C6	6473(3)	1910.7(15)	2171.5(11)	32.9(6)
C7	4195(3)	2324.9(13)	4207.0(11)	28.9(5)
C8	5076(3)	1932.0(12)	4718.5(10)	24.4(5)
C9	4994(2)	1173.6(12)	4817.3(10)	21.8(5)
C10	6586(3)	1283.2(13)	5690.4(11)	28.7(5)
C11	5972(3)	2304.5(13)	5140.2(11)	30.3(5)
C12	7344(3)	925.0(16)	6253.7(14)	44.4(7)
C21	5219(2)	4347.1(12)	3494.2(11)	24.6(5)
C22	4352(3)	3953.0(13)	3050.1(11)	26.9(5)
C23	2937(3)	3750.7(14)	3152.0(13)	33.7(6)
C24	2330(3)	3932.1(14)	3711.6(14)	38.7(6)
C25	3159(3)	4301.8(15)	4171.2(14)	42.0(7)
C26	4578(3)	4501.1(14)	4061.7(12)	35.4(6)
C31	7503(3)	5228.7(12)	3827.6(10)	24.7(5)
C32	6657(3)	5854.0(13)	3898.2(11)	30.3(5)
C33	7145(3)	6453.7(14)	4246.0(12)	34.9(6)
C34	8518(3)	6457.6(14)	4534.0(12)	37.4(6)
C35	9381(3)	5856.9(15)	4480.4(12)	37.9(6)
C36	8882(3)	5252.6(14)	4131.1(11)	30.7(5)
C41	6997(3)	4916.5(12)	2645.9(11)	24.9(5)
C42	8324(3)	4978.8(13)	2358.7(12)	30.3(5)
C43	8442(3)	5325.8(14)	1779.4(12)	38.1(7)
C44	7253(4)	5648.9(15)	1470.2(12)	43.1(7)
C45	5934(3)	5616.9(14)	1744.8(13)	40.3(7)
C46	5820(3)	5247.6(13)	2316.7(11)	30.5(5)

C51	7846(2)	3831.6(13)	3481.4(11)	26.6(5)
C52	7994(3)	3541.4(13)	4099.2(12)	31.6(6)
C53	8733(3)	2901.9(15)	4238.2(14)	40.4(7)
C54	9368(3)	2525.3(15)	3760.1(17)	46.8(8)
C55	9236(3)	2783.0(15)	3149.1(15)	41.4(7)
C56	8484(3)	3424.9(14)	3011.1(13)	32.3(6)
B1	6898(3)	4569.3(14)	3359.2(12)	23.5(5)

Table 3 Anisotropic Displacement Parameters ($Å^2 \times 10^3$) for 19srv333. The Anisotropic displacement factor exponent takes the form: $-2\pi^2[h^2a^{*2}U_{11}+2hka^*b^*U_{12}+\ldots]$.

Atom	**U_{11}**	**U_{22}**	**U_{33}**	**U_{23}**	**U_{13}**	**U_{12}**
Cl1	76.7(6)	39.7(4)	58.5(5)	6.6(3)	37.7(4)	4.3(4)
Cl2	103.2(9)	106.8(9)	42.1(5)	23.7(6)	0.5(5)	52.9(8)
C1S	60(2)	57(2)	42.8(17)	7.4(15)	12.6(15)	16.7(16)
C2S	79(3)	80(3)	42.3(19)	10.3(18)	-0.3(17)	26(2)
O1	46.1(13)	32.1(12)	61.8(15)	30.6(11)	-34.7(12)	-14.3(10)
O1A	58(3)	66(4)	67(4)	-13(3)	-9(3)	-6(3)
O1B	30(2)	48(3)	35(2)	-5(2)	-0.7(18)	5(2)
N1	29.9(10)	19.3(9)	23.5(10)	2.8(8)	-1.2(8)	-1.6(8)
N2	28.2(10)	18.7(9)	26.0(10)	3.1(8)	-2.2(8)	-1.2(8)
N3	27.0(10)	21.8(9)	22.5(10)	5.1(8)	-0.7(8)	-1.7(8)
N4	32.9(11)	21.8(10)	19.8(9)	-0.9(8)	-0.1(8)	-2.8(8)
N5	44.8(13)	26.4(11)	26.7(11)	-3.7(9)	-2.6(9)	-10.4(9)
N6	34.0(11)	18.2(10)	21.2(10)	0.9(8)	-2.8(8)	-1.9(8)
C1	30.5(12)	21.3(11)	26.1(12)	4.6(9)	-2.7(9)	-3.9(9)
C2	25.4(11)	17.0(10)	24.4(11)	6.4(9)	-1.1(9)	1.2(9)

C3	28.0(12)	19.4(11)	28.3(12)	1.0(9)	0.1(9)	-0.4(9)
C4	30.7(13)	26.2(12)	33.0(13)	-2.1(10)	-8.3(10)	1.8(10)
C5	58(3)	66(4)	67(4)	-13(3)	-9(3)	-6(3)
C5A	30(2)	48(3)	35(2)	-5(2)	-0.7(18)	5(2)
C5B	46.1(13)	32.1(12)	61.8(15)	30.6(11)	-34.7(12)	-14.3(10)
C6	31.4(13)	41.5(15)	26.0(12)	3.9(11)	4.6(10)	-6.2(11)
C7	40.1(14)	20.4(11)	26.2(12)	-0.7(9)	2.9(10)	2.5(10)
C8	32.6(12)	20.4(11)	20.6(11)	-1.5(9)	5.0(9)	-1.1(9)
C9	26.6(11)	20.4(11)	18.7(11)	-2.0(8)	5.3(9)	-0.9(9)
C10	34.7(13)	27.1(12)	23.9(12)	-0.7(10)	-1.7(10)	-4.5(10)
C11	44.1(14)	22.0(12)	25.1(12)	-2.6(9)	5.4(10)	-7.3(10)
C12	56.3(18)	36.6(15)	37.9(15)	1.7(12)	-17.6(13)	-6.5(13)
C21	29.2(12)	20.4(11)	24.2(12)	3.6(9)	2.2(9)	-4.5(9)
C22	31.5(12)	23.3(11)	25.7(12)	2.2(9)	1.3(10)	-2.7(10)
C23	30.1(13)	27.0(13)	42.8(15)	5.4(11)	-6.7(11)	-7.8(10)
C24	30.2(13)	27.7(13)	59.4(18)	8.2(12)	13.3(12)	-4.7(11)
C25	50.2(17)	31.5(14)	46.9(16)	-2.4(12)	24.8(13)	-10.4(12)
C26	45.8(15)	32.2(13)	29.5(13)	-4.3(10)	13.4(11)	-16.2(12)
C31	32.0(12)	24.7(11)	17.8(11)	1.5(9)	4.7(9)	-9.9(10)
C32	36.2(13)	27.5(12)	27.4(12)	0.5(10)	4.4(10)	-8.7(10)
C33	50.6(16)	26.2(13)	29.2(13)	-3.5(10)	12.8(11)	-8.7(11)
C34	57.0(17)	31.8(14)	24.0(13)	-5.6(10)	8.2(12)	-20.4(13)
C35	40.8(15)	41.8(16)	30.5(14)	-0.2(11)	-2.5(11)	-21.5(12)
C36	33.5(13)	30.8(13)	27.7(12)	1.2(10)	2.4(10)	-10.7(10)
C41	34.3(12)	18.7(11)	21.6(11)	-4.7(9)	2.4(9)	-8.5(9)
C42	36.4(13)	27.7(12)	27.4(12)	-6.1(10)	6.9(10)	-12.8(10)

C43	54.2(17)	32.9(14)	29.0(13)	-9.8(11)	17.1(12)	-22.0(13)
C44	73(2)	34.3(14)	22.5(13)	1.8(11)	7.3(13)	-19.8(14)
C45	59.8(18)	29.3(14)	31.2(14)	6.9(11)	-1.8(13)	-3.6(13)
C46	41.2(14)	24.5(12)	26.1(12)	2.1(10)	4.7(10)	-3.2(10)
C51	24.8(11)	24.6(12)	30.2(13)	-1.4(10)	-0.2(9)	-9.6(9)
C52	30.9(13)	26.2(12)	36.7(14)	3.5(10)	-5.4(10)	-10.7(10)
C53	38.8(15)	30.4(14)	49.9(17)	7.9(12)	-15.5(13)	-13.0(12)
C54	36.2(15)	23.0(13)	79(2)	0.5(14)	-18.0(14)	-2.8(11)
C55	32.0(14)	31.6(14)	60.1(19)	-13.6(13)	-1.6(13)	-4.2(11)
C56	28.9(12)	28.5(13)	39.0(14)	-5.1(11)	-1.1(10)	-9.6(10)
B1	26.5(13)	23.6(12)	20.6(12)	-1.3(10)	2.7(10)	-6.2(10)

Table 4 Bond Lengths for 19srv333.

Atom	**Atom**	**Length/Å**		**Atom**	**Atom**	**Length/Å**
Cl1	C1S	1.789(4)		C21	C22	1.400(3)
Cl2	C2S	1.764(3)		C21	C26	1.398(3)
Cl2A	C2S	1.711(5)		C21	B1	1.646(3)
C1S	C2S	1.491(5)		C22	C23	1.390(3)
O1	C4	1.426(3)		C23	C24	1.380(4)
O1A	C4	1.428(6)		C24	C25	1.380(4)
O1B	C4	1.455(5)		C25	C26	1.394(4)
N1	N2	1.372(3)		C31	C32	1.406(3)
N1	C1	1.311(3)		C31	C36	1.392(3)
N1	C7	1.474(3)		C31	B1	1.644(3)
N2	C2	1.313(3)		C32	C33	1.388(3)

N3	C1	1.332(3)		C33	C34	1.373(4)
N3	C2	1.367(3)		C34	C35	1.373(4)
N3	C6	1.470(3)		C35	C36	1.399(4)
N4	C9	1.351(3)		C41	C42	1.406(3)
N4	C10	1.332(3)		C41	C46	1.396(3)
N5	C10	1.336(3)		C41	B1	1.645(3)
N5	C11	1.345(3)		C42	C43	1.391(4)
N6	C9	1.334(3)		C43	C44	1.379(4)
C2	C3	1.482(3)		C44	C45	1.383(4)
C3	C4	1.529(3)		C45	C46	1.396(3)
C4	C5	1.428(6)		C51	C52	1.409(3)
C4	C5A	1.455(5)		C51	C56	1.403(4)
C4	C5B	1.426(3)		C51	B1	1.630(4)
C7	C8	1.500(3)		C52	C53	1.386(4)
C8	C9	1.416(3)		C53	C54	1.385(4)
C8	C11	1.365(3)		C54	C55	1.374(4)
C10	C12	1.497(4)		C55	C56	1.394(4)

Table 5 Bond Angles for 19srv333.

Atom	**Atom**	**Atom**	**Angle/°**		**Atom**	**Atom**	**Atom**	**Angle/°**
C2S	C1S	Cl1	111.9(2)		C26	C21	C22	115.1(2)
C1S	C2S	Cl2	112.9(3)		C26	C21	B1	123.4(2)
C1S	C2S	Cl2A	122.8(4)		C23	C22	C21	122.8(2)
N2	N1	C7	120.08(19)		C24	C23	C22	120.2(2)
C1	N1	N2	111.00(19)		C23	C24	C25	119.0(2)

C1	N1	C7	128.9(2)		C24	C25	C26	120.1(3)
C2	N2	N1	104.42(18)		C25	C26	C21	122.7(2)
C1	N3	C2	106.96(19)		C32	C31	B1	119.9(2)
C1	N3	C6	126.5(2)		C36	C31	C32	115.1(2)
C2	N3	C6	126.4(2)		C36	C31	B1	124.7(2)
C10	N4	C9	117.9(2)		C33	C32	C31	122.9(2)
C10	N5	C11	115.4(2)		C34	C33	C32	120.1(3)
N1	C1	N3	107.3(2)		C35	C34	C33	119.0(2)
N2	C2	N3	110.3(2)		C34	C35	C36	120.7(3)
N2	C2	C3	125.1(2)		C31	C36	C35	122.1(3)
N3	C2	C3	124.6(2)		C42	C41	B1	121.7(2)
C2	C3	C4	111.61(19)		C46	C41	C42	115.1(2)
O1	C4	C3	106.22(19)		C46	C41	B1	122.8(2)
O1	C4	C5A	105.5(3)		C43	C42	C41	122.3(3)
O1A	C4	C3	110.1(3)		C44	C43	C42	120.8(3)
O1B	C4	C3	116.4(3)		C43	C44	C45	118.7(2)
C5	C4	O1B	109.1(3)		C44	C45	C46	119.9(3)
C5	C4	C3	110.1(3)		C41	C46	C45	123.2(2)
C5A	C4	C3	116.4(3)		C52	C51	B1	119.0(2)
C5B	C4	O1A	109.3(3)		C56	C51	C52	115.6(2)
C5B	C4	C3	106.22(19)		C56	C51	B1	125.4(2)
N1	C7	C8	112.70(19)		C53	C52	C51	122.6(3)
C9	C8	C7	123.4(2)		C54	C53	C52	119.8(3)
C11	C8	C7	120.6(2)		C55	C54	C53	119.6(3)
C11	C8	C9	115.9(2)		C54	C55	C56	120.3(3)
N4	C9	C8	120.4(2)		C55	C56	C51	122.1(3)

N6	C9	N4	116.5(2)		C31	B1	C21	111.73(19)
N6	C9	C8	123.1(2)		C31	B1	C41	103.17(17)
N4	C10	N5	125.8(2)		C41	B1	C21	111.13(19)
N4	C10	C12	116.6(2)		C51	B1	C21	105.58(18)
N5	C10	C12	117.5(2)		C51	B1	C31	111.16(19)
N5	C11	C8	124.4(2)		C51	B1	C41	114.25(19)
C22	C21	B1	121.4(2)					

Table 6 Hydrogen Bonds for 19srv333.

D	**H**	**A**	**d(D-H)/Å**	**d(H-A)/Å**	**d(D-A)/Å**	**D-H-A/°**
N6	H6A	N4[1]	0.80(3)	2.18(3)	2.984(3)	177(3)
N6	H6B	N2	0.85(3)	2.34(3)	3.088(3)	148(2)

[1]1-X,-Y,1-Z

Table 7 Selected Torsion Angles for 19srv333.

A	**B**	**C**	**D**	**Angle/°**		**A**	**B**	**C**	**D**	**Angle/°**
C4	C3	C2	N2	88.4(3)		C31	B1	C41	C46	-95.6(2)
C4	C3	C2	N3	-88.5(3)		C31	B1	C51	C52	55.5(3)
C8	C7	N1	N2	103.5(2)		C31	B1	C51	C56	-128.2(2)
C8	C7	N1	C1	-77.6(3)		C41	B1	C21	C22	47.4(3)
C9	C8	C7	N1	-62.4(3)		C41	B1	C21	C26	-135.8(2)
C11	C8	C7	N1	120.6(2)		C41	B1	C31	C32	71.1(2)
C21	B1	C31	C32	-48.4(3)		C41	B1	C31	C36	-103.0(2)
C21	B1	C31	C36	137.5(2)		C41	B1	C51	C52	171.77(19)
C21	B1	C41	C42	-163.7(2)		C41	B1	C51	C56	-11.9(3)

C21	B1	C41	C46	24.3(3)		C51	B1	C21	C22	-76.9(3)
C21	B1	C51	C52	-65.8(2)		C51	B1	C21	C26	99.9(3)
C21	B1	C51	C56	110.5(2)		C51	B1	C31	C32	-166.0(2)
C31	B1	C21	C22	162.1(2)		C51	B1	C31	C36	19.9(3)
C31	B1	C21	C26	-21.1(3)		C51	B1	C41	C42	-44.4(3)
C31	B1	C41	C42	76.4(3)		C51	B1	C41	C46	143.6(2)

Table 8 Hydrogen Atom Coordinates (Å×10^4) and Isotropic Displacement Parameters (Å^2×10^3) for 19srv333.

Atom	***x***	***y***	***z***	**U(eq)**
H1SA	9292.1	8427.13	3786.55	64
H1SB	8511.48	9111.14	3446.97	64
H2SA	7890.64	9490.46	4499.33	80
H2SB	9549.49	9583.36	4338.18	80
H2SC	7954.65	9135.58	4675.41	80
H2SD	8731.96	9738.53	4280.56	80
H1	2990.9	2559.22	1572.17	72
H1A	2593.37	811.34	1143.28	96
H1B	1590.17	2133.17	2309.37	57
H1C	6421.56	2558.27	3369.67	31
H3A	2980.09	699.54	2308.69	30
H3B	4331.12	903.36	1902.74	30
H4A	2186.76	1284.81	1330.31	36
H4B	1712.46	1749.91	1927.91	36
H5A	2862.86	1092.41	880.11	96
H5B	1269.16	1419.71	926.51	96

H5C	1715.56	686.81	1294.41	96
H5AA	1643.36	2234.31	2318.91	57
H5AB	724.56	2164.81	1655.01	57
H5AC	712.36	1518.21	2160.11	57
H5BA	4421.76	2080.51	1657.91	72
H5BB	3071.16	2619.51	1689.41	72
H5BC	3342.56	2197.51	1045.31	72
H6C	7039.42	1461.21	2197.02	49
H6D	7127.28	2327.78	2221.92	49
H6E	5934.9	1938.08	1758.12	49
H7A	3153.35	2244.21	4266.37	35
H7B	4385.69	2851.9	4247.02	35
H11	6066.29	2812.71	5080.35	36
H12A	6628.6	777.91	6552.98	67
H12B	8032.2	1266.28	6461.72	67
H12C	7866.11	496.41	6114.91	67
H6A	4140(30)	308(18)	4524(13)	33(8)
H6B	3660(30)	896(15)	4129(14)	34(8)
H22	4748.5	3818.1	2662.41	32
H23	2385.46	3486.83	2835.43	40
H24	1356.03	3804.47	3779.65	46
H25	2762.73	4420.63	4562.69	50
H26	5131	4751.82	4386.08	42
H32	5708.12	5866.45	3698.9	36
H33	6530.1	6861.97	4284.82	42
H34	8864.7	6869.54	4766.78	45

H35	10326.66	5851.69	4682.64	45
H36	9503.44	4845.42	4100.02	37
H42	9169.96	4776.99	2567.46	36
H43	9353.48	5340.57	1594.19	46
H44	7339.31	5888.71	1076.19	52
H45	5107.13	5845.83	1544.63	48
H46	4896.42	5220.35	2490.14	37
H52	7568.96	3794.1	4433.34	38
H53	8805.07	2722.21	4660.47	49
H54	9892.33	2091.39	3854.09	56
H55	9658.21	2522.37	2818.92	50
H56	8401.73	3592.08	2585.04	39

Table 9 Atomic Occupancy for 19srv333.

Atom	***Occupancy***		**Atom**	***Occupancy***		**Atom**	***Occupancy***
Cl2	0.9		Cl2A	0.1		H2SA	0.9
H2SB	0.9		H2SC	0.1		H2SD	0.1
O1	0.5		H1	0.5		O1A	0.25
H1A	0.25		O1B	0.25		H1B	0.25
H4A	0.5		H4B	0.5		C5	0.25
H5A	0.25		H5B	0.25		H5C	0.25
C5A	0.25		H5AA	0.25		H5AB	0.25
H5AC	0.25		C5B	0.5		H5BA	0.5
H5BB	0.5		H5BC	0.5			

8.2 Acetohydroxyacid synthase

8.2.1 3E9Y *Arabidopsis thaliana* AHAS in complex with monosulfuron[7]

Crystal structure of monosulforon bound AHAS binding pocket is shown in **figure 2**. These sulfonylureas do not attach directly to TPP but rather sit locked within the transport channel leading to the active site thereby restricting advancement of substrate molecule to the catalytic centre. TPP present in this crystal structure as the hydroxyethyl adduct.

(a)

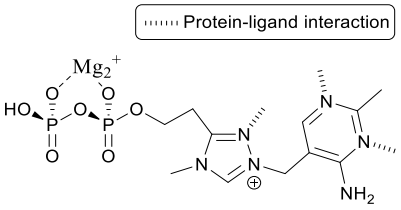

(b)

Figure 2: (a) Natural cofactor Thiamine Pyrophosphate (TPP) 3-D conformation at *arabidopsis thaliana* AHAS active site (b) Structure of Triazolyl Pyrophosphate mimic (TrPP)

Table 8.1: Results of docking TrPP at active site of 3E9Y

No :	Docked Pose	RMSD [a]	B[b]	H-B[c]	L-C[d]	L-T[e]	N-P[f]	R[g]	PLP Fitness	Rank

1		10.2	133.4	9.9	0.0	0.9	9.9	21.7	-282.4	6
2	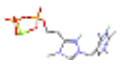	9.1	193.1	13.4	0.0	1.0	13.4	34.8	-367.8	1st
3	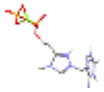	9.1	150.3	-2.8	0.0	1.1	-2.8	36.0	-325.0	3
4	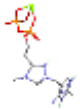	9.8	-3.5	0.0	0.0	1.1	0.0	0.5	16.8	10
5	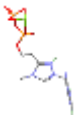	9.4	-5.9	0.0	1.0	0.5	0.0	0.2	15.2	9
6		10.6	176.4	-0.6	0.0	1.1	-0.6	29.9	-305.8	5
7	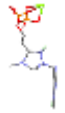	9.5	156.5	8.0	0.0	0.9	8.0	18.8	-344.4	2
8	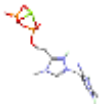	9.4	-6.1	0.0	8.1	0.6	0.0	1.2	11.0	8
9	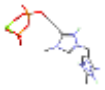	8.4	105.9	-2.1	0.0	1.2	-2.1	25.6	-205.0	7
10	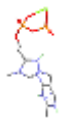	8.7	133.5	6.9	4.7	1.1	6.9	18.6	-324.8	4

[a] RMSD: root mean square deviation of mimic ligand atoms pose from the natural cofactor original pose; [b] B: buried term (polar-non polar); [c] H-B; hydrogen bonding term; [d] L-C; ligand clash term; [e] L-T; ligand torsion term; [f] N-P: non polar term; [g] R: ligand repulsion term.

8.2.2 5IMS *Saccharomyces cerevisiae* AHAS

(a) 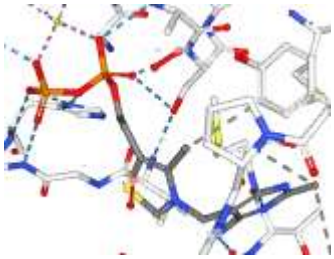 (b) 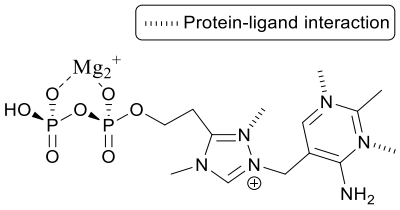

Figure 3: (a) Natural cofactor Thiamine Pyrophosphate (TPP) 3-D conformation at *Saccharomyces cerevisiae* AHAS active site (b) Structure of Triazolyl Pyrophosphate mimic (TrPP)

Table 8.2: Results of docking TrPP at active site of 5IMS AHAS

No:	Docked Pose	RMSD [a]	B[b]	H-B[c]	L-C[d]	L-T[e]	N-P[f]	R[g]	PLP Fitness	Rank
1	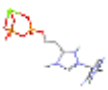	2.9	3.5	-2.9	0	1.8	-20.6	33.5	8.4	2

2	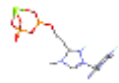	2.9	3.0	-2.9	0	0.9	-11.1	33.8	3.8	1st
3	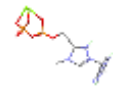	2.9	-1.8	-3.0	0	1.5	-22.0	36.0	9.0	3

[a] RMSD: root mean square deviation of mimic ligand atoms pose from the natural cofactor original pose; [b] B: buried term (polar-non polar); [c] H-B; hydrogen bonding term; [d] L-C; ligand clash term; [e] L-T; ligand torsion term; [f] N-P: non polar term; [g] R: ligand repulsion term.

8.2.3 6BD3 *Saccharomyces cerevisiae* AHAS

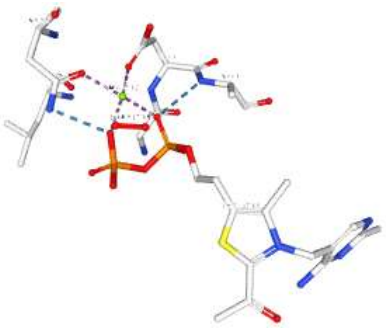

(a)

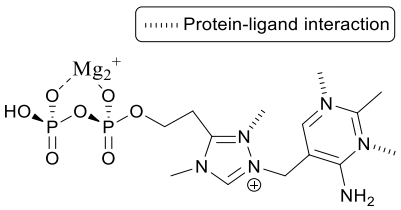

(b)

Figure 4: (a) Natural cofactor Thiamine Pyrophosphate (TPP) 3-D conformation at *Saccharomyces cerevisiae* AHAS active site (b) Structure of Triazolyl Pyrophosphate mimic (TrPP)

Table 8.3: Results of docking TrPP at active site of 6BD3 AHAS

No:	Docked Pose	RMSD [a]	B[b]	H-B[c]	L-C[d]	L-T[e]	N-P[f]	R[g]	PLP Fitness	Rank
1	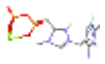	11.5	-7.4	-1.6	0.0	0.3	-34.9	0.4	42.0	8
2		12.2	-7.2	-0.9	0.0	0.2	-35.3	0.5	41.4	5
3	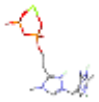	10.1	-7.0	0.0	0.0	0.1	-36.7	1.4	42.3	9
4		11.8	-6.1	0.0	0.0	0.4	-31.3	0.7	34.2	1st
5	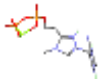	11.7	-7.0	0.0	0.0	0.6	-36.8	0.7	40.1	2
6	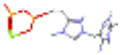	11.3	-8.2	-0.9	0.0	0.8	-34.2	0.6	41.7	6
7		11.3	-7.4	-0.9	0.0	0.3	-35.0	0.4	40.7	4
8	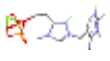	11.2	-8.4	-1.4	0.0	0.4	-33.9	0.6	42.5	10

9	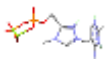	11.3	-8.3	0.0	0.0	0.7	-35.4	0.6	40.5	3
10	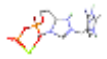	11.5	-6.5	0.0	0.0	0.6	-38.2	0.7	41.8	7

[a] RMSD: root mean square deviation of mimic ligand atoms pose from the natural cofactor original pose; [b] B: buried term (polar-non polar); [c] H-B; hydrogen bonding term; [d] L-C; ligand clash term; [e] L-T; ligand torsion term; [f] N-P: non polar term; [g] R: ligand repulsion term.

8.2.4 6BD9 Saccharomyces cerevisiae AHAS

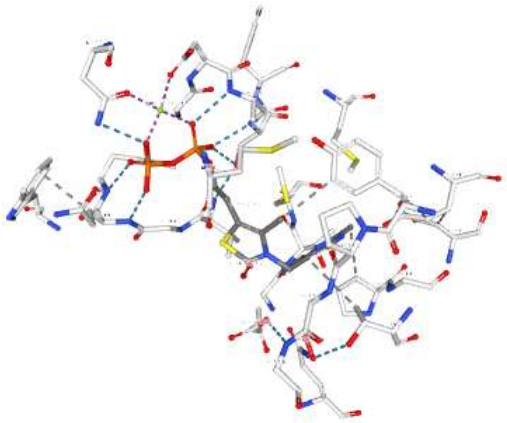

(a)

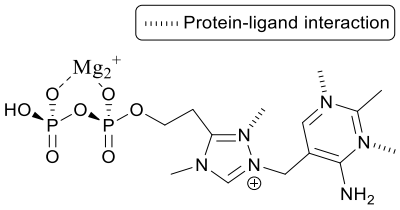

(b)

Figure 5: (a) Natural cofactor Thiamine Pyrophosphate (TPP) 3-D conformation at *Saccharomyces cerevisiae* AHAS active site (b) Structure of Triazolyl Pyrophosphate mimic (TrPP)

Table 8.4: Results of docking TrPP at active site of 6BD9 AHAS

No:	Docked Pose	RMSD [a]	B[b]	H-B[c]	L-C[d]	L-T[e]	N-P[f]	R[g]	PLP Fitness	Rank
1	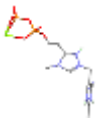	12.5	-3.8	-2.1	1.9	0.3	-27.1	0.8	35.0	5
2	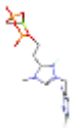	12.9	-7.3	-0.6	0.2	0.6	-36.3	0.9	40.7	10
3		12.0	-7.0	-0.6	0.0	0.7	-23.7	0.6	29.1	2
4	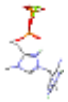	13.0	-5.5	0.0	0.0	0.7	-29.7	0.6	33.4	4
5	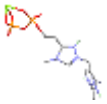	12.5	-6.5	-3.0	0.0	0.7	-32.1	1.1	35.5	6
6		12.9	-7.4	-0.5	1.7	0.6	-35.8	0.7	39.8	9
7		12.8	-7.1	-1.0	0.0	0.6	-35.0	0.8	39.4	8
8		13.4	-8.1	0.0	0.0	0.8	-25.1	0.7	31.3	3

9		13.1	-6.1	-0.5	0.0	0.6	-32.4	0.6	36.6	7
10		13.1	-7.8	-0.4	0.0	0.8	-22.8	0.7	26.7	1st

[a] RMSD: root mean square deviation of mimic ligand atoms pose from the natural cofactor original pose; [b] B: buried term (polar-non polar); [c] H-B; hydrogen bonding term; [d] L-C; ligand clash term; [e] L-T; ligand torsion term; [f] N-P: non polar term; [g] R: ligand repulsion term.

8.2.5 6DEK Crystal structure of Candida albicans AHAS catalytic subunit[8]

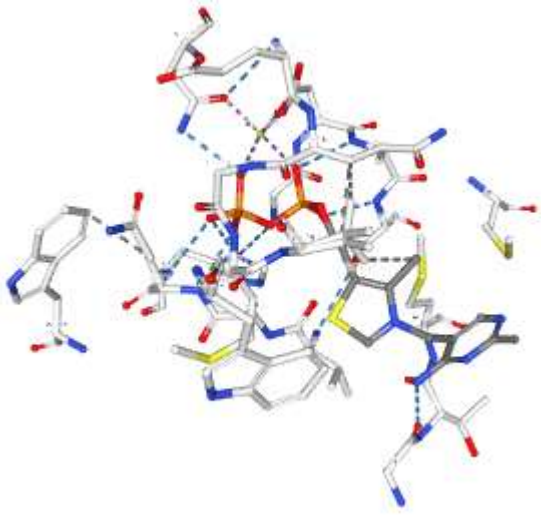

(a)

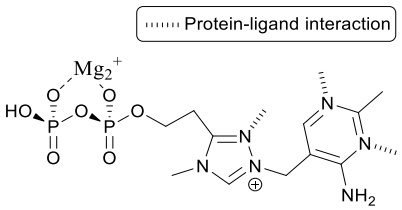

(b)

Figure 6: (a) Natural cofactor Thiamine Pyrophosphate (TPP) 3-D conformation at *Candida albicans* AHAS active site (b) Structure of Triazolyl Pyrophosphate mimic (TrPP)

Table 8.5: Results of docking TrPP at active site of 6DEK AHAS

No:	Docked Pose	RMSD [a]	B[b]	H-B[c]	L-C[d]	L-T[e]	N-P[f]	R[g]	PLP Fitness	Rank
1	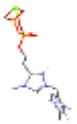	9.4	-1.8	-2.0	0.0	1.0	-54.4	2.5	51.8	6
2	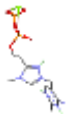	9.3	0.9	-2.0	0.0	0.6	-53.9	2.4	50.0	2
3	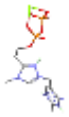	8.5	-2.2	-2.0	0.0	0.9	-52.7	3.0	50.2	3
4	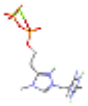	9.3	-8.2	0.0	0.0	0.8	-46.1	2.2	48.9	1
5	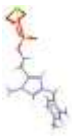	9.4	-0.9	-2.0	0.0	0.9	-54.6	2.5	51.1	5
6	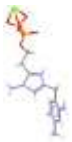	9.5	-0.5	-2.8	0.0	0.7	-54.2	4.1	50.6	4

[a] RMSD: root mean square deviation of mimic ligand atoms pose from the natural cofactor original pose; [b] B: buried term (polar-non polar); [c] H-B; hydrogen bonding term; [d] L-C; ligand clash term; [e] L-T; ligand torsion term; [f] N-P: non polar term; [g] R: ligand repulsion term.

8.3 Benzaldehyde lyase BAL

BAL is a TPP dependent enzyme which promotes the forward and reverse reactions of (*R*)-benzoin to benzaldehyde. This reaction shows very promising applications in asymmetric synthesis.

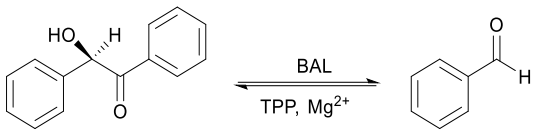

Scheme 2: conversion of (*R*)-benzoin to benzaldehyde

8.3.1 2AG0 Crystal structure of BAL from *Pseudomonas fluorescens*[9]

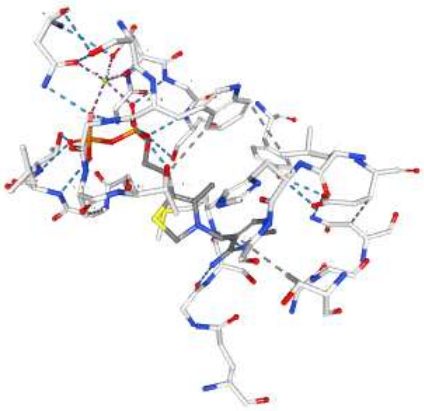

(a)

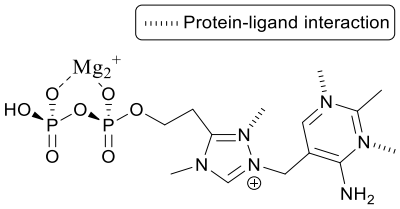

(b)

Figure 7: (a) Natural cofactor Thiamine Pyrophosphate (TPP) 3-D conformation at *Pseudomonas fluorescens* BAL active site (b) Structure of Triazolyl Pyrophosphate mimic (TrPP)

Table 8.6: Results of docking TrPP at active site of 2AG0 BAL

No:	Docked Pose	RMSD [a]	B[b]	H-B[c]	L-C[d]	L-T[e]	N-P[f]	R[g]	PLP Fitness	Rank

1		7.6	-6.7	-0.8	0.0	0.6	-47.1	1.0	51.4	1
2		7.2	-7.7	-1.0	0.0	1.0	-51.0	4.2	52.5	3
3		7.3	-7.9	-1.0	0.0	0.7	-49.8	5.0	51.6	2

[a] RMSD: root mean square deviation of mimic ligand atoms pose from the natural cofactor original pose; [b] B: buried term (polar-non polar); [c] H-B; hydrogen bonding term; [d] L-C; ligand clash term; [e] L-T; ligand torsion term; [f] N-P: non polar term; [g] R: ligand repulsion term.

8.3.2 **2AG1** Crystal structure of BAL from *Pseudomonas fluorescens*[9]

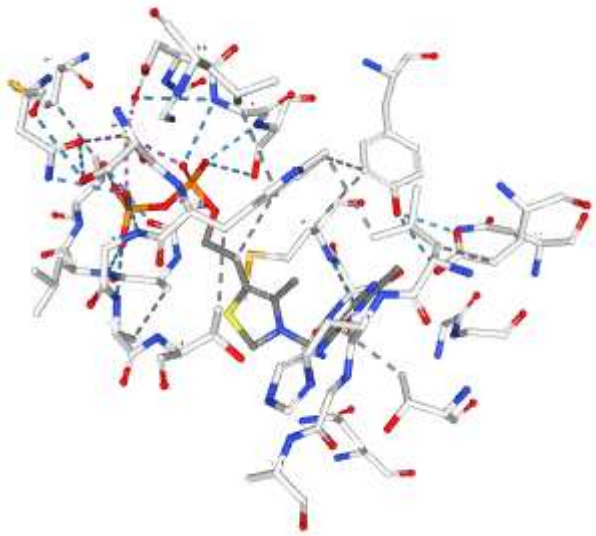

(a)

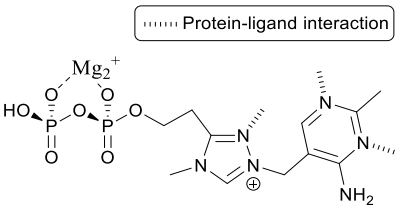

(b)

Figure 8: (a) Natural cofactor Thiamine Pyrophosphate (TPP) 3-D conformation at *Pseudomonas fluorescens* BAL active site (b) Structure of Triazolyl Pyrophosphate mimic (TrPP)

Table 8.7: Results of docking TrPP at active site of 2AG1 BAL

No:	Docked Pose	RMSD [a]	B[b]	H-B[c]	L-C[d]	L-T[e]	N-P[f]	R[g]	PLP Fitness	Rank
1	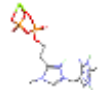	7.3	-4.3	-1.0	0.0	0.7	-54.7	5.1	51.5	3
2	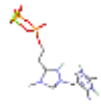	7.4	-10.1	-1.3	0.0	1.1	-52.3	1.9	55.9	7
3	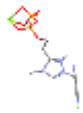	8.7	-8.5	-3.1	0.0	0.9	-43.4	1.7	49.1	1
4	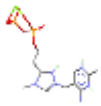	7.5	-9.5	-0.4	0.0	0.7	-50.0	1.5	55.1	5
5	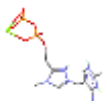	6.9	-8.1	-1.4	0.0	0.9	-40.0	1.1	54.7	4
6	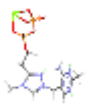	7.1	-6.0	-1.0	0.0	0.7	-48.8	1.0	51.4	2

[a] RMSD: root mean square deviation of mimic ligand atoms pose from the natural cofactor original pose; [b] B: buried term (polar-non polar); [c] H-B; hydrogen bonding term; [d] L-C; ligand clash term; [e] L-T; ligand torsion term; [f] N-P: non polar term; [g] R: ligand repulsion term.

8.3.3 2UZ1 structure of BAL complexed with 2-methyl- 2,4-pentanediol[10]

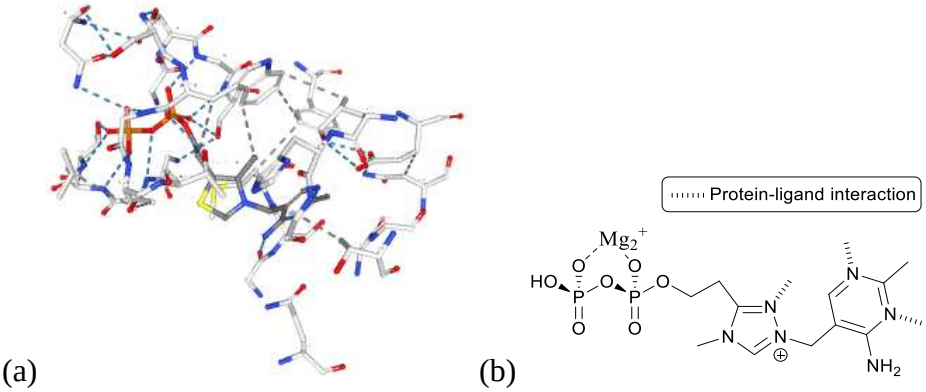

(a) (b)

Figure 9: (a) Natural cofactor Thiamine Pyrophosphate (TPP) 3-D conformation at *Pseudomonas fluorescens* BAL active site (b) Structure of Triazolyl Pyrophosphate mimic (TrPP)

Table 8.8: Results of docking TrPP at active site of 2UZ1 BAL

No:	Docked Pose	RMSD[a]	B[b]	H-B[c]	L-C[d]	L-T[e]	N-P[f]	R[g]	PLP Fitness	Rank
1	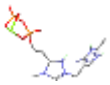	8.2	-11.3	-3.3	0.0	0.5	-42.6	2.4	51.6	7
2		8.4	-2.0	-2.0	0.0	0.9	-36.2	3.6	43.2	2
3		8.3	-8.5	-3.2	0.0	0.7	-35.0	2.9	45.2	3

4	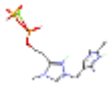	8.6	-9.0	-1.6	0.0	0.4	-48.8	3.6	51.0	6
5	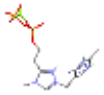	8.2	-10.8	-2.2	0.0	0.5	-46.9	3.2	51.9	8
6	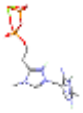	7.1	-12.1	-1.9	0.0	1.2	-42.7	5.6	46.3	4
7		8.8	-3.3	0.0	0.0	0.5	-42.6	1.1	41.9	**1**
8	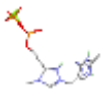	8.3	-11.9	-3.2	0.0	1.1	-41.4	2.2	50.2	5
9		8.3	-11.7	-3.0	0.0	0.4	-46.2	2.1	52.5	9

[a] RMSD: root mean square deviation of mimic ligand atoms pose from the natural cofactor original pose; [b] B: buried term (polar-non polar); [c] H-B; hydrogen bonding term; [d] L-C; ligand clash term; [e] L-T; ligand torsion term; [f] N-P: non polar term; [g] R: ligand repulsion term.

8.3.4 3D7K Crystal structure of BAL in complex with the inhibitor MBP[11]

Methylbenzoyl phosphonate MBP is shown complexed with TPP at the binding pocket of BAL, and no other structural change was detected in comparison with TPP bound BAL.

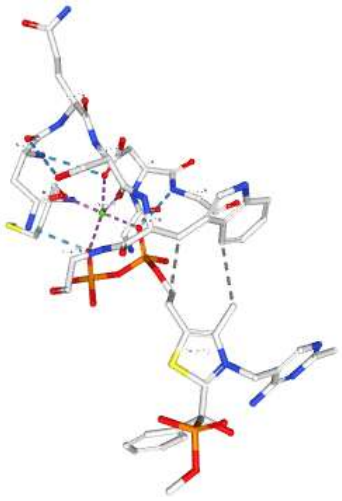

(a)

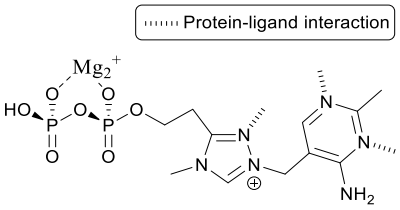

(b)

Figure 10: (a) Natural cofactor Thiamine Pyrophosphate (TPP) complex with MBP 3-D conformation at BAL active site (b) Structure of Triazolyl Pyrophosphate mimic (TrPP)

Table 8.9: Results of docking TrPP at active site of 3D7K BAL

No:	Docked Pose	RMSD [a]	B[b]	H-B[c]	L-C[d]	L-T[e]	N-P[f]	R[g]	PLP Fitness	Rank
1	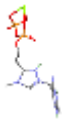	7.8	-10.98	-1.5	0.0	1.0	-38.4	2.9	45.4	4
2	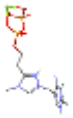	7.8	-8.42	-0.9	0.0	0.5	-44.0	5.2	45.3	3
3		7.4	-6.49	-0.9	0.0	0.7	-39.5	3.2	49.3	10
4	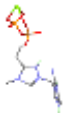	7.8	-11.46	-1.2	0.0	0.6	-42.3	4.2	47.9	7

5	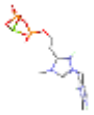	7.6	-2.32	-4.4	1.0	0.5	-27.6	2.6	45.0	2
6	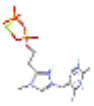	7.4	-3.22	-1.0	0.0	0.7	-24.6	1.6	45.4	5
7		7.3	-6.25	-0.1	0.0	0.6	-38.9	3.9	48.9	9
8		8.2	-9.35	0.0	0.0	0.8	-30.3	1.7	38.0	1
9		7.2	-7.7465	-0.9	0.0	0.6	-45.2	3.2	48.6	8
10	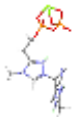	7.7	-8.9481	-2.2	0.0	0.5	-39.3	2.2	47.3	6

[a] RMSD: root mean square deviation of mimic ligand atoms pose from the natural cofactor original pose; [b] B: buried term (polar-non polar); [c] H-B; hydrogen bonding term; [d] L-C; ligand clash term; [e] L-T; ligand torsion term; [f] N-P: non polar term; [g] R: ligand repulsion term.

8.3.5 3IAE Structure of BAL A28S mutant with benzoylphosphonate

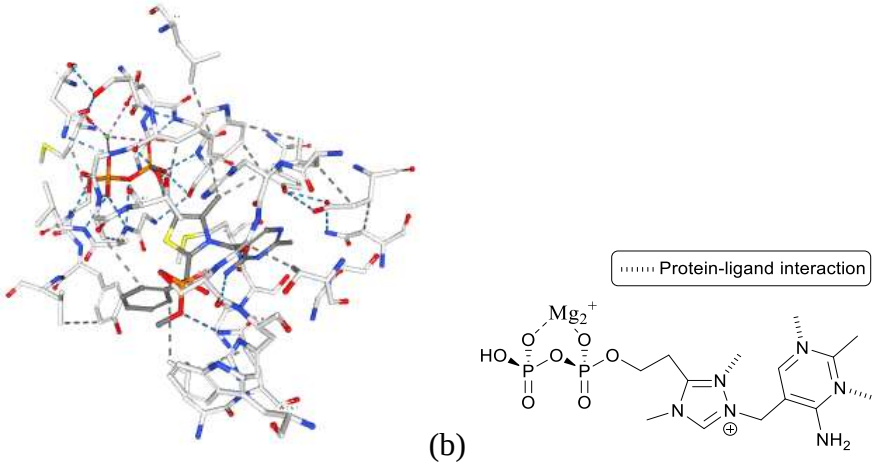

Figure 11: (a) Natural cofactor Thiamine Pyrophosphate (TPP) complex with benzoyl phosphonate at BAL active site (b) Structure of Triazolyl Pyrophosphate mimic (TrPP)

Table 8.10: Results of docking TrPP at active site of 3IAE BAL

No:	Docked Pose	RMSD [a]	B[b]	H-B[c]	L-C[d]	L-T[e]	N-P[f]	R[g]	PLP Fitness	Rank
1	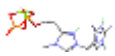	13.1	-6.6	0.0	0.0	0.7	-32.7	0.5	36.4	1
2	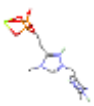	8.8	-12.9	-0.3	0.0	0.7	-25.0	2.6	39.9	4
3	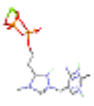	7.9	-6.5	-0.2	0.0	0.6	-48.6	5.5	46.7	9

4	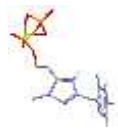	7.4	-8.6	-2.8	0.0	0.6	-38.3	1.2	41.8	6
5		13.9	-5.0	-1.0	0.0	0.9	-37.7	1.5	39.3	3
6		7.2	-9.1	-3.3	0.0	0.5	-28.1	2.3	51.4	10
7		12.1	-8.1	0.0	0.0	0.8	-34.6	0.8	38.8	2
8		7.4	-6.6	-3.1	0.0	0.2	-40.7	1.6	43.4	7
9	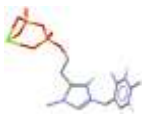	7.8	-4.8	0.0	0.0	0.8	-38.0	4.8	46.2	8
10		8.4	-3.8	0.0	0.0	0.4	-39.4	0.7	40.0	5

[a] RMSD: root mean square deviation of mimic ligand atoms pose from the natural cofactor original pose; [b] B: buried term (polar-non polar); [c] H-B; hydrogen bonding term; [d] L-C; ligand clash term; [e] L-T; ligand torsion term; [f] N-P: non polar term; [g] R: ligand repulsion term.

8.3.6 **3IAF** Structure of BAL A28S mutant with monomethyl benzoylphosphonate[12]

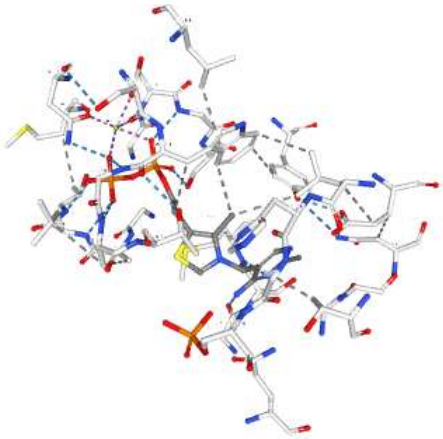

(a)

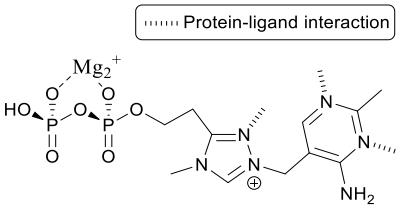

(b)

Figure 12: (a) Natural cofactor Thiamine Pyrophosphate (TPP) complex with monomethyl benzolyl phosphonate at BAL active site (b) Structure of Triazolyl Pyrophosphate mimic (TrPP)

Table 8.11: Results of docking TrPP at active site of 3IAF BAL

No:	Docked Pose	RMSD [a]	B[b]	H-B[c]	L-C[d]	L-T[e]	N-P[f]	R[g]	PLP Fitness	Rank
1		8.6	-10.0	-3.1	0.0	0.4	-47.8	3.5	53.9	1
2		8.4	-12.1	-3.0	0.0	0.7	-36.4	3.0	55.2	3
3		8.5	-11.2	-3.7	0.0	0.6	-35.3	2.8	54.3	2

[a] RMSD: root mean square deviation of mimic ligand atoms pose from the natural cofactor original pose; [b] B: buried term (polar-non polar); [c] H-B; hydrogen bonding term; [d] L-C; ligand clash term; [e] L-T; ligand torsion term; [f] N-P: non polar term; [g] R: ligand repulsion term.

8.4 Benzoylformate decarboxylase

Benzoylformate decarboxylase BFD fosters the non-oxidative conversion of benzoylformate into benzaldehyde **scheme 3** utilizing TPP as cofactor[13]. BFD has been known to help bacteria grow by using (R)-mandelate as food[14]. Several TPP dependent enzymes show comparable active site structure: the glutamate is almost always present, as well as *one dual* histine residue[151617]. However, specificity and substrate selectivity are determined by other residues parked within and around the active site[1819].

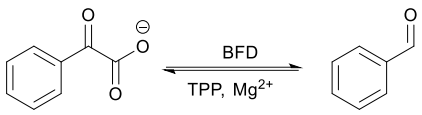

Scheme 3: Decarboxylation of benzoylformate by TPP bound BFD

8.4.1 **1BFD** BFD from pseudomonas putida[20]

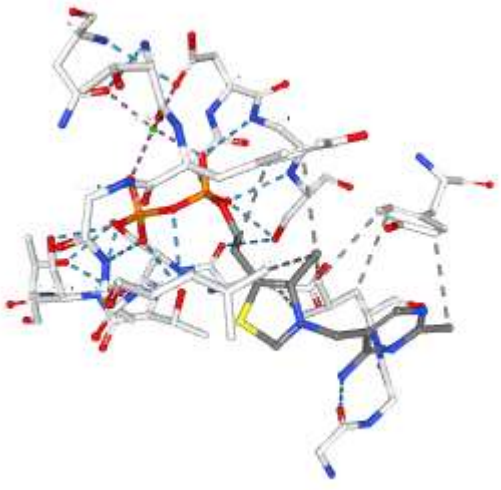

(a)

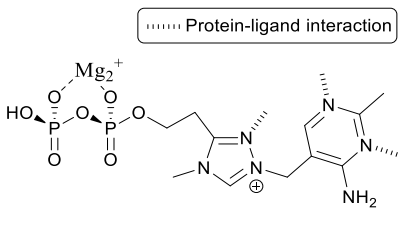

(b)

Figure 13: (a) Natural cofactor Thiamine Pyrophosphate (TPP) at 1BFD BFD active site (b) Structure of Triazolyl Pyrophosphate mimic (TrPP)

Table 8.12 Results of docking TrPP at active site of 1BFD BFD

No:	Docked Pose	RMSD [a]	B[b]	H-B[c]	L-C[d]	L-T[e]	N-P[f]	R[g]	PLP Fitness	Rank
1	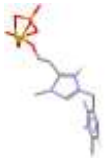	9.5	-4.8	-1.2	0.4	0.4	-23.8	3.1	42.0	1
2	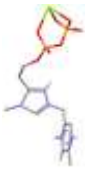	9.0	-6.3	-1.8	0.0	0.9	-40.2	2.8	43.7	5
3	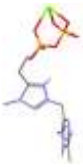	8.9	-9.5	-1.7	0.0	0.8	-39.7	2.5	45.9	8
4		9.4	-2.3	-1.1	0.0	0.8	-43.6	2.9	42.8	3
5	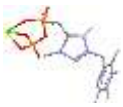	9.3	-2.9	-0.5	0.0	0.4	-42.7	2.7	44.1	6
6	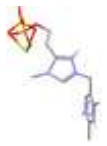	9.1	-3.6	-2.0	1.3	0.6	-9.7	4.0	42.9	4
7		9.1	-6.4	-1.9	0.0	0.8	-41.1	2.0	47.2	10

8	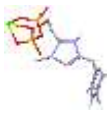	9.4	-7.4	-2.2	0.0	0.7	-40.1	2.6	45.8	7
9	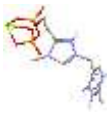	9.2	-8.0	-1.9	0.0	0.7	-40.3	2.1	46.5	9
10	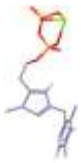	9.0	-3.2	-0.5	0.0	0.7	-47.3	4.3	42.4	2

[a] RMSD: root mean square deviation of mimic ligand atoms pose from the natural cofactor original pose; [b] B: buried term (polar-non polar); [c] H-B; hydrogen bonding term; [d] L-C; ligand clash term; [e] L-T; ligand torsion term; [f] N-P: non polar term; [g] R: ligand repulsion term.

8.4.2 **1PI3** E28Q mutant Benzoylformate Decarboxylase from Pseudomonas Putida

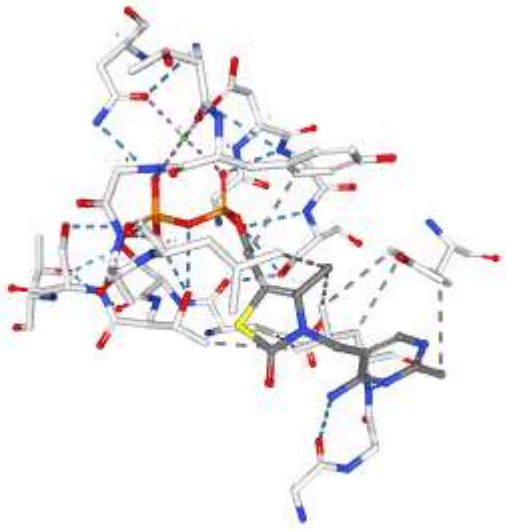

(a)

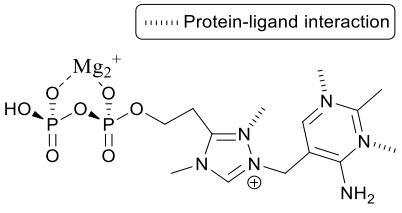

(b)

Figure 14: (a) Natural cofactor Thiamine Pyrophosphate (TPP) at 1PI3 BFD active site (b) Structure of Triazolyl Pyrophosphate mimic (TrPP)

Table 8.13: Results of docking TrPP at active site of 1PI3 BFD

No:	Docked Pose	RMSD [a]	B[b]	H-B[c]	L-C[d]	L-T[e]	N-P[f]	R[g]	PLP Fitness	Rank
1	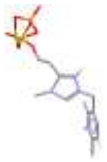	8.1	-4.1	-3.5	0.0	0.6	-42.3	2.6	44.0	7
2	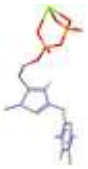	8.1	-4.5	-3.7	0.0	0.6	-42.7	2.2	45.5	9
3	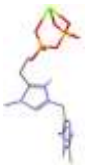	7.9	-6.8	-2.4	0.0	0.6	-38.8	2.2	43.6	6
4		9.0	-0.7	-1.8	0.0	0.5	-17.0	4.3	40.1	4
5	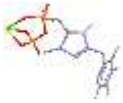	8.4	-1.7	0.0	0.0	1.2	-43.8	5.2	37.0	2
6	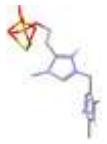	8.5	-5.4	-2.6	0.0	1.2	-41.7	1.3	45.5	8

7	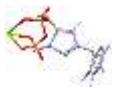	8.2	-1.3	-0.8	0.0	0.6	-37.9	4.0	39.8	3
8	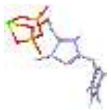	8.3	-5.3	-2.3	0.0	0.8	-41.1	1.3	45.7	10
9	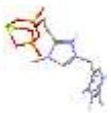	8.6	-1.8	0.0	0.0	0.2	-43.2	2.5	40.3	5
10	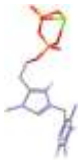	8.9	-0.1	-2.4	0.0	0.6	-40.0	2.7	36.4	**1**

[a] RMSD: root mean square deviation of mimic ligand atoms pose from the natural cofactor original pose; [b] B: buried term (polar-non polar); [c] H-B; hydrogen bonding term; [d] L-C; ligand clash term; [e] L-T; ligand torsion term; [f] N-P: non polar term; [g] R: ligand repulsion term.

8.4.3 **1QPB** PDC from yeast (form b) complexed with pyruvamide [21]

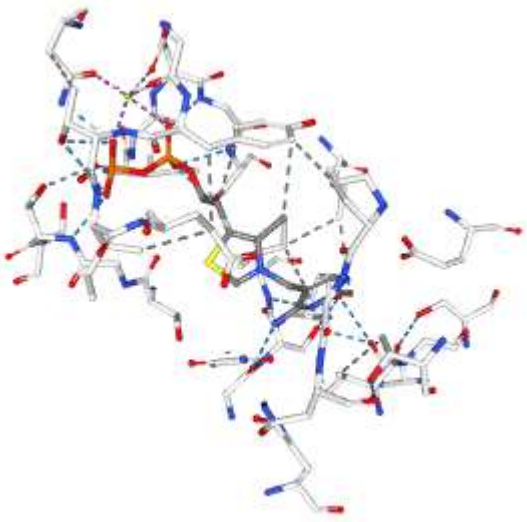

(a)

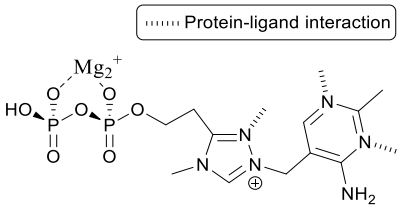

(b)

Figure 15: (a) Natural cofactor Thiamine Pyrophosphate (TPP) at PDC active site (b) Structure of Triazolyl Pyrophosphate mimic (TrPP)

Table 8.14: Results of docking TrPP at active site of 1QPB PDC

No:	Docked Pose	RMSD[a]	B[b]	H-B[c]	L-C[d]	L-T[e]	N-P[f]	R[g]	PLP Fitness	Rank
1		8.4	12.6	-1.6	0.0	1.5	-44.0	10.4	33.5	1
2		8.8	2.4	-2.3	0.0	1.4	-45.4	7.0	47.0	9
3		4.4	-10.1	-1.7	0.0	1.2	-46.8	23.0	48.0	10
4		4.5	-9.8	-1.7	0.0	0.8	-41.5	23.7	46.5	8
5	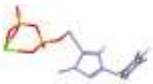	4.6	-3.0	-1.6	0.0	0.8	-44.7	16.5	41.9	6
6	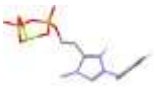	4.4	-4.7	-2.0	0.0	0.4	-16.3	18.9	40.7	5
7	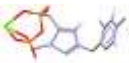	8.6	5.4	-1.0	0.0	1.0	-42.8	7.8	42.3	7

8		4.4	-12.5	-1.0	0.0	1.1	-36.4	22.3	38.2	3
9	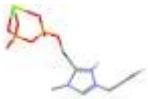	4.5	-5.9	-1.9	0.0	0.6	-40.4	19.3	37.1	2
10	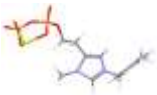	4.4	0.3	-2.0	0.0	0.9	-23.1	17.6	38.8	4

[a] RMSD: root mean square deviation of mimic ligand atoms pose from the natural cofactor original pose; [b] B: buried term (polar-non polar); [c] H-B; hydrogen bonding term; [d] L-C; ligand clash term; [e] L-T; ligand torsion term; [f] N-P: non polar term; [g] R: ligand repulsion term.

8.4.4 **2V3W** structure of the BFD variant L461A from *Pseudomonas putida*[22]

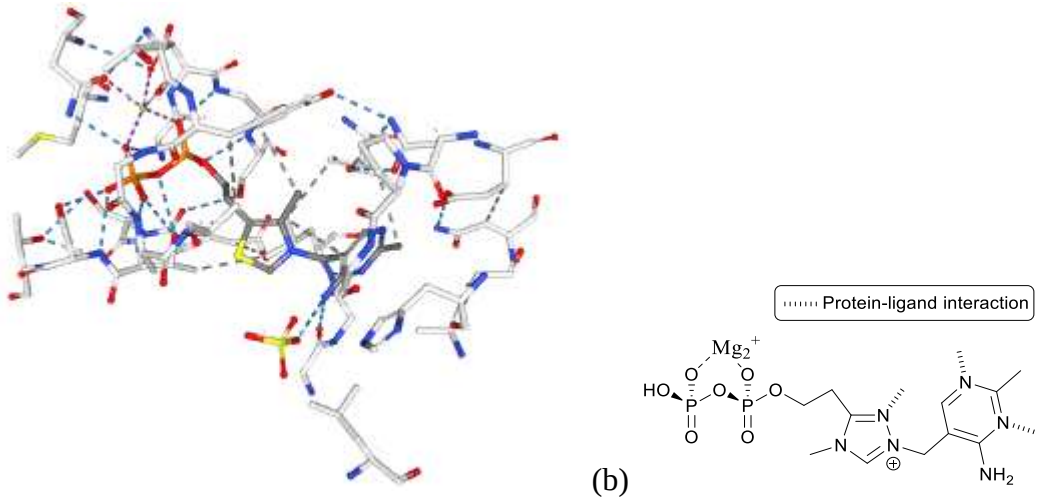

(a) (b)

Figure 16: (a) Natural cofactor Thiamine Pyrophosphate (TPP) at BFD active site (b) Structure of Triazolyl Pyrophosphate mimic (TrPP)

Table 8.15: Results of docking TrPP at active site of 2V3W BFD

No:	Docked Pose	RMSD[a]	B[b]	H-B[c]	L-C[d]	L-T[e]	N-P[f]	R[g]	PLP Fitness	Rank
1	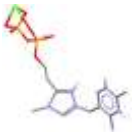	6.7	9.6	-2.5	0.0	1.1	-54.3	13.6	26.8	3
2	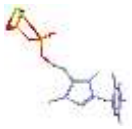	8.4	31.3	-2.9	0.0	1.4	-39.3	4.7	2.1	1
3	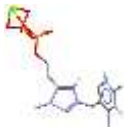	6.9	12.9	-0.4	0.0	0.9	-51.0	8.0	23.7	2
4	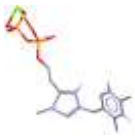	6.7	9.6	-3.2	0.0	1.0	-55.2	14.3	27.0	4

[a] RMSD: root mean square deviation of mimic ligand atoms pose from the natural cofactor original pose; [b] B: buried term (polar-non polar); [c] H-B; hydrogen bonding term; [d] L-C; ligand clash term; [e] L-T; ligand torsion term; [f] N-P: non polar term; [g] R: ligand repulsion term.

8.4.5 **3FSJ** structure of benzoylformate decarboxylase in complex with the inhibitor MBP[23]

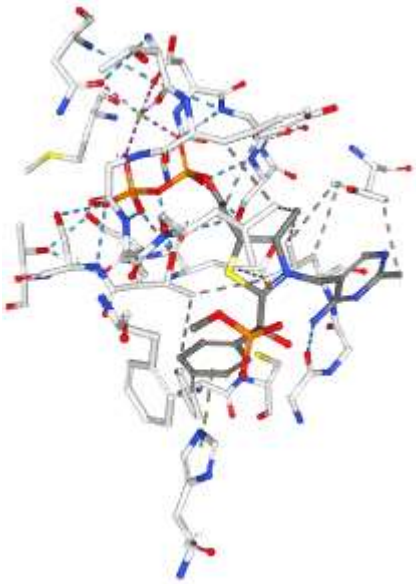

(a)

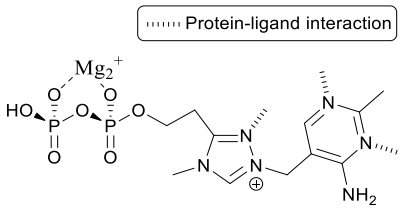

(b)

Figure 17: (a) Natural cofactor Thiamine Pyrophosphate (TPP) complex with methylbenzoylformate (MBP) at BFD active site (b) Structure of Triazolyl Pyrophosphate mimic (TrPP)

Table 8.16: Results of docking TrPP at active site of 3FSJ BFD

No:	Docked Pose	RMSD [a]	B[b]	H-B[c]	L-C[d]	L-T[e]	N-P[f]	R[g]	PLP Fitness	Rank
1	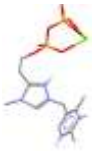	5.3	-4.4	-1.8	0.0	0.4	-34.5	3.4	41.8	2
2		5.8	-7.4	-1.9	0.0	0.5	-42.1	1.5	46.5	4
3	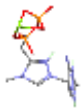	6.9	-9.0	-1.8	0.0	1.5	-47.2	1.0	52.9	10

4	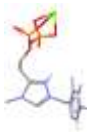	8.9	-8.9	0.0	0.0	0.9	-40.8	0.6	46.8	6
5	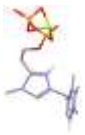	9.0	-9.2	0.0	0.0	0.9	-40.9	0.6	46.8	7
6		6.1	-7.9	-2.1	0.0	1.1	-42.1	1.4	47.2	8
7		8.9	-7.8	0.0	0.0	0.7	-40.9	0.6	46.7	5
8	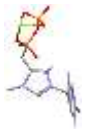	6.9	-10.3	-1.5	0.0	1.3	-46.8	1.5	52.5	9
9	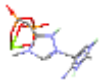	5.8	-6.7	-2.4	0.0	0.5	-41.4	1.7	45.8	3
10	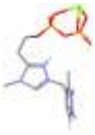	5.6	-3.5	0.0	0.0	0.5	-39.3	1.2	38.4	1

[a] RMSD: root mean square deviation of mimic ligand atoms pose from the natural cofactor original pose; [b] B: buried term (polar-non polar); [c] H-B; hydrogen bonding term; [d] L-C; ligand clash term; [e] L-T; ligand torsion term; [f] N-P: non polar term; [g] R: ligand repulsion term.

8.4.6 4GG1 Crystal Structure of BFD Mutant L403T [24]

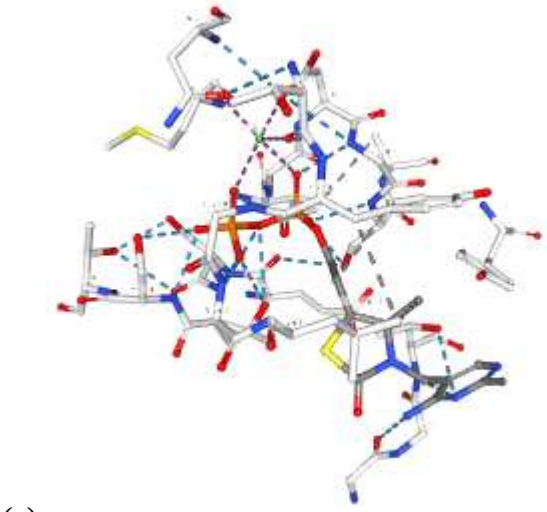

(a)

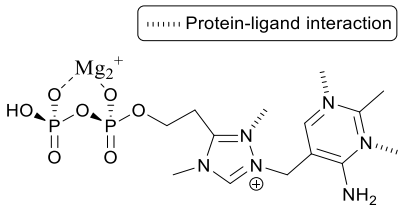

(b)

Figure 18: (a) Natural cofactor Thiamine Pyrophosphate (TPP) at 4GG1 BFD active site (b) Structure of Triazolyl Pyrophosphate mimic (TrPP)

Table 8.17: Results of docking TrPP at active site of 4GG1 BFD

No:	Docked Pose	RMSD *a*	B*b*	H-B*c*	L-C*d*	L-T*e*	N-P*f*	R*g*	PLP Fitness	Rank
1	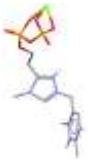	8.6	-0.8		0.0	1.0	-43.5	3.3	39.5	4
2	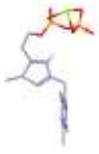	10.5	-8.1		0.1	1.3	-47.6	1.0	49.1	10
3	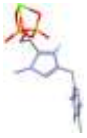	8.6	-4.0		0.0	1.1	-38.2	2.0	40.0	6

4		9.3	-0.8		0.0	0.4	-40.4	2.2	39.9	5
5	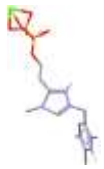	8.6	9.0		0.0	0.6	-48.0	3.6	35.5	2
6	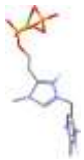	9.0	-5.3		0.0	0.4	-39.9	2.8	39.4	3
7	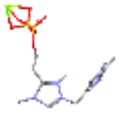	8.9	-8.0		0.0	1.1	-47.7	3.7	49.0	9
8		9.1	-6.4		0.0	0.8	-43.1	3.9	44.3	8
9		11.7	-5.0		0.0	0.8	-27.6	1.3	31.4	1
10	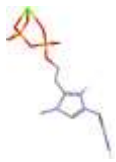	9.2	-3.3		0.0	0.2	-39.4	3.0	40.6	7

[a] RMSD: root mean square deviation of mimic ligand atoms pose from the natural cofactor original pose; [b] B: buried term (polar-non polar); [c] H-B; hydrogen bonding term; [d] L-C; ligand clash term; [e] L-T; ligand torsion term; [f] N-P: non polar term; [g] R: ligand repulsion term.

8.4.7 4GM0 Crystal Structure of BFD Mutant L403N [24]

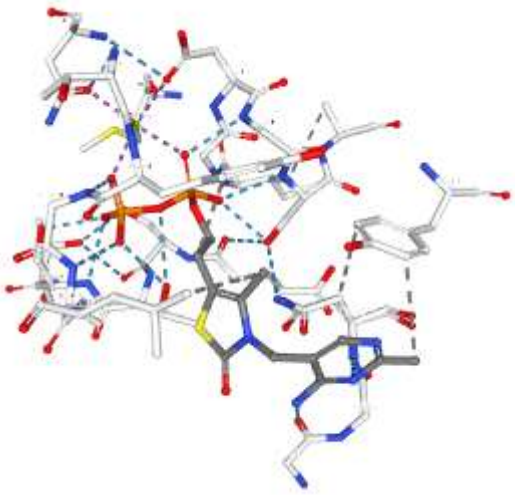

(a)

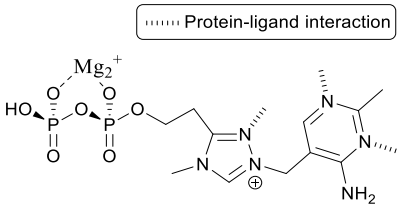

(b)

Figure 19: (a) Native cofactor Thiamine Pyrophosphate (TPP) at 4GM0 BFD active site (b) Triazolyl Pyrophosphate mimic (TrPP)

Table 8.18: Results of docking TrPP at active site of 4GM0 BFD

No:	Docked Pose	RMSD [a]	B[b]	H-B[c]	L-C[d]	L-T[e]	N-P[f]	R[g]	PLP Fitness	Rank
1		9.7	-3.5	-1.3	0.7	0.6	-21.2	0.8	31.5	1
2		9.6	-6.3	-1.0	0.0	0.9	-36.3	1.7	39.7	4
3	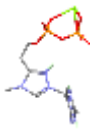	8.0	-4.9	-1.8	0.0	0.3	-36.0	1.5	39.8	5

4	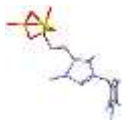	11.0	-6.3	-1.0	0.0	0.9	-36.3	2.7	40.0	7
5	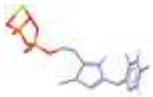	9.6	-11.9	-1.0	0.0	0.9	-29.0	2.2	40.3	9
6		12.5	-8.1	-1.0	0.0	0.4	-30.4	0.9	37.7	2
7	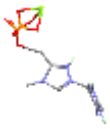	9.0	-2.7	-2.0	0.0	0.7	-36.2	0.8	38.7	3
8	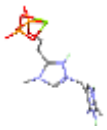	8.7	-4.8	-1.2	0.0	0.3	-37.5	1.3	39.8	6
9	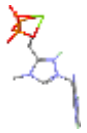	9.0	-7.3	-1.0	0.0	0.5	-35.6	0.9	41.0	10
10	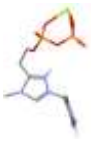	8.0	-5.1	-2.0	0.0	0.4	-36.2	1.4	40.1	8

[a] RMSD: root mean square deviation of mimic ligand atoms pose from the natural cofactor original pose; [b] B: buried term (polar-non polar); [c] H-B; hydrogen bonding term; [d] L-C; ligand clash term; [e] L-T; ligand torsion term; [f] N-P: non polar term; [g] R: ligand repulsion term.

8.4.8 4GM1 Crystal Structure of BFD Mutant L403S[24]

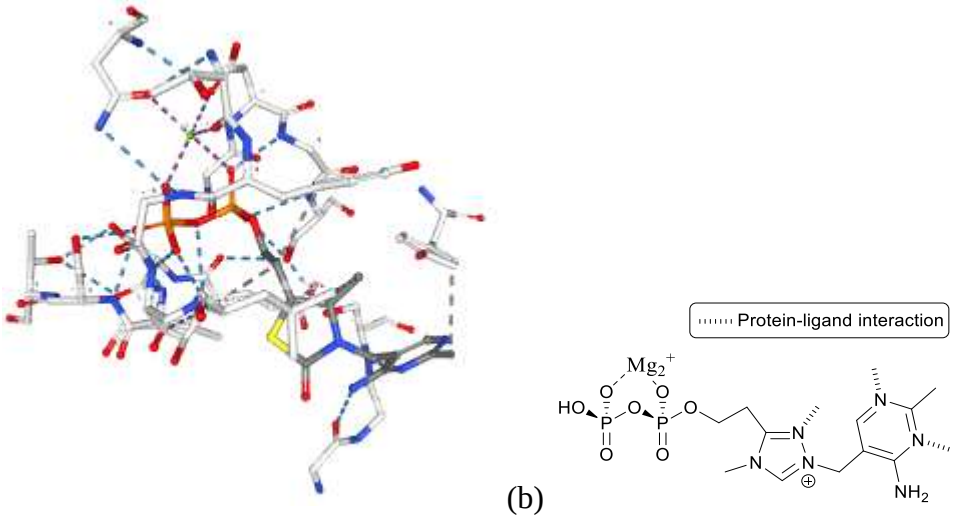

(a) (b)

Figure 19: (a) Natural cofactor Thiamine Pyrophosphate (TPP) at BFD active site (b) Structure of Triazolyl Pyrophosphate mimic (TrPP)

Table 8.19: Results of docking TrPP at active site of 4GM1 BFD

No:	Docked Pose	RMSD [a]	B[b]	H-B[c]	L-C[d]	L-T[e]	N-P[f]	R[g]	PLP Fitness	Rank
1	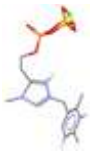	8.4	-10.4	-0.7	0.0	0.6	-41.5	2.8	47.8	8
2		8.9	-8.3	-1.5	0.0	0.4	-28.4	1.9	47.0	3
3		9.0	-8.7	-0.9	0.0	0.4	-41.2	1.7	47.3	5

4	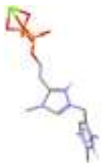	8.9	4.6	-1.7	0.0	0.5	-50.1	5.7	39.9	1
5	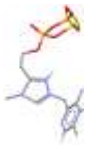	8.3	-10.2	-0.4	0.0	0.4	-42.3	2.6	47.8	6
6	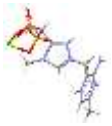	8.8	-8.4	-0.9	0.0	0.4	-39.1	1.5	47.0	4
7	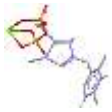	8.9	-8.1	-1.6	0.0	0.3	-43.3	1.6	47.8	7
8		14.2	-9.4	-0.7	0.0	0.5	-49.1	1.2	56.2	10
9		8.4	-10.7	-0.4	0.0	0.7	-43.3	2.0	48.3	9
10	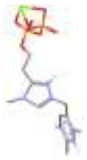	8.9	-7.8	-2.0	0.2	1.0	-37.1	0.6	41.9	2

[a] RMSD: root mean square deviation of mimic ligand atoms pose from the natural cofactor original pose; [b] B: buried term (polar-non polar); [c] H-B; hydrogen bonding term; [d] L-C; ligand clash term; [e] L-T; ligand torsion term; [f] N-P: non polar term; [g] R: ligand repulsion term.

8.4.9 **4K9Q Structure of BFD from *Polynucleobacter necessarius***

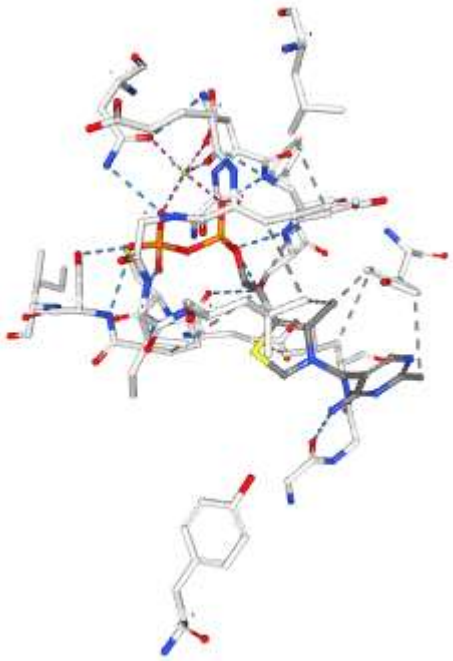

(a)

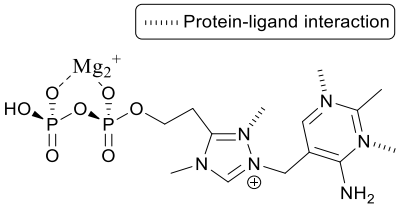

(b)

Figure 21: (a) Native cofactor thiamine pyrophosphate (TPP) at BFD active site (b) Triazolyl pyrophosphate mimic (TrPP)

Table 8.20: Results of docking TrPP at active site of 4K9Q BFD

No:	Docked Pose	RMSD [a]	B[b]	H-B[c]	L-C[d]	L-T[e]	N-P[f]	R[g]	PLP Fitness	Rank
1	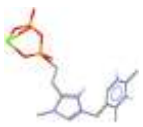	11.3	-8.4	-1.0	0.0	0.4	-34.7	1.3	41.8	8
2	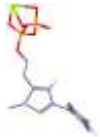	8.9	-2.9	-1.2	1.0	1.4	-42.6	1.2	40.6	6

3		9.3	1.6	-3.0	0.0	1.0	-46.2	1.9	44.1	10
4	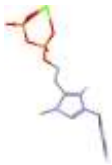	9.9	3.3	-3.7	0.0	0.4	-46.8	1.9	41.5	7
5	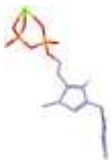	9.9	1.1	-2.7	0.0	0.6	-44.0	1.5	42.3	9
6	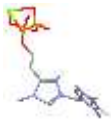	8.9	-0.8	-1.1	1.8	0.9	-43.4	1.0	39.9	5
7		9.0	-1.4	-1.1	0.1	0.9	-41.7	1.7	39.7	4
8		9.1	2.7	-0.9	1.5	0.4	-44.4	1.4	39.3	2
9	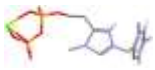	11.7	-10.4	-1.0	0.0	1.0	-30.9	1.1	38.9	1
10		12.4	-8.2	-1.8	0.0	0.9	-32.5	1.0	39.3	3

[a] RMSD: root mean square deviation of mimic ligand atoms pose from the natural cofactor original pose; [b] B: buried term (polar-non polar); [c] H-B; hydrogen bonding term; [d] L-C; ligand clash term; [e] L-T; ligand torsion term; [f] N-P: non polar term; [g] R: ligand repulsion term.

8.4.10 4MPR Structure of BFD tetramer [25]

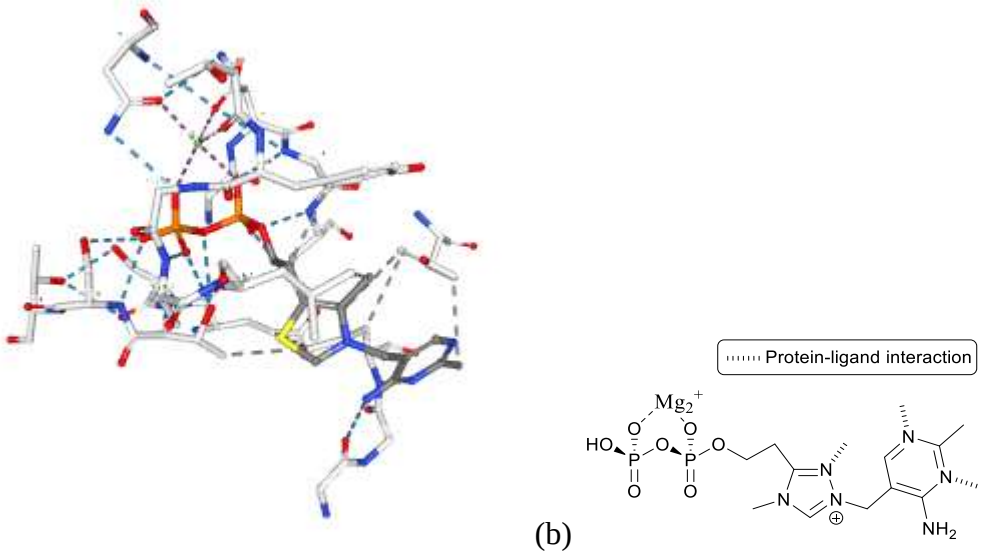

(a) (b)

Figure 22: (a) Natural cofactor Thiamine Pyrophosphate (TPP) at BFD active site (b) Structure of Triazolyl Pyrophosphate mimic (TrPP)

Table 8.21: Results of docking TrPP at active site of 4MPR BFD

No:	Docked Pose	RMSD [a]	B[b]	H-B[c]	L-C[d]	L-T[e]	N-P[f]	R[g]	PLP Fitness	Rank
1	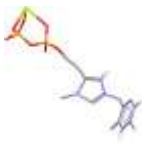	9.9	-8.9	-2.4	0.0	0.7		1.9	46.6	7
2	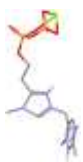	9.2	-9.0	-2.0	0.0	0.7		2.4	43.1	3

3	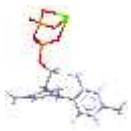	11.2	-6.2	-1.6	0.0	0.8		1.1	47.3	9
4	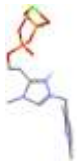	9.0	-8.9	0.0	0.8	1.0		0.8	41.4	1
5	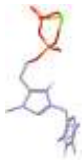	8.9	-6.5	-2.3	0.0	0.8		2.4	43.5	4
6		8.6	-7.0	-2.6	0.0	0.9		0.9	43.7	5
7		11.3	-7.9	-1.0	0.0	0.9		0.7	47.8	10
8	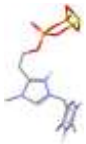	8.6	-5.9	-3.7	0.0	0.8		1.6	46.2	6
9	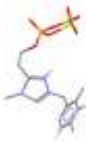	8.6	-5.4	-0.4	0.0	0.6		2.9	42.4	2
10	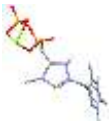	9.5	-5.9	-2.0	0.0	0.5		1.2	46.7	8

[a] RMSD: root mean square deviation of mimic ligand atoms pose from the natural cofactor original pose; [b] B: buried term (polar-non polar); [c] H-B; hydrogen bonding term; [d] L-C; ligand clash term; [e] L-T; ligand torsion term; [f] N-P: non polar term; [g] R: ligand repulsion term.

8.4.11 **5DEI BFD from *Pseudomonas putida***

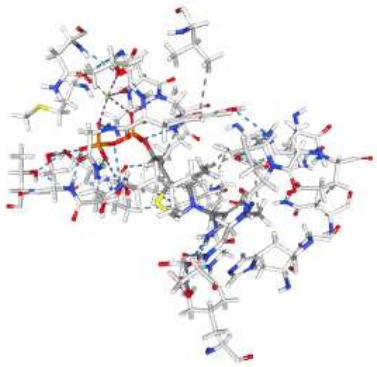

(a)

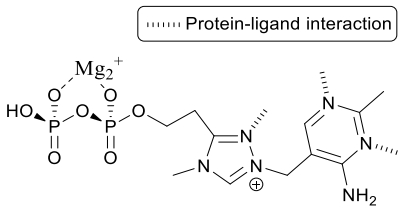

(b)

Figure 23: (a) Natural cofactor Thiamine Pyrophosphate (TPP) at BFD active site (b) Structure of Triazolyl Pyrophosphate mimic (TrPP)

Table 8.22: Results of docking TrPP at active site of 5DEI BFD

No:	Docked Pose	RMSD [a]	B[b]	H-B[c]	L-C[d]	L-T[e]	N-P[f]	R[g]	PLP Fitness	Rank
1	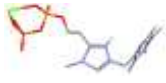	4.0	-5.2	-13.1	0.0	1.0	-44.0	15.0	89.9	8

2	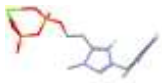	4.0	-6.4	-12.2	3.4	1.3	-43.5	13.9	84.8	3
3	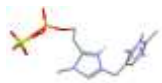	4.0	-2.2	-15.4	0.0	1.2	-19.7	4.7	86.7	5
4	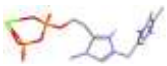	4.3	-9.4	-11.5	0.0	1.1	-41.0	13.0	86.2	4
5	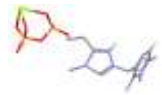	3.9	-7.0	-12.3	7.2	1.3	-42.6	13.6	78.9	1
6		4.2	-10.9	-9.3	0.0	0.8	-46.3	13.3	80.1	2
7	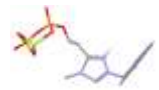	3.8	5.2	-16.3	0.0	1.0	-11.3	3.9	88.8	7
8	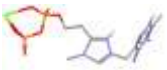	4.0	-9.5	-11.5	7.5	1.2	-44.1	10.0	87.3	6

[a] RMSD: root mean square deviation of mimic ligand atoms pose from the natural cofactor original pose; [b] B: buried term (polar-non polar); [c] H-B; hydrogen bonding term; [d] L-C; ligand clash term; [e] L-T; ligand torsion term; [f] N-P: non polar term; [g] R: ligand repulsion term.

8.4.12 6A50 benzoylformate decarboxylases in complex with cofactor TPP

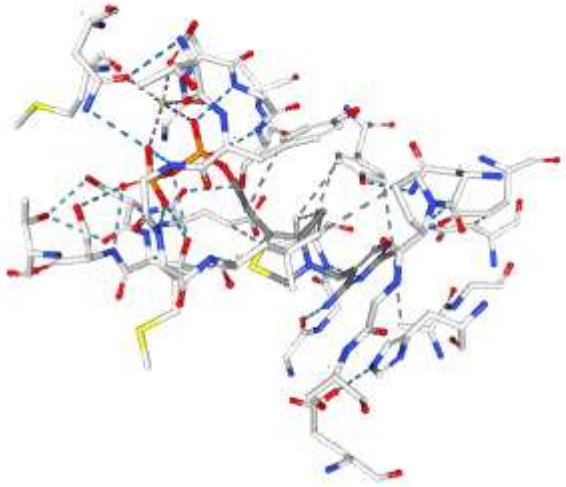

(a)

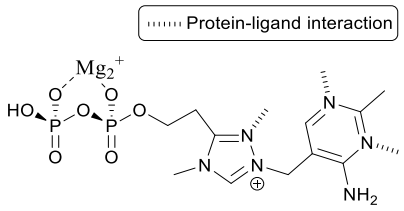

(b)

Figure 24: (a) Native cofactor thiamine pyrophosphate (TPP) at BFD active site (b) Triazolyl Pyrophosphate mimic (TrPP)

Table 8.23: Results of docking TrPP at active site of 6A50 BFD

No:	Docked Pose	RMSD [a]	B[b]	H-B[c]	L-C[d]	L-T[e]	N-P[f]	R[g]	PLP Fitness	Rank
1	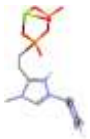	6.8	6.0	-2.3	0.0	0.6	-47.9	22.2	18.7	4
2	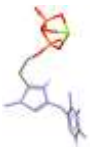	6.8	0.5	-1.7	0.0	0.6	-38.0	35.2	13.6	1
3	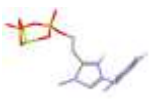	3.0	-1.6	-2.0	0.0	0.5	-17.8	24.1	28.7	9

4	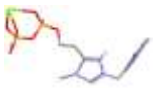	3.3	-9.3	-1.8	0.0	1.2	-36.6	36.2	23.7	6
5		7.1	8.3	-2.0	0.0	1.1	-39.6	24.5	16.9	3
6	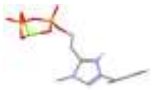	3.6	-2.9	-3.5	0.0	1.1	-22.4	27.0	31.0	10
7	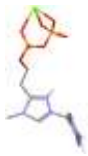	7.2	12.4	-2.9	0.0	0.9	-42.4	20.5	20.9	5
8	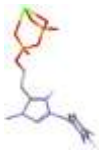	7.3	10.8	-3.3	0.0	1.9	-43.0	27.9	15.7	2
9	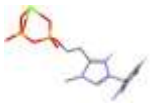	3.0	5.0	-1.9	0.0	1.0	-44.6	23.5	27.2	8
10		2.9	-12.2	-2.0	0.0	1.2	-29.0	30.4	24.9	7

[a] RMSD: root mean square deviation of mimic ligand atoms pose from the natural cofactor original pose; [b] B: buried term (polar-non polar); [c] H-B; hydrogen bonding term; [d] L-C; ligand clash term; [e] L-T; ligand torsion term; [f] N-P: non polar term; [g] R: ligand repulsion term.

8.5 Cyclohexane-1,2-dione hydrolase

Cyclohexane-1,2-dione (CDH) is relatively newly discovered TPP dependent enzyme that catalyses the ring opening reaction of cyclohexane-1,2-dione[26]. Its active site

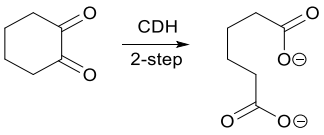

Scheme 3: Conversion of Cyclohexanea-1,2-dione to Adipate

8.5.1 4D5E Crystal Structure of recombinant wildtype CDH[27]

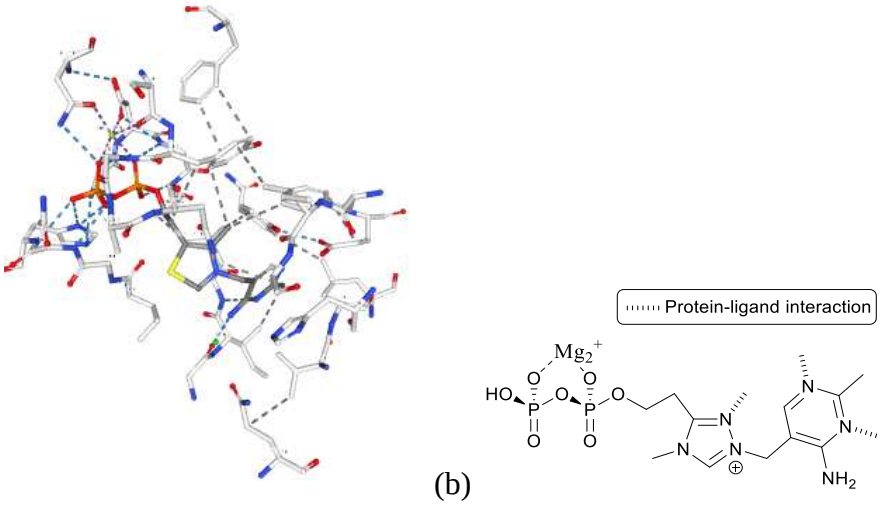

(a) (b)

Figure 25: (a) Natural cofactor Thiamine Pyrophosphate (TPP) at 4D5E CDH active site (b) Triazolyl pyrophosphate mimic (TrPP)

Table 8.24: Results of docking TrPP at active site of 4D5E CDH

No:	Docked Pose	RMSD[a]	B[b]	H-B[c]	L-C[d]	L-T[e]	N-P[f]	R[g]	PLP Fitness	Rank
1	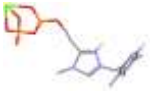	3.9	-6.8	-0.8	0.0	1.1	-29.9	28.6	25.1	3

2	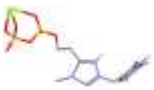	4.1	-4.9	-3.0	0.0	1.1	-28.9	31.9	22.5	2
3	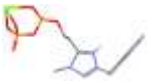	3.9	-6.7	-1.0	0.0	1.4	-27.7	27.8	21.6	1

[a] RMSD: root mean square deviation of mimic ligand atoms pose from the natural cofactor original pose; [b] B: buried term (polar-non polar); [c] H-B; hydrogen bonding term; [d] L-C; ligand clash term; [e] L-T; ligand torsion term; [f] N-P: non polar term; [g] R: ligand repulsion term.

8.5.2 4D5G Structure of recombinant CDH-H28AN484A

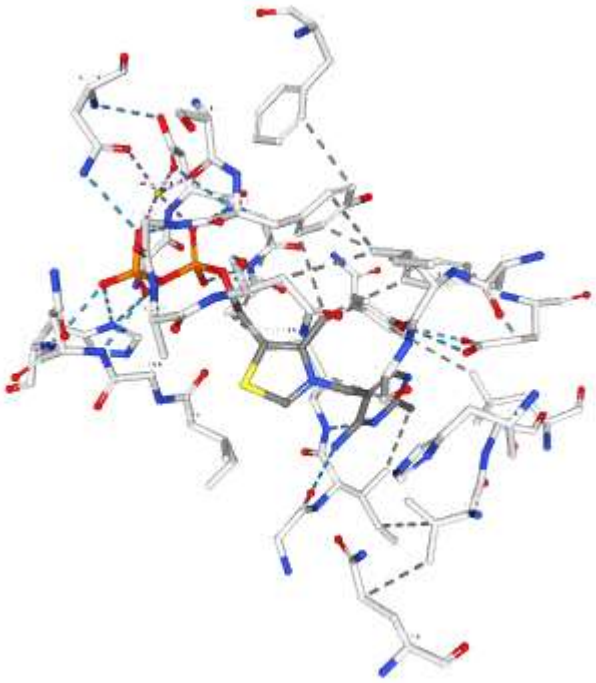

(a)

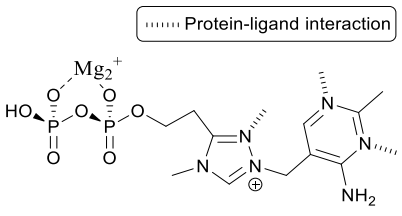

(b)

Figure 26: (a) Natural cofactor Thiamine Pyrophosphate (TPP) at 4D5G CDH active site (b) Triazolyl Pyrophosphate mimic (TrPP)

Table 8.25: Results of docking TrPP at active site of 4D5G CDH

No:	Docked Pose	RMSD [a]	B[b]	H-B[c]	L-C[d]	L-T[e]	N-P[f]	R[g]	PLP Fitness	Rank
1	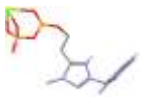	3.0	-4.8	-2.0	0.0	0.8	-28.6	19.6	59.7	2
2		3.0	-5.1	-2.0	0.0	1.0	-26.3	21.1	63.1	3
3	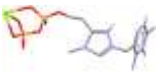	3.0	-6.5	-2.2	0.0	1.3	-23.6	19.1	58.0	1

[a] RMSD: root mean square deviation of mimic ligand atoms pose from the natural cofactor original pose; [b] B: buried term (polar-non polar); [c] H-B; hydrogen bonding term; [d] L-C; ligand clash term; [e] L-T; ligand torsion term; [f] N-P: non polar term; [g] R: ligand repulsion term.

8.6 Pyruvate dehydrogenase

Pyruvate dehydrogenase PDH is the first of three enzymes, E1 to E3, that make up pyruvate dehydrogenase complex (PDC), which catalyses the transformation of pyruvate to acetyl-CoA. PDH employs TPP as cofactor, in converting pyruvate to the hydroxyethyl adduct with the release of carbon dioxide. This adduct then goes on to attack a lysine bound moiety and frees up TPP.

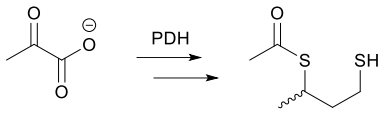

Scheme 5: E1 (PDH) decarboxylation of pyruvate

8.6.1 1L8A E. Coli PDC [34]

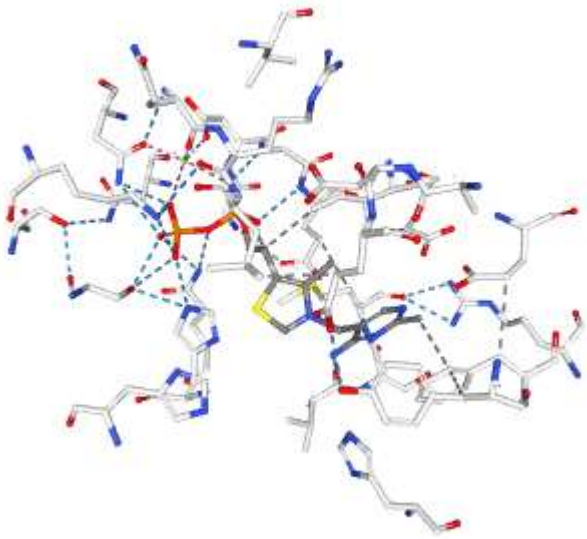

(a)

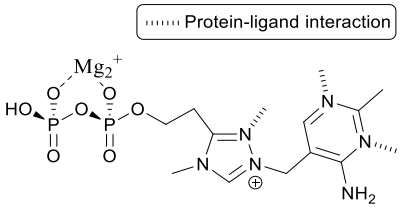

(b)

Figure 40: (a) Native cofactor thiamine pyrophosphate (TPP) at PDH active site (b) Triazolyl pyrophosphate mimic (TrPP)

Table 8.26: Results of docking TrPP at active site of 1L8A PDC

No:	Docked Pose	RMSD [a]	B[b]	H-B[c]	L-C[d]	L-T[e]	N-P[f]	R[g]	PLP Fitness	Rank

1		6.7	10.4	-1.0	0.0	1.5	-34.3	5.9	21.4	2
2	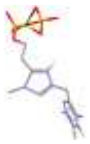	9.2	17.9	-2.3	0.0	1.1	-41.1	1.8	19.4	1
3	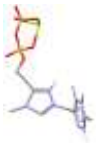	7.0	9.6	-2.0	0.0	1.1	-42.3	3.0	27.9	6
4	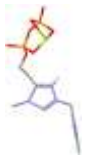	6.9	10.7	-1.9	0.0	1.3	-41.2	6.3	21.4	3
5	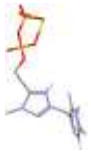	7.0	10.6	-2.0	0.0	0.9	-41.5	1.8	26.2	5
6	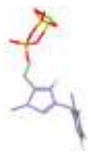	6.7	12.3	-1.9	0.0	0.8	-40.9	3.0	22.5	4

[a] RMSD: root mean square deviation of mimic ligand atoms pose from the natural cofactor original pose; [b] B: buried term (polar-non polar); [c] H-B; hydrogen bonding term; [d] L-C; ligand clash term; [e] L-T; ligand torsion term; [f] N-P: non polar term; [g] R: ligand repulsion term.

8.6.2 1NI4 HUMAN PYRUVATE DEHYDROGENASE [35]

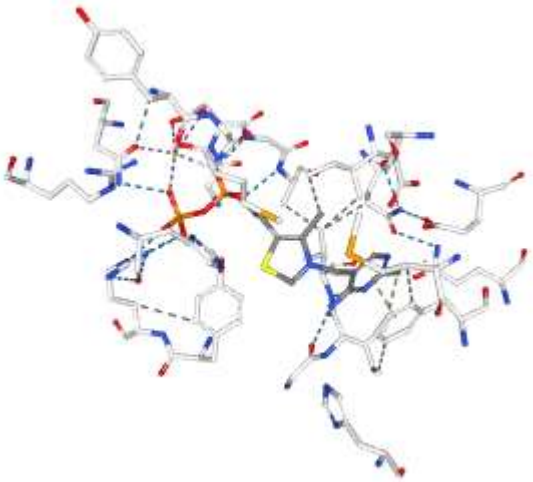

(a)

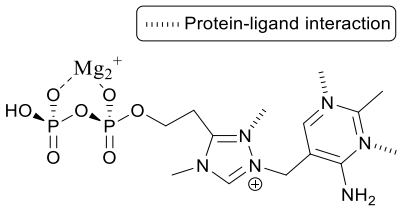

(b)

Figure 41: (a) Natural cofactor Thiamine Pyrophosphate (TPP) at 1NI4 PDH active site (b) Triazolyl Pyrophosphate mimic (TrPP)

Table 8.27: Results of docking TrPP at active site of 1NI4 PDC

No:	Docked Pose	RMSD [a]	B[b]	H-B[c]	L-C[d]	L-T[e]	N-P[f]	R[g]	PLP Fitness	Rank
1	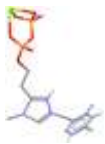	3.2	-12.6	-1.8	0.0	0.6	-35.4	20.6	77.0	3
2	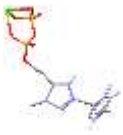	3.1	-12.9	-1.8	0.0	1.6	-30.5	23.8	71.3	1
3	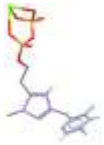	3.2	-13.7	-1.5	0.0	1.4	-31.2	22.3	75.7	2

[a] RMSD: root mean square deviation of mimic ligand atoms pose from the natural cofactor original pose; [b] B: buried term (polar-non polar); [c] H-B; hydrogen bonding term; [d] L-C; ligand clash term; [e] L-T; ligand torsion term; [f] N-P: non polar term; [g] R: ligand repulsion term.

8.6.3 2OZL Human pyruvate dehydrogenase S264E variant [36]

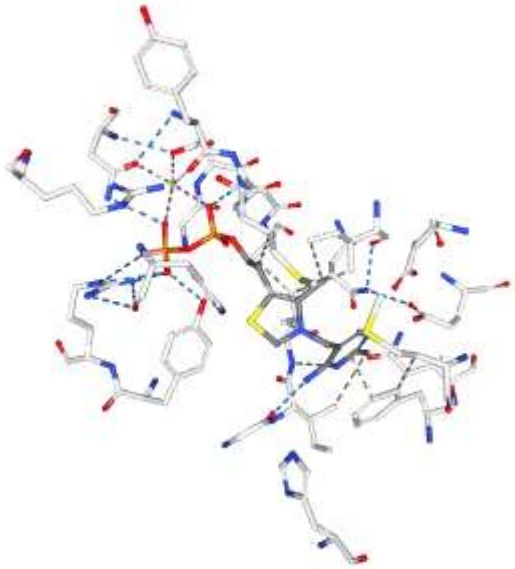

(a)

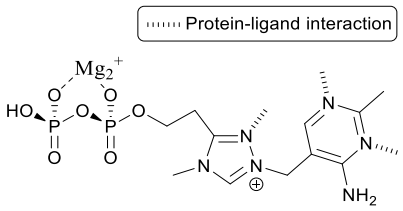

(b)

Figure 42: (a) Natural cofactor Thiamine Pyrophosphate (TPP) at PDH active site (b) Structure of Triazolyl Pyrophosphate mimic (TrPP)

Table 8.28: Results of docking TrPP at active site of 2OZL PDC

No:	Docked Pose	RMSD [a]	B[b]	H-B[c]	L-C[d]	L-T[e]	N-P[f]	R[g]	PLP Fitness	Rank
1	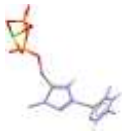	3.94	-5.47	-2.00	0.00	0.96	-35.26	35.93	19.84	1
2	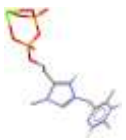	4.02	-4.68	-2.00	0.00	0.84	-32.40	31.76	28.68	2

3		4.00	-5.29	-2.00	0.00	0.81	-33.81	32.08	29.25	3

[a] RMSD: root mean square deviation of mimic ligand atoms pose from the natural cofactor original pose; [b] B: buried term (polar-non polar); [c] H-B; hydrogen bonding term; [d] L-C; ligand clash term; [e] L-T; ligand torsion term; [f] N-P: non polar term; [g] R: ligand repulsion term.

8.6.4 3EXE Crystal structure of the pyruvate dehydrogenase (E1p) component of human pyruvate dehydrogenase complex [37]

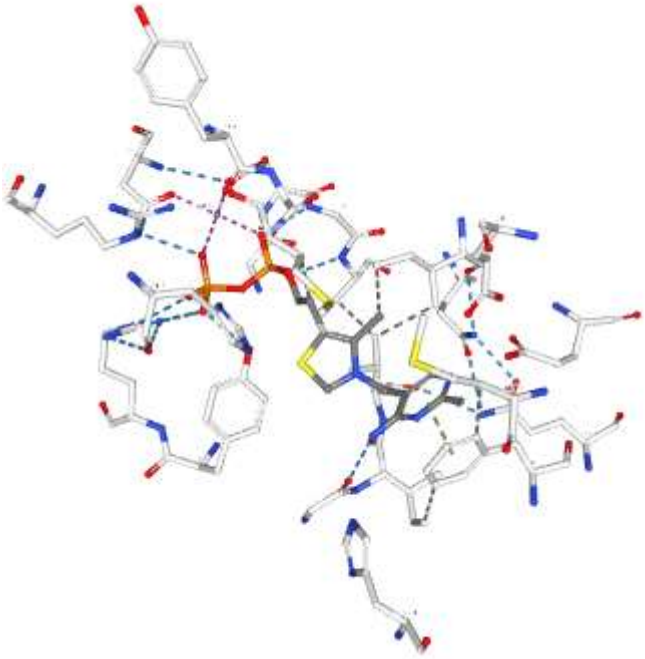

(a)

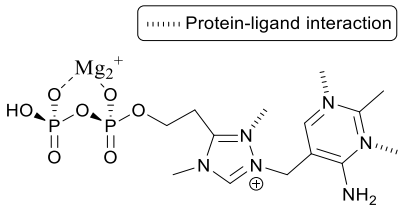

(b)

Figure 43: (a) Natural cofactor Thiamine Pyrophosphate (TPP) at 3EXE PDH active site (b) Structure of Triazolyl Pyrophosphate mimic (TrPP)

Table 8.29: Results of docking TrPP at active site of 3EXE PDC

No:	Docked Pose	RMSD [a]	B[b]	H-B[c]	L-C[d]	L-T[e]	N-P[f]	R[g]	PLP Fitness	Rank

1	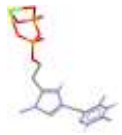	2.8	3.1	-0.3	0.0	1.4	-40.8	37.5	19.0	3
2	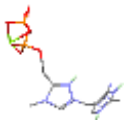	2.9	-1.4	-0.8	0.0	1.2	-42.3	40.3	11.8	2
3	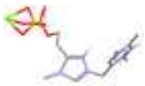	2.8	-4.4	0.2	0.0	1.0	-8.0	37.1	-4.8	1

[a] RMSD: root mean square deviation of mimic ligand atoms pose from the natural cofactor original pose; [b] B: buried term (polar-non polar); [c] H-B; hydrogen bonding term; [d] L-C; ligand clash term; [e] L-T; ligand torsion term; [f] N-P: non polar term; [g] R: ligand repulsion term.

8.6.5 3EXF Crystal structure of the pyruvate dehydrogenase (E1p) component of human pyruvate dehydrogenase complex [37]

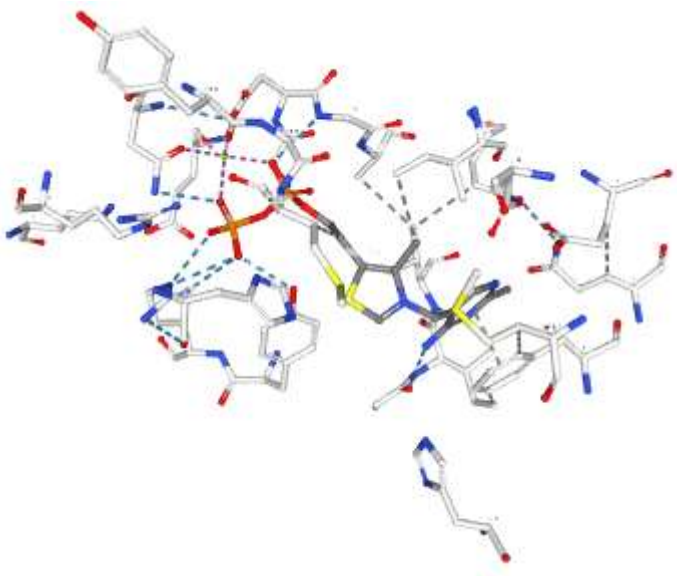

(a)

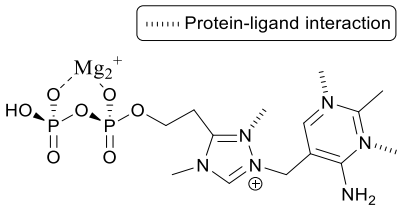

(b)

Figure 40: (a) Natural cofactor Thiamine Pyrophosphate (TPP) at PDH active site (b) Triazolyl Pyrophosphate mimic (TrPP)

Table 8.30: Results of docking TrPP at active site of 5NPU PDC

No:	Docked Pose	RMSD [a]	B[b]	H-B[c]	L-C[d]	L-T[e]	N-P[f]	R[g]	PLP Fitness	Rank
1	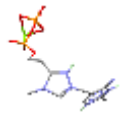	8.6	-14.9	-1.9	0.0	0.9	-35.3	2.4	52.4	3
2	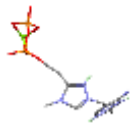	8.9	-14.3	-1.2	0.0	0.7	-44.1	1.6	52.0	2
3	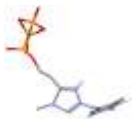	8.8	-14.6	-0.7	0.0	0.8	-45.1	1.7	51.7	1

[a] RMSD: root mean square deviation of mimic ligand atoms pose from the natural cofactor original pose; [b] B: buried term (polar-non polar); [c] H-B; hydrogen bonding term; [d] L-C; ligand clash term; [e] L-T; ligand torsion term; [f] N-P: non polar term; [g] R: ligand repulsion term.

8.7 Pyruvate Decarboxylase

Pyruvate decarboxylase PDC is a very well known, TPP dependent enzyme which has been in use for centuries in the fermentation of carbohydrate to give alcohol. It can exist as four identical sub units each with one active site. PDC promotes the conversion of pyruvic acid to acetaldehyde giving off carbondioxide in the process. For every active site in the PDC tetramer, two Glutamates Glu-477 and -51 are invariably present, and contribute to keeping the TPP bound in a rigid conformation[28].

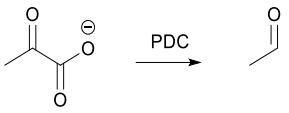

Scheme 4: Decarboyxlation of pyruvate by PDC

8.7.1 **1OVM** Crystal structure of IndolePDC from *Enterobacter cloacae*

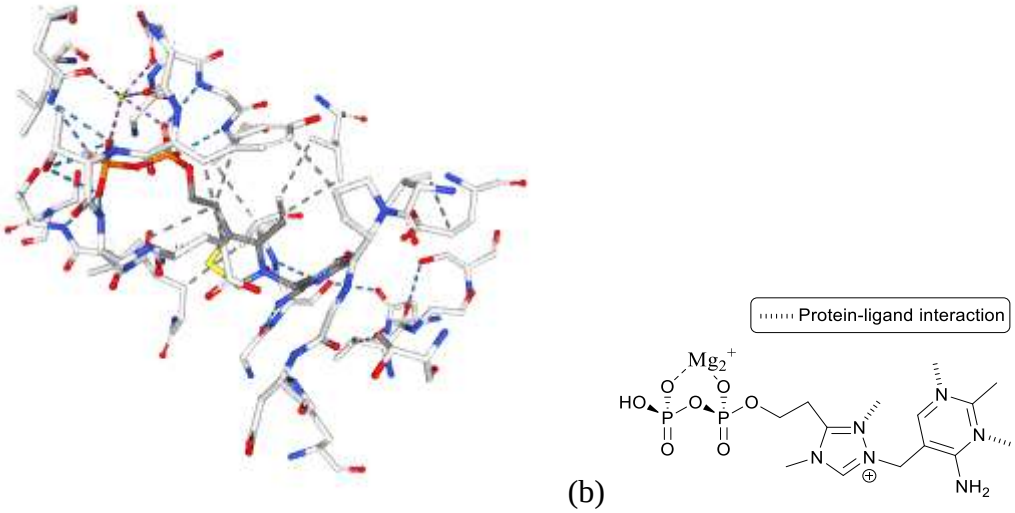

(a) (b)

Figure 27: (a) Natural cofactor Thiamine Pyrophosphate (TPP) at IndolePDC active site (b) Structure of Triazolyl Pyrophosphate mimic (TrPP)

Table 8.31: Results of docking TrPP at active site of 1OVM PDC

No :	Docked Pose	RMSD [a]	B[b]	H-B[c]	L-C[d]	L-T[e]	N-P[f]	R[g]	PLP Fitness	Rank

1		4.0	-5.6	-1.0	0.0	0.5	-41.8	18.2	37.0	4
2	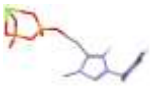	4.3	-9.4	-2.2	0.0	1.2	-41.8	25.6	38.7	5
3	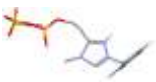	4.0	-5.0	-1.4	0.0	1.4	-30.1	16.0	36.3	3
4		4.2	-1.5	-2.0	0.0	0.6	-17.1	13.9	36.1	2
5		8.7	13.8	-3.0	0.0	0.6	-43.6	6.4	39.2	7
6		8.8	4.5	-3.0	0.0	0.9	-36.5	9.2	41.8	9
7		4.0	-5.3	-1.0	0.0	1.0	-43.2	17.2	41.8	8
8	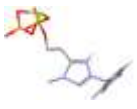	3.9	3.0	-1.0	0.0	0.6	-4.8	19.3	32.3	1
9	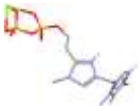	4.0	-9.3	-1.0	0.0	1.2	-45.9	19.1	42.4	10

10	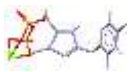	8.7	4.3	-3.0	0.0	1.1	-35.7	9.1	39.0	6

[a] RMSD: root mean square deviation of mimic ligand atoms pose from the natural cofactor original pose; [b] B: buried term (polar-non polar); [c] H-B; hydrogen bonding term; [d] L-C; ligand clash term; [e] L-T; ligand torsion term; [f] N-P: non polar term; [g] R: ligand repulsion term.

8.7.2 **2NXW** Crystal structure of phenylPDC of *Azospirillum brasilense*[18]

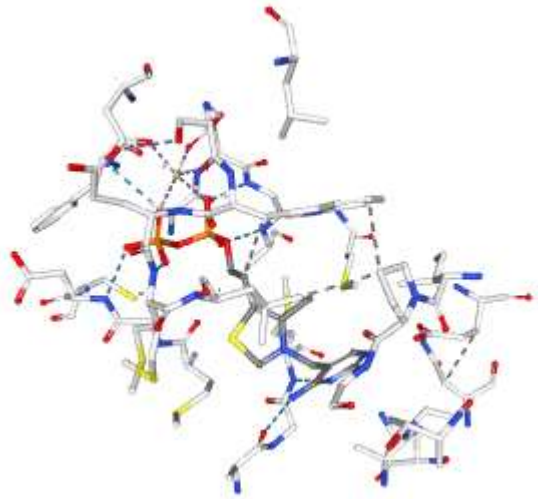

(a)

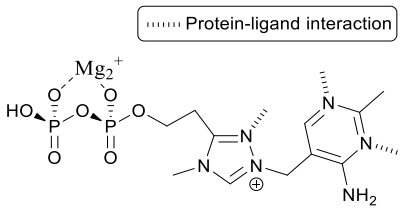

(b)

Figure 28: (a) Natural cofactor Thiamine Pyrophosphate (TPP) at 2NXW phenylPDC active site (b) Structure of Triazolyl Pyrophosphate mimic (TrPP)

Table 8.32: Results of docking TrPP at active site of 2NXW PDC

No:	Docked Pose	RMSD [a]	B[b]	H-B[c]	L-C[d]	L-T[e]	N-P[f]	R[g]	PLP Fitness	Rank
1	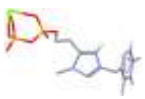	3.8	-9.3	-4.5	2.7	1.1	-36.1	25.7	34.3	2

2	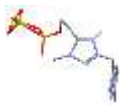	3.8	-13.9	-4.9	0.0	1.9	-48.7	20.3	47.4	3
3	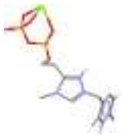	3.9	0.1	-2.7	0.0	1.5	-40.3	28.3	28.3	1

[a] RMSD: root mean square deviation of mimic ligand atoms pose from the natural cofactor original pose; [b] B: buried term (polar-non polar); [c] H-B; hydrogen bonding term; [d] L-C; ligand clash term; [e] L-T; ligand torsion term; [f] N-P: non polar term; [g] R: ligand repulsion term.

8.7.3 **2VJY** PDC from *Kluyveromyces lactis* in complex with the substrate analogue methyl acetylphosphonate [29]

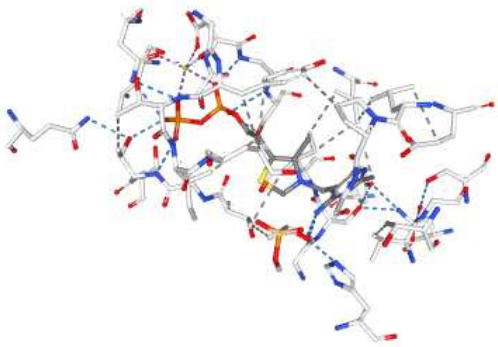

(a)

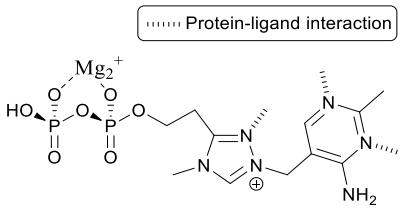

(b)

Figure 29: (a) Natural cofactor Thiamine Pyrophosphate (TPP) at 2VJY PDC active site (b) Structure of Triazolyl Pyrophosphate mimic (TrPP)

Table 8.33: Results of docking TrPP at active site of 2VJY PDC

No:	Docked Pose	RMSD [a]	B[b]	H-B[c]	L-C[d]	L-T[e]	N-P[f]	R[g]	PLP Fitness	Rank

1		9.0	14.1	-3.6	0.0	0.7	-25.6	18.9	22.7	1
2	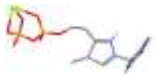	4.3	-9.7	-3.0	0.0	0.9	-36.2	33.5	29.4	2
3	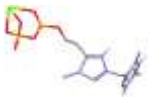	4.3	-10.2	-1.6	0.0	1.0	-31.1	35.0	30.3	3
4		4.3	-7.2	-2.7	0.0	1.1	-42.4	27.3	32.8	4

[a] RMSD: root mean square deviation of mimic ligand atoms pose from the natural cofactor original pose; [b] B: buried term (polar-non polar); [c] H-B; hydrogen bonding term; [d] L-C; ligand clash term; [e] L-T; ligand torsion term; [f] N-P: non polar term; [g] R: ligand repulsion term.

8.7.4 2V4K – Crystal Structure of a Mutant Aspartate Aminotransferase

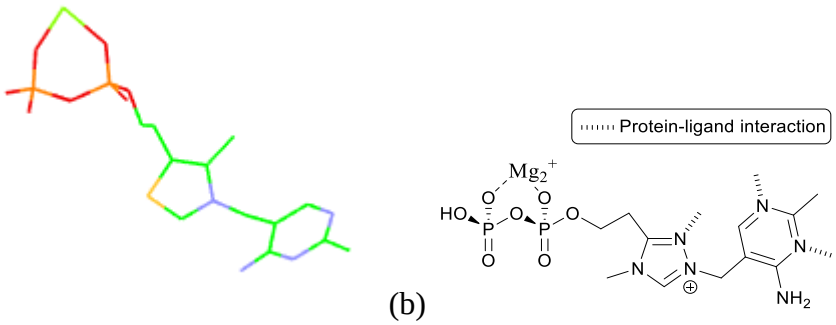

(a) (b)

Figure 30: (a) Natural cofactor Thiamine Pyrophosphate (TPP) at 2V4K PDC active site (b) Structure of Triazolyl Pyrophosphate mimic (TrPP)

Table 8.34: Results of docking TrPP at active site of 2V4K PDC

No:	Docked Pose	RMSD [a]	B[b]	H-B[c]	L-C[d]	L-T[e]	N-P[f]	R[g]	PLP Fitness	Rank
1	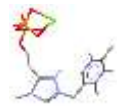	7.8	-1.1	-2.0	0.0	0.3	-5.7	8.0	31.3	6
2	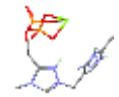	7.5	2.6	-2.0	0.0	0.9	-10.7	7.6	30.7	4
3		8.2	3.9	-2.0	0.0	1.1	-0.9	8.2	32.0	7
4		8.2	-5.6	-2.0	0.0	1.3	-35.5	12.9	37.3	10
5		7.2	-0.9	-4.0	0.0	0.7	-36.8	21.1	30.6	3
6	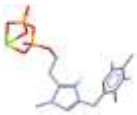	8.2	5.2	-2.0	0.0	0.8	-3.9	8.1	32.3	8
7	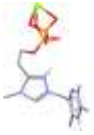	7.0	-8.0	-2.3	0.0	1.3	-31.6	17.3	30.4	2
8		7.7	-7.9	-0.3	0.0	1.1	-35.7	14.6	31.2	5

9	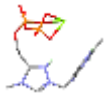	7.7	3.4	-0.4	0.0	1.6	-10.5	7.6	29.0	1
10	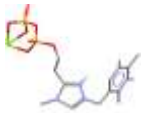	8.3	2.7	-2.0	0.0	0.8	-7.5	10.1	33.0	9

[a] RMSD: root mean square deviation of mimic ligand atoms pose from the natural cofactor original pose; [b] B: buried term (polar-non polar); [c] H-B; hydrogen bonding term; [d] L-C; ligand clash term; [e] L-T; ligand torsion term; [f] N-P: non polar term; [g] R: ligand repulsion term.

8.7.5 2WVA PDC from *Zymomonas mobilis* [30]

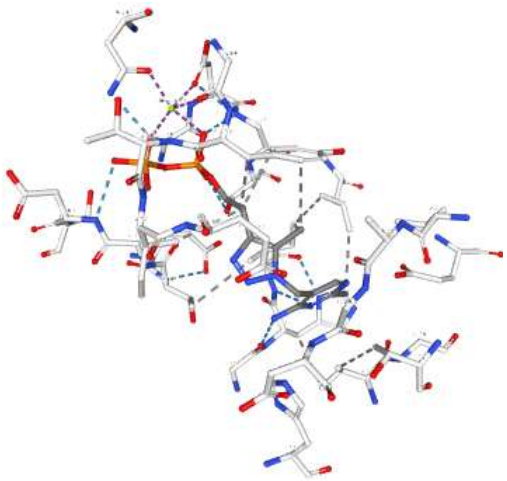

(a)

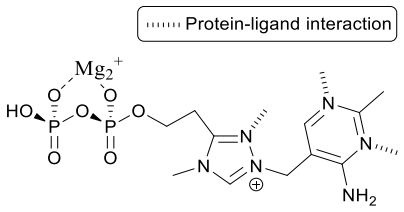

(b)

Figure 30: (a) Natural cofactor Thiamine Pyrophosphate (TPP) at 2WVA PDC active site (b) Structure of Triazolyl Pyrophosphate mimic (TrPP)

Table 8.35: Results of docking TrPP at active site of 2WVA PDC

No:	Docked Pose	RMSD [a]	B[b]	H-B[c]	L-C[d]	L-T[e]	N-P[f]	R[g]	PLP Fitness	Rank

1	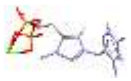	3.6	0.9	-3.1	1.2	1.3	-34.0	13.5	28.1	3
2	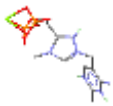	3.8	20.4	-2.5	0.0	2.1	-37.9	11.0	22.6	1
3	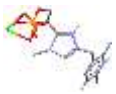	3.6	8.3	-2.9	2.9	1.0	-46.7	13.5	26.6	2
4		3.7	7.9	-3.0	0.1	0.6	-43.2	10.7	30.2	6
5		3.7	9.0	-3.0	0.0	0.6	-43.4	10.4	29.5	5
6	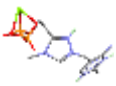	3.7	1.7	-3.0	0.1	0.8	-29.8	17.0	29.3	4

[a] RMSD: root mean square deviation of mimic ligand atoms pose from the natural cofactor original pose; [b] B: buried term (polar-non polar); [c] H-B; hydrogen bonding term; [d] L-C; ligand clash term; [e] L-T; ligand torsion term; [f] N-P: non polar term; [g] R: ligand repulsion term.

8.7.6 2WVG PDC from *Zymomonas mobilis* [30]

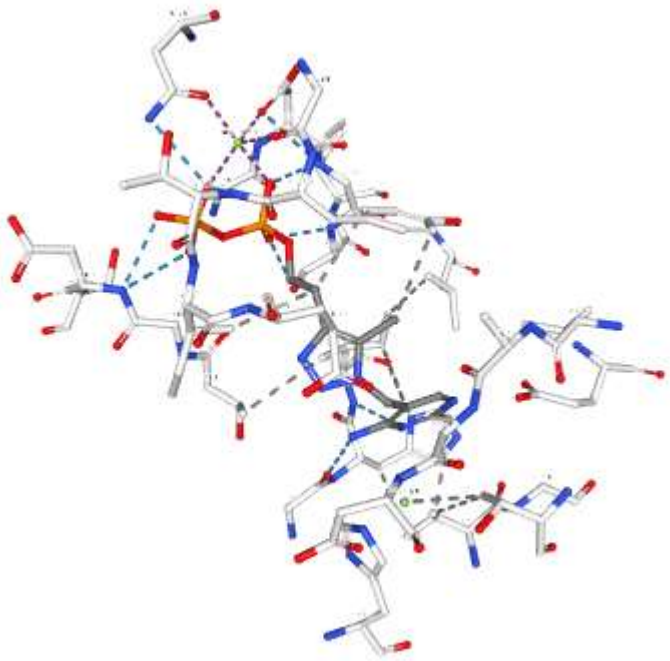

(a)

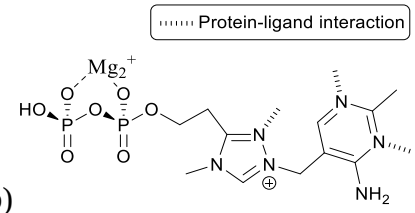

(b)

Figure 32: (a) Natural cofactor Thiamine Pyrophosphate (TPP) at 2WVG PDC active site (b) Structure of Triazolyl Pyrophosphate mimic (TrPP)

Table 8.36: Results of docking TrPP at active site of 2WVG PDC

No:	Docked Pose	RMSD [a]	B[b]	H-B[c]	L-C[d]	L-T[e]	N-P[f]	R[g]	PLP Fitness	Rank
1	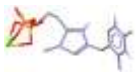	3.5	-4.0	-3.0	0.0	0.4	-33.7	14.3	38.6	9
2	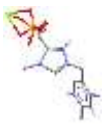	3.6	11.6	-2.3	0.1	0.9	-49.5	10.8	32.0	2
3		3.7	3.7	-1.5	0.8	0.5	-44.0	7.3	38.4	8

4	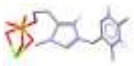	3.3	2.3	-2.9	0.0	0.9	-40.8	10.0	41.2	10
5	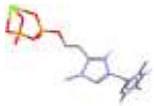	9.4	-12.6	0.3	0.0	0.8	-31.5	27.7	33.6	4
6	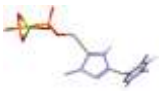	9.3	-9.2	0.3	0.0	1.2	-4.3	22.5	33.5	3
7	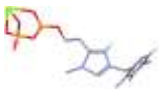	9.2	-13.1	-1.1	0.0	0.7	-30.8	29.2	35.0	5
8	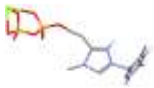	9.3	-12.0	0.3	0.0	1.0	-43.4	24.6	37.7	6
9	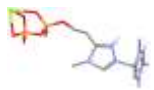	9.2	-13.1	-0.7	0.0	1.4	-40.4	25.7	37.8	7
10	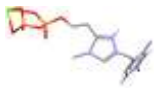	9.4	-12.1	-0.9	6.4	1.3	-41.5	21.7	30.1	1

[a] RMSD: root mean square deviation of mimic ligand atoms pose from the natural cofactor original pose; [b] B: buried term (polar-non polar); [c] H-B; hydrogen bonding term; [d] L-C; ligand clash term; [e] L-T; ligand torsion term; [f] N-P: non polar term; [g] R: ligand repulsion term.

8.7.7 **4COK PDC from *Gluconoacetobacter diazotrophicus*** [31]

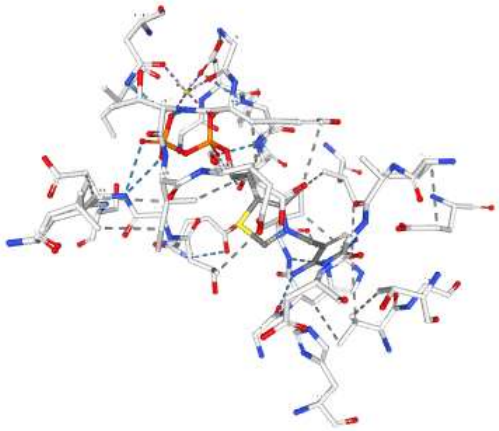

(a)

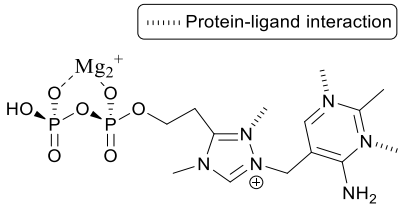

(b)

Figure 33: (a) Natural cofactor Thiamine Pyrophosphate (TPP) at 4COK PDC active site (b) Structure of Triazolyl Pyrophosphate mimic (TrPP)

Table 8.37: Results of docking TrPP at active site of 2NXW PDC

No:	Docked Pose	RMSD *a*	B*b*	H-B*c*	L-C*d*	L-T*e*	N-P*f*	R*g*	PLP Fitness	Rank
1		8.9	7.3	-2.0	0.0	1.1	-30.2	17.6	24.4	1
2		9.0	4.8	-3.2	0.0	0.7	-32.7	19.1	27.8	2
3	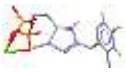	8.9	4.2	-3.2	2.6	0.8	-37.9	15.1	29.9	3

4	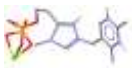	8.8	3.9	-2.9	0.0	1.1	-37.1	12.7	34.4	4

[a] RMSD: root mean square deviation of mimic ligand atoms pose from the natural cofactor original pose; [b] B: buried term (polar-non polar); [c] H-B; hydrogen bonding term; [d] L-C; ligand clash term; [e] L-T; ligand torsion term; [f] N-P: non polar term; [g] R: ligand repulsion term.

8.7.8 4MZX BFD Mutant T377L/A460Y

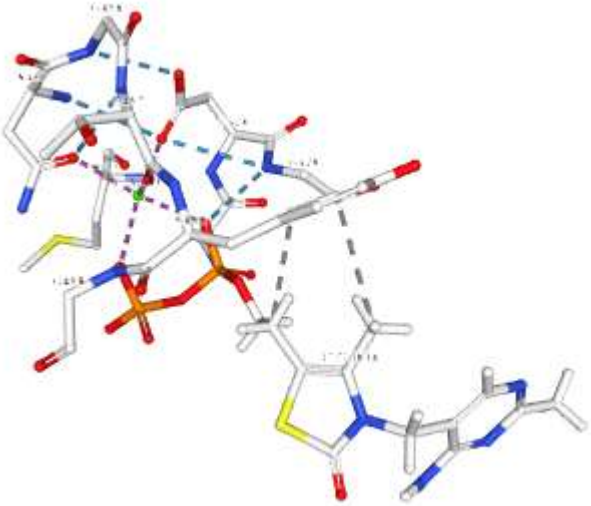

(a)

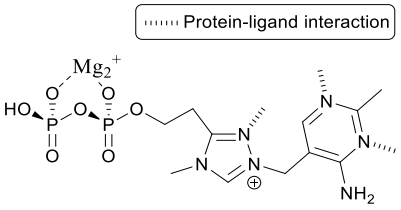

(b)

Figure 34: (a) Natural cofactor Thiamine Pyrophosphate (TPP) at BFD active site (b) Structure of Triazolyl Pyrophosphate mimic (TrPP)

Table 8.38: Results of docking TrPP at active site of 4MZX PDC

No:	Docked Pose	RMSD [a]	B[b]	H-B[c]	L-C[d]	L-T[e]	N-P[f]	R[g]	PLP Fitness	Rank
1	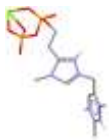	8.8	-5.6	-1.2	0.0	0.6	-47.9	3.7	47.4	10

2	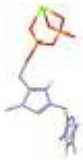	8.5	-7.2	-2.0	0.0	0.7	-39.8	1.9	44.9	6
3	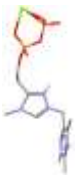	9.0	-5.9	0.0	0.0	1.2	-46.5	2.9	45.0	8
4	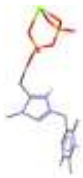	8.9	-5.2	0.0	0.0	1.1	-45.7	2.4	45.0	7
5	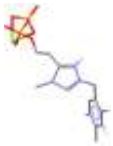	9.3	-5.4	-1.7	0.0	0.5	-7.2	3.1	46.7	9
6	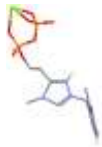	8.7	-3.2	0.0	0.1	0.4	-39.2	1.3	39.5	1
7	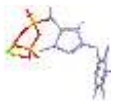	8.6	-6.2	0.0	0.0	1.0	-26.1	5.0	44.3	5
8	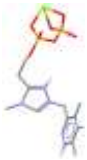	8.7	-3.8	0.0	0.0	0.7	-47.4	3.9	44.3	4
9	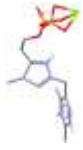	8.7	3.5	-2.0	0.2	0.5	-27.0	4.2	41.2	3

10	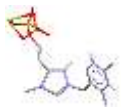	8.6	1.0	-2.0	0.0	0.5	-43.2	1.1	40.1	2

[a] RMSD: root mean square deviation of mimic ligand atoms pose from the natural cofactor original pose; [b] B: buried term (polar-non polar); [c] H-B; hydrogen bonding term; [d] L-C; ligand clash term; [e] L-T; ligand torsion term; [f] N-P: non polar term; [g] R: ligand repulsion term.

8.7.9 **4ZP1** Crystal structure of *Zymomonas mobilis* PDC variant Glu473Ala [32]

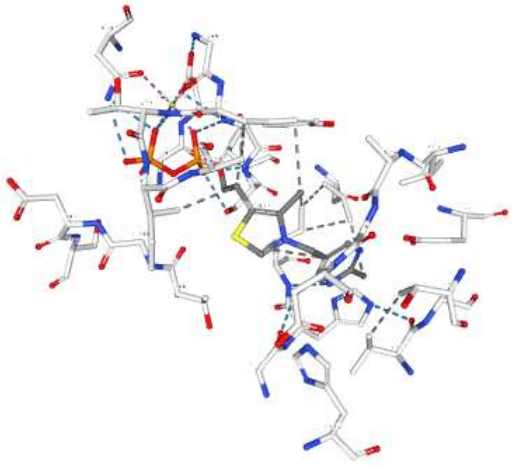

(a)

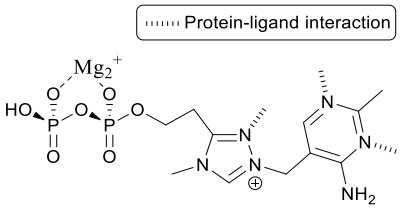

(b)

Figure 35: (a) Natural cofactor Thiamine Pyrophosphate (TPP) at 2ZP1 PDC active site (b) Triazolyl Pyrophosphate mimic (TrPP)

Table 8.39: Results of docking TrPP at active site of 2ZP1 PDC

No:	Docked Pose	RMSD [a]	B[b]	H-B[c]	L-C[d]	L-T[e]	N-P[f]	R[g]	PLP Fitness	Rank
1	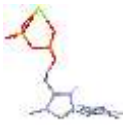	36.1	142.1	0.0	2.8	1.3	132.2	98.8	-293.5	1
2		36.1	138.2	0.0	2.0	1.2	114.4	97.9	-282.3	2

3		36.4	113.5	0.0	2.3	1.2	154.2	98.3	-279.8	3

[a] RMSD: root mean square deviation of mimic ligand atoms pose from the natural cofactor original pose; [b] B: buried term (polar-non polar); [c] H-B; hydrogen bonding term; [d] L-C; ligand clash term; [e] L-T; ligand torsion term; [f] N-P: non polar term; [g] R: ligand repulsion term.

8.7.10 5NPU Crystal structure of an inferred ancestral bacterial pyruvate decarboxylase

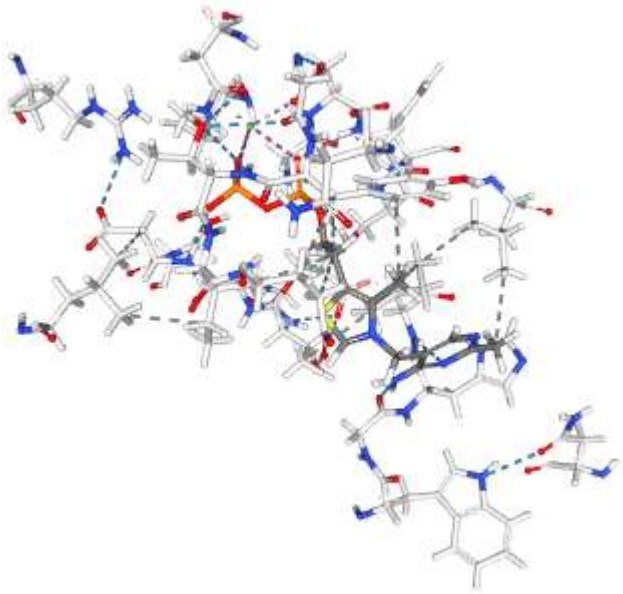

(a)

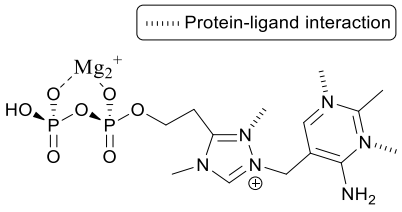

(b)

Figure 36: (a) Natural cofactor Thiamine Pyrophosphate (TPP) at 5NPU PDC active site (b) Structure of Triazolyl Pyrophosphate mimic (TrPP)

Table 8.40: Results of docking TrPP at active site of 5NPU PDC

No:	Docked Pose	RMSD [a]	B[b]	H-B[c]	L-C[d]	L-T[e]	N-P[f]	R[g]	PLP Fitness	Rank
1		3.8	-12.4	-7.0	0.0	1.3	-33.0	0.9	74.2	4

2		5.0	-12.9	-6.9	0.0	1.3	-32.6	3.3	71.9	1
3		3.8	-13.0	-6.5	0.0	1.5	-28.7	0.8	72.0	2
4	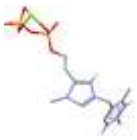	3.8	-12.0	-7.4	0.0	0.8	-33.0	0.8	73.7	3

[a] RMSD: root mean square deviation of mimic ligand atoms pose from the natural cofactor original pose; [b] B: buried term (polar-non polar); [c] H-B; hydrogen bonding term; [d] L-C; ligand clash term; [e] L-T; ligand torsion term; [f] N-P: non polar term; [g] R: ligand repulsion term.

8.7.11 5TMA Zymomonas mobilis pyruvate decarboxylase mutant PDC-2.3 [33]

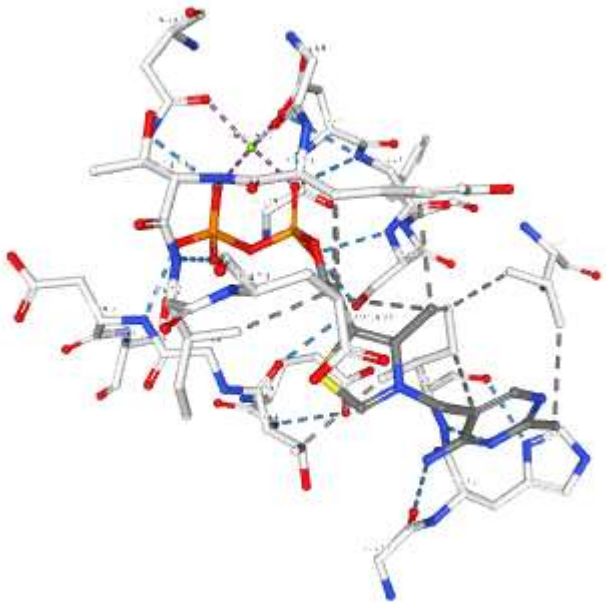

(a)

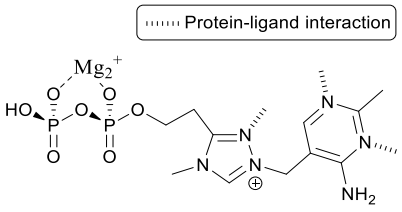

(b)

Figure 37: (a) Natural cofactor Thiamine Pyrophosphate (TPP) at 5TMA PDC active site (b) Structure of Triazolyl Pyrophosphate mimic (TrPP)

Table 8.41: Results of docking TrPP at active site of 5TMA PDC

No:	Docked Pose	RMSD [a]	B[b]	H-B[c]	L-C[d]	L-T[e]	N-P[f]	R[g]	PLP Fitness	Rank
1	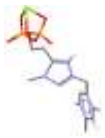	9.1	0.9	-2.5	0.0	0.8	-43.0	5.5	37.9	1
2	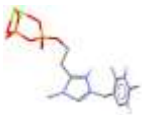	9.3	-4.3	0.0	0.0	0.2	-35.1	0.2	38.6	2
3	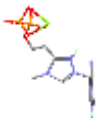	11.2	-8.6	-1.0	0.0	0.6	-41.3	0.9	48.7	8
4	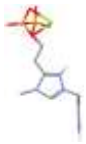	11.2	-9.4	0.0	0.0	0.7	-41.3	0.9	48.4	7
5	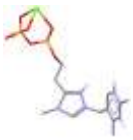	9.0	-7.9	-0.9	0.0	0.8	-36.7	0.7	42.3	4
6	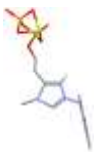	11.8	-8.2	0.0	0.0	0.5	-33.0	0.6	39.7	3
7	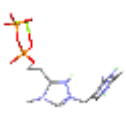	9.9	-7.4	0.0	0.0	0.7	-38.6	0.6	44.0	5

8	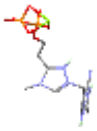	11.3	-7.8	-1.0	0.0	1.1	-40.0	0.7	46.6	6

[a] RMSD: root mean square deviation of mimic ligand atoms pose from the natural cofactor original pose; [b] B: buried term (polar-non polar); [c] H-B; hydrogen bonding term; [d] L-C; ligand clash term; [e] L-T; ligand torsion term; [f] N-P: non polar term; [g] R: ligand repulsion term.

8.7.12 6EFG PDC from Kluyveromyces lactis

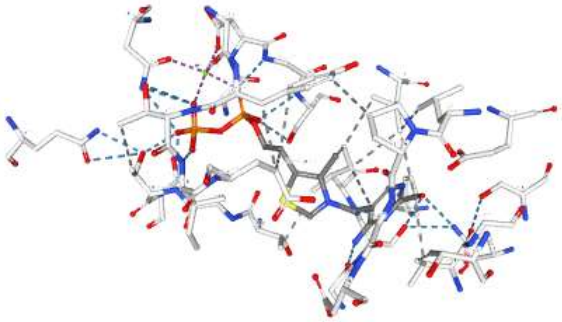

(a)

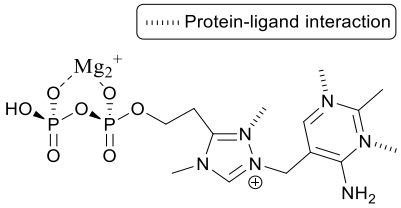

(b)

Figure 38: (a) Natural cofactor Thiamine Pyrophosphate (TPP) at 6EFG PDC active site (b) Structure of Triazolyl Pyrophosphate mimic (TrPP)

Table 8.42: Results of docking TrPP at active site of 6EFG PDC

No:	Docked Pose	RMSD [a]	B[b]	H-B[c]	L-C[d]	L-T[e]	N-P[f]	R[g]	PLP Fitness	Rank
1	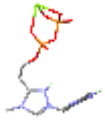	15.9	-6.8	0.0	0.0	0.3	-35.1	0.1	40.5	9

2		14.6	-5.2	0.0	0.0	0.7	-22.6	0.7	28.3	1
3		14.1	-7.2	0.0	0.0	0.4	-31.0	0.6	36.7	7
4		13.9	-7.6	0.0	0.0	0.6	-27.0	1.8	29.6	2
5	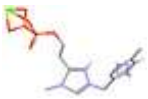	13.8	1.5	-1.0	0.0	0.7	-35.6	0.7	32.3	4
6		16.2	-2.6	0.0	0.0	0.4	-39.3	0.1	39.1	8
7		15.4	-6.5	0.0	0.0	0.7	-32.4	0.7	32.6	5
8		14.1	-7.1	0.0	0.0	0.2	-26.7	0.5	31.6	3
9		14.0	-5.9	-2.7	0.0	0.5	-21.0	0.6	33.0	6
10		15.9	-6.8	0.0	0.0	0.3	-35.1	0.1	40.5	10

[a] RMSD: root mean square deviation of mimic ligand atoms pose from the natural cofactor original pose; [b] B: buried term (polar-non polar); [c] H-B; hydrogen bonding term; [d] L-C; ligand clash term; [e] L-T; ligand torsion term; [f] N-P: non polar term; [g] R: ligand repulsion term.

8.7.13 **6EFH** PDC from Kluyveromyces lactis soaked with pyruvamide

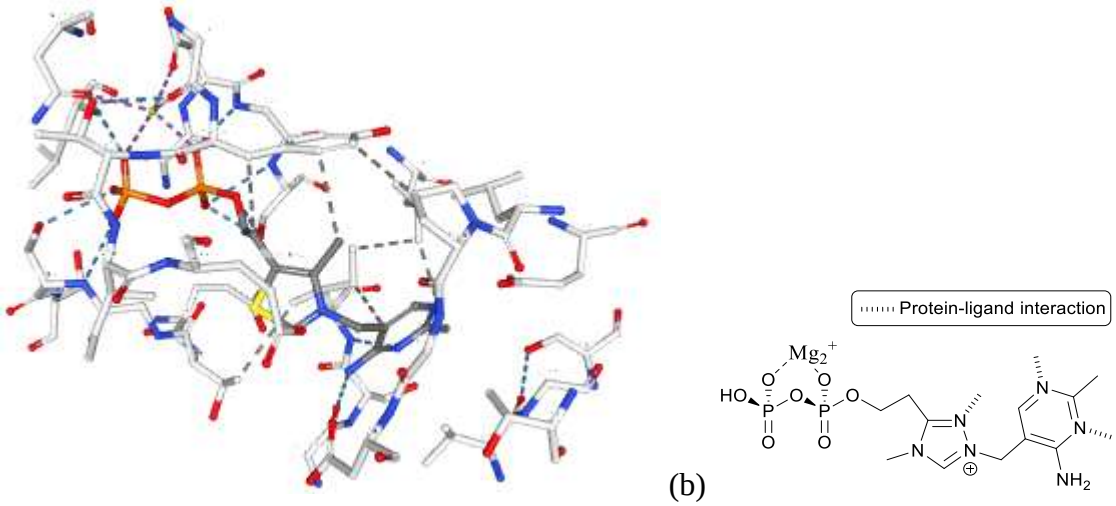

Figure 36: (a) Natural cofactor Thiamine Pyrophosphate (TPP) at PDC active site (b) Structure of Triazolyl Pyrophosphate mimic (TrPP)

Table 8.43: Results of docking TrPP at active site of 6EFH PDC

No:	Docked Pose	RMSD[a]	B[b]	H-B[c]	L-C[d]	L-T[e]	N-P[f]	R[g]	PLP Fitness	Rank
1	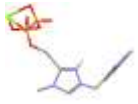	8.6	-3.1	-2.0	0.0	1.5	-37.9	8.9	42.7	5

2		8.8	-8.0	-1.2	0.0	1.5	-40.2	10.1	45.2	9
3	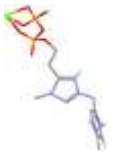	9.1	-1.2	-1.6	0.0	0.8	-29.7	4.0	37.1	2
4	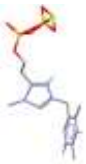	8.9	-6.9	-1.1	0.0	1.2	-25.3	2.0	36.0	1
5	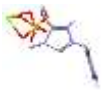	8.7	2.3	-2.0	0.0	1.0	-50.7	2.2	44.8	7
6	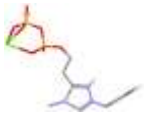	4.6	-5.7	-2.0	0.0	0.7	-38.4	6.6	43.0	6
7	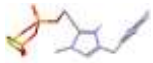	8.7	-6.7	-2.0	0.0	1.2	-43.3	9.9	45.0	8
8	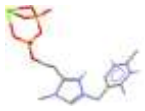	8.9	-3.6	-2.3	0.0	1.3	-36.3	7.5	42.5	4
9		9.1	-0.8	-2.0	0.0	0.3	-50.4	4.6	46.3	10
10		7.4	-0.3	-1.0	0.0	1.0	-32.8	10.2	39.5	3

[a] RMSD: root mean square deviation of mimic ligand atoms pose from the natural cofactor original pose; [b] B: buried term (polar-non polar); [c] H-B; hydrogen bonding term; [d] L-C; ligand clash term; [e] L-T; ligand torsion term; [f] N-P: non polar term; [g] R: ligand repulsion term.

8.8 Transketolase

Transketolase (TK) is a TPP dependent enzyme present in all living organisms. It catalyses two reactions in the pentose phosphate pathway and one in the Calvin cycle of photosynthesis. The substrates must be in the right stereo configuration in order to enter the rather striated channel leading into the active site, this in turn controls the specificity of the enzyme[38].

8.8.1 1ITZ Maize Transketolase in complex with TPP [40]

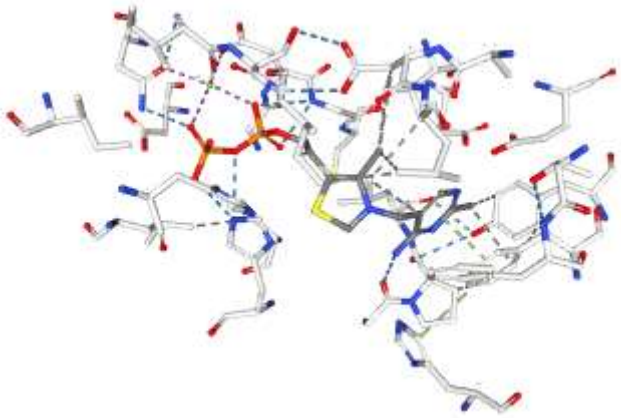

(a) (b)

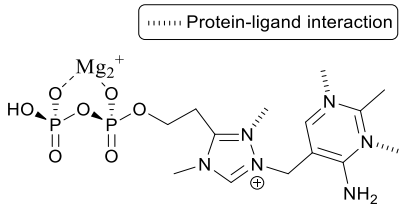

Figure 46: (a) Natural cofactor Thiamine Pyrophosphate (TPP) at TK active site (b) Structure of Triazolyl Pyrophosphate mimic (TrPP)

Table 8.44: Results of docking TrPP at active site of 1ITZ TK

No:	Docked Pose	RMSD [a]	B[b]	H-B[c]	L-C[d]	L-T[e]	N-P[f]	R[g]	PLP Fitness	Rank
1	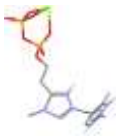	13.3	-4.1	0.0	0.0	0.9	-26.8	1.0	27.5	4
2	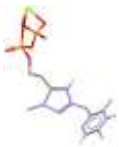	13.4	-6.0	-0.7	0.0	0.7	-22.1	3.8	23.9	2
3	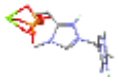	12.6	-2.9	-1.3	0.0	0.8	-26.2	0.9	26.9	3
4		15.4	-5.5	0.0	0.0	1.2	-17.5	0.4	20.2	1
5		13.4	-2.2	-1.0	0.0	0.9	-29.6	0.7	30.0	7
6	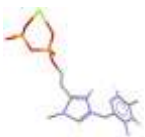	13.3	-5.0	0.0	0.0	0.7	-29.2	1.1	31.8	10
7		13.1	-2.8	0.0	0.0	0.1	-28.9	0.9	31.6	9

8		12.7	-4.1	0.0	0.0	0.7	-26.8	1.6	27.8	5
9		14.7	-6.3	-1.1	0.0	0.8	-24.9	1.6	29.0	6
10	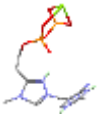	15.0	-8.1	-1.9	0.0	1.1	-25.3	1.1	31.4	8

[a] RMSD: root mean square deviation of mimic ligand atoms pose from the natural cofactor original pose; [b] B: buried term (polar-non polar); [c] H-B; hydrogen bonding term; [d] L-C; ligand clash term; [e] L-T; ligand torsion term; [f] N-P: non polar term; [g] R: ligand repulsion term.

8.8.2 1GPU - Transketolase from from Saccharomyces Cerevisiae [39]

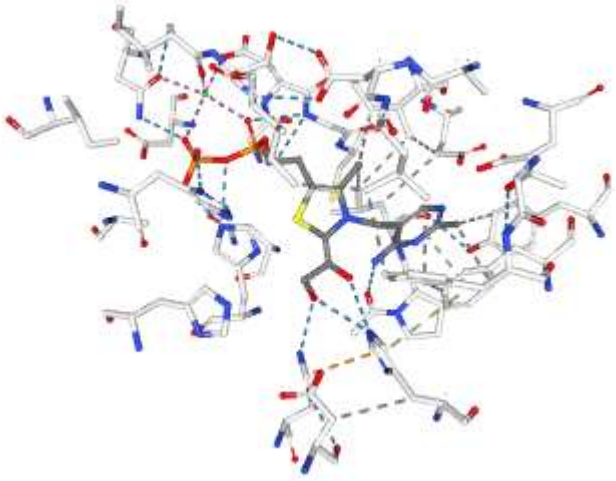

(a)

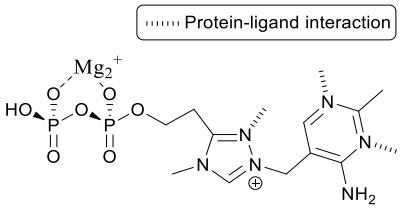

(b)

Figure 45: (a) Natural cofactor Thiamine Pyrophosphate (TPP) at 1GPU TK active site (b) Structure of Triazolyl Pyrophosphate mimic (TrPP)

Table 8.45: Results of docking TrPP at active site of 1GPU TK

No:	Docked Pose	RMSD [a]	B[b]	H-B[c]	L-C[d]	L-T[e]	N-P[f]	R[g]	PLP Fitness	Rank
1	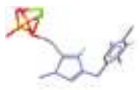	8.6	-5.5	-3.0	0.0	0.6	-31.3	14.6	42.2	4
2	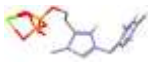	8.7	-9.3	-2.0	0.0	1.1	-37.8	13.8	40.6	2
3	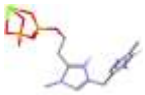	8.9	-3.2	-3.0	0.0	1.0	-24.8	8.8	43.3	5
4		8.8	-8.1	-3.0	0.0	0.6	-35.0	15.1	40.2	1
5		8.8	-5.6	-2.5	0.0	0.8	-22.5	9.5	41.9	3

[a] RMSD: root mean square deviation of mimic ligand atoms pose from the natural cofactor original pose; [b] B: buried term (polar-non polar); [c] H-B; hydrogen bonding term; [d] L-C; ligand clash term; [e] L-T; ligand torsion term; [f] N-P: non polar term; [g] R: ligand repulsion term.

8.8.3 1QGD - Transketolase from Escherichia Coli

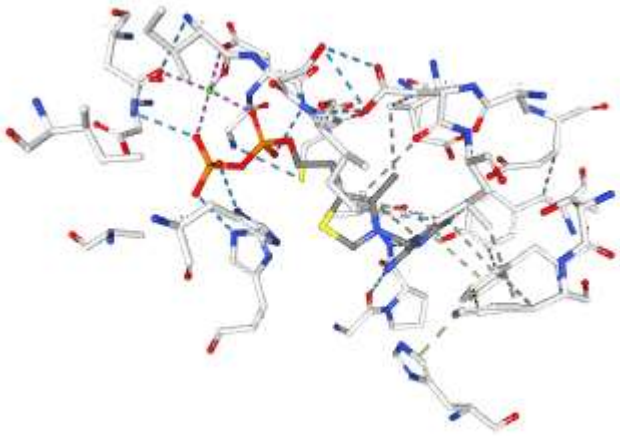

(a)

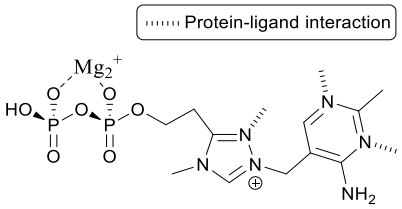

(b)

Figure 47: (a) Natural cofactor Thiamine Pyrophosphate (TPP) at TK active site (b) Triazolyl pyrophosphate mimic (TrPP)

Table 8.46: Results of docking TrPP at active site of 1QGD TK

No:	Docked Pose	RMSD [a]	B[b]	H-B[c]	L-C[d]	L-T[e]	N-P[f]	R[g]	PLP Fitness	Rank
1	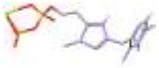	3.8	-5.1	-1.8	0.0	1.1	-36.2	17.4	33.4	7
2	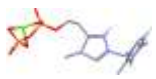	3.8	-2.7	-2.1	0.0	0.9	-46.5	16.3	31.7	3

3	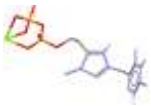	3.9	-4.1	-2.0	0.0	1.6	-30.9	20.1	33.3	6
4	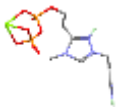	8.3	8.8	-1.3	0.0	1.2	-8.4	10.0	23.2	1
5	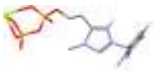	3.8	-4.6	-1.9	0.0	1.1	-35.1	19.0	32.0	4
6		3.9	-2.9	-2.7	0.0	1.1	-53.5	18.1	33.7	8
7	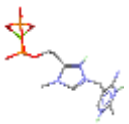	3.9	1.7	-2.6	0.0	1.1	-54.6	17.1	33.1	5
8	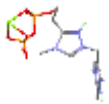	8.3	3.0	-2.4	0.0	0.9	-1.8	15.7	26.9	2
9	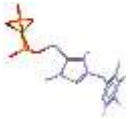	3.9	-0.7	-2.5	0.0	1.2	-53.8	18.7	33.9	10
10	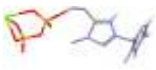	3.8	-6.3	-1.9	0.0	1.8	-36.6	22.3	33.9	9

[a] RMSD: root mean square deviation of mimic ligand atoms pose from the natural cofactor original pose; [b] B: buried term (polar-non polar); [c] H-B; hydrogen bonding term; [d] L-C; ligand clash term; [e] L-T; ligand torsion term; [f] N-P: non polar term; [g] R: ligand repulsion term.

8.8.4 1R9J Transketolase from *Leishmania Mexicana*

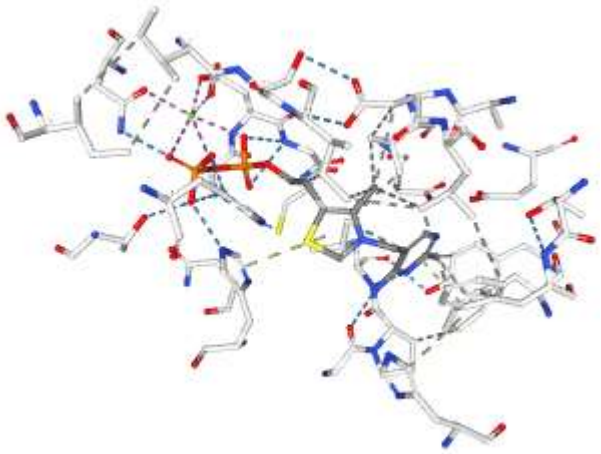

(a)

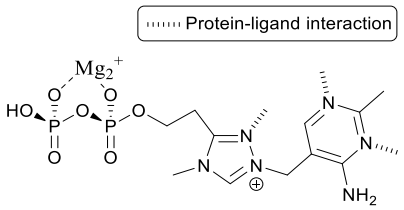

(b)

Figure 48: (a) Natural cofactor Thiamine Pyrophosphate (TPP) at TK active site (b) Structure of Triazolyl Pyrophosphate mimic (TrPP)

Table 8.47: Results of docking TrPP at active site of 1R9J TK

No:	Docked Pose	RMSD [a]	B[b]	H-B[c]	L-C[d]	L-T[e]	N-P[f]	R[g]	PLP Fitness	Rank
1	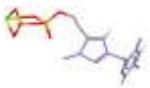	3.3	2.3	-0.5	0.0	1.3	-47.7	20.7	31.9	9
2	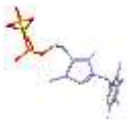	3.1	-1.7	-1.0	0.0	0.9	-54.5	25.2	29.9	7
3		8.8	6.0	-2.7	0.0	1.0	-35.9	10.5	25.2	3
4	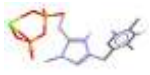	8.7	8.4	-4.4	0.0	1.6	-29.6	12.0	21.2	1

5		3.3	-1.4	0.4	0.0	1.3	-19.6	24.2	28.2	6
6		8.7	7.8	-3.3	0.0	1.4	-28.3	8.4	24.6	2
7	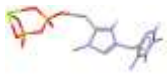	2.7	-2.0	-0.9	0.0	1.3	-40.2	27.4	30.1	8
8	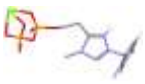	2.7	-3.6	-0.8	9.2	1.0	-38.9	24.1	27.1	4
9	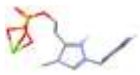	8.7	6.0	-3.1	0.0	0.7	-39.0	8.6	27.4	5
10		3.0	-1.6	-1.3	0.0	1.5	-30.6	24.8	35.4	10

[a] RMSD: root mean square deviation of mimic ligand atoms pose from the natural cofactor original pose; [b] B: buried term (polar-non polar); [c] H-B; hydrogen bonding term; [d] L-C; ligand clash term; [e] L-T; ligand torsion term; [f] N-P: non polar term; [g] R: ligand repulsion term.

8.8.5 3M34 Crystal structure of transketolase in complex with TPP and calcium ion

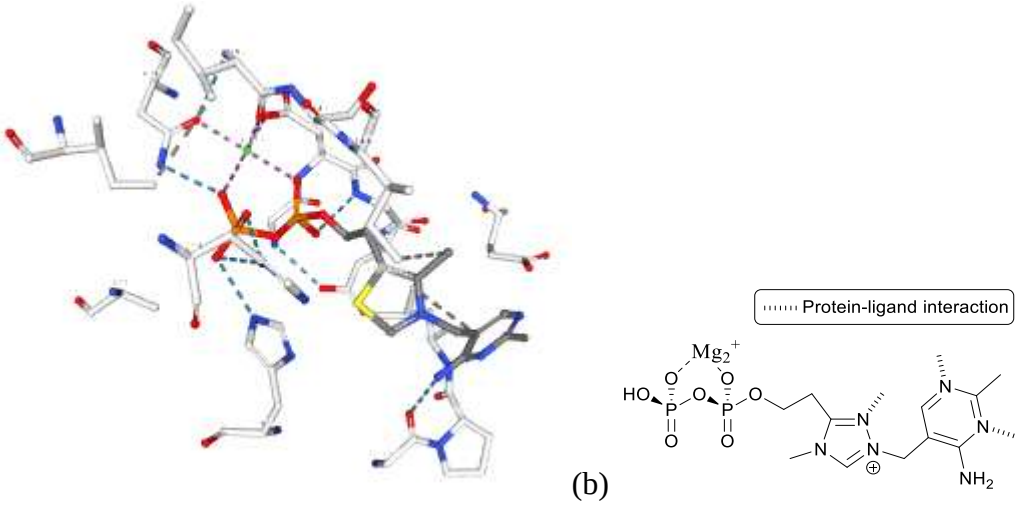

Figure 49: (a) Natural cofactor Thiamine Pyrophosphate (TPP) at 3M34 TK active site (b) Structure of Triazolyl Pyrophosphate mimic (TrPP)

Table 8.48: Results of docking TrPP at active site of 3M34 TK

No:	Docked Pose	RMSD [a]	B[b]	H-B[c]	L-C[d]	L-T[e]	N-P[f]	R[g]	PLP Fitness	Rank
1		9.0	-10.6	-2.6	0.0	0.7	-32.7	2.6	41.0	5
2		9.3	-8.2	-2.0	3.4	0.4	-32.9	1.6	36.0	1
3	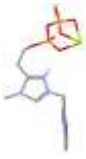	8.2	-11.1	-2.6	0.0	1.0	-28.6	2.9	39.9	2

4	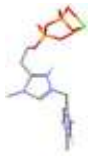	8.3	-11.5	-2.5	0.0	0.6	-37.3	3.3	41.5	7
5	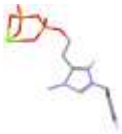	9.2	-9.7	-2.8	0.0	0.4	-34.0	1.9	42.7	10
6	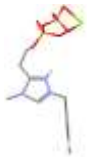	8.4	-11.4	-2.5	0.0	0.7	-38.1	3.4	41.1	6
7	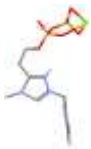	8.2	-11.4	-2.5	0.0	0.7	-35.5	3.3	41.7	9
8	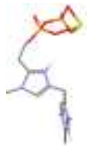	8.2	-11.7	-2.7	0.0	0.7	-33.7	3.3	41.6	8
9	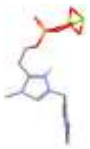	8.2	-11.8	-2.5	0.0	0.5	-27.2	3.6	40.8	4
10	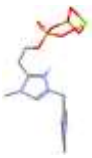	8.2	-11.1	-1.7	0.0	0.9	-32.9	2.7	40.0	3

[a] RMSD: root mean square deviation of mimic ligand atoms pose from the natural cofactor original pose; [b] B: buried term (polar-non polar); [c] H-B; hydrogen bonding term; [d] L-C; ligand clash term; [e] L-T; ligand torsion term; [f] N-P: non polar term; [g] R: ligand repulsion term.

8.8.6 3M49 Crystal Structure of Transketolase Complexed with Thiamine Diphosphate from Bacillus anthracis

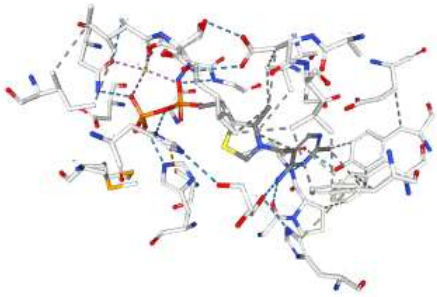

(a)

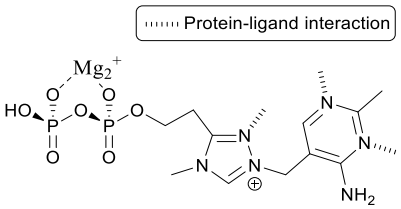

(b)

Figure 50: (a) Natural cofactor Thiamine Pyrophosphate (TPP) at 3M49 TK active site (b) Structure of Triazolyl Pyrophosphate mimic (TrPP)

Table 8.49: Results of docking TrPP at active site of 3M49 TK

No:	Docked Pose	RMSD [a]	B[b]	H-B[c]	L-C[d]	L-T[e]	N-P[f]	R[g]	PLP Fitness	Rank
1		3.9	6.6	-3.0	0.0	1.5	-44.7	21.9	28.2	7
2	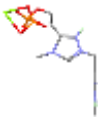	8.6	11.3	-1.7	0.2	1.3	-12.9	21.9	26.6	4
3		8.5	6.8	-1.0	0.0	1.0	-12.7	18.5	32.4	9
4		8.6	10.2	-1.0	1.9	0.8	-11.2	14.8	26.9	6
5		4.2	3.7	-0.3	0.0	1.1	-40.9	27.3	24.7	3

6	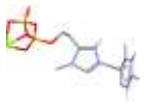	4.0	-1.7	-2.5	0.0	1.5	-18.3	29.0	23.8	2
7		8.5	7.9	-1.2	0.0	1.0	-11.5	19.4	31.3	8
8	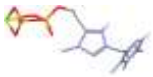	3.9	4.3	-2.1	0.0	1.3	-47.6	17.9	35.6	10
9	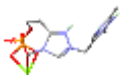	8.5	12.2	-1.2	0.8	1.3	-40.0	16.2	26.9	5
10	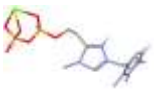	3.9	6.0	-2.0	0.0	1.6	-30.7	26.5	22.7	1

[a] RMSD: root mean square deviation of mimic ligand atoms pose from the natural cofactor original pose; [b] B: buried term (polar-non polar); [c] H-B; hydrogen bonding term; [d] L-C; ligand clash term; [e] L-T; ligand torsion term; [f] N-P: non polar term; [g] R: ligand repulsion term.

8.8.7 3MOS crystal structure of human transketolase[41]

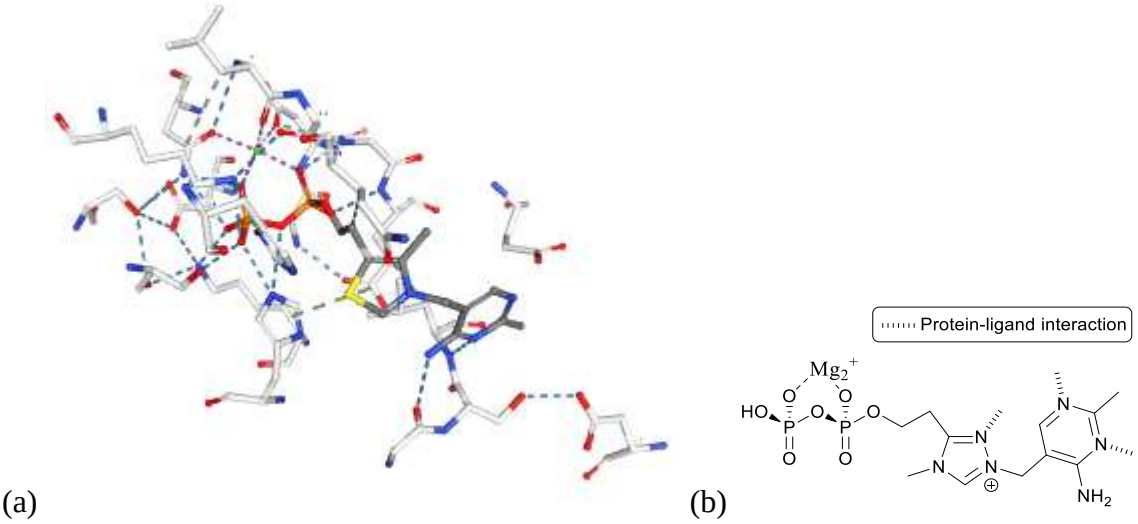

(a) (b)

Figure 51: (a) Natural cofactor Thiamine Pyrophosphate (TPP) at TK active site (b) Structure of Triazolyl Pyrophosphate mimic (TrPP)

Table 8.50: Results of docking TrPP at active site of 3MOS TK

No:	Docked Pose	RMSD[a]	B[b]	H-B[c]	L-C[d]	L-T[e]	N-P[f]	R[g]	PLP Fitness	Rank
1	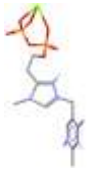	8.8	-5.1	-1.0	1.9	0.7	-37.3	6.3	33.5	2
2	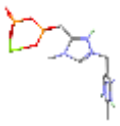	9.0	-6.0	-1.3	1.9	0.4	-32.7	5.1	34.1	3

3	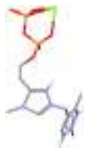	9.0	-8.1	-0.4	0.0	0.3	-31.7	1.4	38.9	5
4	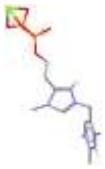	9.5	-6.9	-1.0	1.3	0.6	-34.5	5.3	33.4	1
5	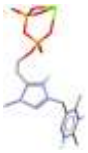	9.0	-7.2	-0.4	0.0	0.4	-33.1	1.4	39.1	7
6	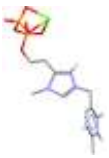	9.6	-9.3	0.0	0.7	0.6	-27.7	1.1	34.2	4
7	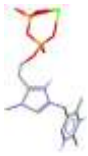	9.0	-6.6	-0.4	0.0	0.3	-33.5	1.4	38.9	6

[a] RMSD: root mean square deviation of mimic ligand atoms pose from the natural cofactor original pose; [b] B: buried term (polar-non polar); [c] H-B; hydrogen bonding term; [d] L-C; ligand clash term; [e] L-T; ligand torsion term; [f] N-P: non polar term; [g] R: ligand repulsion term.

8.8.8 3OOY Crystal structure of human Transketolase

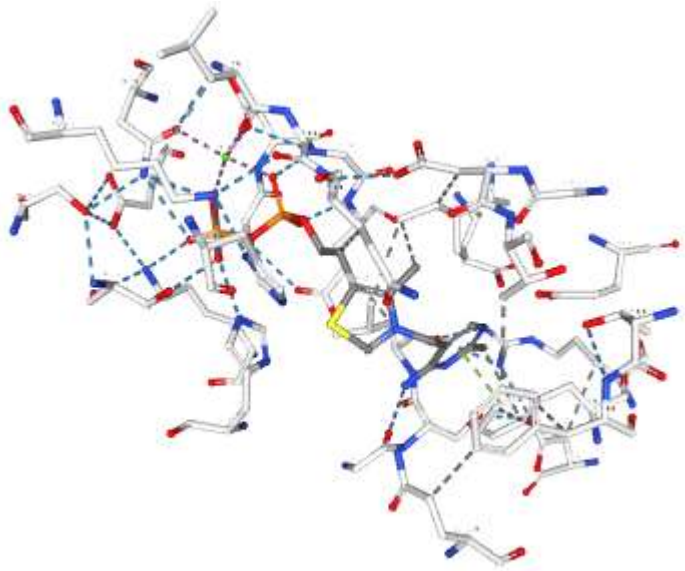

(a)

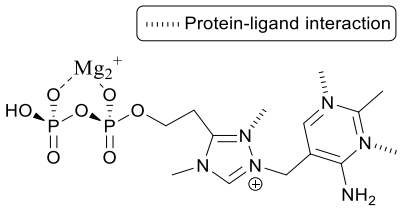

(b)

Figure 52: (a) Natural cofactor Thiamine Pyrophosphate (TPP) at 3OOY TK active site (b) Structure of Triazolyl Pyrophosphate mimic (TrPP)

Table 8.51: Results of docking TrPP at active site of 3OOY TK

No:	Docked Pose	RMSD *a*	B*b*	H-B*c*	L-C*d*	L-T*e*	N-P*f*	R*g*	PLP Fitness	Rank
1	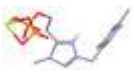	8.1	2.2	-1.0	0.0	1.2	-19.7	5.8	24.4	8
2	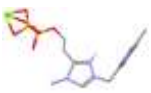	8.3	1.0	0.0	0.0	1.0	-31.4	9.4	24.8	9
3	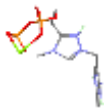	8.1	12.3	0.0	0.0	1.3	-37.5	8.0	22.9	7

4	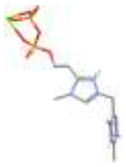	10.9	3.7	-1.5	1.6	1.3	-20.0	1.4	12.0	1
5		10.9	4.3	-1.5	1.7	1.2	-21.3	1.6	12.4	2
6	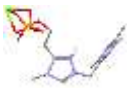	8.2	2.3	-1.0	0.0	0.8	-19.7	9.1	21.5	5
7	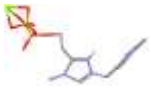	8.3	1.4	0.0	0.0	0.7	-31.4	13.2	18.8	4
8	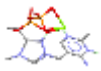	7.7	6.7	-1.7	3.5	0.3	-32.8	15.1	14.3	3
9	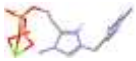	8.3	6.1	0.0	0.0	1.5	-37.2	3.5	22.1	6
10	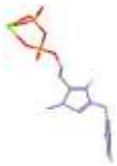	9.0	-8.1	-3.0	0.0	1.1	-35.1	15.3	26.3	10

[a] RMSD: root mean square deviation of mimic ligand atoms pose from the natural cofactor original pose; [b] B: buried term (polar-non polar); [c] H-B; hydrogen bonding term; [d] L-C; ligand clash term; [e] L-T; ligand torsion term; [f] N-P: non polar term; [g] R: ligand repulsion term.

8.8.9 3RIM Crystal structure of mycobacterium tuberculosis Transketolase (Rv1449c)[42]

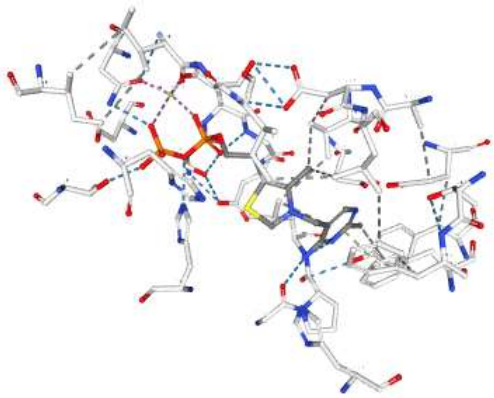

(a)

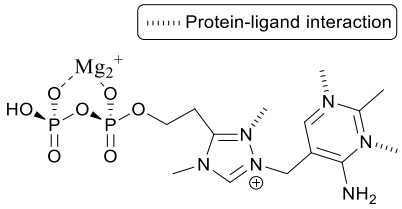

(b)

Figure 53: (a) Natural cofactor Thiamine Pyrophosphate (TPP) at 3RIM TK active site (b) Structure of Triazolyl Pyrophosphate mimic (TrPP)

Table 8.52: Results of docking TrPP at active site of 3RIM TK

No:	Docked Pose	RMSD[a]	B[b]	H-B[c]	L-C[d]	L-T[e]	N-P[f]	R[g]	PLP Fitness	Rank
1	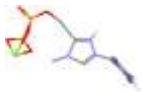	11.6	-9.1	-1.2	0.0	1.1	-4.6	1.9	32.8	2
2	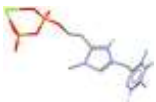	11.4	-8.0	-2.0	0.0	0.7	-33.8	3.9	35.8	8
3	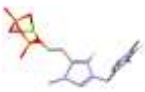	12.2	-3.9	-1.7	0.0	0.6	-34.0	1.7	34.8	5
4	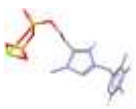	11.6	-7.2	-2.0	0.0	0.9	-32.9	3.4	34.0	3

5		11.9	-4.9	-1.0	0.0	0.6	-34.9	2.2	35.0	6
6	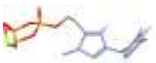	11.1	-7.0	-2.0	0.0	0.9	-30.5	2.5	36.3	10
7	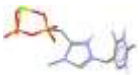	11.6	-4.8	-1.0	0.0	0.2	-35.0	1.7	36.0	9
8		11.7	-2.9	-1.0	0.0	0.3	-32.9	1.5	35.6	7
9		12.3	-9.0	-2.7	0.0	0.5	-11.1	3.2	25.0	1
10	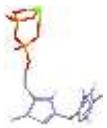	13.1	-3.3	-1.0	0.0	0.9	-35.0	1.2	34.6	4

[a] RMSD: root mean square deviation of mimic ligand atoms pose from the natural cofactor original pose; [b] B: buried term (polar-non polar); [c] H-B; hydrogen bonding term; [d] L-C; ligand clash term; [e] L-T; ligand torsion term; [f] N-P: non polar term; [g] R: ligand repulsion term.

8.8.10 4C7X Thiamine Pyrophosphate Bound Transketolase from Lactobacillus salivarius[43]

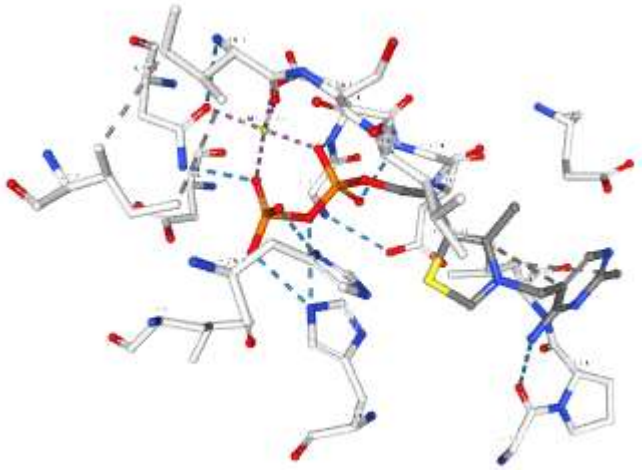

(a)

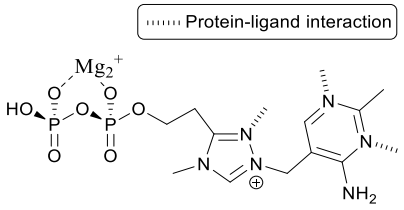

(b)

Figure 54: (a) Natural cofactor Thiamine Pyrophosphate (TPP) at 4C7X TK active site (b) Structure of Triazolyl Pyrophosphate mimic (TrPP)

Table 8.53: Results of docking TrPP at active site of 4C7X TK

No:	Docked Pose	RMSD[a]	B[b]	H-B[c]	L-C[d]	L-T[e]	N-P[f]	R[g]	PLP Fitness	Rank
1	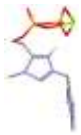	4.6	-6.3	-2.0	0.0	0.5	-32.6	4.5	34.9	3
2		5.6	-6.2	-1.6	0.0	0.3	-31.1	4.4	34.7	2
3	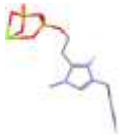	5.8	-4.8	-2.2	0.0	0.8	-33.6	4.6	34.4	1

4	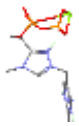	4.6	-6.3	-2.1	0.0	0.3	-33.9	4.5	35.2	4
5	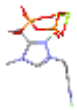	4.4	-6.0	-1.7	0.0	0.4	-34.8	4.6	35.4	5

[a] RMSD: root mean square deviation of mimic ligand atoms pose from the natural cofactor original pose; [b] B: buried term (polar-non polar); [c] H-B; hydrogen bonding term; [d] L-C; ligand clash term; [e] L-T; ligand torsion term; [f] N-P: non polar term; [g] R: ligand repulsion term.

8.8.11 5ND5 Crystal structure of TK from *Chlamydomonas reinhardtii* in complex with TPP [44]

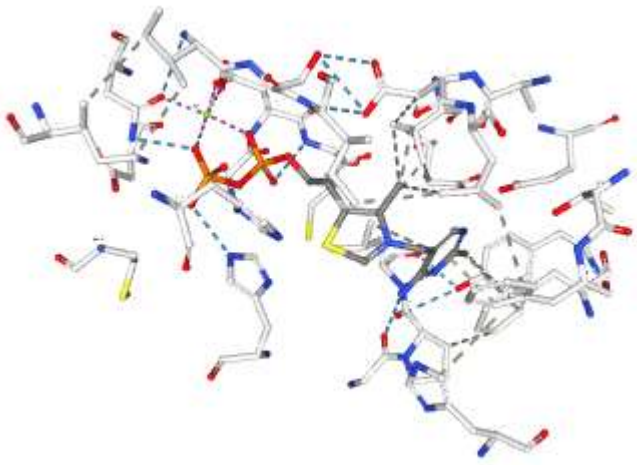

(a)

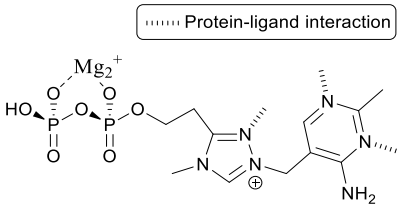

(b)

Figure 55: (a) Natural cofactor Thiamine Pyrophosphate (TPP) at 5ND5 TK active site (b) Structure of Triazolyl Pyrophosphate mimic (TrPP)

Table 8.54: Results of docking TrPP at active site of 5ND5 TK

No:	Docked Pose	RMSD[a]	B[b]	H-B[c]	L-C[d]	L-T[e]	N-P[f]	R[g]	PLP Fitness	Rank
1	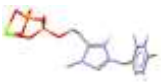	3.1	5.3	-2.8	0.0	1.2	-31.9	24.9	24.6	8
2	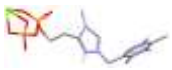	8.9	11.4	-1.3	0.0	1.2	3.5	22.1	18.2	5
3	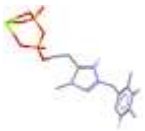	3.1	3.0	-2.9	0.0	1.1	-29.7	29.3	21.7	7
4		3.4	11.4	2.7	0.0	1.3	-38.7	22.0	16.4	4
5	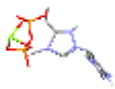	8.5	13.9	-1.9	0.0	0.8	0.6	16.3	14.8	3
6		8.9	15.9	-1.2	0.0	1.8	0.6	24.4	10.9	1
7		2.9	3.9	-2.3	0.0	1.2	-41.2	16.7	31.0	10
8	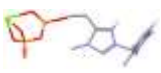	2.9	-0.5	-3.0	0.0	0.9	-30.9	27.9	26.9	9

9	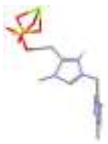	8.9	6.2	-2.6	0.0	1.7	-18.8	21.0	13.2	2
10		8.7	12.7	-2.8	0.0	0.8	4.5	15.6	19.6	6

[a] RMSD: root mean square deviation of mimic ligand atoms pose from the natural cofactor original pose; [b] B: buried term (polar-non polar); [c] H-B; hydrogen bonding term; [d] L-C; ligand clash term; [e] L-T; ligand torsion term; [f] N-P: non polar term; [g] R: ligand repulsion term.

8.8.12 5XS6 Crystal Structure of Transketolase in complex with TPP Pichia Stipitis [45]

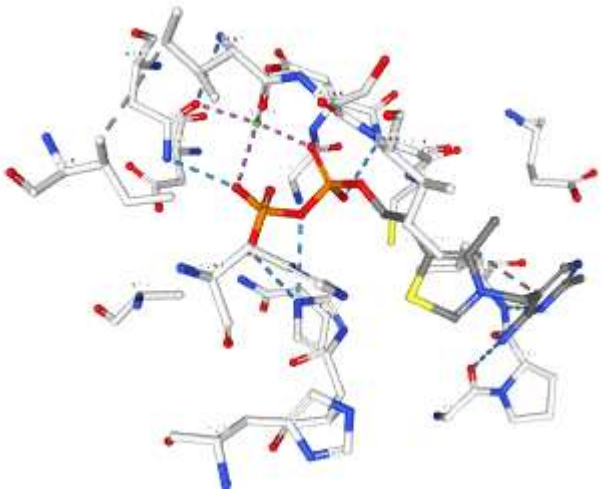

(a)

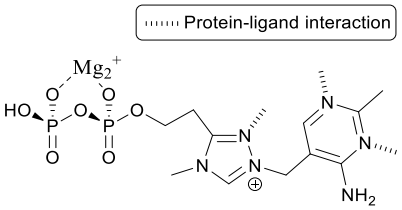

(b)

Figure 56: (a) Natural cofactor Thiamine Pyrophosphate (TPP) at 5XS6 TK active site (b) Structure of Triazolyl Pyrophosphate mimic (TrPP)

Table 8.55: Results of docking TrPP at active site of 5XS6 TK

No:	Docked Pose	RMSD[a]	B[b]	H-B[c]	L-C[d]	L-T[e]	N-P[f]	R[g]	PLP Fitness	Rank
1	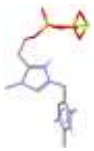	8.2	-10.8	-2.7	0.3	0.5	-34.0	3.3	42.5	9
2		9.6	-6.1	-1.4	0.0	0.5	-39.2	2.0	41.9	5
3	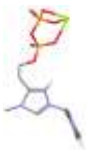	8.9	-5.5	-1.6	0.0	0.4	-38.2	1.1	40.7	3
4	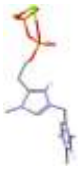	9.0	-11.2	-2.9	0.0	0.4	-33.8	3.8	42.4	8
5		9.7	-6.6	-1.8	0.0	0.7	-39.0	1.7	42.1	7
6	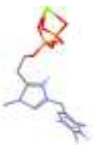	8.8	-5.5	-2.0	2.0	0.4	-35.8	2.1	38.0	2
7		8.8	-10.7	-2.8	0.0	0.5	-23.1	3.6	41.8	4

8	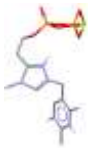	8.2	-11.1	-2.9	0.0	0.5	-32.2	3.4	43.4	10
9		9.1	-9.1	-1.8	0.0	1.0	-37.5	1.9	41.9	6
10		9.0	-2.2	-2.0	0.3	0.5	-37.7	1.6	37.8	1

[a] RMSD: root mean square deviation of mimic ligand atoms pose from the natural cofactor original pose; [b] B: buried term (polar-non polar); [c] H-B; hydrogen bonding term; [d] L-C; ligand clash term; [e] L-T; ligand torsion term; [f] N-P: non polar term; [g] R: ligand repulsion term.

8.9 References

1. Verdonk, M. L., Cole, J. C., Hartshorn, M. J., Murray, C. W. & Taylor, R. D. Improved protein-ligand docking using GOLD. *Proteins Struct. Funct. Genet.* (2003). doi:10.1002/prot.10465
2. Cheng, T., Li, X., Li, Y., Liu, Z. & Wang, R. Comparative assessment of scoring functions on a diverse test set. *J. Chem. Inf. Model.* (2009). doi:10.1021/ci9000053
3. Korb, O., Stützle, T. & Exner, T. E. Empirical Scoring Functions for Advanced Protein−Ligand Docking with PLANTS. *J. Chem. Inf. Model.* **49**, 84–96 (2009).
4. Chipman, D., Barak, Z. & Schloss, J. V. Biosynthesis of 2-aceto-2-hydroxy acids: acetolactate synthases and acetohydroxyacid synthases. *Biochimica et Biophysica Acta - Protein Structure and Molecular Enzymology* (1998). doi:10.1016/S0167-4838(98)00083-1
5. Tittmann, K., Vyazmensky, M., Hubner, G., Barak, Z. & Chipman, D. M. The carboligation reaction of acetohydroxyacid synthase II: Steady-state intermediate distributions in wild type and mutants by NMR. *Proc. Natl. Acad. Sci.* (2005). doi:10.1073/pnas.0408210101
6. McCourt, J. A., Pang, S. S., King-Scott, J., Guddat, L. W. & Duggleby, R. G. Herbicide-binding sites revealed in the structure of plant acetohydroxyacid synthase. *Proc. Natl. Acad. Sci.* **103**, 569–573 (2006).
7. Wang, J. G. *et al.* Crystal structures of two novel sulfonylurea herbicides in complex with Arabidopsis thaliana acetohydroxyacid synthase. *FEBS J.* (2009). doi:10.1111/j.1742-4658.2009.06863.x
8. Garcia, M. D. *et al.* Commercial AHAS-inhibiting herbicides are promising drug leads for the treatment of human fungal pathogenic infections. *Proc. Natl. Acad. Sci.* (2018). doi:10.1073/pnas.1809422115
9. Mosbacher, T. G., Mueller, M. & Schulz, G. E. Structure and mechanism of the ThDP-dependent benzaldehyde lyase from Pseudomonas fluorescens. *FEBS J.* (2005). doi:10.1111/j.1742-4658.2005.04998.x
10. Maraite, A., Schmidt, T., Ansörge-Schumacher, M. B., Brzozowski, A. M. & Grogan, G. Structure of the ThDP-dependent enzyme benzaldehyde lyase refined to 1.65 Å resolution. *Acta Crystallogr. Sect. F Struct. Biol. Cryst. Commun.* (2007). doi:10.1107/S1744309107028576
11. Brandt, G. S. *et al.* Probing the active center of benzaldehyde lyase with substitutions and the pseudosubstrate analogue benzoylphosphonic acid methyl ester. *Biochemistry* (2008). doi:10.1021/bi8004413
12. Brandt, G. S., Kneen, M. M., Petsko, G. A., Ringe, D. & McLeish, M. J. Active-site engineering of benzaldehyde lyase shows that a point mutation can confer both new reactivity and susceptibility to mechanism-based inhibition. *J. Am. Chem. Soc.* (2010). doi:10.1021/ja907064w
13. Hegeman, G. D. Benzoylformate Decarboxylase (Pseudomonas putida). *Methods Enzymol.* (1970). doi:10.1016/0076-6879(71)17262-X

14. Hegeman, G. D. Synthesis of the enzymes of the mandelate pathway by Pseudomonas putida. I. Synthesis of enzymes by the wild type. *J. Bacteriol.* (1966).

15. Rother Neé Gocke, D. *et al.* S-Selective Mixed Carboligation by Structure-Based Design of the Pyruvate Decarboxylase from Acetobacter pasteurianus. *ChemCatChem* (2011). doi:10.1002/cctc.201100054

16. Kutter, S. *et al.* The crystal structure of pyruvate decarboxylase from Kluyveromyces lactis: Implications for the substrate activation mechanism of this enzyme. *FEBS J.* (2006). doi:10.1111/j.1742-4658.2006.05415.x

17. Dobritzsch, D., König, S., Schneider, G. & Lu, G. High resolution crystal structure of pyruvate decarboxylase from Zymomonas mobilis. Implications for substrate activation in pyruvate decarboxylases. *J. Biol. Chem.* (1998). doi:10.1074/jbc.273.32.20196

18. Versées, W., Spaepen, S., Vanderleyden, J. & Steyaert, J. The crystal structure of phenylpyruvate decarboxylase from Azospirillum brasilense at 1.5 Å resolution: Implications for its catalytic and regulatory mechanism. *FEBS J.* (2007). doi:10.1111/j.1742-4658.2007.05771.x

19. Berthold, C. L. *et al.* Structure of the branched-chain keto acid decarboxylase (KdcA) from Lactococcus lactis provides insights into the structural basis for the chemoselective and enantioselective carboligation reaction. *Acta Crystallogr. Sect. D Biol. Crystallogr.* (2007). doi:10.1107/S0907444907050433

20. Hasson, M. S. *et al.* The crystal structure of benzoylformate decarboxylase at 1.6 Å Resolution: Diversity of catalytic residues in thiamin diphosphate-dependent enzymes. *Biochemistry* (1998). doi:10.1021/bi973047e

21. Lu, G., Dobritzsch, D., Baumann, S., Schneider, G. & König, S. The structural basis of substrate activation in yeast pyruvate decarboxylase. A crystallographic and kinetic study. *Eur. J. Biochem.* (2000). doi:10.1046/j.1432-1327.2000.01070.x

22. Gocke, D. *et al.* Rational protein design of ThDP-dependent enzymes - Engineering stereoselectivity. *ChemBioChem* (2008). doi:10.1002/cbic.200700598

23. Brandt, G. S. *et al.* Snapshot of a reaction intermediate: Analysis of benzoylformate decarboxylase in complex with a benzoylphosphonate inhibitor. *Biochemistry* (2009). doi:10.1021/bi801950k

24. Andrews, F. H., Tom, A. R., Gunderman, P. R., Novak, W. R. P. & McLeish, M. J. A bulky hydrophobic residue is not required to maintain the V-conformation of enzyme-bound thiamin diphosphate. *Biochemistry* (2013). doi:10.1021/bi400368j

25. Andrews, F. H., Rogers, M. P., Paul, L. N. & McLeish, M. J. Perturbation of the monomer-monomer interfaces of the benzoylformate decarboxylase tetramer. *Biochemistry* (2014). doi:10.1021/bi500081r

26. Fraas, S. *et al.* Cyclohexane-1,2-dione hydrolase: A new tool to degrade alicyclic compounds. *J. Mol. Catal. B Enzym.* (2009). doi:10.1016/j.molcatb.2009.03.021

27. Loschonsky, S. *et al.* Extended reaction scope of thiamine diphosphate dependent cyclohexane-1,2-dione hydrolase: From C-C bond cleavage to C-C bond ligation. *Angew. Chemie - Int. Ed.* (2014). doi:10.1002/anie.201408287

28. Lobell, M. & Crout, D. H. G. Pyruvate decarboxylase: A molecular modeling study of pyruvate decarboxylation and acyloin formation. *J. Am. Chem. Soc.* (1996). doi:10.1021/ja951830t

29. Kutter, S. *et al.* Covalently bound substrate at the regulatory site of yeast pyruvate decarboxylases triggers allosteric enzyme activation. *J. Biol. Chem.* (2009). doi:10.1074/jbc.M806228200

30. Pei, X. Y., Erixon, K. M., Luisi, B. F. & Leeper, F. J. Structural insights into the prereaction state of pyruvate decarboxylase from zymomonas mobilise. *Biochemistry* (2010). doi:10.1021/bi901864j

31. Van Zyl, L. J., Schubert, W. D., Tuffin, M. I. & Cowan, D. A. Structure and functional characterization of pyruvate decarboxylase from Gluconacetobacter diazotrophicus. *BMC Struct. Biol.* (2014). doi:10.1186/s12900-014-0021-1

32. Wechsler, C. *et al.* Tuning and Switching Enantioselectivity of Asymmetric Carboligation in an Enzyme through Mutational Analysis of a Single Hot Spot. *ChemBioChem* (2015). doi:10.1002/cbic.201500529

33. Sammond, D. W. *et al.* An iterative computational design approach to increase the thermal endurance of a mesophilic enzyme. *Biotechnol. Biofuels* (2018). doi:10.1186/s13068-018-1178-9

34. Arjunan, P. *et al.* Structure of the pyruvate dehydrogenase multienzyme complex E1 component from Escherichia coli at 1.85 Å resolution. *Biochemistry* (2002). doi:10.1021/bi0118557

35. Ciszak, E. M., Korotchkina, L. G., Dominiak, P. M., Sidhu, S. & Patel, M. S. Structural basis for flip-flop action of thiamin pyrophosphate-dependent enzymes revealed by human pyruvate dehydrogenase. *J. Biol. Chem.* (2003). doi:10.1074/jbc.M300339200

36. Seifert, F. *et al.* Phosphorylation of serine 264 impedes active site accessibility in the E1 component of the human pyruvate dehydrogenase multienzyme complex. *Biochemistry* (2007). doi:10.1021/bi700083z

37. Kato, M. *et al.* Structural Basis for Inactivation of the Human Pyruvate Dehydrogenase Complex by Phosphorylation: Role of Disordered Phosphorylation Loops. *Structure* (2008). doi:10.1016/j.str.2008.10.010

38. Nilsson, U., Meshalkina, L., Lindqvist, Y. & Schneidere, G. Examination of substrate binding in thiamin diphosphate-dependent transketolase by protein crystallography and site-directed mutagenesis. *J. Biol. Chem.* (1997). doi:10.1074/jbc.272.3.1864

39. Fiedler, E. *et al.* Snapshot of a key intermediate in enzymatic thiamin catalysis: Crystal structure of the -carbanion of (, -dihydroxyethyl)-thiamin diphosphate in the active site of transketolase from Saccharomyces cerevisiae. *Proc. Natl. Acad. Sci.* (2002). doi:10.1073/pnas.022510999

40. Gerhardt, S. Structure and Properties of an Engineered Transketolase from Maize. *PLANT Physiol.* (2003). doi:10.1104/pp.103.020982

41. Mitschke, L. *et al.* The crystal structure of human transketolase and new insights into its mode of action. *J. Biol. Chem.* (2010). doi:10.1074/jbc.M110.149955

42. Fullam, E., Pojer, F., Bergfors, T., Jones, T. A. & Cole, S. T. Structure and function of the transketolase from Mycobacterium tuberculosis and comparison with the human enzyme. *Open Biol.* (2012). doi:10.1098/rsob.110026

43. Lukacik, P. *et al.* High-resolution structures of Lactobacillus salivarius transketolase in the presence and absence of thiamine pyrophosphate . *Acta Crystallogr. Sect. F Struct. Biol. Commun.* (2015). doi:10.1107/s2053230x1501657x

44. Pasquini, M. *et al.* Structural basis for the magnesium-dependent activation of transketolase from Chlamydomonas reinhardtii. *Biochim. Biophys. Acta - Gen. Subj.* (2017). doi:10.1016/j.bbagen.2017.05.021

45. Hsu, N. S. *et al.* The Mesomeric Effect of Thiazolium on non-Kekulé Diradicals in Pichia stipitis Transketolase. *Angew. Chemie - Int. Ed.* (2018). doi:10.1002/anie.201709799